UNIVERSITÀ DEGLI STUDI DI MILANO

DOTTORATO DI RICERCA IN SCIENZE DELLA TERRA
Ciclo XXXV
DIPARTIMENTO DI SCIENZE DELLA TERRA

ADVANCED MINERALOGICAL AND CRYSTALLOGRAPHICAL TECHNIQUES FOR UNDERSTANDING TRANSFORMATION PROCESSES IN NATURAL MATERIALS AND SYNTHETIC ANALOGOUS

PhD Thesis:

Marco Cantaluppi
ID. nr. R12516

Prof. Nicoletta Marinoni	**Academic Year**	**Prof. Maria Iole Spalla**
Tutor	**2021/2022**	*Coordinator*

Contents

Research Aims

This study aims to compare the Combustion Pyrometamorphism (CP) process involving limestone and marly-limestone belonging to Hatrurim Basin in Israel and the human-made cement manufacture by means of both standard (Reflected and Transmitted Light Microscopy, X-ray Fluorescence, Laboratory X-ray Powder Diffraction, Laboratory Single Crystal X-Ray Diffraction, Electron MicroProbe Analyser, Scanning Electron Microprobe, Calorimetry) and innovative analytical techniques (Micro X-ray Computed Tomography, Synchrotron X-ray Powder Diffraction with *in-situ* and *ex-situ* experiments and Neutron Diffraction), highlighting differences and similarities between natural and synthetic process useful to better understand the geological process and improving cement manufacture.

CP is considered as a complex geological process involving sedimentary sequences in two main stages: (i) 1st stage of High Temperature (HT) (850 – 1650 °C) and Low Pressure (LP) (< 1 km) metamorphism due to the self-ignition of coal seams or methane-rich hydrocarbon gases coming from depth reservoirs; (ii) 2nd stage of LT (< 300 °C) and LP metamorphism in which takes place fluids and gas interactions with previous combusted rocks [1]. Rocks resulting from this multistage process have similar texture, mineral assemblage and chemical composition to several synthetic human-made materials, such as metal-slags, ceramics, anhydrous and hydrated cements [2]. CP is a LP and HT process, representing an uncommon field for petrological studies and metamorphosed rocks: there is a lack of geological and petrological information in the field of extremely HT and LP metamorphism especially for marls and limestone [1,3–6], increasing the difficulties to better explain CP process.

Cement represents the most important building materials used for all constructions ranging from ordinary urban planning (civil houses, road foundations, etc.) to strategical buildings (dams, tunnels, bridges, underground nuclear waste repositories, skyscrapers foundations, etc.). It is obtained by heating at HT a fine mixture of limestone and clay in a rotary kiln [7,8]. Nowadays, cement manufacture represents the 3rd anthropogenic CO_2 emission source due to the high CO_2 emission during the decomposition of limestone. Therefore, many efforts have been made over last decades trying to reduce the greenhouse gases footprint of cement manufacture by designing *green-cements* (also called *eco-friendly cements*), such as Calcium SulfoAluminate Cements (CSA) and Belite Cements (BC), that use alternative and less CO_2 releasing raw materials with lower thermal treatment.

To cope with the aim this project was organised in three main parts: (i) study of rock samples of natural cements (larnite-rich rocks) and their protolith (impure limestones) collected in Israel in Hatrurim Basin region (see chapters 5,8 and 9); (ii) laboratory scale production of two different *green-cements*, High Ferrite Belite Cement S-doped (HFBC S-doped) and Cement S-P-F-doped were laboratory prepared starting with an industrial raw meal and previous collected Israeli limestone, respectively (see chapter 10); (iii) hydration properties comparison between HFBC S-doped and natural anhydrous cement (larnite-rich rocks) (see chapter 11).

The investigation and comparison with conventional and innovative techniques of natural CP rocks and human-made synthetic equivalents led important information useful for both geological and industrial purposes: (i) better understanding on HT and LP metamorphism of limestone, hence clarifying processes occurring during CP (metamorphic reactions, melting points, highest T reached,

microtextural changes, etc.); (ii) predicting the evolution of cement-based materials on long-term hydration (t > 1000 years), crucial for repository of low-emission nuclear waste and strategical buildings (dams, tunnels, bridges, building foundations, etc.); (iii) designing new *green-cements* for reducing cement manufacture CO_2 footprint and waste management by studying the effects of simultaneous dopants (F, P and S), different thermal treatments and raw materials particle size.

LIST OF ABBREVIATION TERMS

ABCSA – Alite Belite Calcium SulfoAluminate Cement
AR – Alumina Ratio
BC – Belite Cement
BCSA – Belite Calcium SulfoAluminate cement
BCSAT – Belite Calcium SulfoAluminate Ternesite cement
BF – Belite Ferrite cement
BFY – Belite-Ferrite-Ye'elimite cement
BYF – Belite-Ye'elimite-Ferrite cement
CP – Combustion Pyrometamorphism
DSC-TGA – Differential Scanning Calorimetry associated with Thermal Gravimetric Analysis
EMPA – Electron MicroProbe Analyser
HF – Hatrurim Formation
HFBCSA – High Ferrite Belite Calcium SulfoAluminate cement
HFBC – High Ferrite Belite Cement
HM – hematite-magnetite buffer
HT – High Temperature
IBF – Instrumental Broadening Function
ICA – Isothermal Calorimetric Analysis
IP – Igneous Pyrometamorphism
LP – Low Pressure
LT – Low Temperature
LOI – Loss On Ignition
LSF – Lime Saturation Factor
LXRPD – Laboratory X-ray Powder Diffraction
MZC – Mottled Zone Complex
NXRD – Neutron Diffraction
PF – Pole Figure
QPA – Quantitative Phase Analysis
QMF – quartz-magnetite-fayalite buffer
QTA – Quantitative Texture Analysis
RLF – Reflected Light Microscopy
RQPA – Rietveld Quantitative Phase Analysis
SCXRD – Single Crystal X-ray Diffraction
SEM – Scanning Electron Microprobe
SR – Silica Ratio
SSA – Specific Surface Area
SXRPD – Synchrotron X-ray Powder Diffraction
TLM – Transmitted Light Microscopy
WM – wustite-magnetite buffer
XRF – X-ray Fluorescence
XRD – X-ray Diffraction
XRPD – X-ray Powder Diffraction
YBF – Ye'elimite-Belite-Ferrite cement
μ-CT – X-ray Computed μ-Tomography

Chapter 1
Pyrometamorphism

1.1 – Introduction

Pyrometamorphism, from the Greek pyro = fire, meta = change; morph = shape or form, is a term firstly used to describe high temperature changes taking place in magma chamber country rocks with or without interchange of material and/or fluids (metasomatism) [1,3]. Nowadays, pyrometamorphism is considered a type of thermal metamorphism distinguished by a large temperature window and LP with a local extension compared to regional metamorphism [4]: therefore, it is a geological process than can occur from the surface to the shallow crust, less than 3-4 km in depth, with a limited extension depending on the width of the heating source [3].

Three different types of pyrometamorphism could be depicted by considering the heating source that also defines the upper limit temperature: (i) flow of mafic magma through conduits at low depth or generally low depth magma chamber with a maximum temperature of ~ 1200 °C [3], commonly reported as Igneous Pyrometamorphism (IP); (ii) spontaneous combustion of coal seams, oil and methane-rich gases, reported as Combustion Pyrometamorphism (CP), reaching theoretically up to 1880 °C and 2045 °C for methane and coal burning in air, respectively [9]; (iii) lightning strikes on the surface involving rocks and/or soil for very short time on the order of μs at temperature almost > 2000 °C leading a fully melting [4,10–12], reported as lighting pyrometamorphism [1,4].

The mineral assemblages of pyrometamorphosed rocks generally fall between sanidinite and hornfels facies, confirming the HT and LP environmental conditions [3]. Pyrometamorphosed rocks are comparatively rare and volumetrically lesser than regional metamorphic rocks [3,4]. Moreover, IP rocks are the most common pyrometamorphosed rocks due to their deeper genesis compared to CP and LP rocks, giving a better preservation from weathering and geomorphological processes, despite only occur to narrow area close to the heating source [1,3]. CP rocks are lesser common than IP ones because they occur close to surface generally below 100 m in depth, due to the needed oxygen availability, thus highly and easily involved in weathering and alteration processes [1,13].

Temperature gradients in pyrometamorphosed field are extreme, varying by hundreds degrees over a few metres or even centimetres, especially for CP and LP [1,13]. Extremely HT could lead the partial melting of rocks, especially in clay-rich and silica-rich protoliths (clayed marls, clays, sandstone, etc.) [14–19], the development of granoblastic, vescicular and/or fluidal textures, and high-temperature mineral assemblages [20,21].

A large variety of HT minerals (e.g., cordierite, mullite, pyroxenes, sanidine, sapphirine, merwinite, rankinite, wollastonite, etc.) which some of them are metastable (e.g., larnite, hatrurite, brownmillerite, mayenite, ye'elimite, etc.) occur only in pyrometamorphosed rocks, and represent the natural analogous to those ones synthetized during laboratory experiments and/or industrial manufactures, such as cement, ceramic and metallurgical slags [20,22–26].

As a consequence, investigation on pyrometamorphosed rocks and the overall pyrometamorphism process could be extremely relevant for both geological purpose, for a deeper

understanding on microstructure development and stability fields of mineral assemblages at HT and LP conditions, and industrial application, mainly improving the production process (i.e., finding alternative raw materials, chemical compositions, thermal treatment, etc.) and/or the properties of final products (i.e., microstructural changes, mineral assemblages, physical and chemical properties, water reactivity, etc.).

1.2 - Combustion Pyrometamorphism

Combustion Pyrometamorphism (CP) should be considered as a rare and complex HT and LP metamorphic process commonly involving sedimentary sequence in two main stages: (i) 1st stage of HT (> 850 °C) and LP metamorphism (prograde stage) leading HT mineral assemblages, microstructural changes and in some cases the partial melting; (ii) 2nd stage of LT (< 300 °C) and LP metamorphism (retrograde stage) characterised by the interaction among prograde rocks, fluids mainly coming from circulating water, and combustion gases [1,25,27,28].

These HT conditions are achieved by the natural self-combustion of coal seams, occurring within the sedimentary sequence, or hydrocarbon gases rising from depth reservoirs [1,27,29]. The local temperature reached by the combustion process strictly depends on the oxygen supply: burning temperature increase with the oxygen supply [13,30]. The highest estimated temperature is ~ 2000 °C related to calcium-rich paralavas composed of glass, wollastonite, diopside and plagioclase occurring in Kazakhstan oil fields [31,32].

Studies indicated that the combustion process falls within the reducing conditions from wustite-magnetite (WM) and quartz-magnetite-fayalite (QFM) buffers [22]. However, the occurrence of many Fe^{3+} bearing minerals, such as brownmillerite ($Ca_2(Al,Fe)_2O_5$), shulamitite ($Ca_3TiFeAlO_8$), Fe-perovskite ($CaTiFe_xO_{3x/2}$), magnetite ($FeFe_2O_3$) and hematite (Fe_2O_3), and Fe^{3+} as ionic substitutes within the crystal structure of some minerals, such as ye'elimite ($Ca_4(AlO_2)_6(SO_4)$) and gehlenite ($Ca_2Al(AlSiO_7)$), suggest that the fO_2 could be also higher as hematite-magnetite buffer (HM) [20,33–35]. Therefore, the oxygen fugacity during CP could change from a portion to another, varying on the basis of the rock texture (fracturing, porosity and permeability) which extremely influences the oxygen supply needed during the combustion.

1.3 – Classification terms used for pyrometamorphosed rocks

Several rock terms are commonly used for pyrometamorphosed rocks, reported as follow [1,27]:

(i) *Hornfels*, used to describe a hard, compact contact metamorphic rock developed at the margin of an igneous body. The rock has a variable grain size, composed of silicates plus oxide minerals and has a subconchoidal fracture, sometimes with signs of partial melting;

(ii) *Emery*, a dark, hard, dense granular rock consisting mainly of corundum, spinel, magnetite and/or ilmenite-hematite resulting from the HT metamorphism of clay-rich sediment and laterite;

(iii) *Porcellanite*, a light coloured, very fine grained, completely recrystallized pyrometamorphosed marl or shale [36];

(iv) *Sanidinite*, melted and recrystallised quartzfeldspatic rock composed of composed of sanidine, biotite, cordierite, orthopyroxene, sillimanite, mullite, spinel, corundum, ilmenite and Ti-magnetite;

(v) *Buchite* or *Clinker*, glassy pyrometamorphosed sandstone composed of glass, oxides and mullite, commonly occurring in xenolithes in basaltic rocks;

(vi) *Paralava*, vesicular, aphanitic, fused shale, sandstone and marl that resembles artificial slag or basalt in physical appearance;

(vii) *Fulgurite*, an irregular, glassy, often tabular or rod-like rock produced by lightning fusion of sand, loose sediment and sometimes rocks.

Those terms are usually found in the past literature and can not represent a valid and unambiguous way to classify pyrometamorphosed rocks. Furthermore, *sanidinite* and *hornfels* terms are used to describe different metamorphic facies [3], and *clinker* is the common term to describe anhydrous cement [7].

In this view, it's necessary to adopt only the metamorphic classification terms recommended by the Subcommission on the Systematics of Metamorphic Rocks (SCMR), which aims to provide systematic schemes for terminology and rock definitions that are widely acceptable and suitable for international use [37]. This classification is based on the use of visible structure features at mesoscopic or microscopic scale (i.e., schistose, gneissose or granofelsic structure) and on the mineral abundance with eventually prefixes and/or suffixes (Fig. 1.1,2). Genetic terms (impactite, folgorite, etc.) are generally avoided and only used when the genetic process of the rock is clearly stated [37].

Schist, *gneiss* and *granofels* are used as fundamental root terms for a systematic terminology clarifying only structural connotation, with no mineralogical or compositional implication: *schist* should be used for metamorphic rocks with well-developed schistose structure (marked by the preferred orientation of inequant mineral grains); *gneiss* should be adopted for metamorphic rocks with poor-developed schistose structure; whereas, *granofels* should be used when no schistose structure occurred. However, the term *schist* accounts several names of rocks that possess a specific name (e.g., phyllite and slate) and with variable schistosity grade. Furthermore, it follows from this classification that a metamorphic rock may have up to three correct names, such as protolith, specific (non-systematic) and systematic names: a metabasalt could be also named as amphibolite and hornblende-plagioclase gneiss; a metalimestone could be also reported as marble and calcite granofels.

SCMR suggests using non-systematic names (specific names) when are well-founded (e.g., phyllites, slate, granulite, eclogite, etc.); therefore, systematic names will be appropriate when no suitable non-systematic names are occurring. The first step of the classification guide is the identification of clear metamorphic structure, which is not occurring a protolith-based name may be applied: protolith-based names are usually adopted for weakly metamorphosed rocks which their pristine texture is partially occurring (e.g., biotite-quartz—feldspar metasandstone, metarhyolite, metagabbro, etc.). If a protolith name is not appropriate or the rock exhibits a metamorphic structure, the next step is (i) the evaluation of well-suitable non-systematic metamorphic rock names or (ii) giving a rock name based on mineral abundance if the main one is > 75vol.%. If none of these conditions well-fit, the schistosity grade of the metamorphic rock is taken into account: the term *schist* should be used if the schistosity is well-defined at < 1 cm; the term *gneiss* should be adopted when the

schistosity is defined at > 1 cm; whereas, the term *granofels* should be used in the case of no schistosity. Furthermore, mineral phase abundance should be added as prefixes after choosing the appropriate classification term among *schist*, *gneiss* and *granofels*: all major constituents (> 5vol.%) should be added as prefixes and placed in order of increasing abundance [37].

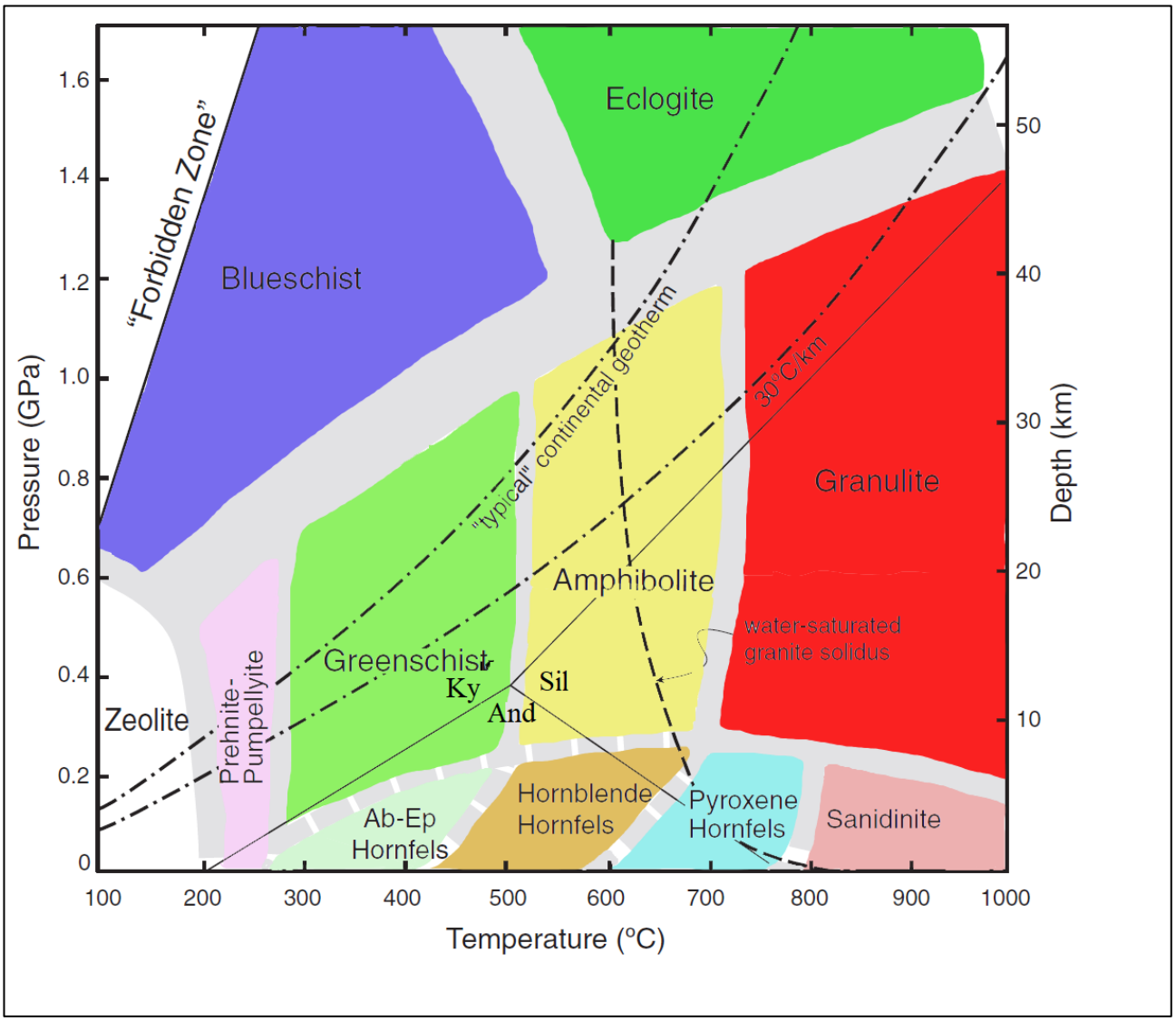

Fig. 1.1 – Temperature (°C) vs Pressure (GPa and km beneath the crust) diagram highlighting the limits of metamorphic facies (modified from [3]); "typical" and average geotherm for continental crust are from Brown et al. (1993) [38].

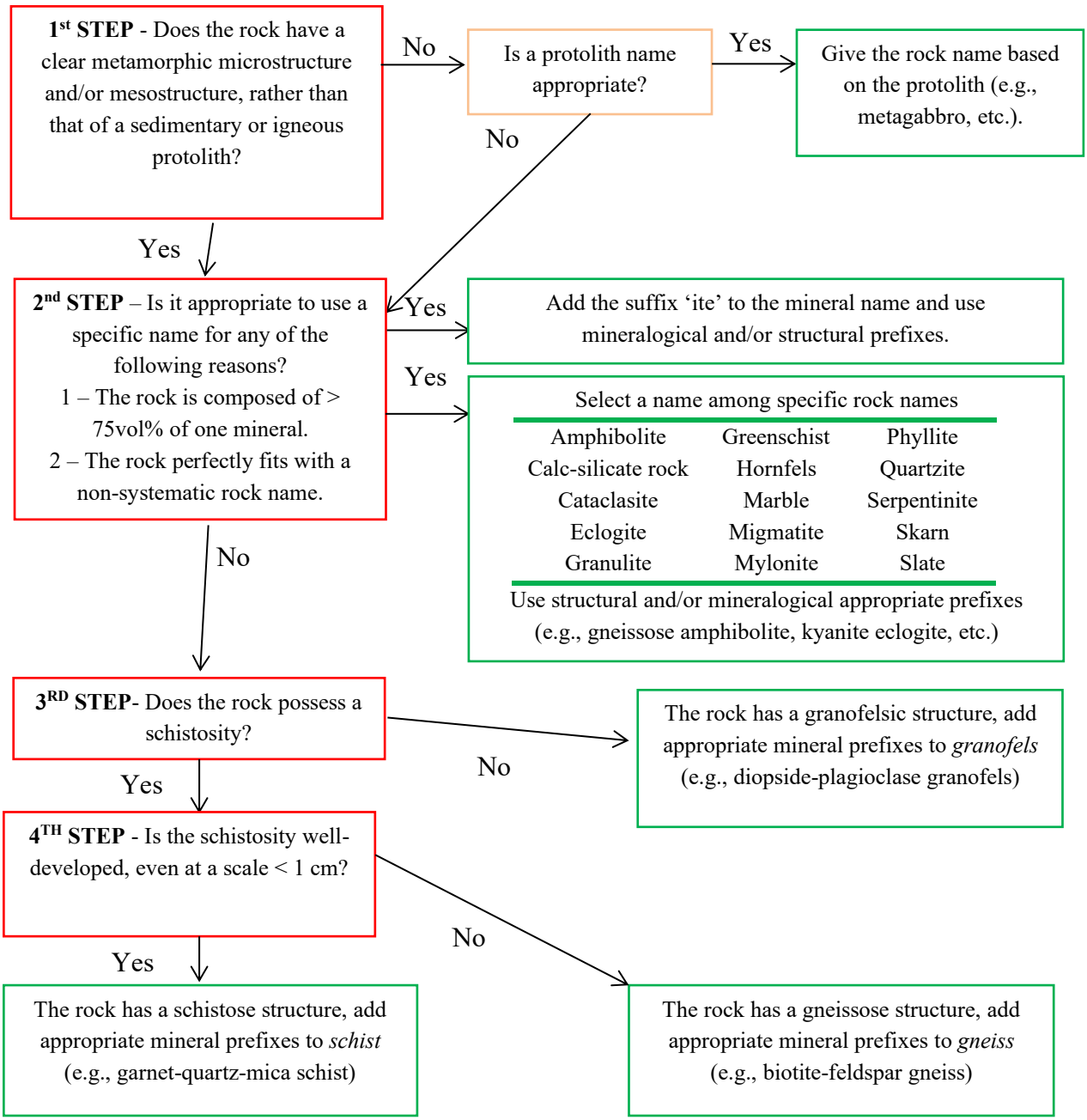

Fig. 1.2 – Flowchart for nomenclature of metamorphic rock [37].

1.4 – Combustion Pyrometamorphosed outcrops

Several outcrops of CP rocks were discovered all over the World, mainly generated by the self-ignition of fractured and shallow coal seams, some examples are followed reported: Madhya Pradesh [39] and Dhanbad [40,41], India; Wyoming and Montana, USA [15–17,42–44]; Hat Creek, British Columbia, Canada [19,45,46]; Ravensworth, Leigh Creek Coalfield, Australia [47–49]; Glenroy valley, New Zealand [50][Tulloh and Campbell, 1993]; Kuznetskiy, southern Siberia, Russia [51,52]; Kenderlyk Depression, Kazakhstan [53]; Northern China [54]; Ringstead Bay, England [55]; Timbuktu, Mali [56,57]; North-Boemia, Czech Republic [Zacek et al., 2005]; Yagnob River Valley, Tadjikistan [58–61]; Uzbekistan [62]; Tul-I-Marmar, Zoh-I-Hait and Tang-I-Gogird, Masjid-I-Sulaiman, Iran [63]; Injana, Iraq [64]; Hatrurim Basin, Nahal Ayyalon, Ma'ale Adummim, Nabi Musa, Jebl Harmun, Hureqanya, Kefar Uriyya, Tarquimiya, Malhata, Nahal Darga, Israel [13,28,29,65–68]; Marqarin, Suweilih, Daba Siwaqa, Jordan [25,69–73]; North-Bohemian Coal Field, Czech Republic [74,75]. Most of the reported CP locations had undergone in HT metamorphism > 1000 °C, almost reaching partial melting as stated by the occurrence of glass and typical high temperature phases (cristobalite, cordierite, mullite, merwinite, bredigite, rankinite, etc.).

Furthermore, there is a clear predominance of clay-rich protolith, sandstone and lacustrine sediments involved in the CP events compared to limestone and marly-limestone protoliths, which could be explained by the higher weathering resistance of the former CP protoliths [1,3]. Only the Hatrurim Basin can be considered as the most important and widest location in which crops out CP rocks of limestone protoliths well preserved: hence, our study was focused especially on this location because of the chance to observe and collect both prograde and retrograde CP rocks, and their corresponding unmetamorphosed protoliths.

1.5 – Combustion Pyrometamorphism in Israel

Many locations across Israel have been claimed as a result of CP events involving sedimentary rocks and the self-ignition of hydrocarbon gases: Hatrurim Basin, Hyrcania, Jebel Harmun, Ma'ale Adumim, Beit Sahur, Nabi Musa, Nahal Ayalon, Kefar Uriyya, Tarqumiya, Nahal Darga and Nahal Malhata [13,28,65,76–78].

The metamorphic rock sequence has almost similar features (mineral assemblages, chemical compositions and textures) among these different locations across Israel: hence, it has been widely called as Mottled Zone Complex (MZC) [79,80] or also Hatrurim Formation [81], because of the major extension of outcrops in the Hatrurim Basin region (Fig. 1.3). The term "Mottled" was used to describe the variegated colours of the rocks in all shades of brown, green, yellow, pink, red and black [1,13,78]. Furthermore, the unusual environmental formation conditions (HT, LP and changes in the fO_2 along the CP sequence) allowed the crystallisation of extremely rare minerals and numerous HT mineral assemblages that were only known in industrial materials and extra-terrestrial rocks [2,82–85]: 195 new minerals have been discovered since 1977 [86].

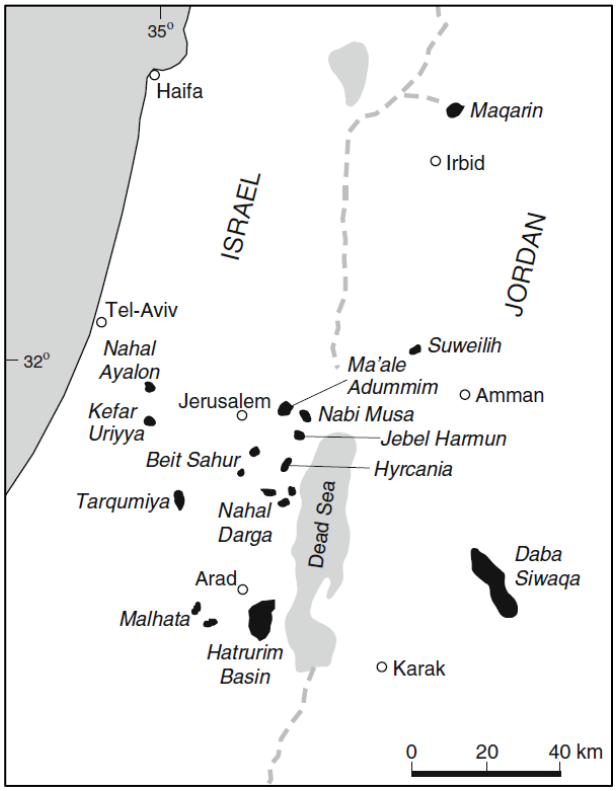

Fig. 1.3 – Spatial distribution of Mottled Zone Complexes (black areas indicate CP locations) among Israel and Jordan (from [1,13]).

Chapter 2
Geological framework of Israel

2.1 – Geological setting

The studied area is located in the northern part of the African Plate, which collided with the Eurasian Plate at the end of the Eocene [87,88] (Fig. 2.1). Before the collision, this area was part of the southern shelf of the Tethys paleo-ocean, which was involved in a typical deposition of carbonate platform across North Africa, Arabian Peninsula and Levant areas [88].

The sedimentary sequence is composed mainly of carbonate sediments, interrupted by sedimentation breaks (*hiatus*) and unconformities, highlighted by the deposition of Nubian sandstone horizons [88]. The overall sedimentary sequence was deformed during Upper Cretaceous (Turonian and Coniacian) due to the beginning of Alpine orogeny related to the closure of Tethys paleo-ocean [88].

Israel and Jordan belong to Arabian-Nubian platform that could be divided in three parts:

(i) Precambrian basement (800-600 Ma) made of granite, gneiss, schists and Pan-African granitoids with dike swarms (600-580 Ma) [89,90];

(ii) Late Precambrian conglomerates and carbonate rocks (580-541 Ma) [89,90];

(iii) Sedimentary sequence composed of shale, dolomite and limestone interrupted by Cambrian, Ordovician, Permian and Lower Cretaceous Nubian sandstone [68,88,91] (Fig. 2.2).

The basement is exposed across Aqaba Bay (southern Israel), southern Dead Sea in Jordan and in some areas along the Levantine Transform Fault; moreover, it's covered unconformable by Late Precambrian rocks. Cambrian to Ordovician sandstone crops out in southern Negev and Dead Sea, while Jurassic rocks occur mainly in Israel in Ramon, Hatira and Hazera craters. Early Cretaceous rocks are exposed in the central parts of the Negev Desert and in the western part of Transjordan Plateau, close to Levantine Transform Fault [88,92] (see Fig. 2.2).

Fig. 2.1 – Structural interpretation of Arabian Plate; the purple rectangle highlights the interested area (modifies from [93]).

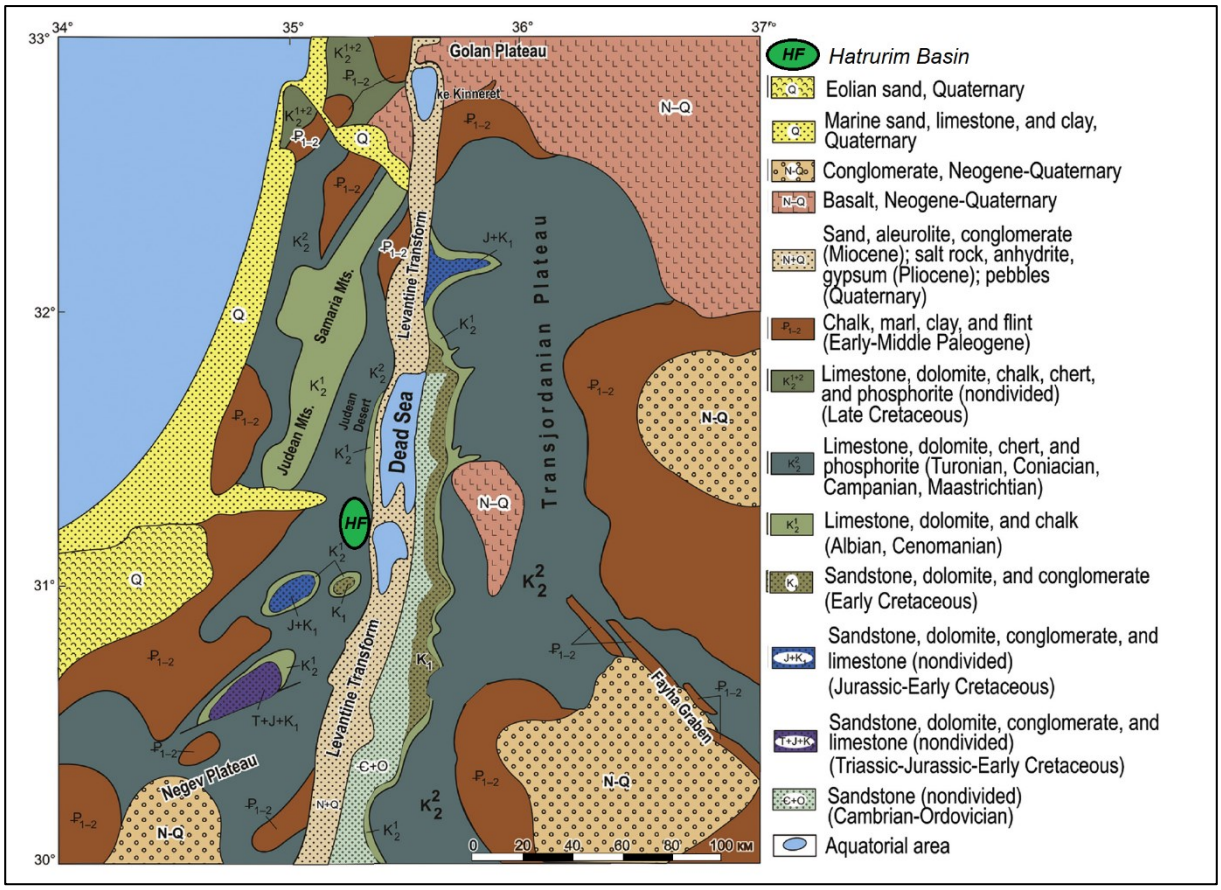

Fig. 2.2– Lithostratigraphic map of South Levant highlighting the Hatrurim Basin (modified from [88]).

2.2 – Geological history from Upper Cretaceous to Holocene

In order to understand the geological setting in the Hatrurim Basin a briefing of the main geological events from Coniaciano (Upper Cretaceous) to Holocene should be considered, which represents the age range of the rocks in the studied area. Starting from Coniaciano, the Early Alpine orogeny created two major structures:

(i) Judean – Samaria Fold Belt, which is related to Syrian Arc;

(ii) Negev and Transjordan Plateaus, which were later divided by the Levantine Transform Fault during Oligocene [88] (Fig. 2.2).

During Campanian and later, the tectonic activity caused folding, followed by a change in the sedimentation: chalky rocks was observed mainly in anticlines; while the deposition of Mount Scopus Group, which is composed of cherts and phosphorite beds (Mishash Formation) later covered by limestone and marls (Ghareb and Taqiye Formation), was observed in synclines. During Eocene, a progressive gradual change in the sedimentation occurred: the transition from Mount Scopus Group to Avedat Group, composed of mainly by limestone, represents reduction in the clay supply [88,94].

From Eocene to Oligocene, a stage of sea regression and uplifting occurred exposing outcrops to erosion and denudation, producing clastic sediments, excepted for some locations in the western part. Over this period two different types of sedimentation in Israel could be recognized [88]:

(i) marine deposition in the western part, forming Saqiye Group;

(ii) continental sedimentation in the eastern and southern part, forming Tiberias Group, which also includes conglomerates of Hazeva Formation cropping out in the Hatrurim Basin [13].

In late Oligocene, the opening of the Levantine Transform Fault and Red Seas Rift produced a displacement of about 100 km between the two limbs and the formation of a chain of rhomb-shaped grabens [93,95–99].

During Miocene to Pleistocene, tectonics activity produced a dense network of subordinate faults:

(i) Transjordan Plateau was broken by E-W and NE-SW striking faults, with smaller vertical displacement (50-70 m), spacing of 10-20 km and traced for 10-50 km, plus a network of minor faults oriented NW-SE, which produced many grabens;

(ii) Levantine microplate (Sinai microplate) was broken by NE-SW striking faults, extending for 20-30 km with a vertical displacement ranging from 200 to 300 m, plus several E-W and NW-SE faults with less extension and slight vertical displacement [67].

In particular over the period from Miocene to Pleistocene, considering the eastern part of Israel close to Dead Sea, three stages could be recognized: (i) 1st stage (late Miocene, 8-10 Ma) of deposition of 2-3 km of continental conglomerates belonging to Hazeva Formation; (ii) 2nd stage (late Miocene to Pliocene, 3-6 Ma) of rapid subsidence produced a deep topographic trough, and the basin was invaded by the Mediterranean Sea forming an elongated seawater arm called Sedom Lagoon with deposition of 2-3 km of evaporites (Sedom Formation) [100]; (iii) 4rd stage (early Pliocene to Pleistocene) of cut off of the Sedom Lagoon from the Mediterranean Sea, producing hypersaline condition with deposition of 3-4 km of lacustrine and fluvial sediments (Samra Formation) [100].

During Pliocene to Pleistocene, alluvial and proluvial pebbles were deposited in Transjordan Plateau; whereas coastal sedimentation in Israel was composed by sands, pebbles, clays and evaporates [67,90,101].

Over the period from Miocene to Holocene, several basalts exhibitions occurred only in Jordan area, which are strictly related to the extension of Levantine Transform Fault [67,102]. Three main age groups of these basaltic flows were identified: (i) middle Miocene (18 – 9 Ma); (ii) late Miocene (8 – 6 Ma); (iii) Pliocene – Holocene (< 5 Ma).

2.3 – Sinai microplate tectonic framework

Sinai microplate experienced stronger tectonic deformation compared to Arabian microplate; furthermore, central and southern Israel were mainly folded, whereas Northern Israel was mainly faulted [103]. In general, two main structural elements are observed among Sinai microplate (Fig. 2,3):

(i) folds associated with reverse faults, which have a trend between NNE-SSW and NE-SW, related to compression stage [103];

(ii) normal faults, which have trends from N-S to NNE-SSW [103].

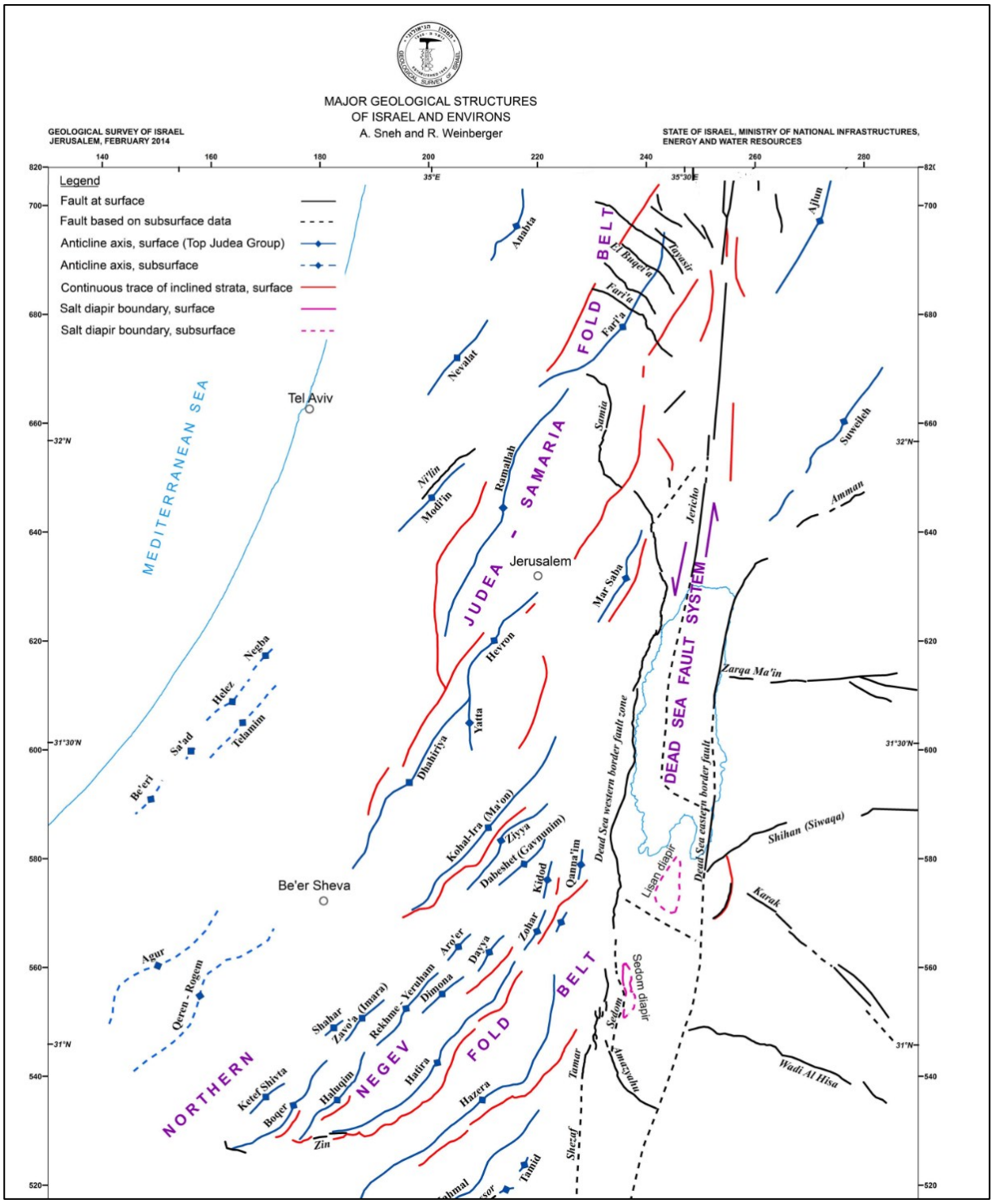

Fig. 2.3 – Map showing major tectonic structures among Israel and Jordan, scale 1:500'000 [102].

2.3.1 – Tectonic Setting of Hatrurim Basin

Hatrurim Basin is in the central-eastern part of Israel, represents a rectangular syncline with several minor structures strictly related to the Syrian Arc fold system: (i) Gurim anticline, where crops out Mishash Formation; (ii) Morag and (iii) Hatrurim adjacent synclines (Fig. 2.4a,b). Moreover, Gurim anticline is asymmetric with *SE* flank steeper than its NE one, and toward NE forms a saddle from which Mt. Ye'elim rises (Fig. 2.4a). Many additional folds are located on the south and east of the

basin but are less clear than northern ones [13]. CP rocks don't exhibits any preferred orientation of joints, explained by the inducted recrystallization, cracking and later hydration processes due to the CP [13].

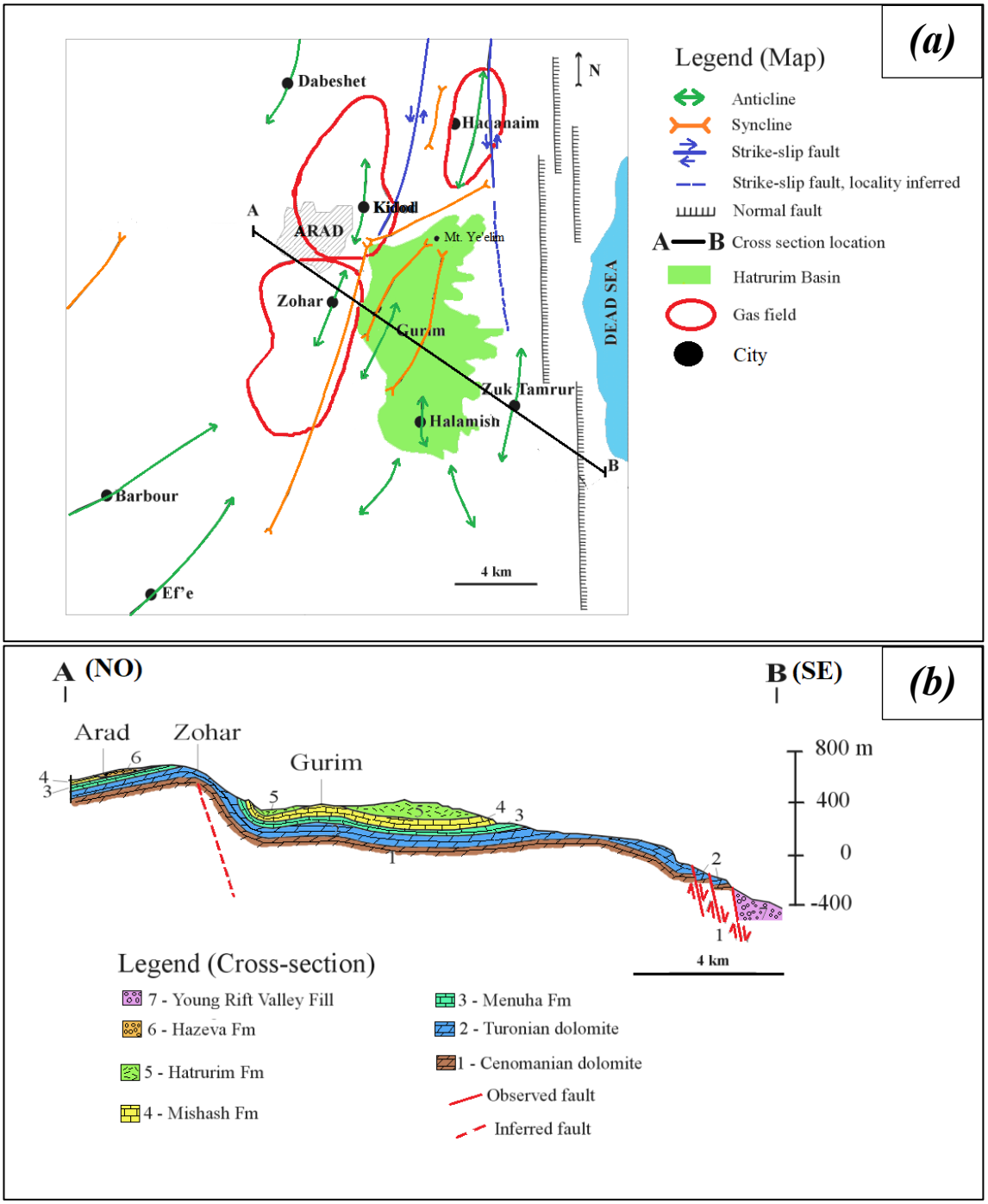

Fig. 2.4 – (a) General map highlighting the relation between Hatrurim Basin, geological structures and gas reservoirs; (b) geological cross-section passing through Hatrurim Basin (modified from [22]).

Chapter 3
Lithostratigraphy of Hatrurim Basin

3.1 – Sedimentary sequence

The sedimentary sequence involved in the CP event in the Hatrurim Basin is composed of phosphoric chert (Mishash Formation), marine rocks (Ghareb and Taqiye Formation) and terrigenous-clastic rocks (Hazeva Formation), from to the bottom to the top, with ages varying from Upper Cretaceous to Pliocene [13,104,105]. The majority of outcrops are belonging to Mishash, Menuha and Nezer Formation; whereas, Ghareb Formation crops out in some locations close to Arad city and on the southeast from Hatrurim Basin. Taqiye Formation outcrops are reported only in some location in the northeaster part of the Hatrurim Basin. Furthermore, both Ghareb and Taqiye Formation are made of limestone that are easily weathered, therefore the outcrops commonly form hummocky landscape [13]. In Fig. 3.1 is reported the geological map (scale 1:50’000) of the studied area, and in Fig. 3.2 the legend of the lithostratigraphic sequence. In Fig. 3.3 is reported the difference in thickness and features of lithostratigraphic sequence from Upper Campanian to Upper Paleocene between syncline and anticline locations in Negev [106].

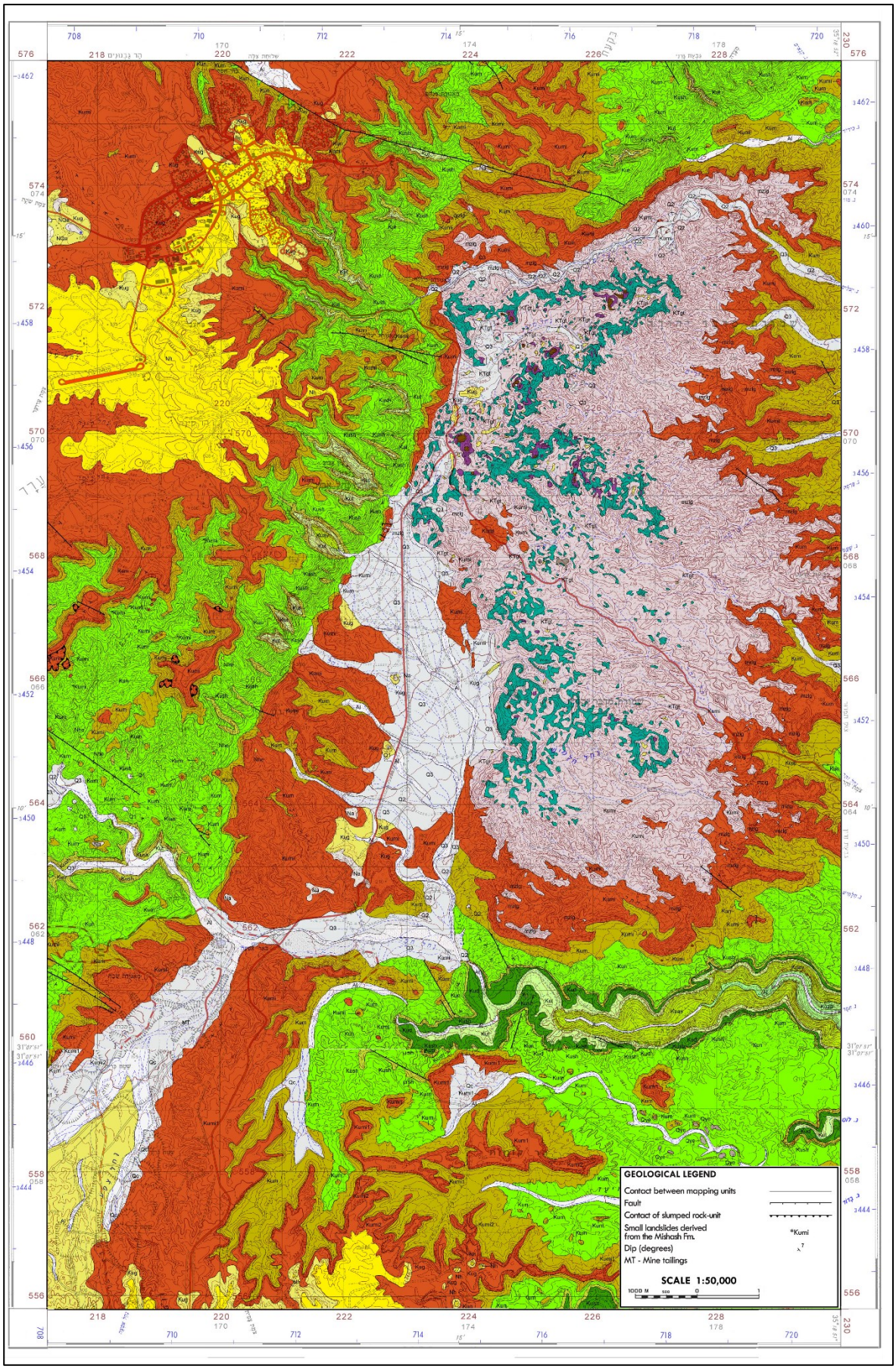

Fig. 3.1 – Geological Map of Hatrurim Basin and its surrounding area (scale 1:50'000) [104,105].

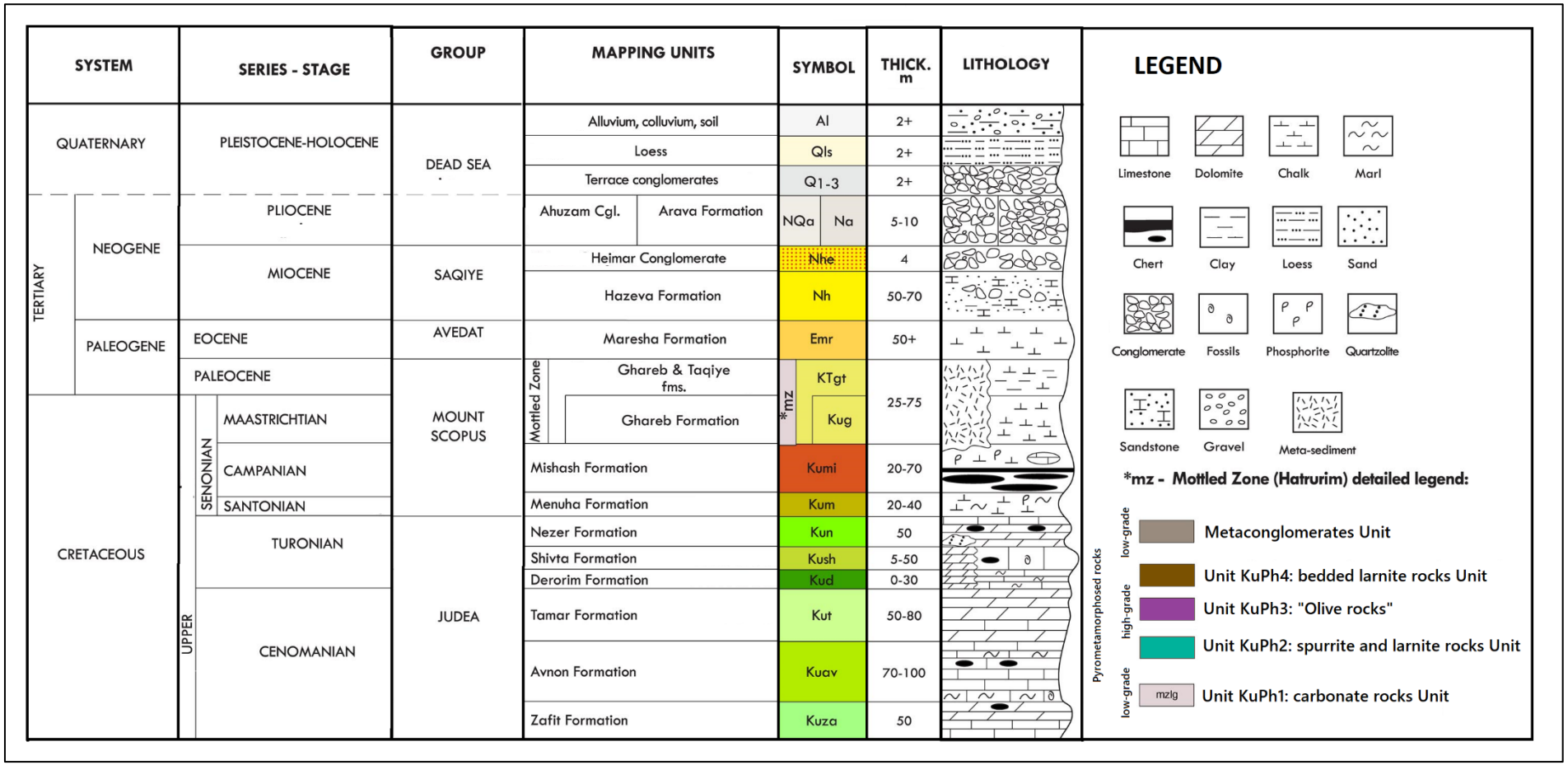

Fig. 3.2 – Lithostratigraphic sequence of the studied area including the pyrometamorphosed rocks of the Hatrurim Basin [104].

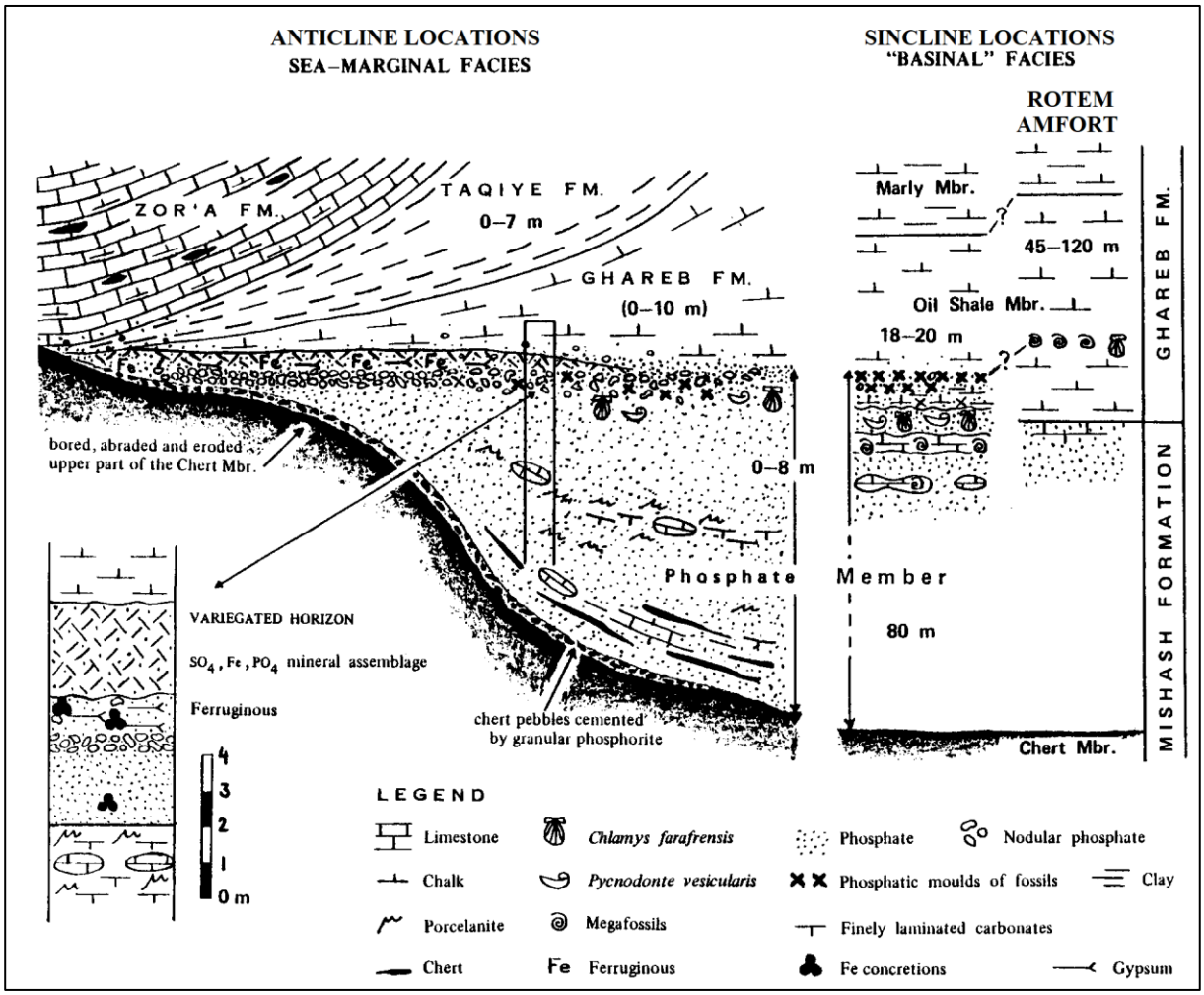

Fig. 3.3 – Stratigraphic section of Late Cretaceous – Early Paleocene formations in synclinal and anticlinal regions in Negev, highlighting differences in the thickness [106].

3.1.1 – Mishash Formation (Campanian- Early Maastrichian)

Mishash Formation is composed of chert layers and calcareous, oolitic, phosphate layers alternating with phosphatic chalk, grey marls and limestone, with a maximum thickness of ~ 130 m and an average of ~ 60 m. It's widely developed in the synclinal areas of the Negev and reaches its maximum in the north-central part of the region, where is normally mined [107–109]. The depositional environment has claimed as marine and lagoonal [101]. This formation is overlaid by a condensed layer composed of calcite, dolomite and fluorapatite with the absence of fauna, representing a depositional hiatus [110] A condensed layer is almost widespread in Negev, indicating the transition between Mishash and Ghareb Formation: the condensed layer is composed of approximately 20wt.% dolomite, 45wt.% fluorapatite, 35wt.% calcite and no fauna is observed [111]. Bentor and Vroman [80] firstly distinguished three different facies:

(i) Flinty-chalky facies, deposed in synclinal area, consisting of flint layers separated by chalky beds and occasionally limestone;

(ii) Chalky facies, deposed in synclinal area, consisting of chalks with subordinate flint layers, mainly developed in Judean Desert;

(iii) Flinty facies, deposed in anticlinal area, consisting of thick flint layers.

Whereas, Soudry et al [112] later divide Mishash Formation in two members:

(i) Main Chert Member, represents the base of this formation, consisting of brecciated grey to reddish chert with occasionally partially silicified chalk and porcellanite. This member varies in thickness from 20 to 30 m;

(ii) Phosphate Series Member, represents the upper portion of this formation which is well developed in synclines, consisting of an alternation of nodular phosphorite layers, phosphatic chalk, porcellanite, and friable carbonates. The thickness varying from 80 m to 8 meters in synclines and anticlines, respectively [106]. Phosphatic nodules consist of phosphate pellets, coated grains and fish bone fragments, which at optical microscopy usually revealed a matrix of cryptocrystalline phosphate with weakly anisotropic features on crossed nicols [106]. The formation of phosphate nodules is explained by cyclic repetition of low and high-energy episodes associated with a microbial activity of sulphide-oxidizing bacteria depending on the position of the anoxic-oxic surface [110]. Furthermore, hard carbonate concretions ranging in size from centimeters to a few meters are commonly found, which are made of hard matrix supported limestone with well-preserved fish bones, intense microsparitization and silicification at their margins. The formation of carbonate concretions are related to the decomposition of organic matter in anoxic conditions which leads an increase in pH and a dissolution of opal [113]

Only the upper part of Mishash Formation (Phosphate Series Member) was involved in the CP event. Therefore, Mishash Formation could be considered as the stratigraphic basis upon which the Hatrurim Formation rests [13].

3.1.2 – Ghareb Formation (Early to Upper Maastrichtian)

Ghareb Formation is mainly composed of yellow and pink, limonitic, marly chalk with phosphate nodules and rare grey gypsiferous shales [101]. Rare dolomites bodies appear only in the upper part. Outcrops are generally well exposed in on synclines in the Negev Desert [13]. The depositional environment of Ghareb Formation is recognized as open marine deposition environment with a thicker sequence close to synclines with at the base organic-rich rocks, while in anticlines the sequence is thinner with a lack of bituminous lithotypes [101,114].

This formation is commonly divided in two members by the carbonate content which increases from the bottom to the top:

(i) Lower Member (Early to Middle Maastrichtian), which is represented by poor bedded bituminous marls and chalky marls with siliceous chalk in the basal part, cut by several gypsum-rich veins [13,115]. The calcite content is up to 72wt.% within this member [13]. When it contains up to 26% of organic matter as bitumen it is called Oil Shale Member [78,116]. This Member is also called Marl Member [114]. Little well-rounded phosphatic pellets (< 1 cm) occur within the Lower Member, especially in the Oil Shale Member, suggesting a low-rate of deposition and a low-energy environment [106];

(ii) Upper Member (Middle to Upper Maastrichtiano), which is mainly poor bedded bituminous limestone and marly limestone, with at least 86wt.% of calcite and strongly jointed [13].

This member has a wide range of organic matter content from 15 to 30wt.% [78,116]. The Upper Member is also called Chalky Member [114].

Several outcrops are exposed around the eastern margin of the southern part of Hatrurim Basin. The thickness of the formation ranging from 30 to 80 m, but locally can reaches up to 170 m, and seems to increase toward southeast [28]. The stratigraphic age is between 65 and 72 Ma, which is in good agreement with $^{40}K/^{40}Ar$ data (64-74 Ma) [117] and paleontological data that claimed a late Campanian to Maastrichian age [101]. The Ghareb Formation overlies the Mishash Formation conformably and it's also conformably overlain by Taqiye Formation. Benthic foraminifers are generally greater than planktonic foraminifers in Ghareb Formation, confirming the increase of deep compared to Mishash Formation [118].

Studies [118] highlighted diagenetic process of replacement of gypsum by calcite in organic-rich part of Ghareb Formation explained by a three steps process: (i) sediments were deposited on the bottom of an hypersaline stratified lagoon, which the upper part were oxygenated and rich in foraminifers; (ii) organic matter accumulated on the anoxic hypersaline bottom with crystallisation of gypsum in foraminifer tests due to hypersaline condition; (iii) sulphate-reduction bacteria activity due to anoxic condition released Ca^{2+}, H_2S and HCO_3^- that leads an oversaturation and later precipitation of $CaCO_3$.

The beginning of CP is recognizable by a pronounced recrystallization of microfossils, hardness increase and lighting of colours which occurs during the initial prograde stage at low temperature [13].

3.1.3 – Taqiye Formation (Late Maastrichtian-Upper Paleocene)

Taqiye Formation consists of green shale at the base, passing gradually upwards into argillaceous chalks and chalky limestone, which sometimes appear gypsiferous, bituminous and limonitic, containing marcasite concretions [101]. This formation is divided in two members:

(i) Lower Member (Late Maastrichtian to Middle Paleocene), which is mainly composed of marls, with a wide clay content and sometimes dolomitic, and clays reaching up to 80 m. Several concretions of pyrite, marcasite and rarely barite occur in this member [13]. Clays content is composed of montmorillonite (up to 80wt.%), kaolinite (up to 50wt.%) and illite (up to 20wt.%); the calcite content has an increasing upward trend [94];

(ii) Hafir Member, which represents a sequence of well bedded chalks, with chert concretions at the base and many marly beds at the top. The thickness reaches up to 30 m and rapidly decreases toward anticlines [13,94]. The clay assemblage is composed of sepiolite (up to 20wt.%), palygorskite (up to 60wt.%) and montmorillonite (up to 90wt.%) [94].

The bituminous part occurs only in few locations limited in synclines and the organic content reaches up to 25% [13,80]. The overall thickness is up to 150 m, but the average is around 50 m [28,94]. The stratigraphic age ranges between 59 and 65 Ma, which is in good agreement with $^{40}K/^{40}Ar$ data (74-152 Ma) [94,117].

3.1.4 – Hazeva Formation (Oligocene-Miocene)

Hazeva Formation is composed of clastic rocks and overlies unconformably the Taqiye Formation. The thickness is extremely variable from 50 to 500 m. This formation is divided in three members, described from the bottom to the top [13,119]:

(i) Zefa Member (Oligocene), consisting of coarse gravel and breccia grading upward to sandy marls. Most of pebbles are well rounded up to 50 cm composed of chert, flint, with minor limestone and chalk. The upper part of this member is overlain by a white fine-grained sand, containing limestone, flint and orthoquartzite pebbles up to a few centimeters [13,120];

(ii) Shahaq Member (Early to Middle Miocene) representing an autochthonous polymictic conglomerate;

(iii) Rotem Member (Upper Miocene) made of gravelly sandstone, also representing the end of the Miocene.

Rarely this formation is partly metamorphosed and mineralized with retrograde minerals especially in cracks and veinlets [13,80,112].

3.1.5 – Paleoenvironmental reconstruction from Late Campanian to Upper Palaeocene

The sedimentary sequence from Late Campanian to Upper Paleocene in central-eastern Israel (Northern Negev) took place in shallow marine environment within NE-SW elongated basins with an overall deepening of the continental shelf toward NW. Basins were formed by tectonic activity during Campanian, creating high and low on the continental shelf. The sedimentary sequence could be divided in three stages with different environmental conditions:

(i) a first stage of Lower Chert Member (Mishash Formation) deposition, composed of brecciated chert layers, interbedded chalks, and phosphate organic-rich carbonates suggesting an open marine environment;

(ii) a second stage with the deposition of Phosphate Member (Mishash Formation), composed of nodular phosphorite layers, porcellanite and phosphatic chalks, changing to a lagoon environment conditions with cyclic changes in sea level and tectonic activity;

(iii) a third stage (from Early Maastrichtian to Upper Paleocene) of Ghareb and Taqiye Formations deposition, that are represent by marly limestone and chalky marls, highlighting an overall deepening of marine conditions with local temporary restricted conditions resulting in bituminous-rich rocks.

3.2 – Pyrometamorphosed sequence – Hatrurim Formation

The sedimentary sequence from the upper part of Mishash Formation to the lower part of Hazeva Formation has undergone in combustion pyrometamorphism in the northern Negev, resulting in metamorphic rocks sequence called Hatrurim Formation (HF) or also Mottled Zone Complex (MCZ) [13,28,65]. The area involved in the CP event is called Hatrurim Basin, which represents an arid area of ~ 40 km^2, with an entire section up to 190 m of metamorphic rocks [13]. Two main ages of CP events were recognized by K–Ar dating, one at 2.3-4 Ma and an older at 16 Ma [117].

HF is divided into five mapping units basing on the stratigraphic position in the sequence: Unit KuPh1, carbonate rocks unit; Unit KuPh2, spurrite and larnite rocks unit; Unit KuPh3, calcite-zeolite-garnet and anorthite-diopside hornfels unit; Unit KuPh4, bedded larnite rocks unit; metaconglomerate unit (Fig. 3.4). The concept of mapping the metamorphic units was the direct correlation between unmetamorphosed and pyrometamorphosed rocks [13,78]. Due to the rarity and limited exposure of metamorphosed outcrops of Mishash Formation, no dedicated metamorphic unit was created [13]. Some outcrops of unmetamorphosed Ghareb and Taqiye Formation occur in Hatrurim Basin, and paleontological studied confirmed their age and the stratigraphic position [78].

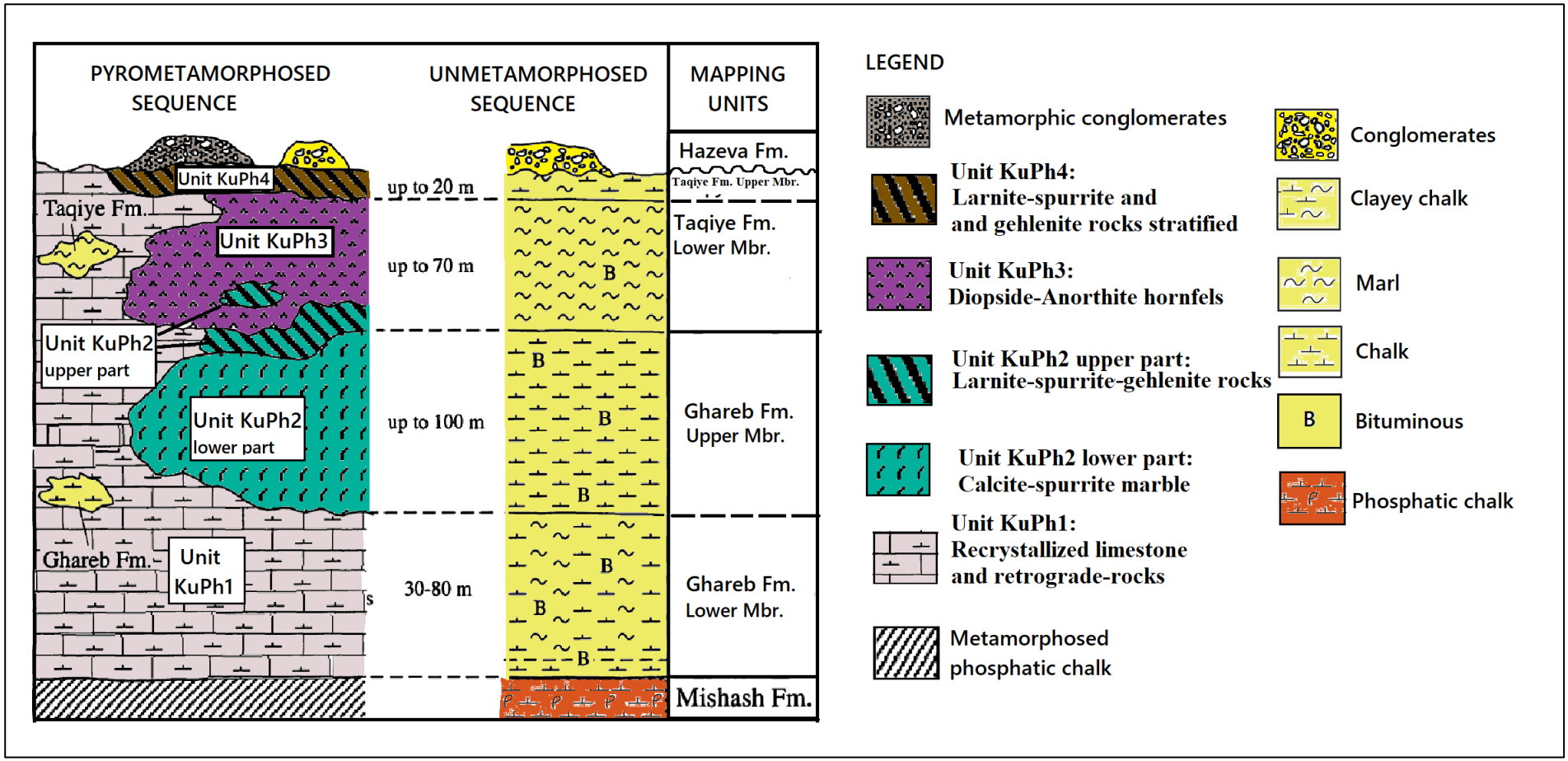

Fig. 3.4 – Stratigraphic sequence and correlation between sedimentary sequence (from Late Campanian to Upper Paleocene) and pyrometamorphosed sequence occurring in Hatrurim Basin (modified from [13]).

3.2.1 – Metamorphosed Mishash Formation

Only the Phosphate Series Member is slightly affected by CP, and due to its small outcrops no mapping unit was dedicated to this lithotype [13]. The metamorphism of Mishash Formation produces a darkening of layers, progressive decarbonation of francolite ($Ca_{5-1/2x}[(PO_4)_{3-x}(CO_3)_x](F,OH)$) into fluorapatite and a general recrystallization [121]. The high-grade facies is represented by apatite-rich marble with reddish to green colour, due to the presence of apatite [13].

3.2.2 – Unit KuPh1: carbonate rocks Unit

This unit is made of mainly low-grade and retrograde metamorphic rocks, which cover ~ 70% area of the entire Hatrurim Basin, and lesser high-grade rocks. Despite the low-grade rocks occur in all parts of the stratigraphic section, they commonly occur at the base of the metamorphosed sequence. Typically, this unit forms badlands landscape with light colours and soft terrains [13]. Most outcrops are coated by a white to yellow porous crust made of calcite, gypsum and sometimes halite varying in thickness from 0.1 to 1 m. Misoriented veinlets, considered as retrograde veins, are composed of secondary calcite, gypsum and volkonskoite ($Ca_{0.3}(Cr^{3+},Fe^{3+},Mg)_2(Si,Al)_4O_{10}(OH)_2 \cdot 4H_2O$) [13]. This unit is composed of three metamorphic grades:

(i) prograde low-grade metamorphosed carbonates, resulting from low-temperature metamorphism of Late Cretaceous marine rocks, composed of calcite, apatite, zeolites and hydrogarnet;

(ii) numerous lens bodies ranging from 1 to 10 m of gehlenite or larnite rocks (high-grade metamorphic rocks). Gehlenite lenses are composed of gehlenite, garnet (andradite-grossularia), fluorapatite, nagelschmidtite and wollastonite, crossed by retrograde veinlets of calcite, tobermorite, portlandite and hydrogarnet; larnite lens always occur close to gehlenite lens and consist hard dark-brown rocks of larnite, brownmillerite, mayenite or ye'elimite and fluorapatite.

(iii) retrograde metamorphosed rocks, resulting from low-temperature processes (sulfation, carbonation and hydration) involving prograde metamorphic rocks. Retrograde process is more pervasive for larnite lens compared to other prograde rocks, forming pseudoconglomerates: pebbles up to 10 cm of anhydrous larnite rock, surrounded by light coloured cement composed of calcite, portlandite, hydrogarnet, tobermorite, aragonite, halite, jennite, ettringite, afwillite, iron oxides and fluorapatite.

The transition between low-grade rocks and high-grade lens is generally irregular, often by retrograde rocks. Moreover, Ghareb and Taqiye Formation outcrops, which are in contact with Unit KuPh1, are always surrounded only by low-grade metamorphic rocks [13]. Furthermore, metric bodies of lizardite-rich rocks occur in the upper part of Unit KuPh1, consisting of calcite, lizardite, hematite, gypsum and dolomite, explained by the metamorphism of dolostone belonging to Lower Member of Ghareb Formation [13].

3.2.3 – Unit KuPh2: spurrite and larnite rocks Unit

This unit is dominated by spurrite and larnite rich rocks which are the corresponding metamorphosed Lower and Upper Members of Taqiye and Ghareb Formations, respectively. The average metamorphic grade of Unit KuPh2 is higher compared to Unit KuPh1. The unit is divided in two sub-units by the mineral assemblage and stratigraphic position:

(i) calcite-spurrite marble subunit, forming cliffs without bedding, and representing the CP of Upper Member of Ghareb Formation. The mineral assemblage is composed of spurrite and calcite, as major phases, and brownmillerite, mayenite, apatite and garnet, as minor minerals. Marbles are usually crisscrossed by white to beige coloured veinlets of calcite, volkonskoite, gypsum, zeolites and other hydrated phases. Hematite concretions from 1 mm to 10 cm in size rarely occur. Moreover, marbles were also used in the past as dimension stone called "Arad Marble", as confirmed by the numerous dismissed quarries [13];

(ii) larnite-spurrite-gehlenite rocks subunit occurs above the calcite-spurrite marble unit, also among Unit KuPh3 as lens bodies. This subunit should correspond to the metamorphism of rocks belonging to Upper Member of Ghareb Formation and Lower Member of Taqiye Formation. It's composed of mainly larnite-rich rocks, minor spurrite marble and gehlenite-rich rocks. The former and the latter are very similar in chemical composition and mineral assemblage respect to larnite and gehlenite rock lens belonging to KuPh1 [13].

The contact between calcite-spurrite-gehlenite and calcite-spurrite subunits is usually irregular.

3.2.4 – Unit KuPh3: calcite-zeolite-garnet and anorthite-diopside hornfels Unit

Unit KuPh3 accounts rocks with a wide metamorphic grade, representing the metamorphism of Lower Member of Taqiye Formation: the wide range of clay content of Taqiye Formation is reflected by the various mineral assemblages of metamorphosed rocks, ranging from calcite-spurrite marble, for limestone and marls, to anorthite-diopside hornfels, for marly claystone. Outcrops mainly occur in the northern Hatrurim Basin. The unit is divided in four subunits, representing an increase of metamorphic grade which is toward the upper part:

(i) calcite-hydrogrossular rocks subunit, also called low-grade olive rocks, which has the same metamorphic grade of low-grade metamorphosed carbonates belonging to Unit KuPh1. The rocks are light-green meta-chalk, with sporadic hematite or barite concretions. Calcite-hydrogrossular rocks are porous and soft, mainly composed of calcite and hydrogrossular with minor aragonite, aluminous serpentine, vaterite, hematite, zeolites, garnet (andradite-grossular) and apatite;

(ii) calcite-zeolite-garnet rocks subunit, also called medium-grade porous olive rocks, which represents the most abundant subunit of Unit KuPh3. The subunit is composed of zeolites (mainly thomsonite and gismondine, with less phillipsite and chabasite), calcite, diopside, garnet (andradite-grossular), hydrogarnet and minor maghemite, hematite, serpentine, aragonite and vaterite;

(iii) anorthite-diopside hornfels subunit, also called high-grade dense olive rocks, composed of two rocks varying in textures: (a) hornfels which are massive, fine grained and homogeneous, mainly composed of diopside, anorthite, grossular, wollastonite and minor

calcite, zeolites, serpentine, andradite and gehlenite; (b) paralavas with fluidal texture, lens shape, fine grained, mainly composed of diopside, anorthite, K-feldspar, Fe-Ti oxides and glass, with minor calcite, zeolite, apatite, pyrrothyte, fayalite and tridymite [22]. Rocks usually contain hematite-maghemite concretions varying in shape from spherical to elongated and from few millimeters to centimeters in size [13]. Studied on paralavas estimated a formation temperature between 1220-1500 °C using the normative component of paralavas [22], and 1000-1200 °C considering the hematite-corundum pair [35]. Whereas, glass composition indicates that temperature of quenching ranging from 950-1150 °C [13,22];

(iv) gehlenite-wollastonite hornfels subunit, also called high-grade gehlenitic dense olive rocks, composed of grey to olive-brown, fine grained and hard rocks. This subunit generally occurs in the upper part of Unit KuPh3 and represents the high-grade metamorphism of Lower Member of Taqiye Formation. Hornfels are composed of gehlenite, wollastonite, garnet (andratite-grossular) and diopside with granoblastic texture. Veins filled with thomsonite, jennite, tobermorite, calcite and hydrogarnet sometimes occur [13,28].

3.2.5 – Unit KuPh4: bedded larnite rocks Unit

This unit overlies Unit KuPh3 and represents the high-grade metamorphism of Hafir Member belonging to Taqiye Formation. Most of outcrops occur in the northern Hatrurim Basin on top of hills. Outcrops exhibit a bedding, forming banks from 10 cm to 2 m thick, with no clear relation with mineral or clear texture changes [13]. Rocks are frequently cut by retrograde light-coloured veinlets filled by hydrates minerals such as hydrogarnet, tobermorite, chabasite, thomsonite, jennite, ettringite, portlandite and calcite. This unit includes two different rocks reflecting changes in metamorphic grade:

(i) larnite rocks representing highest metamorphic grade in the sequence with an estimated forming temperature 1200-1400 °C. All occurring features are similar to larnite lens of Unit KuPh1, composed of brown to black, fine grained and hard rocks. Two main mineral assemblages can occur basing on the occurrence of gehlenite as major mineral: one made of larnite, ye'elimite, brownmillerite, shulamitite, spinel and fluorapatite; whereas, the other composed of larnite, gehlenite, mayenite, brownmillerite, shulamitite, spinel and fluorapatite [122];

(ii) spurrite-calcite marbles with an estimated forming temperature between 850-950 °C, which are composed of spurrite, calcite and mayenite. Minerals assemblage and textural features are similar to spurrite-calcite subunit (Unit KuPh2) ones.

3.2.6 – Metaconglomerates Unit

A small number of metaconglomerates outcrops occur in Hatrurim Basin [80,123]. Metaconglomerates have a metamorphic grade varying from very low to medium, increasing when the thickness is lower. There are three major areas where metaconglomerates outcrops are exposed: (i) close to the centre of Hatrurim Basin; (ii) in the north-eastern part of Hatrurim Basin at an elevation from 290 m to 370 m; (iii) in the south-western zone close to Gurim anticline. The degree

of cementation of metaconglomerates increases with the metamorphic grade. These metaconglomerates are poorly sorted and polymictic, containing chert and phosphorite pebbles from Mishash Formation, sandstone of Hazeva Formation, rare limestone pebbles belonging to Judea Group and CP pebbles [13]. The matrix of these metaconglomerates is varying from grey to red, composed of calcite, quartz and orthoclase grains. Metamorphosed rocks consist mainly of quartz, feldspar, calcite, apophyllite and zeolites [117].

Chapter 4
Combustion Pyrometamorphism event in Hatrurim Basin

Many theories have been made explaining the genesis of Hatrurim Basin invoking a volcanic [124,125], tectonic [126], sedimentary [79] or hydrothermal [80,127] genesis. The metamorphic event could be considered as isochemical, except for low-grade rocks due to the weathering process and interaction with water and gases [13,128].

The pressure during the combustion was governed by the load pressure of rock column, hence, the highest pressure reached was of 25 atm at the base of metamorphosed sequence [129]. Due to the interaction between rocks and fluids/gases, the composition of gases can play an important role in the stability field of minerals. Carbon dioxide should be the main constituent of the vapour phase, released both by the combustion of fuel and by the breakdown of calcite. H_2O may also be an important component phase especially at low temperature. SO_2 should be considered especially at high temperature (> 1200 °C) when anhydrite and ternesite start to decompose. The oxygen fugacity among Hatrurim Basin rocks during the combustion should be in the range from HM and QFM buffers [130,131]. Whereas, the estimated highest temperature for Hatrurim Basin should not exceed the eutectic point of 1280 °C of the coexistence of larnite-brownmillerite-mayenite [129,132].

Fission track analysis ($^{40}Ar/^{39}Ar$ and $^{40}K/^{40}Ar$ analysis) revealed a range of ages for CP rocks in Hatrurim Basin, ranging from 1.2 to 5 Ma with an average of 3 Ma [13,78,117]. K–Ar dating method used K-bearing minerals mainly coming from KuPh3 and Metaconglomerate Units. This age range should be related to the opening of Dead Sea rift due to the strict relation with neotectonics activity [88]. U-Th dating method on hydration veins revealed a wide range from 45 to 450 ka with an average of 150 ka [133]. The combustion event lasted from 300 to 1000 days as estimated by using the conduction heat equation [134] assuming the distance measured on field between high-grade metamorphic and unmetamorphosed rocks, a foci temperature of 750 °C and a thermal conductivity of $1 \cdot 10^{-6}$ m^2/s [28].

Afterwards, nowadays two main models are used to explain the formation of Hatrurim Basin:

(i) self-ignition bitumen model, in which the bituminous rocks represent the fuel for combustion process [13];

(ii) mud volcanism model, where methane-rich hydrocarbon gases from deep reservoirs toward to surface represent the fuel for the combustion [66].

The self-ignition bitumen model for CP for MZC has been widely accepted by the geological community, but recent studies highlighted criticalities mainly focused on the mechanism of triggering the combustion, the occurrence of brecciated-cement bodies and strict correlation between hydrocarbon deposits and MZCs.

4.1 – Self-ignition bitumen combustion model

This model claims an in-situ spontaneous combustion of bituminous matter occurring in the original sedimentary rocks (Ghareb and Taqiye Formation) as a source of heat. The self-ignition of bitumen was triggered by a first intense cracking, due to neotectonic event related to Dead Sea Transform Fault, and later oxidizing of sulphide minerals, giving enough energy to start the combustion [78,123,129]. Isotopic studies on carbon and oxygen confirmed the hypothesis of the involvement of bitumen (organic matter) in the combustion: spurrite ($Ca_5(SiO_4)_2CO_3$) crystals are strongly enriched in C^{12}, suggesting a CO_2 coming from an organic source during the spurrite formation at high temperature (650-950 °C) [123,128].

In general, three main features control the CP event: (i) the availability of organic matter in the protoliths; (ii) the access of oxygen by joints, essential for the combustion; (iii) rapid exposure and following oxidation of sulphides and subsequent combustion of organic matter [13]. A slow oxidation of bituminous protoliths leads a low oxidation of sulphides and organic matter without reaching the self-ignition point [13]. Therefore, the oxygen supply represents the chief controlling factor, depending on the grade of crack and deep of system: higher fracturing grade and closer to surface, higher is the oxygen availability, therefore higher temperature could be reached. Drilling in the Hatrurim Basin in Halamish, Gurim and Mt. Ye'elim locations confirmed up to 120 m of CP rocks from the surface, followed by unmetamorphosed sedimentary rocks [13]. The occurrence of several dike-like structures in Hatrurim Basin suggests a combustion process with numerous foci representing locations of high temperature combustion and releasing of combustion gases [13].

The self-ignition bitumen combustion model for Hatrurim Basis depicts a three steps process: (i) a rapid removal of clastic rocks (Hazeva Formation), which were covering the bituminous sequence; (ii) followed by a rapid exposure, starting the oxidation of sulphide minerals and organic matter; (iii) self-ignition of bitumen in several locations, creating foci in which high temperature are reached and combustion gases are released.

4.2 –Mud vulcanism model

Despite the self-ignition of bituminous rocks is the most accepted model there are several inconsistencies: (i) bituminous chalk has an insufficient porosity to sustain a combustion process; (ii) presence of brecciated and pipe-like bodies and rock fragments belonging to formations ~ 2-3 km beneath the surface; (iii) the evidence of very high-temperature mineral assemblages, which can not be explained by low-calorific fuel as bituminous limestone; (vi) the occurrence of relatively high concentration of U-Th, REE, trace elements and noble metals, large-scale dolomitization and calcite-barite enrichments suggest the occurrence of hydrothermal activity common in mud vulcanism system [135]. Therefore, many authors invoked the mud volcanism as a genetic process for Hatrurim Basin.

Mud vulcanism is a geological process related to neotectonic deformation, which causes movement of oil, gases and brine in hydrocarbon reservoirs: the overpressure of these deep reservoir causes the rinse of mainly hydrocarbon gases and lesser brine toward the surface along

faults produced by neotectonic activity. Furthermore, conical hills commonly occur on mud vulcanism fields, which are composed of brecciated and cemented rocks [67,135]. The overheated and pressured hydrocarbon-rich fluids when reaches the surface causes hydrofracturing of outcrops and self-ignites in contact with oxygen due to high pressure and temperature. The combustion of hydrocarbon gases produces a rapid increase in temperature forming high-grade metamorphic rocks; whereas, after the combustion low-grade metamorphic rocks are formed, both from simply weathering process or by hydrothermal low-temperature brines forming metasomatized and brecciated-cements rocks. The release of brines coming from deep reservoirs is not always occurring after the gas combustion [63,67].

Many features occur in Hatrurim Basin and in nowadays mud volcano locations, helping in understanding the formation process [67]:

(i) pyrometamorphosed field are always located close to shear zones or flexures, indicating that tectonic activity is key-factor;
(ii) the widespread occurrence of fractured rocks especially close for high temperature facies, which is consistent with hydro-explosion during the rinse of gases;
(iii) great thickness and extension of pyrometamorphosed rock, indicating a prolonged process of combustion powered by hydrocarbons release;
(iv) wide range of minerals assemblages and chemical composition, not explained by the correlation of metamorphism of protoliths but rather by extrusion and metamorphism of ancient rocks;
(v) the occurrence of extensive and pervasive hydrothermal alteration, which is commonly found in mud volcanism locations;
(vi) the close spatial occurrence between pyrometamorphosed rocks and oil, gases and asphalts reservoir.

Further studies investigated the occurrence and the formation of reservoirs in Israel, revealing f useful features to lend credence to mud volcanism model. In the western flank of the Dead Sea there are three main gas fields (Zohar, Kidod and Haqanaim), plus several oil, asphalt and light oil exhibitions (Fig. 7a) [88]. The origin of hydrocarbon reservoirs beneath the Northern Negev is related to hydrocarbon maturation, migration and accumulation in the western flank of Dead Sea rift, which took place during the last 3-6 Ma: hydrocarbons fluids were originated from the Senonian bituminous rocks buried in the graben and migrated westward accumulating in anticline structural traps [100].

Studies on gas of the Zohar, Kidod and Haqanaim reservoirs revealed composed a composition of 90-96% of methane, 2-4% ethane, propane and butane and <1 % CO_2 [136], which could better represent the fuel for CP due to its high calorific power.

Chapter 5
Field trip in Hatrurim Basin

A field trip was performed in the northern part of Negev Desert on the south from Arad city, in order to highlight (i) geological features at mesoscale (from 1 to 10 cm) and macroscale (from 10 cm to 10 m) observing outcrops, and collecting (ii) rocks samples from main formations, especially for calcareous protoliths (Ghareb Formation) and the corresponding high-grade metamorphic rocks (KuPh2,4), useful for mesoscale and microscale (from 5 μm to 1 cm) laboratory investigations. The field trip was dived in two trips (Table 5.1 and Fig. 5.1):

- 1st trip, focused on outcrops of sedimentary rocks close to Arad city and the north-western part of Hatrurim Basin (from Stop-1 to 8);
- 2nd trip, focused on outcrops on Mt. Ye'elim, which represents one of highest mountain in the Hatrurim Basin, where crops out high-grade metamorphic rocks of KuPh4 close to the top (Stop-9).

STATION	***SHORT DESCRIPTION***	***N (°)***	***E (°)***	***GOOGLE MAPS LINK***
	1st Trip			
Stop-1 Northern Arad	*Phosphate-rich limestone with chert layers (Phosphate Series Member, Mishash Fm.)*	31.265264	35.205141	STOP-1
Stop-2 Northern Arad	*Extremely weathered limestone with hard limestone concretions (Lower Member, Ghareb Fm.)*	31.262028	35.207855	STOP-2
Stop-3 Road 258 to Mezad Tamar	*Viewpoint of Hatrurim Basin highlighting Gurim and Zohar anticline, Morag and Hatrurim synclines*	31.095152	35.205860	STOP-3
Stop-4 Road 31at Hatrurim Junction	*Light-brown fine-grained rocks with iron-rich nodules and hydrations veins (Unit KuPh3,4)*	31.220569	35.250128	STOP-3
Stop-5 Road 31 at Morag Quarry	*Calcite-spurrite rocks with green and white hydration veins: Arad Marble (Unit KuPh2)*	31.23529	35.25182	STOP-4
Stop-6 Wadi Morag and Gurim anticline hill	*Brown to black hard rocks crisscrossed by numerous hydration veins (UnitPh3,4)*	31.23640	35.26346	STOP-5
Stop-7 Desert walking trail	*Extremely weathered limestone forming soft terrains (weathered Ghareb Fm.)*	31.22872	35.25315	STOP-6
Stop-8 Roten Amfort Plant	*Phosphatic soft limestone collected from phosphate mining plant (Lower Member of Ghareb Fm.)*	31.11490	35.190171	STOP-7
	2nd Trip			
Stop-9 Mt. Ye'elim	*Hard, black and fine-grained rocks with brown and white hydration veins (KuPh4)*	31.242633	35.278923	STOP-8

Table 5.1 – Locations of stops during the field trip in the Hatrurim basin with a brief description of rocks.

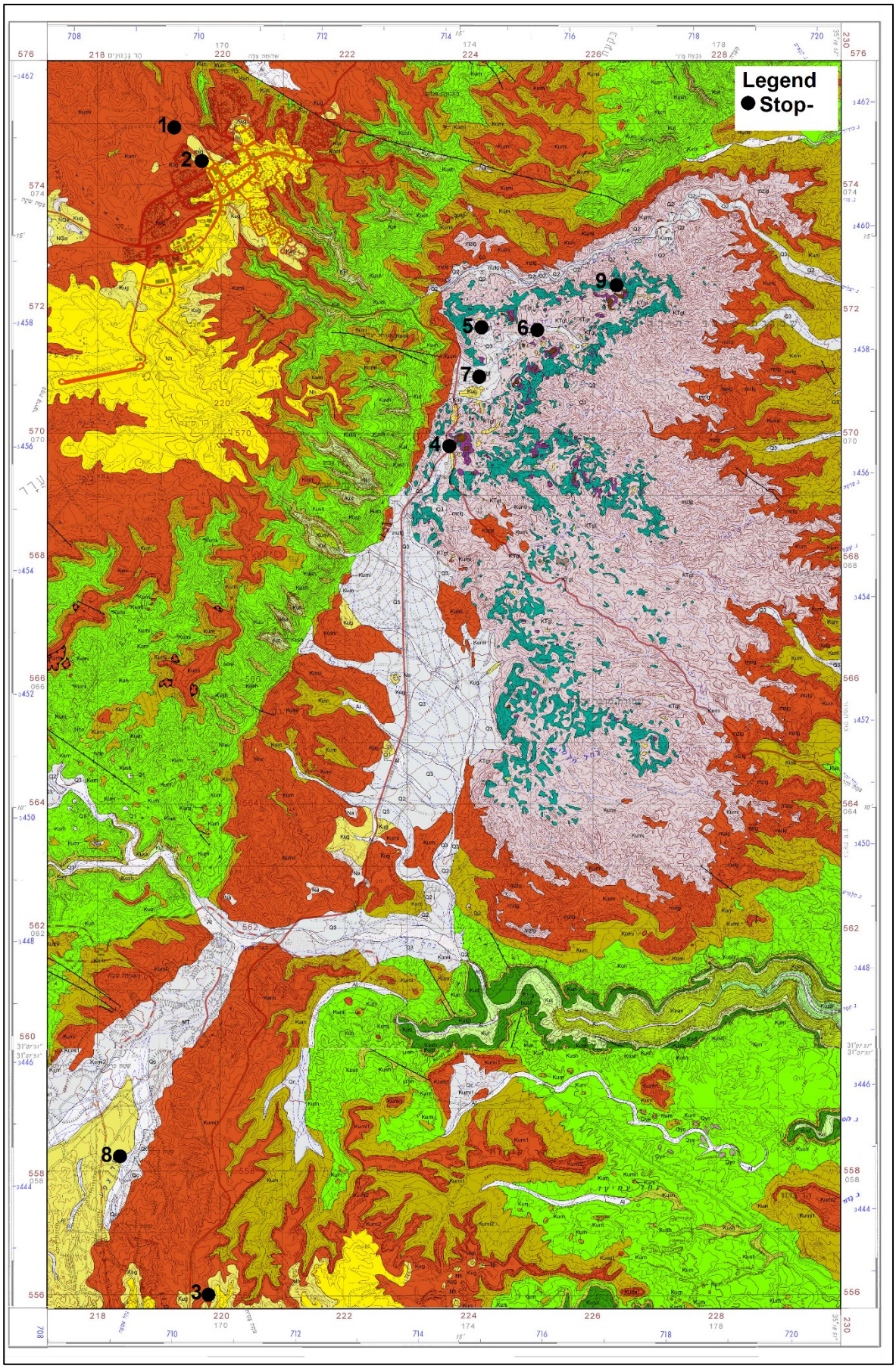

Fig. 5.1 – Field trip stops plot on the Geological Map (scale 1:50’000) [104,105].

5.1 – Stop-1

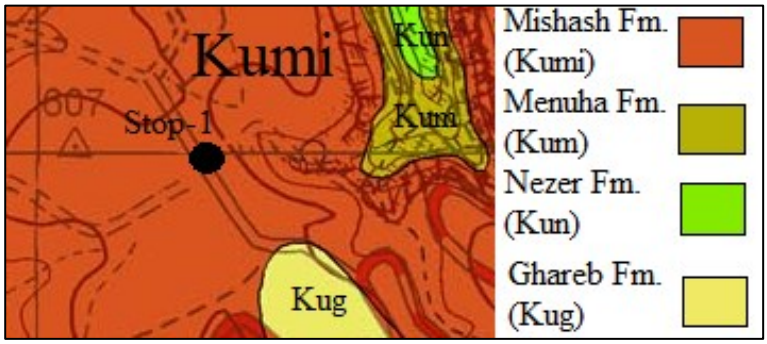

Fig. 5.2 – Geological Map (1:50'000 [104]) reporting the sampling location of Stop-1 in the northern part of Arad city where crops out Mishash Fm.

This stop is located in the northern part of Arad city, close to Hatsfoni Park, where is exposed the unmetamorphosed sedimentary sequence of the upper part of Mishash Formation (Upper Member, Phosphate Series Member): an alternation of black chert layers of 5-20 cm and soft limestone or porcellanite ranging from 5-40 cm thick. Sometimes within soft stratified limestone and porcellanite rounded nodules of hard limestone up to 50 cm diameter occur. Limestone rich parts of this formation form hummocky landscape (Fig. 5.4), whereas porcellanite horizons, chert layers and concretions are better preserved. The dip of geological strata varies from sub-horizontal to N45°/25°; moreover, sometimes strata is undulated and changes in thickness. The outcrops are in good agreement with the sedimentary description of Burg [13], but no clear evidences of high-grade phosphatic layers and the lack of the ~1 m thick condensed layer (see section 4.1.1) [106,114,137], which the latter represents a clear marker horizon between Mishash Formation and Ghareb Formation. Considering the thickness of the entire Mishash Formation (for anticline locations is 40-45 m [106]), the geological map (Fig. 3.1) and features of Ghareb Formation (see section 3.2.1), the boundary between Mishash and Ghareb Formation should be in the upper part of the outcrop reported in Fig. 5.4, above the 15 cm thick chert layer in the middle.

Fig. 5.3 – Eastern view of Stop-1, highlighting the stratigraphic position of Lower Member of Mishash Formation (Chert Member) by the occurrence of black chert layers.

Fig. 5.4 – Upper Member (Phosphate Member) of Mishash Formation, consisting of phopshatic porcellanite and phosphatic limestone with several hard limestone nodules.

5.2 – Stop-2

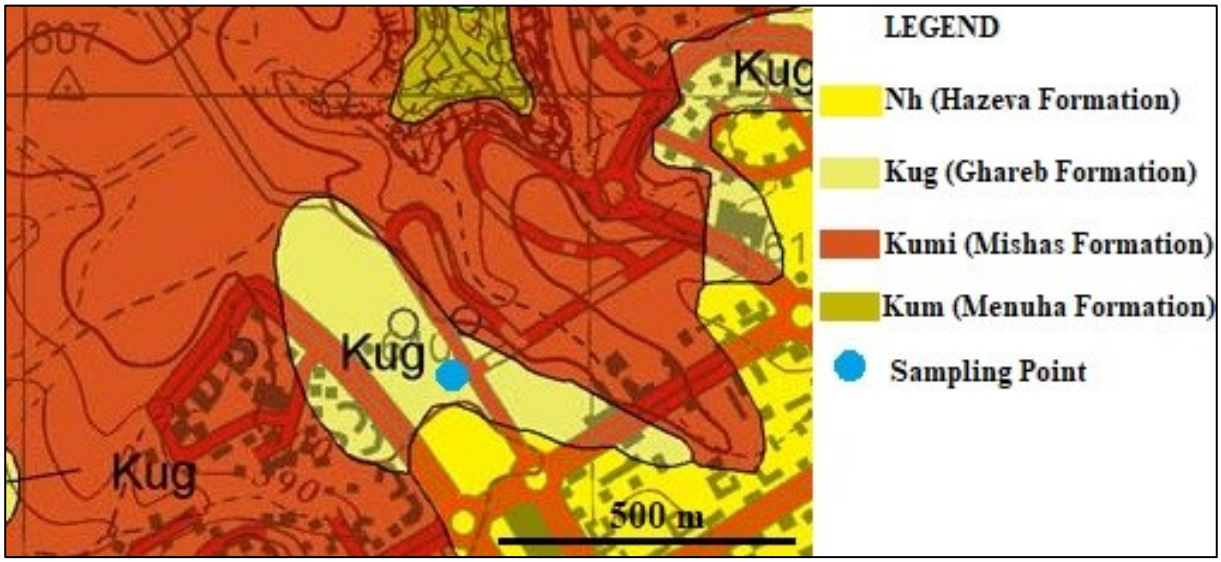

Fig. 5.5 – Geological Map (1:50'000 [104]) reporting the sampling location of Stop-2 in the northern part of Arad city where crops out weathered Ghareb Fm.

This stop is located approximately 300 m toward SW from Stop-1 on the west side of Yerushalayim Street (Fig. 5.5). Outcrops belong to Lower Member of Ghareb Formation, they are little and extremely weathered forming hummocky landscape (Fig. 5.6): poor bedded limestone, completely altered in soft and light calcareous sand, with several hard limestone pebbles (up to 50 cm) which remain unaltered. No evidence of bitumen, probably due to the intense weathering and oxidation processes. In some parts of the outcrops the dip of strata is clear and ranging from sub-horizontal to N12°/15°. There isn't a clear contact between the Lower Member of Ghareb Formation and the upper part of Mishash Formation, probably because of the very pervasive weathering.

Fig. 5.6 – Lower Member of Ghareb Formation intensely weathered, forming a hummocky landscape partially covered by small bushes; occurrence of dense lenticular-shaped hard fine-grained limestone.

5.3 – Stop-3

This stop is located on the road from Arad to Mezad Tamar (road 258) after passing the river Nahal Heimar. This location permits to get an overview of the entire Hatrurim Basin observing it from the south, from west to east are highlighted: Zohar anticline, where Turonian and Campanian sedimentary rocks are exposed; Gurim anticline, which is bordered by Morag and Hatrurim syncline on the west and east flank respectively (Fig. 5.7). Black layers place the top of the Mishash Formation, which represents the “Bake-Line” [28]: the stratigraphic position of the lower part of Hatrurim Formation (Fig. 5.8).

Fig. 5.7 – Overview of the Hatrurim Basin from the southern part close to Rotem Amfort mining plant.

Fig. 5.8 – Overview of the Hatrurim Basin from the southern part, close to Rotem Amfort mining Plant, observing toward east; the Bake-Line is highlighted by the black layers representing the heated upper part of Mishash Formation.

5.4 – Stop-4

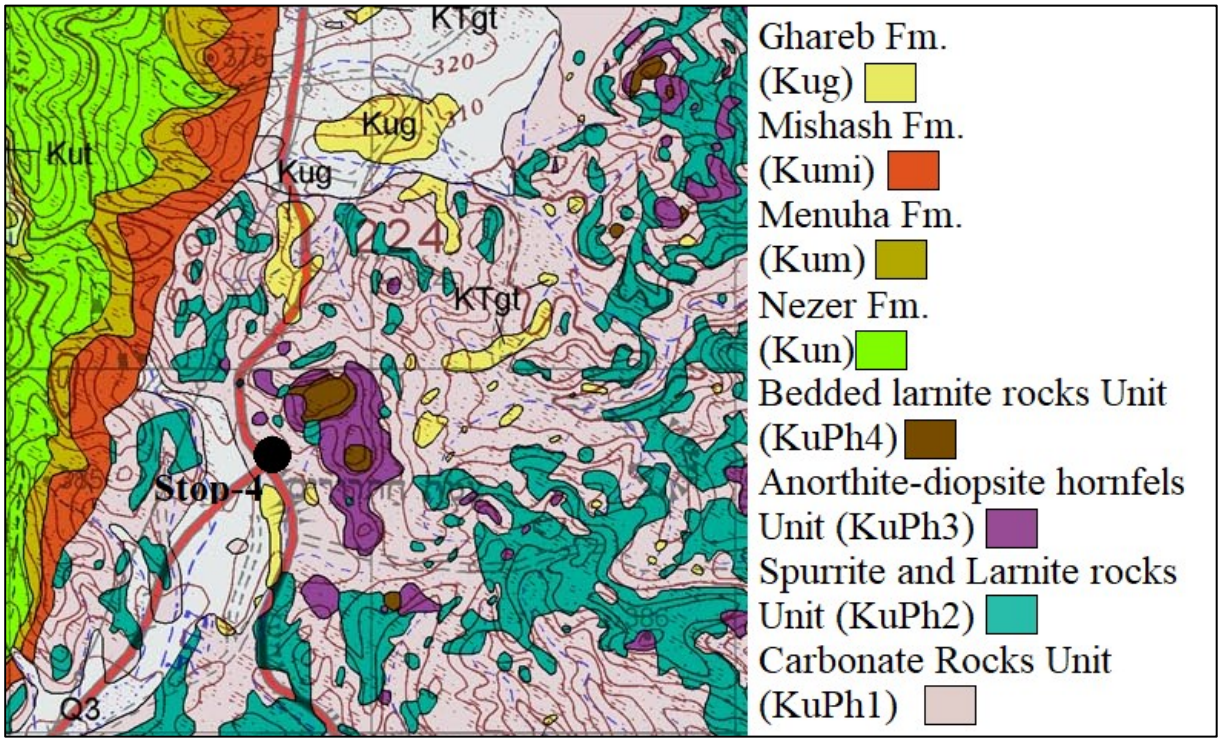

Fig. 5.9 – Geological Map (1:50'000 [104]) reporting the sampling location of Stop-4 at Hatrurim Junction where crops out well preserved outcrops of CP rocks.

This stop is located on the Hatrurim crossroad, also called Hatrurim Junction, where the road 31 from Arad to Neve Zohar crosses the road 258 to Nahal Heimar. In this location there are two main conical hills (~ 380 m) belonging to Gurim anticline, which are separated by a little saddle (Fig. 2.4a). These hills are mainly covered by slope quaternary deposit from the bottom to the half of the hills, whereas Hatrurim Formation rocks crop out only in the upper part. Top hills are composed of brown to dark-brown, hard, homogeneous and fine-grained rocks (anorthite-diopside hornfels) belonging to Unit KuPh3 with light brown to white weathering colour surface (Fig. 5.10,11). In addition, centimetric ferruginous nodules with dark brown millimetric rim are widespread (Fig. 5.12a,b). No evidence of rocks belonging to Unit KuPh4, despite this unit is reported on the geological map. 8 m below the top hills, gehlenite-wollastonite hornfels rocks (Unit KuPh3) crop out: rocks are greenish on fresh fracture and reveal dark brown to black weather colour surface. The contact between different metamorphic grades inside Unit KuPh3 is not constant and seems to be an irregular transition surface. Gehlenite-wollastonite dense olive rocks are composed of dark-green parts, varying in size from a few millimetres to centimeters, separated by a light matrix composed of retrograde minerals (Fig. 5.13a,b). These retrograde minerals have coarser grain size respect to prograde metamorphic minerals and sometimes exhibit a druse structure (Fig. 5.13b). There is a millimetric green transition between dark-green dense parts and the light matrix (Fig.5.13a), suggesting a reaction boundary between them.

Fig. 5.10 – Overview of the Hatrurim Junction toward NE where Hatrurim Formation crops out on the top of two conical hills.

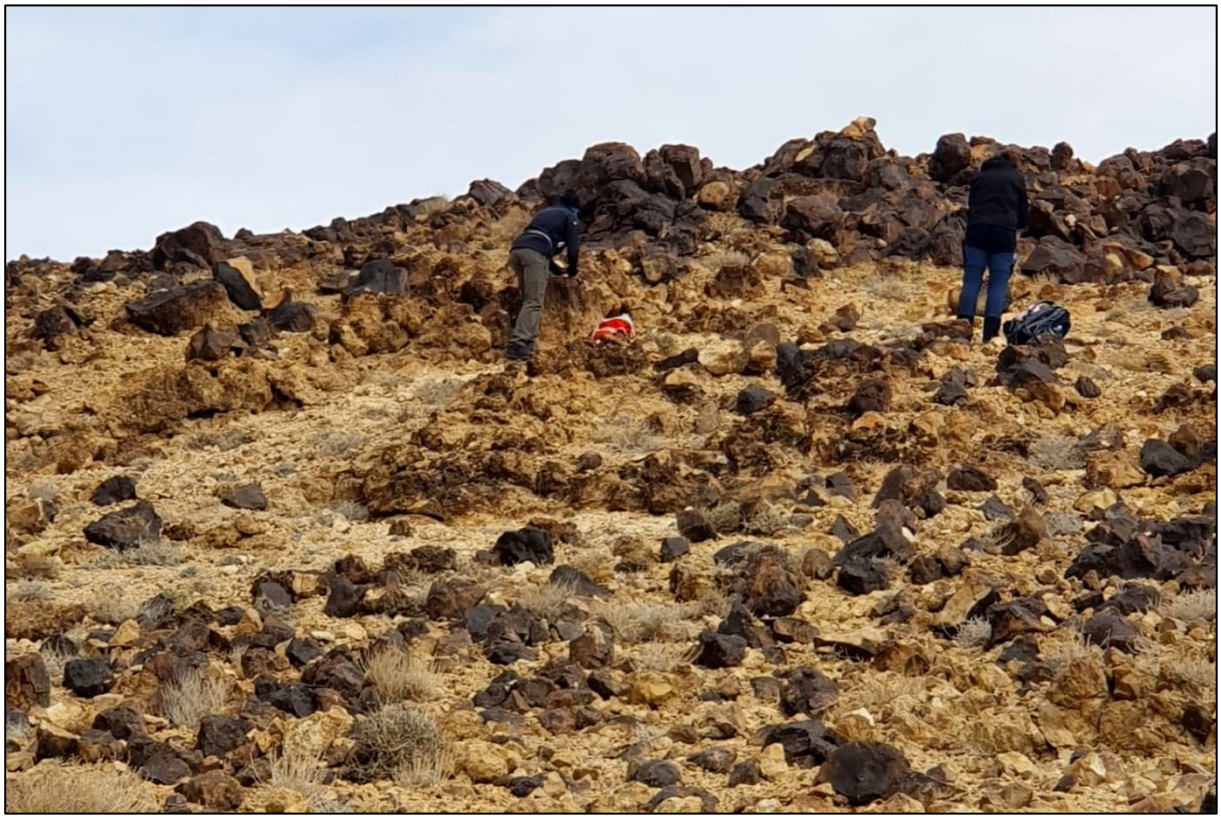

Fig. 5.11 – Outcrops of high-grade dense and medium-grade porous olive rocks (Unit KuPh3) which are characterized by dark-brown and yellow weathered colour, respectively.

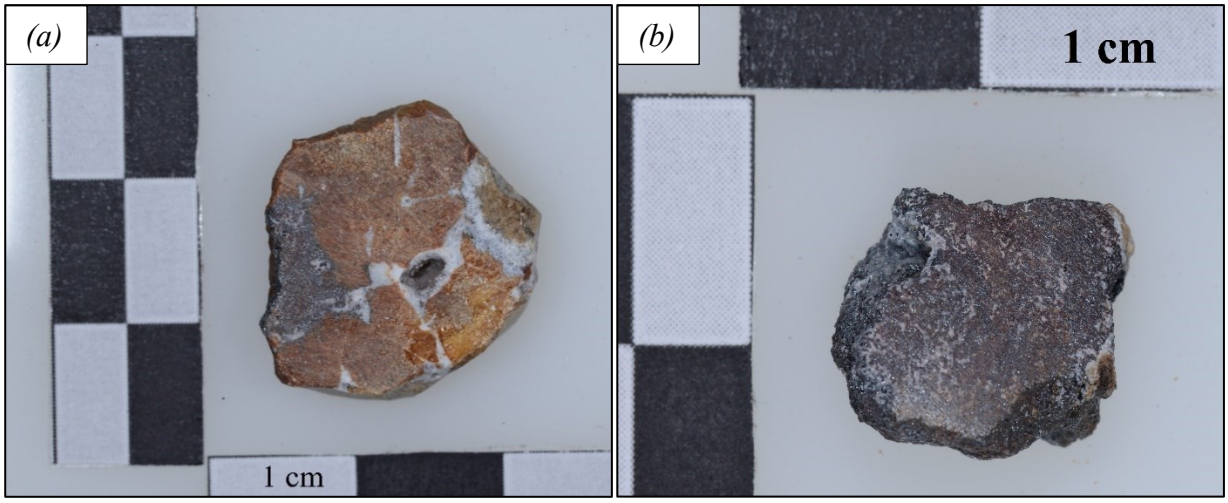

Fig. 5.13 – Anorthite-wollastonite hornfels (high-grade dense olive rocks, Unit KuPh3) (a) highlighting the microstructure composed of brown parts separated by a white millimetric veins and some metallic nodules; (b) details of a centimetric metallic nodule made of magnetite and hematite.

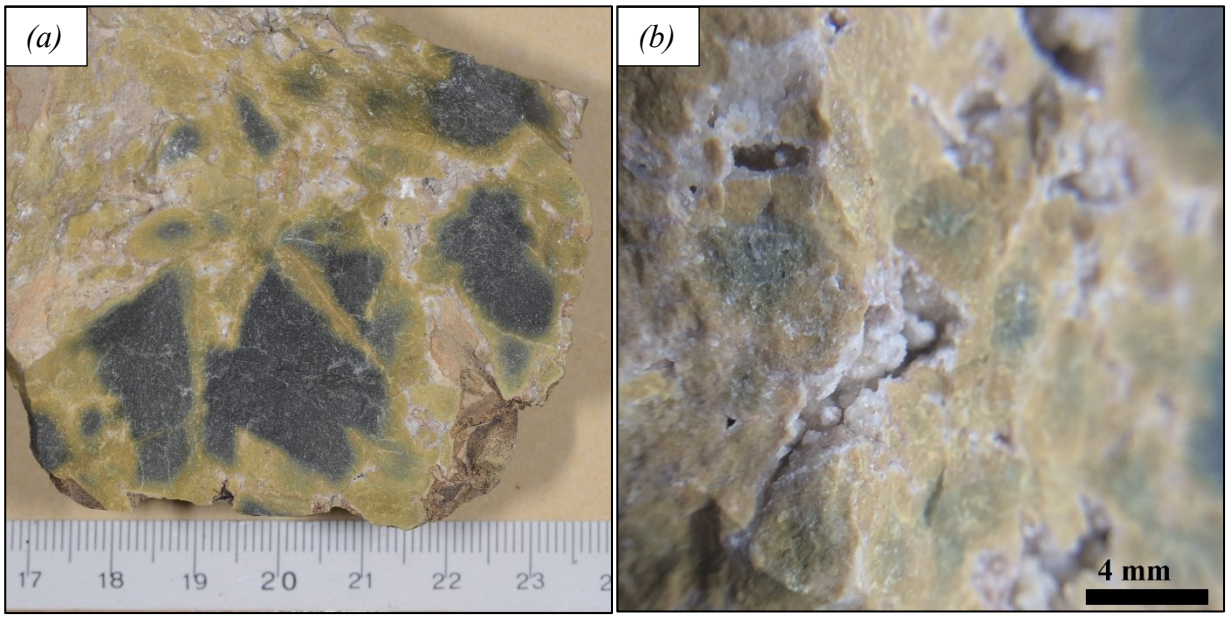

Fig. 5.13 – Gehlenite-wollastonite rock (Unit KuPh3) (a) details of the internal structure composed of dark green centimetric parts separated by a light green less dense matrix in which can occurs voids filled by crystals; (b) enlargement of a void filled by white crystals.

5.5 – Stop-5

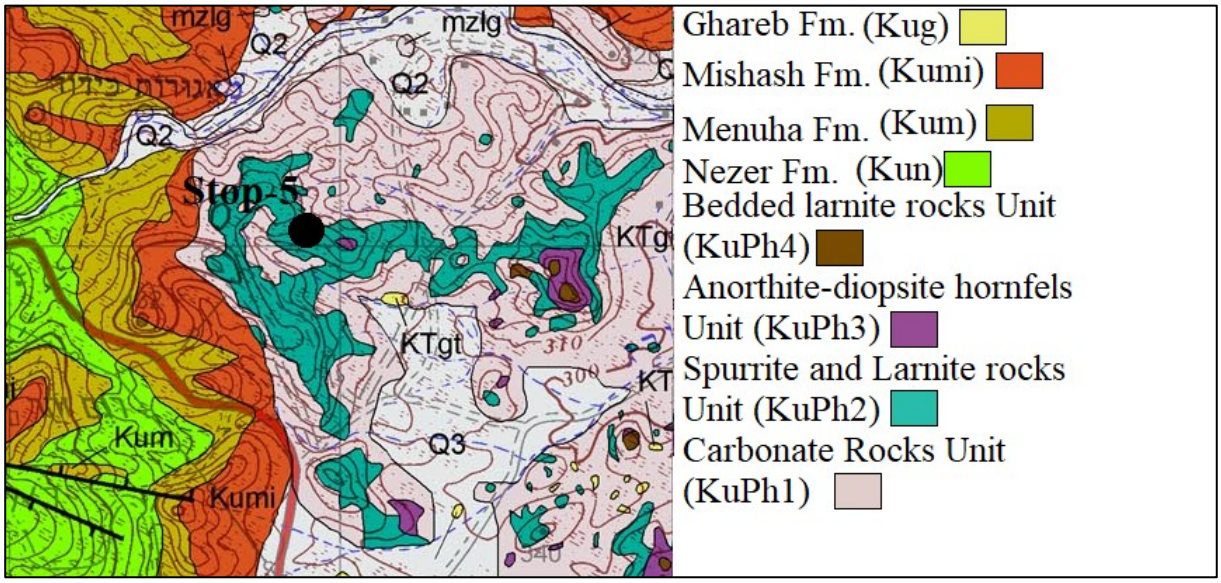

Fig. 5.14 – Geological Map (1:50'000 [104]) reporting location of Stop-5 at the abandoned Arad Marble quarry, where crops out well preserved outcrops of KuPh2 rocks.

This stop is located around 1 km north from previous stop-4 along a wide walking trail that starts from road 31 and leads to a hill surrounded by two wadi channels (Fig. 5.14). This area represents an abandoned quarry of "Arad Marble", which is a dimension stone widely used for popular floor tiles. In fact, several rock blocks from 40 cm to 2 m in diameter commonly occur, which are strictly related to human activity (Fig. 5.15). Outcrops are small and mainly clustered on the top of hill, whereas the other parts are covered by chaotic blocks, probably related to caving activity and slope quaternary deposit (Fig. 5.16). Outcrops are composed of mainly calcite-spurrite marble subunit belonging to Unit KuPh2: dark-grey, homogeneous, fine grained, dense and hard to break rocks composed of calcite and spurrite (Fig. 5.17,18). Furthermore, it is also frequently crisscrossed by white and green veinlets (Fig. 5.18). The weathering surface colour is light brown to light-yellow (Fig. 5.17).

Fig. 5.15 – An overview from the base of the "Arad Marble" quarry hill along the walking trail, highlighting the occurrence of several rock blocks related to quarry activity.

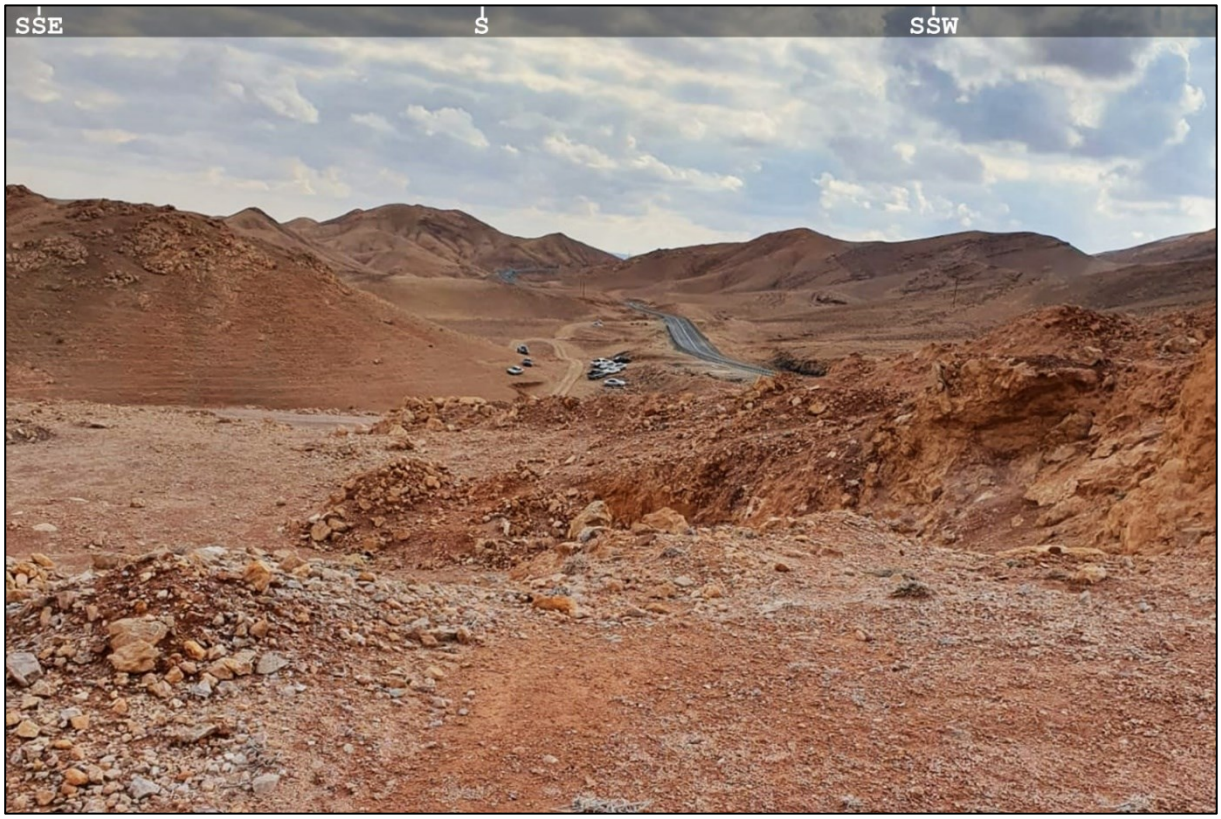

Fig. 5.16 – An overview from the top of the hill where are exposed small outcrops of Unit KuPh2.

Fig. 5.17 – A block of larnite-gehlenite-spurrite rock with white surface colour, black colour on fresh fracture, very hard to break, homogeneous and crisscrossed by numberless light veinlets without preferred orientation.

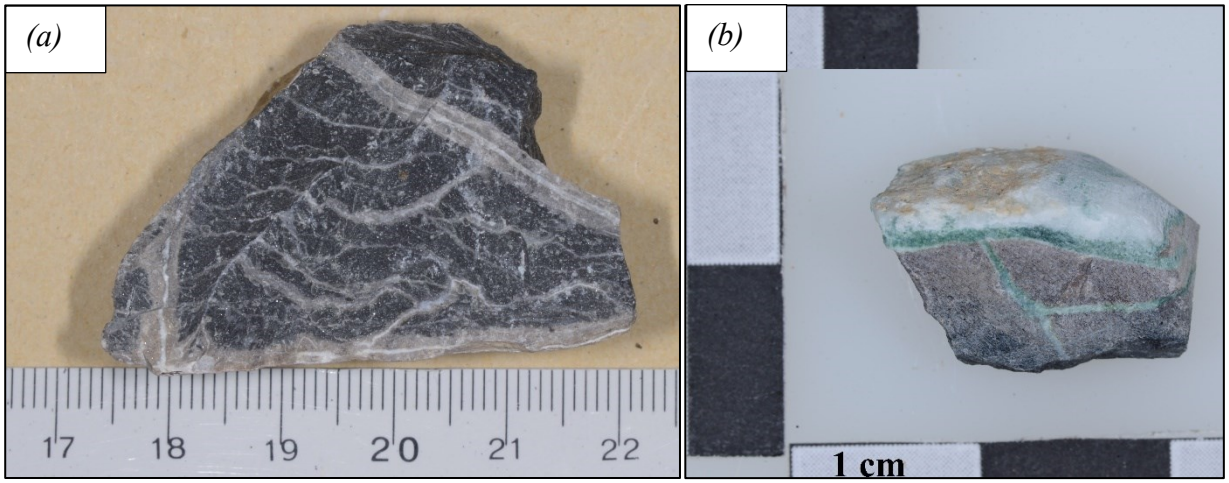

Fig. 5.18 – Calcite-spurrite rock samples composed of hard, fine grained dark parts crisscrossed by millimetric veinlets ranging from (a) light grey to (b) green.

5.6 – Stop-6

STATION	SHORT DESCRIPTION	N (°)	E (°)	GOOGLE MAPS LINK
Stop-6.1 Wadi Morag top	*Lower part of Hatrurim Formation*	31.23562	35.27070	STOP-6.1
Stop-6.2 Wadi Morag base	*Outcrops of Unit KuPh1 and pseudoconglomerates*	31.23291	35.26989	STOP-6.2
Stop-6.3 Gurim Anticline top hill	*Outcrops of bedded larnite rocks unit close to the top of the hill*	31.23356	35.26682	STOP-6.3

Table 5.2 – Positions of relevant geological features belonging to Stop-6.

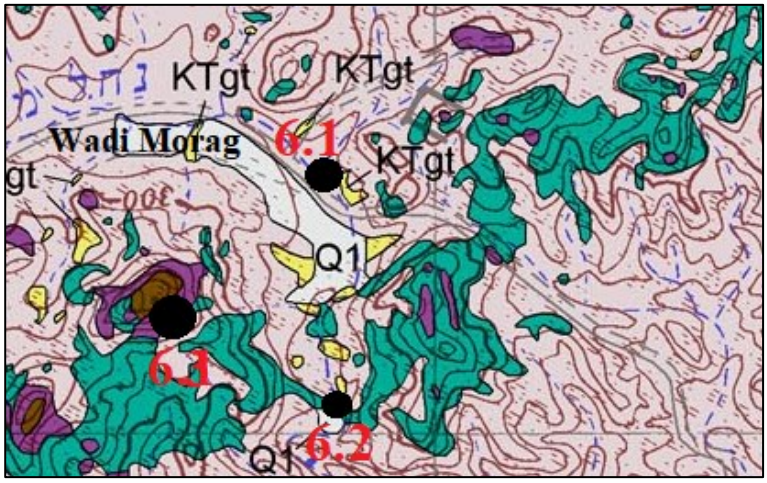

Fig. 5.19 – Geological Map (1:50'000 [104]) reporting location of Stop-6.

This stop is located 1.5 km east from the base of the previous hill, along the walking trail parallel to Wadi Morag, also called Nahal Morag (Fig. 5.19). Following the Wadi Morag toward SE, several outcrops of Unit KuPh1 are exposed: a mixture of low-grade and retrograde metamorphosed carbonates; considering the stratigraphic position, they should be related to the CP of Ghareb Formation (Fig. 5.20). Low-grade metamorphosed carbonates are fine grained, heterogeneous in hardness and porosity with locally a slight recrystallization. Retrograde metamorphosed carbonates are mainly represented by pseudoconglomerates, which occur as rounded to elliptical pebbles, with brown to light-purple colour on fresh fracture both crisscrossed by numerous white little veinlets and surrounded by a light coloured and soft matrix (Fig. 5.21,22).

Close to Wadi Morag channel toward west a hill of Gurim anticline occurs in which crops out Unit KuPh3,4 (Fig. 5.23). This conical hill reveals important features of the upper part of Mottled Zone Complex (Fig. 5.24). In the upper half part of the hill, approximately at 340 m, Unit KuPh3 crops out with its typical black weathered colour and slight bedding as occurred at Stop-4; low-grade olive rocks appear mainly in bottom part, while medium-grade porous olive rocks and high-grade dense olive rocks crop out the middle and the upper portion of this layer, respectively. Black scoriaceous rocks occur within the upper portion of Unit KuPh3. Moreover, elongated ferruginous concretion with black colour, metallic lustre and centimetric diameter are commonly found in high-grade dense olive rocks.

Above the Unit KuPh3, Unit KuPh4 crops out with a clear bedding (Fig. 5.24-27), especially close to the top of the hill. Several beds with black weather surface colour, variating in thick from 5 to 15 cm, dense, homogeneous and hard with olive colour in fresh surface occur only close to the transition between the transition between Unit KuPh3 and Unit KuPh4. These rocks are very similar to high-grade dense olive rocks, but with a very prominent bedding respect to olive rocks that occur below. This stratigraphic position should be related the transition between the Upper Member of Ghareb Formation and Hafir Member (Taqiye Formation). Above this stratigraphic position, Unit KuPh4 appears with its common features: hard to break, dense, fine grained, black to brown fresh colour surface, light-yellow to light-brown on weathered surface and crisscrossed by numberless light veinlets. Strata has a dip from subhorizontal to 350-10°N/25°. In details, calcite-spurrite rocks are composed of: (i) black portions made of mainly calcite and spurrite and minor brownmillerite, larnite, mayenite and fluorapatite, representing the prograde metamorphic part (Fig. 5.28a); (ii) light-brown rounded parts are made of jennite, ettringite, apophyllite, secondary calcite, brucite, katoite and minor spurrite and brownmillerite; (iii) white submillimetric veins composed of secondary calcite, ettringite, jennite and minor aragonite and katoite (Fig. 5.28b). These bedded rocks are related to the CP of Hafir Member (Ghareb Formation) because the latter represents the stratigraphic unit which has a well pronounced bedding.

Fig. 5.20 – Overview of Wadi Morag toward *SE* at Stop-6.1, highlighting several outcrops of Unit KuPh1 on the flanks of the channel.

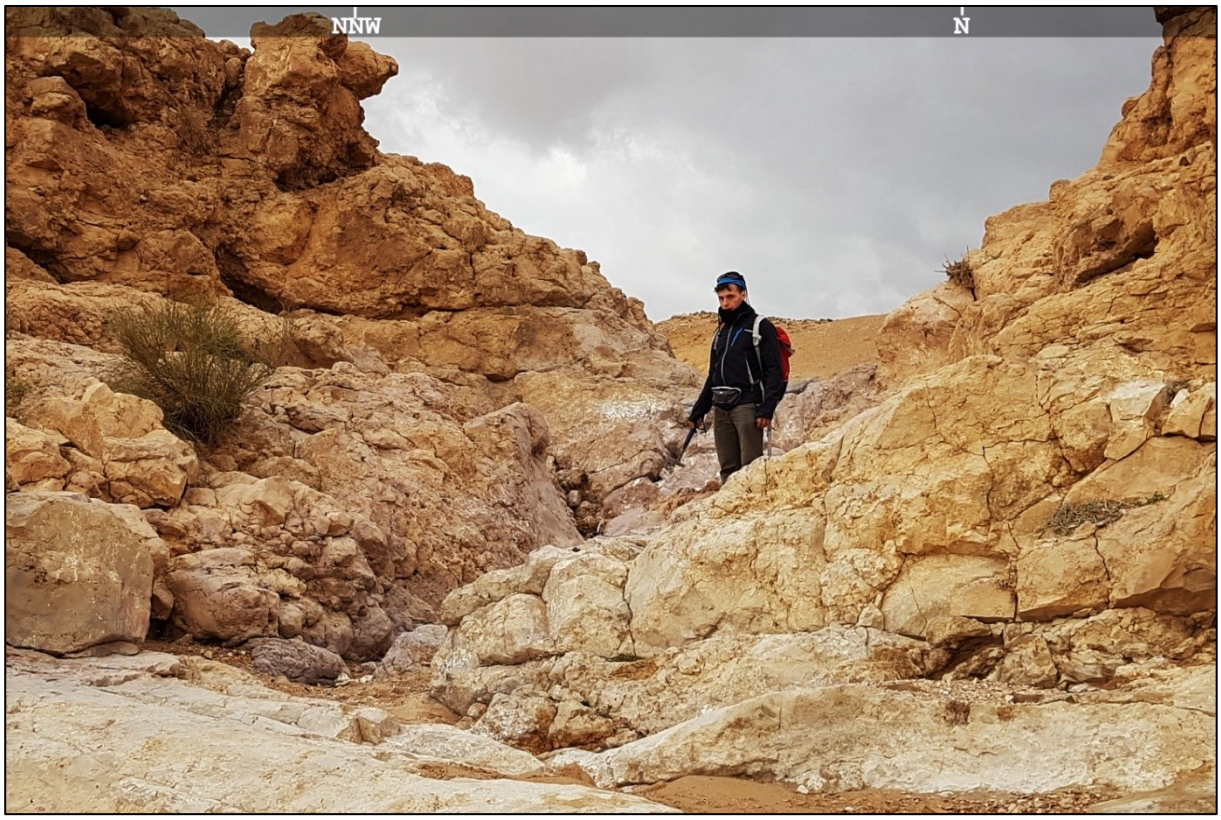

Fig. 5.21 – The main outcrop in Wadi Morag where retrograde and low-grade carbonates occur.

Fig. 5.22 – Pseudoconglomerates of Unit KuPh1 in Wadi Morag; dark purple centimetric elongated pebbles of high-grade metamorphic rocks (larnite-rich rocks) are crisscrossed by numerous withe veinlets.

Fig. 5.23 – Conical hill on the west of Wadi Morag, where is exposed the upper part of Hatrurim Formation starting with Unit KuPh3 from the upper half of hill, highlighted by the black layers, and Unit KuPh4 close to the top.

Fig. 5.24 – Outcrop close to the base of Unit KuPh4 (Stop-6.3), where a sequence of bedded centimetric layers of olive rocks (gehlenite-wollastonite hornfels with dark weathered colour) and calcite-spurrite marble (light weathered colour layers) crop out, belonging to Unit KuPh3 and Unit KuPh4, respectively.

Fig. 5.25 – The top of the hill on Gurim Anticline where thick bedded calcite-spurrite marble crops out with light-yellow weathered surface and black to brown colour on fresh fracture.

Fig. 5.26 – An overview from the hilltop toward NE viewing the Wadi Morag channel and the Mt. Ye'elim.

Fig. 5.27 – Bedded calcite-spurrite marble (350-15°N/15-25°) of Unit KuPh4 on the top of the hill.

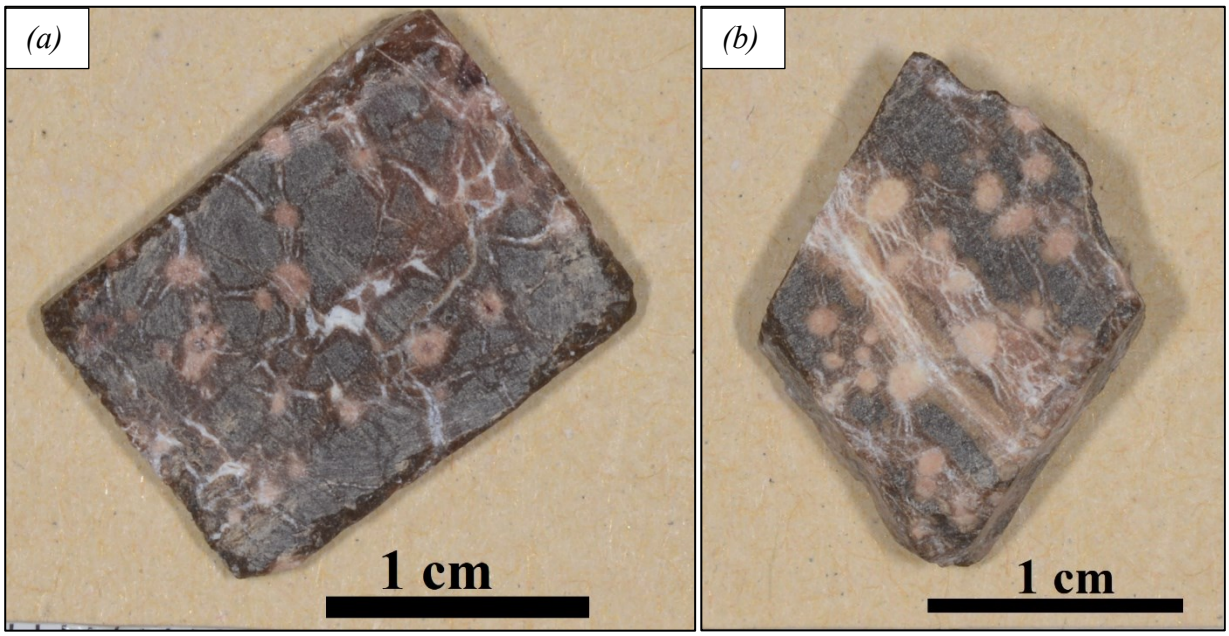

Fig. 5.28 – Bedded calcite-spurrite marble sample (Unit KuPh4) highlighting the texture made of (a) black parts (calcite, spurrite and minor brownmillerite) related to prograde metamorphism and light-brown rounded elements (jennite, ettringite, calcite and brucite) and (b) white submillimetric veins (calcite, jennite, ettringite and minor aragonite).

5.7 – Stop-7

Return to the main road and head toward south on road 31 for ~ 300 m and take the left on the off-road toward east (Fig. 5.29). Several metric outcrops of Ghareb Formation occur, but rocks are extremely weathered. In this location, Ghareb Formation occurs with poor bedding, light colour, very soft and without hard nodules as saw in Stop-2 (Fig. 5.30).

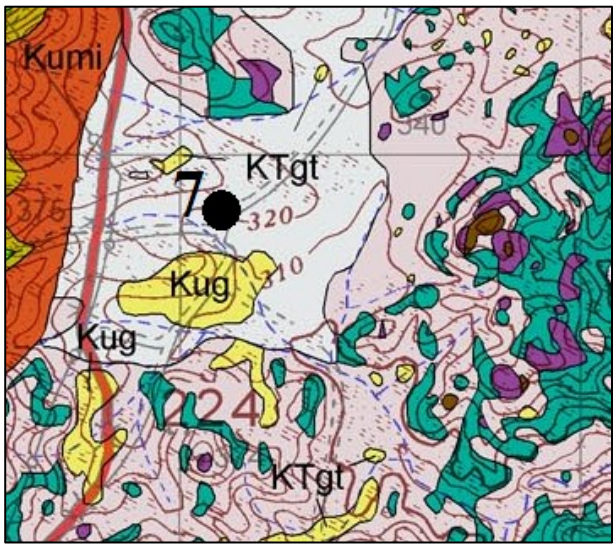

Fig. 5.29 – Geological Map (1:50’000 [104]) reporting location of Stop-7.

Fig. 5.30 – Outcrop of weathered Lower Member of Ghareb Formation close to a wadi channel.

5.8 – Stop-8

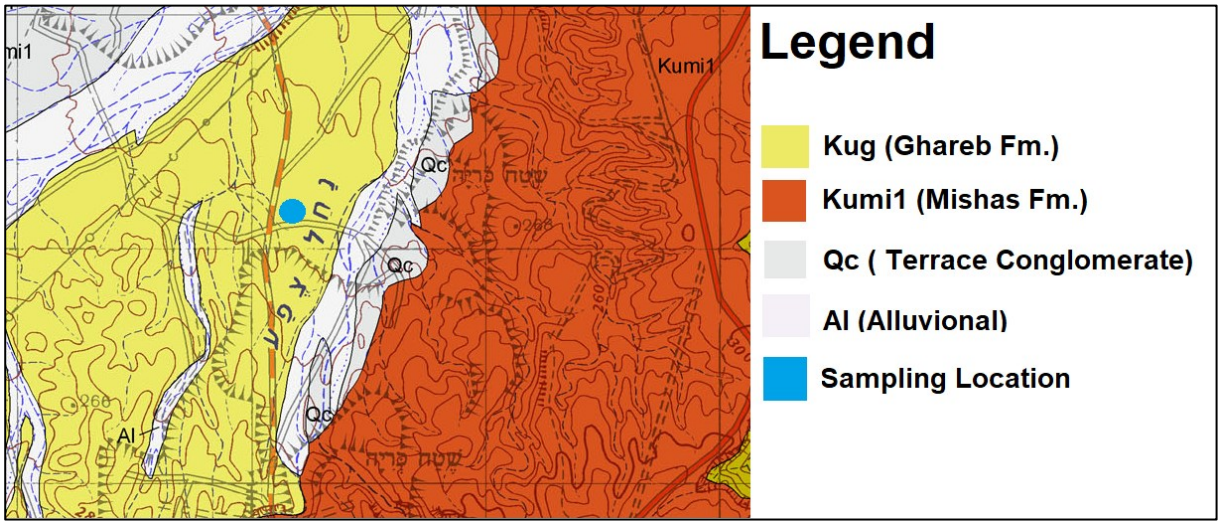

Fig. 5.31 – Geological map (1:50’000 [105]) reporting with a blue circle the location of sampling in the Rotem Amfort Plant.

Return to road 31 and head for Rotem Amfort mining plat along road 258 (Fig. 5.31). This mining plant caves Phosphate Series Member of Mishash Formation and there are several vertical cross sections where fresh Lower Ghareb Formation is exposed (Fig. 5.32,33). This bottom part of Ghareb Formation is frequently rich in organic content as bitumen (Fig. 5.32). There is an increase in thickness of strata from the bottom to the top Lower Member of Ghareb Formation, but bedding is more evident in the former and the dip is usually subhorizontal (Fig. 5.33). This lower part of Ghareb Formation is made of phosphatic- and gypsum-rich limestone, very soft and easily weathered.

Fig. 5.32 – Overview of Rotem Amfort mining plant highlighting dark-grey outcrops of Ghareb Formation rich in bitumen and the following bitumen-free light-yellow chalky parts.

Fig. 5.33 – Vertical cross section in Rotem Amfort mining plant, where is exposed the Lower Part of Ghareb Formation rich in bitumen, representing the grey to black lower portion, whereas the light-yellow upper portion represents the chalky part.

5.9 – Stop-9

On the western part of Arad city take the walking trail starting from Keden Street and head for south since Wadi Ye'elim, also called Nahal Ye'elim, passing through Nahal Pra'im. After that, head for east for east for 1 km, passing through the Beduin Village, and take the main watershed at the base of Mt. Ye'elim. This mountain is one of the highest mountain in Negev Desert and has an SW-NE elongated shape, with *SE* flank steeper than NW one, where streams head to Wadi Ye'elim and to Wadi Morag, respectively. Geological features of Hatrurim Formation are quite the same saw stop-6, excepted for a less clear bedding of KuPh4, but with wider outcrops. Moreover, decacentimetric blocks with black to brown colour on fresh surface, very dense, hard, homogeneous and fine grained are common in the upper part of KuPh4 layer. These blocks are surrounded by a millimetric soft white layer probably related to hydration process. The dip of strata ranging from subhorizontal to 350-15°/15-25° in *SE* and NW flank, respectively.

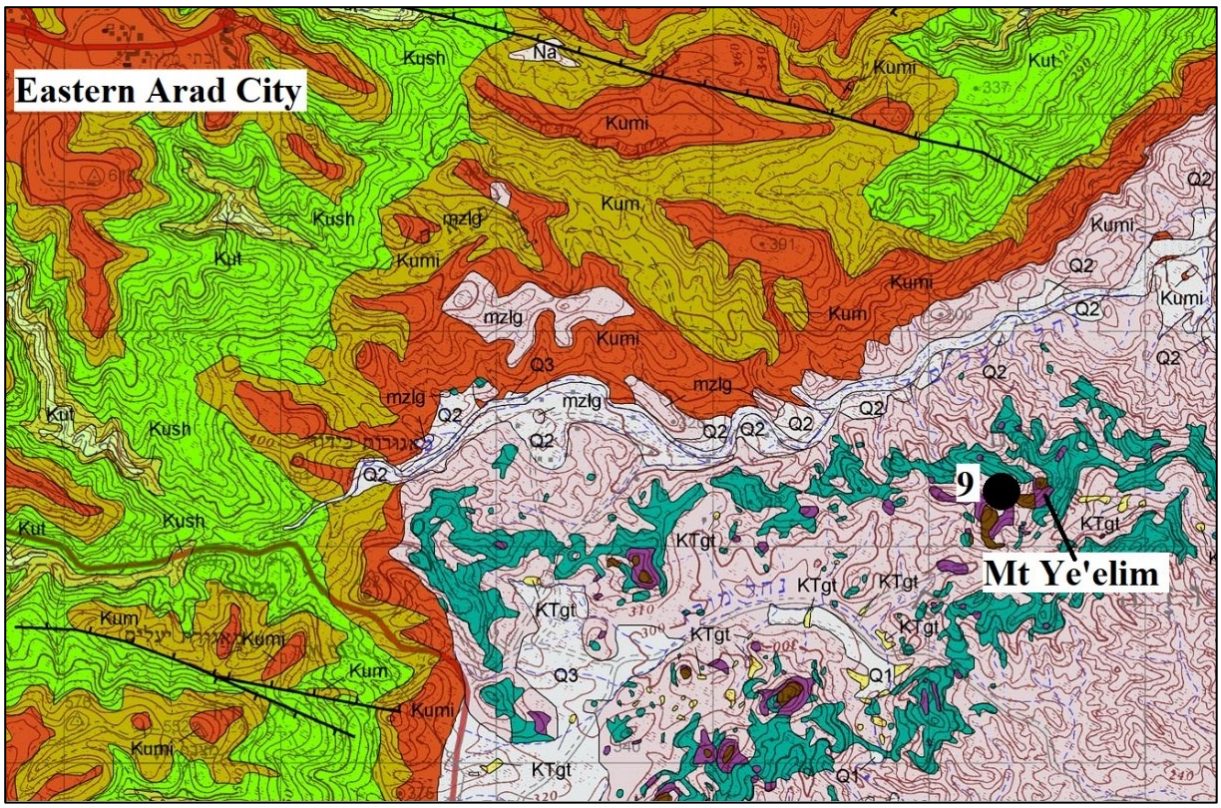

Fig. 5.34 – Geological map (1:50'000 [104]) highlighting the location of Mt. Ye'elim related to Stop-9 of the field trip, in which crops out Unit KuPh4 with larnite rocks.

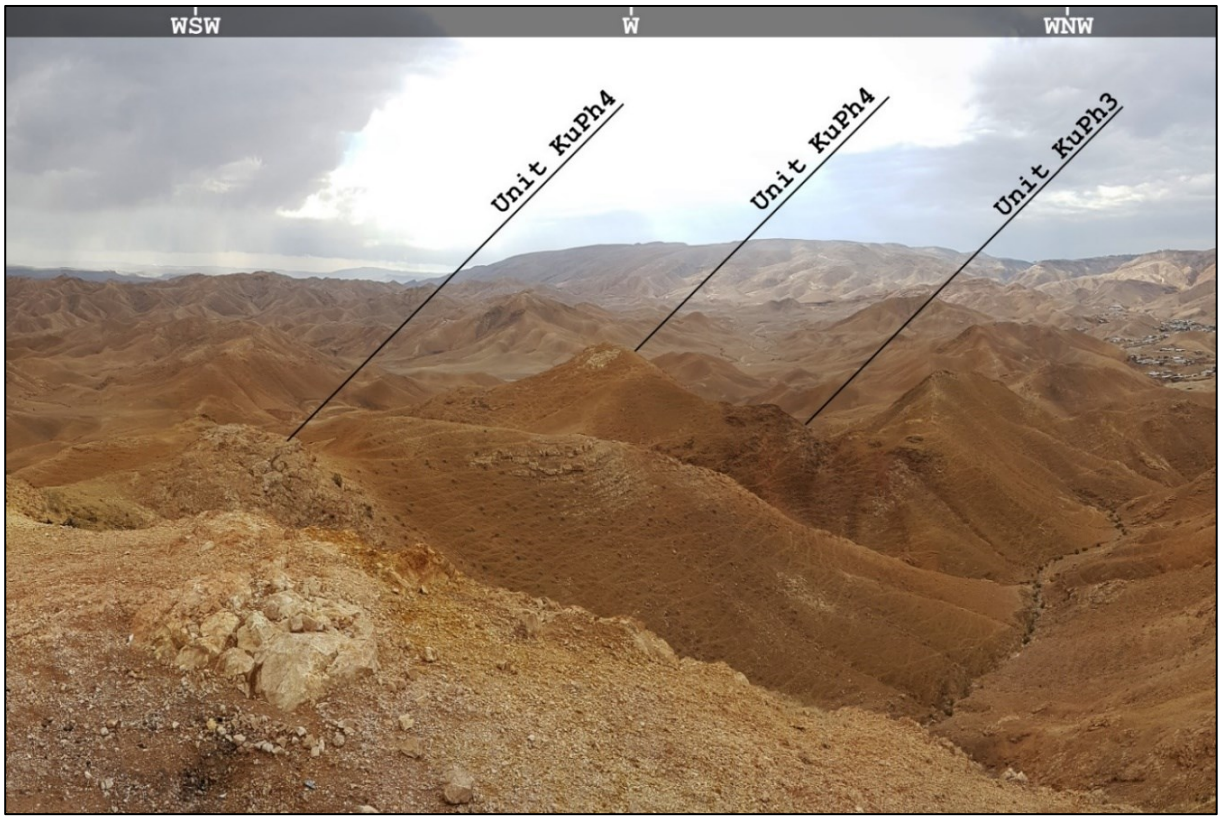

Fig. 5.35 – Overview from the top of Mt. Ye'elim toward west, viewing outcrops of Unit KuPh4 and KuPh3, which is recognized by the black colour. On the right of the photo is visible Wadi Ye'elim and faraway the Beduin Village.

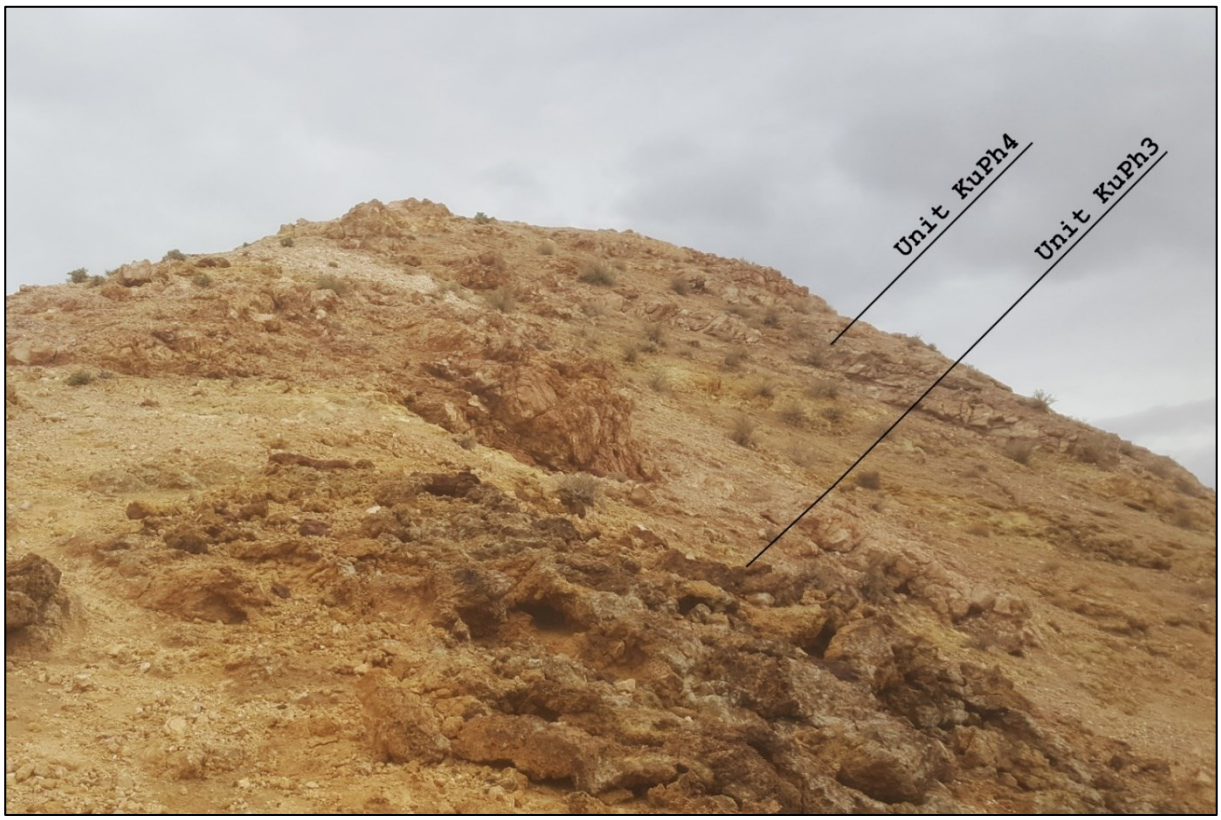

Fig. 5.36 - Eastern flank of Mt. Ye'elim on the half upper part, where anorthite-wollastonite hornfels (Unit KuPh3) at the bottom and bedded larnite rocks (Unit KuPh4) at the top crop out.

Fig. 5.37 – Outcrop on the top of Mt. Ye'elim of larnite rocks (Unit KuPh4), composed of decacentimetric brown fragments surrounded by white to light-yellow retrograde matrix and veins.

Fig. 5.38 – Larnite rocks outcrops on fresh surface with dark colours (anhydrous parts) and retrograde veinlets with light-brown and white layers at the borders and the middle, respectively.

Fig. 5.39 – Details of brown fragments (anhydrous part related to HT event) surrounded by light matrix and often crisscrossed by millimetric white veins, representing the retrograde process.

5.10 – Crystal phase assemblage among field trip rocks

Crystal phases identification was performed by means of LXRPD analysis to identify and recognize mineral assemblage useful to select rocks for further investigation and to compare results with bibliographic ones. Moreover, QPA was performed using the Rietveld method (RQPA) on the XRD patterns, obtaining the wt.% of each occurring crystal phase previously identified.

In Table 5.3 are reported results coming from only sedimentary rocks collected among Stop-1,2,8, highlighting calcite as the main crystal phase followed by apatite, quartz and gypsum. Whereas, in Table 5.4 RQPA results are reported only for CP rocks revealing a wide range of mineral assemblages depending on the position within the metamorphic sequence, texture and if secondary process occurred (e.g., larnite pseudoconglomerates, calcite-spurrite rocks, etc.). Larnite-rich rocks occur only in two locations (Stop-9 and 6) which they represent locations of HT combustion (> 1000 °C).

$Minerals/_{Stops}$	***Stop-1***	***Stop-2***	***Stop-8***
Calcite $(CaCO_3)$	*76*	*75-95*	*78*
Quartz $(\alpha\text{-}SiO_2)$	*3*	*1-2*	*3*
Apatite $(Ca_5(PO_4)_3(OH,F,Cl))$	*7*	*1-15*	*3*
Kaolinite *($Al_2(Si_2O_5)(OH)_4$)*	*7*	*n.d.*	*4*
Illite *($K(Al,Mg,Fe)_2(Si,Al)_4O_{10}[(OH)_2,H_2O]$)*	*7*	*n.d.*	*<5*
Gypsum *($CaSO_4 \cdot 2H_2O$)*	*n.d.*	*n.d.*	*3-5*
Goethite *($FeO(OH)$)*	*n.d.*	*n.d.*	*<2*
Fluorite *(CaF_2)*	*n.d.*	*<1*	*n.d.*

Table 5.3 – Semiquantitative analysis results for sedimentary rocks by means of XRPD analysis; values are reported in wt.%; n.d., not detected crystal phase.

Minerals / Stops	Stop-4		Stop-5		Stop-6			Stop-9	
	Bulk	Nodules	Bulk	Veins	6.1	6.2*	6.3^	Bulk	Veins
Calcite $(CaCO)_3$	27	11	80	78	78	1	23	-	43
Quartz (SiO_2)	-	1	-	-	1	<1	-	-	-
Aragonite ($CaCO_3$)	-	-	-	13	-	-	-	-	16
Vaterite ($CaCO_3$)	-	-	-	-	-	-	-	-	15
Spurrite ($Ca_5(SiO_4)_2(CO_3)$)	-	-	18	3	-	-	52	-	-
Larnite (β-Ca_2SiO_4)	-	-	-	-	-	62	5	81	3
Gehlenite ($Ca_2Al_2SiO_7$)	38	22	-	-	-	-	-	-	-
Wollastonite ($CaSiO_3$)	24	38	-	-	-	-	-	-	-
Plagioclase ($CaAl_2Si_2O_8$)	11	-	-	-	-	-	-	-	-
Mayenite ($Ca_{12}Al_{14}O_{33}$)	-	-	-	-	-	1	5	3	-
Ye'elimite ($Ca_4(AlO_2)_6(SO_4)$)	-	-	-	-	-	15	-	6	-
Brownmillerite ($Ca_2(Al,Fe)O_5$)	-	-	-	-	-	1	3	1	-
Shulamitite ($Ca_3TiFeAlO_8$)	-	-	-	-	-	3	-	3	-
FluorApatite ($Ca_5(PO_4)F$)	-	-	-	-	2	9	4	3	-
Hematite (Fe_2O_3)	-	16	-	-	-	-	-	-	-
Magnetite ($FeFe_2O_4$)	-	6	-	-	-	-	-	-	-
Spinel ($(Mg,Fe)(Fe,Al)O_4$)	-	-	-	-	-	3	-	3	3
Gypsum ($CaSO_4 \cdot 2H_2O$)	-	-	-	-	2	-	-	-	2
Brucite ($Mg(OH)_2$)	-	-	-	-	-	-	2	-	-
Katoite ($Ca_3Al_2(OH)_{12}$)	-	-	-	-	17	1	1	-	10
Gismondine ($CaAl_2Si_2O_8 \cdot 8H_2O$)	-	2	-	-	-	-	-	-	-
Thomsonite ($NaCa_2Al_5SI_5O_{20} \cdot 6H_2O$)	-	3	-	-	-	-	-	-	-
Ettringite ($Ca_6Al_2(OH)_{12}(SO_4)_3 \cdot 26H_2O$)	-	-	2	3	-	1	3	-	3
Tobermorite ($Ca_5Si_6O_{16}(OH)_2 \cdot 4H_2O$)	-	-	-	2	-	1	1	-	5
Jennite ($Ca_9Si_6O_{18}(OH)_6 \cdot 8H_2O$)	-	-	-	-	-	1	2	-	-

Table 5.4 – Semiquantitative analysis results for CP rocks by means of XRPD analysis and Rietveld analysis; values are reported in wt.%; *pseudoconglomerates; ^rock analysed as a bulk, without separating different portions (white veins, hydrated rounded parts and black portions); - phase below the limit of detection; e.s.d. is below 3% for major phases (≥ 10wt.%) and < 10% for minor phases (< 10 wt.%).

Chapter 6
Cement manufacture

6.1 – Ordinary Portland Cement

Ordinary Portland Cement (OPC) represents the most important and widespread building material used for both traditional constructions and strategical building (damps, tunnels, skyscrapers, nuclear power plants, etc.). This material is made of mainly anhydrous clinker (~ 95wt.%) and minor amount of gypsum (~ 5wt.%), in order to control the setting [7,8]. OPC is classified as a hydraulic binder because when is mixed with water, commonly with a 0.5 water cement ratio, forms a paste that becomes harder over the time: OPC should reach his characteristic strength resistance after 28 hydrations days. OPC is called mortar when is mixed with water and sand; whereas, when more inert occurs is called concrete that could be also reinforced with steel bars (reinforced concrete) as normally occurring in foundations.

Clinker, which represents the main part of cement, is obtained by heating at high temperature (~ 1450 °C) a mixture of limestone and clay, or marls, in a rotary kiln. All the latter raw materials are normally caved from quarries, grinded as fine powders, mixed and chemical controlled. At high temperature during the thermal treatment the raw meal partially melts nodulizing and is completely converted to a mixture of tricalcium silicate (hatrurite, Ca_3SiO_5), dicalcium silicate (larnite, β-Ca_2SiO_4), ferrite (brownmillerite, $Ca_2(Al,Fe)_2O_5$) and tricalcium aluminate (celite, $Ca_3Al_2O_6$), where the calcium silicate part represents ~ 85wt.%. Clinker nodules are grinded and mixed with a natural or synthetic sulphate-bearing source (anhydrite, bassanite or gypsum) obtaining cement.

During the hydration the increase in the mechanical resistance is mainly due to the calcium silicate phases (hatrurite and larnite) that produce an amorphous gel, which is gradually converted into calcium silicate hydrated phases [7,8].

6.2 – World cement production

Nowadays, the global cement production is still increasing mainly because of the continuous population rise, requiring new buildings, and the development of Eastern countries [138]: the global leader in cement production is China followed by India, which their productions represents more than 50wt.% world production from 2002; whereas several countries (Japan, USA, Iran and Turkey) maintained unchanged their production over the years [139,140].

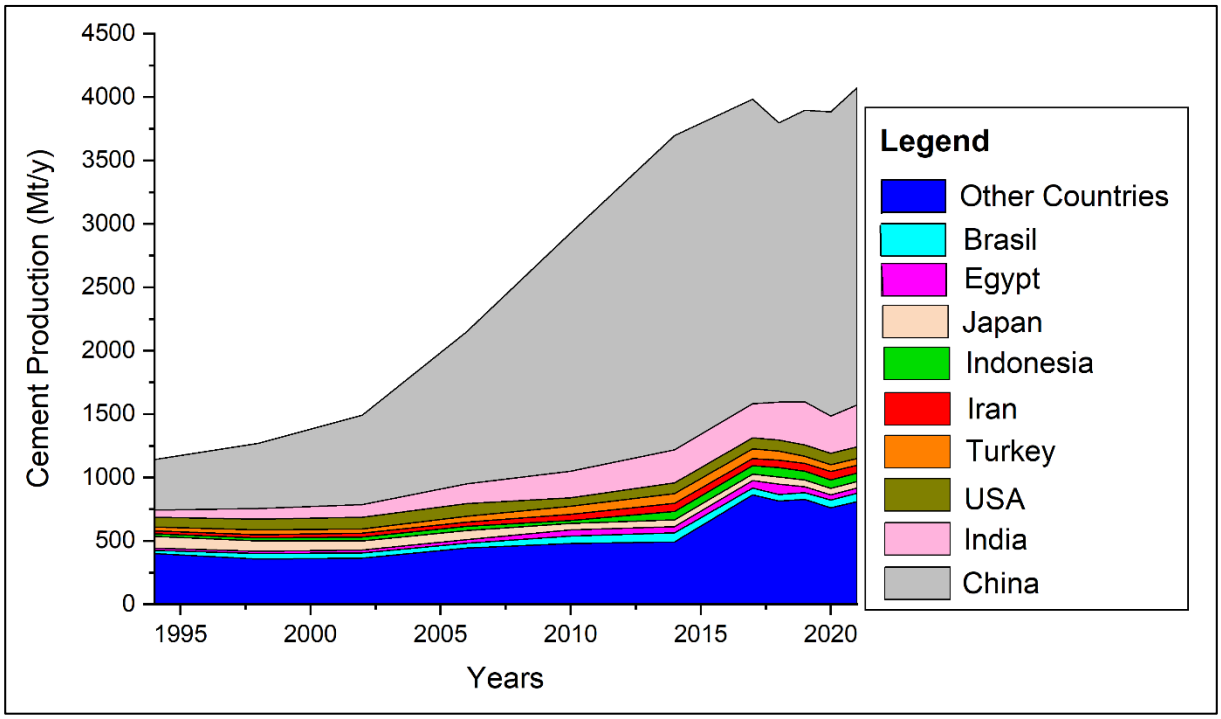

Fig. 6.1 – World cement production between 1994 to 2021 [139].

6.3 – ENVIRONMENTAL SUSTAINABILITY AND *GREEN-CEMENTS*

Global, the cement industry accounts for approximately 5wt.% of current anthropogenic CO_2 emissions [141], and its contribution is still raising over the time due to the overall cement demand increase. It has been estimated that the production of 1 kg of cement releases an average 1.17 kg CO_2, depending on many factors related to the energy production and the type of cement plant [142,143]. 0.51 kg CO_2 (~ 43wt.% CO_2) is released during the decarbonation of calcite, during the thermal treatment; whereas, 0.43-0.48 kg CO_2 (~ 41wt.% CO_2) comes from the combustion of the fuel in the rotary kiln. The rest of CO_2 concerns the quarrying of raw materials (0.082 kg CO_2, 7wt.%), transportation of raw materials and final cement (0.035 kg CO_2, 3wt.%) and grinding of raw materials and clinker nodules (0.06 kg CO_2, 5wt.%). Moreover, OPC requires 1.7 kg of quarried raw material, ~ 0.2 l of liquid fuel and 0.151 kWh of electric energy per kg of clinker. Therefore, a huge consumption of natural resources (raw materials, fuels, gravel, sand and water for making cement), land use (limestone, clay and inert quarries, raw materials and cement storage) and electric energy are needed to produce OPC.

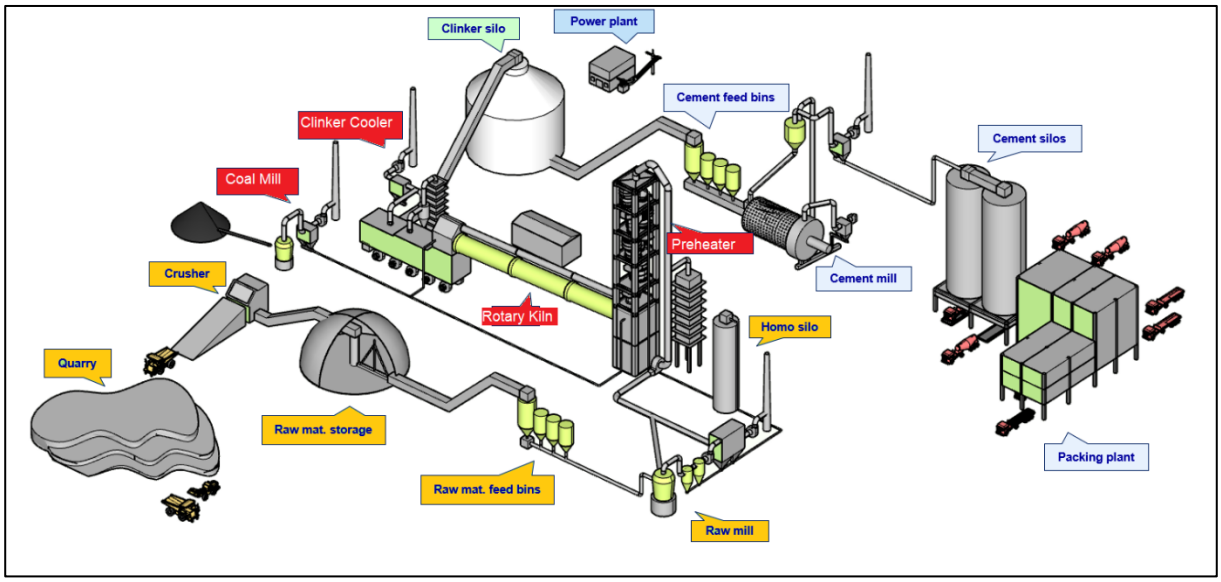

Fig. 6.2 – Cement manufacture scheme highlighting all the main steps concerning the raw meal preparation (quarrying, crushing, storing and mixing), pyro-processing (preheating at 900 °C, firing in the rotary kiln at 1450 °C and quenching) and final cement preparation (clinker grinding, clinker and gypsum mixing, storing and packing of cement).

In order to reduce the global warming, which is strictly related to the emission of greenhouse gases from human activity, changes in industry plants and energy production are required; hence, alternatives in cement manufacture are high priority research. Over the past twenty years many solutions have been proposed mainly concerning: (i) substituting parts of cement with reactive materials (fly ashes, calcite, pozzolanic and volcanic materials) reducing the consumption of cement but maintaining similar, if not better, mechanical properties [7,8,132]; (ii) using alternative raw materials and/or wastes coming from other industries (metallurgical slags, ashes from burning plants, mine tailings, etc.), reducing the amount of new raw materials quarried (limestone, clays, marls, sand, etc.), improving the thermal treatment by changing the melt properties, grinding and disposal costs due the general fine grain and inertization by thermal treatment, respectively; (iii) design of new cements, also called *green-cements* or *eco-friendly cements*, that are produced at lower temperature (1300-1350 °C), with a wide range of raw materials, also wastes and a lower CaO wt.%, hence releasing less CO_2 compared to OPC. Moreover, *green-cements* could be also mixed with other cement types (Calcium Aluminate Cements and OPC) and the above-mentioned reactive materials.

One of most relevant *green-cements* is Belite Cement (BC) which is made at 1350 °C, 100 °C less than OPC, with a lower CaO wt.%, saving an overall 10wt.% CO_2 emission concerning 3wt.% and 7wt.% CO_2 emissions from fuel burning and decarbonation, respectively (Table 6.1) [144]. BC is made of larnite, celite or mayenite ($Ca_{12}Al_{14}O_{33}$) and brownmillerite; hence, the mechanical strength is mainly due to the hydration of larnite. Therefore, two drawbacks occur: (i) low-hydration rate of larnite, leading low strength at early hydration; (ii) high-hardness in clinker milling process, because of the hardness of belite compared to hatrurite [145,146]. Another important *green-cements* is Calcium SulfoAluminate cement (CSA) or Belite Calcium SulfoAluminate cement (BCSA), defined basing on the amount of ye'elimite ($Ca_4Al_6SO_{16}$): CSA is composed of mainly ye'elimite (50-70wt.%), larnite (10-20wt.%) and minor amount of

brownmillerite (2-10wt.%) and anhydrite (0-10wt.%); whereas, BCSA is made of larnite (45-65wt.%), ye'elimite (15-35wt.%), brownmillerite (8-16wt.%) and anhydrite (0-5wt.%) [76,147–149]. However, a nomenclature based on the mineral abundance could be used to classify cement materials: BC could be replaced by Belite-Ferrite (BF) cement; CSA could be replaced by Ye'elimite-Belite-Ferrite cement (YBF); BCSA as Belite-Ye'elimite-Ferrite cement (BYF). Both CSA and BCSA are produced at lower temperature 1300-1350 °C and require less CaO: their production releases 20-35% less CO_2 compared to OPC manufacture. Moreover, these *green-cements* highlighted a rapid setting, early strength, shrinkage compensation and good sulphate resistance; but, supply of Al-rich raw materials (synthetic alumina or bauxite), which is extremely limited, the lower strength at medium hydration age, due to the larnite hydration, and the limited knowledge at long-term hydration, represent the main drawbacks [148].

Crystal Phase	***kg CO_2 / kg of component***
Hatrurite (Ca_3SiO_5)	0.578
Larnite (Ca_2SiO_4)	0.511
Celite ($Ca_3Al_2O_6$)	0.490
Brownmillerite ($Ca_2(Al,Fe)_2O_5$)	0.360
Ye'elimite ($Ca_4Al_6SO_{16}$)	0.216
Krotite ($CaAl_2O_4$)	0.278

Table 6.1 – Amount of CO_2 released during the synthesis of each cement crystal phases [148,149].

Therefore, the research could still do many steps forward reducing anthropogenic CO_2 by also developing new *green-cements* trying to overcome drawbacks related to: (i) low-hydration rate of BC, by means of dopants, mineraliser or alternative raw materials [147,150]; (ii) alternative Al-rich wastes instead of expensive bauxite for BCSA and CSA manufacture, reducing the costs of synthetising ye'elimite and for the disposal of Al-wastes [151,152]; (iii) improving the knowledge on the hydration of these cements, especially at long hydration stage.

6.4 – Cement chemist notation

In cement and concrete scientific literature, a shorthand notation that leaves the oxygen out is widely used to make crystal phase chemical formula shorter. This notation is also used to describe chemical reactions during clinkering and hydration of phases (Table 6.2).

Oxide	CaO	SiO_2	Al_2O_3	Fe_2O_3	P_2O_5	K_2O	Na_2O	MgO	CO_2	H_2O	SO_3
Symbol	C	S	A	F	P	K	N	M	$\bar{C}$	$\bar{H}$	$\bar{S}$

Table 6.2 – Cement Chemists Notation reporting the symbols used for all the main elements.

6.5 – Clinker mineralogy

In this section the main crystal phases occurring in OPC are reported and their crystal structure, polymorphism and hydration mechanisms are described.

6.5.1 – Hatrurite, tricalcium silicate (Ca_3SiO_5, C_3S)

Hatrurite, also called alite, (tricalcium silicate, Ca_3SiO_5, C_3S) represents the main component of OPC clinker. Seven different polymorphs are known, stable at different temperature window at ambient pressure: triclinic ones (T1, T2 and T3) a low temperature; monoclinic polymorphs at temperature between 980 and 1070 °C (M1, M2 and M3); the rhombic structure at temperature higher than 1070 °C. Hatrurite can be described as nesosilicate, made of isolated $[SiO_4]^{4-}$ tetrahedrons and Ca-O polyhedrons. Each calcium site has a variable coordination number with the oxygen, but the mean of Ca coordination is used to distinguish some polymorphs.

T1	⇄	***T2***	⇄	***T3***	⇄	***M1***	⇄	***M2***	⇄	***M3***	⇄	***R***
	620 °C		*920 °C*		*980 °C*		*990 °C*		*1060 °C*		*1070 °C*	

Table 6.3 – Polymorphic transitions occurring during heating of hatrurite at ambient pressure.

Considering the date reported in Table 6.3, the T1 polymorph should be one occurring in OPC but due to ionic substituents inside the crystal structure, acting as mineraliser, M1 and M3 are normally occurring in cement manufacture. Moreover, several low-intensity Bragg peaks in OPC patterns highlighted the occurrence of superstructures for hatrurite, increasing unit cell dimension and atomic positions.

The proposed crystal structures for hatrurite highlighted similarities in the occurrence of symmetry elements among polymorphs: the hexagonal plane *H*; the rhombohedral axis a_R from the rhombic polymorph; the monoclinic plane *M*. Moreover, R polymorph could be described represented with an orthohexagonal unit cell (R_{OH}) or with a hexagonal one (R_H). The proposed average unit cell for monoclinic polymorphs (<M>) has elements in common with the R polymorph: (i) $a_{<M>}$ // to a_R; (ii) $b_{<M>}$ // to $b_{<OH>}$; $c_{<M>}$ // to $-a_{OH}$.

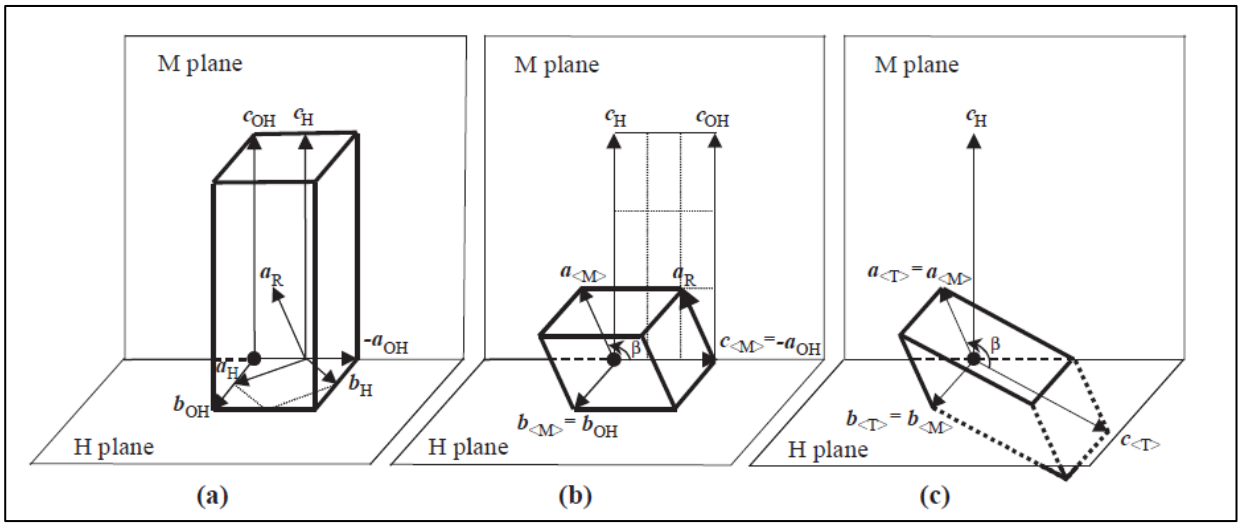

Fig. 6.2 – Different unit cells for hatrurite polymorphs and their crystallographic relations: monoclinic plane M; hexagonal plane H; a_R vector of the rhombohedral cell; a_H, b_H and c_H for hexagonal cell; a_{OH}, b_{OH} and c_{OH} for orthohexagonal cell; $a_{<M>}$, $b_{<M>}$ and $c_{<M>}$ for monoclinic cell; $a_{<T>}$, $b_{<T>}$ and $c_{<T>}$ for triclinic cell .

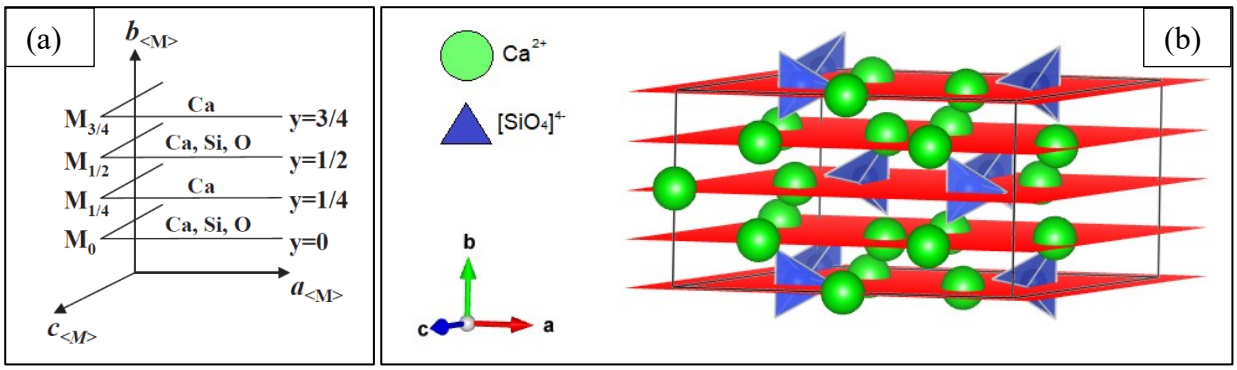

Fig. 6.3 – (a) monoclinic planes (M) occurring in the monoclinic structure; (b) hatrurite monoclinic crystal structure highlighting the positions of monoclinic planes in red.

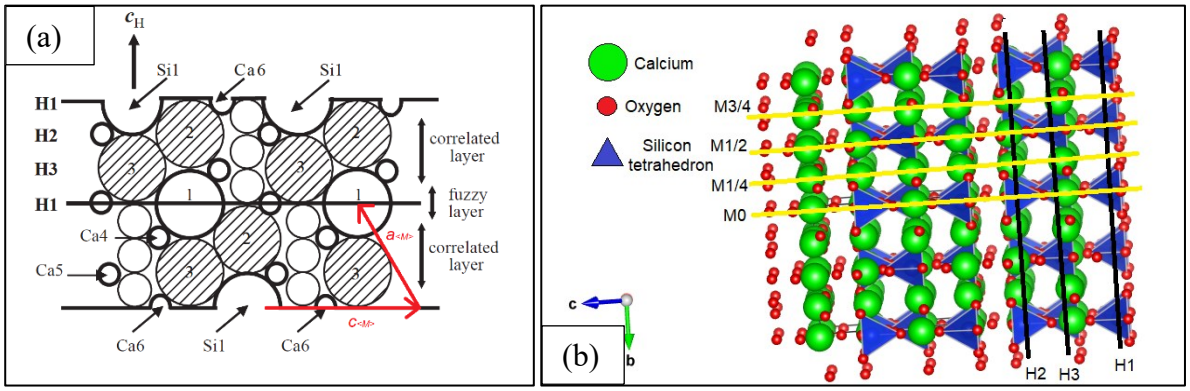

Fig. 6.4 – (a) monoclinic plane M_0 highlighting the three hexagonal planes H1,2,3; (b) hatrurite monoclinic crystal structure highlighting the positions of four monoclinic planes in yellow and three hexagonal planes in black.

	Reference	Space Group	Symbol	a (Å)	b (Å)	c (Å)	α (°)	β (°)	γ (°)	V (Å^3)	Z
T1	[153]	$P\bar{1}$	G	11.67	14.24	13.72	105.5	94.33	90	2190.3	18
T1	[154]	$P\bar{1}$	<T>	9.303	7.041	18.39	90.39	143	89.63	725	6
T2	[155] (T=682°C)	$P\bar{1}$	-	11.7416(2)	14.2785(2)	13.7732(2)	105.129(1)	94.415(1)	89.889(1)	2222.02(8)	18
T3	[156]	$P\bar{1}$	G	11.6389(2)	14.1716(3)	13.6434(3)	104.982(2)	94.622(1)	90.107(2)	2166.199(3)	18
M1	[157]	Pc	<M>	9.2912	7.059	12.2575	90	116.03	90	722.4	6
M1	[158]	Pc	M'1	27.8736(2)	7.0590(5)	12.2575(8)	90	116.030(6)	90	2167	18
M1	[158]	Pa	M-1	12.2575	7.0590	25.0462	90	90.06	90	2167	18
M2	[159]	Cm	-	12.342	7.143	25.434	90	90	90	2242	?
M3	[160]	Cm	<M>	12.235	7.073	9.298	90	116.31	90	721	6
M3	[160]	Am	<M>	9.298	7.073	12.235	90	116.31	90	721	6
M3	[161]	Im	M'3	18.7159(9)	7.0330(4)	36.694(9)	90	116.038(4)	90	4294	36
M3	[161]	Cm	M-3	33.083	7.027	18.499	90	94.12	90	4289	36
M3	[162]	Cm	M-3	33.1078(6)	7.0355(1)	18.5211	90	94.137(1)	90	4302.9(2)	36
R	[163] (T = 1200 °C)	$R\bar{3}m$	R-H	7.135	7.135	25.586	90	90	120	1128	9
R	[163] (T = 1200 °C)	Pmmm	R-OH	12.358	7.135	25.586	90	90	90	2256	18

Table 6.4 – Crystallographic parameters for different published crystal structures of hatrurite [164].

Furthermore, the average monoclinic unit cell <M> has two main structural crystallographic elements (Fig. 6.2,3,4):

- Four monoclinic planes (M_0, $M_{1/4}$, $M_{1/2}$ and $M_{3/4}$) in which layers of only calcium ions ($M_{1/4}$ and $M_{3/4}$), alternate to layers composed of calcium, silicon tetrahedron and isolated oxygen bonded with calcium (M_0 and $M_{1/2}$);
- Three hexagnonal planes (H1,2,3), in which the second and third (H2,3) are composed of silicon tetrahedron oriented up and down, respectively; whereas the first hexagonal plane is made of silicon tetrahedron with high variability orientation and widely spaced among them.

The hydration on hatrurite is main responsible of the strength at 28 hydration days in OPC. Its hydration is complex but could be summarised by the following reaction:

$$2Ca_3SiO_5 + 6H_2O \rightarrow Ca_3Si_2O_4(OH)_6 + 3Ca(OH)_2$$

This hydration forms portlandite and an amorphous gel CSH (Calcium-Silicate-Hydrated phase), which is gradually converted into crystallite phases as tobermorite, jennite and afwillite over the time. It has been estimated that 70wt.% of hatrurite completely hydrated in 28 days and the 100wt.% after one year.

6.5.2 – Dicalcium silicate (Ca_2SiO_4, C_2S)

Dicalcium silicate (Ca_2SiO_4, C_2S) has five different polymorphs as a function of temperature at ambient pressure (Table 6.4).

	– – – – – – – 730 °C – – – – – – – –→							
γ	←	***β***	⇄	***α'$_L$***	⇄	***α'$_H$***	⇄	***α***
Calcio-olivine		***Larnite***				***Flamite***		
	< 500 °C		*680 °C*		*1160 °C*		*1425 °C*	

Table 6.4 – Dicalcium silicate polymorphic transitions as a function of temperature at ambient pressure.

These polymorphic transitions are not always reversible: heating γ-Ca_2SiO_4 (also called, calcio-olivine), the transition to larnite is skipped and the crystal directly turns into α'$_L$-Ca_2SiO_4 at 730 °C; whereas during the cooling, all the polymorphic transitions occur in absence of ionic substituents. This particular behaviour is related to the metastability of the larnite polymorph. The transitions occurring at high temperatures are described as displacive changes in the crystal structure [165].

The most common polymorph occurring in OPC is β-Ca_2SiO_4 (also called belite), with sometimes minor of flamite, which is not the low temperature polymorph: the occurrence of ionic substituents in the crystal structure affects the stability field of high temperature polymorphs, increasing its stability field toward lower temperature, as occurring for tricalcium silicate phase.

	Space group	a (Å)	b (Å)	c (Å)	α (°)	β (°)	γ (°)	V (Å³)	Z	Ref.
γ	*Pnma*	*11.232*	*6.773*	*5.083*	*90*	*90*	*90*	*386.69*	*4*	[166]
	Pbnm	*5.081*	*11.224*	*6.778*	*90*	*90*	*90*	*386.54*	*4*	[167]
β	*$P2_1/c$*	*5.480*	*6.760*	*11.150*	*90*	*123.55*	*90*	*344.2*	*4*	[166]
	$P2_1/n$	*5.48(2)*	*6.76(2)*	*9.28(2)*	*90*	*94.33(5)*	*90*	*342.8(1)*	*4*	[168]
	$P2_1/n$	*5.502(1)*	*6.745(1)*	*9.297(3)*	*90*	*94.59(4)*	*90*	*343.9(1)*	*4*	[169]
	$P2_1/n$	*5.5172(4)*	*6.76996(6)*	*9.32298(8)*	*90*	*94.336(2)*	*90*	*347.228(1)*	*4*	[170]
	$P2_1/n$	*5.50684(1)*	*6.74839(1)*	*9.30320(2)*	*90*	*94.590(1)*	*90*	*344.62(1)*	*4*	[171]
	$P2_1/n$	*5.5051(3)*	*6.7551(5)*	*9.3108(5)*	*90*	*94.513(4)*	*90*	*345.17(1)*	*4*	[172]
α'_L	*$Pna2_1$*	*20.810*	*9.496*	*5.600*	*90*	*90*	*90*	*1106.63*	*12*	[173]
α'_H	*Pnma*	*6.748*	*5.494*	*9.261*	*90*	*90*	*90*	*343.33*	*4*	[166]
	Pnma	*6.871*	*5.601*	*9.556*	*90*	*90*	*90*	*367.8*	*4*	[174]
	Pnma	*6.8588(2)*	*5.4301(2)*	*9.4052(3)*	*90*	*90*	*90*	*350.29(2)*	*4*	[175]
α	*$P6_3/mmc$*	*5.532*	*5.532*	*7.327*	*90*	*90*	*120*	*192.73*	*2*	[174]
	$P\bar{3}m1$	*5.419*	*5.419*	*7.022*	*90*	*90*	*120*	*178.58*	*2*	[166]

Table 6.5 – Crystallographic parameters for published dicalcium silicate polymorph crystal structures.

Furthermore, these high temperature phases are more reactive with water, hence their occurrence enhances the hydration reactivity of OPC.

All the polymorphs of dicalcium silicate could be considered as nesosilicate composed of isolated silicate tetrahedrons and polyhedron of calcium. Differences in coordination number for calcium polyhedron occur among polymorphs: calcio-olivine has a crystal structure similar to olivine and 6 has coordination number for calcium sites; larnite has two calcium sites, one with 7 and 8 for coordination number; whereas, all the high temperature polymorphs (α'_L, α'_H and α) have higher calcium coordination number 8 for one site and up to 10 for the other [172]. Afterwards, the transition from the HT modifications to the room temperature one is accompanied by (i) a rotation of silicon tetrahedron, (ii) decrease in the sizes of the coordination sphere around calcium sites and (iii) a progressive reduction of the shared edges for calcium polyhedron with other calcium polyhedron and silicon tetrahedron.

More in detail, larnite (β-Ca_2SiO_4) crystal structure could be represented as nesosilicate structure with two different calcium sites (Ca1,2) (Fig. 6.5). One calcium site (Ca1) forms distorted seven-vertex polyhedron that builds zig-zag calcium polyhedron chain along [100] (Fig. 6.7a,b). Whereas the other calcium site (Ca2) forms distorted polyhedron with 8 coordination number building layers // to (-101) sharing faces to other Ca2 polyhedrons along [010] and one edge along [-101] (Fig. 6.6a,b). Furthermore, these layers made of Ca2 atoms have channels along [100] in which the zig-zag chain of Ca1 atoms occurs. Each Ca1 polyhedron is sharing 4 faces with 4 Ca2 polyhedrons belonging to a layer and one oxygen to another layers (Fig. 6.7b). Isolated silicon tetrahedrons occur between Ca2 layer to another, and each tetrahedron is sharing two edges with two Ca2 polyhedrons and one edge with Ca1 polyhedron (Fig. 6.5a,b) [172].

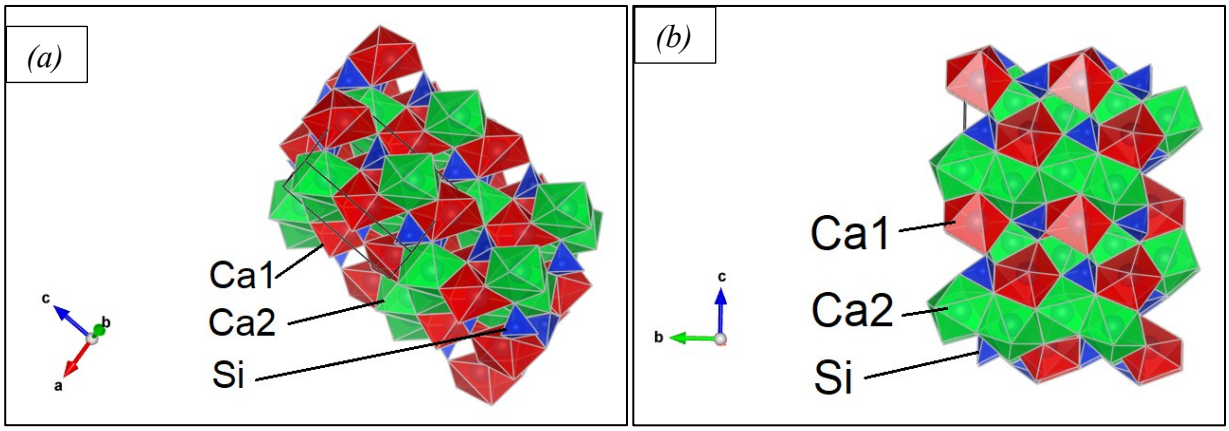

Fig. 6.5 – Crystal structure representation of larnite [169] along b (a) and a (b) vectors; green Ca2, red Ca1 and blue silicon tetrahedron.

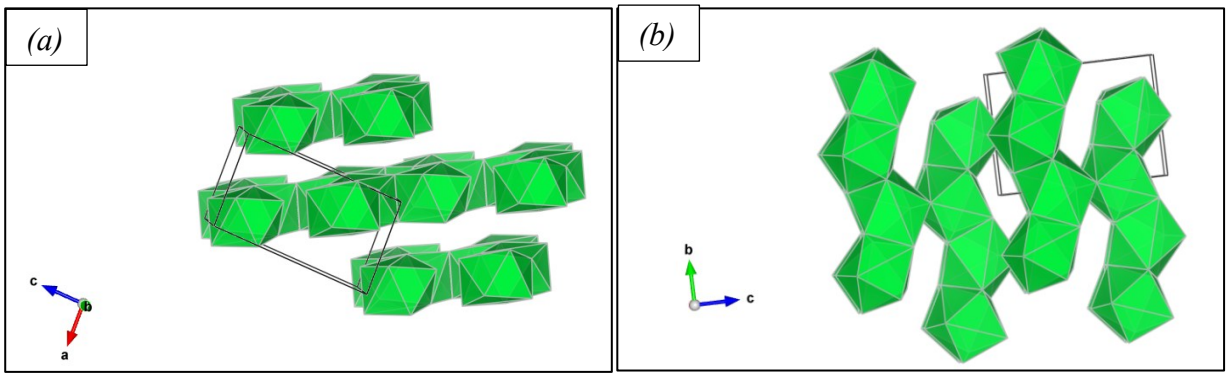

Fig. 6.6 – Crystal structure representation of larnite [169] only considering the Ca2 polyhedrons forming layers // to (-101) (a), and channels along [100] (b); in green Ca2.

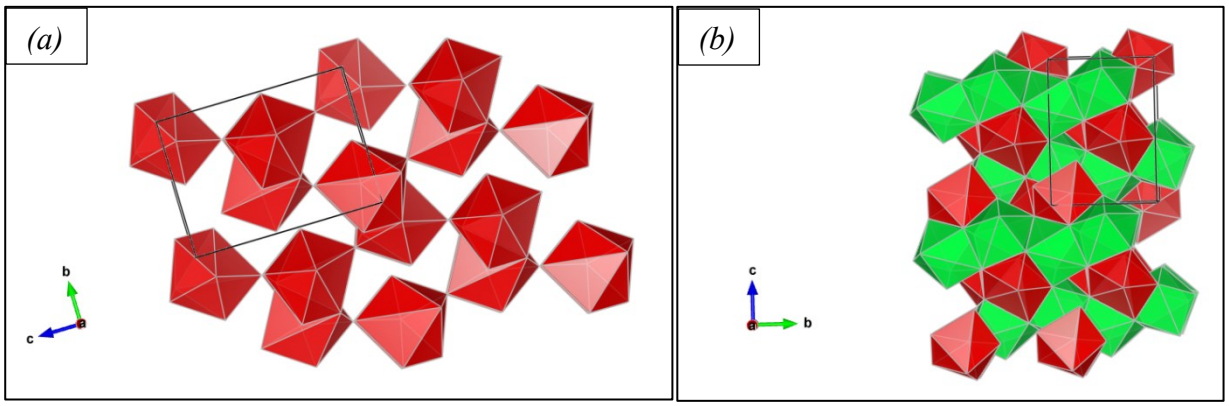

Fig. 6.7 – Crystal structure representation of larnite [169] only considering (a) the Ca1 atomic position forming chains along [100], and (b) all calcium polyhedrons; in green Ca2 and red Ca1.

Still in calcio-olivine (γ-Ca_2SiO_4) crystal structure there are two calcium sites (Ca1,2): Ca2 forms layers // to (010) with each distorted octahedron is sharing 4 oxygens with other 4 calcium polyhedrons belonging to the same layer, one edge with one silicon tetrahedron and three oxygens to other 3 tetrahedrons; Ca1 forms chains along [001] between the Ca2 layers, in which each Ca1 atom shares one edge with the other Ca1 belonging to the same chain (Fig. 6.8a,b).

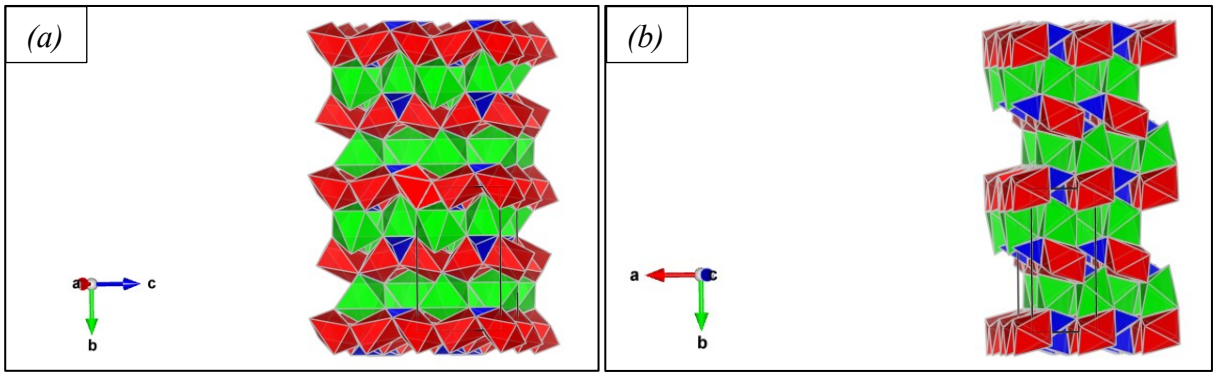

Fig. 6.8 – Crystal structure representation of calcio-olivine [176] along a (a) and c (b) vectors; green Ca2, red Ca1 and blue silicon tetrahedron.

Only larnite and other HT polymorphs highlighted a hydration reactivity at room temperature, whereas calcio-olivine has only a slight hydration reactivity at higher temperatures and long curing time. The hydration reaction is similar to hatrurite one, but requires less water and produces less portlandite, as reported in the following reaction:

$$2Ca_2SiO_4 + 4H_2O \rightarrow Ca_3Si_2O_4(OH)_6 + Ca(OH)_2$$

Cements rich in larnite highlighted a slow development of strength due to the low hydration rate of dicalcium silicate, but produce higher mechanical resistance after long hydration time [7,8].

6.5.3 – Tricalcium aluminate (celite, $Ca_3Al_2O_6$, C_3A)

Tricalcium aluminate (celite, $Ca_3Al_2O_6$) normally occurs in OPC as interstitial phase with brownmillerite in the range of 5-8 wt.%. Pure tricalcium aluminate has not polymorph only having the cubic form (Table 6.6). Its crystal structure is made by tetrahedron forming $[Al_6O_{18}]^{-18}$ rings of six $[AlO_4]^{-5}$ tetrahedron, sharing 2 corners. Two similar aluminium sites occur forming the six-members ring; whereas, six different calcium sites occur, witch five of them with an octahedron coordination and one coordinated to eight oxygens [177] (Fig. 6.9).

Tricalcium silicate can replace part of calcium with sodium forming a solid solution by substituting one calcium with two sodium: one sodium is replacing the calcium and the other is hosted in the middle of one aluminium ring (Table 6.6) [178,179]. The progressive ionic substitution modifies the crystal structure passing from cubic to orthorhombic and monoclinic (Table 6.6).

Celite exhibits an extremely fast reactivity in contact with water turning into dicalcium aluminate octahydrate which is gradually converted into hydrogarnet, as reported in the following reactions [7,177]:

$$2Ca_3Al_2O_6 + 27H_2O \rightarrow 3Ca_2Al(OH)_6Al(OH)_43H_2O + 2Al(OH)_3$$

$$3Ca_2Al(OH)_6Al(OH)_43H_2O \rightarrow 2Ca_3Al_2(OH)_{12} + 2Al(OH)_3 + 9H_2O$$

These reactions complete withing a few hours causing a fast stiffening, asl known as “flash setting”, not allowing a right workability of the cement paste during the hanging [8]. Therefore, adding a sulphate-bearing phase (gypsum, bassanite or anhydrite) retards the hydration of celite an inhibits the “flash setting” allowing the right workability of cement paste, extremely important for concrete making. The following reaction highlights the reactivity of celite in the presence of water and sulphate, producing a layer on celite crystal of ettringite (belonging to Aft phases) [7]:

$$Ca_3Al_2O_6 + 32H_2O + CaSO_4 \rightarrow Ca_6(Al(OH)_6)_2(SO_4)_3 26H_2O$$

Because the added amount of sulphate-bearing phase is not stochiometric enough to react with all the celite, after a few hours, the ettringite reacts with the remaining celite forming monosulfate phase (belonging to AFm phases) as reported in the next reaction [7]:

$$Ca_6(Al(OH)_6)_2(SO_4)_3 26H_2O + Ca_3Al_2O_6 + 4H_2O \rightarrow 3Ca_4(Al(OH)_6)_2(SO_4)6H_2O$$

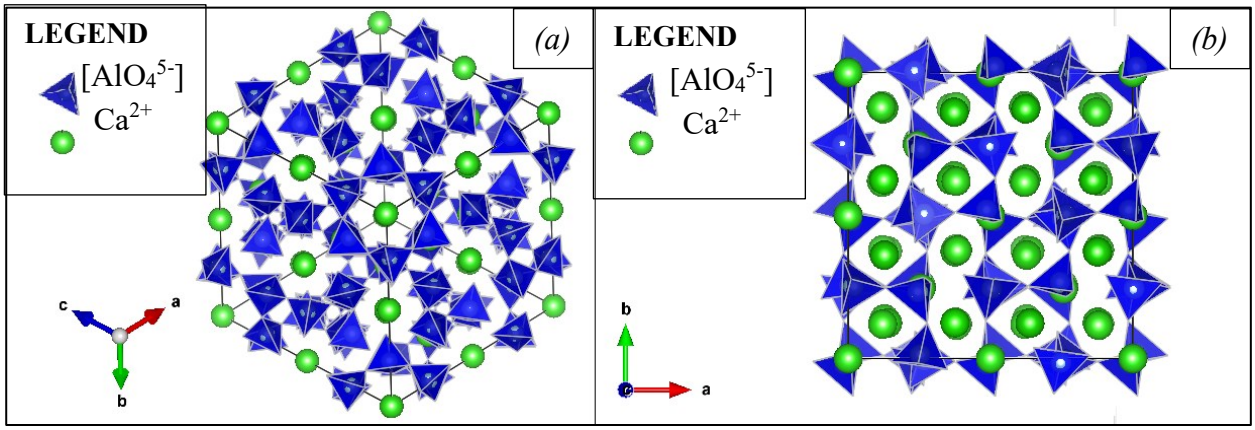

Fig. 6.9 – Celite crystal structure observed (a) along (111) the threefold symmetry axis, (b) along (001) direction.

Space group	*x*	*a (Å)*	*b (Å)*	*c (Å)*	*α (°)*	*β (°)*	*γ (°)*	*V (Å³)*	*Z*
$Pa\bar{3}$	*0-0.04*	*15.263(3)*	*15.263(3)*	*15.263(3)*	*90*	*90*	*90*	*3555.7*	*8*
$P2_13$	*0.04-0.16*	*15.248(2)*	*15.248(2)*	*15.248(2)*	*90*	*90*	*90*	*3545.2*	*8*
Pbca	*0.16-0.20*	*10.879(1)*	*10.845(2)*	*15.106(2)*	*90*	*90*	*90*	*1782.3*	*4*
$P2_1/a$	*0.20-0.25*	*10.844(2)*	*10.855(2)*	*15.122(4)*	*90*	*90*	*90.4(1)*	*1786.8*	*4*

Table 6.6 – $Na_{2x}Ca_{3-x}Al_2O_6$ structure modifications as a function of Na_2O ionic substitution [179].

6.5.4 – Tetracalcium aluminium ferrite (brownmillerite, $Ca_2(Al,Fe)_2O_5$, C_4AF)

Tetracalcium aluminium ferrite, also called brownmillerite ($Ca_2(Al,Fe)_2O_5$) occurs in clinker as an interstitial phase in a concentration ranging from 5-15wt.% [7]. Brownmillerite represents a solid solution between srebrodolskite ($Ca_2Fe_2O_5$), which is the pure iron-rich one, and dicalcium aluminate ($Ca_2Al_2O_5$), representing the pure aluminium-rich one, but at room temperature and ambient conditions this solid solution is limited to $x = 0.7$ considering a general formula $Ca_2(Al_xFe_{1-x})_2O_5$ [180]. Tetracalcium aluminium ferrite is usually considered as $x = 0.5$ in OPC [7].

Brownmillerite crystal structure is made of alternated octahedron and tetrahedron layers both developed along plane (101): each octahedron shares four corners with other four octahedrons and two corners with two tetrahedrons belonging to different layers (Fig. 6.10). Most of Al^{3+} is hosted inside tetrahedron site, whereas Fe^{3+} prefers the octahedron site: at $x = 0.325$ around 75% of tetrahedron sites are occupied by Al^{3+}; instead, at $x > 0.325$ Al^{3+} is equal spread among tetrahedron and octahedron sites [180]. Calcium occurs in one atomic site between a layer to another forming a distorted polyhedron made of eight bonds with oxygen (Fig. 6.10). Passing from the pure end member rich in iron to the one normally occurring in OPC, an increase in the symmetry by passing from *Pcmn* to *Ibm2* occurs (Table 6.7), also highlighted by a gradual reduction in all cell parameters and volume [180].

Space group	*x*	*a (Å)*	*b (Å)*	*c (Å)*	*α (°)*	*β (°)*	*γ (°)*	*V (Å³)*	*Z*
Pnma	*0*	*5.4268(3)*	*14.7631(5)*	*5.5969(2)*	*90*	*90*	*90*	*448.40*	*4*
Pnma	*0.22*	*5.3986(3)*	*14.6631(7)*	*5.5910(2)*	*90*	*90*	*90*	*442.59*	*4*
I2mb	*0.28*	*5.3808(3)*	*14.6131(8)*	*5.5911(3)*	*90*	*90*	*90*	*439.63*	*4*
I2mb	*0.50*	*5.3269(3)*	*14.4687(9)*	*5.5433(2)*	*90*	*90*	*90*	*427.24*	*4*
I2mb	*0.68*	*5.2991(4)*	*14.4434(9)*	*5.5099(3)*	*90*	*90*	*90*	*421.71*	*4*

Table 6.7 – Crystallographic parameters for the solid solution $Ca_2(Al_xFe_{1-x})_2O_5$, highlighting the changes in space group and gradual reduction in volume and cell parameters [180].

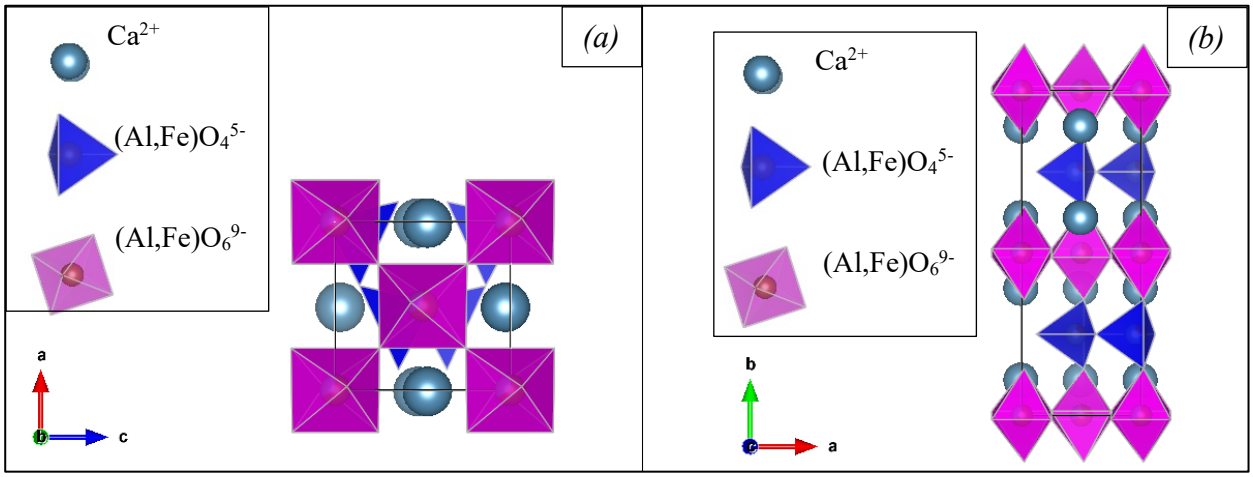

Fig. 6.10 – Crystal structure representation of brownmillerite ($Ca_2(Al,Fe)_2O_5$, Ibm2) (a) along [010] and (b) [001] highlighting the tetrahedron and octahedron layers, and the position of calcium site between these two layers.

Brownmillerite reacts slower than celite with water, producing in absence and presence of $CaSO_4$ a Afm and Aft phase, respectively, as reported in the next two hydration reactions [7,8]:

$$Ca_4(Al,Fe)_2O_5 + 21H_2O \rightarrow Ca_4(Al_{0.67}Fe_{0.33}(OH)_6)_2(OH)_2 \cdot 12H_2O + \frac{4}{3}Fe(OH)_3$$

$$Ca_4(Al,Fe)_2O_5 + 3CaSO_4 2H_2O + 30H_2O \rightarrow Ca_6(Al(OH)_6)_2(SO_4)_3 26H_2O + Ca(OH)_2 + 2Fe(OH)_3$$

6.5.5 – Ye'elimite ($Ca_4Al_6SO_{16}$, $C_4A_3\bar{S}$)

Ye'elimite represents a minor crystal phase in OPC when is burned at lower temperature with high sulphur content and the main phase in CSA cements. Ye'elimite has been described with cubic or orthorhombic structural models. This crystal phase is a sodalite tectoaluminate crystal structure, made of a framework of aluminium tetrahedron forming six and four-member rings; calcium atoms are bonded with six oxygens and occur in the centre of six-member rings, which are aligned along diagonals considering the cube shape; sulphur tetrahedrons occurs in the same direction of calcium atoms in the cube centre and at its apexes.

A concentration of more ionic substituents, mainly as Fe^{3+} substituting Al^{3+}, increase the stability field at room temperature of the cubic form, whereas, lower amount of dopants allows the orthorhombic crystal structure: cubic form represents the high temperature polymorph which is stabilised at room temperature with ionic substituents, as commonly occurring for other calcium silicate phases (tricalcium and dicalcium silicates).

Ye'elimite reacts fast with water especially in the presence of a sulphate-bearing phase (gypsum, bassanite, anhydrite) leading the formation of monosulphate phase or ettringite, respectively, as reported in the following reactions:

$$Ca_4(AlO_2)_6(SO_4) + 2CaSO_4 + 38H_2O \rightarrow Ca_6(Al(OH)_6)_2(SO_4)_3 26H_2O + 2Al(OH)_3$$

$$Ca_4(AlO_2)_6(SO_4) + 18H_2O \rightarrow Ca_4(Al(OH)_6)_2(SO_4)\ \ 6H_2O + 4Al(OH)_3$$

6.6 – Minor elements effects on clinker

OPC and *BC* are represented by the chemical system $CaO\text{-}SiO_2\text{-}Al_2O_3\text{-}Fe_2O_3$, whereas, also SO_3 should take into consideration for BCSA. Raw materials used to prepare the starting raw meal for clinkerisation are not completely pure, even the fuel has sulphur, Pb and other minor components, leading important changes in clinker production (i.e., melting point, melt properties, stability of crystal phases, decomposition of calcite, etc.) if their contents are not limited. Most changes due to minor elements regard the viscosity and surface tension of liquid phase changes its viscosity and surface tension depending on the type of chemical species. Several studies have been made on understanding the source and the effects of minor elements also with different concentration [7,8,181]. However, only the effects of minor elements found in our study case are below reported and described:

(i) sodium and potassium improve the stability of HT dicalcium silicate polymorphs and increase the viscosity of melt by favouring tetrahedron polymerisation of aluminium and iron [7,8,181]. Furthermore, alkali stabilises HT polymorphs of dicalcium silicate, enhancing hydration reactivity [147,150,182], while increase the stability of M_1-hatrurite and orthorhombic celite [183];

(ii) sulphur reduces viscosity of melt by favouring octahedron polymerisation, but they both improve hatrurite formation only at low content [184,185]. Furthermore, SO_3 acts reducing the stability field of hatrurite until it disappears at $SO_3 \geq 3.7$wt.% [186], allowing only CaO-

C_2S-C_3A-C_4AF as final mineral assemblage. However, several experiments reported C_3S occurrence even at higher SO_3 content in the raw meal, but most results highlighted a final SO_3 content in the clinker lower than in the starting raw meal [187–190]: sulphur could be lost at high temperatures, leading a gradual reduction of the overall SO_3 content, hence allowing C_3S formation. SO_3 also avoids the increase of viscosity in the liquid phase by alkali, but only when $SO_3/(Na_2O+K_2O) \geq 1$ [7,8]. Different ionic substitution have been identified occurring in calcium silicate clinker phases: (i) $2^{IV}Al^{3+} + {}^{IV}S^{6+} \rightarrow 3^{IV}Si^{4+}$ or $3^{IV}Al^{3+} + 2^{IV}S^{6+} \rightarrow 5^{IV}Si^{4+}$ only involving tetrahedrons; (ii) $2^{IV}Al^{3+} + 4^{IV}S^{6+} + 3\ V.^{2+} \rightarrow 6^{IV}Si^{4+} + 3\ Ca^{2+}$ leading the formation of calcium vacancies [187]; (iii) $V.^{2+} + {}^{IV}S^{6+} \rightarrow {}^{IV}Si^{4+} + Ca^{2+}$ leading the formation of calcium vacancy [191]. Sulphur has been considered as M_1-C_3S and β-C_2S stabiliser [7,8,158,164,183]. Several studies added phosphogypsum as sulphur source in the starting raw meal, observing a strong improvement of clinkering reactions at lower temperature as low as 1200 °C [189,192]. Similar results were obtained by adding both phosphogypsum and fly ashes as SO_3 source [193].

(iii) Phosphorous could be considered as a mineraliser and fluxer reducing the melt viscosity, as for sulphur, and improving hatrurite formation but only at P_2O_5 < 1wt.% [194]; whereas, at higher content (> 2wt.% in the raw meal) strongly reduces hatrurite crystallisation by increasing dicalcium silicate stability due to the C_2S-C_3P complete solid solution at high temperature [195–199]. Ionic substitutions involving phosphorous inside dicalcium and tricalcium silicate phases are the same: (i) $2^{IV}P^{5+} + Vac.^{2+} \rightarrow 2^{IV}Si^{4+} + Ca^{2+}$ when phosphorous is alone [200]; (ii) ${}^{IV}P^{5+} + Na^{+} \rightarrow {}^{IV}Si^{4+} + Ca^{2+}$ when sodium is occurring with phosphorous [7,175]; (iii) ${}^{IV}P^{5+} + {}^{IV}Al^{3+} \rightarrow 2^{IV}Si^{4+}$ when aluminium is available [200]. Furthermore the C_3S primary crystallisation field is extended up to 13wt.% [201]. Even a different phosphorous source could have different effects on clinkering: HPO_4^{4-} tends to be enriched in the melt improving hatrurite formation by reducing the viscosity; whereas, $H_2PO_4^{4-}$ and PO_4^{3-} increase dicalcium silicate stability leading a reduction of hatrurite crystallisation [202];

(iv) Fluorine is usually added in the raw meal in the form CaF_2, reducing calcite decarbonation at 600 °C, melting point and the viscosity of the liquid phase: fluorine enhance clinkering and hatrurite formation at temperature as low as 1230 °C [203–205]. However, high CaF_2 content (~ 1.5wt.%) forms an eutectic point at 1170 °C among C_3S-C_2S-$C_9S_3CaF_2$, strongly reducing the melting point of OPC raw meal [201,206]. Furthermore, $C_9S_3CaF_2$ melts at T > 1175 °C forming R-C_3S, α-C_2S and liquid [201,206]. Fluorine could be hosted at HT in mayenite, considering the substitution between fluorine and oxygen [207], and hatrurite by two main substitutions: (i) $2F^{-1} + V'' \rightarrow 2O^{-2} + Ca^{2+}$ [208,209], leading calcium vacancy; (ii) $F^{-1} + {}^{IV}Al^{3+} \rightarrow O^{-2} + {}^{IV}Si^{4+}$ in the presence of aluminium, leading a global reduction of negative charge [210–214]. When fluorine is alone added to OPC raw mixture stabilises M_1-C_3S [215].

Combing minor elements has stronger influences on crystal phase stability, polymorphism of crystal phases, clinkering reactions, melting point and melt properties. Moreover, the effects of

simultaneous occurrence of minor elements could not be predicted by simply considering the multiple effects of each single dopant [7,8,150]. However, the most important result of simultaneous minor elements doping is the overall reduction of clinkerisation temperature. Some cement kilns operated adding 1wt.% and 0.3wt.% of $CaSO_4$ and CaF_2 to raw mixtures, respectively, reducing the clinkerisation to 1250 °C and saving around 5% of fuel consumption [216,217]. When fluorine is combined with sulphur in OPC raw meal fluorellestadite is formed only when $F/SO_3 > 0.158$, otherwise no fluorine phase occurs [218]. The addiction of phosphorous, sulphur and fluorine has been tested only on BCSA raw meal adding phosphate rock acid-insoluble residue reaching ~ 1wt.% F, ~ 1.5wt.% P_2O_5 and ~ 5wt.% SO_3 doping, revealing an optimal temperature formation at 1200 °C with a phase assemblage composed of α'_H-C_2S, β-C_2S, orthorhombic and cubic ye'elimite [219].

6.7 – Cement control quality parameters

Three main control quality parameters are usually used in cement manufacture to predict ratio among phases and the improvement of clinkering reactions [8]. These values are calculated starting from XRF of raw meals.

Silica Ratio (SR) is defined as the ratio $SiO_2/(Al_2O_3 + Fe_2O_3)$ which for Ordinary Portland Cement varies from 2 to 3, and its increase leads to a rise of silicate phases and a reduction of melt at high T reducing clinkering reactions.

Alumina Ratio (AR) is calculated as the ratio between aluminium and iron oxides (Al_2O_3/Fe_2O_3) which has a value from 1 to 4 for OPC and defines the abundance of brownmillerite compared to Al-rich phases. The reduction of AR leads an increase of brownmillerite occurrence.

Lime Saturation Factor (LSF) is an important quality control parameter defined as the ratio $CaO/(2.8\,SiO_2 + 1.2\,Al_2O_3 + 0.65\,Fe_2O_3)$ which for OPC usually falls in the range 0.92-1.02. This value controls the proportion between hatrurite and larnite in OPC; furthermore, when the value 1 is obtained lime (CaO-free) should occurs at the clinkerisation temperature (1350-1450 °C). Furthermore, in the case of high-MgO content, which has a strong impact on alite phase formation, LSF formula has been slightly modified: if MgO < 2wt.% $(CaO + 0.75\,MgO)/(2.8\,SiO_2 + 1.2\,Al_2O_3 + 0.65\,Fe_2O_3)$; if MgO > 2wt.% $(CaO + MgO)/(2.8\,SiO_2 + 1.2\,Al_2O_3 + 0.65\,Fe_2O_3)$.

However, all these formulas do not take into account the potential effects of other minor elements (e.g., SO_3, P_2O_5, CaF_2, $CaCl_2$, etc.) on changing crystal phase distribution and abundance, and melt properties.

Chapter 7
Materials and Methods

7.1 – Materials

7.1.1 – Natural rocks: Limestone and Combusted Pyrometamorphosed Rock

Natural limestone samples belonging to the Lower Member of Ghareb Formation were collected during the field trip (Stop-2, outcrops in Arad City, and Stop-8, outcrops in the Rotem Amfort mine) were investigated by XRF, for chemical investigation, RQPA on LXRPD data, obtaining mineralogical and crystallographic information, TLM and RLF for microtextural investigation. Only *RM* sample was further studied with NXRD on bulk samples for textural analysis, SXRPD, μ-CT with *in-situ* and *ex-situ* experiment and SCXRD. In Table 7.1 XRF results are reported for studied limestone and bibliographic ones. Detailed description related to textural, mineralogical and crystallographic information on limestone samples are accounted in Chapter 8.

Samples *SO* and *SE* were collected at Stop-2 from hard limestone concretions with metric size (see section *3.1.2*, Fig. 5.6) and rounded shape inside weathered outcrops of Ghareb Formation. These hard nodules should be related to process during diagenesis involving decomposition of organic matter with reduction conditions, as commonly occurring in Mishash Formation [113] (see section *3.1.1*, Fig. 5.4). Both samples represent phosphatic-rich limestone with differences in textural features: *SO* forms the textural homogeneous part composed of mainly calcite (> 95wt.%) and minor quartz, apatite and fluorite, which is classified as a calci-mudstone; *SE* represents the heterogeneous part composed of mainly calcite and apatite, and minor quartz, which is classified as phosphatic wackestone. Therefore, XRF revealed that these samples are mainly composed of CaO due to the general absence of quartz and clays.

Sample *RM* was collected at Stop-8 from fresh quarry face of Lower Member of Ghareb Formation (see section 5.8, Fig. 5.33). *RM* is composed of calcite, kaolinite, gypsum, apatite, quartz and minor goethite, and classified by textural features as a phosphatic calci-mudstone.

Only larnite-rich rocks (Natural CP rocks) were deeply studied for the comparison with the corresponding synthetic green-cement. Larnite-rich rocks were collected on Stop-6.2 (*6BWO*) and Stop-9 (*YC2O*), and were analysed by XRF, RQPA on both LXRPD and SXRPD, RLM, SEM/EMPA and μ-CT. *YC2O* was also studied with NXRD for textural investigation; moreover, this sample was selected to prepare cement by adding natural gypsum (*3GNat*), coming from Toledo mine (Spain), making a comparison on hydration properties with synthetic belite cement by means of DSC-TGA, ICA and XRPD at different hydration time (1, 3, 7, 28 days). Table 7.2 reports the XRF results for *YC2O*, *6BWO* and bibliographic values for larnite-rich rocks.

$Sample/_{Oxide}$		CaO	SiO_2	Al_2O_3	Fe_2O_3	MgO	SO_3	P_2O_5	TiO_2	K_2O	Na_2O	SrO	LOI	TOT^*
SO		55.72	1.54	0.87	1.1	0.21	0.12	0.48	0.09	0.15	0.11	0.05	39.32	99.76
SE		54.21	2.01	0.25	0.35	0.18	0.21	8.91	0.03	0.12	0.08	0.05	34.02	100.42
RM		47.12 [68.38]	11.76 [17.07]	3.34 [4.85]	2.45 [3.56]	0.23 [0.33]	1.89 [2.74]	1.75 [2.54]	0.05 [0.07]	0.15 [0.22]	0.11 [0.16]	0.07 [0.10]	31.50	100.41 [100.02]
Lower Ghareb Fm. (Marl Member) Bibliographic Values [220]	***Min.***	32.00	2.40	0.60	0.30	0.30	0.10	0.19	0.04	0.31	0.29	0.02	32.00	94.97
	Average	33.58	9.83	3.90	1.84	0.51	5.79	1.65	0.16	0.42	0.74	0.03	42.15	99.52
	Max	44.10	14.00	6.00	3.50	1.12	11.90	5.70	0.24	0.40	2.00	0.06	49.33	101.35

Table 7.1 – X-ray Fluorescence results for limestone protoliths belonging to Ghareb Formation, also bibliographic values [220] are reported for making comparison; e.s.d. below 0.1 wt%; values reported in square brackets do not take into account LOI; *sum of analysed oxides and LOI.

$Sample/_{Oxide}$		CaO	SiO_2	Al_2O_3	Fe_2O_3	MgO	SO_3	P_2O_5	TiO_2	K_2O	Na_2O	SrO	BaO	LOI	TOT
6BWO		56.04	23.30	9.56	3.32	1.05	3.42	2.46	0.52	0.21	0.38	0.11	0.11	0.58	101.06*
YC2O		53.11	25.20	9.40	3.01	2.02	1.62	0.95	0.33	0.21	0.29	0.19	0.12	3.42	99.87*
Larnite Rocks (Unit KuPh1,2,4) Bibliographic Values [2,20,221]	***Min.***	50.80	21.00	7.92	2.42	0.81	1.35	0.78	0.32	0.09	0.0	0.12	0.01	0.75	97.50
	Mean	52.06	23.55	10.78	4.53	1.16	2.81	2.00	0.40	0.74	0.33	0.18	0.10	1.72	99.53*
	Max	56.00	26.10	12.14	5.81	1.78	5.32	3.84	0.45	2.43	0.72	0.29	0.50	2.42	100.40

Table 7.2 – X-ray Fluorescence results for sampled larnite-rich rocks belonging to Unit KuPh1,2,4, and bibliographic values [2,20,221] for making comparison; e.s.d. below 0.1 wt%; *sum of analysed oxides and LOI.

7.1.2 – Synthetic green-cements

Different *green-cement*s were synthetised at laboratory scale at different temperatures observing changes on mineral assemblage, crystallographic features and microtexture among them and with natural larnite-rich rocks (*6BWO* and *YC2O*).

Heated samples were obtained by using a RHF 14/3 Carbolite laboratory oven with always an increasing temperature rate of 2 °C/min; whereas the heating time at the selected temperature was of 2, 8 and 4 hours for samples heated at 700-900, 1000-1200 and 1250-1350 °C, respectively. Samples *RM* and *BC* were heated as pellets obtained by pressing grinded powders in a pellet pressing die with an internal diameter of 11 mm and using a hydraulic press at 60 kN for 1 min. The correct working of the laboratory oven thermocouple (Type R) was checked by using Process Temperature Control Rings (PTCR). Samples burned at T ≥ 1000 °C were firstly heated at 950 °C for 1 hour accounting a complete decarbonation, followed by grinding of powders and pellets of ~ 1.5 g were re-obtained for the subsequent heating. Samples obtained at T ≥ 1250 °C were heated in a sealed Pt crucibles reducing the loss of volatile elements (Na_2O, SO_3, Cl and F) [150,222]. After the heating cycle, samples were always slowly cooled by simply turning off the SiC heating elements, accounting an average 2-3 °C/min of cooling rate. The choice of a slow cooling instead of a quenching, which the latter is normally performed in cement plant, was driven by the chance of trying to reduce the energy expenditure to obtain cement.

Sample *BC* has a chemical composition compatible with a High Ferrite Belite Cement [223,224] doped with sulphur. The choice of preparing cement with this chemical composition was driven by the chance of designing a new type *green-cements* that has the potential to (i) reduce the overall CO_2-footprint of cement plant, because it's heated at lower T than OPC, and (ii) leading the re-use of Fe and S-rich wastes, mainly coming from metallurgic [225] and chemical industry [226], respectively. *BC* was prepared by adding iron oxide (2wt.%), kaolinite (6wt.%) and gypsum (4wt.%) to a standard OPC raw meal (Table 7.3), which is made of limestone and clay. Sample *BC* was heated at 700, 800, 900, 1000, 1100, 1200, 1250, 1300 and 1350 °C. Moreover, 300 g of *BC* heated at 1350 °C were used for hydration experiments by adding natural gypsum, coming from Toledo mine (Spain), and investigated by means of DSC-TGA, ICA and XRPD at different hydration time (1, 3, 7, 28 days).

RM samples collected at Stop-8 should represent the most similar protolith of natural larnite rocks occurring in Hatrurim Basin; therefore, heating *RM* is important for a better understanding of the CP event and highlights changes occurring during heating. Furthermore, nowadays, the phosphatic gypsum-rich limestone (*RM*) represents a massive by-product waste of the Rotem Amfort phosphatic mine plant that has a similar chemical composition with OPC raw meal doped with P_2O_5, SO_3 and F. The occurrence of dopants elements could improve the clinkering reactions, reducing the temperature and heating time for making cement: therefore, *RM* could be directly re-used as an alternative cement raw material to design a new type of *green-cements*. Some *RM* samples were grinded, homogenised, and pellets were heated at 700, 800, 900, 1000, 1100, 1200, 1250, 1300 and 1350 °C. Whereas, some *RM* fragments (labelled as *RF*) were directly heated at 900, 1200 (*RFa* and *RFb*), 1250 and 1350 °C, reproducing similar heating conditions of natural larnite rocks and highlighting the effect of the texture during heating.

Element	OPC	BC		Bibliographic values	
	Starting raw meal	*Raw meal Before heating*	*After Heating (T 1350 °C)*	*BCSA* [148]	*OPC-HF* [224]
CaO	42.21	38.45	57.50	48.12-52.58	63.83
SiO_2	13.75	14.88	23.21	15.25-19.69	18.53
Al_2O_3	4.22	5.25	7.42	15.45-17.17	6.83
Fe_2O_3	1.95	3.71	5.52	2.60-7.66	5.67
MgO	0.64	0.56	0.91	0.20-1.66	0.96
SO_3	0.02	2.05	3.31	4.40-7.88	1.04
P_2O_5	0.01	0.08	0.14	-	0.31
TiO_2	0.19	0.17	0.25	0.40-0.62	0.31
K_2O	0.59	0.52	0.90	0.10-0.30	0.31
Na_2O	0.01	0.08	0.16	0.10-0.30	0.32
SrO	0.01	0.08	0.17	-	0.05
LOI	35.80	34.80	0.89	-	0.58
TOT	99.40	100.63	100.38	98.50-101.30	99.74
LSF	0.97	0.75	0.77	0.69-0.71	1.00
AR	1.68	1.34	1.42	2.76-7.31	1.20
SR	2.63	1.79	1.66	1.00-1.13	2.71

Table 7.3 – XRF results from BC sample before heating (starting raw meal) and after firing at 1350 °C; moreover, BCSAF and OPC-HF bibliographic values are reported as comparison; e.s.d. below 1wt.%.

7.2 – Methods

7.2.1 – Bibliographic research on combustion pyrometamorphism and geological framework of Hatrurim Basin

Detailed bibliographic research on CP, especially for CP event occurred in Hatrurim Basin, was made in order to get information on what have been already done and studied on this location and in particular on larnite-rich rocks.

7.2.2 – Field trip in Hatrurim Basin

The Field trip in Hatrurim Basin (see chapter 5) was prepared on the base of the bibliographic research, choosing study locations in which rocks collection and geological features at different observation scale were available.

7.2.3 – Transmitted and Reflected Light Microscopy (TLM and RLM)

Polished and thin sections were studied using Zeiss Axioscope 5 Polarizing Microscope Reflected Transmitted Light. Thin sections were only made for limestone protoliths (*RM, SO* and *SE*).

Whereas, polished sections were made for natural larnite-rich rocks (*6BWO* and *YC2O*) and *green-cements* heated at different temperatures (*RM* and *BC* at 1200, 1250, 1300 and 1350 °C, *RFa, RFb*): samples were embedded in epoxide resin under vacuum system for improving impregnation, due to the high porosity of some samples, following by a dry-out polishing with SiC abrasive papers with decreasing the grain size and finished with diamond paste (~ 1 μm). After the polishing procedure, polished sections were cleaned using pure hexane (C_6H_{14}) removing all the residues.

Polished sections of *YC2O, RFa, RFb, BC* heated at 1350 °C and *RM* heated at 1200, 1250, 1300 and 1350 °C were also studied with Nital etching (5% HNO_3 and 95% C_2H_5OH) for highlighting differences among common cement phases: drops of Nital were applied on polished sections for 10 sec. later washed by pure ethanol (C_2H_5OH).

7.2.4 – X-ray Fluorescence (XRF)

The elemental composition of natural larnite-rich rocks (*6BWO* and *YC2O*), limestone (*RM*, *SO* and *SE*), starting raw meals for synthetising *green-cement* (*BC* before and after heated) was measured by means of X-ray Fluorescence using a Bruker S8 Tiger WDXRF spectrometer with a Rh X-ray tube, operating at 50 kV and 80 mA. The quantification was performed by a calibration of a group of 56 reference standards. The measurements were carried out by using fused glass discs prepared by mixing 0.875 g of fine powdered sample with 6.125 g LiB_4, used as a low-melting reagent, overall corresponding to a 1:7 ratio sample/LiB_4. The prepared mixture was carefully homogenized in a Pt crucible and heated for 15 min at 1000 °C using a CLAISSE FLUXER-BIS! Automatic apparatus. After the complete melting, the melt was poured into a Pt-plate and slowly cooled forming glass discs that were directly used for the chemical analysis. Loss On Ignition (LOI) was determined gravimetrically by weighting the samples before and after the thermal at 1000 °C for 45 min.

7.2.5 – X-ray Powder Diffraction at Laboratory and Synchrotron scale (LXRPD/SXRPD)

XRD analysis was performed to study the phase assemblage of sample. LXRPD was performed at the University of Milan at the Earth Science Department studying all the samples, excepted the ones related to the hydration of *BC* and *Nat* that were analysed at the Servicios Centrale de Apoyo a la Investigation (SCAI) at the Department of Inorganic Chemistry. The two different instrumental set-ups are reported in Table 7.4. The sample loading was back-loading, but in the case of little amount of powder a zero-background sample holder was used, which is made of Si single crystal cut along (100) plane, and ethanol as powder dispersing media. Limestone samples (*RM, SO* and *SE*) and synthetic *green-cement* heated at 1250, 1300 and 1350 °C were also analysed by XRD adding ~ 4wt.% of Si NIST 640c [227] as an internal standard for accounting a better cell parameters refinement of crystal phases.

LXRPD – Instrumental Set-Up	***Study of natural and anhydrous synthetic rocks (University of Milan)***	***Hydration study (University of Malaga)***
Diffractometer (geometry)	PANanalytical X'Per Pro (Bragg-Brentano, θ-2θ)	PANanalytical X'Per Pro (Bragg-Brentano, θ-2θ)
Incident Beam		
X-ray Tube type (kV, mA)	Cu $K\alpha_{1,2}$ (40, 40)	Cu $K\alpha_{1,2}$ (45, 40)
Monochromator	-	Ge(111)
Soller Slit (width, ° 2θ)	0.02	0.04
Incident mask (width, mm)	6.60	-
Antiscatter Slit (width, ° 2θ)	0.5	1
Fixed Divergency Slit (width, ° 2θ)	0.25	0.5
Diffracted Beam		
Antiscatter Slit (height, mm)	5.5	1.52
Soller Slit (width, ° 2θ)	0.02	0.04
Filter (thickness, mm)	Ni (0.02)	-
Detector (active height unit, ° 2θ)	X'Celerator (2.122)	X'Celerator (2.122)
Data Collection Set-Up		
Start and end angle (° 2θ)	4 – 130	4 – 70
Step Size (° 2θ)	0.02	0.02
Count time per each step (sec)	60	280

Table 7.4 – LXRPD instrumental set-ups for investigation of natural and anhydrous synthetic rocks, performed at the University of Milan, and studying the hydration of natural larnite-rich rocks and *green-cements* at the University of Malaga.

SXRPD analysis was performed at Elettra synchrotron facility (Trieste, Italy) at the beamline MCX and at ESRF synchrotron facility (Grenoble, France) at the beamline ID22, both with *ex-situ* and *in-situ* experiments. The choice of performing SXRPD analysis was driven by: (i) the complexity crystal phase assemblage of natural larnite-rich rocks both anhydrous and hydrated ones, especially on minor crystal phases, (ii) the chance of obtaining highly accurate and precise data on crystal structure parameters and compare between natural *vs* synthetic materials (larnite cell parameters, crystallite size and microstrain differences); (iii) the availability of performing HT *in-situ* experiments with high d-spacing resolution and fast data collection.

Ex-situ experiments at MCX beamline were performed on limestone (*RM*), natural larnite-rich rocks (*6BWO*, *YC2O*), natural hydrated larnite-rich rocks (*6BWV*, *YC2V*) and laboratory hydrated larnite-rich rocks (*6BWO* after 3 weeks of hydration). The experimental set-up used is reported in Table 7.5 (Fig. 7.1). The monochromatic radiation was selected by using a double crystal Si(111). Borosilicate glass capillaries with an internal diameter of 1 mm were used as sample holders for the data collection (Fig. 7.2).

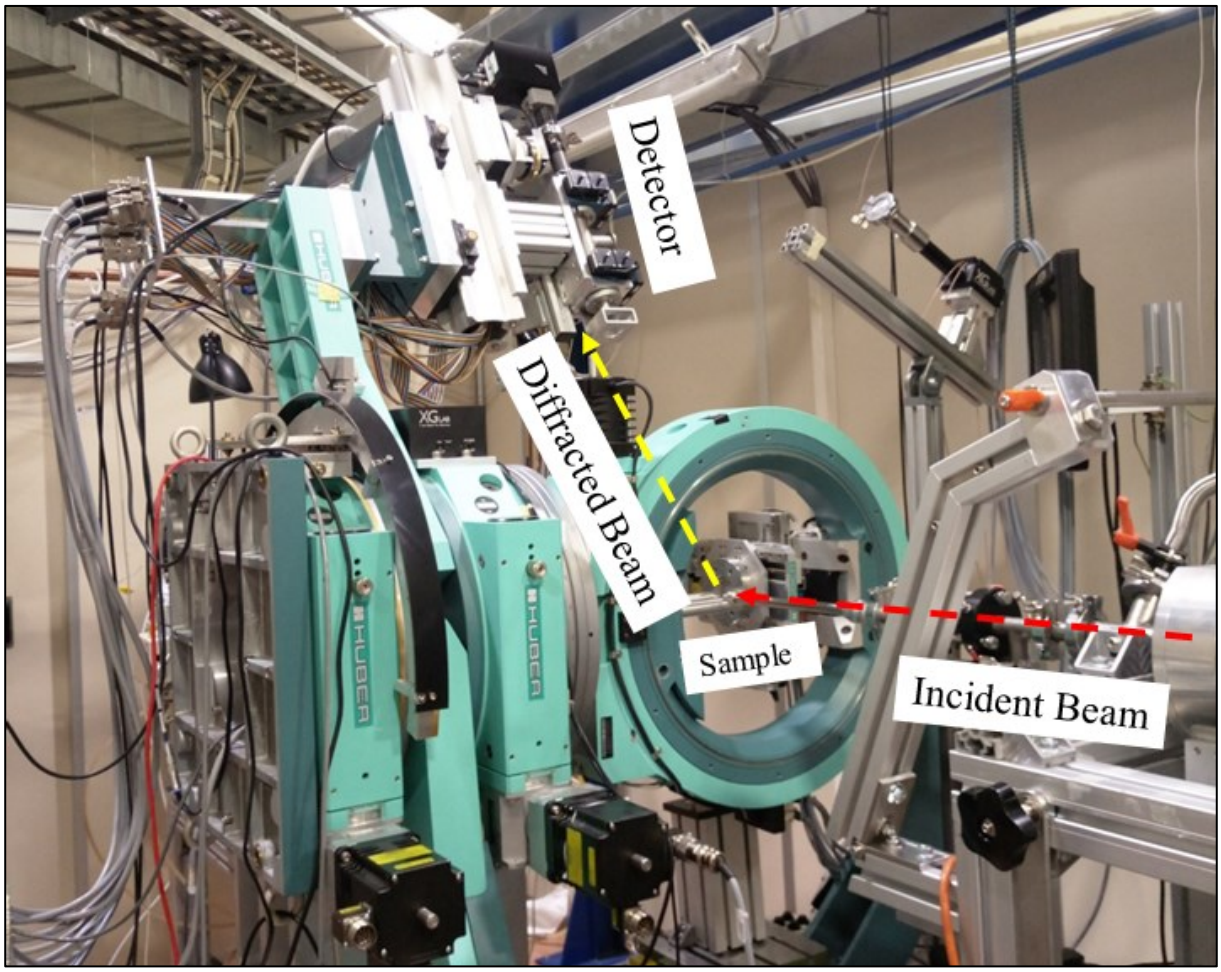

Fig. 7.1 – SXRPD diffractometer at MCX beamline of Elettra synchrotron, highlighting the experimental set-up used of ex-situ experiments.

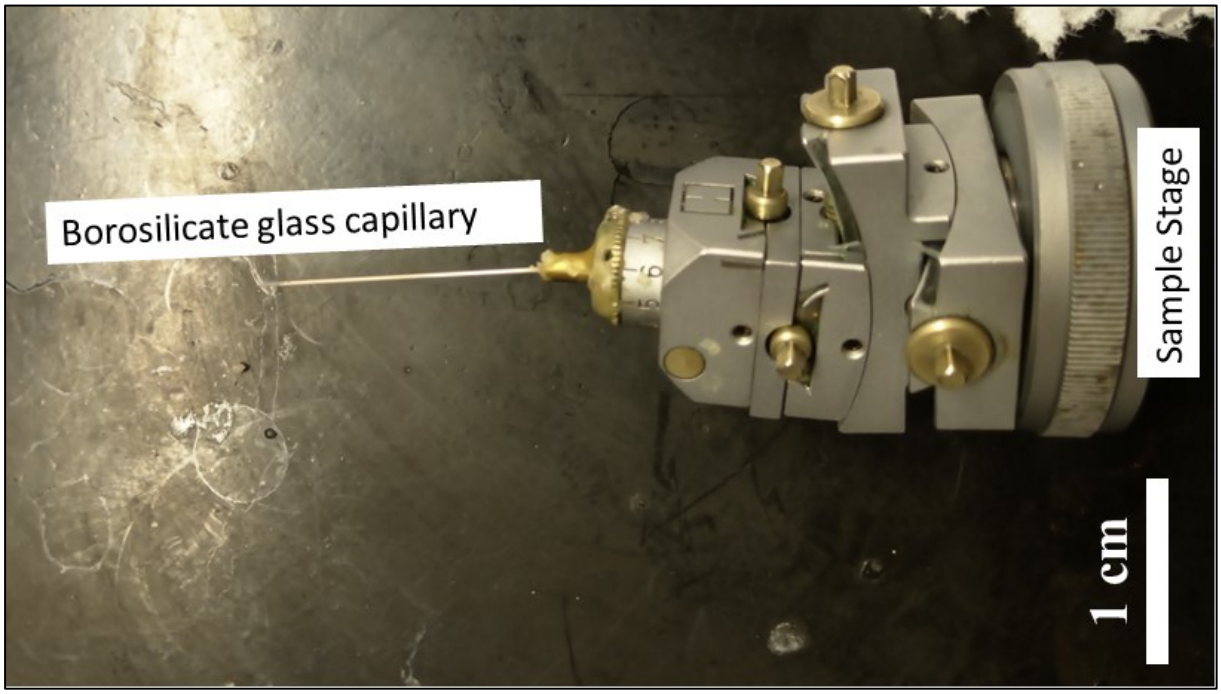

Fig. 7.2 – Sample stage set-up for ex-situ experiments at MCX beamline at Elettra synchrotron.

HT *in-situ* experiment at MCX beamline was performed with the same λ of *ex-situ* experiments on natural limestone (*RM*) using a furnace and heating from room temperature to 1000 °C: an increasing temperature rate of 10 °C/min till 800 °C and of 5 °C/min from 800 to 1000 °C; data collection was performed at room temperature, 500, 600, 700, 750, 800, 850, 900, 925, 950, 1000 °C and after heating at 25 °C; before each collection a stabilising time of 15 min was waited, in order to reach the thermodynamic equilibrium. The furnace has a linear hole that allows to exit the diffracted beam that reaches a translating image plate [228–231] (Fig. 7.3,4). Pure SiO_2 glass capillary was used as sample holder; furthermore, the capillary base was open allowing the escape of gases mainly released during the decarbonation of calcite, avoiding the over pressuring and explosion of the capillary (Fig. 7.5).

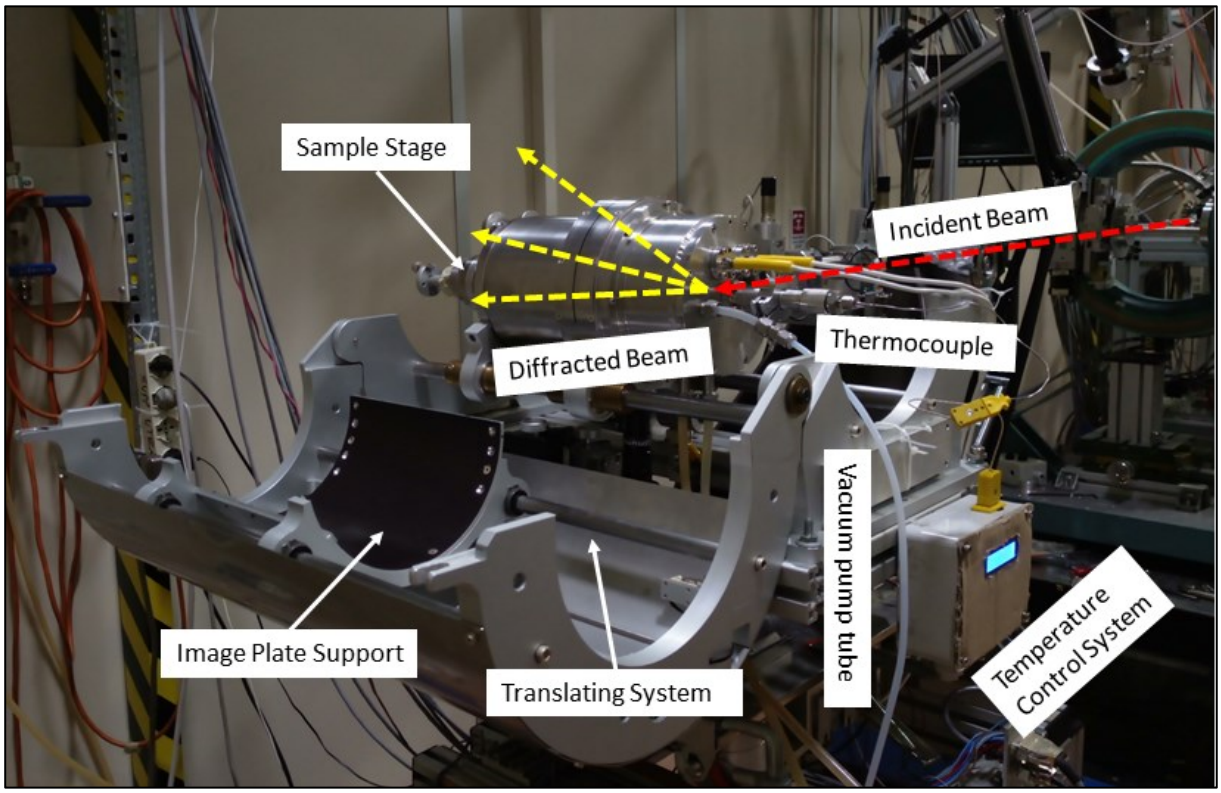

Fig. 7.3 – Instrumental set-up used for in-situ experiment at MCX beamline at Elettra synchrotron.

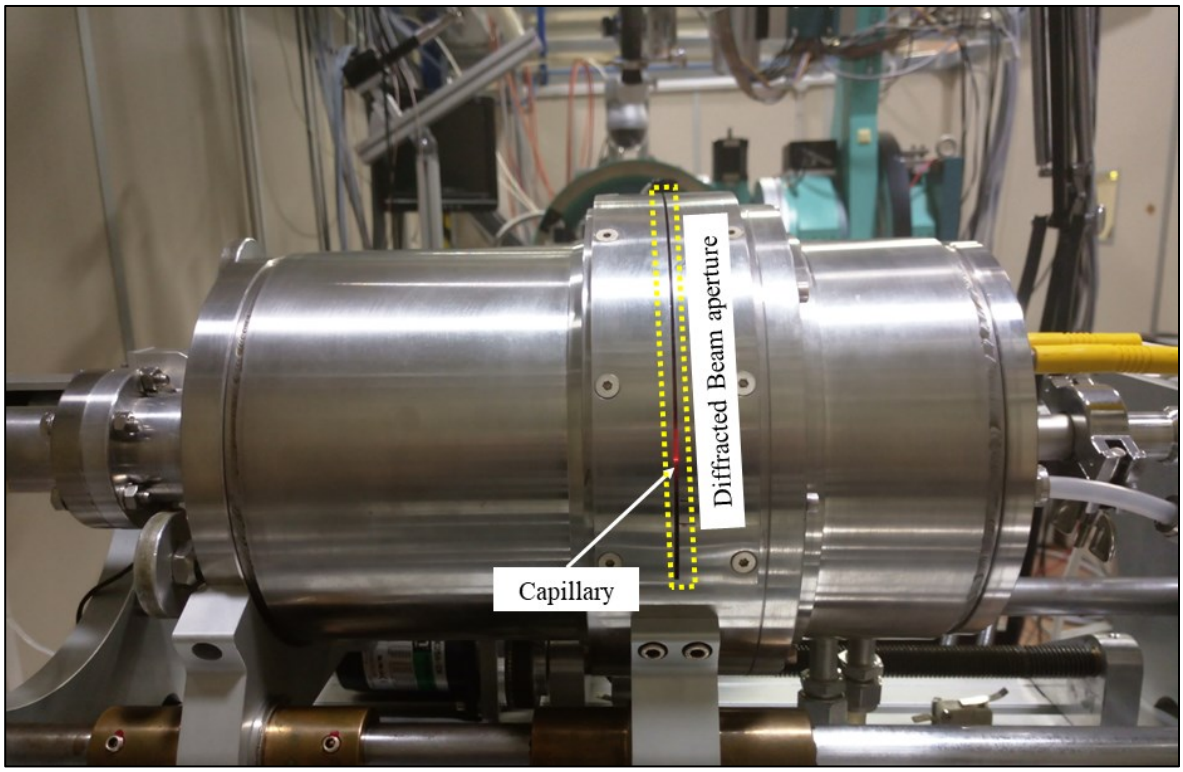

Fig. 7.4 – MCX beamline oven operating at 1000 °C, highlighting the position of the heated capillary after the data collection at high-temperature.

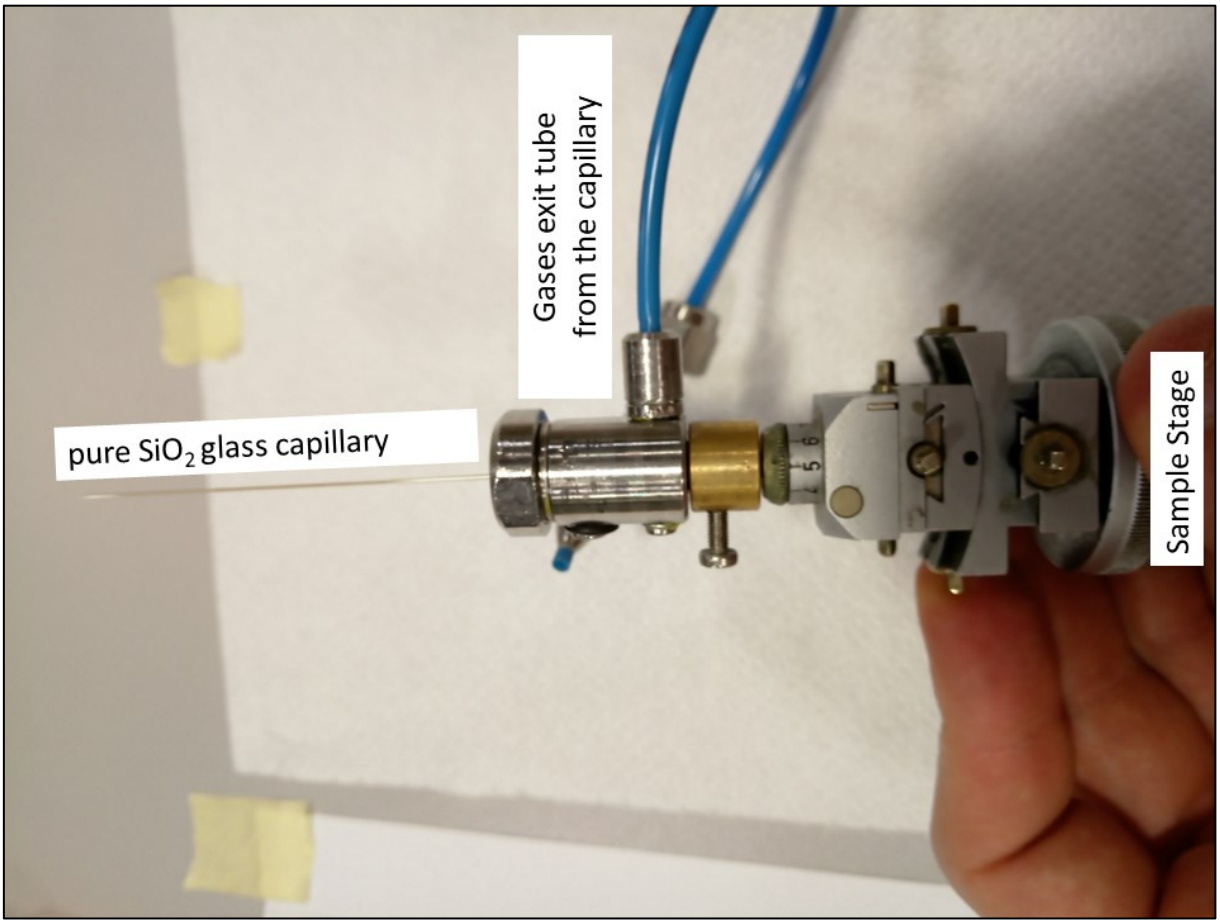

Fig. 7.5 – Sample stage set-up for high-temperature in-situ experiment at MCX beamline at Elettra synchrotron.

Synchrotron Facility, Beamline	***Elettra, MCX***	***ESRF, ID22***
Monochromatic λ (Å)	1.033	0.354109
Geometry	Debye Scherrer	Debye Scherrer
start and end angle (° 2θ, Å)	4 – 65 °, 14.78 – 0.96 Å	0.002 – 52.916 °, 10020 – 0.3974 Å
Detector	Fast scintillator counter	Multi-analyser stage (9 Si(111) associated with Point Sensitive Detectors) [232]
Step Size (° 2θ)	0.01	0.002
Count per each step (sec)	4	0.42

Table 7.5 – SXRPD instrumental set-ups for ex-situ experiments performed at Elettra and ESRF synchrotron facilities.

Ex-situ experiments at ID22 beamline were performed on natural larnite-rich rocks (*6BWO* and *YC2O*), natural hydrated larnite-rich rocks (*6BWV* and *YC2V*) and on anhydrous *green-cements* heated at 1200 °C (*RM_1200* and *BC_1200*) [233–235]. Borosilicate capillaries were used as sample holder for *ex-situ* experiments.

High-temperature *in-situ* experiments at ID22 beamline were performed on natural limestone (*RM*), previously decarbonated at 900 °C for 2 hours, which were heated from room temperature to ~ 1250 °C by using a halogen-bulb mirror furnace made of three 150 W halogen lamps (Fig. 7.7,8). Pt-capillaries with an internal diameter of 0.6 mm and 0.04 mm wall thickness were used as sample holder filled with the decarbonated limestone powder (Fig. 7.6). To ensure the maximum efficiency of the furnace, the lamps filaments must lie in the same plane of the sample rotation axis, focusing thus a 4 mm section along this axis. Moreover, filled Pt-capillaries were also sealed at the ends by argon arc welding machine, avoiding the escape of volatile elements (F, Cl and SO_2) at HT. The furnace technical configuration allows no direct temperature measurements on the sample during heating. Therefore, platinum from the capillary was used as an internal standard to control the reached temperature by considering the thermal expansion coefficients [236] (*Eq.*1) and the cell parameter expansion obtained by Rietveld refinement: *Eq.2* reports the formula to obtain the achieved temperature in kelvin by considering the thermal expansion coefficients (*Eq.1*), the cell parameter value at room temperature measured in Å (a_0) and the observed increase in the cell parameter (Δ_{a_0}, Å).

(Eq.1) $$\frac{\Delta_{a_0}}{a_0} = 7.543 * 10^{-6}(T - 291) + 7.543 * 10^{-9}(T - 291)^2$$

(Eq.2) $$T(°K) = \left(-7.543 * 10^{-6} + \frac{\sqrt{(-7.543*10^{-6})^2 - 4(2.362*10^{-9})\left(-\frac{\Delta_{a_0}}{a_0}\right)}}{2\,(2.362*10^{-9})} \right) + 291$$

Two different experimental data collections were used (Table 7.6): (i) one Pt-capillary was analysed at different selected temperatures (916, 966, 1029, 1040, 1060, 1077, 1095, 1111, 1133, 1150, 1182 °C) with an heating rate of 15 °C/min from room temperature to 900 and 5 °C/min from 900 to 1200 °C, moreover, a stabilising time of 10 min before data collection was used; (ii) the other

experiment was performed by heating the Pt-capillary from room temperature to 1250 °C with an heating rate of 15 °C/min till 900 °C and 5 °C/min from 900 to 1250 °C, and data was collected after each ~ 13 °C of increasing temperature without a stabilising time. Both experiments were also analysed at 25 °C before and after heating by a fast cooling, in order to highlight differences in the crystal phase assemblage from high to room temperature. The 2nd High-Temperature *in-situ* experimental set-up, which has no stabilising time before data collection, was chosen trying to reproduce similar conditions occurring in rotary kiln in cement plant [7,8,132].

Synchrotron Facility, Beamline	***ESRF, ID22***	
Instrumental Set-Up	**1st HT *in-situ* experiment** (stabilising time of 10 min)	**2nd HT *in-situ* experiment** (no stabilising time)
Monochromatic λ (Å)	0.354109	0.354109
Geometry	Debye Scherrer	Debye Scherrer
Start and end angle (° 2θ, Å)	0.002 – 42.92°, 10020 – 0.484 Å	0.002 – 42.92°, 10020 – 0.484 Å
Detector	Multyanalyser stage (9 Si(111) associated with Point Sensitive Detectors) [232]	Multyanalyser stage (9 Si(111) associated with Point Sensitive Detectors) [232]
Step Size (° 2θ)	0.002	0.002
Count per each step (sec)	0.05	0.01

Table 7.6 – SXRPD instrumental set-ups for the two in-situ experiments performed at ID22 beamline at ESRF synchrotron facility.

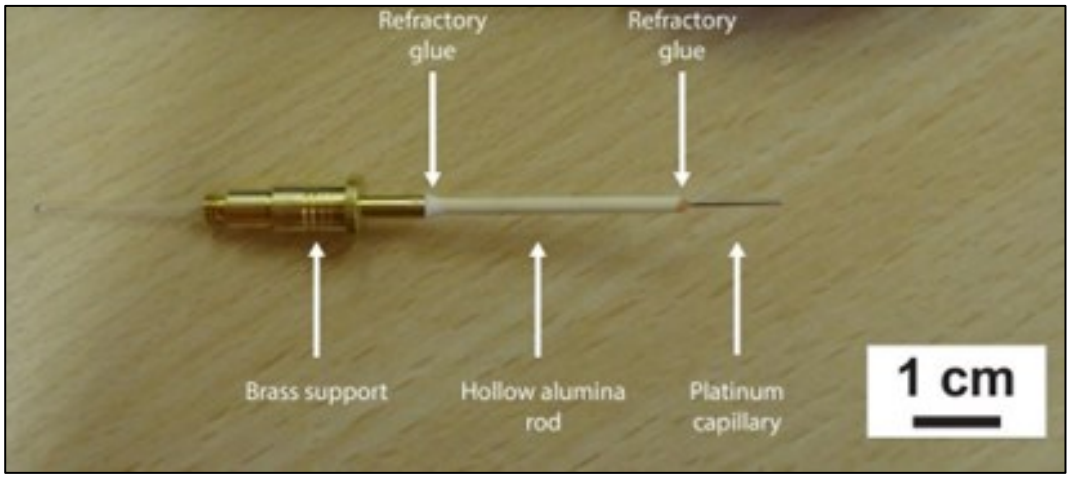

Fig. 7.6 – Sample configuration of high-temperature in-situ experiments at ID22 at ESRF synchrotron.

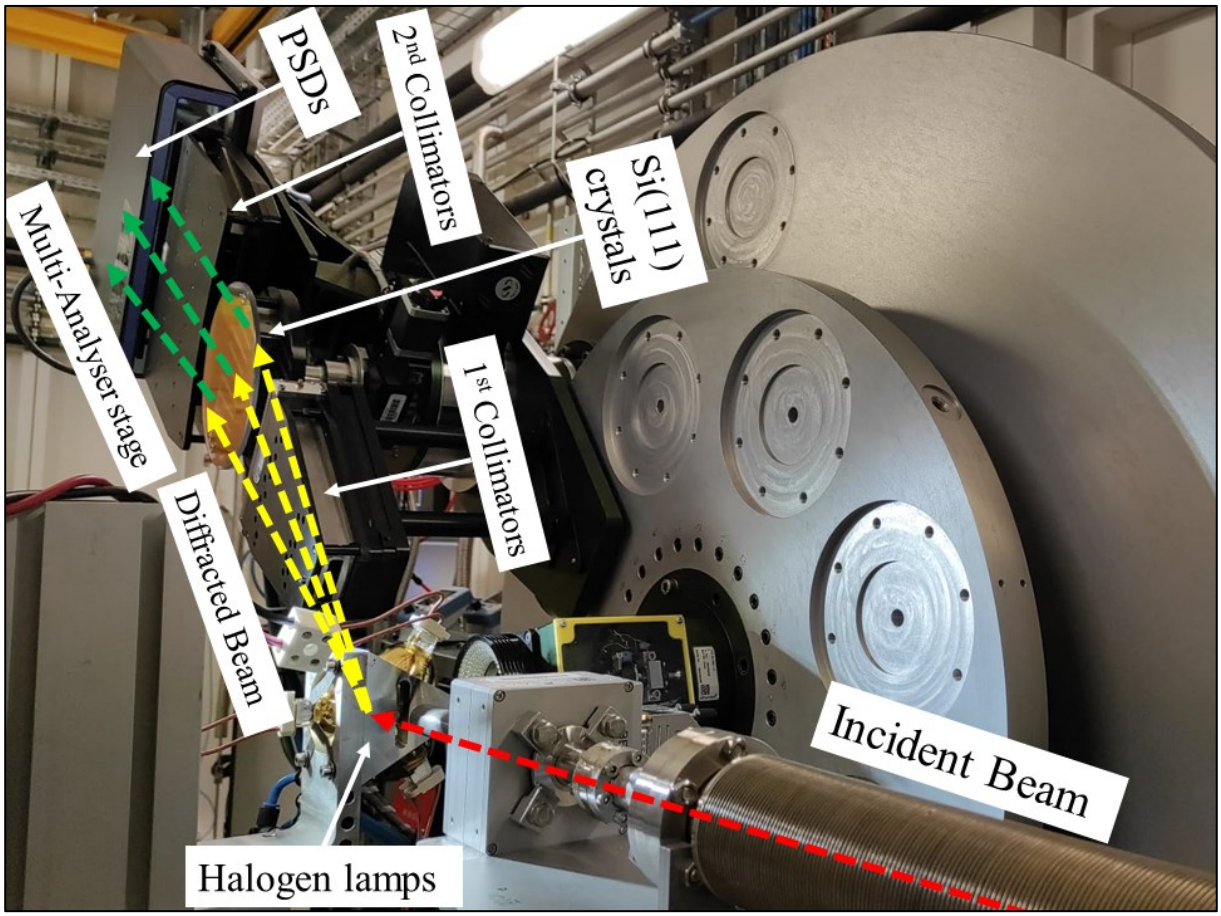

Fig. 7.7 – Instrumental configuration at ID22 beamline at ESRF synchrotron used for in-situ and ex-situ experiments, excepted the halogen lamps for the latter.

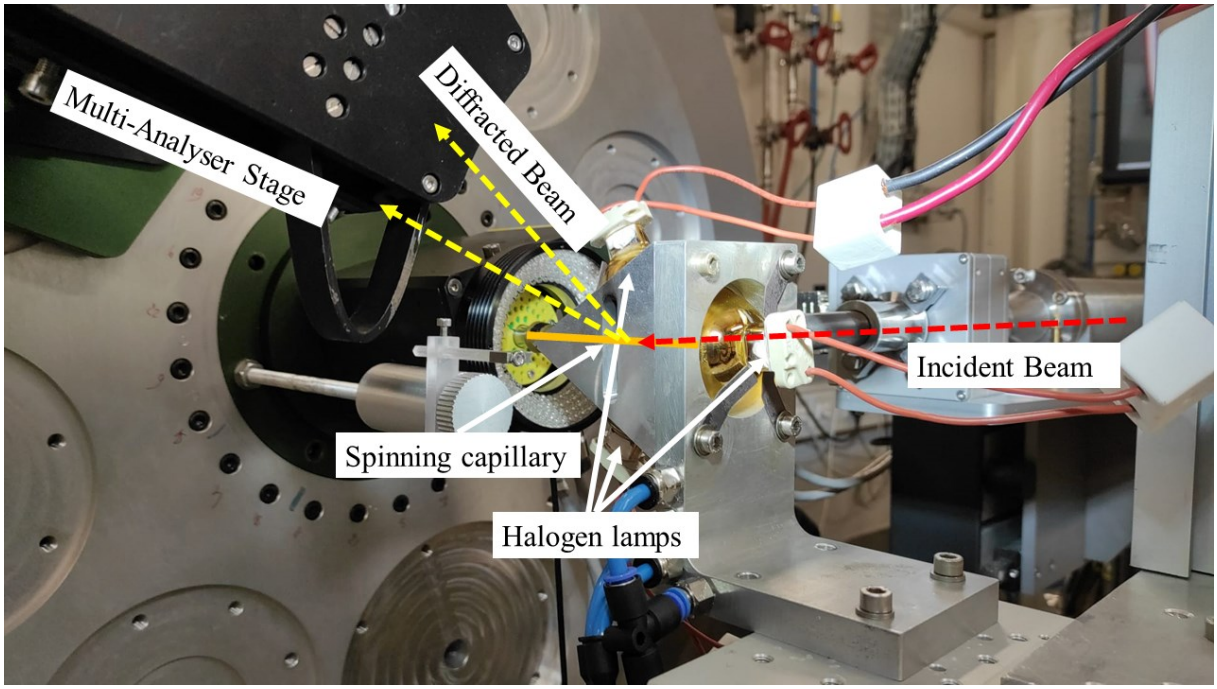

Fig. 7.8 – Instrumental configuration at ID22 beamline at ESRF synchrotron used for in-situ and ex-situ experiments, excepted the halogen lamps for the latter.

7.2.6 – Qualitative phase analysis, Rietveld Quantitative Phase Analysis (RQPA) and refinement strategy

Qualitative phase analysis of XRD data was performed by means of PANalytical X'Pert HighScore v. 1.0b software [237] associated with the Powder Diffraction File (PDF-2) [238], leading a fast and visual identification of occurring crystal phases in the sample. Whereas, Crystallography Open Database (COD) was used for searching the available crystal structures for the next Rietveld refinement method [239–244].

The Rietveld method accounts the quantitative crystal phase analysis in powder studied by XRD, and nowadays it is widely used in industry for studying complex mixtures [245–247]. The Rietveld method uses a least square approach to optimize a theoretical line profile until it matches in the best possible way the measured one obtained from XRD analysis: *Eq.3* reports the function that has to be minimized (S_y), w_i is the statistical weight, $Y_i(obs)$ and $Y_i(calc)$ represent the observed and calculated pattern at each *i*-point.

(Eq.3) $S_y = \sum_i w_i |Y_i(obs) - Y_i(calc)^2|$

The $Y_i(calc)$ is obtained by the *Eq.4* as the sum of the contributions of the background $Y_{bck}(2\theta_i)$ and the intensity from the crystal phases. The latter contribution is calculated by considering the scale factor for each α-phase (S_α), the multiplicity (m_k) and the structure factor (F_k) of reflections *k*, $h(2\theta_i - 2\theta_k)$ representing the profile function describing the intensity along the pattern, P_k representing the additional corrections (preferred orientation of crystals, systematic extinctions, etc.) and $L_p\,(2\theta_i)$ corresponding to the Lorentz polarization correction factor.

(Eq.4) $Y_i(calc) = Y_{bck}(2\theta_i) + \sum_{\alpha=1}^{m} S_\alpha \sum_k m_k\, |F_k|^2 h(2\theta_i - 2\theta_k) P_k L_p\,(2\theta_i)$

The profile function ($h(2\theta_i - 2\theta_k)$) is described by a convolution of more functions. The software used for RQPA in this work is GSAS-ii [248] that uses a pseudo-Voigt function [249,250] considering for the FHWM a Gaussian (σ^2) and Lorentizian broadening (γ): *U*, *V* and *W* are coefficients from Caglioti equation [251], whereas *P* is the Scherrer coefficient for Gaussian broadening; *X* is the Lorentzian Scherrer broadening and *Y* describes the strain broadening.

(Eq.5) $\sigma^2 = Utan^2\theta + V\,tan\theta + W + P/cos^2\theta$

(Eq.6) $\gamma = {}^{X}/_{cos\theta} + Y\,tan\theta$

FWHM Gaussian and Lorentzian broadening parameters are used to describe the overall Instrumental Broadening Function (IBF) that is obtained by collecting a pattern of a standard and refining the parameters (*U, V, W, X* and *Y*). Furthermore, in GSAS-ii a refinable parameter *SH/L* is used to account the peak asymmetry which has a strong impact on Bragg peaks at low angle [252,253]. In GSAS-ii micro-strain (*Eq.7*) and crystallite size (*Eq.*8) is normally considered as full Lorentzian broadening, hence for each α crystal phase included in the Rietveld refinement two additional terms are added to FWHM Lorentzian broadening (γ): (i) Y_α used for calculating the

micro-strain; (ii) X_α accounting the crystallite size broadening. S_α represents the micro-strain parameter for a specific α-phase, is dimensionless and accounts lattice deformations, vacancies and defects of the lattice; whereas *K* represents the Scherrer constant depending on the shape of crystallite (for a sphere as crystallite shape, $K = 0.89$). C_α represents the crystallite size for a α phase reported in Å, accounting the average dimension of lattice domain. T. In the case of considering the effect of micro-strain and crystallite size broadening as a mixture of Lorentzian and Gaussian broadening two more equations will be considered using P (*Eq.*5) and U (*Eq.*6) refinable parameters for each crystal phase, as for Y_α and X_α [254]. An increase in micro-strain is equal to an increase in broadening, whereas an increase in crystallite size acts as a sharpening of Bragg peaks for a specific α-phase. The general equation used to represent the crystallite size is $\beta(2\theta) = {\lambda K}/{D\ cos\theta}$ [255,256], where *D* represents the crystallite size and *β(2θ)* the integral breadth corresponding to peak broadening; whereas the general equation for micro-strain is $e = {\beta(2\theta)}/{4\ tan\theta}$, where *e* is the micro-strain value [257].

(*Eq.7*) $S_\alpha = \frac{\pi}{18000} Y_\alpha\ 100\%$

(*Eq.8*) $C_\alpha = \frac{18000\ K\ \lambda}{\pi\ X_\alpha} 100\%$

The refinement strategy for performing the RQPA on XRD data was the following: (i) obtaining the IBF for each instrument by using LaB_6 NIST 660a and Si NIST 640c for laboratory and synchrotron diffractometers, respectively, refining *U*, *V*, *W*, *X*, *Y* and *SH/L*, which the latter is used to describe the peak asymmetry [227]; (ii) using a Chebyshev polynomial function with 10 terms to describe the background function, which were refined during the refinements; (iii) refining the scale factor for each occurring crystal phase; (iv) refining the zero error parameter of the diffractometer; (v) refining the cell parameters of crystal phases, always after three refinements cycle of the previous step; (vi) refining the crystallite size and micro-strain separately and alternatively for three times, due to their high correlation. Crystallite size and micro-strain were refined only for main crystal phases; moreover, they were together refined only for synchrotron data, since no correlation error occurred [248]. Furthermore, when Si NIST 640c [227] was added as an internal standard, only the cell parameters of other phases were refined, obtaining more precise values.

The goodness of fitting was measured by considering three Rietveld parameters that are calculated by the GSAS-ii software after each refinement cycle:

1. R_{exp} (Rietveld expected pattern), $R_{exp} = \sqrt{\frac{\sum M-P}{\sum w_m {Y_i}^2(obs)}}$, where *M* represents the overall number of observed points, *P* the refined parameters and w_m is the reciprocal of the variance;
2. R_{wp} (Rietveld weighted pattern), $R_{wp} = \sqrt{\frac{\sum w_m [Y_i(obs)-Y_i(calc)]^2}{\sum w_m {Y_i}^2(obs)}}$;
3. χ^2, also called as GoF (Goodness Of Fitting) $GoF = R_{wp}/R_{exp}$.

In order to quantify the amount of amorphous phase during the hydration process of *green-cements* (*3GBC* and *3GNat*) content the internal standard method was applied [258–260]: adding 20wt.% of α-SiO_2 Quartz (NIST 755 [227]). The amorphous fraction (W_A, wt.%) is obtained from the following *Eq.9*, where *Ws* (wt.%) and R_S (wt.%) represents the know amount of added internal crystalline standard and the Rietveld result (wt.%) for the internal standard, respectively:

$$(Eq.9)\ W_A = \frac{1}{100 - W_S}\left(1 - \frac{W_S}{R_S}\right) * 10^4$$

The amorphous content includes not only the amorphous phase, which normally produces a hump in the XRD pattern from 5.6 to 2.5 Å [261], but also all crystal phases that were not included in the Rietveld refinement: a good amorphous evaluation requires to identify all occurring crystal phases. Therefore, the "real" weight percent of each crystal phase (W_α, wt.%) is obtained by using the calculated concentration for each crystal phase (R_α, wt.%) and the amorphous content (W_A), as reported in the following *Eq.10*:

$$(Eq.10)\ W_\alpha = \frac{R_\alpha}{\left(\sum_{\alpha=1}^{n} R_\alpha\right)}(100 - W_A)$$

7.2.7 – Single Crystal X-ray Diffraction (SCXRD)

Laboratory SCXRD was performed on crystals picked up from the 5wt.% HCl residue of dark-submetallic anisotropies in Ghareb Formation limestone (*RM*) using a stereomicroscope, which were identified as titanite ($CaTiSiO_5$) crystals. Diffraction data collection used a Rigaku Oxford Diffraction XtaLAB Synergy diffractometer, equipped PhotonJet (Mo) X-ray Source operating at 50 kV and 1 mA, with a monochromatized Mo*K*α radiation and equipped with a HyPix hybrid photon counter (HPC) detector working at 62 mm from the crystal. A step scan 0.5° and an exposure time 80 s per frame was used. Intensity data was extracted, scaled and corrected for absorption using CrysAlisPro v. 1.171.40.36a [262].

Synchrotron SCXRD was performed on rhombic-shape crystals of hatrurite (Ca_3SiO_5) picked up from the synthetic *green-cement RM* heated 1350 °C as pellets at X06DA (PXII) beamline at the synchrotron light source of Paul Scherrer Institute (PSI) [263–268]. Diffraction data collection used a monochromatic radiation source (λ = 0.70848 Å), a 90 x 45 μm focused beam, PILATUS 2M-F detector with a detector distance of 90 mm, multi-axis PRIGoniometer and sample changer CATS.

Collected data was analysed (peak hunting, peak indexing, unit cell finding and space group identification) by mean of CrysAlisPro v. 1.171.40.36a [262].

7.2.8 – Scanning Electron Microprobe analysis and Electron MicroProbe microAnalyser (SEM/EMPA)

Scanning Electron Microprobe analysis and Electron MicroProbe microAnalyser were performed for obtaining microtextural, punctual chemical composition and variability on natural larnite-rich rocks and synthetic *green-cements*. Samples were prepared as reported in section 7.2.3 and a

covering of a sputtered graphite layer was applied to ensure same electric conductivity on the surface sample.

Scanning Electron Microprobe (SEM) analysis was performed by means of a JOEL JSM-IT 500 in Energy Dispersive X-ray Spettroscopy (EDS) at the laboratory of the Earth Science Department "Ardito Desio" of the University of Milan, with an accelerating voltage of 20 kV, a spot size of 1 μm, a beam current of 10 nA, a counting time of 60 s on peaks and 20 s on backgrounds. The following samples were studied by means of SEM-EDS: *6BWO* and *YC2O*, corresponding to natural larnite-rich rocks; *BC* heated at 1200, 1300 °C, representing the laboratory *green-cements* rich in belite, ferrite and ye'elimite; Ghareb Formation heated at 1200 °C as pellets (*RM_1200*) and fragments (*RFa* and *RFb*), corresponding on *green-cements* doped with P, S and F.
Electron MicroProbe microanalysis was performed by mean of a JEOL JXA-8200 Electron MicroProbe Analyser (EMPA) in Wavelength Dispersive X-ray Spectroscopy (WDS), with an accelerating voltage of 15 kV, an electron probe spot size of 1μm, a beam current of 10 nA, a counting times of 30 s on peaks and 10 s on backgrounds. The following elements were measured: Si, Al, Ca, Fe, K, Mg, Na, S, P, Ti, Cr and F for all samples, and also Cl for natural larnite-rich rocks. Natural kyanite (Al_2SiO_5, for Al, Si, TAP), anorthite ($CaAl_2Si_2O_8$, for Ca. PET), fayalite (Fe_2SiO_4, for Fe, LIF), K-feldspar ($KAlSi_3O_8$, for K, PET), olivine ($(Mg,Fe)_2SiO_4$, for Mg, TAP), omphacite ($(Na,Ca)(AlMg)Si_2O_6$, for Na TAP), anhydrite ($CaSO_4$, for S, PET), fluorapatite ($Ca_5(PO_4)_3F$, for F and P, PET and LDE), chromite ($MgCr_2O_3$, for Cr, PET) and titanite ($CaTiSiO_5$, for Ti, PET) and sylvite (KCl, for Cl, LDE) have been employed as standards. Raw data were corrected for matrix effects using a conventional ΦρZ routine in the JEOL soft-ware package [269].
These polished sections were also investigated by means of a Zeiss EVO MA15 Scanning Electron Microscope operating with an acceleration current of 15 kV and 4 nA, a beam size of 100 nm and a working distance of 11 mm, with an image resolution of 1024 x 730 pixels. Microstructural analysis was performed using detection of BackScattered Electrons (BSE). Elemental maps were obtained studying the distribution of Al, Fe, S, P and F using WDS method on representative sample portions with a pixel size of 0.20 x 0.20 μm^2, a counting time of 30 ms. The following samples were studied using EMPA-WDS: *6BWO* and *YC2O* for natural larnite-rich rocks; *BC* heated at 1250, 1300 and 1350 °C; *RM* heated at 1200, 1250, 1300 and 1350 °C; Ghareb Formation samples heated at 1200 °C as fragments (*RFa*).

Elaboration of BSE images was carried out by means of Image-Pro PLUS v 4.5.0.29 and ImageJ v. 1.53 software [270–272].

7.2.9 – X-ray microComputed Tomography at synchrotron scale (μ-CT)

3D imaging experiments were performed at SYRMEP beamline at Elettra synchrotron, in order to obtain 3D microtextural information (porosity, permeability, connectivity of pores, crystals dimensions, preferred orientations, etc.) and crystal phase identification based on differences in density; furthermore, high-temperature *in-situ* experiment was performed on a fragment of Ghareb Formation revealing microtextural changes (calcite decomposition, incipient melting temperature, pores evolution, etc.) occurring during heating.

Both *in-situ* and *ex-situ* experiments were performed using a white-beam with 2.4 GeV filtered by Al-foils selecting an average energy of 27.9 keV. Using a polychromatic radiation allows higher photon flux, decreasing the scanning time increasing the thickness of sample. The samples were located at 16 m from the source and the maximum X-ray beam size was 160 mm (h) x 4 mm (v). Images were acquired using a microscope system based on a 16-bit, 2048 x 2048 pixels, water-cooled sCMOS detector coupled with a 17 μm-thick LSO:Tb scintillator screen. Experiments performed on cylindrical samples with ~ 1.5 mm diameter.

Ex-situ investigations used a pixel size of 0.9 μm, a 15 cm as sample-detector distance, 300 ms of exposure time, 2000 projections (0.09° rotation along z axis) and 2048 slices (3.84 mm of investigated length). Moreover, two experiments for each sample were carried out for increasing the analysed volume also considering an overlapping of 448 slices from a portion to the other, hence studying an overall 3648 slices (~ 3.28 mm of length). The following samples were analysed: *YC2O*, *6BWO*, *YC2V, 6BWV* and *BC* heated at 1350 °C.

HT *in-situ* experiment was performed on fragment of Ghareb Formation using 2.4 μm pixel size, 20 cm sample-detector distance, 350 ms of exposure time, 1000 projections (0.18° rotation along z axis) and 1600 slices (~ 1.84 mm of studied length). The furnace used for HT experiments is based on induction heating by application of radiofrequency signal on an electrically conducting object [273] (Fig. 7.9,10). Because the heat is generated inside on the graphite furnace, the sample can be fast heated and cooled, reproducing similar conditions occurring in rotary kiln. The heating element of the furnace is an induction coil controlled by HGT-1200/0.45 N high-frequency generator. For the experiment an alumina crucible with an internal diameter of 3.9 mm and a vertical size of 7 mm was used and located inside the graphite furnace. The graphite furnace is surrounded by a pure SiO_2 glass tube and is placed in the middle of two zirconia rods. In order to avoid oxidation of graphite furnace a continuous nitrogen flux is maintained during the experiment. The oxygen fugacity cannot be directly measured, but previous experiments [273] highlighted a fO_2 10^{-3} at 1000 °C, between HM and NNO buffers, corresponding to similar conditions in rotary kiln. The temperature control is performed by increasing or decreasing the amperage of the generator; before the experiment a heating calibration curve was measured using a S-type Pt-Rh/Pt thermocouple, a FLUKE 54 II temperature controller and positioning the thermocouple inside the crucible instead of the sample. An increasing temperature rate of 10 °C/min and a stabilising time of 15 min; data collections were made at room temperature, 900, 1150, 1250 and at 25 °C after heating at 1350 °C for 30 min of fragment of Ghareb Formation. The measurement at 1350 °C as not carried out because of the movement of the sample during melting, inhibiting the reconstruction. Moreover, in order to make a comparison between *in-situ* and laboratory prepared heated sample, also Ghareb Formation fragments heated at 900, 1250 and 1350 °C (*RF*) were analysed at room temperature with the same *in-situ* instrumental set-up.

Image processing was made using two softwares: (i) ImageJ [270,272] to treat sample slices identifying voids and high density phases; (ii) VGStudio Max v. 3.4 for 3D reconstruction importing sample volume and voids as separated elements. The volume of voids was calculated by the ratio between void pixels and sample pixels obtained from ImageJ Analyse Particle function.

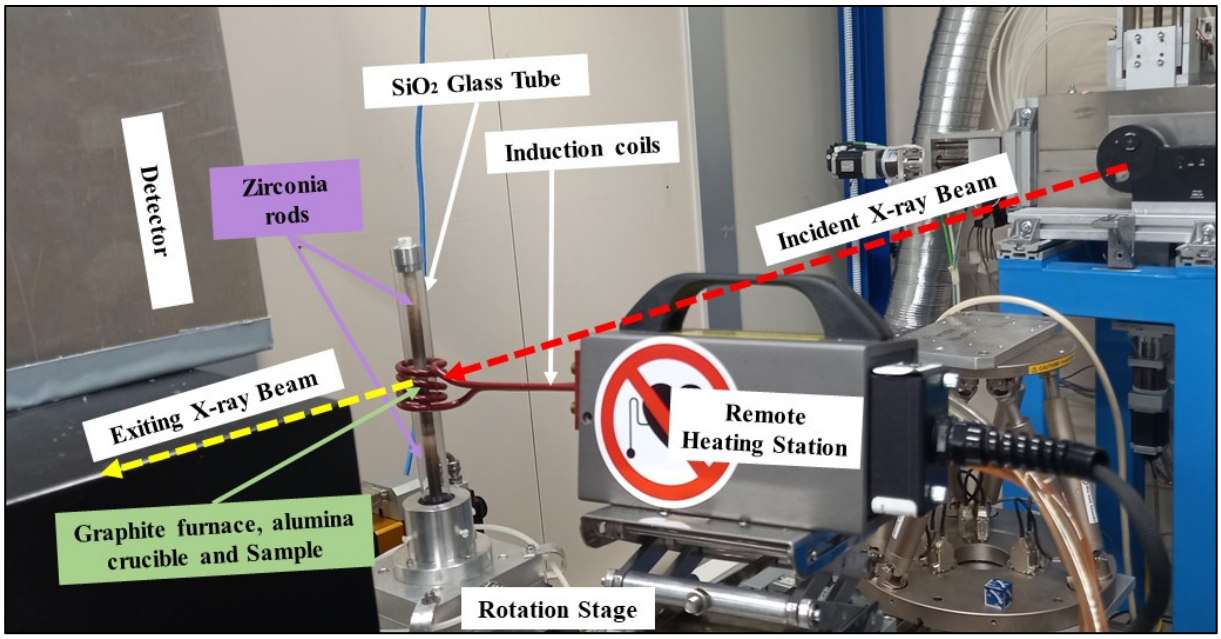

Fig. 7.9 – High-temperature in-situ experimental set-up, highlighting the heating system configuration.

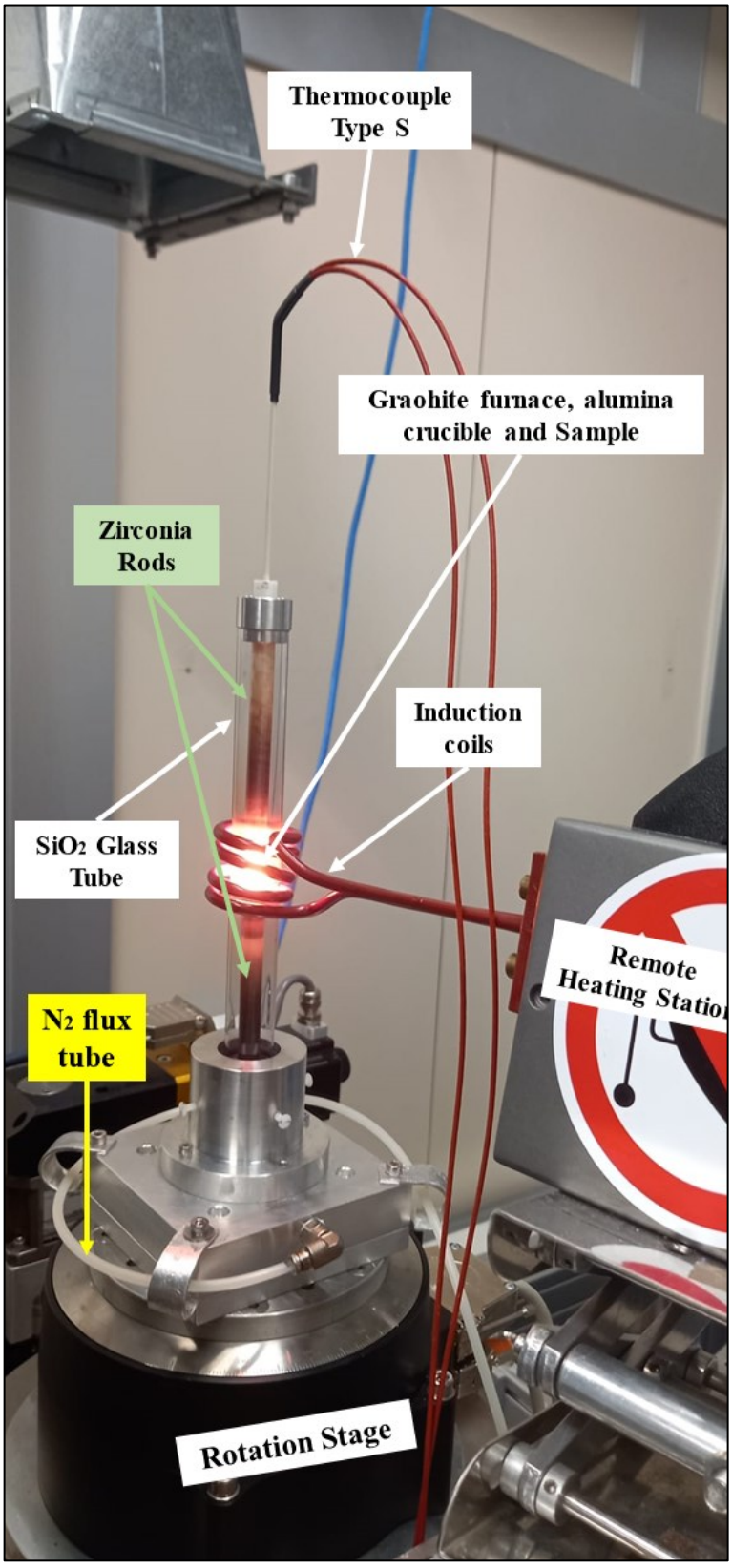

Fig. 7.10 – High temperature in-situ experimental set-up at 1350 °C.

7.2.10 – Neutron Diffraction for Quantitative Texture Analysis (NXRD-QTA)

Neutron Diffraction represents a non-disruptive method for Quantitative Texture Analysis (NXRD-QTA), also called Crystallographic Preferred Orientation (CPO) [274]. This method uses the high penetration and high flux of neutrons available at the nuclear reactor at the Institute Laue-Langevin (ILL) in Grenoble (France), allowing the study of samples with volumes ~ 1 cm^3. Measurements were performed using the D1B diffractometer with a monochromatic radiation of λ = 2.526039 Å selected with a pyrolytic graphite (002) monochromator, a flux = $6*10^6$ $ncm^{-2}s^{-1}$, a maximum beam size 2 x 5 cm^2. XRD data are collected rotating the sample around two axes with a goniometer (φ from 0 to 340° by 20° of increase for each step; χ from 0 to 100° by 10° of increase for each step) collecting an overall 180 patterns. A curved position-sensitive detector with an angular range 2θ with a resolution of 0.2° was used.

Rietveld texture analysis was carried out by means of MAUD software [275–278], by considering during the RQPA all the phases but only the major crystal phases were included in the texture analysis by EWIMV method [279] obtaining the Orientation Distribution Function. Successively, for each selected crystal phase used for QTA main Bragg peaks should be selected to obtain the Pole Figures (PFs) representing the orientation of lattice planes selected respected to the sample orientation [280]. In the PFs pole densities are reported as multiples of the random distribution (m.r.d.): an increase in the m.r.d. for a selected lattice plane of the projection is linked to an increase of the preferred orientation of that crystal phase [281].

The refinement strategy included the refinement of a Chebyshev polynomial function with 5 parameters, cell parameters of crystal phases, scale factor of phases, crystallite size and microstrain only for major crystal phases and the zero offset of the diffractometer. Only after some refinement cycles the EWIMV was calculated for the selected phases, later obtaining the PFs for main Bragg peaks. The following samples were analysed: *YC2O* as natural larnite-rich rocks; Ghareb Formation fragment and pellet; heated Ghareb Formation fragment and pellet at 1200 °C.

7.2.11 – Measurement of density

Measurements of real density were carried out by means of helium Pycnometer (Accupyc II 1340 Pycnometer, Micromeritics) at the Servicios Centrales de Apoyo a la Investigation (SCAI) at the University of Malaga. Experiments were performed at room temperature on powder samples of around 3 g in a sample chamber of 10 cm^3 and with pressure of 13.45 psi of He.

Natural larnite-rich rocks powder (*Nat*) and *green-cements BC* synthetized at 1350 °C, both with and without the 3wt.% gypsum addition (*3GNat* and *3GBC*), were analysed.

7.2.12 – Specific Surface Area measurement (BET and Blaine methods)

Specific Surface Area (SSA) measurement is fundamental for hydration of cement because hydration reactions occur on the crystal surface. Therefore, having a similar SSA among samples is required for making comparison of hydration reactivity of cements.

SSA analysis with BET method was carried out by means of MICROMERITICS ASAP 2420 instrument, at room temperature, with an inert gas (N_2) and ~ 0.8 g of sample powder.

SSA analysis with Blaine method was measured following UNE-EN196-6:2010 using the Blaine Fineness Tester (UTCM-0240 Blaine Air Permeability Apparatus) [282].

Both methods were carried out at the Servicios Centrales de Apoyo a la Investigation (SCAI) at the University of Malaga. Natural larnite-rich rocks powder (*Nat*) and *green-cements BC* synthetized at 1350 °C, both with and without the 3wt.% gypsum addition (*3GNat* and *3GBC*), were analysed.

7.2.13 – Cement pastes preparation and Stopping hydration procedure

Cement pastes were prepared by mixing water and cement (*3GNat* and *3GBC*) always with water/cement ration of 0.5. Powder and water were mixed mechanically for 210 sec at 800 rmp at room temperature. The prepared pastes were cast into hermetically closed PolyTetraFluoroEthylene (PTFE) cylinders (Fig. 7.11), followed rotated at 16 rmp for 24 hours of hydration at constant temperature. After this time, the cylinders of pastes were demoulded and stored in vessel maintaining constant temperature and water saturation point (Fig. 7.12).

Cement pastes were prepared for *3GNat* and *3GBC* samples and analysed at 1, 3, 7 and 28 days of hydration by means of LXRPD and DSC-TA. For stopping the hydration, strictly required for LXRPD investigation, a two steps process was followed using a Whatman device with filter of 2.5 μm pores coupled with a vacuum pump: (i) grinded powder sample was washed twice with isopropanol (C_3H_8O); (ii) following, a washing with diethyl ether ($(C_2H_5)_2O$). A portion of the dry powders was manually mixed with 20wt.% of quartz as an internal standard, whereas the other part was used for DSC-TA experiments.

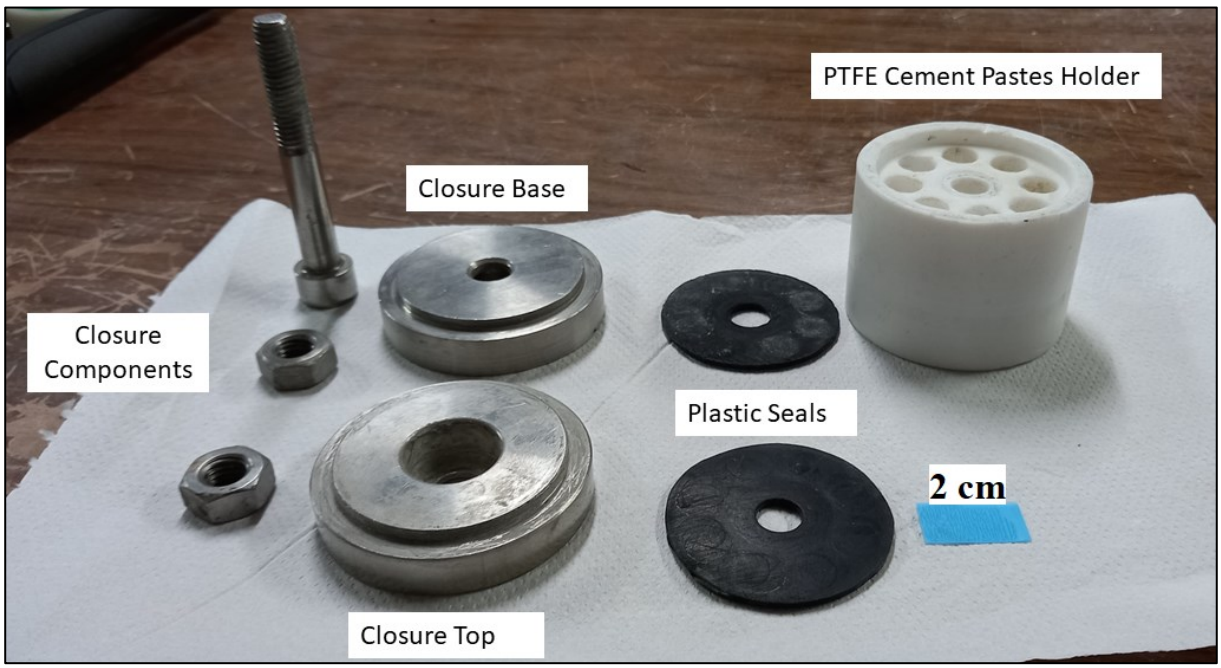

Fig. 7.11 – Cement pastes holder which is based on PTFE with 8 cylindrical holes for hosting pastes and a closure system made of two steel bases, plastic seals, a screw and bolts.

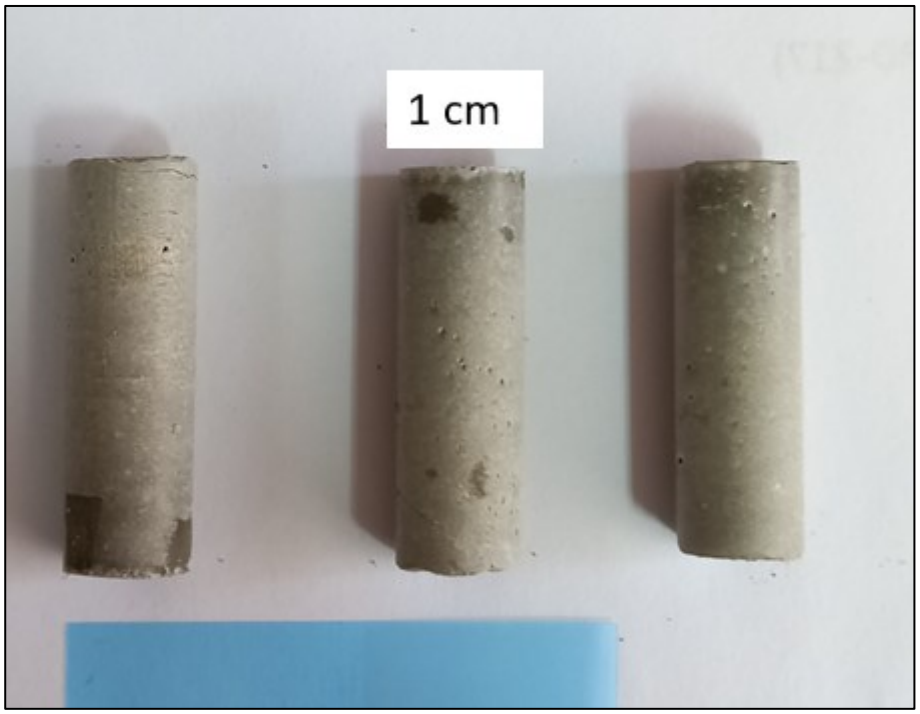

Fig. 7.12 – Cement pastes demoulded after 24 hours of hydration from the PTFE holder.

7.2.14 –ThermoGravimetric Analysis (TGA)

Thermogravimetric Analysis was carried out for obtaining the amount of underreacted water inside (free water content) the pastes and the amount of bonded water inside crystal structures (hydrated crystal phases and hydrated amorphous phases). *3GNat* and *3GBC* samples were studied by TGA at 1, 3, 7 and 28 hydration days.

Analysis was performed using SDT Q600 Analyser instrument, heating the sample (~ 0.08 g) in a platinum crucible from room temperature to 1000 °C with an heating rate of 10 °C/min and oxidating condition. For calculating the Free Water Content (FWC) the following equations (Eq.11,12,13,14) were used [283].

$$(Eq.11)\ \ DSW = (100 - WL_{0-45^\circ C})$$

$$(Eq.12)\ BWC = \frac{WL_{45-550^\circ C}}{100} * DSW$$

$$(Eq.13)\ FWC = CWC - (\frac{BWC}{(100 - BWC)} * CC)$$

$$(Eq.14)\ CWC = FWC + BWC$$

In the Eq.11 is calculated the Dry Sample Weight (DSW) corresponding to the difference between 100 and the wt.% loss at 45 °C. The Eq. 12 leads to the calculate the Bonded Water Content representing the wt.% of water in the dry sample that is bonded both as crystal and amorphous structure. Finally, in the Eq.13 the FWC is calculated by considering the starting Cement Water Content (CWC) during pastes preparation, which was always of 33.33wt.%, BWC and Cement

Content (CC) during pastes preparation, which was of 66.67wt.%. Therefore, the sum of FWC and BWC at a specific time of the hydration is equal to CWC (Eq.14).

7.2.15 – Isothermal Calorimetric Analysis on cement pastes

Isothermal Calorimetric Analysis was performed in an eight-channels Thermal Activity Monitor instrument using glass ampoules, as cement paste holder (Fig. 7.13,14). Furthermore, next to each channel there's another one used for adding the standard, which pure water or sand are commonly used [284]. In order to collect data from the beginning of the hydration, an automatic admix device was used to mix the samples inside the calorimeter by shaking the sample during the first 2 min [285]. The heat released during the hydration was measured till 7 days maintaining a constant temperature of 20 °C.

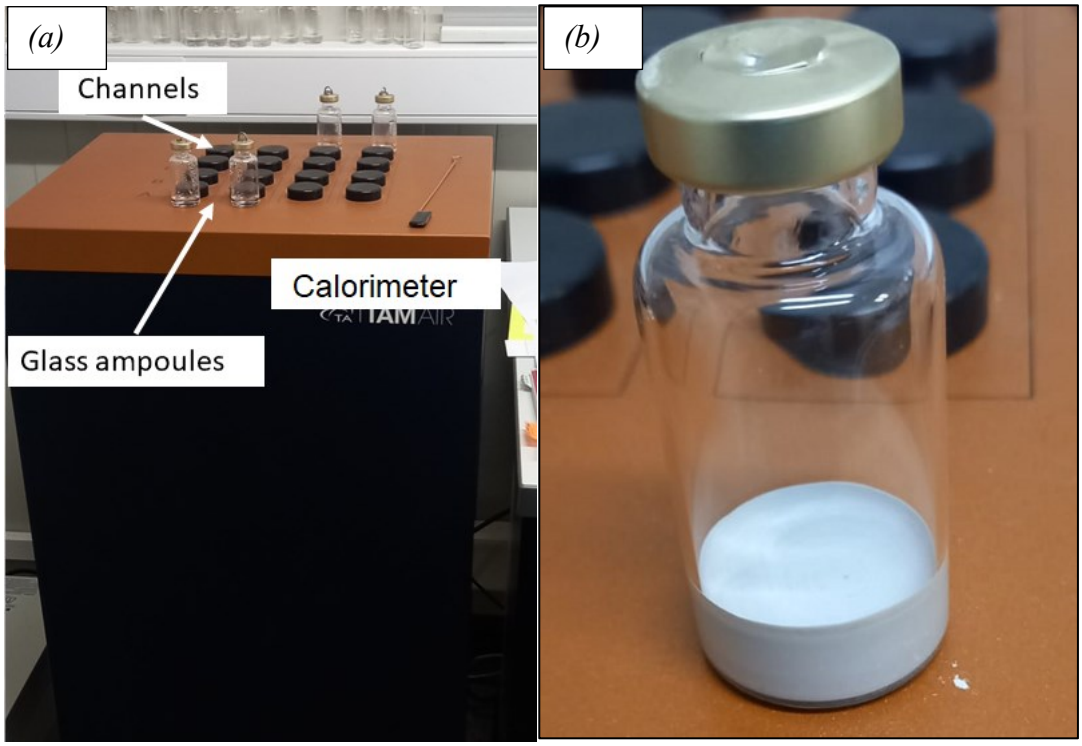

Fig. 7.13 – (a) Thermal Activity Monitor instrument, highlighting the eight-channels for samples and eight-channels for the standard; (b) glass ampoules partially filled with cement pastes after 7 days of hydration.

NATURAL ROCKS						
Larnite rich-rocks				***Phosphatic-gypsum-rich limestone***		
Anhydrous Parts	*Hydrated Veins*	*Anhydrous Parts*	*Veins*	*Hard nodules*		*Soft Limestone*
SAMPLE LABELLING						
YC2O	*YC2V*	*6BWO*	*6BWV*	*SE*	*SO*	*RM*
ANALYTICAL TECHNIQUES						
LXRPD	*LXRPD*	*LXRPD*	*LXRPD*	*LXRPD*	*LXRPD*	*LXRPD*
SXRPD	*SXRPD*	*SXRPD*	*SXRPD*	-	-	*SXRPD*
NXRD	-	-	-	-	-	*NXRD*
RLM	*RLM*	*RLM*	*RLM*	*TLM*	*TLM*	*TLM*
-	-	-	-	-	-	*SCXRD*
SEM-EDS	-	*SEM-EDS*	-	-	-	-
EMPA-WDS	-	*EMPA-WDS*	-	-	-	-
μ-CT	*μ-CT*	*μ-CT*	*μ-CT*	-	-	*μ-CT*

Table 7.6 – Analytical techniques used on natural limestone (larnite-rich rocks and natural limestone collected during field trip) and the used sample labelling.

SYNTHETHIC GREEN-CEMENTS									
High Ferrite Belite Cement S-doped			***Belite Cement P-S-F Doped***						
Powder			*Powder*				*Fragments*		
SAMPLE LABELLING									
BC			*RM*				*RF*	*RFa,b*	*RF*
700–1100 °C	*1200 °C*	*1250-1350 °C*	*In-situ experiments*	*700-1100 °C*	*1200°*	*1250-1350 °C*	*900 °C*	*1200 °C*	*1250-1350 °C*
ANALYTICAL TECHNIQUES									
LXRPD	*LXRPD*	*LXRPD*	-	*LXRPD*	*LXRPD*	*LXRPD*	*LXRPD*	*LXRPD*	*LXRPD*
-	*SXRPD*	-	*SXRPD in-situ*	-	*SXRPD*	-	-	-	-
-	-	-	-	-	*NXRD*	-	-	*NXRD*	-
-	*RLM*	*RLM*	-	-	*TLM*	*TLM*	-	*RLM*	-
-	-	-	-	-	-	*SCXRD*	-	-	-
-	*SEM-EDS*	-	-	-	*SEM-EDS*	-	-	*SED-EDS*	-
-	-	*EMPA-WDS*	-	-	*EMPA-WDS*	*EMPA-WDS*	-	*EMPA-WDS*	-
-	-	*μ-CT*	*μ-CT in-situ*	-	-	-	*μ-CT*	-	*μ-CT*

Table 7.7 – Analytical techniques used on synthetic *green-cements* (Belite-High Ferrite-Ye'elimite Cement and Belite Cement P-S-F doped as powder and fragments).

HYDRATION STUDY BETWEEN NATURAL AND SYNTHETIC CEMENT						
SYNTHETIC GREEN-CEMENTS		***NATURAL LARNITE-RICH ROCKS***				
Belite High Ferrite Ye'elimite Cement		***Low Ye'elimite (labelled as YC2O = Nat)***		***High Ye'elimite (labelled as 6BWO)***		
BC heated 1350 °C	*+3wt.% Gypsum*	*Powder*	*+3wt.% Gypsum*	*Fragments*	*Powder*	
SAMPLE LABELLING						
BC	*3GBC (1,3,7,28 hydration days)*	*Nat*	*3GNat (1,3,7,28 hydration days)*	*6BWO_H5m (5 hydration months)*	*6BWO_H3w (3 hydration weeks)*	*6BWO_H3m,4m (3,4 hydration months)*
ANALYTICAL TECHNIQUES						
LXRPD	*LXRPD*	*LXRPD*	*LXRPD*	*LXRPD*	*LXRPD*	*LXRPD*
Density	*Density*	*Density*	*Density*	-	*SXRPD*	-
SSA-Blaine	*SSA-Blaine*	*SSA-Blaine*	*SSA-Blaine*	-	-	-
SSA-BET	*SSA-BET*	*SSA-BET*	*SSA-BET*	-	-	-
TGA	*TGA*	*TGA*	*TGA*	-	-	-
-	*ICA*	-	*ICA*	-	-	-

Table 7.8 – Analytical techniques used to make comparison between the hydration of natural vs synthetic cement.

Chapter 8
Study on protoliths of larnite-rich rocks

Thin sections were made on samples belonging to Ghareb Formation collected at the Stop-2 (section 5.2), from hard nodules, and Stop-8 in the Rotem Mine outcrops (section 5.8). All samples were analysed by means of X-ray Fluorescence (XRF, Table 7.1), X-ray Powder Diffraction (XRPD) on bulk rock powders and on the residual rock powders after HCl 5wt.% treatment, highlighting the bulk chemical composition and quantitative crystal phase analysis, respectively. Moreover, samples from Stop-8 were also studied by mean of Neutron Diffraction (NXRD), highlighting preferred orientation of minerals.

8.1 – Microtextural results by Light Microscopy

Thin sections coming from the Stop-2 belong to the Lower part of Ghareb Formation which was intensively weathered in this location leading a hummocky landscape with ill-defined stratification and a several hard-dense limestone concretions ranging from 10 – 60 cm in diameter. By means of Transmitted Light Microscopy (TLM) and Reflected Light Microscopy (RLM) analysis on thin sections two microfabrics were recognized (Table 8.1):

(i) phosphatic wackestone (sample labelled as *SE*) consisting of phosphatic pellets ranging in size from 30 – 2000 μm, fish bones (up to ~ 500 μm), and characterized by an intense sparitization of micrite matrix (Fig. 8.3,4); rare iron-rich nodules (< 250 μm) or fractures composed of hematite partially converted to goethite were observed by RFL investigation (Fig. 8.4e,f);

(ii) phosphatic calci-mudstone (sample labelled as *SO*) consisting of phosphatic pellets ranging in size from 30 – 250 μm (Fig. 8.1) and characterized by a sparitization of micrite matrix (Fig. 8.1,2); a major increase in microsparite crystals occurs locally in spherical zones, probably related to the sparitization of foraminifers (Fig. 8.1c,d, 8.2a); fracture filled with euhedral calcite crystals (up to 200 μm) occurred (Fig. 8.2c,d); increase in the amount of phosphatic pellets and/or less sparitization of micrite were generally related to a darkening in colour at 1 nicol (Fig. 8.1).

Afterwards, *SE* and *SO* samples highlighted similar features: (i) matrix supported texture; (ii) medium to intense sparitization process; (iii) occurrence of phosphatic matter as fish bone fragments and pellets.

Samples coming from Stop-9 (labelled as *RM*) belong to the lower part of Ghareb Formation; they are very soft chalk rich in gypsum and apatite (Table 8.1). Thin sections preparation rose many difficulties; hence, also binocular microscopy investigation was performed helping to get more textural information of *RM* samples and leading a comparison with *SO* and *SE* ones (Fig. 8.5c,d). Results highlighted that *RM* could be considered as phosphatic calci-mudstone, revealing similar features to *SO*: (i) the occurrence of rounded pellets with 20 – 250 μm in size that

should represent phosphatic pellets (Fig. 8.5d); (ii) white prismatic fragments with 20 – 100 μm in size that could be claimed as fish bone fragments (Fig. 8.5c); (iii) fine calcite matrix, which had not undergone to a wide sparitization as for *SO* and *SE* (Fig. 8.5a,b).

Samples / Location / Age /Formation	***Microfacies types (if more than one present)***	***Texture (according to Dunham*** [286] ***and Embry & Klovan*** [287]***)***	***Components***	***Diagenetic Features***	***Depositional environment***
Stop-2 / *Arad City / Late Cretaceous (Early Maastrichtian) / Lower Member of Ghareb Formation (Marl Member)*	*SE*	*Phosphatic wackestone*	*Phosphatic nodules/pellets (30 - 2000 µm) and fish bone fragments up to 500 µm*	*Intense sparitization which obliterated the original texture; occurrence of prismatic calcite crystals (40 – 200 µm) filling fractures*	*Marine environments with low to medium-energy conditions and microbial activity on the seabed producing apatite-phosphatic pellets.*
	SO	*Phosphatic calci-mudstone*	*Phosphatic nodules/pellets (30 –250 µm)*	*Sparitization which obliterated the original texture; bioclasts (foraminifers) recrystallization into microsparite*	*Marine environments with low-energy conditions and microbial activity on the seabed producing apatite-phosphatic pellets.*
Stop-9 */ Rotem Amfort Mine / Late Cretaceous (Early to Middle Maastrichtian) / Lower Member of Ghareb Formation (Marl Member)*	*RM*	*Phosphatic calci-mudstone* [288]	*phosphatic pellets were identified; furthermore, studies reported planktonic and benthonic foraminifers with a clear prevail of the former* [114,137]	-	*Open marine environment with low-energy deposition (middle to outer continental shelf or on the upper part of the continental slope* [289,290]*; hypersaline and anoxic conditions on the bottom;*

Table 8.1 – Description of main features of unmetamorphosed samples (limestone and marly limestone) collected in Northern Negev (Israel) during field trip.

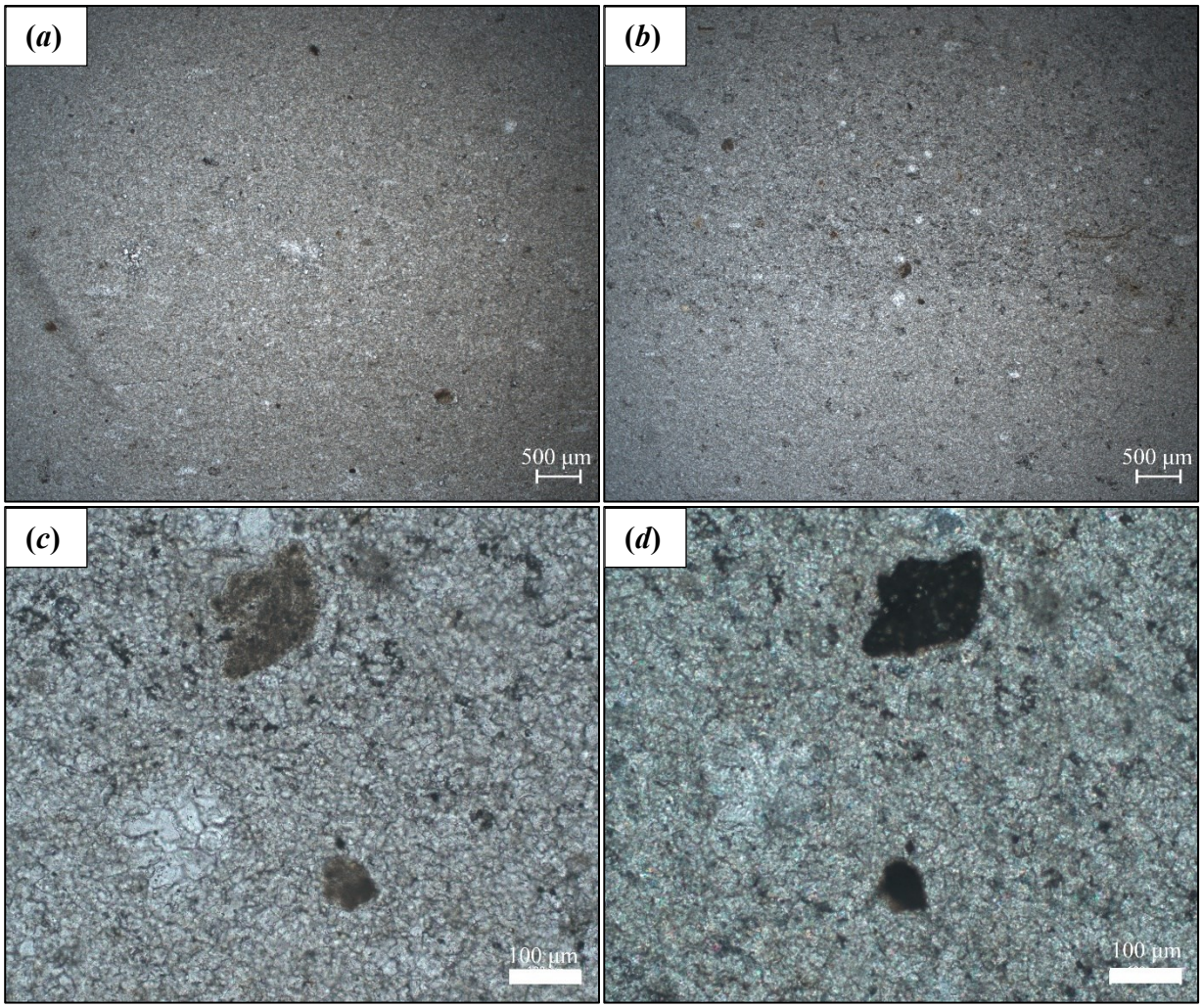

Fig. 8.1 - Optical micrographs of sample *SO* collected at Stop-2: (a) general overview of *SO* samples in parallel nicols, which represents a calci-mudstone with brown phosphatic pellet and a clear sparitization which obliterate the original texture; (b) marking horizon of general increase in phosphatic pellets and decrease in sparitization of matrix upward in the section observed in parallel nicols; (c) enlargement of marking horizon of Fig. 8.1a in parallel nicols; (d) enlargement of marking horizon of Fig. 8.1a in crossed nicols, revealing isotropic feature of phosphatic pellets and high interference colour of calcite.

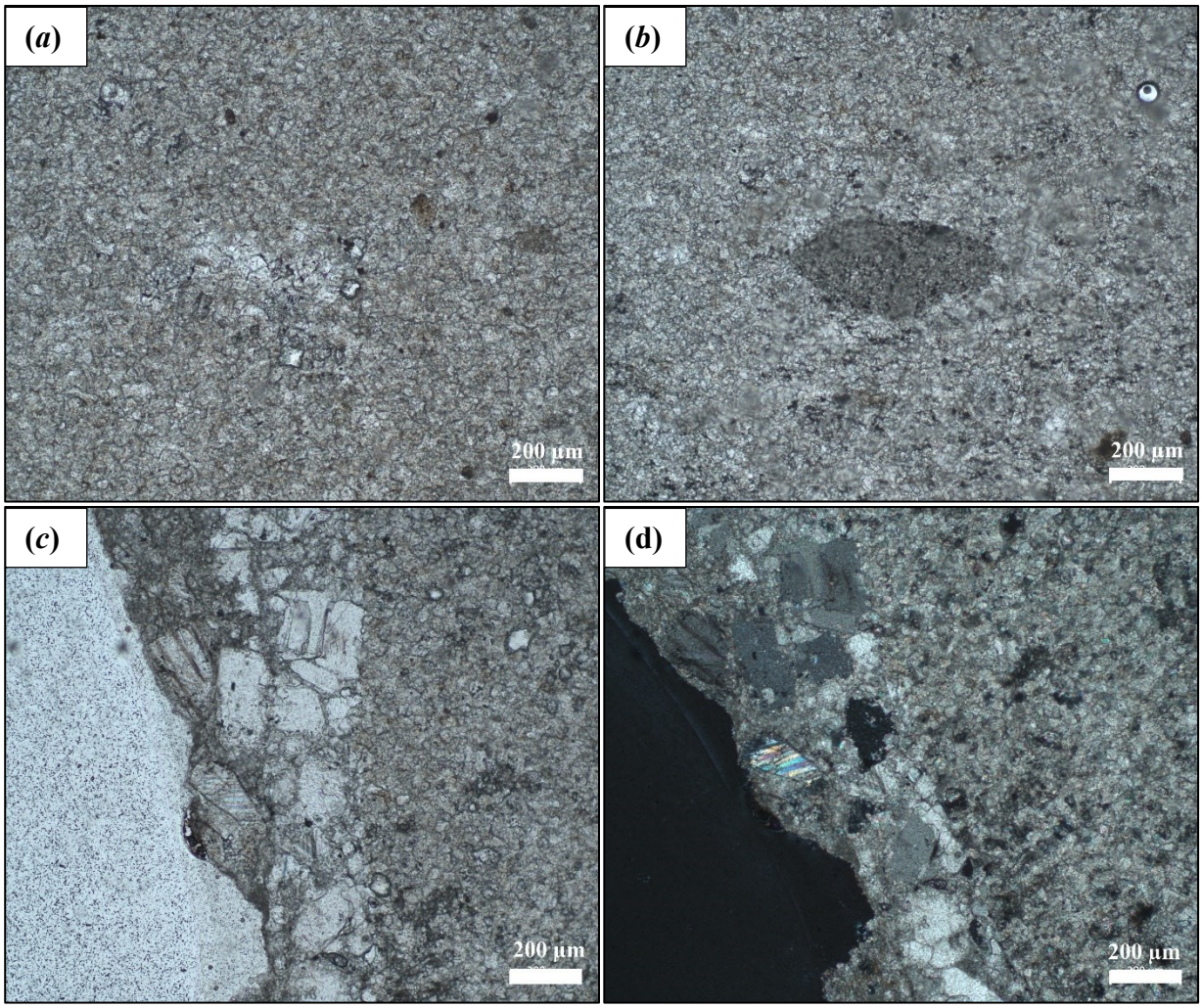

Fig. 8.2 – Optical micrographs of sample *SO* collected at Stop-2: (a) details of the sparitization of the matrix at parallel nicols, with the occurrence of some euhedral rhomb-shaped calcite crystals; (b) biggest phosphatic pellet observed at parallel nicols in *SO* sample; (c) fracture filled with big euhedral rhomb-shaped calcite crystals at parallel nicols; (d) fracture filled with big euhedral rhomb-shaped calcite crystals at crossed nicols.

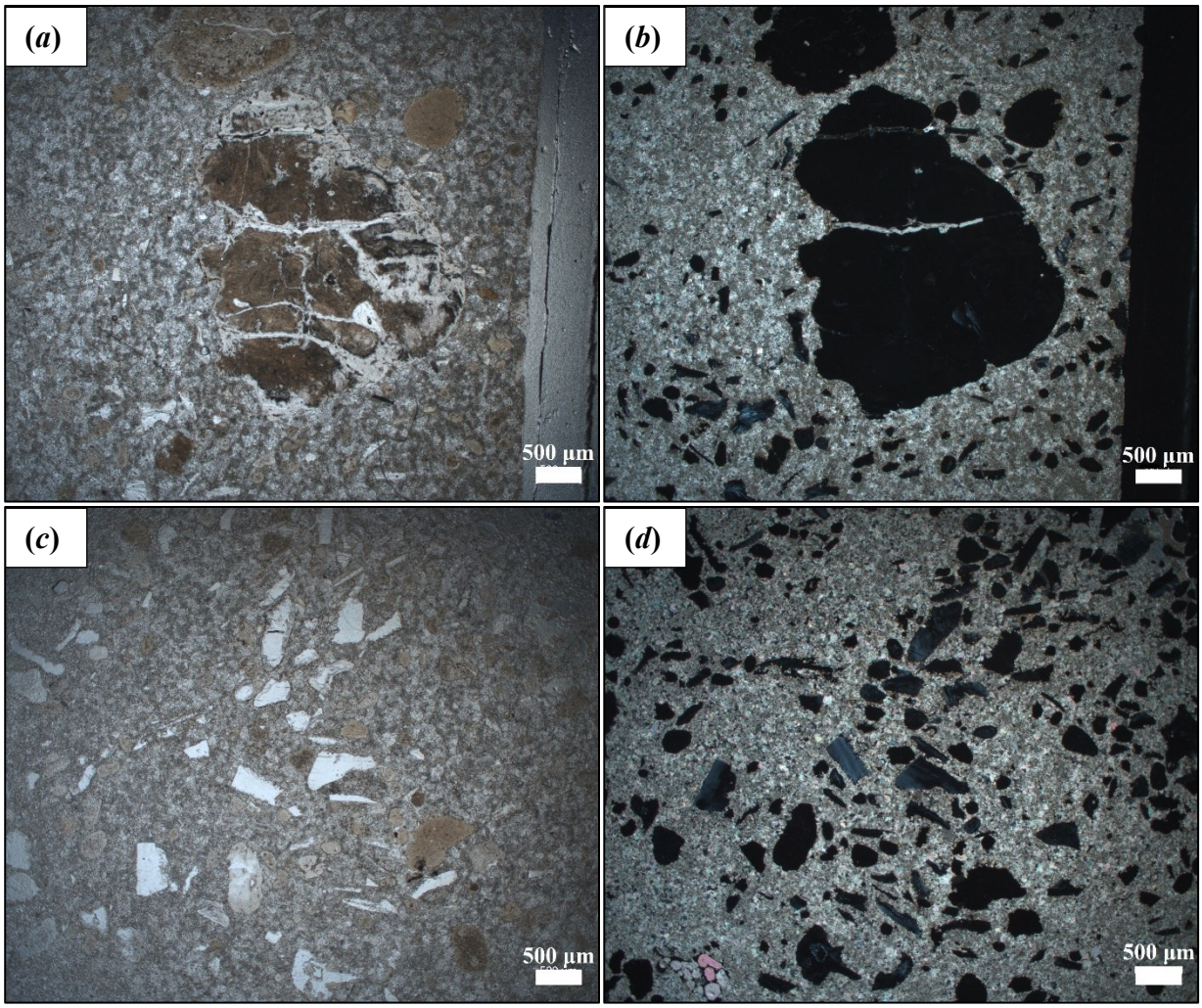

Fig. 8.3 – Optical micrographs of sample *SE* collected in Stop-2: (a) centimetric phosphate pellet not well preserved and fractured; (b) centimetric phosphate pellet observed at crossed nicols, revealing its isotropic features and some fractures cemented by calcite; (c) fish bone fragments associated with phosphate pellets at parallel nicols; (d) fish bone fragments associated with phosphate pellet at crossed nicols, revealing the isotropic feature of phosphate pellet and anisotropic feature of fish bone with grey-bluish interference colours and undulated extinction.

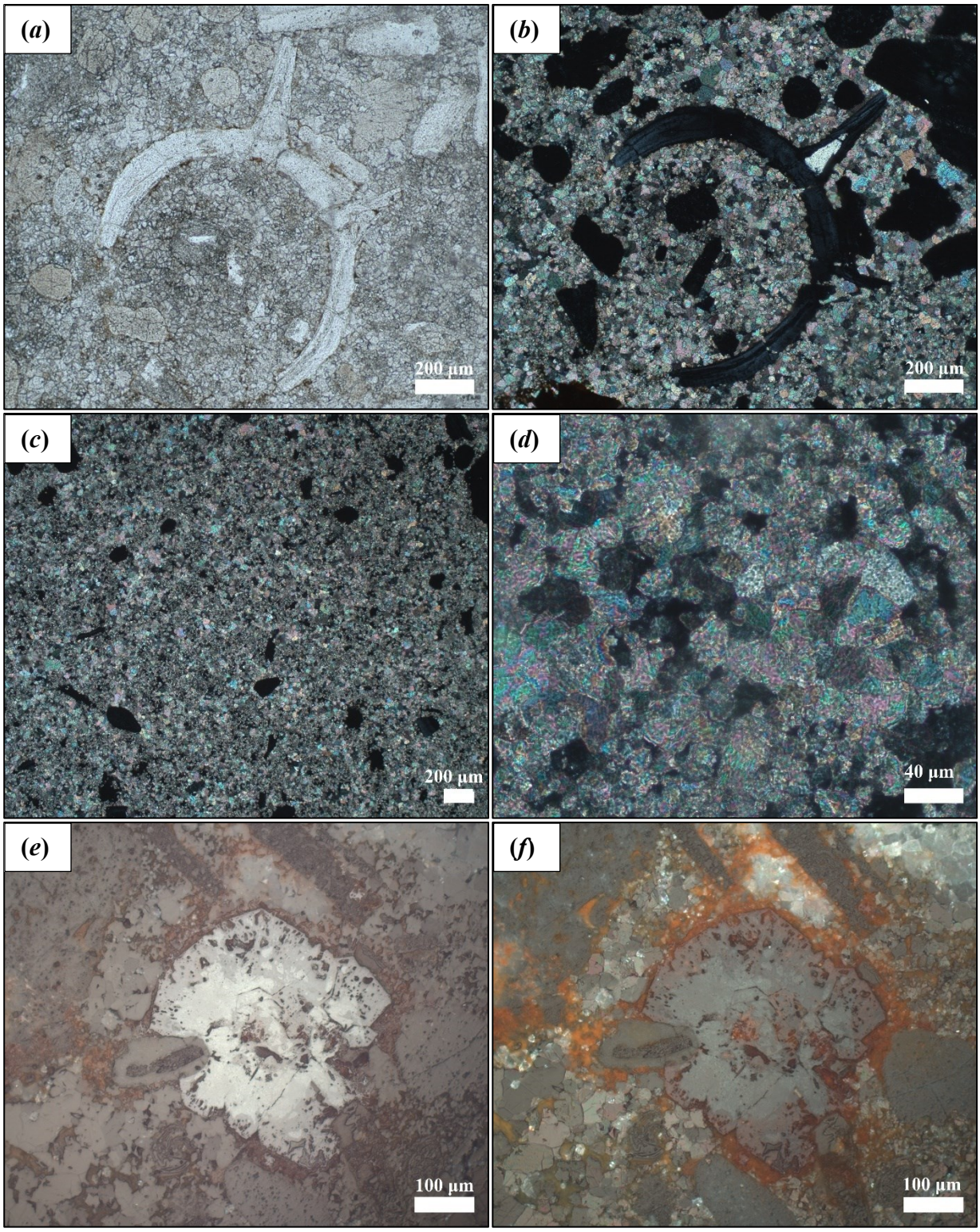

Fig. 8.4 – Optical micrographs of sample *SE* coming from Stop-2: (a,b) preserved fish vertebra at parallel and crossed nicols, revealing anisotropic feature and internal portion filled a single crystal of calcite; (c) intense sparitization of micrite matrix observed at crossed nicols; (d) enlargement of picture (c) highlighting the grain size of microsparite crystals; (e,f) RLM image at parallel and crossed nicols of Fe-rich nodule of hematite (light-grey at one nicols, light-grey bluish at two nicols with deep red internal reflections) with hexagonal shape crystals partially converted to goethite (grey at one nicols, darker and brownish that hematite at two nicols);

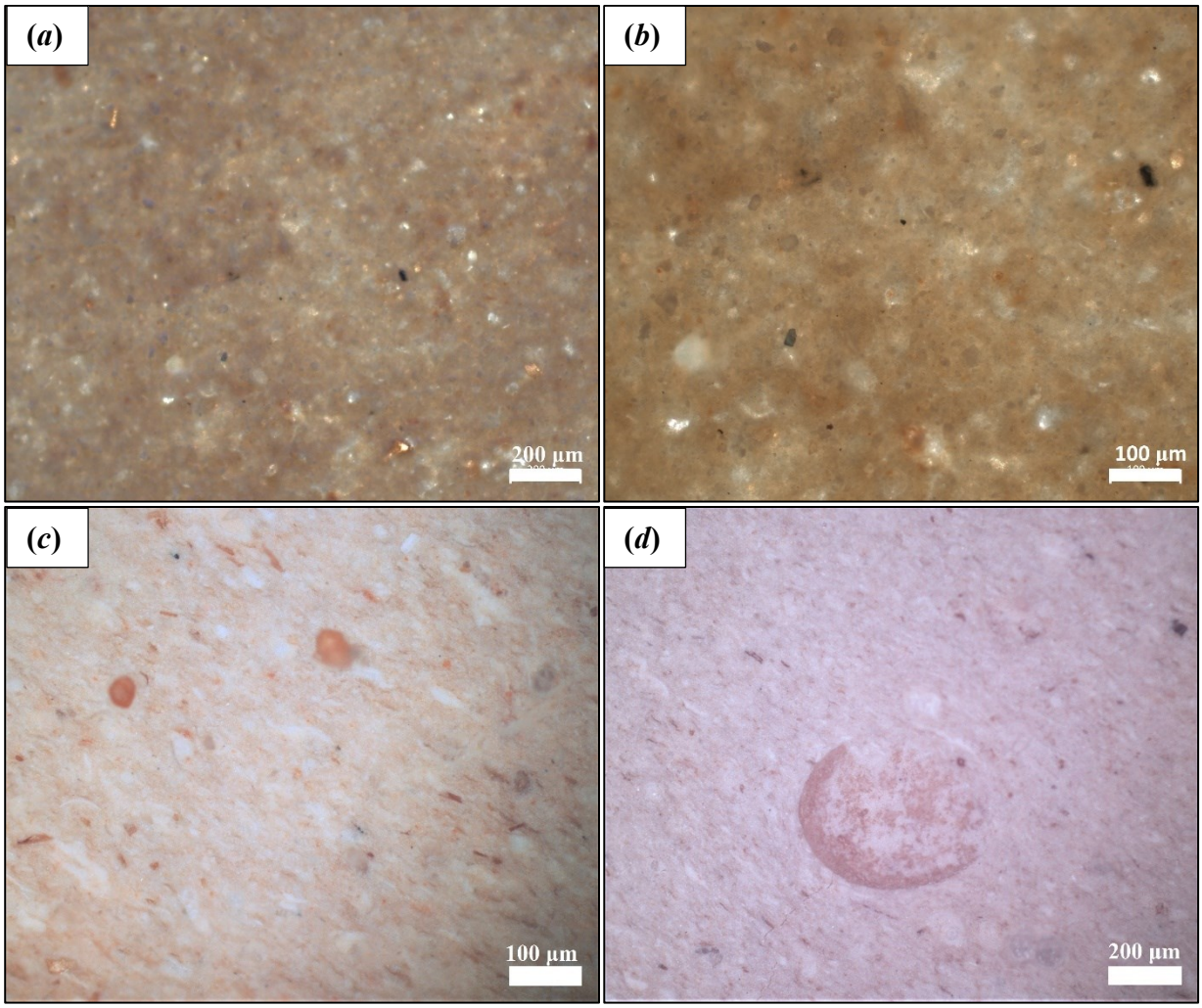

Fig. 8.5 – Optical micrographs of sample *RM* collected at Stop-9: (a) overview of the thin section of sample *RM* at parallel nicols; (b) magnification of the Fig. 8.5a at parallel nicols highlighting the matrix. (c,d) binocular microscopy images highlighting the occurrence of rounded to elliptical brown elements 30-200 µm in size and white prismatic fragments up to 100 µm claimed as phosphatic pellets and fish bone fragments, respectively, as in *SO* and *SE* samples.

8.2 – Mineralogical and crystallographic results of protolith

LXRPD and SXRPD analysis highlighted that calcite represents the main component of all studied limestone passing from 78 to 98wt.% for *RM* and *SO* samples, respectively (Table 8.2, Fig. 8.6,7,9). Higher variation occurs for apatite that represents the main component for *SE* (Fig. 8.8) and minor phase for *RM* and *SO*, as observed by TLM. Quartz always represents a minor crystal phase reaching the lowest value of < 1wt.% for *SO*. Fluorite is an accessory phase only for *SO* and *SE* samples. Microcline was detected only in *SO* and *RM* 5wt.% HCl residues and represents a minor phase (Table 8.3, Fig. 8.12,14,15). Furthermore, gypsum and kaolinite only occurred in *RM* as minor crystal phases. Comparing XRF results (Table 7.1) among limestone samples highlighted: (i) a similar chemical composition for *SO* and *SE*, excepted for the latter than has a higher P_2O_5 wt.% justified by the increase in apatite; (ii) *RM* is different compared to *SE* and *SO*, with higher SO_3, SiO_2 and Al_2O_3 as confirmed XRD analysis due to gypsum, quartz and clays, respectively; (iii) *RM* chemical composition falls in compositional range of Ghareb Formation rocks [220], excepted for higher CaO content due to higher $CaCO_3$ wt.%.

Clay minerals composition was better studied on 5wt.% HCl residues, especially for *SO* and *SE*, revealing differences among samples: kaolinite occurs only in *RM* with illite and low amount of montmorillonite; whereas, illite and montmorillonite occur for *SE* and *SO*, which *SO* has an equal amount of both clays (Table 8.3). No clays were clearly detected by LXRPD for *SE* and *SO* bulk samples, because > 90wt.% is made of calcite and apatite; while, illite and kaolinite were clearly detected by LXRPD and SXRPD for *RM*, because represent ~ 9wt.% of the bulk sample (Fig. 8.12-15).

More accurate observation on *RM* hand samples identified some anisotropies (Table 8.8): (i) red submillimetric layers with decicentimetric later continuity (Fig. 8.18, 19), richer in gypsum and goethite compared to bulk rock; (ii) millimetric white soft veins with no preferred orientation and centimetric lateral continuity (Fig. 8.16,17), mainly composed of gypsum (> 90wt.%) and minor amount of calcite (< 7wt.%) and quartz (< 1wt.%); (iii) sparce millimetric rounded black portions (Fig. 8.20,21). 5wt.% HCl treatment on black portions was performed to better reveal other phases, excepting calcite and other HCl soluble minerals, due to peak overlapping. Black portions residue is made of clay minerals (montmorillonite, kaolinite, illite), bernalite ($Fe(OH)_3 \cdot 0.25H_2O$), quenstedtite ($Fe_2(SO_4)_3 \cdot 11H_2O$) and quartz as major phases and minor amount of gypsum and goethite (Table 8.4). Furthermore, SCXRD was performed on submillimetric prismatic crystals all identified as titanite ($CaTiSiO_5$) (Fig. 8.21,22, Table 8.6).

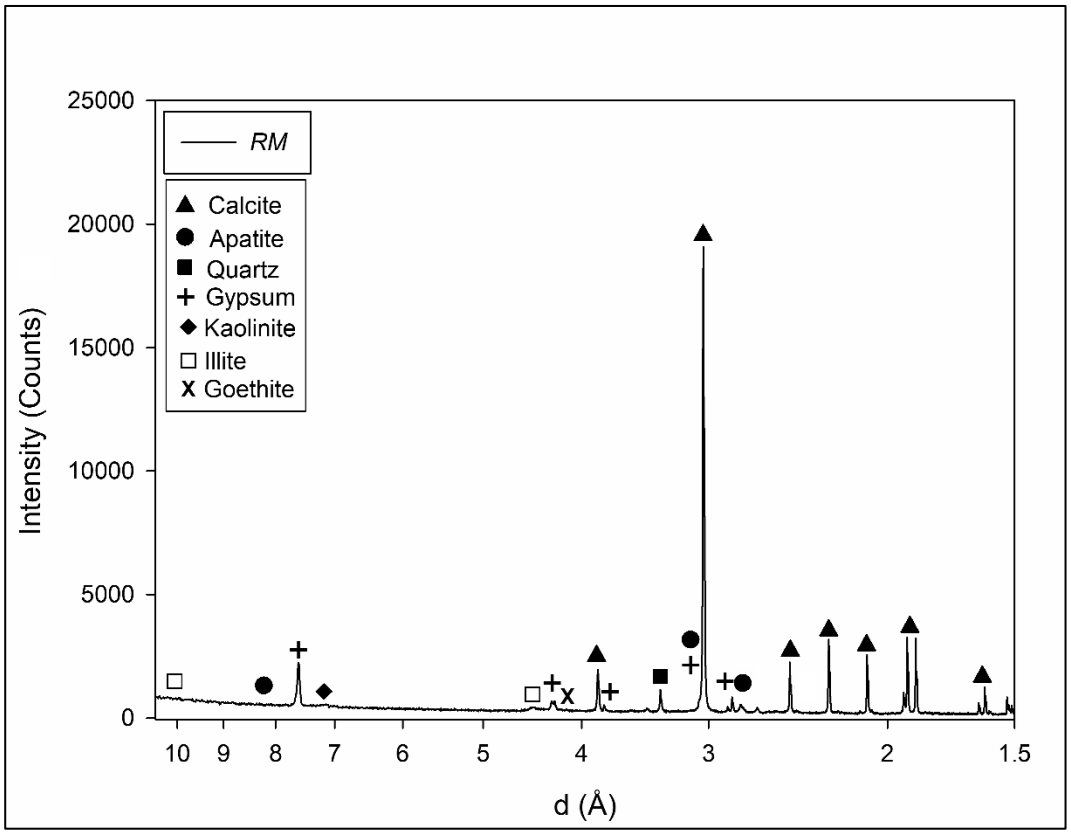

Fig. 8.6 – LXRPD pattern of *RM* sample highlighting main Bragg peaks of occurring crystal phases.

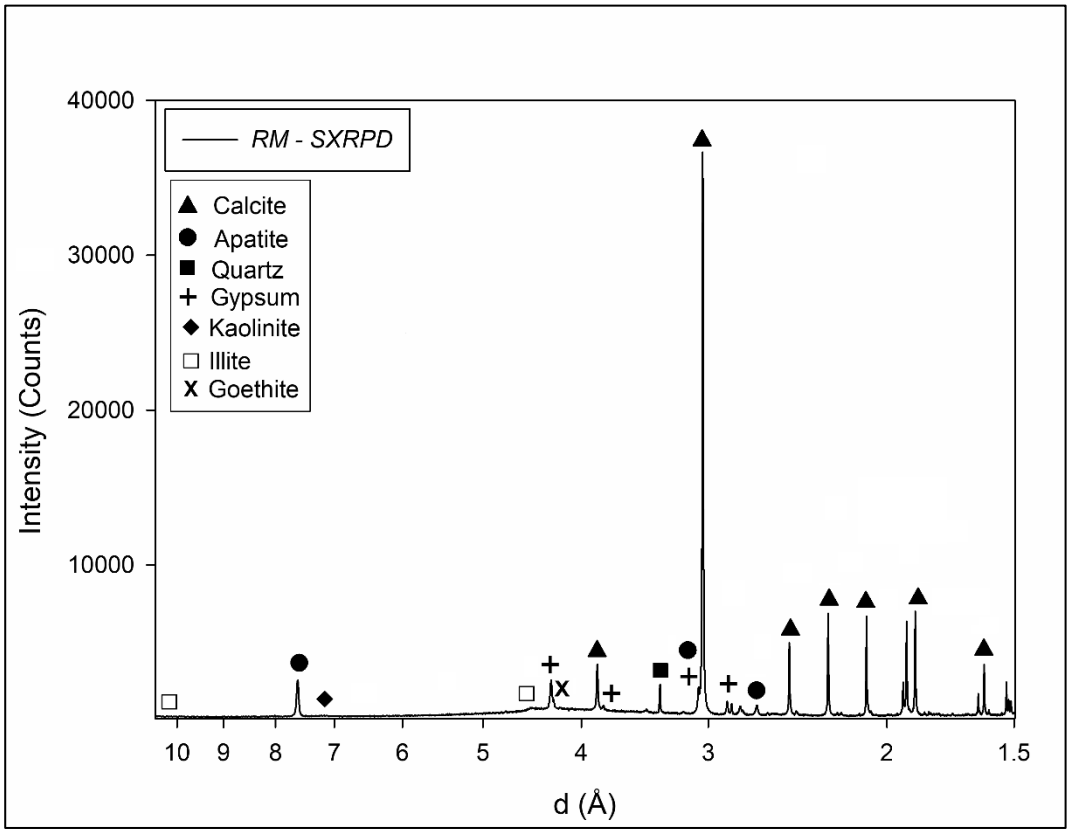

Fig. 8.7 – SXRPD pattern of *RM* sample collected at MCX (Elettra, Trieste), highlighting main Bragg peaks of occurring crystal phases.

SXRPD was performed only on *RM,* obtaining more accurate RQPA, especially on minor phases and crystallographic parameters (cell parameters, crystallite size and microstrain values): RQPA from SXRPD revealed values with lower *e.s.d.* compared to LXRPD (Fig. 8.6,7, Table 8.2), due to higher spatial resolution and intensity/background; quantification of preferentially oriented minerals (illite, kaolinite and montmorillonite along (001), gypsum along (010) and calcite along (104) is improved using synchrotron facility due to the Debye-Scherrer geometry in capillary; the better quantification of Fe-rich crystal phases, such as goethite for *RM*, using synchrotron radiation compared to normal Cu $K\alpha_{1,2}$ one which increases the background contribute. More in details, the simultaneous refinement of crystallite size and microstrain parameters with GSAS-ii on LXRPD pattern was not allowed due to a strong correlation of these two parameters, leading unrealistic values; while no correlation was detected refining SXRPD pattern: therefore, RQPA from SXRPD gave more realistic values highlighting lower crystallite size and higher microstrain compared to LXRPD (Table 8.5).

No relevant changes on cell parameters occurred among limestone samples revealing similar crystallographic parameters close to the pure calcite, as confirmed by the low amount of MgO by means of XRF varying in the range 0.18-0.23wt.% (Table 8.5). Assuming Mg^{2+} as the only substituent of Ca^{2+} in calcite and considering the bibliographic cell parameters from pure calcite to Mg-rich calcite, a straight-line equation could be calculated (Fig. 8.10): when $^{VI}Mg^{2+} \rightarrow {}^{VI}Ca^{2+}$ inside calcite crystal structure a progressive cell parameters reduction occurs, due to the different ionic radius ($^{VI}Ca^{2+}$ = 1.00 Å and $^{VI}Mg^{2+}$ = 0.72 Å [291]). Therefore, the calculated straight-line equation ($y = -87.279x + 367.78$, with R^2 = 0.9785) could be used to quantify the MgO wt.% in calcite and compare with XRF results: *SO* calcite has 0.008364 mol MgO equal to 0.3204wt.% of MgO; *SE* calcite has 0.003780 mol MgO equal to 0.1447wt.% of MgO; whereas, *RM* calcite has no MgO contribute due to the similar cell volume to the pure calcite. Results confirmed the low content of MgO with are comparable to XRF values (Table 7.1).

Considering both crystallite size and microstrain values for calcite, hard concretions (*SO* and *SE*) have higher values, whereas, soft apatite-gypsum-rich chalk (*RM*) has lower ones: calcite peaks in *RM* and *SE* LXRPD patterns, which they have similar calcite wt.% (Table 8.2), revealed comparable peak broadening till ~ 43° 2θ (~ 2.10 Å) (Fig. 8.11a); whereas, at high 2θ (~ 84° 2θ, ~ 1.15 Å), *SE* highlighted larger FWHM compared to *RM*, due to higher broadening contribute of microstrain at high 2θ despite the larger crystallite size (Fig. 8.11b).

Comparing *RM* anisotropies (red layer and veins) and bulk rock LXRPD cell parameters and microstrain are almost similar for all samples, while crystallite size value is higher for red layers (Table 8.5).

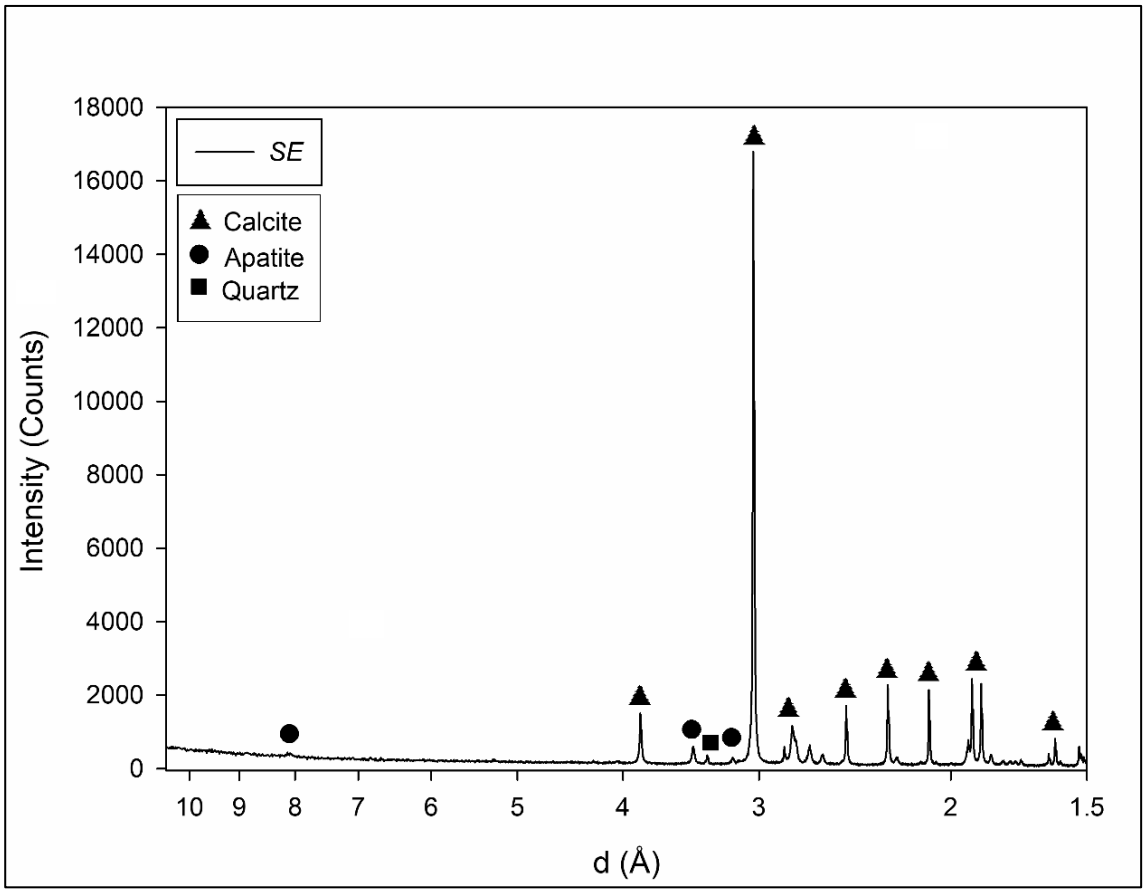

Fig. 8.8 – XRPD pattern of *SE* sample highlighting main Bragg peaks of occurring crystal phases.

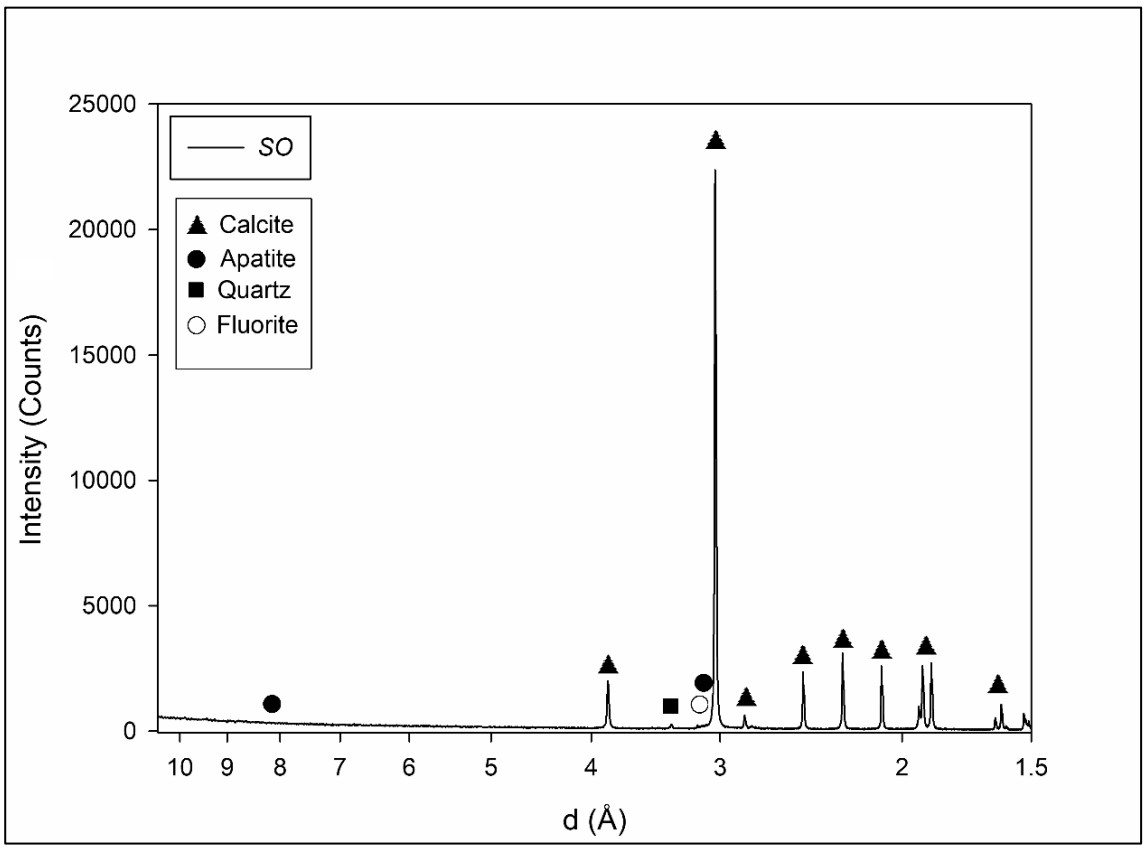

Fig. 8.9 – XRPD pattern of *SO* sample highlighting main Bragg peaks of occurring crystal phases.

Sample	*Instrumental Set-Up*	*Calcite $CaCO_3$*	*Quartz SiO_2*	*Apatite $Ca_5(PO_4)_3F$*	*Gypsum $CaSO_4{\cdot}2H_2O$*	*Kaolinite $Al_2Si_2O_5(OH)_4$*	*Illite*$^+$	*Geothite FeO(OH)*	*Fluorite CaF_2*	*Rexp*	*Rwp*	*GoF*
SO	***LXRPD***	98.69(.27)	0.62(4)	0.69(7)	*n.d.*	*n.d.*	*n.d.*	*n.d.*	0.31(3)	7.08	11.20	1.58
SE	***LXRPD***	77.58(.27)	1.02(5)	21.40(.16)	*n.d.*	*n.d.*	*n.d.*	*n.d.*	*n.d.*	7.02	12.00	1.71
RM	***LXRPD***	78.90(.27)	2.91(9)	3.77(.11)	3.72(.12)	4.71(.21)	5.73(.23)	0.26(7)	*n.d.*	4.86	8.95	1.84
	SXRPD (MCX)	78.12(.21)	2.49(6)	3.44(8)	4.21(.10)	4.84(.16)	4.29(.18)	1.25(9)	*n.d.*	4.46	9.18	2.06

Table 8.2 – XRPD results (wt.%) for limestone protoliths; e.s.d. is reported in rounded brackets; $^+K(Al,Mg,Fe)_2(Si,Al)_4O_{10}[(OH),H_2O]$; n.d., not detected.

Sample	*Quartz SiO_2*	*Apatite $Ca_5(PO_4)_3F$*	*Microcline $KAlSi_3O_8$*	*Kaolinite $Al_2Si_2O_5(OH)_4$*	*Illite*$^+$	*Montm.*°	*Geothite FeO(OH)*	*Fluorite CaF_2*	*Rexp*	*Rwp*	*GoF*
SO	24.94(.56)	*n.d.*	17.41(1.00)	*n.d.*	18.21(1.09)	21.03(.44)	*n.d.*	18.41(.37)	7.59	14.054	1.85
SE	11.26(.23)	56.78(.49)	*n.d.*	*n.d.*	20.80(.68)	6.32(.16)	*n.d.*	4.84(.17)	5.83	12.719	2.18
RM	30.66(.38)	*n.d.*	6.78(.49)	30.02(.63)	25.87(.75)	2.31(.14)	3.54(.30)	*n.d.*	4.22	6.07	1.44

Table 8.3 – XRPD results (wt.%) for 5wt.% HCl treated limestone; e.s.d. is reported in rounded brackets; $^+K(Al,Mg,Fe)_2(Si,Al)_4O_{10}[(OH),H_2O]$; °Montmorillonite, $Na_{0.2}Ca_{0.1}(Al,Mg)_2Si_4O_{10}(OH)_2{\cdot}10H_2O$; n.d., not detected.

Sample / Minerals	*RM*		
	Red Layers	***Veins***	***HCl Residue Black Portions***
Calcite $CaCO_3$	67.29(.59)	6.65(.15)	-
Quartz SiO_2	4.62(.17)	0.27(5)	11.18(.55)
Gypsum $CaSO_4 \cdot 2H_2O$	16.57(.32)	93.08(.32)	1.46(.12)
Microclino $KAlSi_3O_8$	*n.d.*	*n.d.*	0.83(.30)
Kaolinite $Al_2Si_2O_5(OH)_4$	4.20(.48)	*n.d.*	13.01(1.31)
Illite $^{+}$	*n.d.*	*n.d.*	8.43(1.81)
Montm. $^{\circ}$	*n.d.*	*n.d.*	19.57(.57)
Geothite FeO(OH)	7.34(.26)	*n.d.*	3.54(.30)
Bernalite *	*n.d.*	*n.d.*	29.26(1.00)
Quenstedtite $^{+}$	*n.d.*	*n.d.*	16.27(1.39)
Rexp	4.74	4.50	6.49
Rwp	6.62	13.42	11.69
GoF	1.40	2.98	1.80

Table 8.4 – XRPD results (wt.%) for anisotropies in *RM* samples; e.s.d. is reported in rounded brackets; $^{+}K(Al,Mg,Fe)_2(Si,Al)_4O_{10}[(OH),H_2O]$; °Montmorillonite, $Na_{0.2}Ca_{0.1}(Al,Mg)_2Si_4O_{10}(OH)_2 \cdot 10H_2O$; $^{*}Fe(OH)_3 \cdot 0.25H_2O$; $^{+}$ $Fe_2(SO_4)_3 \cdot 11H_2O$.

	Sample	a (Å)	c (Å)	V (Å³)	Crystallite size (μm)	μstrain ($\Delta d/d \cdot 10^6$)
	SO (LXRPD)	4.9865(1)	17.0455(2)	367.05(1)	1.43(8)	2434(19)
	SE (LXRPD)	4.9879(2)	17.0547(3)	367.45(1)	1.55(.11)	2665(27)
RM	***Bulk (SXRPD)***	4.9900(1)	17.0648(2)	367.98(1)	0.38(2)	2084(65)
	Bulk (LXRPD)	4.9900(2)	17.0624(3)	367.94(1)	0.65(3)	1321(30)
	Veins (LXRPD)	4.9896(8)	17.060(1)	367.83(5)	0.59(.12)	1586(171)
	Red Layers (LXRPD)	4.9893(3)	17.0618(5)	367.81(3)	1.10(.10)	1474(40)
	Pure Calcite ($CaCO_3$)	4.9890	17.0620	367.78	-	-
	Low-Mg Calcite ($Ca_{0.97}Mg_{0.03}CO_3$) *[ICSD 89-1304]*	4.9780	16.9880	364.57	-	-
	Medium-Mg Calcite ($Ca_{0.86}Mg_{0.14}CO_3$) *[ICSD 86-2335]*	4.9673	16.9631	362.47	-	-
	High-Mg Calcite ($Ca_{0.871}Mg_{0.129}CO_3$) *[ICSD 86-2336]*	4.9382	16.8320	355.47	-	-
	High-Mg Calcite ($Ca_{0.86}Mg_{0.14}CO_3$) *[ICSD 43-0697]*	4.9410	16.8640	356.55	-	-

Table 8.5 – Crystallographic values for calcite in limestone samples and referee values from pure to Mg-rich calcite.

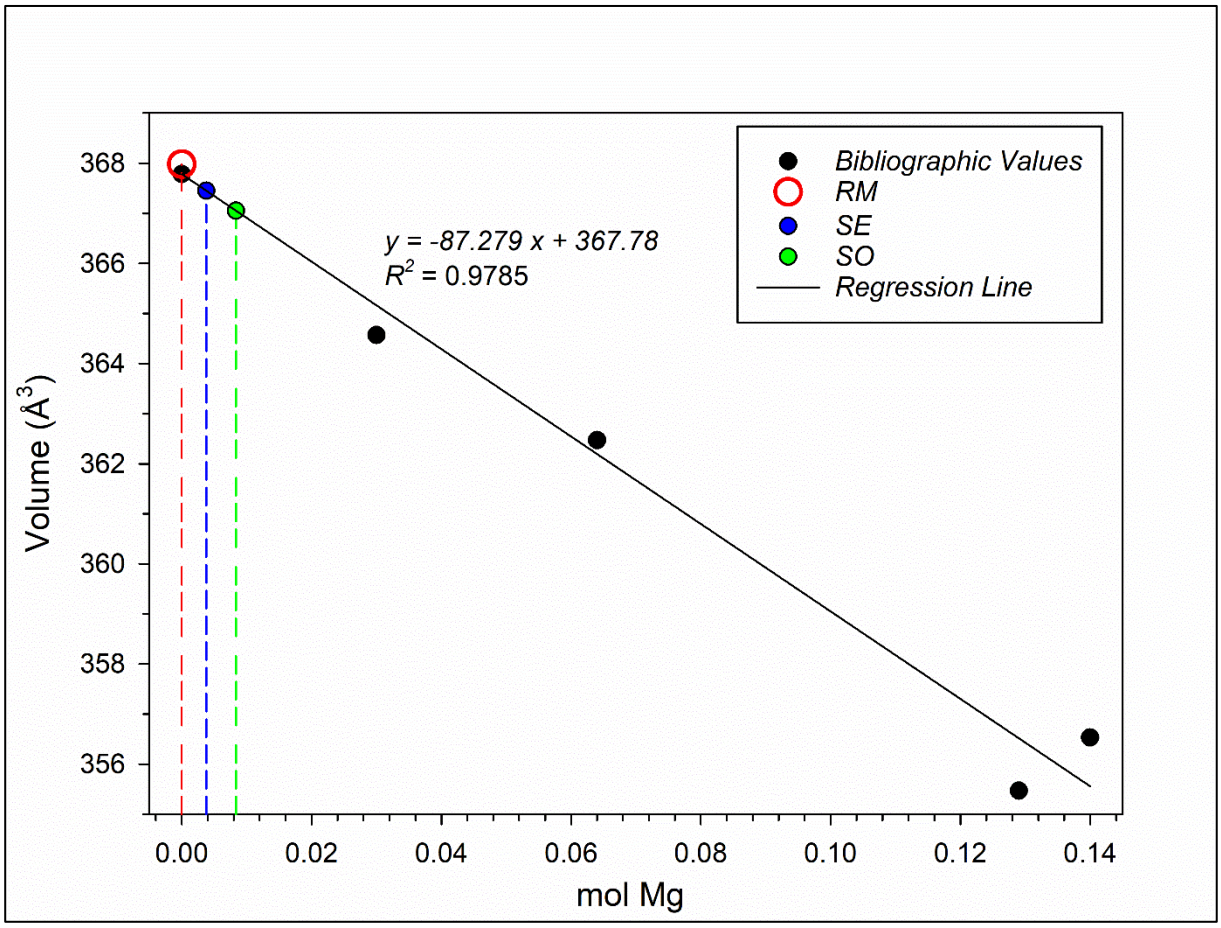

Fig. 8.10 – Plot of mol Mg content in calcite ($(Ca_{1-x},Mg_x)CO_3$)) for limestone samples (RM, *SE* and SO) obtained by using the regression line calculated by referee values (see Table 8.5).

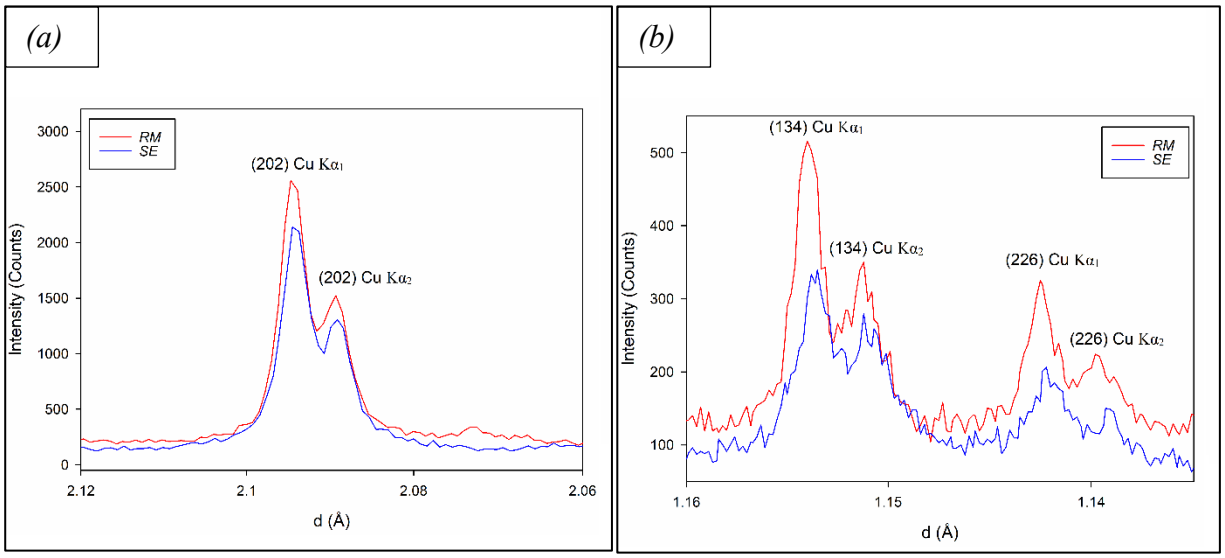

Fig. 8.11 – LXRPD patterns of *RM* (red line) and *SE* (blue line) highlighting differences in the peak broadening of calcite varying in d (Å): (a) (202) calcite peak at medium 2θ (~ 43°, 2.10 Å), revealing a similar peak broadening for *RM* and *SE* samples; (b) (134) and (226) Bragg peaks at high 2θ (~ 86°, 1.15 Å), showing sharper peaks for RM, while *SE* has wider and lesser intensity calcite peaks due to the larger microstrain value.

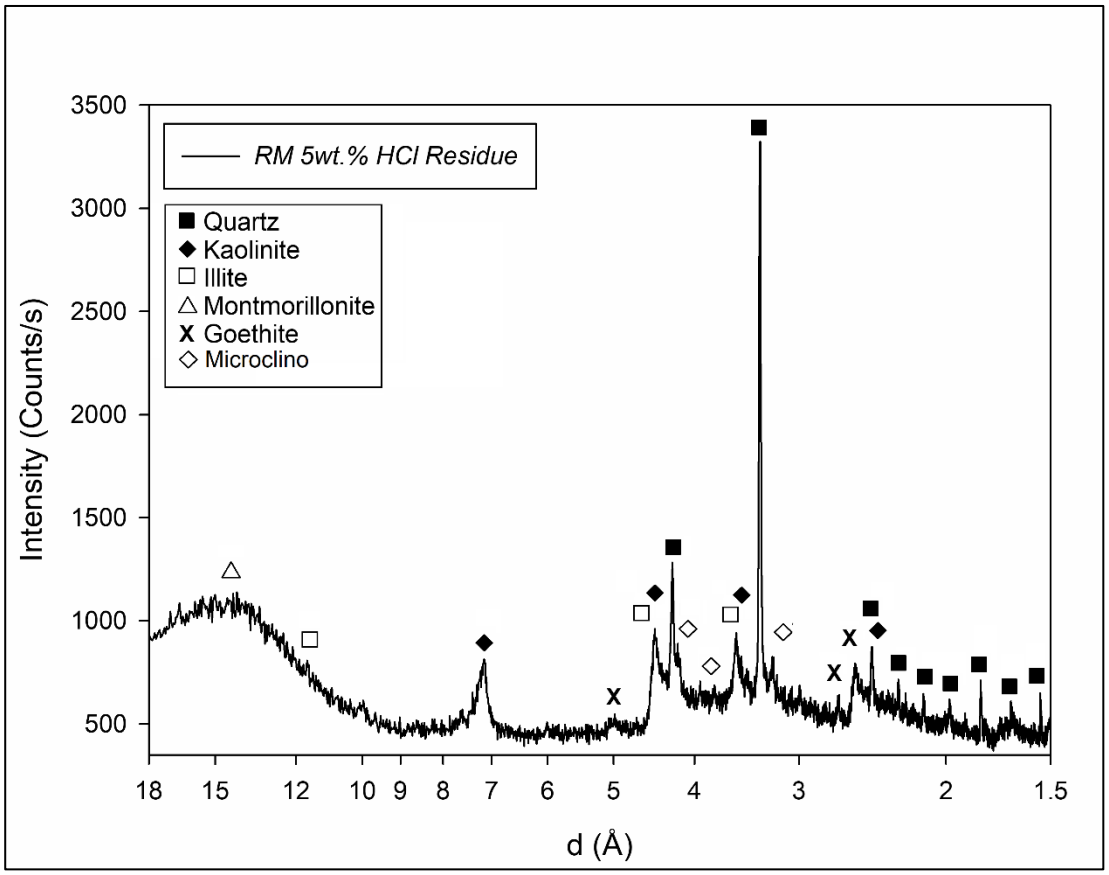

Fig. 8.12 – LXRPD pattern of *RM* sample treated with 5wt.% HCl, highlighting main Bragg peaks of occurring crystal phases.

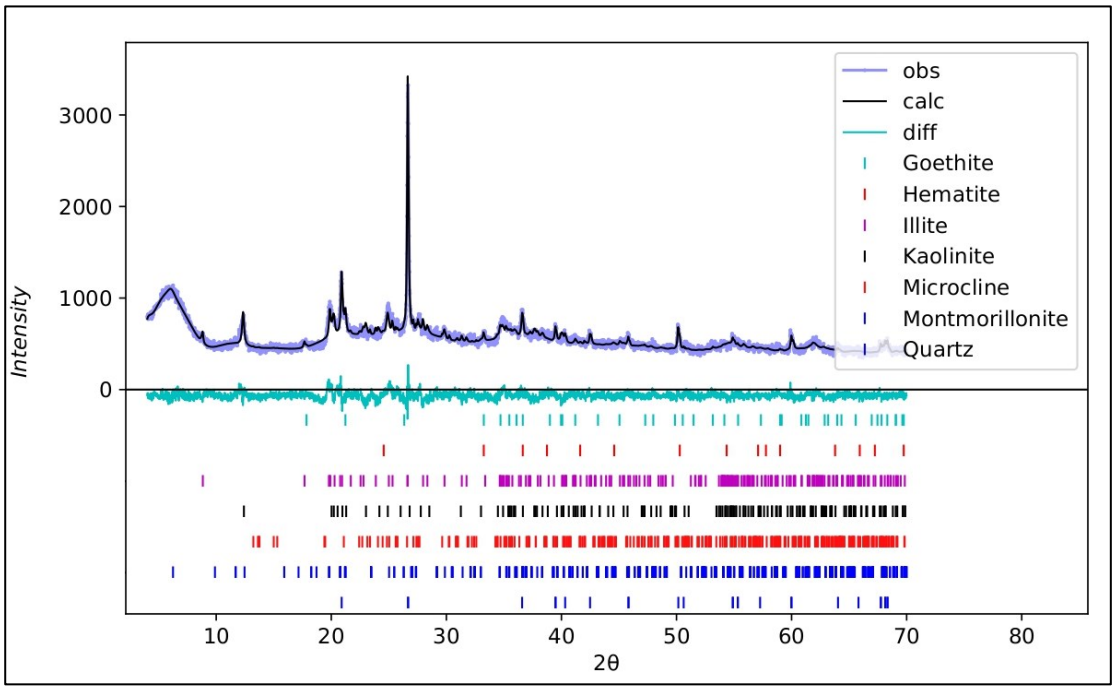

Fig. 8.13 – Rietveld analysis pattern of *RM* sample treated with 5wt.% HCl obtained with GSAS-ii software; light blue, black and cyan lines represent the observed, calculated and difference patterns, respectively; the coloured vertical lines below the pattern highlight the Bragg peaks of each crystal phases.

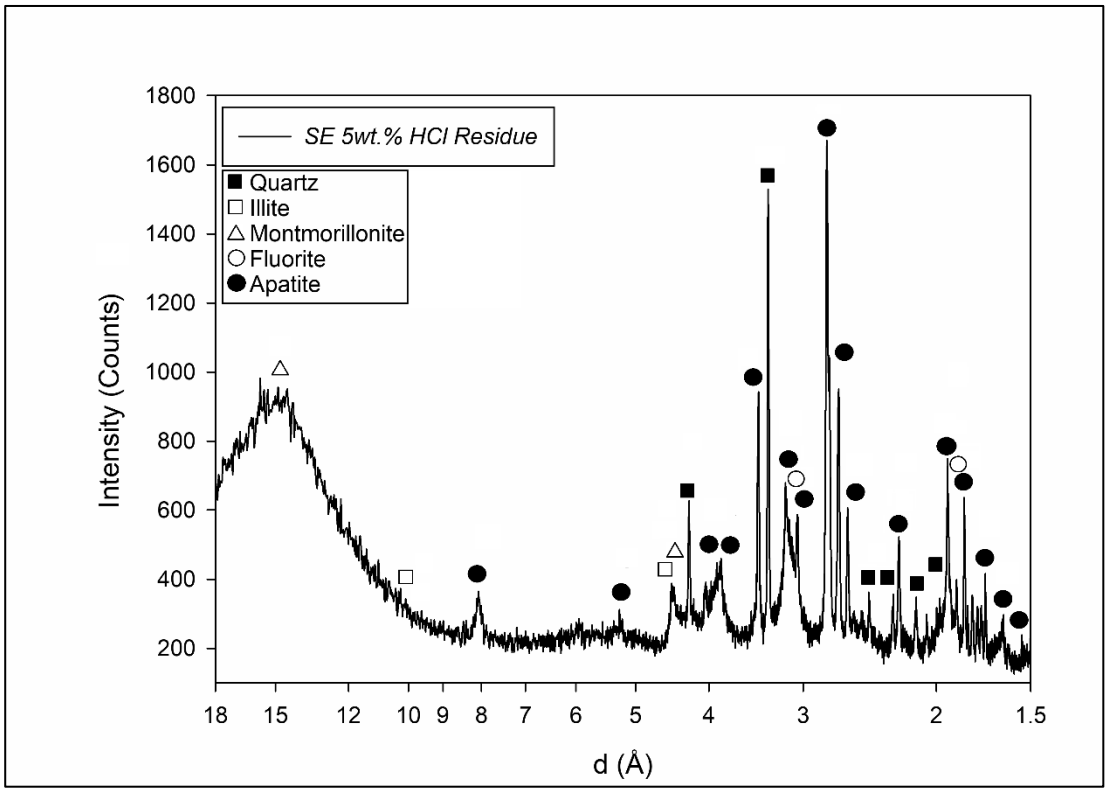

Fig. 8.14 – LXRPD pattern of *SE* sample treated with 5wt.% HCl, highlighting main Bragg peaks of occurring crystal phases.

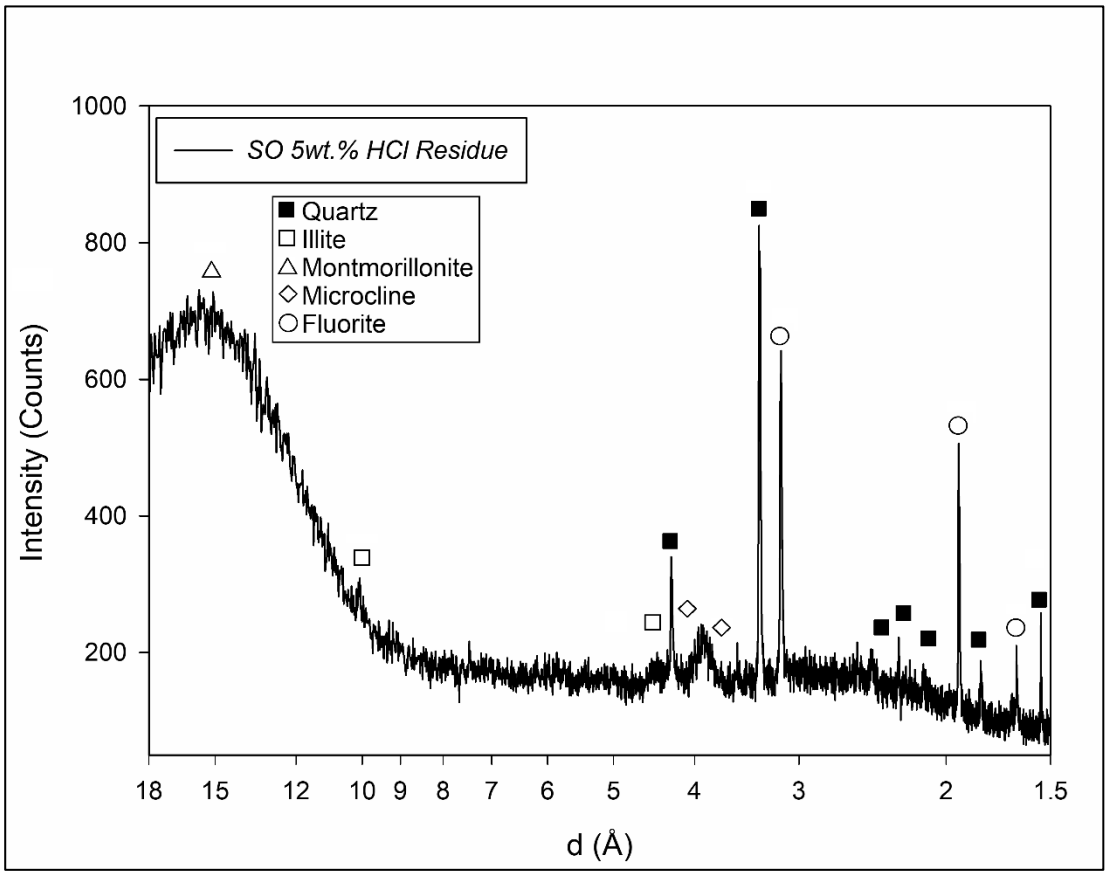

Fig. 8.15 – LXRPD pattern of *SO* sample treated with 5wt.% HCl, highlighting main Bragg peaks of occurring crystal phases.

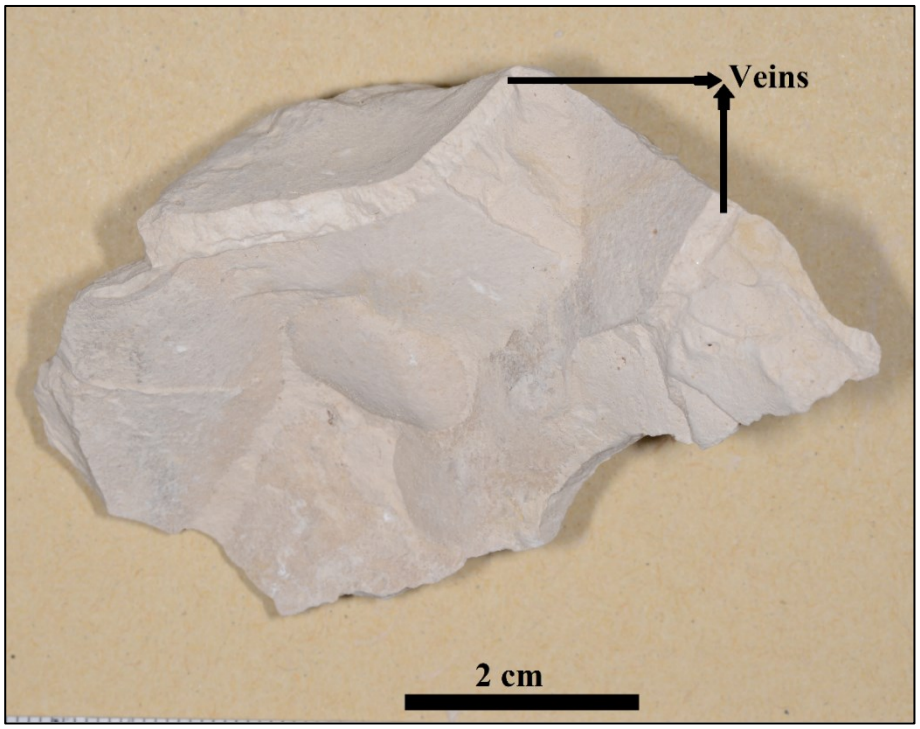

Fig. 8.16 – *RM* fragment highlighting the occurrence of two millimetric white veins without preferred orientation, mainly composed of gypsum and minor amount of calcite and quartz.

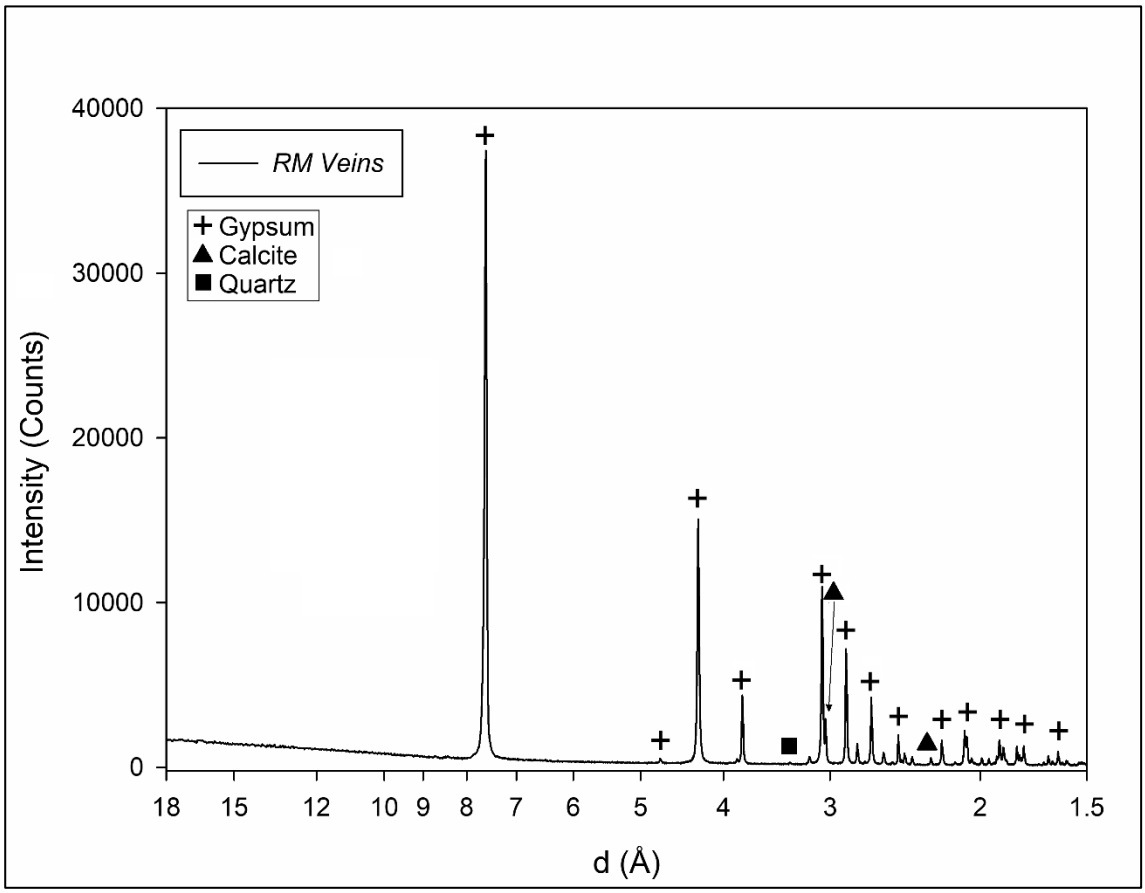

Fig. 8.17 – LXRPD pattern of *RM* veins, highlighting main Bragg peaks of occurring crystal phases.

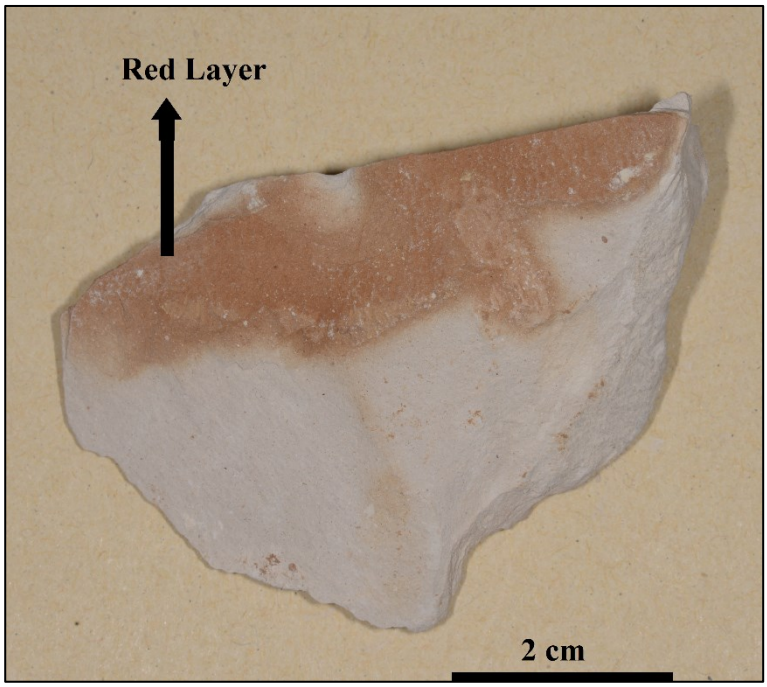

Fig. 8.18 – *RM* fragment showing the submillimetric thick red layer richer in gypsum and goethite, responsible for the red colour, compared to the bulk rock (Table 8.2).

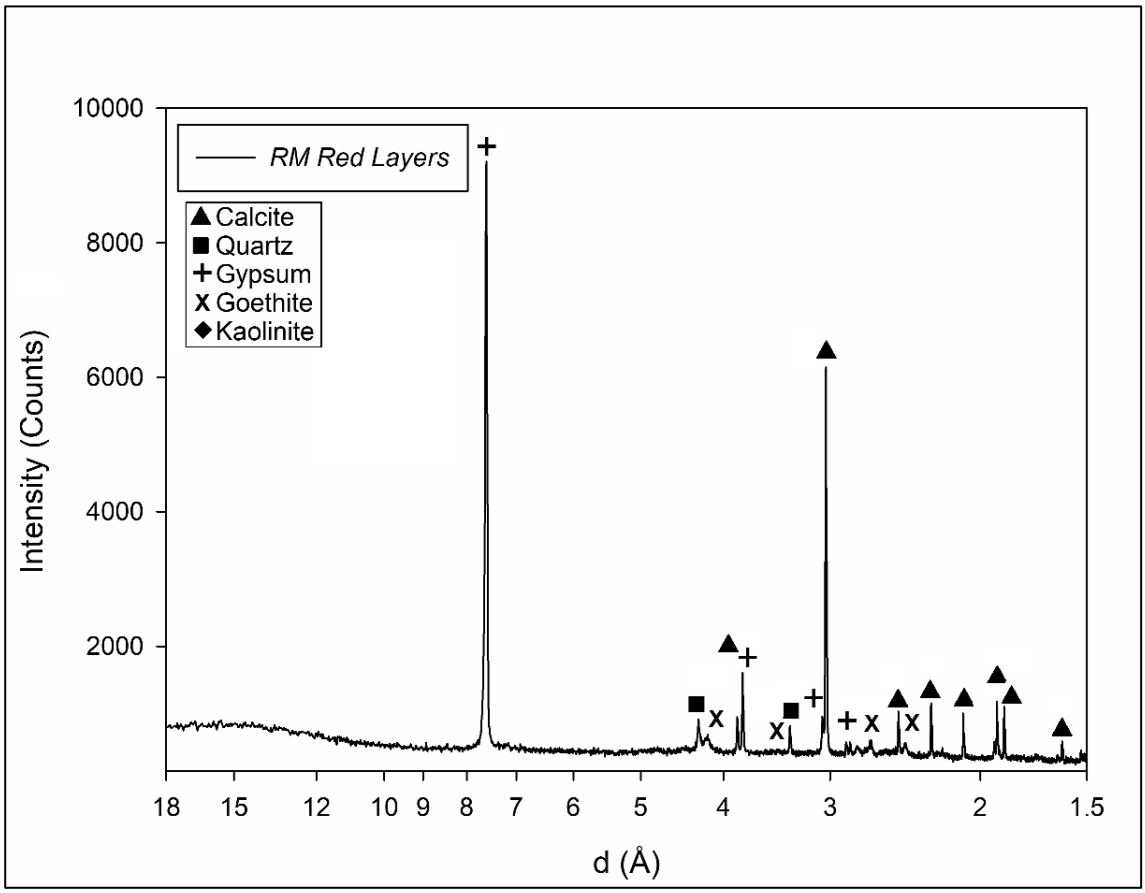

Fig. 8.19 – XRPD pattern of *RM* red layers, highlighting main Bragg peaks of occurring crystal phases.

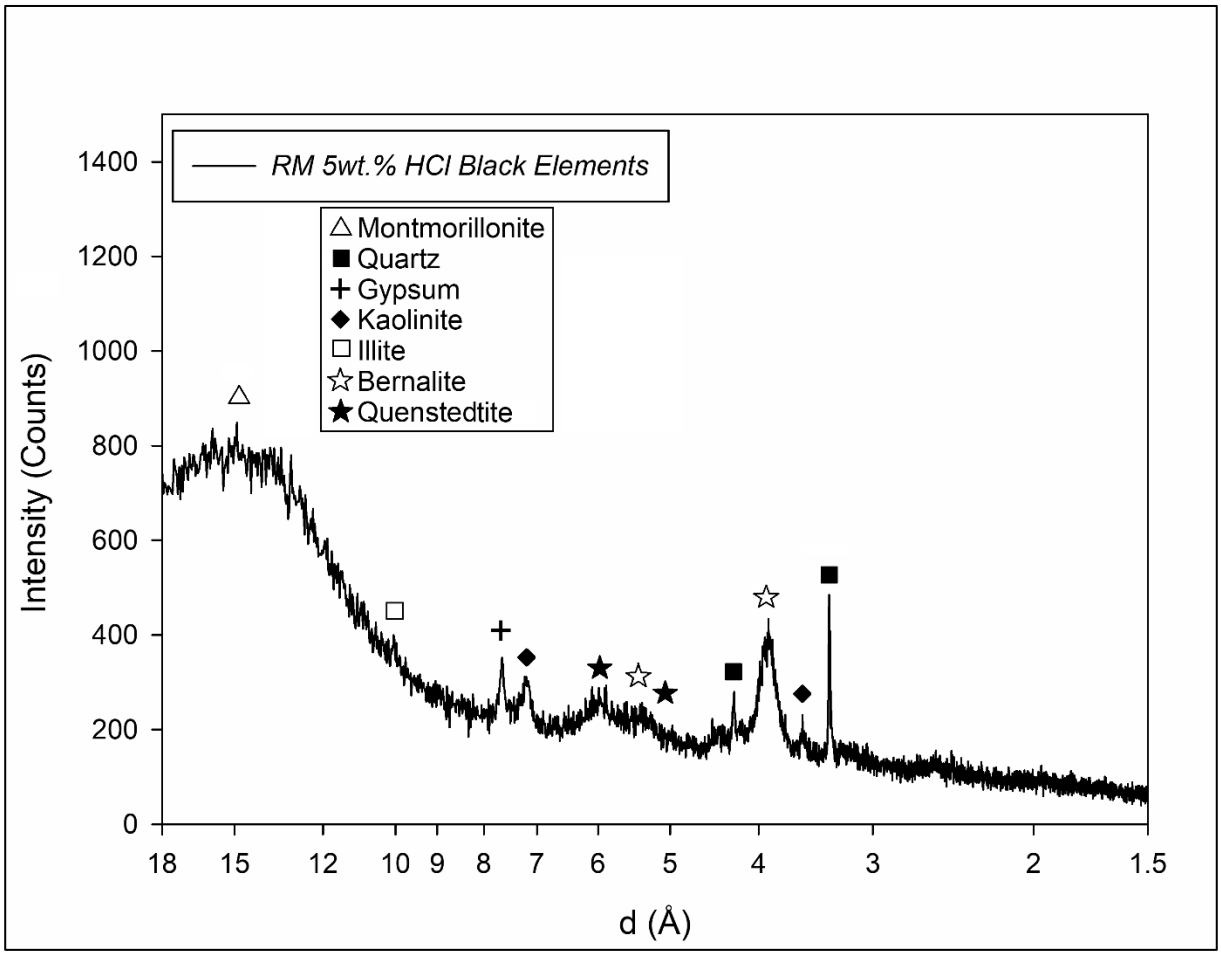

Fig. 8.20 – LXRPD pattern of *RM* black portions treated with 5wt.% HCl, highlighting main Bragg peaks of occurring crystal phases.

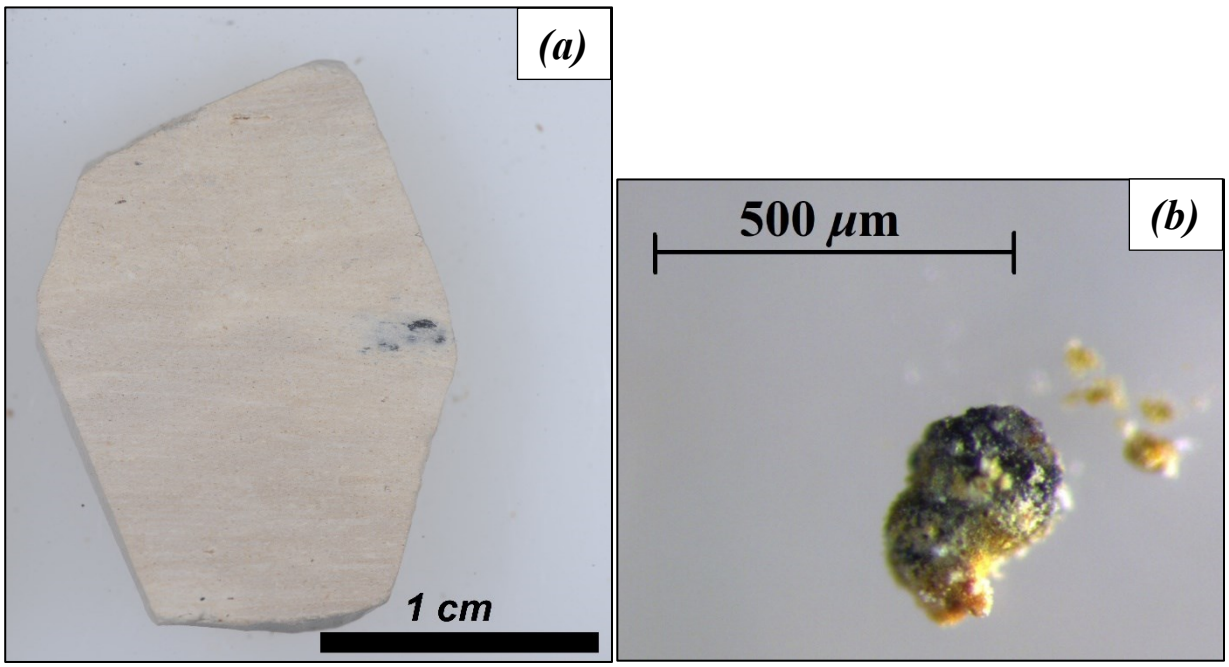

Fig. 8.21 – (a) *RM* sample with elliptical black portions; (b) black portion found in *RM* samples, highlighting colours, shape and dimension.

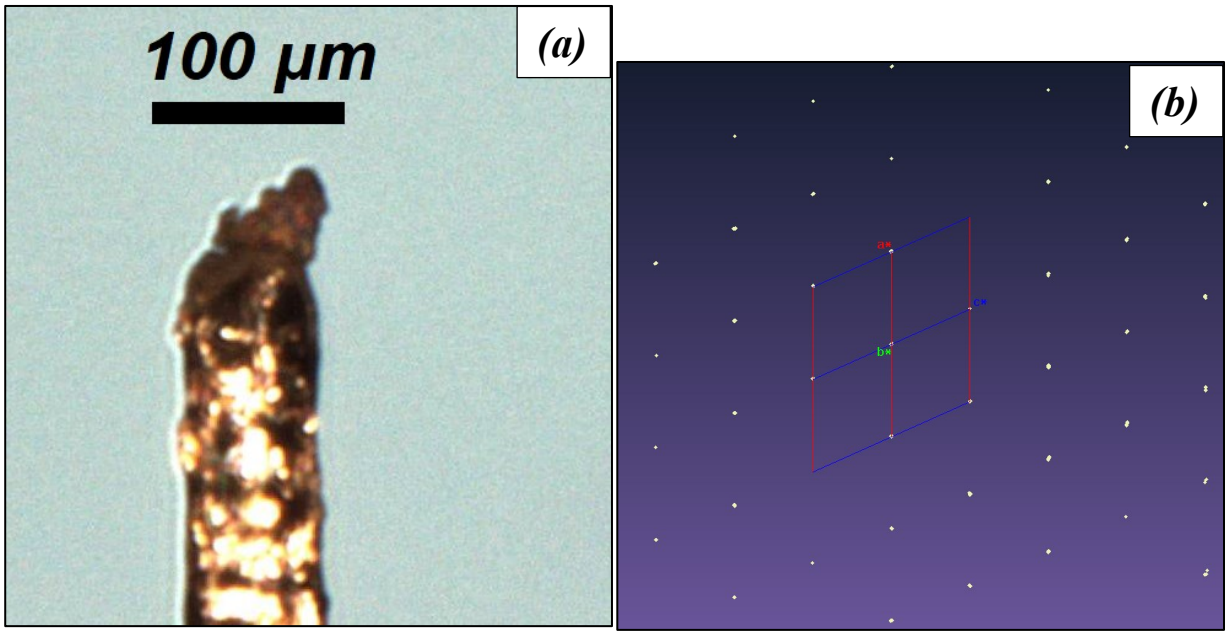

Fig. 8.22 – (a) image of the analysed single crystal (titanite) found in a black portion, mounted on a glass fiber; (b) reciprocal space projection of Bragg peaks along b vector (h0l).

Crystal size (mm)	0.09 x 0.05 x 0.06
Space Group	$C2_{/c}$
a (Å)	6.5588(9)
b (Å)	8.7063(9)
c (Å)	7.0629(9)
α (°)	90.03(1)
β (°)	113.86(2)
γ (°)	89.98(1)
V (Å^3)	368.85(8)
Range for data collection, θ (°)	4.100-28.541
Reciprocal space range *hkl*	$-8 \leq h \leq 8$
	$-10 \leq k \leq 11$
	$-8 \leq l \leq 8$
Set of measured reflections	498
Absorption correction method	multi-scan SCALE3 ABSPACK

Table 8.6 – Parameters and results from SCXRD investigation on titanite crystal found in a black portion of *RM* sample.

NXRD analysis on *RM* fragments revealed no clear preferred orientation of calcite crystals, as reported in the reconstructed pole figures (Fig 8.23). Reconstructed pole figures for calcite Bragg peaks with higher relative intensity ((104), (202) and (018)) should be more considered than others with lower relative intensity ((006), (110) and (1010)): the highest intensity peak (104) and (202) showed no preferred orientation; while, a very slight orientation occurs for *c* axis in the (018) pole figure which is clearer in (006) and (1010) low-intensity peaks pole figures. Therefore, if a preferred orientation occurs, it would be observed especially on high intensity peaks ((104), (202), etc.). The fitting pattern of RQPA associated with texture analysis is reported in Fig 8.24, showing the goodness of fitting.

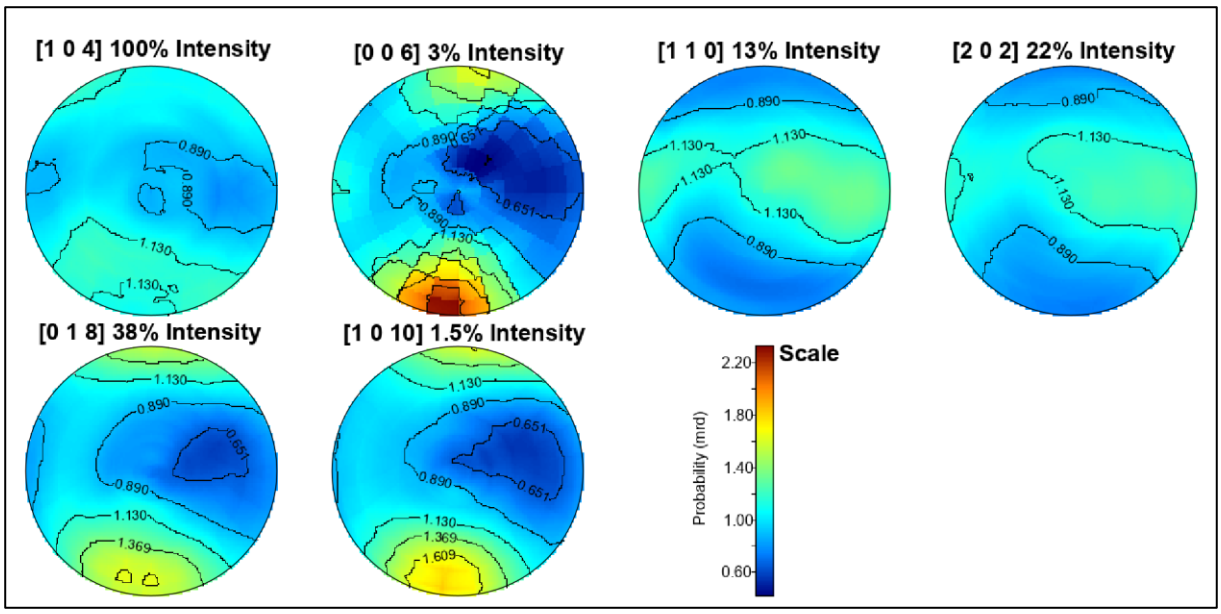

Fig. 8.23 – Reconstructed Pole Figures for main Bragg peaks for calcite in *RM* sample studied by Neutron synchrotron Diffraction.

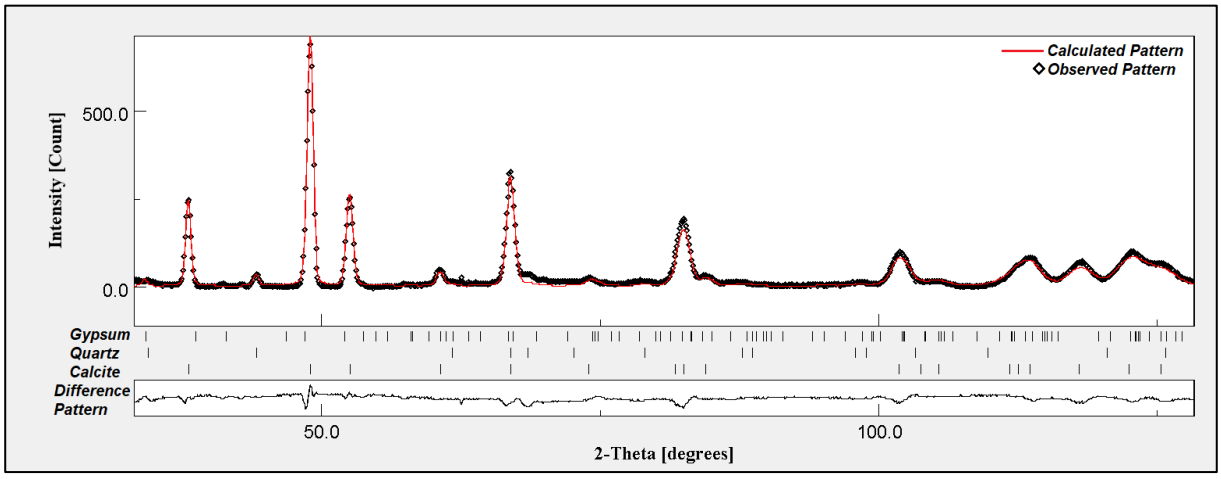

Fig. 8.24 – Fitting result of the sum of Neutron synchrotron Diffraction patterns performed with Maud software [275–278,292].

8.3 – Discussion

Considering for all samples the stratigraphic position, textural (macro and micro scale) and mineralogical features observed: sample *RM* represents the lower part of Ghareb Formation made of phosphatic-gypsum rich limestone deposited during Early Maastrichtian transgressive phase in an open marine environment with low-energy conditions and microbial activity on the bottom responsible of the phosphate enrichment [118,293] (Table 8.1); whereas, samples *SE* and *SO* are hard nodules of phosphatic wackestone and calci-mudstone, respectively, which should represent the phosphatic-gypsum rich limestone (*RM*) involved in a diagenetic process of sparitization that obliterated the original sedimentary texture (Table 8.1), likely related to a precipitation of $CaCO_3$ and dissolution of SiO_2 in anoxic conditions rich in organic matter, as widely found in Upper Member of Mishash Formation [113,118].

RQPA for both bulk and 5wt.% HCl residues for all samples (*RM, SE* and *SO*) are in good agreement with features observed during the LM textural investigation: (i) hard nodules (*SE* and *SO*) are made of mainly calcite and apatite, as fish bones and pellets, and very low amount of quartz and clay minerals, which were only detected in the residues; (ii) phosphatic wackestone (*SE*) has higher amount of apatite compared to phosphatic calci-mudstone (*SO*), as observed during TLM; (iii) apatite-gypsum rich limestone (*RM*) is made of mainly calcite and apatite as *SO* with higher amount of clay minerals, quartz and gypsum (Table 8.2,3).

XRD results for *RM* highlighted the same mineral assemblage of other studies but different clay content was observed: Ghareb Formation collected at Rotem Amfort Mine (Stop-8, *RM*, Table 8.2) revealed high kaolinite content compared to Arad city outcrops [294], which no kaolinite occurs and montmorillonite plus illite represent the overall clay content (Table 8.3). Clay content change could be related to differences in depositional environment, such as anticlinal (Arad) and synclinal (Rotem Amfort Mine) locations, current direction and weight of detrital contribution [295]. Kaolinite is considered as detrital mineral formed on land in humid climate under acid weathering conditions and transported to the basin [294–296]; while, illite and montmorillonite genesis in Ghareb Formation has been claimed as a result of conversion of detrital volcanic rocks in warm water with stratified high salinity basin, as suggested by the widespread gypsum occurrence and in agreement with the depositional environment [294]. Furthermore, the occurrence of phosphate nodules and the P_2O_5 content are similar with previous studies [106,297,298], all reporting phosphatic pellets above the Oil Shale Member in Ghareb Formation.

Considering all the features of the hard concretions of phosphatic limestone of Ghareb Formation (*SO* and *SE*), they should be related to a similar, or even the same, genetic process of the hard limestone concretions occurring in Mishash Formation [106]: (i) fluorite occurs as minor mineral in both *SO* and *SE* samples, suggesting a diagenetic process involving fluids also rich in F^{-1}; (ii) low amount of quartz and higher of calcite compared with the pristine phosphatic calci-mudstone (*RM*) occur, suggesting a dissolution of SiO_2 and a precipitation of $CaCO_3$; (iii) higher crystallite size of calcite compared to *RM*, suggesting a coarsening of crystals as occurs during sparitization of micrite cement. Therefore, *RM* should be considered as the pristine limestone of *SE* and *SO,* which undergone in a secondary process.

A detailed study to calculate MgO contents from calcite cell parameters obtained by RPQA (Fig. 8.10, Table 8.5) showed a good agreement with XRF data, excepted for *RM*, which underestimated the MgO content suggesting that should be contained also in clay minerals.

Apatite-gypsum rich limestone (*RM*) showed three different anisotropies, such as (i) gypsum veins, (ii) millimetric black nodules and (iii) goethite-rich layers, which the first two were also reported in previous studies (Table 8.4, Fig. 8.16,18,21). Gypsum veins were also reported in several studies as millimetric veins with no preferred orientation [13,299]. Fe-rich black nodules were found in other studies, reporting pyrite in the centre and limonite on the border with sometimes barite and clays (montmorillonite, illite and kaolinite), especially occurring in the Oil Shale Member (bituminous-rich limestone) [13,299,300]. The formation of limonite is due to the gradual decomposition of pyrite in oxidating condition. Black nodules observed in this study are composed of Fe-bearing phases (goethite, bernalite, questedtite), clays, quartz and calcite. Fe-bearing phases are represented by hydroxides (goethite and bernalite) and hydrated sulphate (quenstedtite), suggesting an environmental condition of oxidation and arid climate [301]: pyrite oxidation produces ferric hydroxide and hydrous iron sulphate minerals which gradually loss the water content [302]. Moreover, SCXRD revealed the first evidence of titanite crystals inside Fe-rich black nodules in Ghareb Formation, representing a TiO_2 source (Fig. 8.22, Table 8.6). None study reported the occurrence of millimetric goethite-rich layers, but rather clay-rich strata [13,299].

Detailed diffractometric analysis (SXRPD) on *RM* revealed the same mineral assemblage obtained at laboratory scale (LXRPD) (Table 8.2,5), but synchrotron data refinement gave (i) more reasonable crystallite size and microstrain values which were refined at the same time during Rietveld method with no correlation error [248]; (ii) more accuracy and precision on the quantification of minor crystal phases and crystallographic parameters due to the geometry, intensity and wavelength of the radiation [303]. Furthermore, NXRD texture analysis figured out no clear preferred orientation of calcite (Fig. 8.23,24), which represents the main crystal phase that its preferred orientation may influence the growth of Ca-rich HT minerals (larnite, hatrurite, etc.) during CP.

8.4 – Conclusion

The study of Ghareb Formation which represents with also Taqiye Formation the protoliths of Larnite-rich rocks, with both traditional (field trip, bibliographic study, LM, XRF, SCXRD and LXRPD) and innovative methods (SXRPD, NXRD and µ-CT all performed at synchrotron scale) revealed features at different observation scale that can have an influence on the texture, crystal phase assemblage and distribution on larnite-rich rocks during the CP event.

Our results are in good agreement with previous study on this sedimentary formation, highlighting the deposition in an open marine environment with low-energy conditions, stratification of water, high salinity and microbial activity; leading the formation of calci-mudstone rich in apatite, occurring as fish bone fragments and pellets, gypsum, also occurring as millimetric veins, and clays. Furthermore, the occurrence of hard limestone nodules in Ghareb Formation, with same features of hard concretions in Mishash Formation, pointed out the local development of secondary process marked by the dissolution of quartz, sparitization and precipitation of calcite, due to the development of anoxic condition and organic matter. Anisotropies occurring in Ghareb Formation, such as gypsum veins, red goethite-rich layers and Fe-rich black nodules, should be considered during the further investigation on larnite-rich rocks, due to their influence on texture and phase distribution.

Chapter 9
Study on larnite-rich rocks

Larnite-rich rocks were formed by the complex process of CP involving limestone and marls, which is made of two main stages: (i) 1st stage of HT combustion (prograde stage) leading changes in texture and mineral assemblage mainly due decomposition of calcite and reactions involving lime and Si-Al-rich minerals (quartz and clays); (ii) 2nd stage of LT processes (retrograde stage) mainly marked by the hydration of HT rocks principally occurring in fractures and exposed surface. Rocks formed by this two stages process represent the natural corresponding of anhydrous and hydrated cement materials: therefore, the study of CP rocks gives important information for both clarifying CP process and improving cement manufacture.

Larnite-rocks collected at Stop-6.1 (labelled as *6BWO* and *6BWV*) and Stop-9 (labelled as *YC2O* and *YC2V*) during the field trip in Hatrurim Basin were deeply studied by both traditional and innovative techniques (Table 7.6) leading detailed information on microtexture, mineral assemblage and crystallographic features of occurring crystal phases.

9.1 – Results

Polished sections of larnite-rich rocks collected at two different stratigraphic positions, such as Stop-9 (sample labelled as *YC2O*, which should correspond to the CP of the top of Taqiye Formation) and Stop-6.1 (sample labelled as *6BWO*, related to the HT combustion of Ghareb Formation close to the base of the sequence), were studied by means of RLM revealing microtextural features. The identification of minerals was made by considering crystal shape, reflectivity (brightness at // nicols) and bibliographic descriptions of both larnite-rich rocks [2,21,34,78,122] and cement materials [304]:

(i) larnite occurs at // nicols as a low reflective mineral (gangue) with dark grey colour and low pleochroism only visible in big polygonal crystals, at + nicols only slight anisotropy from light brown to darker colours (Fig. 9.3c,d);

(ii) fluorapatite occurs as hexagonal prism crystals with darker colour and bigger size than larnite ones at // nicols, often with high reflective minerals microinclusions (Fig. 9.2c,d);

(iii) spinel is found as rounded to pseudocubic crystals with grey colour at // nicols, whereas, at + nicols shows dark grey colour and yellowish to reddish internal reflections (Fig. 9.1c,d;9.2e,f;9.3e,f);

(iv) ye'elimite occurred as anhedral crystal shape and low crystal size, with dark colour at // nicols, no pleochroism, anisotropy and internal reflections;

(v) shulamitite (tabular to acicular crystals [21]) and brownmillerite (tabular to prismatic crystals [26]) have both light grey colour and no pleochroism at // nicols, and no anisotropy and internal reflections at + nicols (Fig. 9.1c,d;9.2e,f;9.3e,f);

(vi) CSH minerals and calcite occur with dark grey colour, distinguished at + nicols due to lighter colour and common internal reflection of calcite [305] (Fig. 9.1a,b;9.3a,b).

Both samples (*YC2O* and *6BWO*) should be considered as ye'elimite-larnite granofels falling in the sanidinite facies (> 800 °C [3]), due to the occurrence of larnite (HT crystal phase) [1], highlighting similar features:

(i) a homogenous matrix rich in low reflective minerals with grey to dark grey colours, identified as mainly larnite and fluorapatite, with sparce lighter minerals at // nicols, such as brownmillerite, shulamitite and spinel (Fig. 9.1a,b,c,d);

(ii) general low crystal size (< 50 μm), especially for low reflective minerals, making difficult the crystal phase identification (Fig. 9.1c;9.2b);

(iii) nodules of 150-500 μm often occur with an elliptical shape, made of mostly shulamitite, brownmillerite and spinel, showing higher crystal size compared to ones in the matrix (Fig. 9.1c,d;9.2e,f;9.3e,f). The matrix inside the nodules is composed of darker minerals, such as larnite and apatite if no hydration occurred (Fig. 9.1c,d), and CSH minerals and calcite if nodules are inside hydration veins (Fig. 9.3a,b);

(iv) submillimetric hydration veins with no preferred orientation often highlighting at + nicols a central white part rich in calcite and brown borders made of CSH minerals (Fig. 9.1a,b;9.3a,b). Furthermore, spinel almost occurs only in brown borders along with CSH minerals inside two parts made veins (Fig. 9.1a,b).

More in details, *YC2O* has lower crystal size (10-20 μm) compared to *6BWO* (25-50 μm), especially for shulamitite and brownmillerite inside nodules (Fig. 9.1e,f,3e,f). Brownmillerite and shulamitite could also occur as intergrowth of skeletal crystals inside nodules (Fig. 9.3e,f). Nital etching (section 7.2.3) was used on *YC2O* sample allowing detailed microtextural investigation: (i) larnite, which represents the main and only etching reactive mineral in larnite-rich rocks, turned to dark brown colour at // nicols (Fig. 9.2), leading a better estimation of its modal distribution, with no noticeable changes at + ones (Fig. 9.2b); (ii) other crystal phases were better distinguished, especially apatite showing its euhedral hexagonal prism shape with numerous lighter inclusions of brownmillerite-shulamitite and spinel (Fig. 9.2c,d).

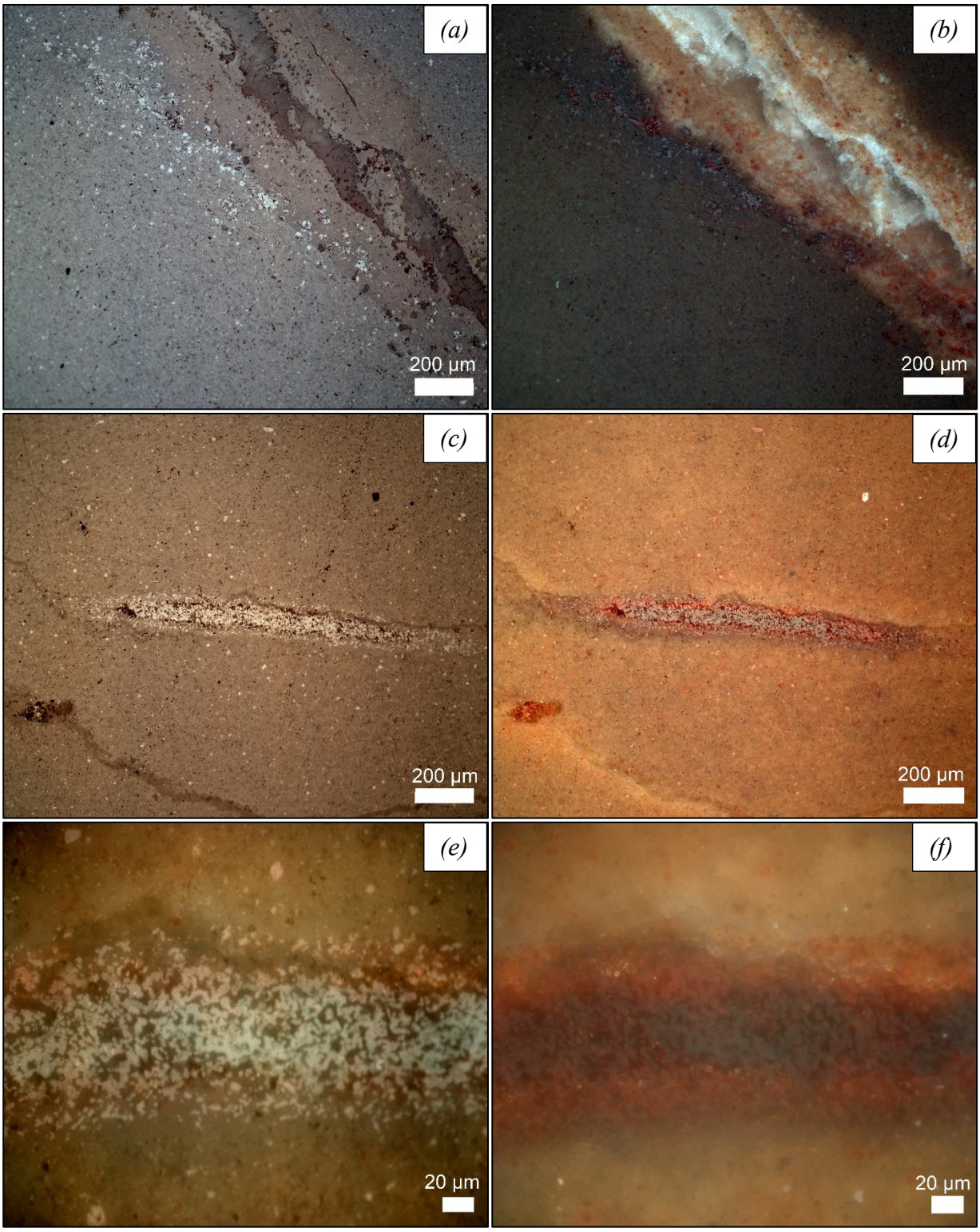

Fig. 9.1 – RLM images for larnite-rich rock (*YC2O* collected at Stop-9), at // (left) and + (right) nicols: (a,b) overview at low magnification including submillimetric hydration vein, which has a white central portion (calcite-rich part) and brown borders of CSH minerals and unreacted spinel; (c,d) elliptical light grey nodule rich in high reflective mineral (spinel, shulamitite, brownmillerite) and a matrix of low reflective ones (apatite, larnite, etc.); (e,f) light grey nodule at high magnification highlighting rounded spinel enrichment with reddish internal reflections at + nicols.

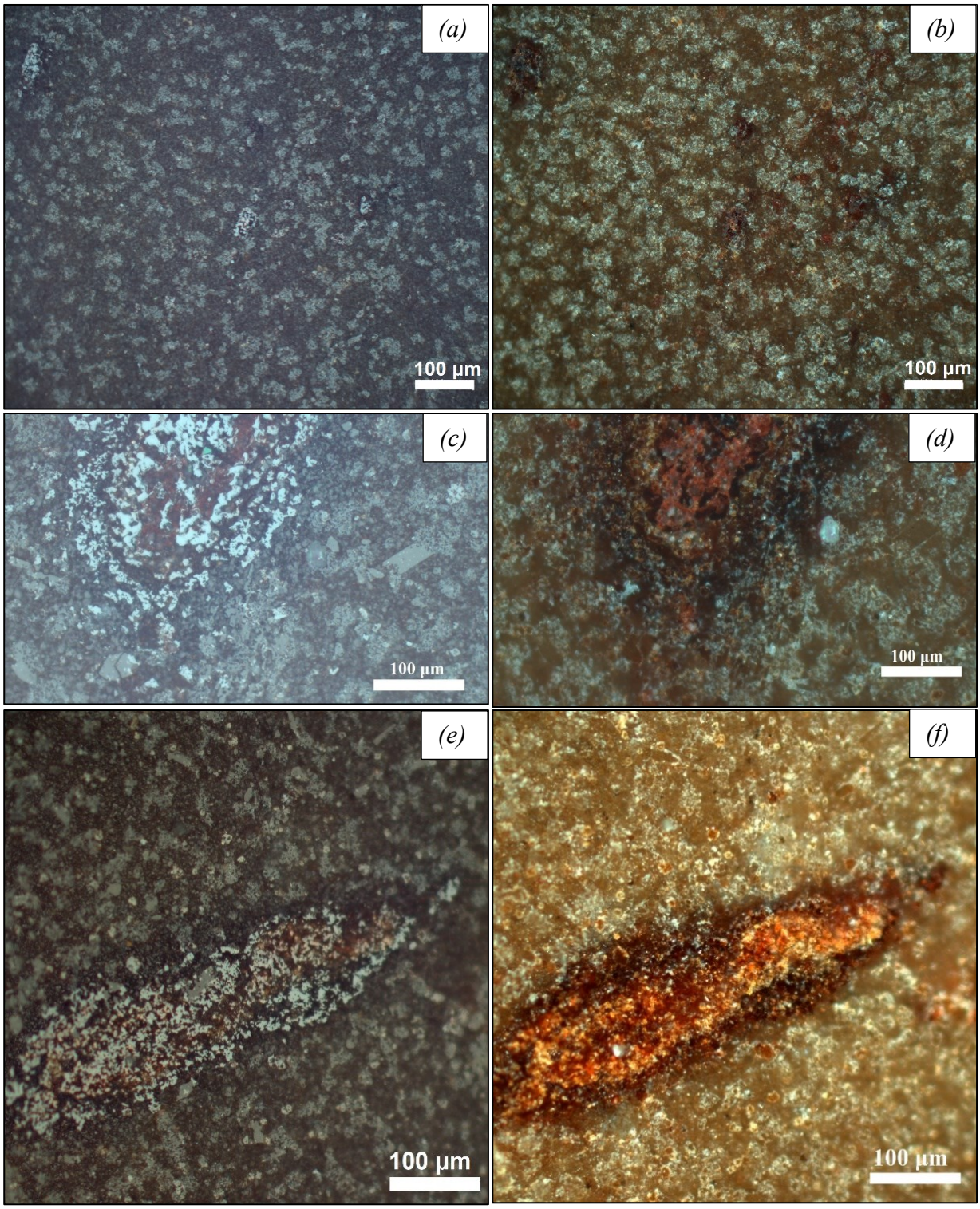

Fig. 9.2 – RLM images for larnite-rich rock (*YC2O*) polished section etched with Nital (see section 7.2.3 [304]), at // (left) and + (right) nicols: (a,b) overview of natural Belite Clinker etched with Nital, showing an overall brown color at // nicols due to larnite abundance representing main etching reactive mineral; (c,d) occurrence of several apatite crystals showing the euhedral hexagonal prism shape rich in light inclusions close to a light grey nodule; (e,f) submillimetric light grey elliptical nodule mainly rich in spinel, also revealing its yellowish to reddish internal reflections, and with a matrix of dark grey minerals.

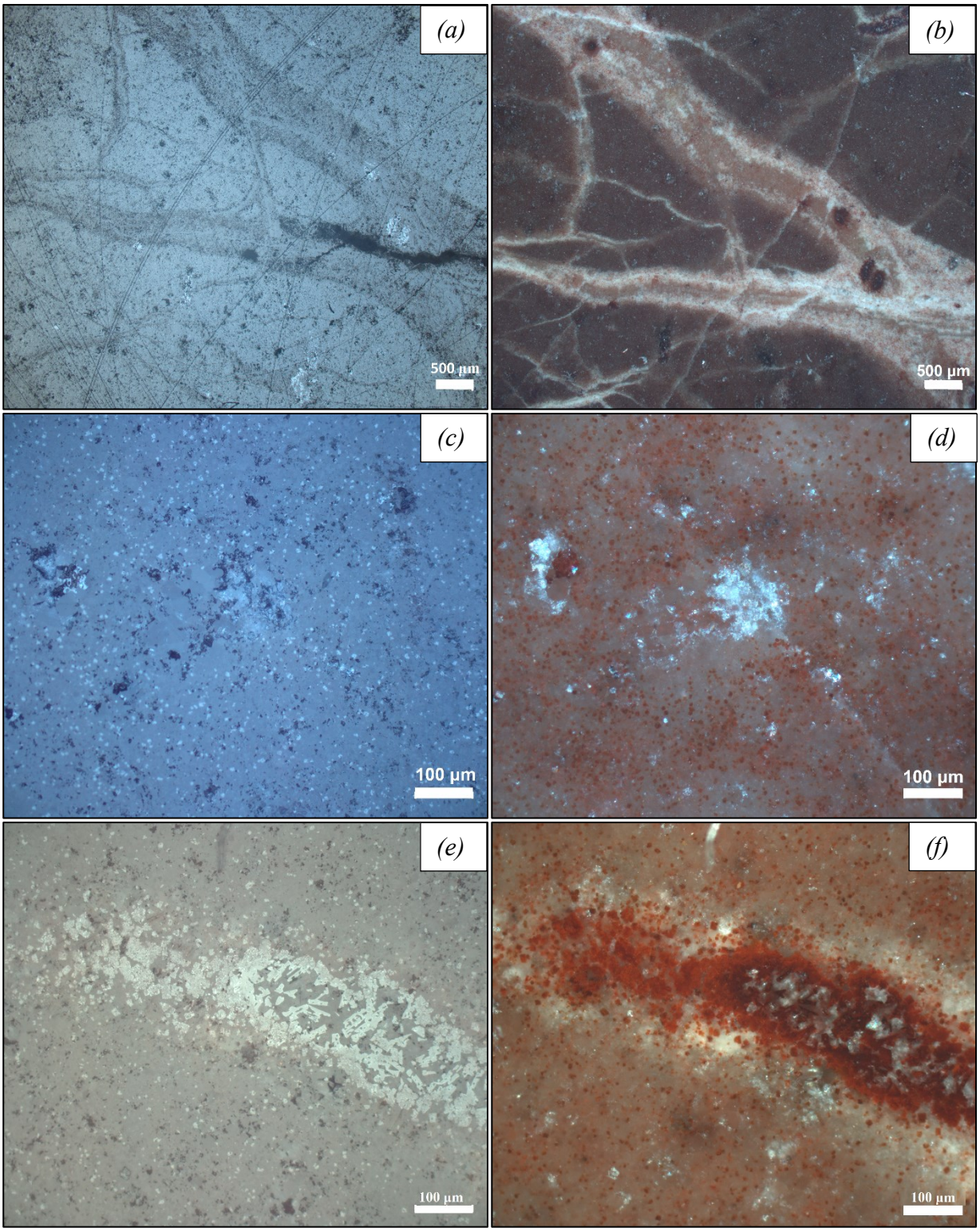

Fig. 9.3 –RLM images for larnite-rich rock (*6BWO*, collected at Stop-6.1), at // (left) and + (right) nicols: (a,b) overview of larnite-rich rock crossed by numerous submillimetric to micrometric hydration veins with black-brown rounded elements rich in spinel at + nicols; (c,d) coarser larnite polygonal crystals (~ 35 µm) showing pleochroism from dark to medium grey and slight anisotropy; (e,f) elliptical submillimetric light grey nodule with a left part rich in spinel (cubic to rounded crystals with grey color rarely zonated and with reddish internal reflections) and a right part rich of shulamitite and brownmillerite (prismatic and skeletal crystals) and a matrix of darker minerals.

XRD analysis with synchrotron and laboratory radiations was made on both samples (*6BWO* and *YC2O*) and their relative hydrated veins (*6BWV* and *YC2V*), obtaining the wt.% of phases and crystallographic parameters by RQPA. Furthermore, anisotropies occurring in larnite-rich rocks, such as black submetallic nodules, white and brown veins, were studied clarifying their nature.

Results highlighted five main similarities among *6BWO* and *YC2O* samples (Table 9.1): (i) same mineral assemblage occurs for both samples considering crystal phases formed during the 1st HT stage of CP, excepted for the occurrence of low amount of brownmillerite only in *6BWO* and ternesite for *YC2O* (Fig. 9.5,9); (ii) larnite represents the main mineral (always > 60wt.%), but *6BWO* has ~ 10wt.% less than *YC2O*; (iii) fluorapatite and ye'elimite occur in both samples, but are more enriched in *6BWO* representing the 3rd and 2nd minerals in abundance order, respectively; (iv) spinel and shulamitite are always present with almost similar wt.%; (v) mayenite occurs in both samples with higher wt.% in *YC2O* (Fig. 9.9). Moreover, minerals related to the 2nd stage of CP occur in larnite-rich rocks representing 2-7wt.%, despite no hydration veins or weathered surfaces were used to obtain powders: (i) ettringite, gibbsite and nordstrandite occur in both samples, but were identified only at SXRPD (Fig. 9.4,6,8); (ii) quartz, jennite and calcite were found only in *6BWO*, especially on synchrotron pattern (Fig. 9.4,6)*;* (iii) gibbsite and afwillite occur only in *YC2O* (Fig. 9.8,9).

Differences between synchrotron and laboratory results should be related to a different investigated volume, that should be higher for laboratory conditions, despite the diffraction geometry at synchrotron (Debye–Scherrer with capillary) leads to higher number of crystals available for diffraction. Furthermore, quantitative changes are also related to minor minerals, Fe-rich crystal phases and minerals with distinctive Bragg peaks at low 2θ (hydrated minerals, brownmillerite and ternesite), which are better quantified with SXRPD (Table 9.1).

Results of crystallographic parameters on larnite were reported and compared with bibliographic data in Table 9.2, including natural crystal, pure synthetic and from clinker nodules: (i) *6BWO* and *YC2O* larnite crystals have both same cell parameters, with no differences between synchrotron and laboratory results; (ii) larnite from Hatrurim Basin rocks has crystallographic parameters close to natural larnite crystals sampled in skarn carbonate xenolith in volcanic structure in northern Caucasian belt [172]; (iii) synthetic pure larnite has lowest cell parameters, whereas, crystals from clinker nodules showed the highest; (iv) microstrain showed similar values for all samples, while crystallite size is higher for *6BWO*, as highlighted by sharper Bragg peaks and in good agreement with RLM evidences (Fig. 9.1c,d;3c,d).

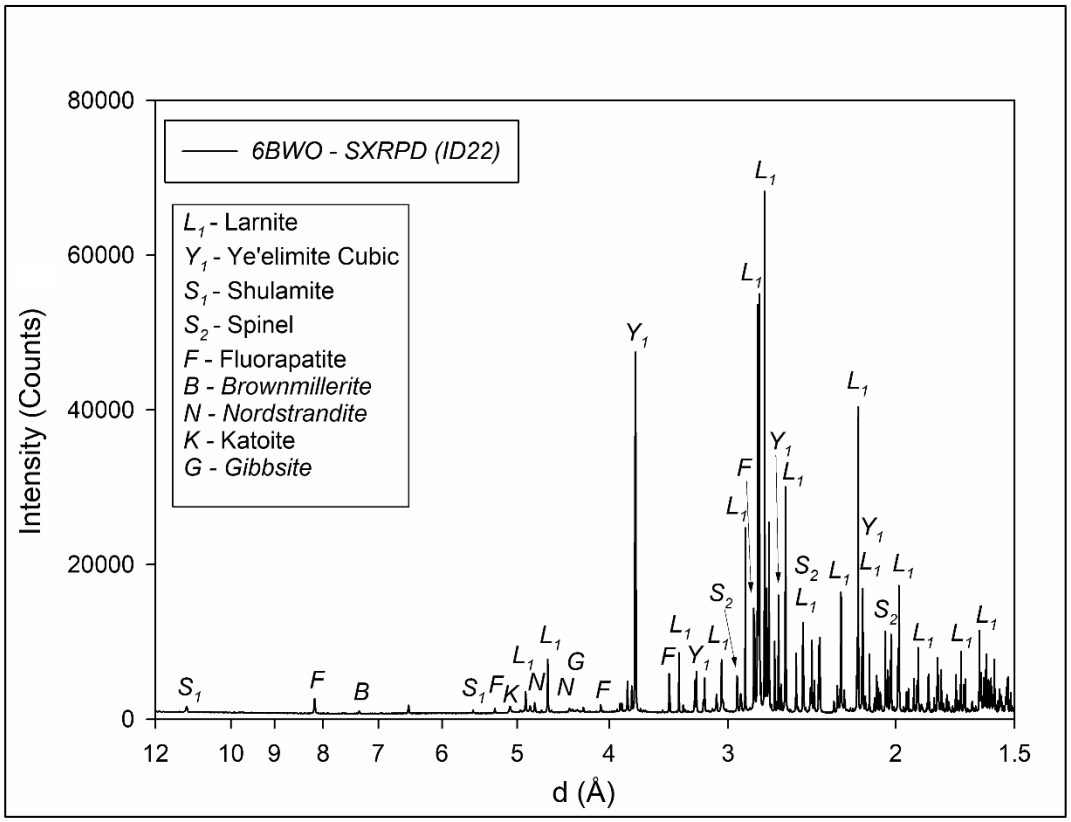

Fig. 9.4 – SXRPD patter of *6BWO* sample collected at ID22 beam line (ESRF) highlighting main mineral Bragg peaks.

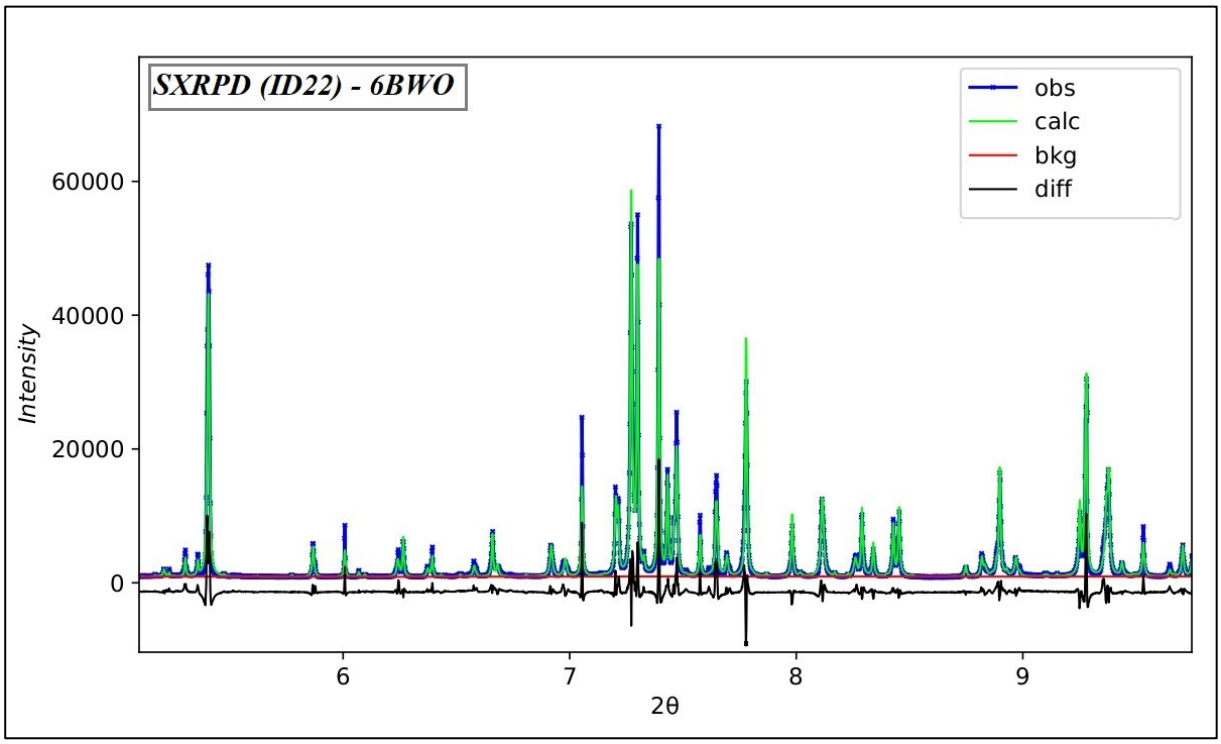

Fig. 9.5 – Fitting of SXRPD patter of *6BWO* sample collected at ID22 beam line (ESRF) by means of GSAS-ii software at 5-10 ° (2θ) (3.98-2.1 Å), highlighting the goodness of peaks fitting; in blue the observed pattern; calculated pattern in green; the background in red; in black the difference point by point between observed and calculated patterns.

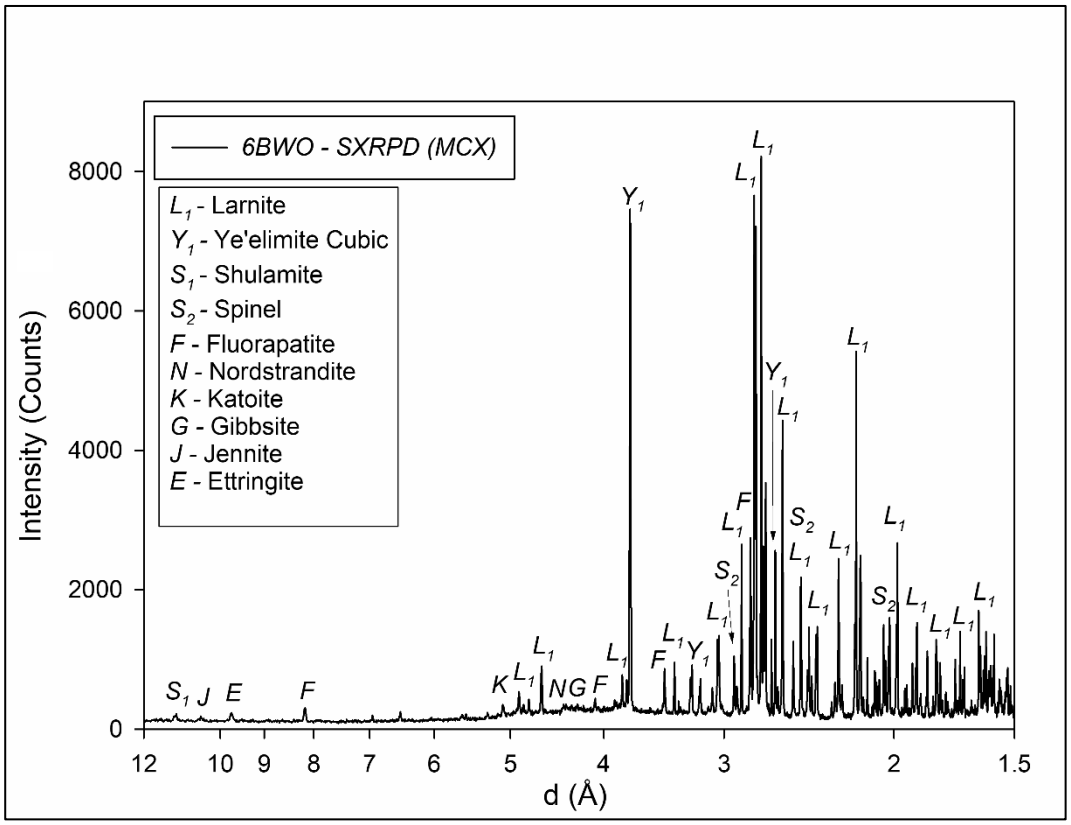

Fig. 9.6 – SXRPD patter of *6BWO* sample collected at MCX beam line (Elettra) highlighting main mineral Bragg peaks.

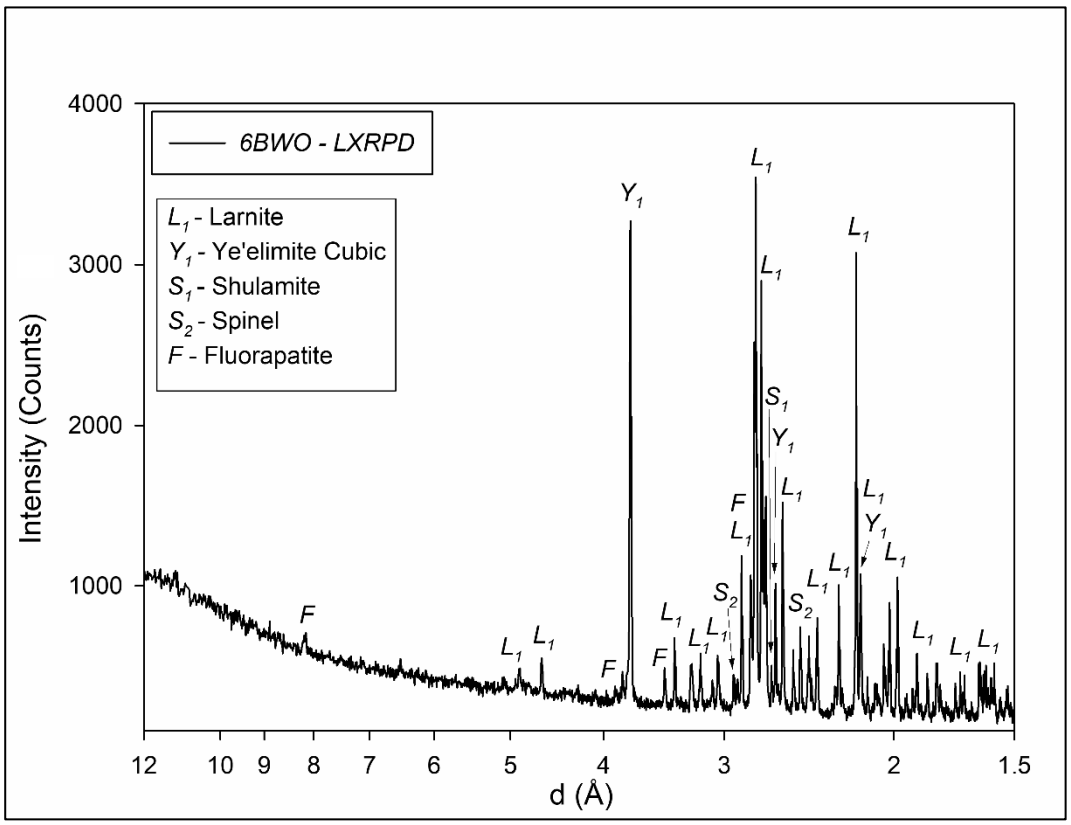

Fig. 9.7 – LXRPD patter of *6BWO* sample and showing main mineral Bragg peaks.

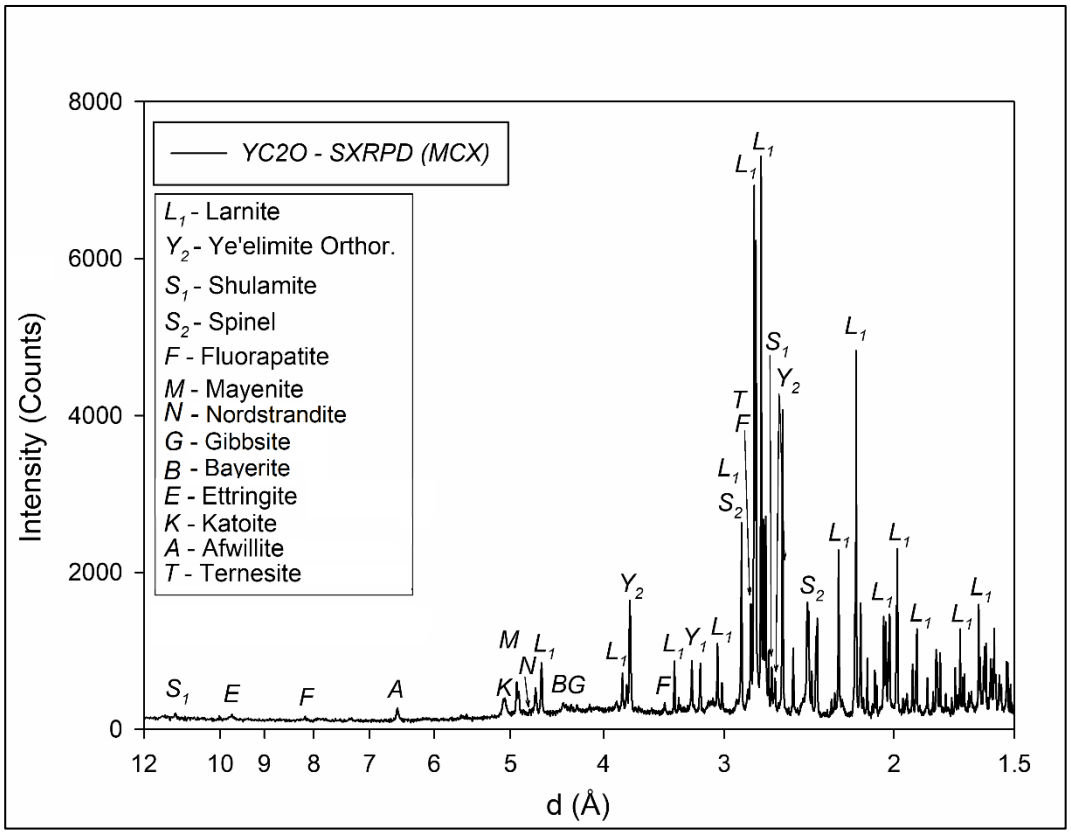

Fig. 9.8 – SXRPD patter of *YC2O* sample collected at MCX beam line (Elettra) highlighting main mineral Bragg peaks.

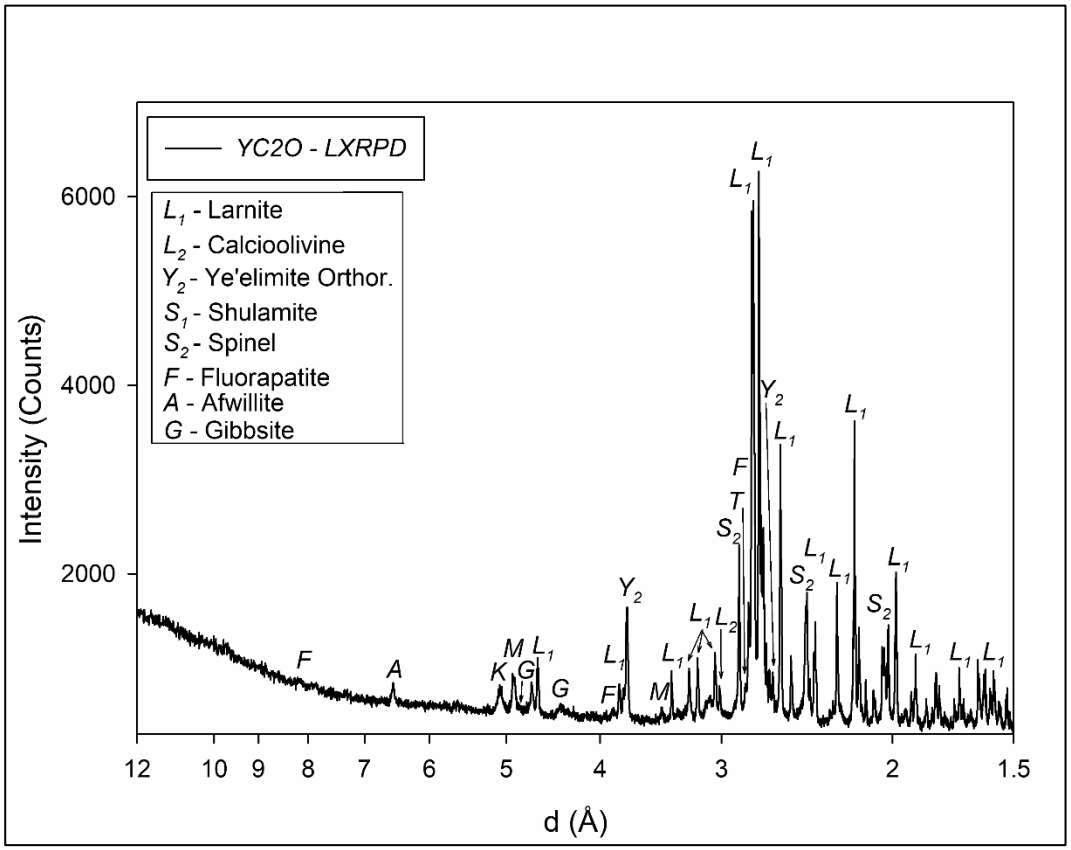

Fig. 9.9 – LXRPD patter of *YC2O* sample and highlighting main mineral Bragg peaks.

Sample / Minerals	6BWO SXRPD (MCX)	6BWO SXRPD (ID22)	6BWO LXRPD	YC2O SXRPD (MCX)	YC2O LXRPD
Larnite β-Ca_2SiO_4	62.72(.22)	68.15(.14)	64.25(.32)	77.60(.32)	73.32(.22)
Calciolivine γ-Ca_2SiO_4	-	-	-	-	2.14(.10)
Spinel $(Mg,Fe)(Fe,Al)_2O_4$	4.39(6)	4.04(3)	3.73(.10)	2.52(6)	5.54(7)
Brownmillerite $Ca_2(Al,Fe)_2O_5$	-	0.18(2)	0.86(1)	-	-
Shulamitite $Ca_3TiFeAlO_8$	2.10(6)	2.08(3)	2.54(.13)	2.57(9)	2.59(7)
Ye'elimite $Ca_4(AlO_2)_6SO_4$	15.46(.15)$^{\$}$	14.98(9)$^{\$}$	17.01(.20)$^{\$}$	4.86(.12)$^{+}$	4.84(.10)$^{+}$
Mayenite $Ca_{12}Al_{14}O_{33}$	0.23(4)	0.09(2)	-	2.50(.10)	1.68(6)
Fluorapatite°	10.07(.17)	8.41(7)	10.86(.26)	2.64(.14)	2.88(.10)
Ternesite $Ca_5(SiO_4)_2SO_4$	-	-	-	1.36(.16)	-
Quartz α-SiO_2	0.29(3)	0.11(1)	-	-	-
Calcite $CaCO_3$	1.61(6)	0.52(3)	0.80(7)	-	-
Katoite $Ca_3Al_2(OH)_{12}$	0.92(7)	0.67(3)	-	1.30(9)	2.26(8)
Ettringite§	0.56(6)	-	-	0.45(7)	-
Jennite $Ca_3Si_6O_{18}(OH)_6{\cdot}8H_2O$	0.33(5)	-	-	-	-
Afwillite $Ca_3(SiO_4)_2(OH)_6$	-	-	-	2.25(.13)	3.61(.12)
Gibbsite $Al(OH)_3$	0.75(7)	0.43(4)	-	0.62(8)	-
Nordstrandite $Al(OH)_3$	0.58(7)	0.37(4)	-	0.58(8)	-
Bayerite $Al(OH)_3$	-	-	-	0.76(8)	1.13(8)
Rexp	5.33	0.95	5.62	5.43	3.90
Rwp	11.68	10.58	9.84	13.89	7.26
GoF	2.23	14.68	1.75	2.56	1.86

Table 9.1 – Rietveld analysis results for natural larnite-rich rocks by means of XRPD analysis at synchrotron (SXRPD) and Laboratory scale (LXRPD); e.s.d., are reported in rounded brackets; $ ye'elimite cubic form; + ye'elimite orthorhombic form; § $Ca_6Al_2(OH)_{12}(SO_4)_3{\cdot}26H_2O$; °$Ca_5(Si_{x/2}, S_{x/2}, P_{1-x}O_4)_3F$, fluorapatite-ellestadite solid solution; -, not detected crystal phase.

Sample	*Instrumental Set-Up*	*a* (Å)	*b* (Å)	*c* (Å)	*β* (°)	*Cell Volume (V/Z)*	*Crystallite Size (μm)*	*μ-strain* ($\Delta d/d \cdot 10^6$)
6BWO	***SXRPD (MCX)***	5.50994(8)	6.75829(8)	9.3156(2)	94.5243(8)	86.453(3)	1.46(.17)	1655(51)
	SXRPD (ID22)	5.50899(3)	6.75733(3)	9.31427(6)	94.5067(4)	86.4155(5)	1.21(.14)	1767(21)
	LXRPD	5.5084(2)	6.7554(2)	9.3113(3)	94.532(2)	86.352(1)	1.55(.16)	1708(34)
YC2O	***SXRPD (MCX)***	5.50871(9)	6.75519(8)	9.3113(2)	94.536(1)	86.353(1)	0.65(2)	1751(24)
	LXRPD	5.5087(8)	6.75517(9)	9.3113(2)	94.536(1)	86.353(1)	0.57(2)	1584(23)
Pure Larnite [169]	***SCXRD***	5.502(1)	6.745(1)	9.297(1)	94.59(2)	85.975(3)	-	-
Clinker Larnite [170]	***NXRPD***	5.5172(4)	6.76996(6)	9.32298(8)	94.336(5)	86.807(3)	-	-
Natural Larnite [172]	***SCXRD***	5.5051(3)	6.7551(3)	9.3108(5)	94.513(4)	86.293(1)	-	-

Table 9.2 – Crystallographic results for Larnite (β-Ca_2SiO_4) occurring in natural larnite-rich rocks compared to bibliographic values coming from pure, clinker and natural larnite crystals; it is also reported the instrumental set-up used to collect the data; e.s.d. is reported in rounded brackets; - not available data.

Diffractometric study both performed at synchrotron and laboratory scale on the hydrated parts of larnite-rich rocks revealed (Fig. 9.10,11; Table 9.3): (i) $CaCO_3$ represents > 75wt.% for both hydrated samples (*6BWV* and *YC2V*); (ii) all three calcium carbonate polymorphs occur in *YC2V*; (iii) spinel is always found, but higher in *YC2V*; (iv) fluorapatite and gypsum have similar abundances; (v) higher variability in CSH minerals occurs in *6BWV* compared to *YC2V*, but was only observed for synchrotron pattern; (vi) spurrite occurs only in *6BWV*.

Sample / Minerals	***6BWV***		***YC2V***	
	SXRPD (ID22)	***LXRPD***	***SXRPD (ID22)***	***LXRPD***
Fluorapatite°	3.01(7)	2.05(2)	2.68(8)	4.13(.17)
Spinel $(Mg,Fe)(Fe,Al)_2O_4$	0.21(3)	0.41(7)	1.70(5)	2.18(9)
Calcite $CaCO_3$	79.89(.23)	79.83(.38)	48.17(.24)	48.45(.39)
Aragonite $CaCO_3$	2.02(7)	2.54(.13)	19.00(.18)	14.80(.23)
Vaterite $CaCO_3$	-	-	16.51(.17)	13.61(.19)
Katoite $Ca_3Al_2(OH)_{12}$	0.33(5)	-	3.38(9)	10.15(.25)
Spurrite $Ca_5Si_2O_8CO_3$	4.65(.12)	5.05(.20)	-	-
Ettringite§	4.16(.10)	5.86(.14)	0.56(6)	-
Jennite $Ca_3Si_6O_{18}(OH)_6{\cdot}8H_2O$	0.20(4)	-	-	-
Gypsum $CaSO_4{\cdot}2H_2O$	0.54(4)	1.32(9)	0.79(6)	1.58(.11)
Plomberite $Ca_5H_2Si_6O_{18}{\cdot}6H_2O$	-	-	0.97(9)	-
Tobermorite 11Å $Ca_5H_2Si_6O_{18}{\cdot}4H_2O$	2.12(.10)	2.79(.13)	5.31(.14)	3.87(.16)
Thaumasite $Ca_3(SO_4)[Si(OH)_6](CO_3){\cdot}12H_2O$	0.37(5)	-	0.20(4)	-
Bulfoteinite $Ca_2SiO_2(OH,F)_4$	0.47(8)	-	-	-
Apophyllite $KFCa_4Si_8O_{20}{\cdot}8H_2O$	0.40(6)	-	-	-
Bayerite $Al(OH)_3$	1.13(8)	-	0.73(7)	1.23(.13)
Rexp	1.54	5.77	2.10	5.44
Rwp	14.47	11.02	13.35	8.71
GoF	9.38	1.91	6.35	1.60

Table 9.3 – Rietveld analysis results for two natural hydrated larnite-rich rocks by means of XRPD analysis at synchrotron (SXRPD) and Laboratory scale (LXRPD); e.s.d. is reported in rounded brackets; §$Ca_6Al_2(OH)_{12}(SO_4)_3{\cdot}26H_2O$; °$Ca_5(Si_{x/2}, S_{x/2}, P_{1-x}O_4)_3F$, fluorapatite-ellestadite solid solution; -, not detected crystal phase.

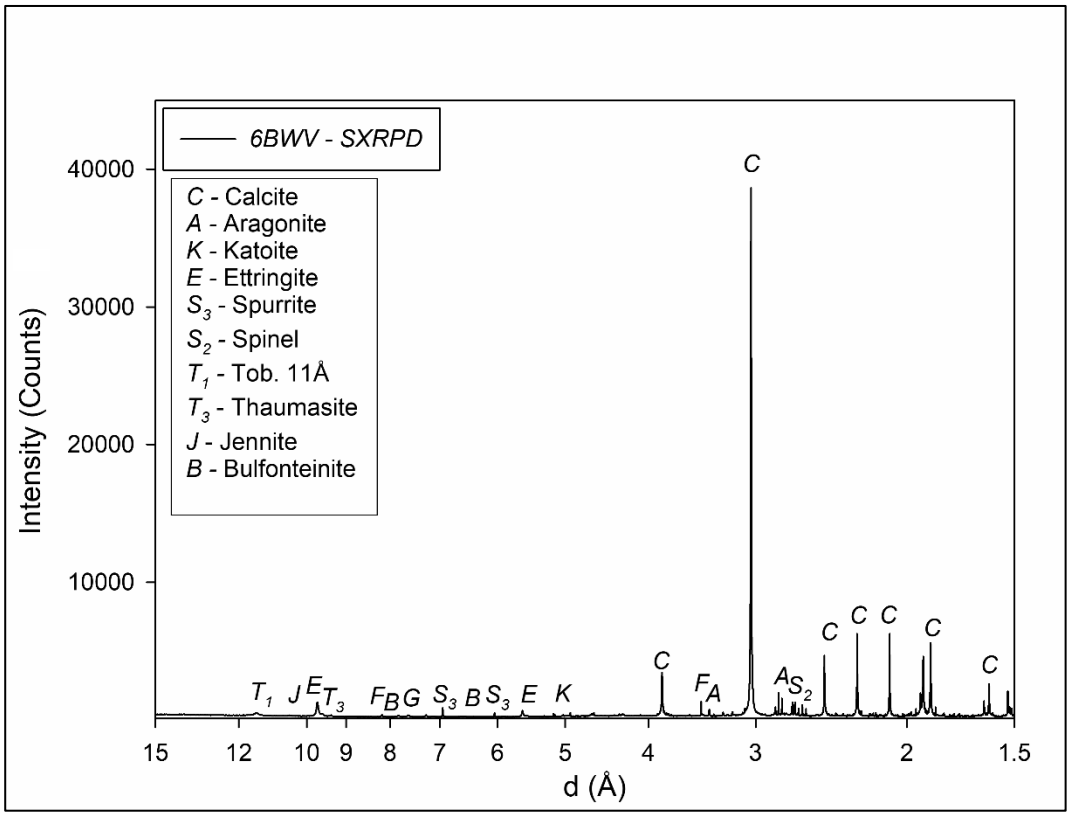

Fig. 9.10 – SXRPD pattern of *6BWV* collected at beam line ID22 (ESRF) highlighting main Bragg peaks.

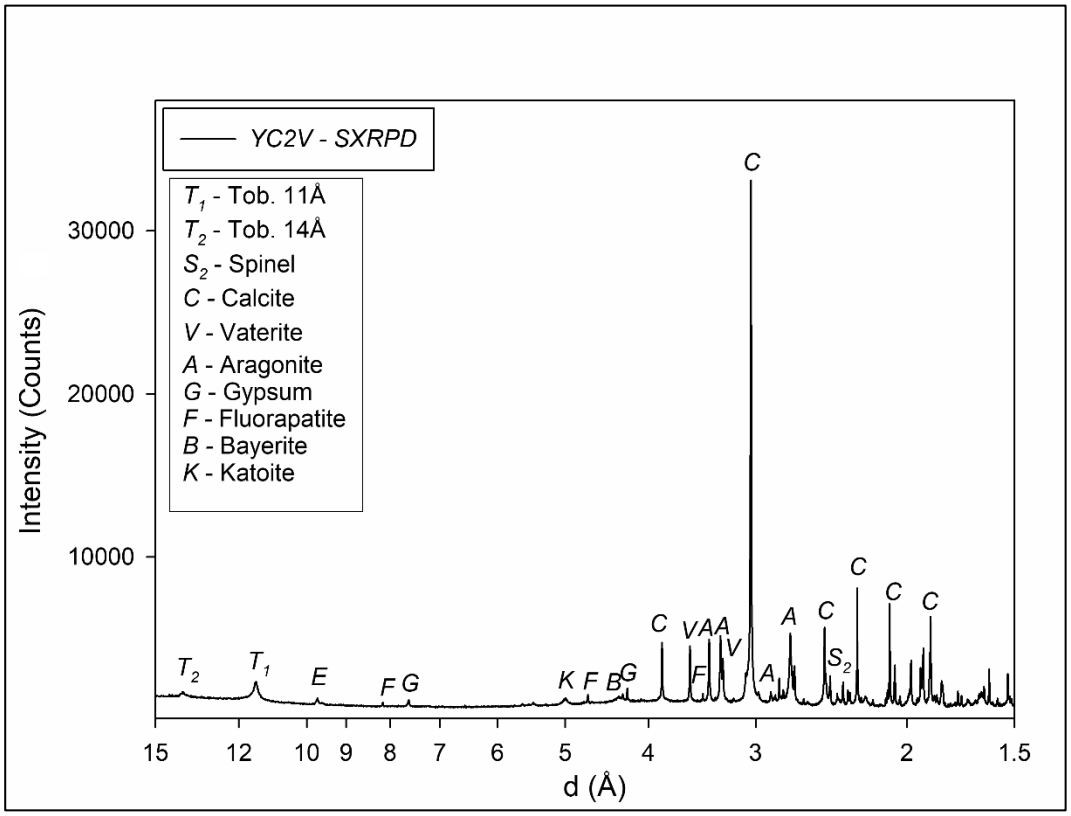

Fig. 9.11 – SXRPD pattern of *YC2V* collected at beam line ID22 (ESRF) highlighting main Bragg peaks.

Crystallographic parameters for calcite in hydrated parts of larnite-rich rocks highlighted cell parameters extremely close to pure bibliographic calcite (Table 8.4;9.4). Crystallite size and microstrain values were both simultaneous refined during Rietveld method for only synchrotron patterns without giving high correlation errors; whereas, these two parameters were separately refined for laboratory data: therefore, synchrotron results should be considered as a better evaluation for crystallite size and microstrain values for calcite. Both samples showed similar values, with lower ones for laboratory data compared to synchrotron ones (Table 9.4).

Sample / Crystallographic parameters	***6BWV***		***YC2V***	
	SXRPD (ID22)	***LXRPD***	***SXRPD (ID22)***	***LXRPD***
***a* (Å)**	4.98972(7)	4.9905(3)	4.9878(2)	4.9887(7)
***c* (Å)**	17.0781(2)	17.0759(6)	17.0977(4)	17.098(1)
***V* (Å^3)**	368.232(5)	368.30(3)	368.374(8)	368.51(7)
***Crystallite Size* (Å)**	0.41(1)	0.27(3)	0.35(3)	0.19(5)
μStrain ($^{\Delta d}/_{d} \cdot 10^6$)	3119(51)	2697(45)	3558(123)	2902.0(183.2)

Table 9.4 – Crystallographic results for calcite in two natural hydrated larnite-rich rocks by means of XRPD analysis at synchrotron (SXRPD) and Laboratory scale (LXRPD); e.s.d. is reported in rounded brackets.

Sample / Minerals	***White***	***Brown***	***Black***
Fluorapatite°	-	4.31(.25)	-
Shulamitite $Ca_3TiFeAlO_8$	-	2.43(.20)	-
Spinel $(Mg,Fe)(Fe,Al)_2O_4$	-	1.36(.21)	13.93(.36)
Calcite $CaCO_3$	95.82(.39)	24.58(.39)	6.67(.34)
Aragonite $CaCO_3$	-	8.12(.40)	-
Vaterite $CaCO_3$	-	19.15(.40)	-
Quartz SiO_2	0.68(6)	-	-
Katoite $Ca_3Al_2(OH)_{12}$	-	8.55(.42)	22.25(.61)
Ettringite§	0.75(.12)	3.00(.30)	18.86(.54)
Gypsum $CaSO_4{\cdot}2H_2O$	-	11.15(.31)	-
Tobermorite 11Å $Ca_5H_2Si_6O_{18}{\cdot}4H_2O$	2.75(.14)	4.25(.32)	38.30(.65)
Plomberite $Ca_5H_2Si_6O_{18}{\cdot}6H_2O$	-	6.13(.28)	-
Gibbsite $Al(OH)_3$	-	1.67(.29)	-
Bayerite $Al(OH)_3$	-	2.70(.32)	-
Rexp	5.71	5.64	4.80
Rwp	10.45	13.53	11.52
GoF	1.83	2.40	2.40

Table 9.5 – RQPA results for hydrated larnite-rich rocks anisotropies (black elements, white and brown vein portions) by means of LXRPD; e.s.d. is reported in rounded brackets; §$Ca_6Al_2(OH)_{12}(SO_4)_3{\cdot}26H_2O$; °$Ca_5(Si_{x/2}, S_{x/2}, P_{1-x}O_4)_3F$, fluorapatite-ellestadite solid solution; -, not detected crystal phase.

Hydrated veins of larnite-rich rocks often displayed an internal division: (i) millimetric to subcentimetric white central part sometimes made of mainly calcite (> 95wt.%) and minor amount of hydrated minerals (Fig. 9.1a,b); (ii) millimetric to subcentrimetric brown borders composed of calcium carbonate polymorphs, representing > 50wt.%, calcium hydrated minerals (CSH minerals, ettringite, katoite, gypsum, aluminium hydroxides) and less reactive phases as spinel, fluorapatite-ellestadite and shulamitite, as observed in RLM (Fig. 9.1a,b); (iii) millimetric black rounded to elliptical nodules commonly found inside brown borders consisting of calcium hydrated minerals, mainly tobermorite, and spinel that represents > 10wt.% (Fig. 9.3a,b).

Microtextural investigation performed by SEM with BSE images on natural larnite-rich rocks pointed out the following features: (i) samples highlighted homogenous granoblastic polygonal microtexture with no preferred distribution, excepted for the occurrence of spinel and shulamitite-rich nodules as observed during RLM analysis (Fig. 9.13,15). Furthermore, *6BWO* showed higher crystal size, approximately twice larger, compared to *YC2O*, leading a better identification of minerals (Fig. 9.13d:9.15d); (ii) larnite always occurs as polygonal crystals with larger size in *6BWO* (15-20 μm) compared to *YC2O* (< 10 μm) with grain triple junctions (Fig. 9.13d); (iii) ye'elimite is always anhedral with xenomorphic larnite inclusions and occurs close to voids; (iv) fluorapatite is found as euhedral hexagonal prism crystals full of inclusions of other minerals (poikilitc texture [3]) and has largest crystal size reaching ~ 50 μm in *6BWO* (Fig. 9.12); (v) spinel occurs as rounded to psedocubic crystals often zonated with a dark core and lighter rims, also forming dense aggregates with different sizes (Fig. 9.12); (vi) shulamitite is found as euhedral prismatic to acicular crystals with 10-15 μm and < 10 μm in *6BWO* and *YC2O*, respectively, and rarely occurs as rounded aggregates (Fig. 9.15c).

Elemental map on *6BWO* was performed by means of EMPA analysing S, P and Fe (Fig. 9.14): fluorapatite showed a phosphorous-rich core and rims progressively higher in sulphur confirming a trend from fluorapatite to fluorellestadite end member in the complete s.s.; larnite showed rare phosphorous-rich spots, but no S and Fe-rich spots occurred; shulamitite has higher concentration of Fe compared to spinel, representing a distinctive feature.

Abundances of crystal phases was also calculated for *6BWO* from a BSE image (Fig. 9.12a) calculating modal distribution and assuming that as vol.% and multiplying for crystal density: results from modal distribution showed a mismatching with RQPA one, showing lesser amount of larnite and twice content of fluorapatite and spinel (Table 9.6, Fig. 9.12b).

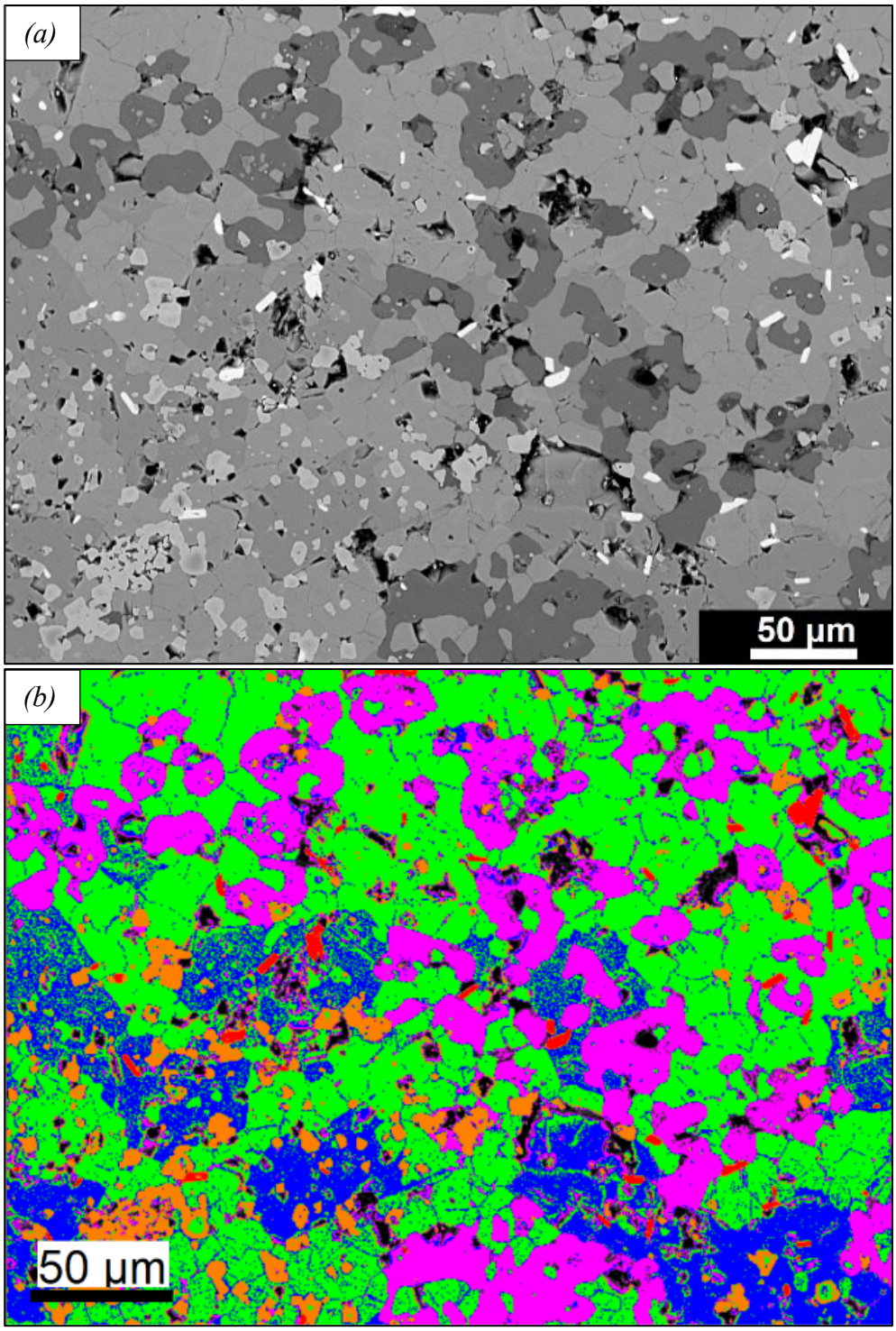

Fig. 9.12 - BSE image of *6BWO* (larnite-rich rock): (a) overview highlighting low crystal size, homogenous microtexture with anhedral dark grey ye'elimite, pseudohexagonal fluorapatite in grey, polygonal larnite in grey, rounded zonate spinel in light grey and prismatic shulamitite in white; (b) segmented image with shulamitite in red, spinel in orange, larnite in green, fluorapatite in blue, ye'elimite in purple and voids in black.

Minerals	*modal% = vol.%*	*Crystal density (g/cm³)*	*Calculated wt.%*
Larnite	*46.39*	*3.32* [169]	*50.24*
Fluorapatite	*18.01*	*3.20* [306]	*23.38*
Ye'elimite	*22.53*	*2.61* [307]	*15.24*
Spinel	*7.51*	*3.58* [308,309]	*9.89*
Shulamitite	*1.01*	*3.84* [310]	*1.29*
Voids	*4.55*	-	-

Table 9.6 – Results of modal crystal phase distribution for Fig. 9.12 and calculated wt.% obtained using crystal density and assuming modal% as vol.%.

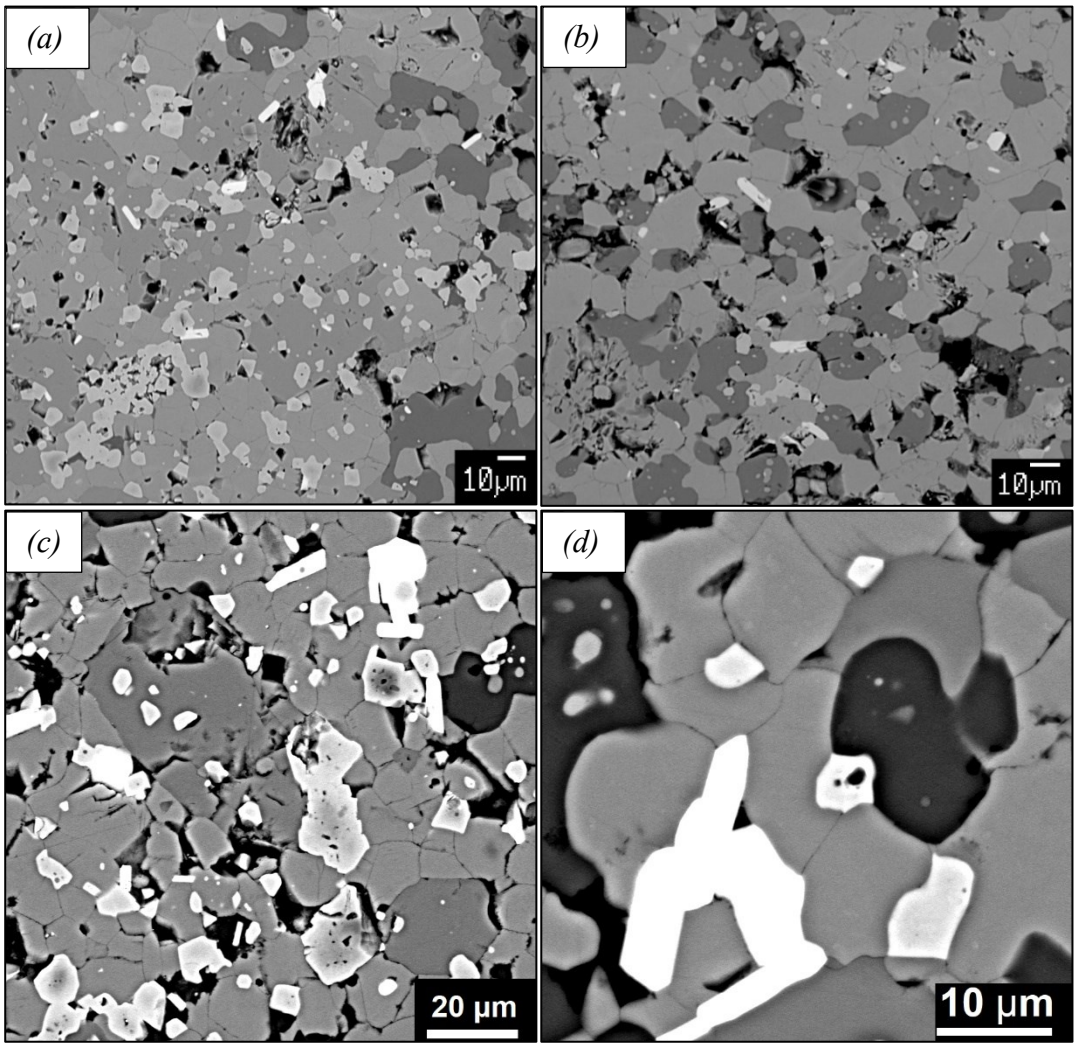

Fig. 9.13 - BSE images acquired at SEM for *6BWO* at different magnification grade:(a) enlargement on a portion rich in spinel occurring as sparce crystals and dense aggregates (~ 30 µm); (b) ye'elimite-rich portion always as dark grey anhedral crystals with often anhedral larnite inclusions; (c) hexagonal fluorapatite crystals with inclusions and euhedral zoned spinel with darker core and lighter rims; (d) polygonal euhedral larnite crystals with triple junctions, prismatic to acicular shulamitite, anhedral ye'elimite and subhedral spinel crystals.

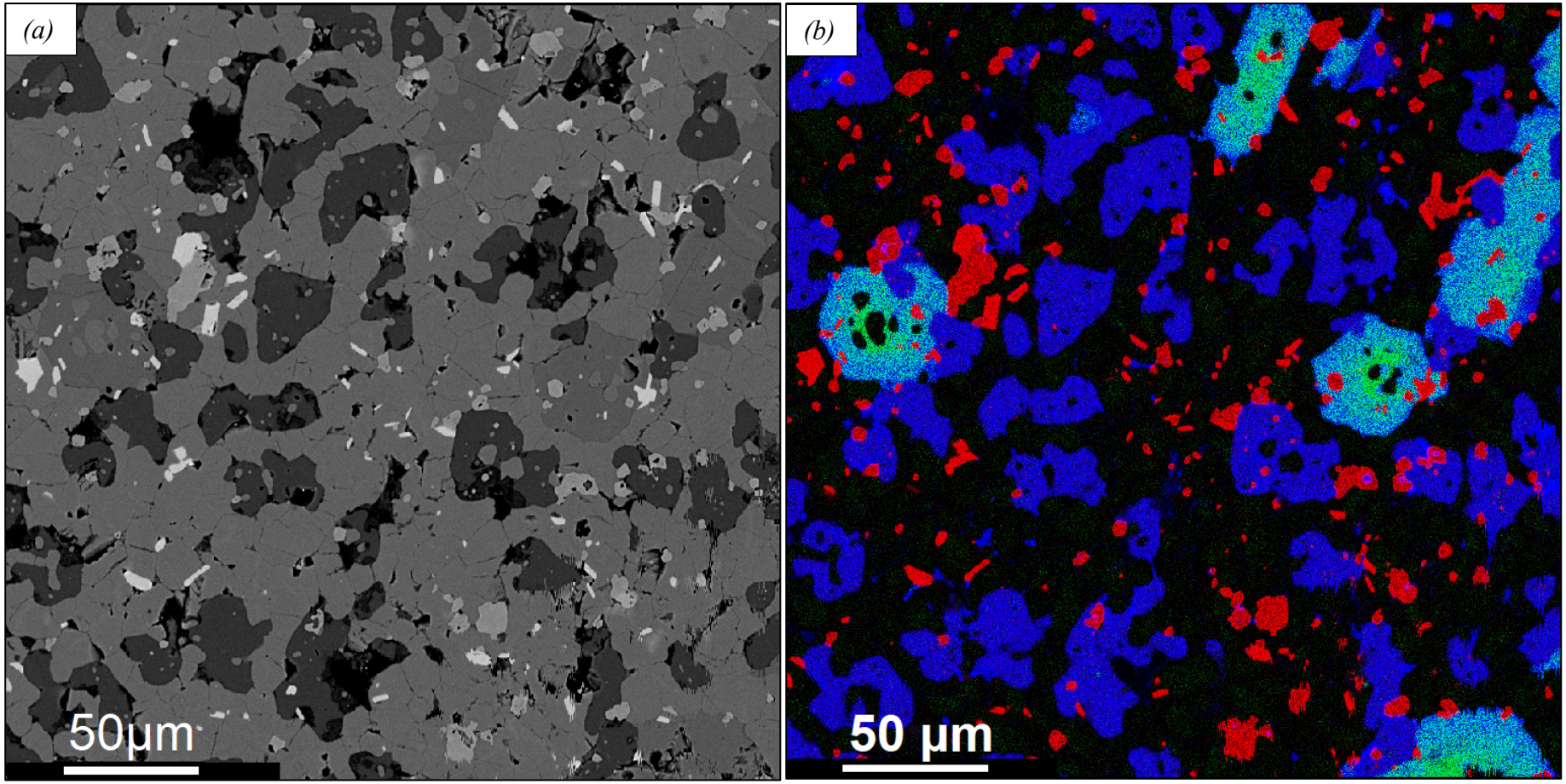

Fig. 9.14 – (a) BSE images of *6BWO* highlighting polygonal larnite in grey, anhedral ye'elimite dark grey, pseudohexagonal fluorapatite in grey (darker than larnite), spinel in light grey and shulamitite in white; (b) elemental map of the previous BSE image obtained by EMPA with 0.3 µm pixel size, analyzing Fe (as red), P (as green) and S (as blue).

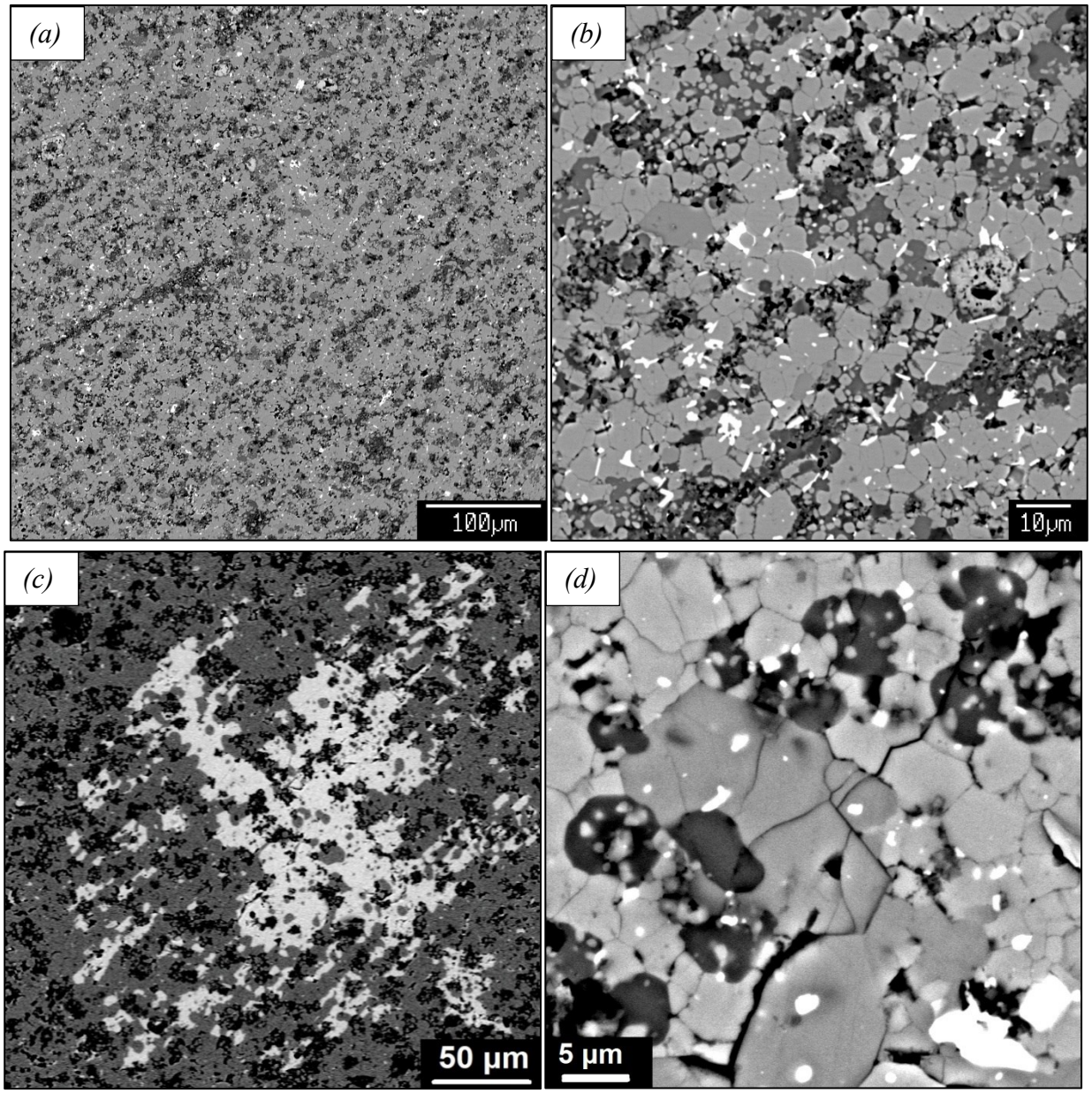

Fig. 9.15 - BSE images acquired at SEM for *YC2O* sample at different magnification grade:(a) low grade magnification grade image revealing the homogenous texture, abundance of larnite (grey) and some enrichment of spinel and shulamitite (light grey and white, respectively); (b) granoblastic microtexture with polygonal to rounded larnite (grey), euhedral hexagonal fluorapatite with inclusion (grey), anhedral ye'elimite (dark grey), rounded spinel often zoned with darker core (light grey) and prismatic shulamitite (white); (c) shulamitite-rich nodule with larnite as matrix (d) microtexture details at high magnification with polygonal larnite with triple junctions, euhedral hexagonal fluorapatite, anhedral ye'elimite with inclusions and sparce white shulamitite crystals.

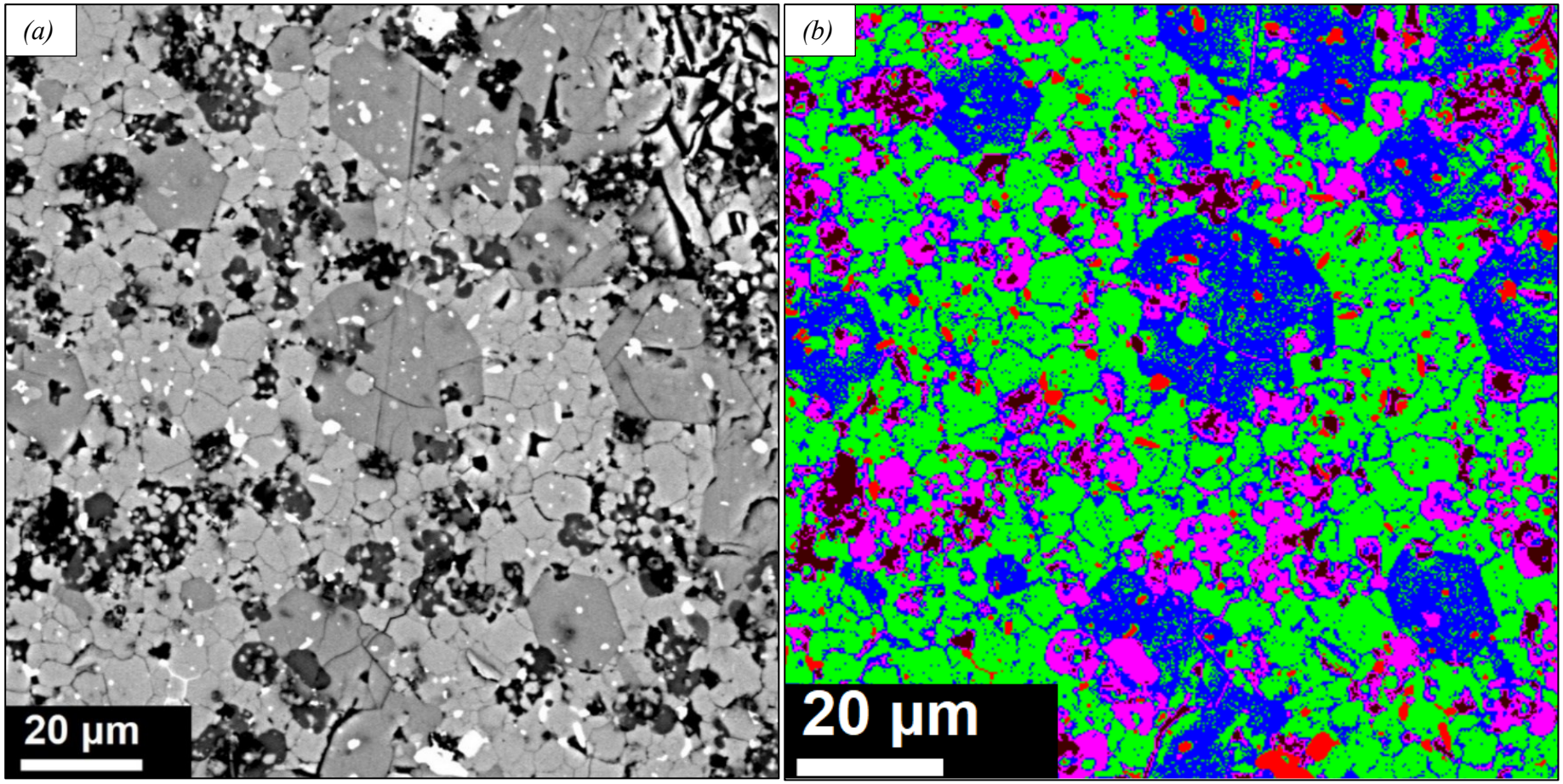

Fig. 9.16 – BSE images acquired at SEM for *YC2O* sample: (a)granoblastic microtexture with polygonal larnite crystals (grey), euhedral hexagonal fluorapatite, anhedral ye'elimite (dark grey), prismatic shulamitite (white) and rounded spinel (white); (b) segmentation of Fig.9.16a, shulamitite and spinel in red, larnite in green, fluorapatite in blue, ye'elimite in purple and voids in black.

Punctual chemical investigation on main crystal phases occurring in natural larnite-rich rocks was performed by means of EMPA, and results were also compared with bibliographic ones [20]. Larnite crystals on both studied samples showed a chemical composition close to the pure dicalcium silicate (Ca_2SiO_4) with only low amount of Na^+ and P^{5+} as major ionic substituents of $^{XIII}Ca^{2+}$ and $^{IV}Si^{4+}$, respectively (Fig. 9.17). Our results are in good agreement with bibliographic values, confirming only phosphorous and sodium as vicariants in the crystal structure.

Elements / Samples		***6BWO***		***YC2O***		***Bibliographic values*** [20]	
		average (n = 23)°	***max.-min.***	***average (n = 10)°***	***max.-min.***	***average (n = 41)°***	***max.-min.***
F		0.00	0.00-0.00	0.00	0.00-0.00	*n.a.*	*n.a.*
Na_2O		0.54(.20)	0.92-0.23	0.26(4)	0.32-0.20	0.44(.22)	0.94-0.08
P_2O_5		1.62(.66)	2.65-0.63	0.66(.14)	0.95-0.47	1.16(.46)	2.28-0.38
Fe_2O_3		0.13(8)	0.37-0.02	0.22(9)	0.39-0.08	0.10(9)	0.71-0.02
K_2O		0.13(4)	0.23-0.07	0.07(1)	0.44-0.09	0.09(4)	0.18-0.02
MgO		0.01(3)	0.13-0.0	0.10(1)	0.08-0.06	0.05(6)	0.02-0.31
SO_3		0.06(7)	0.26-0.0	0.04(3)	0.59-0.00	0.05(5)	0.17-0.03
CaO		62.52(.67)	63.86-61.03	61.68(.71)	62.35-60.10	64.13(.72)	65.71-62.23
Al_2O_3		0.16(7)	0.34-0.04	0.34(1)	1.33-0.05	0.21(.17)	0.80-0.02
Cl		0.01(9)	0.03-0.00	0.01(1)	0.02-0.00	*n.a.*	*n.a.*
TiO_2		0.09(2)	0.1-0.00	0.03(2)	0.1-0.00	0.09(6)	0.39-0.04
SiO_2		33.28(.71)	34.52-31.96	33.57(.58)	34.30-32.51	33.36(.77)	35.13-31.92
Cr_2O_3		0.01(2)	0.08-0.00	0.02(3)	0.07-0.00	0.02(3)	0.12-0.02
Total		98.53(.66)	100.2-97.6	97.01(71)	97.90-95.97	99.70	99.49-100.05
General formula X_2YO_4							
X	**Ca^{2+}**	1.938(.019)	1.968-1.895	1.944(.014)	1.961-1.910	1.97	2.01-1.87
	Mg^{2+}	0.001(1)	0.006-0.000	0.004(9)	0.026-0.000	0.0	0.01-0.0
	Na^+	0.030(.011)	0.050-0.010	0.015(2)	0.018-0.011	0.02	0.09-0.01
	K^+	0.005(2)	0.009-0.002	0.003(1)	0.003-0.002	0.0	0.11-0.0
Y	**Si^{4+}**	0.963(.019)	0.993-0.930	0.987(.011)	1.000-0.988	0.96	1.00-0.75
	P^{5+}	0.040(.016)	0.065-0.015	0.016(4)	0.024-0.012	0.03	0.05-0.0
	Al^{3+}	0.005(2)	0.012-0.001	0.012(.014)	0.047-0.002	0.01	0.02-0.01
	Fe^{3+}	0.003(2)	0.008-0.000	0.005(2)	0.010-0.002	0.0	0.02-0.0
	S^{6+}	0.001(2)	0.006-0.000	0.001(1)	0.002-0.000	0.0	0.001-0.0
	Ti^{4+}	0.001(1)	0.003-0.000	0.001(1)	0.001-0.000	0.0	0.001-0.0
O^{2-}		4		4		4	

Table 9.7 – EMPA results for larnite crystals in larnite-rich rocks (*6BWO* and *YC2O*), and bibliographic values [20] are reported for comparison; general formula was obtained by negative charges normalization; *n.a., not analysed element; °number of analysis.

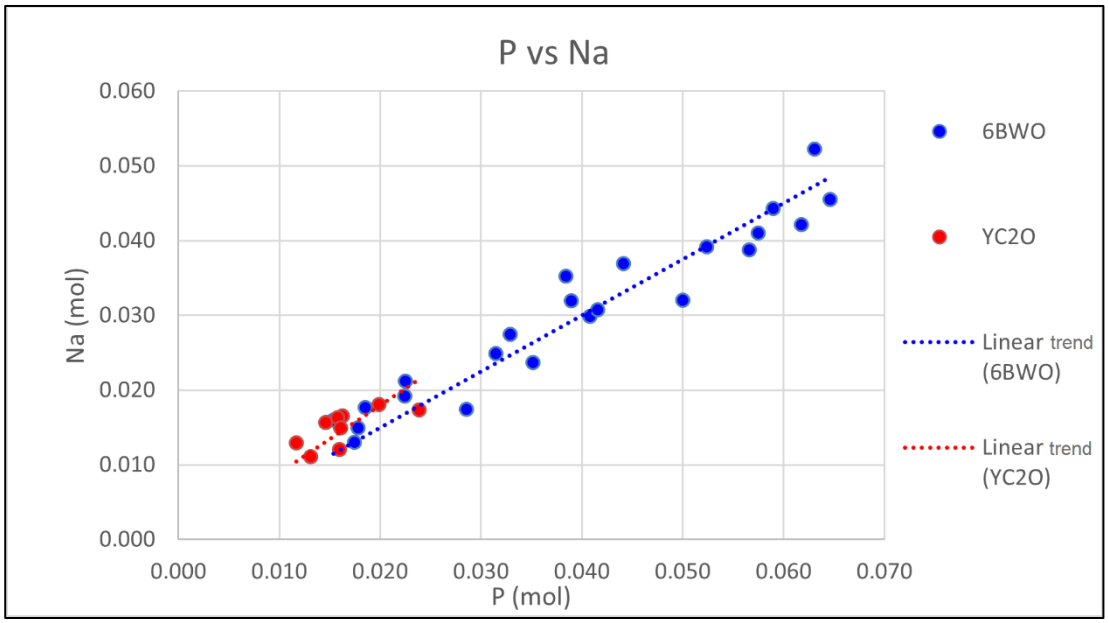

Fig. 9.17 – EMPA results on Na and P molar content for larnite in *6BWO* and *YC2O* showing a positive correlation trend in both samples.

Analysed ye'elimite crystals highlighted the same chemical composition in both samples and bibliographic values, with a general pure formula similar only showing a slight ionic substitution of $^{IV}Fe^{3+}$ and $^{IV}Si^{4+}$ inside *Y* atomic site instead of $^{IV}Al^{3+}$ (Table 9.8). Moreover, bibliographic values showed a wider concentration of Fe_2O_3 compared to our larnite-rich rocks studied [122].

Fluorapatite crystals revealed an average chemical composition falling approximately in middle considering fluorapatite and fluorellestadite as the end member of the solid solution. Whereas, bibliographic values displayed a mean major enrichment in phosphorous with higher variation compared to *6BWO* and *YC2O* (Table 9.9). Furthermore, 2/3 of *Z* atomic site is hosted by fluorine and the remaining 1/3 by (OH), with a slightly higher fluorine concentration in bibliographic values compared to our larnite-rich rocks [122].

Only shulamitite crystals were found in natural larnite-rich rocks during EMPA analysis and no brownmillerite occurred, despite it was identified in *6BWO* during SXRPD (Table 9.1). Shulamitite has an average chemical composition almost similar in all samples and bibliographic values [122], highlighting an enrichment in Fe^{3+} $(Ca_3(Al_{0.225},Si_{0.025},Fe_{0.75})_2(Ti_{0.91},Fe_{0.09})O_8)$ in both *Y* and *Z* sites compared to the pure shulamitite (Table 9.10). Bibliographic values displayed a wider composition range of iron and aluminium. Because Al^{3+} and Fe^{3+} can both occur in octahedron and tetrahedron sites, a general *Z* site was considered with all elements excepted Ti^{4+} that is hosted in a specific octahedron site (*Y* site) in the lattice. Inside *Y* atomic site along with Ti^{4+} could also occur some Fe^{3+} and very low amount of Al^{3+} [310]. In addition, Al^{3+} mostly occurs inside tetrahedron site and minor in octahedron site instead of Fe^{3+} [310].

Elements / Samples		*6BWO*		*YC2O*		*Bigliographic values* [20]	
		average (n = 17)°	*max.-min.*	*average (n = 10)*	*max.-min.*	*average (n = 51)*	*max.-min.*
F		0.00	0.00-0.00	0.00	0.00-0.00	*n.a.*	*n.a.*
Na_2O		0.11(2)	0.15-0.06	0.10(2)	0.15-0.06	0.14(9)	0.32-0.02
P_2O_5		0.37(.28)	0.99-0.04	0.50(.28)	0.99-0.12	0.19(.13)	0.47-0.02
Fe_2O_3		1.96(.17)	2.25-1.68	2.01(.15)	2.23-1.72	2.03(1.04)	6.60-0.77
K_2O		0.10(5)	0.22-0.03	0.08(3)	0.13-0.05	0.07(3)	0.17-0.02
MgO		0.05(7)	0.30-0.01	0.07(8)	0.30-0.01	*n.a.*	*n.a.*
SO_3		12.83(.29)	13.24-12.17	12.81(.39)	13.44-12.12	12.80(.67)	13.69-10.93
CaO		35.69(.56)	36.51-34.72	35.68(.84)	36.78-34.67	36.01(.64)	38.49-34.98
Al_2O_3		47.60(.23)	48.13-47.15	47.61(.20)	48.12-47.34	47.61(1.41)	49.12-46.16
Cl		0.01(7)	0.02-0.00	0.00(1)	0.01-0.00	*n.a.*	*n.a.*
TiO_2		0.03(3)	0.13-0.00	0.04(4)	0.124-0.001	*n.a.*	*n.a.*
SiO_2		0.73(.27)	1.37-0.40	0.79(.22)	1.22-0.45	0.89(.71)	3.90-0.12
Cr_2O_3		0.04(5)	0.14-0.00	0.05(4)	0.10-0.00	*n.a.*	*n.a.*
Total		98.52(.97)	101.38-97.80	99.75(1.33)	101.58-97.82	99.74	100.12-99.64
General formula $X_4[YO_2]_6ZO_4$							
	Ca^{2+}	3.92(3)	3.97-3.85	3.91(5)	4.01-3.88	3.95	3.98-3.95
	Fe^{2+}	0.02(4)	0.12-0.0	0.04(5)	0.17-0.01	0.02	0.22-0.01
X	**Mg^{2+}**	0.01(1)	0.05-0.0	0.01(1)	0.05-0.00	*n.a.*	*n.a.*
	Na^{+}	0.02(5)	0.03-0.01	0.02(1)	0.03-0.01	0.03	0.03-0.01
	K^{+}	0.01(1)	0.03-0.01	0.01(1)	0.02-0.01	0.01	0.02-0.01
	Si^{4+}	0.08(3)	0.14-0.04	0.08(2)	0.12-0.05	0.09	0.20-0.02
	P^{5+}	0.03(2)	0.08-0.01	0.04(2)	0.08-0.01	0.01	0.028-0.0
Y	**Al^{3+}**	5.76(6)	5.90-5.60	5.74(8)	5.82-5.59	5.75	5.92-5.68
	Fe^{3+}	0.13(4)	0.17-0.13	0.12(6)	0.17-0.03	0.14	0.18-0.6
	Cr^{3+}	0.01(1)	0.01-0.00	0.01(1)	0.01-0.00	*n.a.*	*n.a.*
Z	**S^{6+}**	0.99(2)	1.01-0.95	0.98(2)	1.01-0.94	0.99	1.00-0.99
O^{2-}		16		16		16	

Table 9.8 – EMPA results for ye'elimite in natural larnite-rich rocks (*6BWO* and *YC2O*) and bibliographic values reported for comparison; molar values was calculated by negative charge balance; Fe^{2+} molar value was empirically estimated only when *Y* site was > 2 when iron was considered all as Fe^{3+}; bibliographic values [20] are reported for comparison; *n.a., not analysed element; °number of analysis.

Elements / Samples		*6BWO* average (n = 17)°	*6BWO* max.-min.	*YC2O* average (n = 10)	*YC2O* max.-min.	*Bigliographic values* [20] average (n = 25)	*Bigliographic values* [20] max.-min.
F		2.51(.18)	3.04-2.28	2.51(.15)	0.02-0.01	2.90(.47)	4.022.20
Na_2O		0.03(3)	0.07-0.00	0.01(2)	0.52-0.00	0.02(1)	0.26-0.03
P_2O_5		22.09(3.02)	28.71-18.76	23.22(2.98)	28.68-18.74	28.37(6.37)	39.68-15.11
Fe_2O_3		0.17(.11)	0.52-0.06	0.19(8)	0.02-0.00	0.22(1)	0.80-0.02
K_2O		0.01(2)	0.06-0.00	0.01(1)	0.02-0.00	0.03(5)	0.21-0.02
MgO		0.01(2)	0.07-0.00	0.00(1)	0.02-0.00	*n.a.*	*n.a.*
SO_3		9.66(2.20)	13.54-5.07	8.92(1.88)	13.61-5.01	7.13(3.87)	15.53-0.65
CaO		53.99(1.75)	56.78-50.80	53.66(1.35)	56.88-50.45	55.56(.26)	56.27-55.07
Al_2O_3		0.03(2)	0.09-0.00	0.02(1)	0.04-0.00	*n.a.*	*n.a.*
Cl		0.02(1)	0.04-0.00	0.00(1)	0.01-0.00	0.02(5)	0.21-0.01
TiO_2		0.04(2)	0.07-0.00	0.02(2)	0.04-0.00	*n.a.*	*n.a.*
SiO_2		8.90(1.56)	11.01-5.49	8.28(1.48)	10.44-5.40	6.32(2.57)	11.94-1.73
Cr_2O_3		0.08(6)	0.17-0.0	0.04(3)	0.15-0.00	*n.a.*	*n.a.*
Total		97.54(2.99)	102.12-92.50	96.87(2.01)	102.63-98.59	100.57	101.58-100.11
General formula $X_{10}[YO_4]_6Z_2$							
X	**Ca^{2+}**	10.00(2)	10.03-9.95	10.01(2)	10.04-9.99	10.02	9.87-9.94
	Mg^{2+}	0.01(5)	0.02-0.00	0.00	0.00-0.00	*n.a.*	*n.a.*
	Na^{+}	0.01(1)	0.02-0.0	0.01(1)	0.01-0.00	0.01	0.04-0.0
	K^{+}	0.01(4)	0.02-0.0	0.01(2)	0.01-0.00	0.01	0.01-0.0
Y	**Si^{4+}**	1.54(.27)	1.93-0.94	1.44(.31)	1.84-0.92	1.06	1.58-1.12
	P^{5+}	3.24(.48)	4.28-2.60	3.44(.54)	4.32-2.60	4.04	4.40-3.41
	Al^{3+}	0.01(1)	0.02-0.00	0.01(1)	0.01-0.00	*n.a.*	*n.a.*
	Fe^{3+}	0.02(1)	0.07-0.01	0.02(2)	0.06.0.01	0.03	0.07-0.04
	S^{6+}	1.25(.26)	1.66-0.70	1.16(.30)	1.67-0.70	0.90	1.58-0.52
	Ti^{4+}	0.01(1)	0.01-0.00	0.00	0.01-0.00	*n.a.*	*n.a.*
	Cr^{3+}	0.01(1)	0.01-0.00	0.01(1)	0.02-0.00	*n.a.*	*n.a.*
Z	**F^{-1}**	1.38(.13)	1.77-1.23	1.39(.15)	1.77-1.25	1.54	1.68-1.46
	Cl^{-1}	0.00	0.01-0.0	0.00	0.01-0.0	0.01	0.07-0.0
	$^{§}(OH)^{-1}$	0.62(.13)	0.77-0.23	0.61(.15)	0.74-0.23	0.45	0.54-0.25
O^{2-}		25		25		25	

Table 9.9 – EMPA results for fluorapatite s.s. in larnite-rich rocks (*6BWO* and *YC2O*) and bibliographic values [20] are reported for comparison; *n.a., not analysed element; °number of analysis; $^{§}(OH)^{-1}$ molar value was calculated to fill the *Z* atomic site.

Elements / Samples	*6BWO*		*YC2O*		*Bigliographic values* [20]
	average (n = 11)°	*max.-min.*	*average (n = 11)*	*min.-max.*	*average (n =5)*
F	0.00	0.00-0.00	0.00	0.00-0.00	*n.a.*
Na_2O	0.05(3)	0.10-0.00	0.06(4)	0.10-0.00	*n.a.*
P_2O_5	0.01(2)	0.06-0.00	0.01(2)	0.04-0.00	*n.a.*
Fe_2O_3	30.87(.46)	31.63-29.84	30.75(.59)	31.63-29.73	30.13
K_2O	0.03(1)	0.05-0.01	0.03(2)	0.05-0.01	*n.a.*
MgO	0.15(1)	0.18-0.13	0.16(1)	0.18-0.14	*n.a.*
SO_3	0.04(4)	0.11-0.0	0.05(4)	0.11-0.0	*n.a.*
CaO	40.83(.30)	41.17-40.11	40.89(.20)	41.17-40.61	42.79
Al_2O_3	5.42(.27)	5.86-5.11	5.43(.26)	5.86-5.11	5.93
Cl	0.00(3)	0.01-0.0	0.00(2)	0.01-0.00	*n.a.*
TiO_2	17.78(.24)	18.05-17.22	17.81(.18)	18.05-17.57	19.35
SiO_2	0.78(6)	1.01-0.63	0.81(.13)	1.00-0.63	1.08
Cr_2O_3	0.17(6)	0.31-0.10	0.17(7)	0.31-0.10	0.02
Total	96.12(.50)	96.72-95.10	96.16(.42)	96.63-95.57	99.93
General formula X_3 Y Z_2 O_8					
X **Ca^{2+}**	2.99(1)	3.02-2.97	3.00(2)	3.02-2.97	3.00
X **Mg^{2+}**	0.02(1)	0.02-0.01	0.02(1)	0.02-0.01	*n.a.*
X **Na^{+}**	0.01(1)	0.01-0.00	0.01(1)	0.01-0.0	*n.a.*
X **K^{+}**	0.00	0.01-0.00	0.00	0.01-0.0	*n.a.*
Z **Si^{4+}**	0.05(1)	0.07-0.04	0.06(1)	0.07-0.04	0.07
Z **Al^{3+}**	0.44(2)	0.47-0.41	0.46(2)	0.05-0.39	0.46
Z **Fe^{3+}**	1.50(3)	1.63-1.53	1.50(3)	1.63-1.51	1.43
Z **Cr^{3+}**	0.01(1)	0.02-0.01	0.01(1)	0.02-0.00	0.00
Y **Ti^{4+}**	0.91(1)	0.93-0.89	0.92(1)	0.92-0.90	0.95
Y **$^{§}Fe^{3+}$**	0.09(1)	0.07-0.11	0.08(1)	0.08-0.10	0.05
O^{2-}	8		8		8

Table 9.10 – EMPA results for shulamitite in larnite-rich rocks (*6BWO* and *YC2O*) and bibliographic values [20] are reported for comparison; *n.a., not analysed element; °number of analysis; §molar Fe^{3+} calculated to fulfil the *Y* octahedral atomic site which mainly hosts Ti^{4+}[34].

Spinel crystals revealed an average chemical composition in the middle between magnesioferrite ($MgFe_2O_4$) and spinel ($MgAl_2O_4$) with a slight enrichment in iron for bibliographic values (Table 9.11, Fig. 9.18).

Elements / Samples		*6BWO*		*YC2O*		*Bigliographic values* [20]	
		average (n = 11)°	*max.-min.*	*average (n = 5)*	*min.-max.*	*average (n = 43)*	*min.-max.*
F		0.06(5)	0.18-0.0	0.01(1)	0.02-0.0	*n.a.*	*n.a.*
Na_2O		0.05(6)	0.17-0.02	0.01(2)	0.05-0.0	*n.a.*	*n.a.*
P_2O_5		0.04(5)	0.16-0.02	0.01(1)	0.02-0.0	*n.a.*	*n.a.*
Fe_2O_3		50.21(6.55)	57.18-32.65	52.48(1.47)	53.89-50.84	58.20	67.14-58.48
K_2O		0.17(.38)	1.25-0.01	0.01(1)	0.01-0.0	*n.a.*	*n.a.*
MgO		22.60(.94)	23.94-20.62	22.27(.14)	22.45-22.10	19.86	20.16-19.67
SO_3		0.26(.53)	1.66-0.0	0.01(1)	0.01-0.0	*n.a.*	*n.a.*
CaO		1.17(.54)	2.74-0.81	0.92(.20)	1.01-0.55	0.95	1.31-0.79
Al_2O_3		23.67(6.02)	39.56-19.21	21.64(1.05)	22.99-20.76	16.69	19.59-10.56
Cl		0.01(1)	0.03-0.0	0.01(1)	0.02-0.0	*n.a.*	*n.a.*
TiO_2		0.17(6)	0.21-0.13	0.16(9)	0.24-0.0	0.18	0.25-0.01
SiO_2		0.09(5)	0.15-0.02	0.06(4)	0.10-0.01	*n.a.*	*n.a.*
Cr_2O_3		0.90(.46)	1.28-0.40	1.00(.59)	1.48-0.0	1.18	2.65-0.21
Total		99.42(1.74)	101.01-97-89	98.59(.76)	99.29-97.34	§100.29	§99.96-100.31
General formula X Y_2 O_4							
	Ca^{2+}	0.04(1)	0.09-0.02	0.03(1)	0.03-0.02	0.04	0.03-0.05
X	**Mg^{2+}**	1.00(2)	1.03-0.97	1.00(1)	1.01-0.99	0.92	0.93-0.91
	Fe^{2+}	0.00	0.02-0.0	0.00	0.00-0.00	0.01	0.05-0.0
	Fe^{3+}	1.13(.17)	1.25-0.68	1.19(3)	1.22-1.14	1.35	1.60-1.34
Y	**Cr^{3+}**	0.02(1)	0.03-0.01	0.02(1)	0.04-0.03	0.01	0.06-0.0
	Al^{3+}	0.84(.18)	1.30-0.70	0.77(4)	0.82-0.73	0.61	0.70-0.51
O^{2-}		4		4		4	

Table 9.11 – EMPA results for spinel in larnite-rich rocks (*6BWO* and *YC2O*) and bibliographic values [20] are reported for comparison; molar values were obtained by negative charge balance; *n.a., not analysed element; °number of analysis; §total wt.% reported including also V_2O_3, Mn_2O_3, NiO, ZnO and CuO wt.% that were not analysed in our elements routine analysis; Fe^{2+} molar value was empirically estimated when Y site was > 2 considering only Fe^{3+} by negative charge balance.

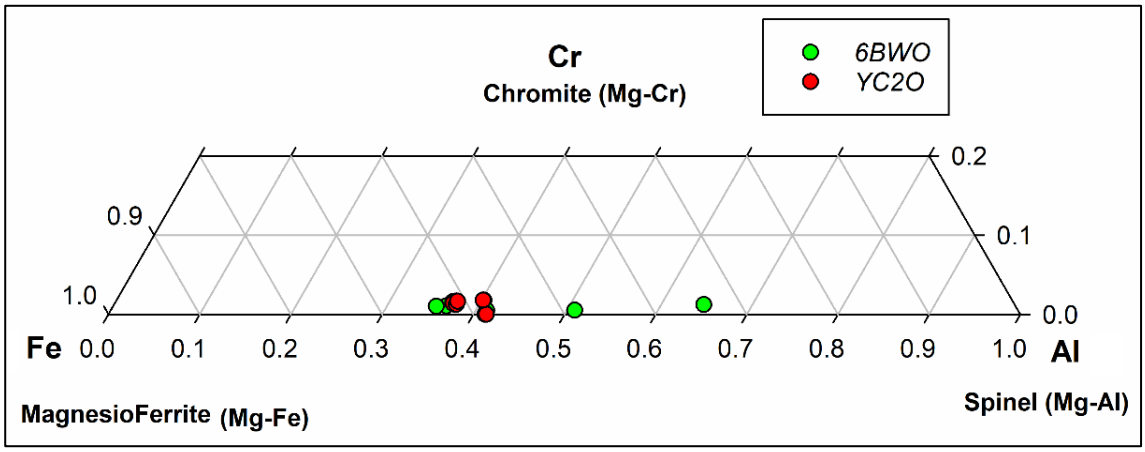

Fig. 9.18 – Ternary diagram displaying the chemical composition variation of spinel in larnite-rich rocks considering the octahedron site fulfilled by Mg and chromite, magnesioferrite and spinel (Mg-Al) as end members.

Mayenite crystals rarely occurs in *YC2O*, as confirmed XRD data, and were not easily recognised in BSE due to similar grey scale of ye'elimite (Table 9.1). Our results agree well with bibliographic one highlighting a slight ionic substitution among Al^{3+} and Fe^{3+}, while differences are related to elements in *W* site (Table 9.12): mayenite in *YC2O* has a both F^{-1} and Cl^{-1} inside *W* site, with a prevalence of the latter; whereas, F^{-1} and $(OH)^{-1}$ represent the major vicariants with only low amount of chlorine for bibliographic data (Table 9.18). *W* atomic site in *YC2O* was considered with only F^{-1} and Cl^{-1}, whereas bibliographic results also took into account $(OH)^{-1}$ content because its occurrence was proved by Raman spectroscopy [207].

Elements / Samples		***YC2O***		***Bibliographic values*** [20]	
		average (n = 4)°	***max.-min.***	***average (n = 13)***	***min.-max.***
F		0.82(6)	0.87-0.74	1.56	-
Na_2O		0.03(2)	0.05-0.00	0.07	-
P_2O_5		0.00(1)	0.02-0.00	0.05	-
Fe_2O_3		2.71(7)	2.78-2.65	2.75	-
K_2O		0.01(1)	0.01-0.00	0.02	-
MgO		0.01(1)	0.02-0.01	*n.a.*	*n.a.*
SO_3		0.01(2)	0.05-0.00	0.04	-
CaO		44.38(.32)	44.76-44.04	46.62	-
Al_2O_3		45.07(.38)	45.52.44.70	47.79	-
Cl		2.26(5)	2.32-2.21	0.69	-
TiO_2		0.02(2)	0.03-0.01	*n.a.*	*n.a.*
SiO_2		0.26(6)	0.32-0.20	0.31	-
Cr_2O_3		0.02(3)	0.05-0.00	*n.a.*	*n.a.*
Total		95.60(.65)	96.35-94.99	99.90	-
General formula X_{12} Y_{14} $O_{33-x/2}$ W_x normalised to 66 negative charges§					
X	**Ca^{2+}**	11.98(9)	11.99-11.97	11.92	-
	Mg^{2+}	0.10(9)	0.01-0.00	*n.a.*	*n.a.*
Y	**Fe^{3+}**	0.51(1)	0.53-0.49	0.49	-
	Cr^{3+}	0.01(1)	0.01-0.00	*n.a.*	*n.a.*
	Al^{3+}	13.39(3)	13.43-13.36	13.44	-
	Ti^{4+}	0.01(1)	0.01-0.00	*n.a.*	*n.a.*
W	**F^{-1}**	0.66(5)	0.70-0.60	1.18	-
	Cl^{-1}	0.97(2)	0.99-0.94	0.28	-
	$(OH)^{-1}$	*n.a.*	*n.a.*	0.64	-
O^{2-}		32.19(.15)	32.17-32.10	32	-

Table 9.12 – EMPA results for mayenite in larnite-rich rock (*YC2O*) and bibliographic values [20] are reported for comparison; *n.a., not analysed element; -, not available data; °number of analysis; §formula was calculated normalizing to 66 negative charges.

NXRD for Quantitative Texture Analysis was performed on rock fragment of *YC2O* larnite-rich rock. Only larnite was considered for identifying preferred orientation due to its abundance and importance during the following hydration process. Results revealed no preferred orientation for

larnite crystals, because values are close to 1 of multiple of random distribution (m.r.d.) (Fig. 9.20). In Fig. 9.19 is highlighted the goodness of fitting for the sum of overall 180 patterns collected.

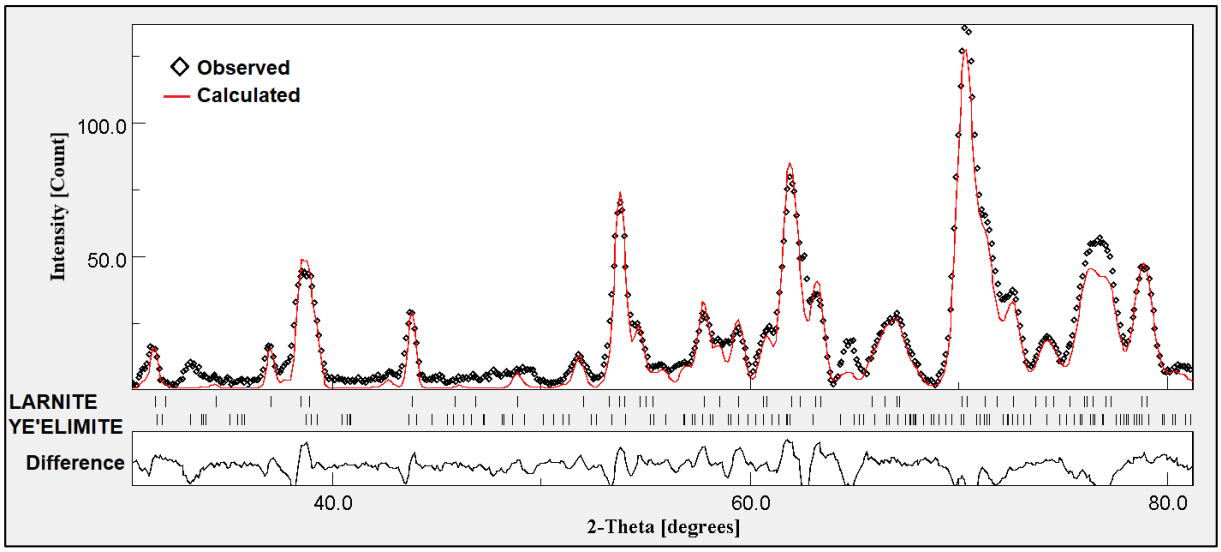

Fig. 9.19 – Fitting result of the sum of Neutron Synchrotron Diffraction patterns performed by Maud [275–278,292].

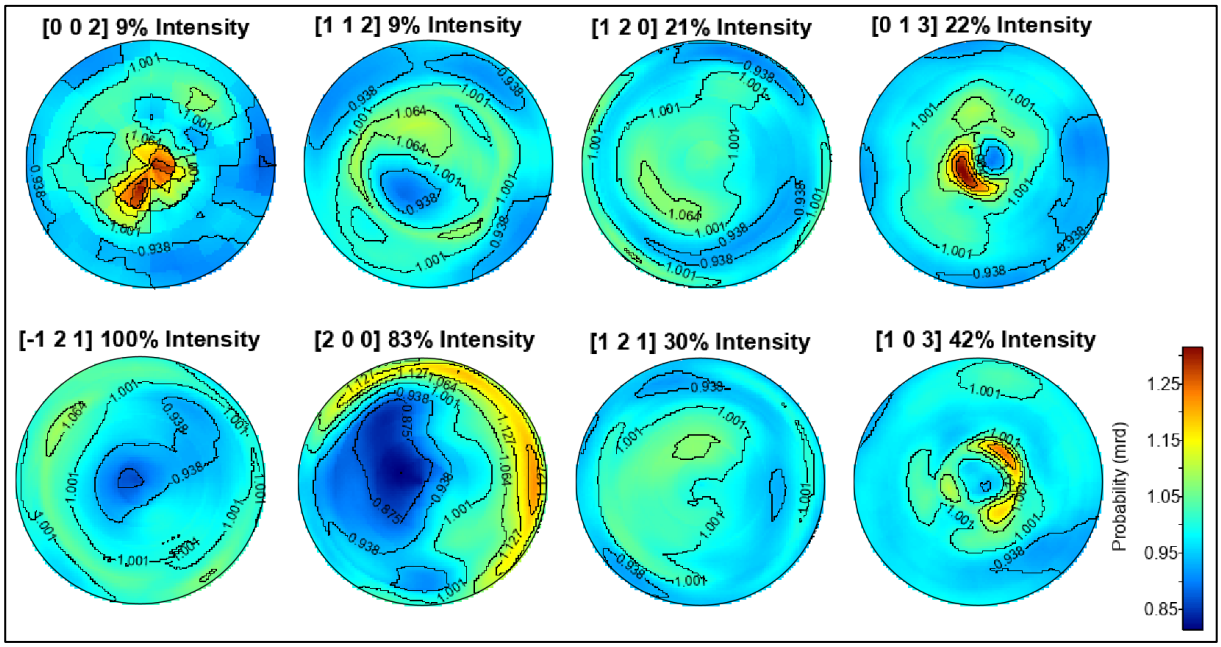

Fig. 9.20 – Reconstructed Pole Figures for main Bragg peaks for larnite in *YC2O* studied by NXRD, showing no preferred orientation of crystals.

Larnite crystal structure refinement was made on SXRPD pattern of *6BWO* starting from the crystal structure model of Jost et al. [169]. *6BWO* sample was used instead of *YC2O* for larnite crystal structure refinement because of the larger crystallite size (Table 9.2) leading a better estimation of atomic position due to sharper and higher Bragg peaks. Scale factors of all crystal phases plus atomic positions and Uiso parameters of larnite were simultaneously refined after RQPA by means of GSAS-ii. Because of the goodness of RQPA before structure refinement, the wt.% of crystal

phases did not change. No remarkable changes occur in the refined crystal structure model (Fig. 9.21; Table 9.13), excepted for a general increase of Uiso parameter for all atomic sites (Table 9.14,15). Furthermore, a slight reduction in bond distances between Si-O is found (Table 9.16) with no changes in angle values of O-Si-O (Table 9.17); whereas, a little increase for most bonds between Ca-O occurs (Table 9.18,19).

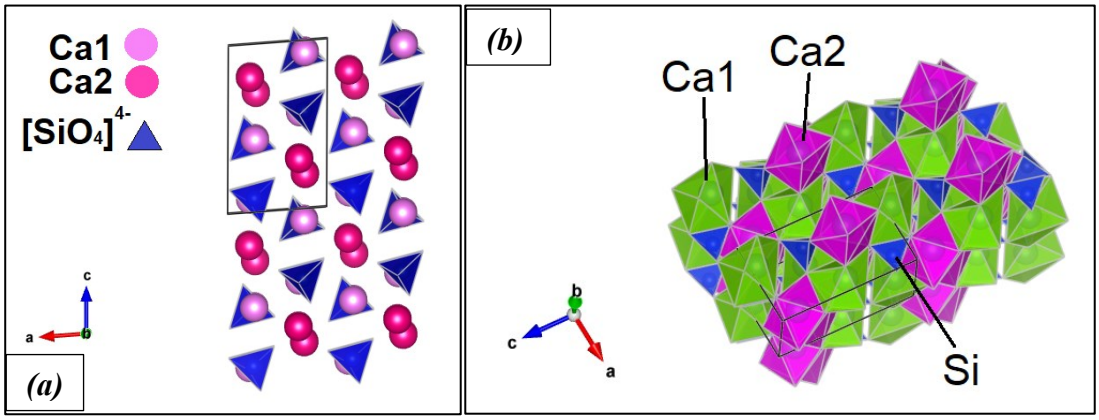

Fig. 9.21 – Crystal structure of the refined larnite along b vector ([010] direction): (a) highlighting the nesosilicate structure with two different calcium sites (Ca1,2); (b) the different coordination polyhedral for Ca1 and Ca2, 7 and 8, respectively.

Crystal Phase	Larnite (β-Ca_2SiO_4)
Space Group	$P2_1/n$
***a* (Å)**	5.50901(2)
***b* (Å)**	6.75729(2)
***c* (Å)**	9.31423(5)
***β* (°)**	94.5077(3)
***V* (Å^3)**	345.659(1)
Z	4
R-Factor (%)	2.58
Number of Reflections	2597
Range of d (Å) investigated	0.5178 – 5.4637
Rexp	0.916
Rwp	9.216
GoF	10.06

Table 9.13 – Crystallographic parameters and values of the Rietveld refinement for refined larnite crystal structure of *6BWO* sample analysed with SXRPD (ID22).

Label	Type	x	y	z	frac.	Uiso	m*
Ca1	Ca^{2+}	0.2719(2)	0.34286(2)	0.5698(1)	1	0.0093(3)	4
Ca2	Ca^{2+}	0.2796(2)	0.99789(2)	0.2982(1)	1	0.0064(3)	4
Si1	Si^{4+}	0.2330(3)	0.78222(2)	0.5819(2)	1	0.0031(4)	4
O1	O^{2-}	0.2794(6)	0.0010(5)	0.5598(4)	1	0.0149(9)	4
O2	O^{2-}	0.0238(6)	0.7487(5)	0.6900(3)	1	0.0113(9)	4
O3	O^{2-}	0.4826(6)	0.6721(5)	0.6376(3)	1	0.0096(9)	4
O4	O^{2-}	0.1574(6)	0.6719(5)	0.4308(3)	1	0.0149(9)	4

Table 9.14 – Atomic positions of refined larnite crystal structure for *6BWO* collected at SXRPD (ID22) by means of Rietveld method with GSAS-ii; e.s.d. is reported is rounded brackets; *multiplicity number of the atomic site.

Label	Type	x	y	z	frac.	Uiso	m*
Ca1	Ca^{2+}	0.2738(2)	0.3428(2)	0.5694(3)	1	0.00480	4
Ca2	Ca^{2+}	0.2798(2)	0.9976(2)	0.2981(3)	1	0.00380	4
Si1	Si^{4+}	0.2324(3)	0.7814(2)	0.5817(2)	1	0.00240	4
O1	O^{2-}	0.2864(10)	0.0135(8)	0.5599(6)	1	0.01150	4
O2	O^{2-}	0.0202(9)	0.7492(8)	0.6919(8)	1	0.00849	4
O3	O^{2-}	0.4859(9)	0.6682(8)	0.6381(8)	1	0.00799	4
O4	O^{2-}	0.1558(9)	0.6710(8)	0.4264(8)	1	0.00786	4

Table 9.15 – Atomic positions and crystallographic parameters of Jost et al. model [169]; e.s.d. is reported in rounded brackets; *multiplicity number of the atomic site.

Bond	New Bond Distances (Å)	Previous Bond Distances (Å)
(Si1-O1)	1.57627	1.61464
(Si1-O2)	1.60538	1.62737
(Si1-O3)	1.61303	1.64586
(Si1-O4)	1.61751	1.65870

Table 9.16 – Bond distance values for atomic site Si1 connected with 4 oxygens, calculated for new and previous larnite crystal structures.

Angle	New Angles (°)	Previous Angles (°)
(O3-Si1-O2)	111.64	111.74
(O2-Si1-O4)	109.43	110.15
(O4-Si1-O3)	102.83	102.83
(O1-Si1-O3)	110.49	110.97
(O1-Si1-O2)	110.59	109.44
(O1-Si1-O4)	111.70	111.46

Table 9.17 – Angle values for atomic site Si1 and oxygens belonging to silicon tetrahedron, calculated for new and previous larnite crystal structures.

Bond	New Bond Distances (Å)	Previous Bond Distances (Å)
(Ca2-O2)	2.41098	2.39159
(Ca2-O4)	2.63861	2.62844
(Ca2-O1)	2.67392	2.64908
(Ca2-O3)	2.41872	2.40076
(Ca2-O2)	2.40149	2.38768
(Ca2-O1)	2.43789	2.44495
(Ca2-O4)	2.48379	2.45098
(Ca2-O3)	2.63102	2.65097

Table 9.18 – Bond distance values for atomic site Ca2, which is connected with 8 neighbour oxygen, calculated for new and previous larnite crystal structures.

Bond	New Bond Distances (Å)	Previous Bond Distances (Å)
(Ca1-O3)	2.44573	2.42614
(Ca1-O1)	2.25181	2.23208
(Ca1-O2)	2.50612	2.50840
(Ca1-O3)	2.56547	2.55348
(Ca1-O4)	2.36684	2.37210
(Ca1-O4)	2.62450	2.64872
(Ca1-O2)	2.87626	2.89715

Table 9.19 – Bond distance values for atomic site Ca1, which is connected with 7 neighbour oxygens, calculated for new and previous larnite crystal structures.

Cilyndric millimetric size samples of *6BWO* (Fig. 9.22a), *YC2O* (Fig. 9.23a) and *YC2V* (Fig. 9.25a) were studied by means of synchrotron X-ray μ-CT, obtaining detailed information on the voids, fractures, high and low density phases distribution. Results on *6BWO* (Fig. 9.22) highlighted a low porosity (3.69vol.%) mainly occurring along fractures (Fig. 9.22c,d) in which low density phases are abundant (C-S-H, ettringite, katoite, etc.). Furthermore, high density phases (shulamitite and spinel) are wide distributed (Fig. 9.22c,e).

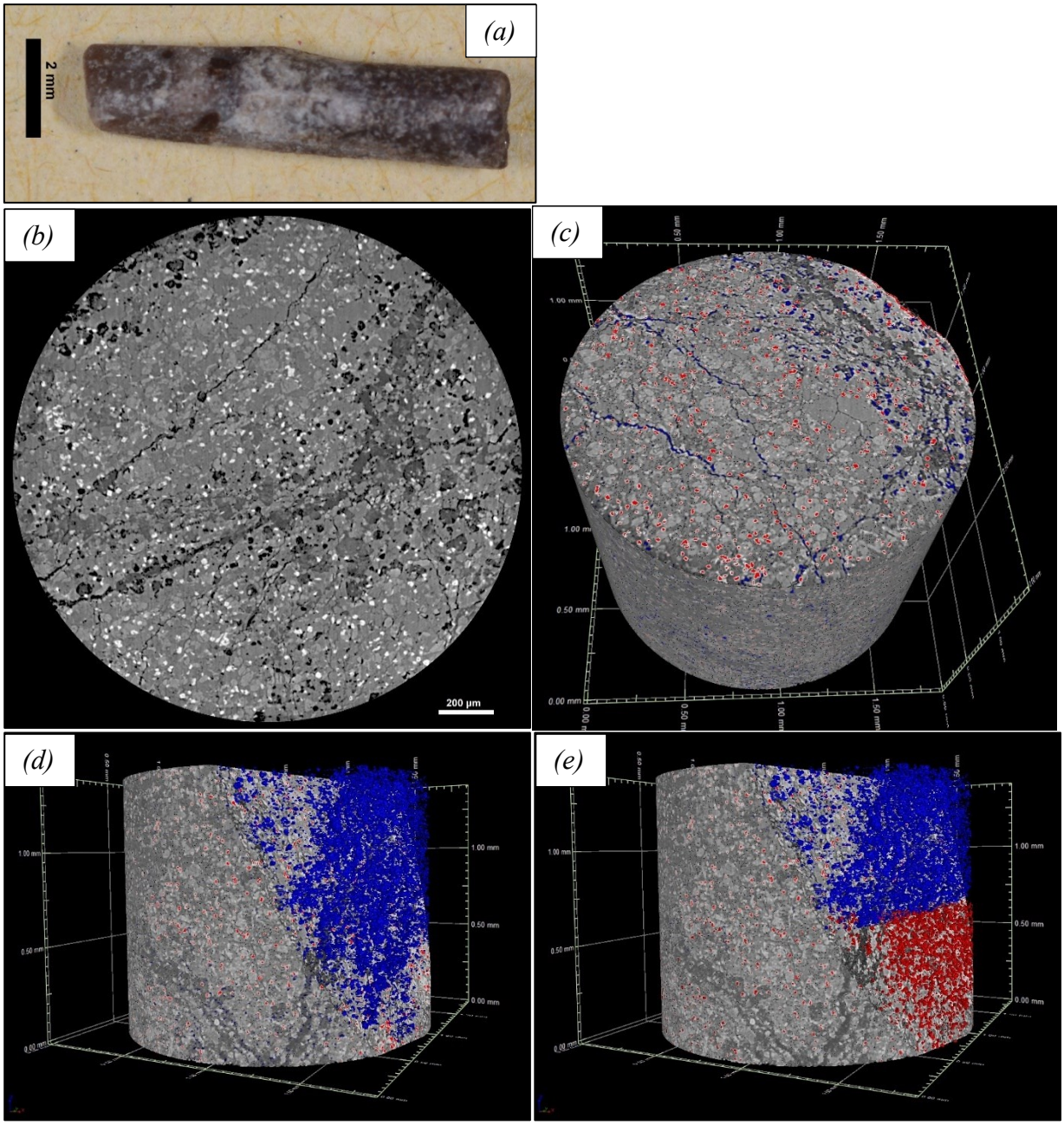

Fig. 9.22 – Ye'elimite-larnite rock fragment (*6BWO*) studied by means of synchrotron X-ray μ-CT: (a) cylindric millimetric rock fragment with no macroscopic vein or inhomogeneities; (b) sample slice highlighting density changes in grey scale, with voids in black, shulamitite and spinel in white, other anhydrous minerals in medium grey and dark grey hydrated crystal phases; (c) volume rendering reporting in red high density minerals (shulamitite and spinel) and in blue voids; (d) volume rendering with a clipping plane showing voids distribution in blue; (e) volume rendering with a clipping plane of the sample revealing in the half bottom high density phases in red, voids in blue in the half top.

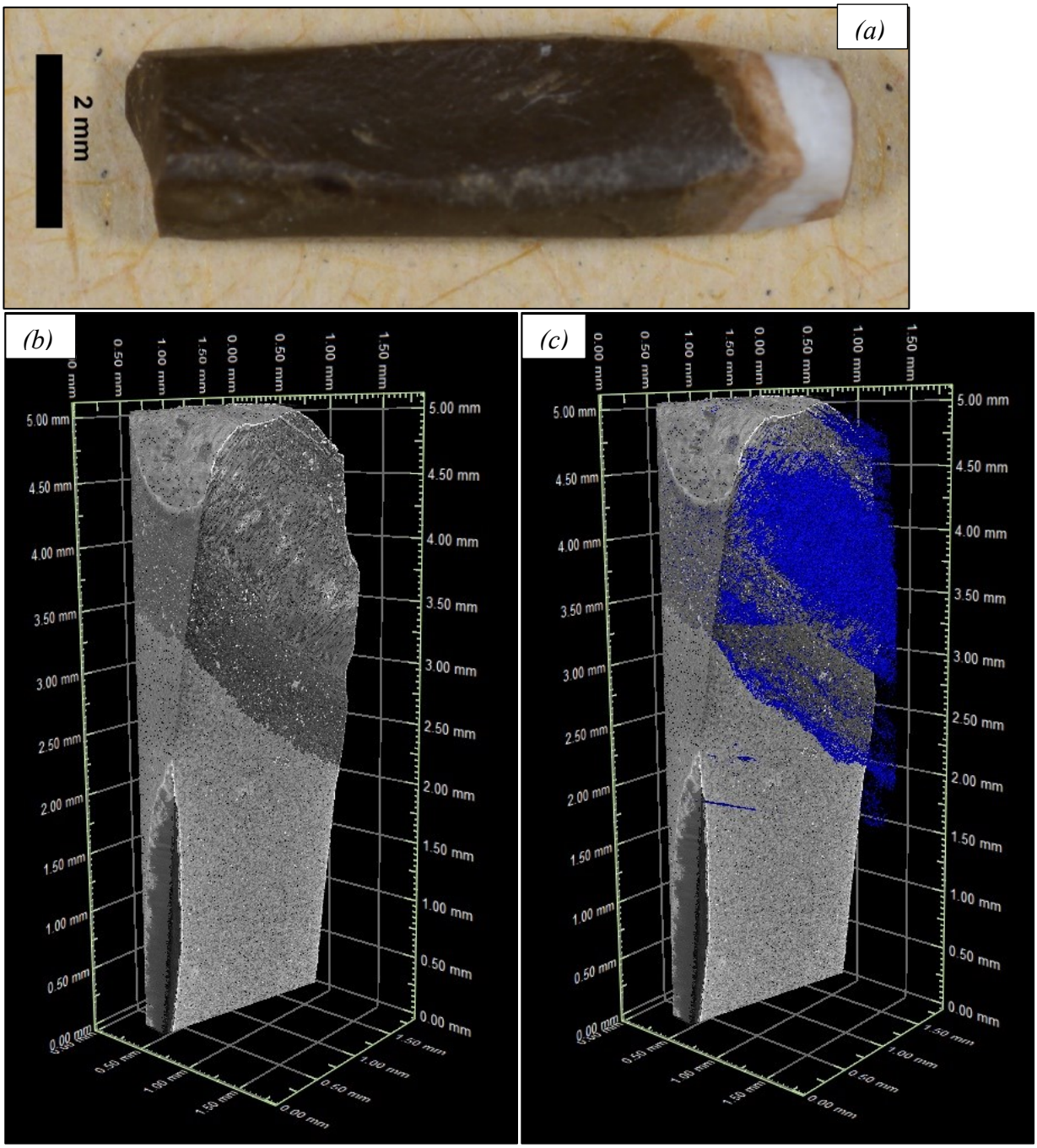

Fig. 9.23 – Ye'elimite-larnite rock fragment (*YC2O*) studied by means of synchrotron X-ray μ-CT: (a) cylindric millimetric size sample with dark brown portion corresponding to anhydrous part (rich in larnite, ye'elimite, spinel, fluorapatite and shulamitite), and a millimetric hydration vein made of light brown part (C-S-H phases rich) and white portion (calcite rich); (b) volume rendering with a clipping plane parallel to the sample elongation clearly showing the hydration vein on the top; (c) volume rendering with a clipping plane parallel to the sample elongation and highlighting in blue voids, which are mainly occurring in the hydration vein especially in the white portion.

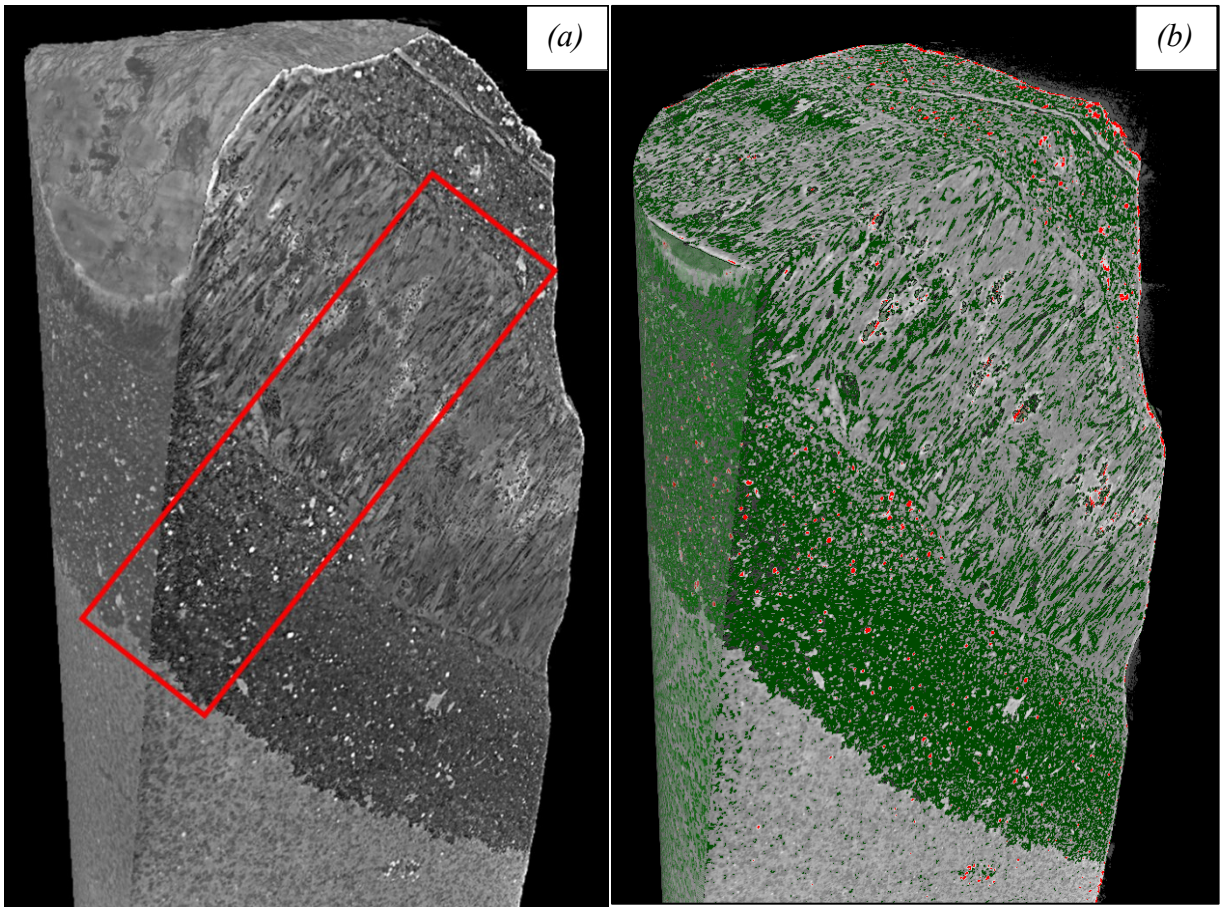

Fig. 9.24 – Detail on the hydration vein in ye'elimite-larnite rock fragment (*YC2O*) studied by means of synchrotron X-ray μ-CT: (a) volume rendering with a clipping plane showing the internal division of the hydration vein (darker portion) and the sharp transition to the anhydrous part (bottom lighter portion); (b) volume rendering reporting in green low-density crystal phases (C-S-H phases, ettringite, etc.), revealing the brown portions of the hydration vein (Fig. 9.23a), and in red high density phases (shulamitite and spinel) which are mainly occurring in the anhydrous portion and vein rims.

Sample *YC2O* (Fig. 9.23a) is mostly made of anhydrous dark brown portion and the remaining by a submillimetric hydration vein composed of a white central part and two light brown rims. Volume rendering of the sample clearly revealed microstructural details: (i) white vein portion is made of denser phases compared to light brown one (Fig. 9.23b); (ii) voids mainly occurred in the hydrated vein without a preferred distribution in light brown rims and with a preferred elongation perpendicular to rims in the central white part (Fig. 9.23c,24a,25); (iii) high density phases (shulamitite and spinel) occurred in anhydrous part and light brown vein rims (Fig. 9.25b,26). In Fig. 9.25 is reported a volume rendering only considering a region perpendicular to the sample vein (Fig. 9.23a,24a) highlighting that most voids occur in the white part of the vein with an elongated shape associated with a reduction in high-density phases (Fig. 9.26).

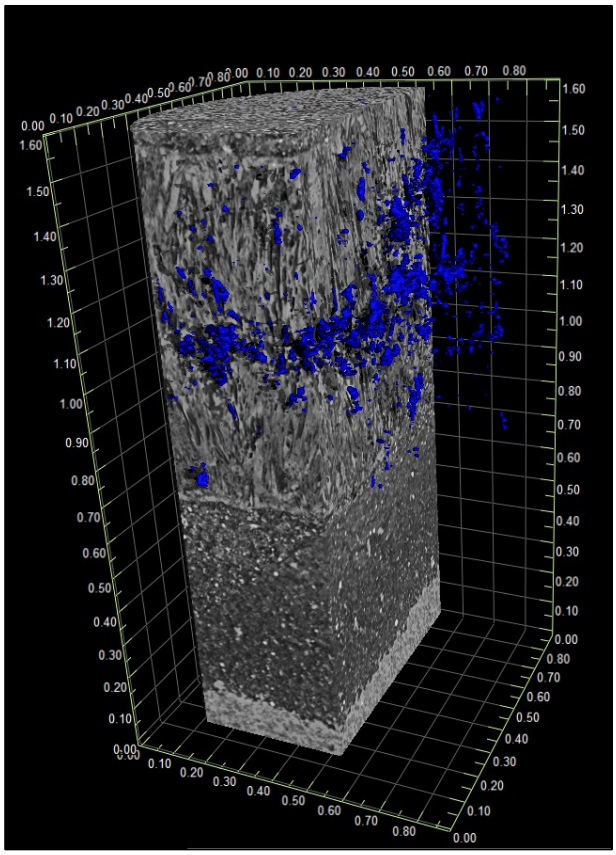

Fig. 9.25 – Volume rendering of sample *YC2O* only considering the red box in Fig. 9.24a; in blue are reported voids which are mainly occurring inside white vein part.

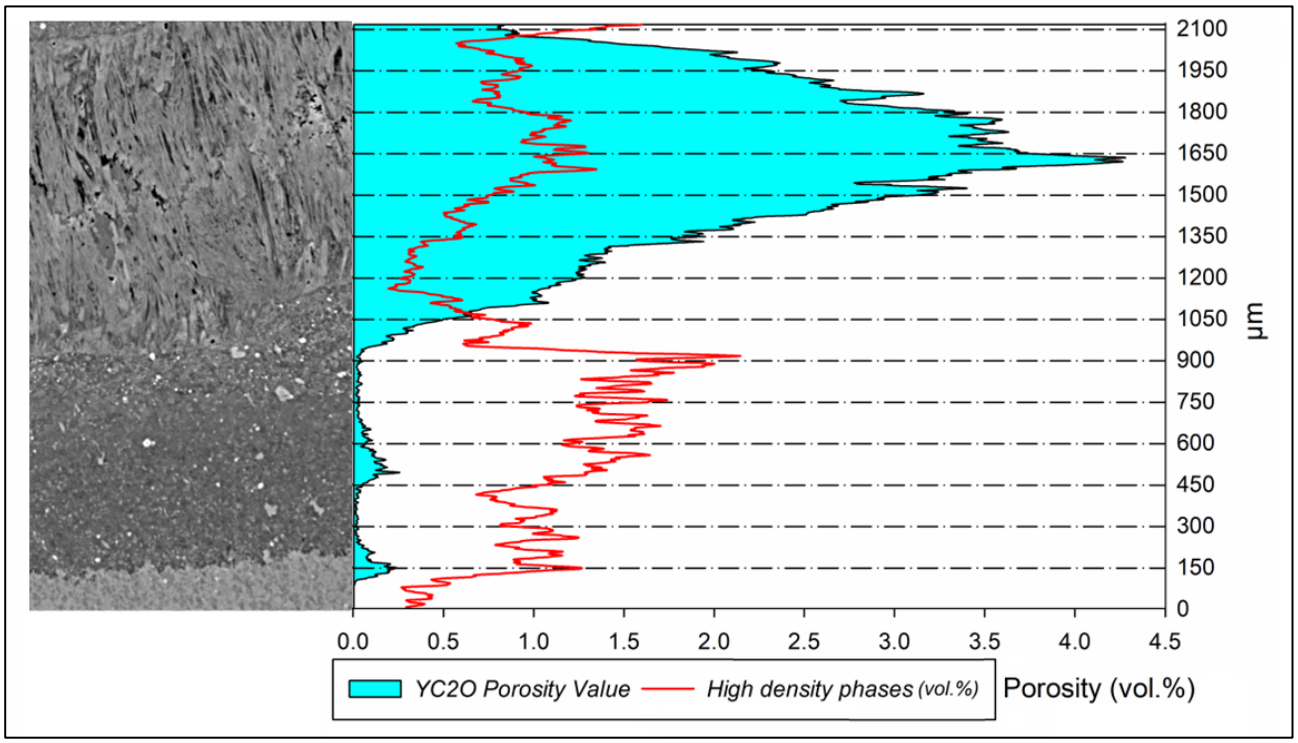

Fig. 9.26 – Variation of porosity (vol.%) and high-density phases (vol.%) in sample *YC2O* perpendicular to the vein.

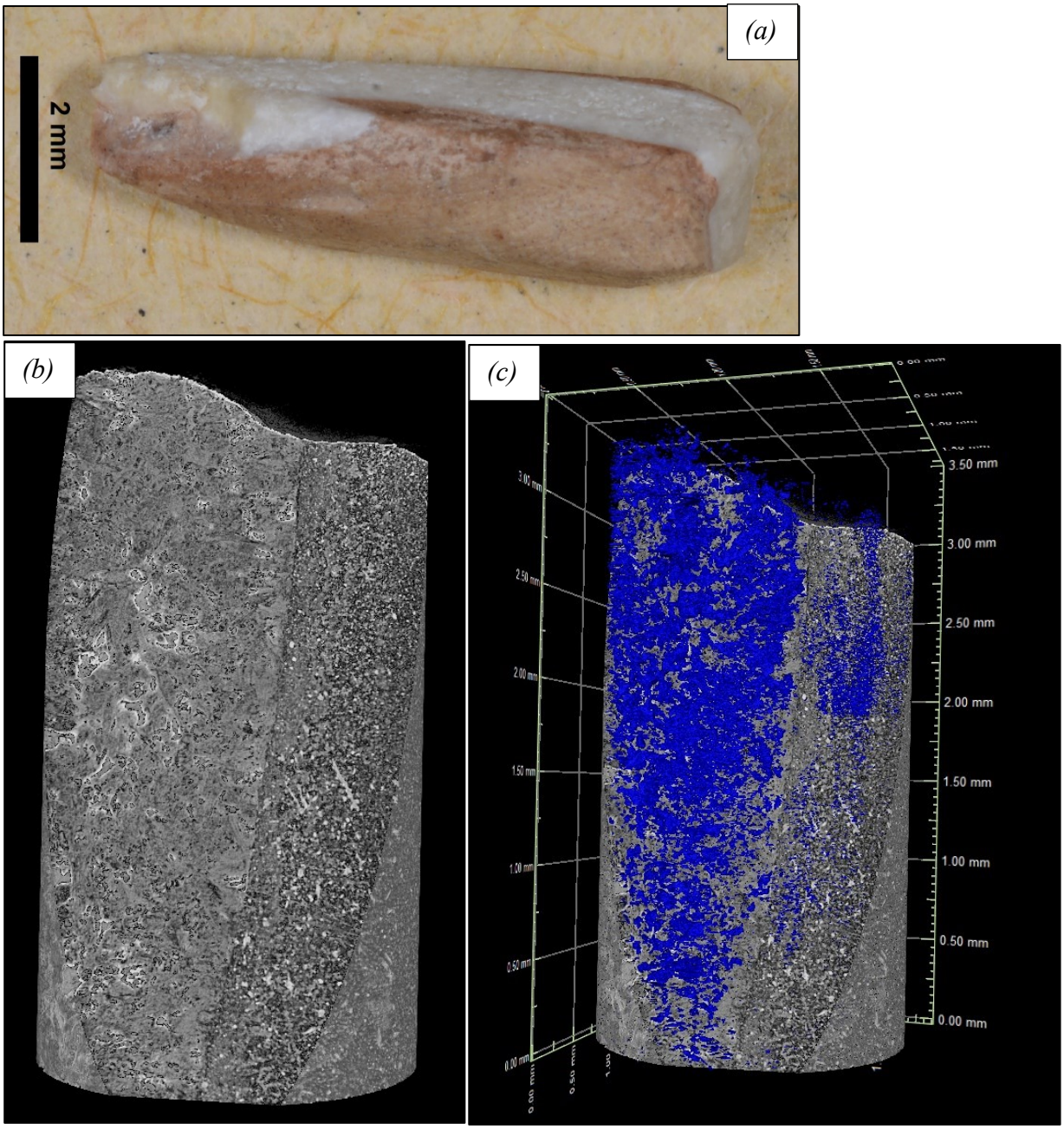

Fig. 9.27 – Hydrated ye'elimite-larnite rock fragment (*YC2V*) studied by means of synchrotron X-ray µ-CT: (a) cylindric millimetric sample with a central white portion (calcite-rich) and two brown sides (C-S-H and ettringite-rich portion) parallel to the sample elongation; (b) volume rendering of the bottom-right part of the sample (a) with a clipping plane parallel to the elongation highlighting a darker right part (brown vein portion) rich in high density phases, and a left lighter part (white vein portion); (c) volume rendering of the bottom-rich part of the sample (a) with a clipping plane showing in blue voids which are mainly occurring in the left sample potion (white vein part).

YC2V sample (Fig. 9.27a) represents a fragment of a hydration vein with two light brown rims and a central calcite-rich part. µ-CT results highlighted the internal sharp transition between the light brown rims (portion rich in hydrated phases), marked by darker colour corresponding to lower density areas, and white calcite-rich vein core featured by lighter colour (Fig. 9.27b). Furthermore, only inside light brown rims high density phases occurred. Voids differently occurred in light brown than white portions: (i) white calcite-rich portion has 9.72vol.% with larger pores and more elongated; (ii) light brown rims have 4.87vol.% with small pores (Fig. 9.27c)

9.2 – Discussion

Samples of natural anhydrous (*6BWO* and *YC2O*) and hydrated (*6BWV* and *YC2V*) larnite-rich rocks were collected during field trip in Hatrurim Basin (see sections 5.6 and 5.9) and were studied by means of both conventional and innovative techniques, leading detailed information on mineral assemblage, crystallographic parameters and textural features at different observation scales.

Three differ types of larnite-rich rocks have been found in Hatrurim Basin and other CP locations among Israel and Jordan (Fig. 1.3) [29,67,311,312], which are distinguished by the mineral assemblage: (i) larnite-mayenite paragenesis as main minerals and with accessory spinel, brownmillerite, shulamitite and fluorapatite-ellestadite; (ii) larnite-gehlenite paragenesis with minor mayenite, brownmillerite, spinel and fluorapatite-ellestadite; (iii) larnite-ye'elimite association as major constituents and brownmillerite, spinel, shulamitite and fluorapatite-ellestadite [20,21]. Larnite-mayenite and larnite-ye'elimite are the most common associations, whereas, larnite-gehlenite is rare in Hatrurim Basin [20]. Our HT samples from Hatrurim Basin both belongs to larnite-ye'elimite rocks with spinel, shulamitite, fluorapatite-ellestadite and low mayenite, while brownmillerite and ternesite represent minor minerals of *6BWO* and *YC2O* (Table 9.1, Fig. 9.4,8), respectively.

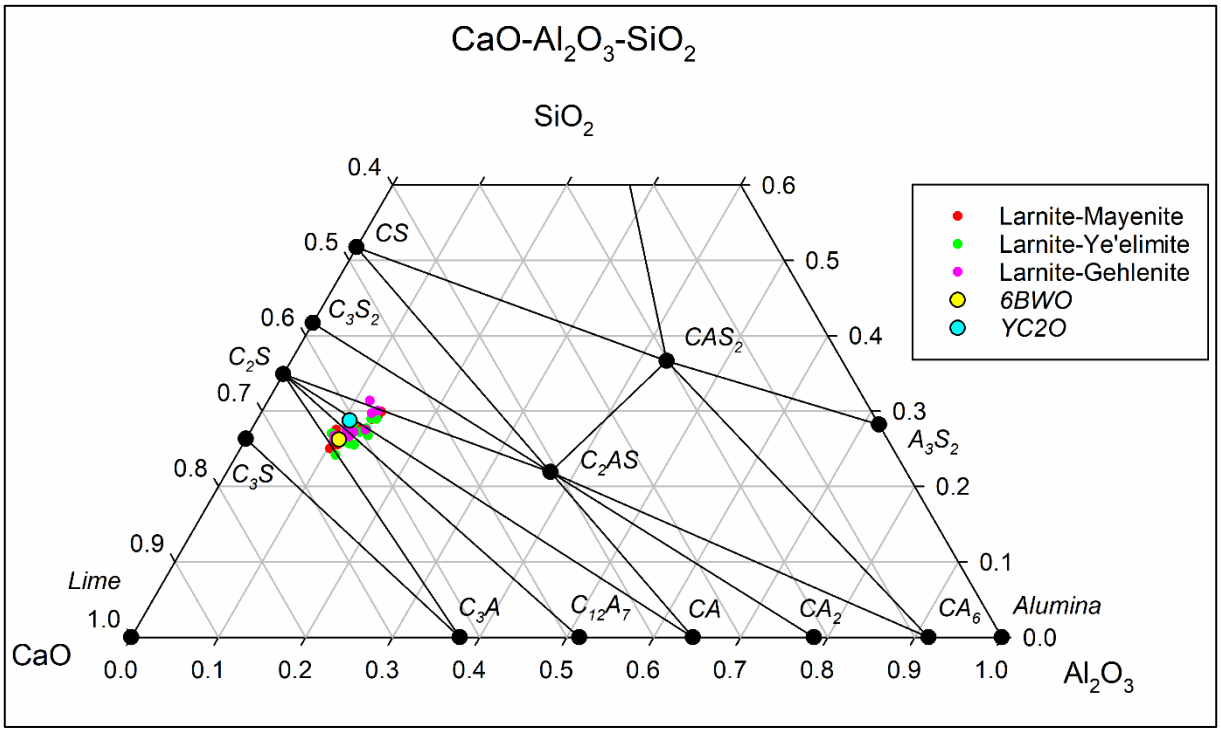

Fig. 9.22 – CaO-Al_2O_3-SiO_2 ternary diagram (weight unitary scale) using the cement nomenclature (CaO=C, SiO_2=S and Al_2O_3=A) and reporting crystal phases assemblages stable below the liquidus considering the invariant points [8]; chemical composition of different larnite-rich rocks are plotted, mostly falling in three crystal phases assemblages, such as C_2S-C_3A-$C_{12}A_7$, C_2S-$C_{12}A_7$-CA and C_2S-C_2AS-CA [8].

The main chemical composition difference among three larnite-bearing assemblages is the sulphur content: larnite-mayenite < 0.11wt.%; larnite-gehlenite 0.15-0.6wt.%; larnite-ye'elimite > 1.4wt.%. P_2O_5 wt.% is not a distinguishing element for these mineral associations because showed a wide

content from 0.78-4wt.% [20,29,220,313,314], leading a change in the wt.% of fluorapatite and the occurrence of flamite (HT polymorph of dicalcium silicate, also reported as α'_H-C_2S, Table 6.4) [7,85,175]. Changes on chemical composition are well reflected by variation in wt.% of crystal phases: *6BWO* has higher content of SO_3 and P_2O_5 leading an increase in ye'elimite and fluorapatite s.s. compared to *YC2O* (Table 9.1, Fig. 9.4,8).

Considering the pure phase diagram CaO-Al_2O_3-SiO_2 all larnite-rich rock types are mainly displayed in three different mineral associations (Fig. 9.22): larnite-celite-mayenite (C_2S-C_3A-$C_{12}A_7$); larnite-mayenite-krotite (C_2S-$C_{12}A_7$-CA); larnite-gehlenite-krotite (C_2S-C_2AS-CA). Even though celite and krotite should occur in several larnite-rich rocks considering the pure ternary phase diagram, none of these two crystal phases have been found; whereas, gehlenite (C_2AS) has been found for chemical composition in which it should not occur, even in association with mayenite [20,220] although no tie-line mayenite-gehlenite exists (Fig. 9.22) [8]. Furthermore, the association C_2S-$C_{12}A_7$-$C_4A_3\bar{S}$-C_4AF (larnite-mayenite-ye'elimite-brownmillerite) and C_2S-$C_5S_2\bar{S}$-$C_4A_3\bar{S}$-C_4AF (larnite-ternesite-ye'elimite-brownmillerite) in the pure system CaO-SiO_2-Al_2O_3-Fe_2O_3-SO_3 are considered stable at temperature ~ 1250 °C; whereas $C_{12}A_7$ and $C_5S_2\bar{S}$ simultaneous occurrence is not stable over the same temperature range [315], despite was found in *YC2O* sample. This mismatching with bibliographic evidences could be explained by: (i) lack of thermodynamic equilibrium during CP, especially in the case of no or slight partial melting that reduces the reactivity and the spatial amplitude of chemical equilibrium; (ii) local chemical composition inhomogeneities leading changes on the mineral assemblage from the main one of the bulk-rock (e.g. spinel and brownmillerite-shulamitite-rich nodules, Fig. 9.1c,d;9.2e,f); (iii) minor elements effects (MgO, P_2O_5, SO_3, Na_2O, TiO_2 and F) that could change the stability field of phases, melting point and melt properties [7,8]. For example, increasing the MgO content enlarges the stability field of gehlenite and stabilises spinel [316]; increasing SO_3 content stabilises ye'elimite that starts forming by the reaction between krotite or mayenite and anhydrite at temperature 1000-1100 °C [317] even depending on the sulphur fugacity [318]; P_2O_5 associated with SO_3, SiO_2 and F stabilises fluorapatite-ellestadite s.s. (Fap-ell) crystals that in association with larnite start melting at 1220±5 °C and completely melts at 1240 °C [319], releasing F, SO_2 and P_2O_5 that reduce the viscosity of Al-Fe-Si melt promoting metamorphic reactions [7,8].

A positive correlation between sedimentary protoliths and metamorphic rocks occurs considering CaO, Al_2O_3 and SiO_2 contents: previous study revealed that all rocks lay on the line SiO_2/Al_2O_3 = 2.7-2.4 and CaO content varies from very CaO-rich rocks, belonging to upper Ghareb Formation corresponding to calcite-spurrite marble (Unit KuPh2), to the lowest, belonging to Taqiye Formation (marls and clays) corresponding to anorthite-diopside hornfels subunit (Unit KuPh3) [28,220]. Our metamorphic samples *6BWO* and *YC2O* showed a SiO_2/Al_2O_3 of 2.43 and 2.63, respectively (Table 7.2, Fig. 9.22), being in good agreement with previous results [28].

Textural features observed during field trip are in good agreement with bibliographic data, reporting outcrops of larnite-rich rocks made of anhydrous dark brown parts crisscrossed by millimetric to subcentimetric hydration veins often showing an internal division without preferred orientation [13,20,28]. Larnite-rich rocks are found (i) on the top hills in the upper part of metamorphic sequence in northern and central Hatrurim Basin as massive outcrops (*YC2O*, Fig. 5.37,38), whereas (ii) in the lower part of metamorphic sequence crop out as bodies with

centimetric to metric in size (*6BWO*) inside LT rocks (Unit KuPh1, Fig. 5.21). Considering the stratigraphic position of collected larnite-rich rocks: (i) *YC2O* sample is correlated to the CP of Hafir Member (Upper Member of Taqiye Formation), due to its slight stratification and the occurrence above the Unit KuPh3 Olive dense rocks subunit, which is easily recognized by the dark brown weathering colours of strata cropping out in all Hatrurim Basin hills (Fig. 5.10,23,24,35,26) corresponding to clay-rich protoliths of Taqiye Formation [13,28]; (ii) *6BWO* is correlated to the CP of Ghareb Formation due to its stratigraphic position below Unit KuPh3 and occurrences inside retrograde rocks (Fig. 5.21,22). Despite the different stratigraphic position, samples showed the same mineral assemblage C_2S-$C_4A_3\bar{S}$-M_2FA-$C_{10}P_3F_2$-C_8T_2FA-$C_{12}A_7$ (larnite-ye'elimite-spinel-fuorapatite-ellestadite-shulamitite-mayenite) excepted at synchrotron scale (SXRPD) that revealed the occurrence of ternesite and minor brownmillerite for *YC2O* and *6BWO*, respectively (Table 9.1; Fig. 9.4,8).

Considering our results and bibliographic ones, larnite-rich rocks revealed similar microtextural features both at different stratigraphic position and location in the Hatrurim Basin: larnite is always the major constituent with rounded to polygonal crystal shape; brownmillerite occurs as prismatic to tabular crystals; shulamitite has acicular crystals; ye'elimite always appears anhedral with inclusions; fluorapatite-ellestadite has peciloblastic hexagonal prism shape; spinel occurs as rounded to psedocubic crystals. Larnite-rick rocks has a general low crystal size (5-35 μm) with fluorapatite, brownmillerite and shulamitite as euhedral bigger crystals [20,21,26,34,320], but in few locations the crystal size is coarser enough to separate single crystals for further study [117].

Combustion temperature in Hatrurim Basin was not homogenous due to features of the combustion event: combustion of methane-rich gases took place at foci in which the temperature was extremely high (up to 1650 °C [16]) leading the thermal metamorphism of country rocks. For most mineral assemblages peak temperatures between 500-950 °C were estimated [321]. Several studies attempted to estimate the highest temperature reached in Hatrurim Basin rocks: first study revealed a general temperature formation between 1000 to 1100 °C [78]; studies on paralavas, representing anorthite-diopside hornfels subunit belonging to Unit KuPh3, estimated a temperature formation between 1125-1310 °C considering pseudowollastonite-anorthite-gehlenite assemblage [29]; orthorhombic $FeAlO_3$ occurrence in hematite and corundum in anorthite-diopside hornfels pointed out a temperature close to 1318 °C [322–325]. Larnite-ye'elimite (*6BWO* and *YC2O*) rocks should be formed at $T \geq 950$ °C, due to the lack of spurrite that decomposes at higher temperature; the occurrence of ye'elimite delimits the lower temperature range at 1000 °C, when starts to crystallise by the reaction of krotite or mayenite and anhydrite, and the higher one at 1300-1350 °C, when decomposes to krotite, mayenite and sulphuric gas [317,318,326].

Flamite represents a HT polymorph of dicalcium silicate and has been found in a few locations in larnite-ye'elimite and larnite-mayenite rocks usually high in P_2O_5 and low fluorellestadite suggesting HT combustion followed by a fast cooling [122]. The occurrence of flamite at room temperature along with larnite strictly requires the stabilisation of α-C_2S (also reported as *Rss*, Fig. 9.23) during heating followed by a fast cooling in the field flamite+α-C_2S (*Rss*+α'-C_2S, Fig. 9.23): a slow cooling from HT leads a complete transition from α-C_2S to flamite that at lower temperature firstly fully turns into α'$_L$-C_2S and later to larnite (β-C_2S), completely

missing the occurrence of flamite at room temperature [7,8]. Higher content of P_2O_5, also if associated with other ionic substituents (K_2O, Na_2O, B_2O_3, etc.), enlarges the stability field of flamite and α-C_2S at lower temperature (Fig. 9.23): phosphorous substitutes silicon creating cation vacancies and promoting HT polymorphs $Ca^{2+} + 2^{IV}Si^{4+} \rightarrow Vac^{2+} + 2^{IV}P^{5+}$ [7,8]. Flamite chemical composition in larnite-rich rocks in Hatrurim Basin showed a variable enrichment in phosphorous associated with lower amount of potassium and sodium: considering the molar content for flamite crystals, the ionic substitution among potassium, sodium and phosphorous is limited ($Ca^{2+} + {}^{IV}Si^{4+} \rightarrow (K, Na)^{+} + {}^{IV}P^{5+}$), whereas the ionic substitution leading calcium vacancies is the prevalent [20]. The minimum temperature combustion for larnite-rich rocks in which flamite occurred could be estimated considering the binary phase diagram Ca_2SiO_4-$Ca_3P_2O_8$ (Fig. 9.23) and chemical compositions of larnite and flamite occurring in Hatrurim Basin: larnite in *6BWO* has 0.05 mol P (Table 9.8, ~ 5wt.% of $Ca_3P_2O_8$, (a) in Fig. 9.23), which at 1198 °C falls in the field *Rss*+α'-C_2S, which *Rss* (α-C_2S) has ~ 0.13 mol P (~ 12wt.% of $Ca_3P_2O_8$, (a1) in Fig. 9.23), nevertheless, no flamite crystal was found in *6BWO*; the lowest P_2O_5-rich flamite found in larnite-rich rocks has ~ 0.12 mol P (~ 11wt.% of $Ca_3P_2O_8$, (c) in Fig. 9.23) which should be formed from a quenching of *Rss* (α-C_2S) with the same P molar content in the field *Rss*+α'-C_2S with α'-C_2S of ~ 0.4 mol P (~ 4wt.% of $Ca_3P_2O_8$) at a temperature of ~ 1225 °C. Therefore, 1225 °C should represent the minimum combustion temperature considering the lowest P_2O_5-rich flamite and larnite association in larnite-rich rocks, which should be close to the quenching temperature. Flamite crystals were not found in our samples probably due to: (i) a slower cooling instead of quenching that inhibits the flamite formation thanks to the complete transition α-C_2S →α'-C_2S; (ii) the rarity and low size of flamite oriented lamellas (< 2 μm) in larnite crystals, which are common for higher P_2O_5 larnite-rich rocks; (iii) lower combustion temperature compared to larnite-rich rocks with flamite.

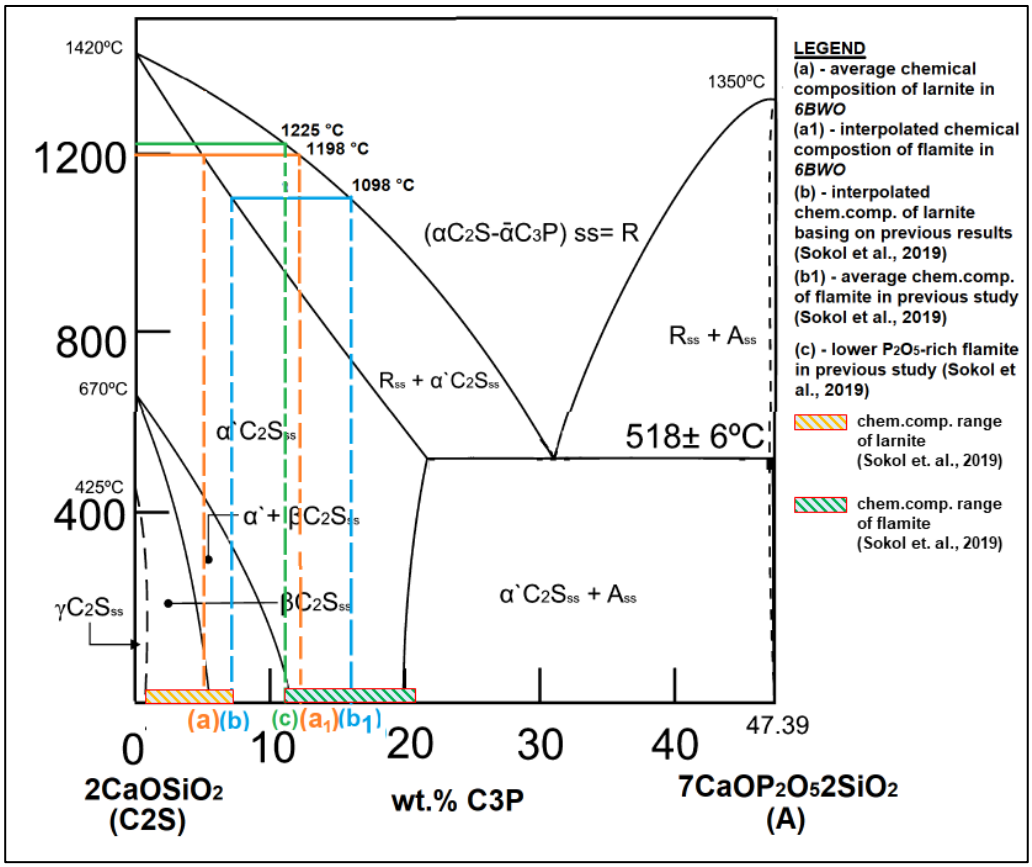

Fig. 9.23 – $2CaOSiO_2$-$7CaO2SiO_2P_2O_5$ binary diagram (wt.% of C_3P) reporting crystal phases and polymorphic transition occurring during heating, especially the field Rss (α-C_2S) and α'-C_2Sss [196]; point (a) represents the average chemical composition obtained for larnite crystals in *6BWO* sample, and (a1) is the calculated chemical position of flamite that should be found in the case of quenching at 1198 °C; point (b1) represents the average chemical composition of flamite in previous study [20], whereas (b) is the correlated chemical composition of larnite crystals in the case of quenching at 1098 °C; point (c) is the lowest P_2O_5-rich flamite found in larnite-rich rocks [20]; the shaded orange rectangle represents the compositional range of all studied larnite, whereas the green one is the compositional range of all studied flamite crystals [20].

Fluorapatite-ellestadite s.s. often occurs in larnite-rich rocks as euhedral peciloblastic hexagonal prism with a P-rich core and S-rich rims (Table 9.9.; Fig. 9.14,16), suggesting that fluorellestadite was crystallising and in equilibrium with other phases during combustion at HT: fluorellestadite in association with larnite slowly starts to melt incongruently at 1220±5 °C and is fully melted at T > 1240 °C, forming liquid and C_2S [319]. Therefore, larnite-rich rocks with fluorapatite-ellestadite euhedral with S-rich rims, as our samples (*6BWO* and *YC2O*), should have been combusted at T ≤ 1220 °C, which could also explain the lack of flamite in these samples. Furthermore, *in-situ* experiments on Ghareb Formation (*RM*) reported in the next chapter figured out the evolution of mineral association during heating and the stability field of fluorapatite-ellestadite.

The occurrence of a liquid phase during combustion of larnite-rich rocks protolith is still an open debate: considering the ternary phase diagram CaF_2-Ca_2SiO_4-$CaSO_4$, the association Ca_2SiO_4-$CaSO_4$-$Ca_{10}(Si_3S_3O_{12})F_2$ (larnite-anhydrite-fluorellestadite) starts melting at ~ 1200 °C and the complete melting of anhydrite completes at ~ 1205 °C, leading Ca_2SiO_4-$Ca_{10}(Si_3S_3O_{12})F_2$-liquid assemblage [319]; studied on heating of fluorellestadite-brownmillerite assemblage showed a first melting from 1208 to 1193 °C, depending on the amount of brownmillerite [190]; experiments in

the system CaO-SiO_2-Al_2O_3-Fe_2O_3-SO_3-F with chemical compositions close to CSA cements and similar to larnite-rich rocks, highlighted a first melting point at 1180-1187 °C [190,204]. Therefore, larnite-rich rocks should have reached the melting point (1180-1200 °C) if low-P_2O_5 flamite occurs (Fig. 9.23), especially if is considered the occurrence of minor elements as P_2O_5, MgO, Na_2O, K_2O, TiO_2, etc. that act lowering the melting point of the system [3,7]. Furthermore, the occurrence of barite ($BaSO_4$), arcanite (K_2SO_4) and calciolangbeinite ($Ca_2K_2(SO_4)_3$), often on the boundaries between larnite and ternesite-silicocarnotite s.s. (tern-silc) [327,328], suggests the participation of a S-rich melt that was progressively enriching in all elements not retained in main crystal phases as ionic substituents, which during cooling crystallised S-rich alkali phases: the system Na_2SO_4-K_2SO_4-$CaSO_4$ starts melting at T ~ 800 °C and with KCl at T < 700 °C [7,8]; hence, during cooling calciolangbeinite, arcanite and aphthitalite ($(KNa)_3Na(SO_4)_2$) could crystallise from a sulphate-rich melt as interstitial phases, as commonly occurring in cement systems.

Considering the microtexture of brownmillerite and shulamitite, which always occur as euhedral prismatic and tabular crystals also forming nodular aggregates along with spinel, and the evidence of a fast cooling, they should have been in equilibrium with other phases and not reached a full melting: anhydrous cements are obtained at HT above the melting point, such as OPC at T ≥ 1338 °C (hatrurite-larnite-celite-brownmillerite), BC at T ≥ 1280 °C (larnite-mayenite-celite-brownmillerite) [7,8] and CSA cements at T ≥ 1249 °C (larnite-ye'elimite-brownmillerite-mayenite-celite) [190], followed by a quenching, leading a microtexture made of subhedral to euhedral calcium silicates crystals in a xenomorphic matrix of mainly brownmillerite, celite and mayenite [7,8,150].

Ternesite-silicocarnotite s.s. sometimes occurred in larnite-rich rocks, as in *YC2O* sample (Fig. 9.8; Table 9.1), as minor mineral with subhedral to euhedral crystals [122,329]. Its occurrence limits the combustion temperature from 1020 to ~ 1288 °C in open and close system, respectively: pure ternesite starts forming at ~ 1000 °C by the reaction $2Ca_2SiO_4 + CaSO_4 \rightarrow Ca_5(SiO_4)_2(SO_4)$, and decomposes by the reaction $Ca_5(SiO_4)_2(SO_4) \rightarrow 2Ca_2SiO_4 + SO_2 + \frac{1}{2}O_2 + CaO$. The latter reaction takes place depending on O_2 and SO_2 fugacity: considering operating conditions in OPC kiln (2% v/v O_2 [330] and from -2.5 to -4 of fSO_2 in $\log_{10}$ [318]), which should be comparable to CP events ones, ternesite upper stability temperature varies from 1164 to 1259 °C at low and high fSO_2, respectively [330].

The simultaneous occurrence of Fe^{3+} and low amount of Fe^{2+} as magnetite in spinel in larnite-rich rocks suggests an oxygen fugacity close to HM (hematite-magnetite) buffer [331], but previous study highlighted that the oxygen fugacity during CP in Hatrurim Basin varied from a location to another moving from condition above HM buffer, confirmed by essenite-hematite association in anorthite-diopside hornfels, to QFM (quartz-fayalite-magnetite) [130].

Ca-Ti-rich phases (Fe-rich perovskite, nataliukite ($Ca_4Ti_2Fe_2O_{11}$) and shulamitite) could be helpful in estimating the combustion temperature but requires the simultaneous occurrence of two Ti-rich phases that were found only for larnite-mayenite and larnite-gehlenite rocks [21]: according to the diagram $CaTiO_3$-$CaFeO_{2.5}$ the disordered cubic Fe-perovskite-Shulamitite paragenesis is stable at T > 1160 °C, representing the minimum temperature reached for larnite-rich rocks; whereas, disordered cubic Fe-perovskite-shulamitite paragenesis at T < 1160 °C transforms to orthorhombic Fe-perovskite-nataliukite or nataliukite-shulamitite, depending on the chemical

composition. However, brownmillerite-shulamitite paragenesis that is the most common in larnite-ye'elimite rocks is useless as geothermometer because does not have crystallographic changes at HT.

Punctual chemical investigation by EMPA highlighted a good agreement with bibliographic results on larnite-ye'elimite rocks [122], and elemental maps highlighted a zoning for spinel and fluorapatite: spinel often shows an Al-rich and Fe-rich core and rim, respectively; fluorapatite-ellestadite always highlights a P-rich core and S-Si-rich rim (fluorellestadite). Moreover, larnite crystals from *YC2O* have a chemical composition close to the pure dicalcium silicate with only a slight P_2O_5 content.

Crystal structure refinement was made on larnite using the Rietveld method on SXRPD pattern highlighting no significant changes in atomic positions and crystallographic parameters compared to larnite occurring in OPC or *BC* [169]. Quantitative texture analysis by NXRD showed no preferred orientation of larnite, suggesting no influence by the pristine limestone texture during the combustion and crystallisation of larnite.

Hydration veins are extremely common in larnite-rich rocks especially in the case of bodies of larnite-rich rocks inside KuPh1 carbonate Unit (*6BWO*) usually forming a complex stockwork of veinlets [13,28] (Fig. 5.22,9.3a,b). Hydration veins related to KuPh4 Unit, especially when related to larnite-rich rocks, often show an internal structure made of a central millimetric white part and brown borders rich in submillimetric black nodules (Fig. 9.1a,b,9.3a,b). Veins should be considered as little fractures in larnite-rich rocks formed during heating by the decarbonation of calcite and spurrite (~ 650-950 °C [332,333]) and volume shrinkage during fast cooling from HT. Calcite is always occurring and represents the main mineral of white parts, whereas in brown portions and black nodules is less abundant. Also other calcium carbonate polymorphs occur (vaterite and aragonite) but only in brown borders: these two minerals are less stable and tend to transform in calcite over the time, especially in the case of a temperature rise [334,335]. Isotopic studies on hydration veins claimed an interaction of CO_2, which is mainly from atmospheric and minor coming from the combustion gases, and calcium hydrated phases (portlandite, CSH and CA$\bar{S}$H phases) during recarbonation process [123]. U-Th dating highlighted a wide range of ages from 35 ka to > 450 ka, suggesting that hydration process continued developing over the time and probably started since after finishing the HT event [336]. Brown vein parts are made of hydrated minerals, such as CSH minerals (tobermorite 14Å, also called plomberite, and 11Å), aluminium hydroxide polymorphs (gibbsite and bayerite), calcium carbonate (calcite, aragonite and vaterite), katoite and ettringite, associated with low amount or less water-reactive phases, such as spinel, fluorapatite s.s. and shulamitite (Table 9.3). Shulamitite should react with water by the reaction $Ca_3TiAlFeO_8+5H_2O\rightarrow CaTiFe^{3+}AlO_8{\cdot}3H_2O+2Ca(OH)_2$ [34], but it is still occurring in hydrated veins, hence, could be considered as a low water-reactive phase. Despite ternesite has been reported in several larnite-ye'elimite rocks [20], as for *YC2O*, no ternesite occurred in hydration veins due to the interaction with water: ternesite has been considered as low or no water-reactive phase [7], however, recent studies figured out its moderately water-reactivity leading jennite, or in general CSH phases, gypusm and portlandite by the following reaction $3Ca_5(SiO_4)_2(SO_4) + 20H_2O \rightarrow Ca_9Si_6O_{18}(OH)_6{\cdot}8H_2O + 3CaSO_4{\cdot}2H_2O + 3Ca(OH)_2$ [337,338]. Furthermore, hydrated black nodules only occur inside brown hydrated parts revealing an enrichment in spinel that justifies the

dark colour: black hydrated nodules have the same texture (shape and size) and enrichment in spinel as the ones occurring inside anhydrous larnite-rich rocks. Therefore, brown hydrated parts should be considered as pristine larnite-rich rocks close to open fractures that undergone in hydration by the circulating water. On the other hand, white veins should be formed from precipitation of circulating pore solution in fractures resulting from the hydration of larnite-rich rocks: water coming from weathering interacts with anhydrous HT minerals (larnite, ye'elimite, anhydrite, hatrurite, etc.) leading a progressive conversion to hydrated crystal phases (CSH, CA$\bar{S}$H and CAH phases, aluminium hydroxides, portlandite, etc.) by the initial formation of amorphous gel phases, especially CSH and AH_3, resulting in high pH (~ 12) pore solution that can move inside pores and fractures. Consequently, the circulating Ca-rich pore solution mainly crystallises calcite and minor gypsum, ettringite and tobermorite because the majority of CSH, CAH and CA$\bar{S}$H and AH_3 minerals are mostly retained in brown vein portions.

The system C_2S-$C_4A_3\bar{S}$-$C\bar{S}$-H_2O could be used to predict the mineral association after early hydration time (~ 72 hydration days) [339]. Larnite-ye'elimite rocks could fall in two different minerals association fields only depending on ye'elimite content because anhydrite rarely occurs: kuzelite($Ca_4Al_2(OH)_{12}(SO_4)\cdot 6H_2O$)–CSH–stratlingite($Ca_4Al_2(OH)_{12}[AlSi(OH)_4]_2\cdot 2H_2O$)–katoite with high ye'elimite (~ 15wt.%); kuzelite-CSH-katoite-portlandite with medium to low ye'elimite (< 15wt.%). However, no kuzelite and stratlingite occurred in our sample and previous studies: lack of kuzelite, also called monosulfate phase [340], could be explained by an interaction with sulfate-rich solutions converting kuzelite into ettringite; whereas, stratlingite absence could occur in the case of higher availability of $Ca(OH)_2$ leading the formation of katoite and CSH gel [339]. Nevertheless, ettringite-katoite or katoite-gypsum associations that occur in our samples are not considered stable in the system C_2S-$C_4A_3\bar{S}$-$C\bar{S}$-H_2O; hence, more complex long-term reactions should be taken into account to explain mineral association in hydrated larnite-rich rocks: ettringite could react with CO_2 forming calcite, gypsum, gibbsite and water by the reaction $Ca_6Al_2(OH)_{12}(SO_4)_3\cdot 26H_2O+3CO_2 \rightarrow 3CaCO_3+3CaSO_4\cdot 2H_2O+2Al(OH)_3+23H_2O$ [341]; portlandite reacts with CO_2 forming calcite and water following the reaction $Ca(OH)_2 + CO_2 \rightarrow CaCO_3 + H_2O$ [341]; CSH minerals interacts with CO_2 producing calcite, amorphous silica and water as reported in the reaction $CSH + CO_2 \rightarrow CaCO_3 + SiO_2 + H_2O$ [341]. Moreover, SXRPD study on hydrated veins highlighted apophyllite and bulfoteinite as minor phases, suggesting fluorine and potassium activities in the circulating water [78], confirming a more complex and wide chemical composition of pore solution compared to OPC one [7].

9.3 – Conclusion

Larnite-ye'elimite rocks collected at Hatrurim Basin were deeply studied by both traditional and innovative techniques revealing important information on mineral assemblage, texture at different observation scales and crystallographic features.

Ye'elimite-larnite granofels represents a type of larnite-rich rock richer in sulphur as showed by ye'elimite occurrence. Ye'elimite-larnite granofels has microtextural features characterized by low crystal size and granoblastic texture with polygonal larnite, coarse euhedral fluorapatite, acicular-prismatic shulamitite, prismatic brownmillerite and subhedral spinel. Mineral assemblage of main minerals is quite the same among different samples with changes observed by SXRPD only on minor minerals occurrence, such as mayenite, ternesite and brownmillerite.

Larnite-rich rocks could not have reached the thermodynamic equilibrium considering the relation between bulk chemical composition and final mineral assemblage if are compared to bibliographic and thermodynamic data. However, previous experiments were made on pure chemical systems, hence the simultaneous effects of minor elements (e.g., P_2O_5, TiO_2, F, MgO, etc.) were not considered despite should strongly affect stability field of minerals. Furthermore, previous experiments in the CaO-SiO_2-Al_2O_3-SO_3-Fe_2O_3 system were performed on homogenous fine powder in controlled oven with also fixed atmosphere; while, larnite-rich rocks were formed during heating of limestone outcrops leading the influence of inhomogeneities during combustion (e.g., black submetallic nodules rich in spinel and brownmillerite-shulamitite crystals) that allow local changes in mineral assemblage.

Considering the mineral assemblage, the upper limit of combustion temperature should be $\leq$ 1220 °C, due to the stability of fluorellestadite as highlighted by EMPA and XRD analysis. However, the occurrence of a low-T melt seems to be confirmed by (i) the occurrence in several larnite-rich rocks of alkali sulphate phases as interstitial phases, as commonly occurring in OPC, and by (ii) experiments in the system CaO-SiO_2-Al_2O_3-Fe_2O_3-SO_3-F that highlighted the occurrence of a first melt at T > 1180-1187 °C. Flamite-larnite association in larnite-rich rocks could be used as a tool to estimate the minimum combustion temperature considering flamite P_2O_5 content: results revealed a wide temperature range with a maximum temperature of 1225 °C for low P_2O_5-rich flamite occurring in larnite-rich rocks.

Hydration veins inside larnite-rich rocks often show an internal structure with a central white part and brown borders also with a differentiation in the mineral assemblage: white parts are mainly composed of calcite and minor phases (tobermorite, ettringite and quartz); brown parts are made of no water-reactive phases (shulamitite, fluorapatite s.s. and spinel) and hydrated crystal phases ($Al(OH_3)$ polymorphs, CSH minerals, ettringite, calcium carbonate polymorphs, gypsum and katoite) plus black rounded nodules enriched in spinel and hydrated minerals. White parts represent pristine fractures formed both during heating of limestone and shrinkage during cooling, which allowed a water-rock interaction path leading the hydration of anhydrous larnite-rich rocks: the resulting Ca-rich circulating pore solution led the crystallisation and infilling of fractures, producing white calcite-rich parts. Moreover, complex late reactions involving first-stage hydration minerals and CO_2 occurred leading gypsum, calcium carbonate polymorphs and quartz crystallisation.

Chapter 10
Synthesis of *green-cements*

This chapter is focused on the results of laboratory-made *green-cements* synthetised starting from two quite different raw meals: (i) *RM* raw meal, representing the grinded powder of phosphatic and gypsum-rich calci-mudstone belonging to Ghareb Formation collected at Rotem Amfort Mine at Stop-8 in Hatrurim Basin (see section 5.8; sample *RM* in Table 7.1); (ii) *BC* raw meal, corresponding to Belite Cements doped with low-amount of sulphur (< 3.5wt.%; sample *BC* in Table 7.3) and with higher amount of Fe_2O_3 compared to ordinary BCs [148], which could be considered as High Ferrite Belite Cement sulphur doped [223,224].

The choice of selecting these two raw meals was driven by the chance of designing new types of doped *green-cements* for both reducing the CO_2-footprint of cement manufacture and increasing the recovery of industrials wastes: (i) *RM* represents a huge volume waste coming from the phosphatic mine activity, which could lead a sulphur pollution in surface water streams (< 250 mg/l following Italian laws, D.Lgs 152/06) due to the gypsum occurrence (up to 15wt.% in bulk rock) that is high soluble; (ii) *BC* belongs to sulphur doped BCs, being similar to BCSA cements that require higher amount of Al_2O_3 compared to OPC, but the limited availability of suitable Al-sources limits their production, therefore, a partial replacement of Al_2O_3 by Fe_2O_3-rich sources or wastes could be considered as a solution thank to the complete and partial solid solution of brownmillerite ($Ca_2(Al_xFe_{1-x})_2O_5$) and ye'elimite ($Ca_4(Al_{1-x}Fe_xO_4)_6(SO_4)$), respectively.

Samples were heated at different temperatures from 700 to 1350 °C and studied by means of RLM with Nital etching, XRD with RQPA and SEM-EMPA, highlighting mineral assemblage and microtextural changes occurring over the temperature. Only *RM* was studied with *in-situ* experiments at synchrotron scale facilities from room temperature to 1244 °C, revealing metamorphic reactions and changes in crystal phase assemblage.

Ex-situ heating experiments on *RM* rock fragments (labelled as *RF*) were performed trying to highlight the effects of grain size and natural anisotropies on mineral assemblage, abundances of crystal phases, crystallographic parameters and microtexture after heating. Furthermore, results of *RM* and *RF* led a direct comparison with natural larnite-ye'elimite rocks helping in clarifying heating process occurred in Hatrurim Basin due to the similar protoliths and heating conditions.

Moreover, mineral assemblage, abundance of crystal phases, crystallographic parameters, microstructural features and quantitative texture analysis were obtained by means of both conventional and innovative analytical techniques, leading detailed information useful for a better understanding of processes occurring during heating and cooling for *green-cements*. A summary of labels and analytical techniques performed on all samples is reported on Table 7.7.

10.1 – Results

Table 10.1 reports cement raw meal parameters (LSF, AR and SR) which are be useful to predict the behaviour during heating, such as amount of melt at HT, free-lime content and amount of silicate and Fe-Al-rich phases: *RM* has higher amount of LSF compared to *BC* leading the occurrence of free-lime at high temperature; AR is almost similar among the two ram meals, whereas, SR is lower for *BC* suggesting higher amount of liquid phase at the same heating temperature and a lower amount of silicate phases.

Parameters / Sample	***RM***	***BC***
LSF	1.22	0.75
AR	1.36	1.34
SR	2.03	1.79

Table 10.1 – Raw meal parameters calculated for *BC* and *RM* mixtures using XRF values (Table 7.1,3) [7].

LXRPD results of *ex-situ* experiments related to *BC* raw meal are reported Fig. 10.1,2 highlighting changes on the mineral assemblage during heating:

(i) calcite starts decomposing at T < 700 °C and completely turned in CaO and CO_2 in the range 700-800 °C;

(ii) larnite is stable at T > 700 °C and continuously increased over the entire temperature range, excepted between 1000-1100 °C when ternesite crystallised;

(iii) larnite represented the only dicalcium silicate polymorphic occurring in all *BC* samples;

(iv) brownmillerite and srebrodolskite occurred at T > 700 °C; the latter was stable till 1250 °C with a strong increase at T ~ 1000 °C, linked with the hematite consumption, followed by a gradual reduction related to the increase of brownmillerite;

(v) celite crystallised at T > 700 °C and slowly reduced at T > 900 °C along with anhydrite crystallising orthorhombic ye'elimite;

(vi) mayenite crystallised at T > 700 °C and at T > 1000 °C reacted with anhydrite to crystallise ye'elimite, which the latter reached its maximum content at 1000 °C. Mayenite reappeared at 1200 and 1350 °C as minor crystal phase;

(vii) periclase occurred only after the complete calcite decomposition and did not react with other phases even at high temperature;

(viii) k-feldspar was an ever-present crystal phase till 1250 °C.

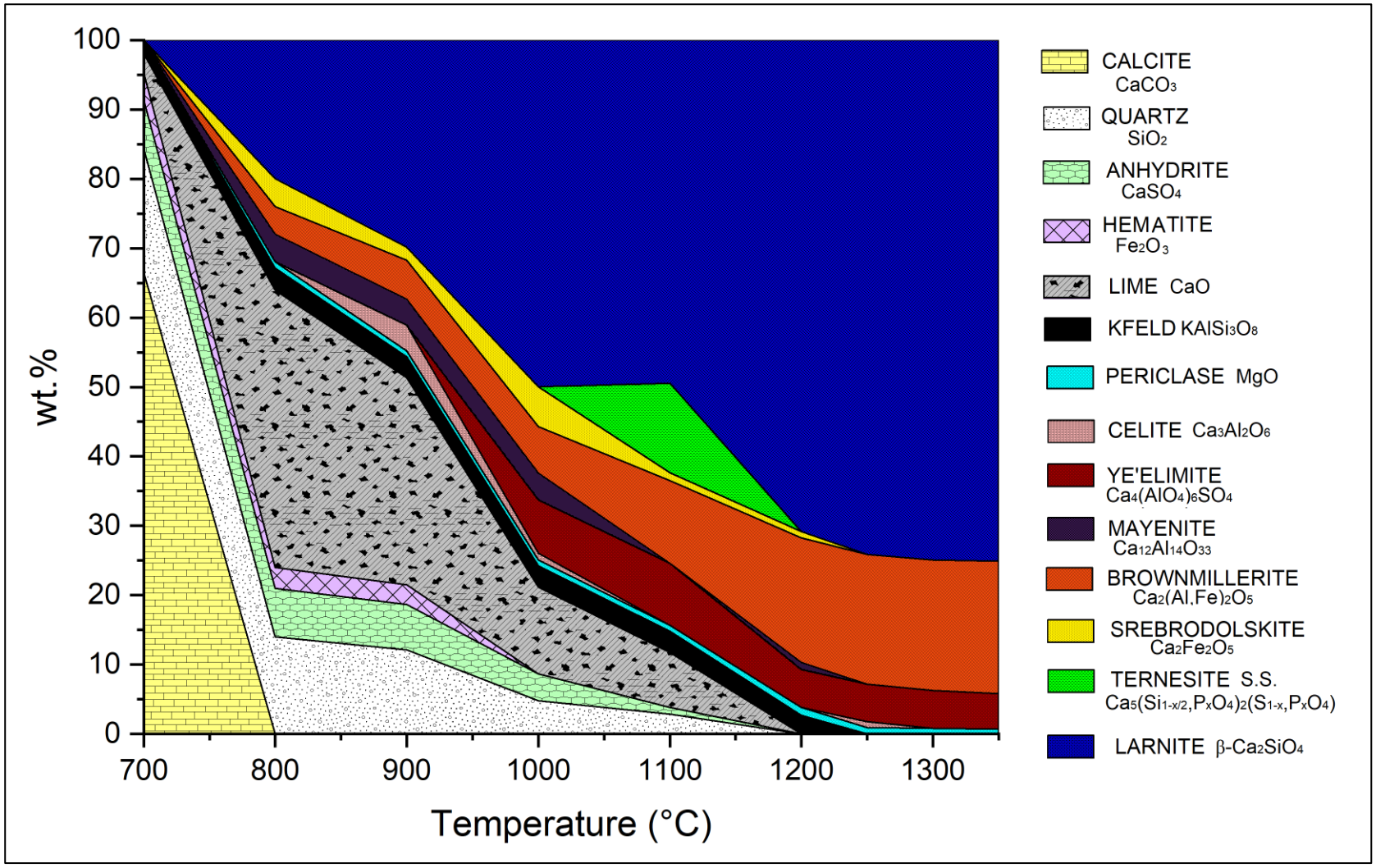

Fig. 10.1 – RQPA results for *ex-situ* experiments on *BC* sample at different heating temperature (700, 800, 900, 1100, 1200, 1250, 1300, 1350 °C), highlighting wt.% of occurring crystal phases.

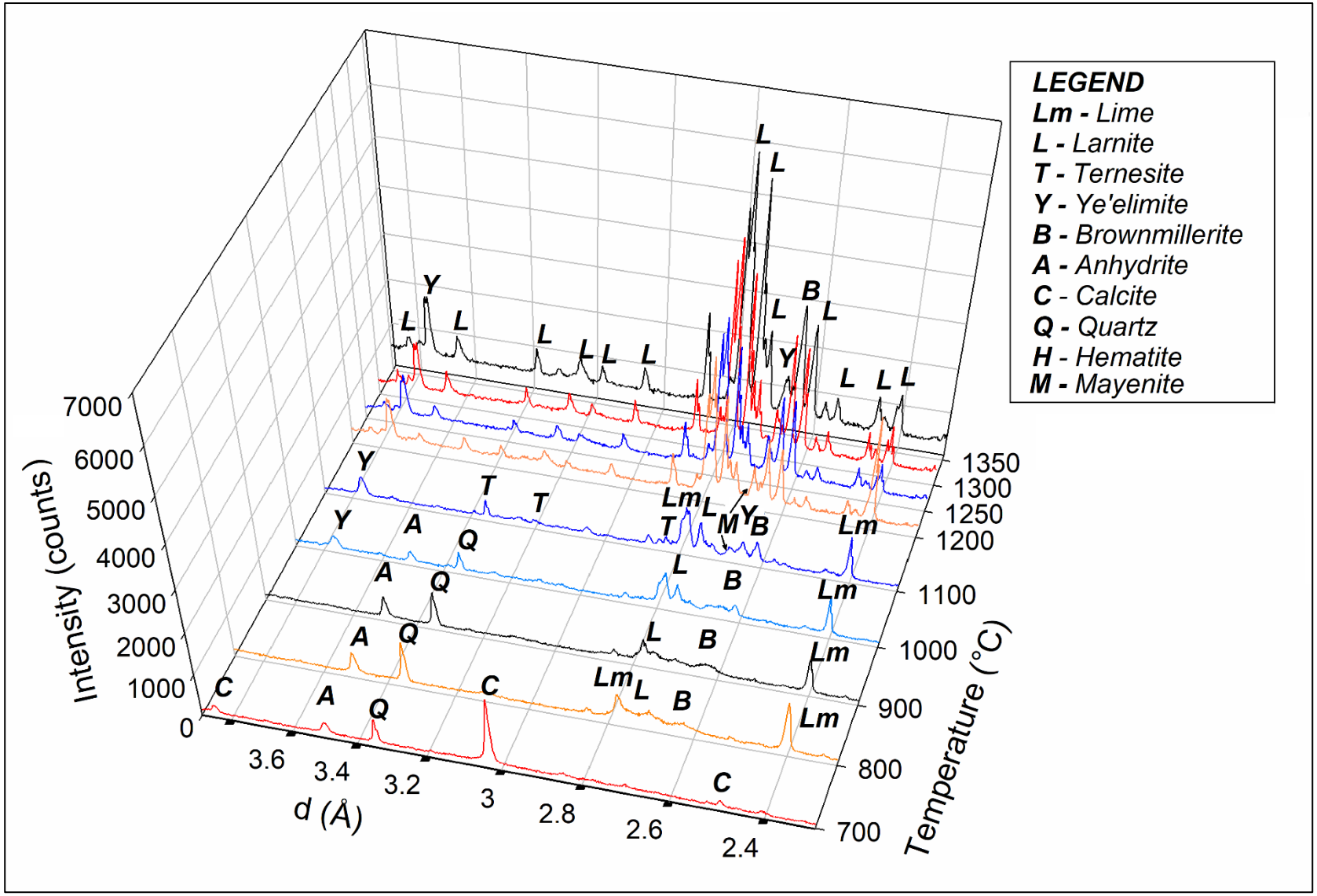

Fig. 10.2 – *Ex-situ* LXRPD patterns of *BC* sample heated at different temperatures reported on Y axes; main Bragg peaks of occurring crystal phases are highlighted.

Ex-situ results on *RM* raw meal highlighted several important features (Fig. 10.3,4): (i) β-C_2S was already stable at ~ 700 °C along with common OPC phases occurring during heating (C_2F, C_4AF, $C_5S_2\bar{C}$, C_2AS, $C_{12}A_7$, anhydrite, lime and remaining calcite) plus fluorapatite-ellestadite s.s.; (ii) $C_5S_2\bar{S}$ appeared at 1000 °C and increased till 1200 °C, leading the decrease of β-C_2S, later followed by a break down at > 1200 °C; (iii) C_2AS and C_3A were transient minor phases stable at 700-800 °C and 800-1000 °C, respectively; (iv) C_4AF gradually increased till 1100 °C, strictly related to the consumption of C_2F, later remaining with an almost constat content; (v) $C_4A_3\bar{S}$ is stable at T > 1000 °C, increased till 1200 °C, followed by a decrease up to 1250 °C that led the grow of $C_{12}A_7$; (iv) fluorapatite-ellestadite s.s. increased up to 1000 °C, followed by a slight reduction before 1200 °C and a steeper one from 1200-1250 °C; (v) C_3S and α'$_H$-C_2S started being both stable at T > 1200 °C, with the breakdown of $C_5S_2\bar{S}$, reaching their maximum content at T ~ 1250 °C and later significatly decreasing at higher temperatures.

In Fig. 10.3 are reported all *RM ex-situ* patterns highlighting the main Bragg peaks of crystal phases, revealing the phase assemblage during heating: the complete breakdown of calcite occurred at T > 700 °C, observed by the disappearence of its main Bragg peaks (~ 3.03 Å) and the intensity increase of lime ones (~ 2.4 and 2.8 Å); ye'elimite and ternesite grow at 1100 °C revealed by the rise of their distinctive peaks at 3.75 Å and 3.4-3.2 Å, respectively.

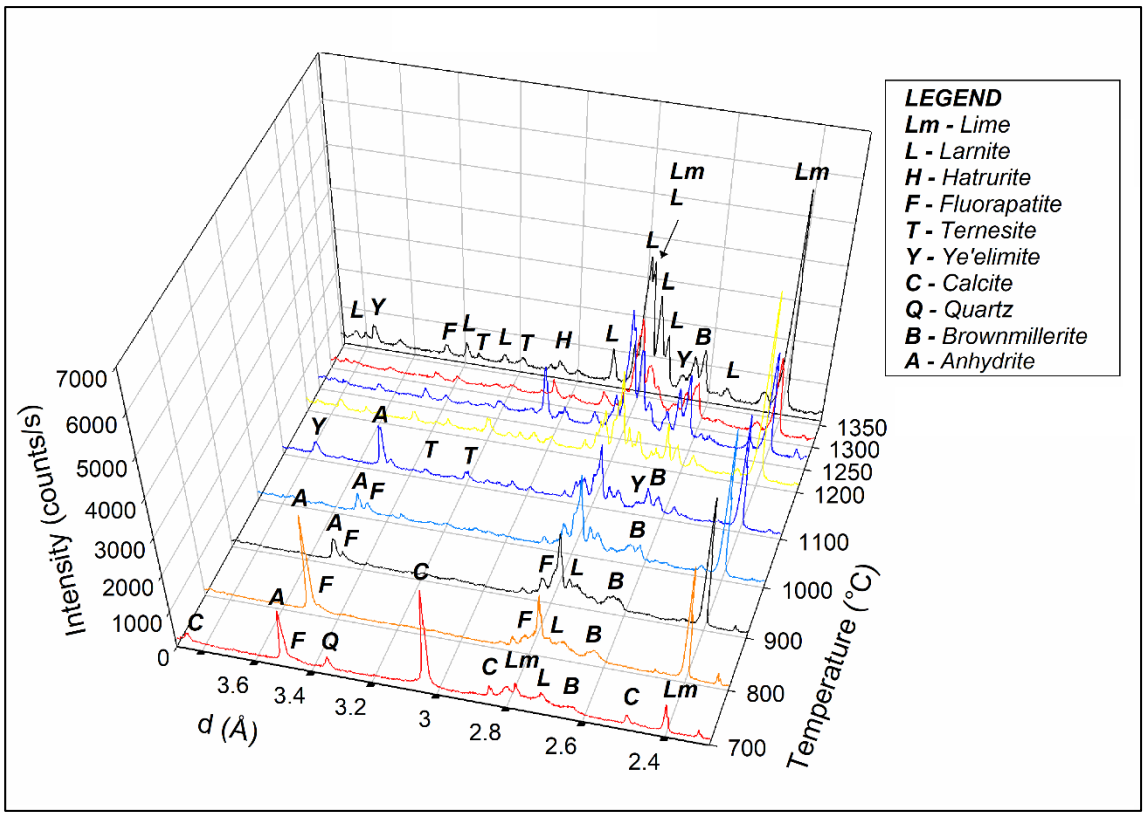

Fig. 10.3 – Ex-situ LXRPD patterns of *RM* sample previously heated in pellets at different temperatures reported on Y axes; main Bragg peaks of major crystal phases are highlighted.

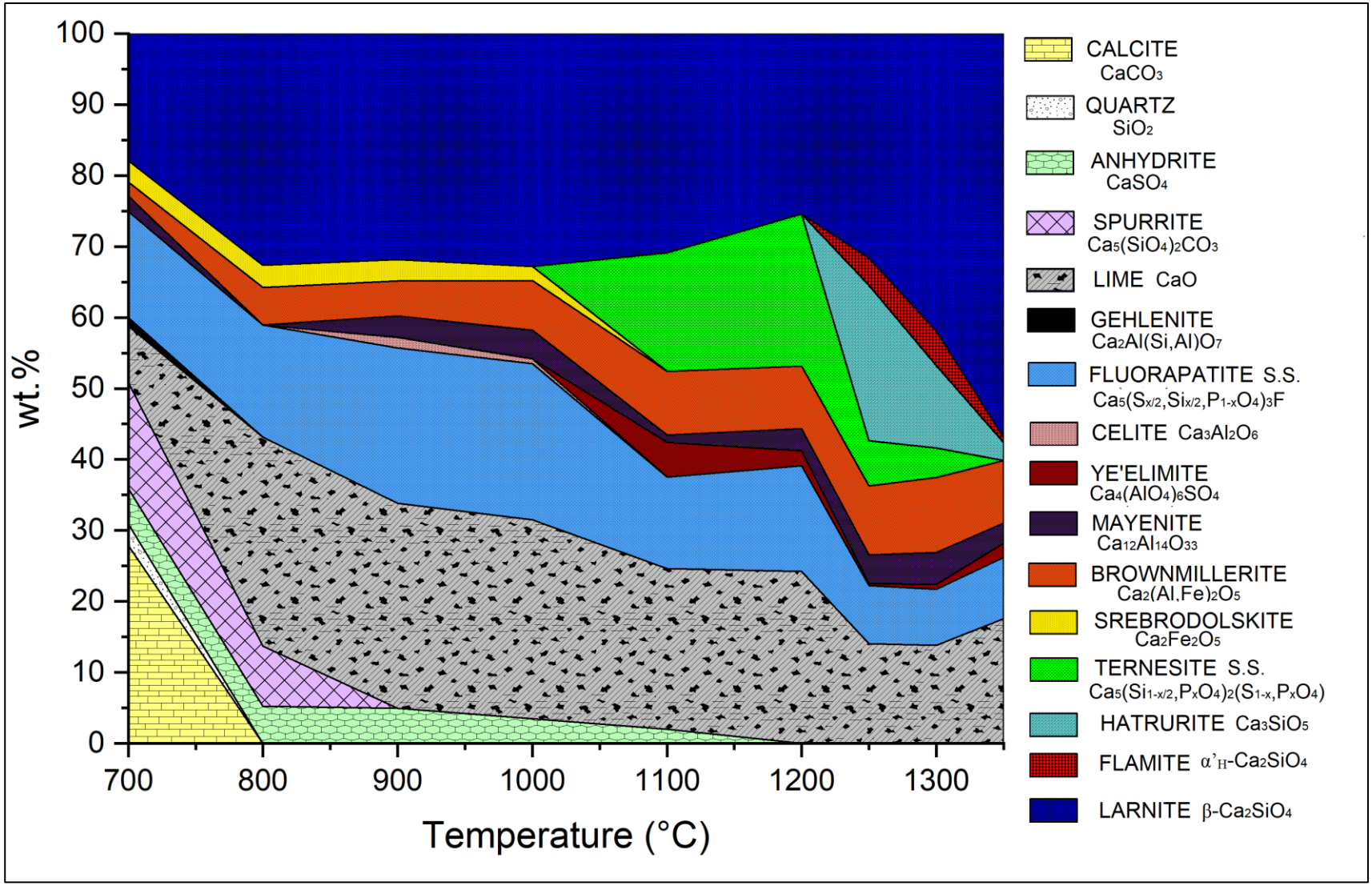

Fig. 10.4 – RQPA results for *ex-situ* experiments on *RM* sample at different heating temperatures (700, 800, 900, 1100, 1200, 1250, 1300, 1350 °C), highlighting wt.% of occurring crystal phases.

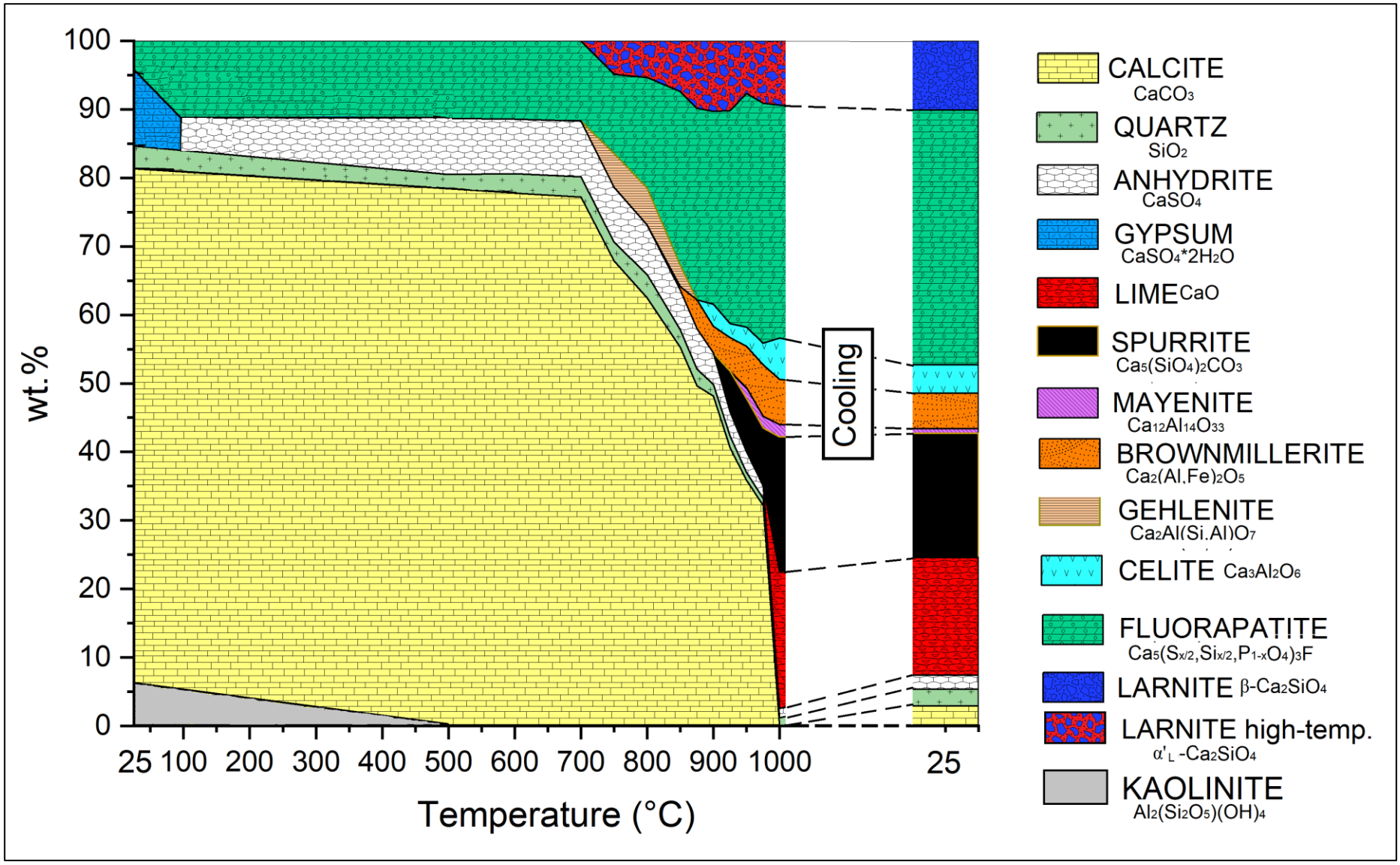

Fig. 10.5 – RQPA results for *in-situ* experiments on *RM* sample at different temperature from room temperature to 1000 °C and at 25 °C after cooling performed at MCX beamline at Elettra synchrotron.

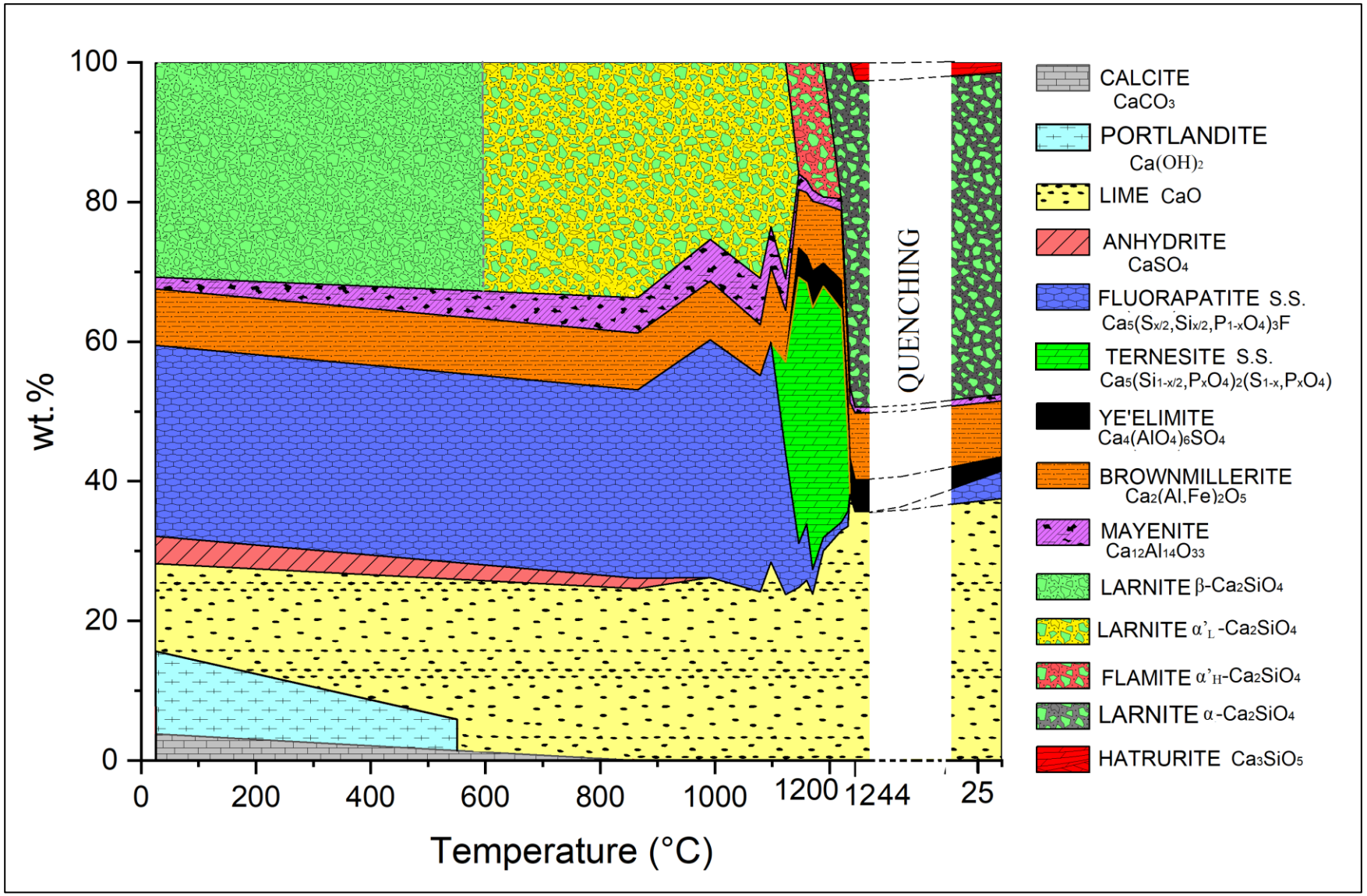

Fig. 10.6 – RQPA results for *in-situ* experiments on *RM* sample continuously heated without stabilisation time before data collection, and fast data collection (2 min) performed at ID22 beamline at ESRF synchrotron facility.

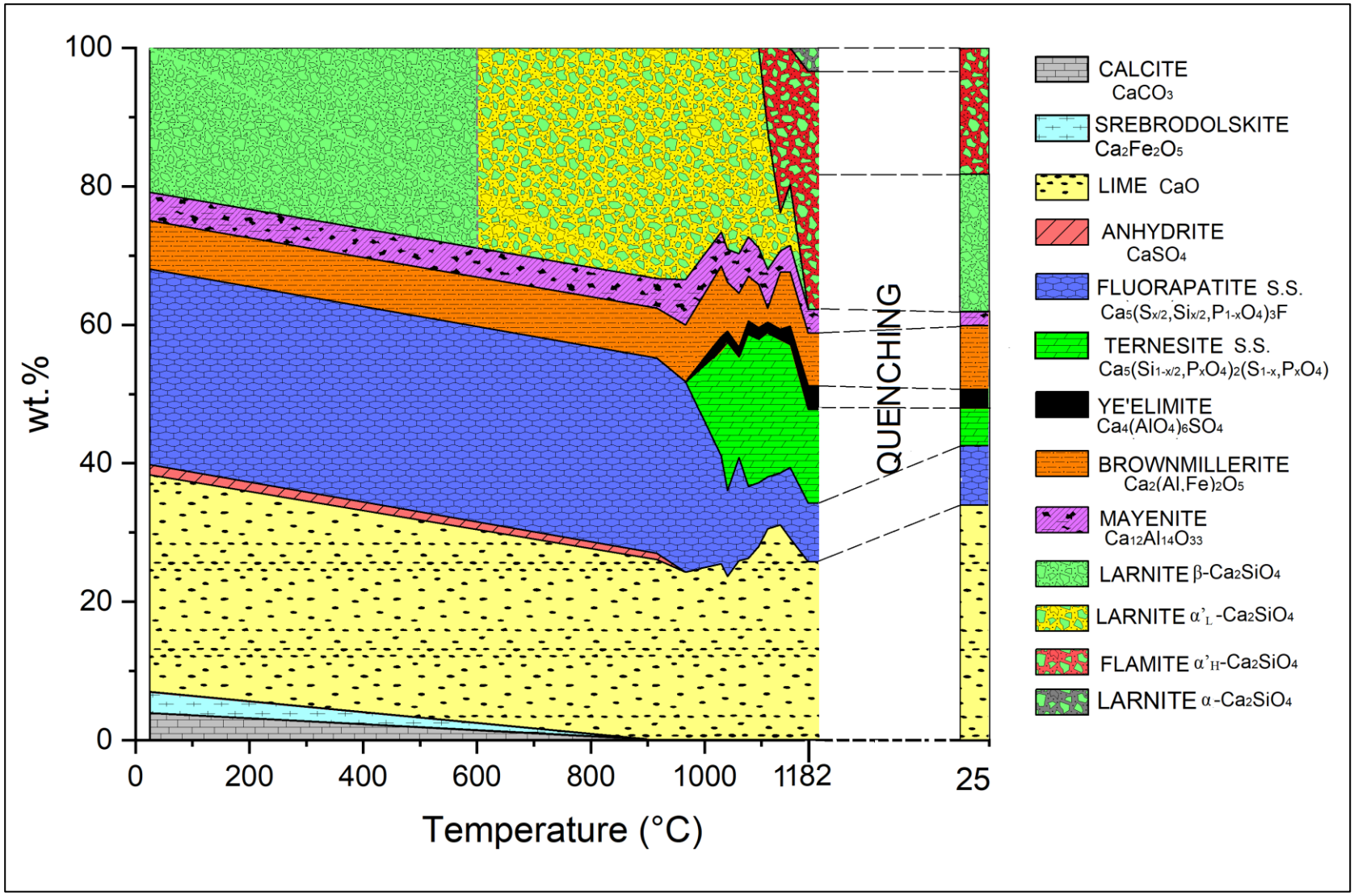

Fig. 10.7 – RQPA results for *in-situ* experiments on *RM* sample at ID22 heated with ramps and stabilisation time before data collection (10 min) performed at ID22 beamline at ESRF synchrotron facility.

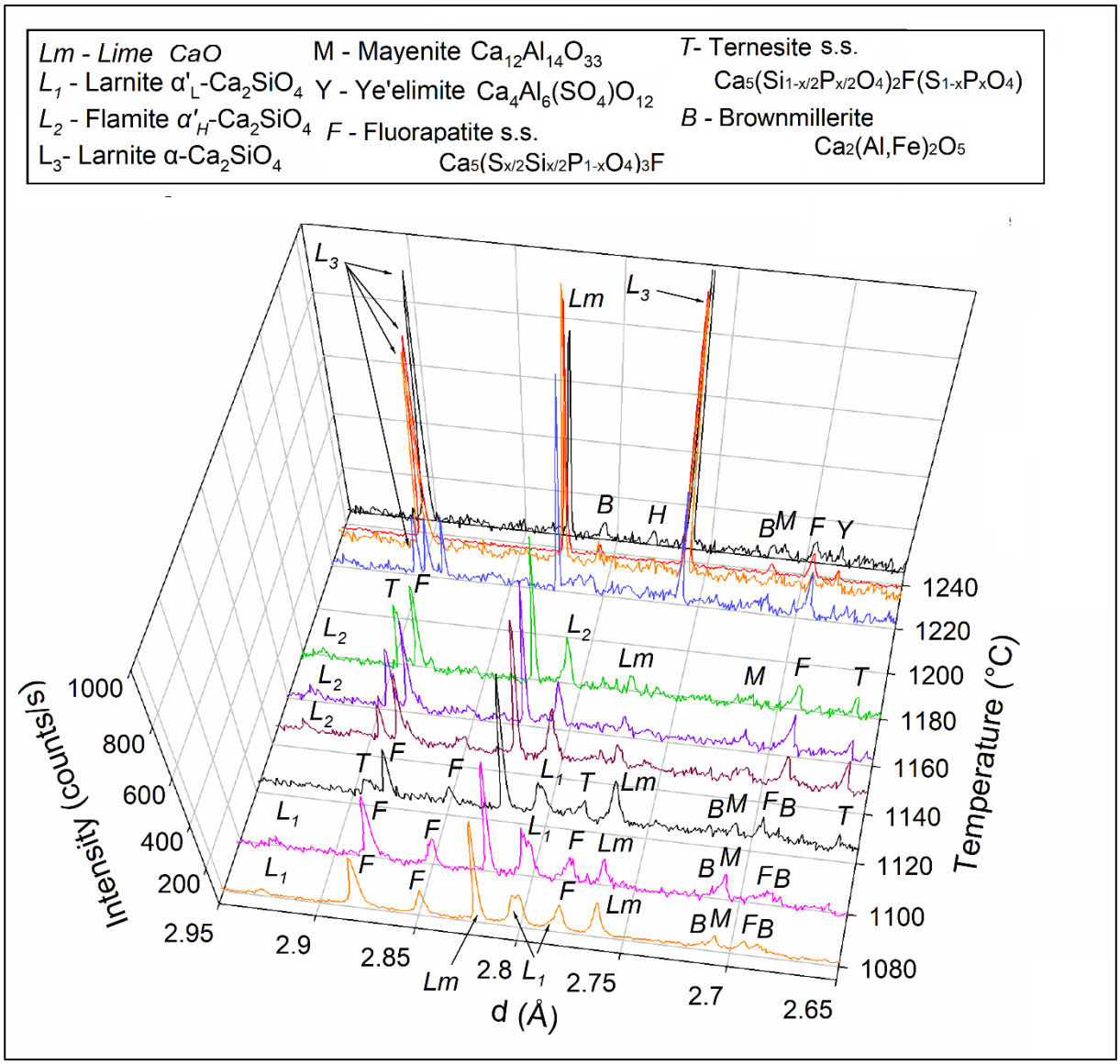

Fig. 10.8 – In-situ SXRPD patterns of *RM* raw meal heated in Pt-capillary at different temperature reported on Y axes and no stabilisation time was used before data collection; main Bragg peaks of major crystal phases are highlighted.

In-situ HT experiment from RT to 1000 °C on *RM* raw meal showed metamorphic reactions and polymorphic transition occurring when phosphatic-gypsum-rich limestone (Ghareb Fm.) is heated as a powder (Fig 10.5). No change or particular reaction occurred up to 700 °C, excepeted the gypsum → anhydrite transition and clay minerals break down [342,343]. However, several important changes occurred from 700 to 1000 °C:

(i) dicalcium silicate started crystallising as α'$_L$-C_2S polymorph at 700-750 °C, according with bibliographic data [7], and gradually increased by the reaction between lime and β-quartz at higher temperature;

(ii) calcite continuosly decreased and completely decomposed at 975-1000 °C, when unreacted free lime was detected;

(iii) fluorapatite, which should be considered as a solid solution with from pure apatite to ellestadite (Fap-ell), grew over the entire temperature range, especially from 700 to 850 °C, by consuming α'$_L$-C_2S and anhydrite, and/or quartz, lime and anhydrite;

(iv) gehlenite was a minor and transient crystal phase stable till 900 °C, after which celite crystallised. Whereas, mayenite and brownmillerite occurred at T > 950 °C and > 875 °C, respectively;

(v) spurrite was stable from 900 °C and steeply grew till 1000 °C representing a major constituent.

During cooling, the polymorphic transition from α'_L-C_2S to β-C_2S and a partial recarbonation of lime to calcite occurred. Furthermore, quartz was still detected despite the capillary lasted around 17 min at 1000 °C before quenching. The final mineral assemblage at room temperature is lime, larnite, anhydrite, spurrite, mayenite, celite, brownmillerite, fluorapatite-ellestadite s.s., quartz, anhydrite and calcite.

HT synchrotron *in-situ* experiments were performed on *RM* raw meal, previously heated at 900 °C for 2 hours for reducing CO_2 during heating, with two different experimental set-ups: (*i*) sealed Pt-capillary heated at different temperatures with 10 min of stabilising time before data collection for improving the achievement of thermodynamic equilibrium and making a direct comparison with *ex-situ* results (Fig. 10.7); (*ii*) sealed Pt-capillary heated up to ~ 1250 °C without a stabilising time before data collection attempting to reproduce cement kiln heating conditions (Fig. 10.8).

In-situ experiment performed with the stabilising time pointed out seven main important features: (i) SXRPD showed the occurrence of minor amount of low crystalline calcite even after an heating at 900 °C, whereas, *ex-situ* LXRPD did not showed calcite content from 800 °C (Fig. 10.3,4); (ii) fluorapatite-ellestadite s.s. showed the same trend of *ex-situ* experiments with a first steep decrease from 966 to 1029 °C strictly related to the crystallisation of ternesite and ye'elimite, followed by a gradual reduction till 1182 °C; (iii) ternesite, after its crystallisation at T > 966 °C, increased up to 1111-1133 °C consuming Fap-ell and C_2S, after which decomposed even during cooling (~ 1182 °C) halving its wt.%; (iv) α'_L-C_2S decreased during the grow of ternesite and turned into α'_H-C_2S from 1111-1150 °C, whereas at T > 1150 °C only α'_H-C_2S and α-C_2S were stable; (v) flamite (α'_H-C_2S) was found even after quenching from HT with a wt.% major than only α-C_2S one at HT, whereas, *ex-situ* experiments showed the occurrence of flamite only at T > 1200 °C with a slow cooling; (vi) srebrodolskite and anhydrite reduced and disappeared at 916 and 966 °C, respectively, and no celite and gehlenite occurred as minor phases; (vii) brownmillerite and mayenite remained stable over the entire explored temperature window, but the latter showed a slight reduction starting from 1060 °C related to ye'elimite crystallisation.

In-situ experiments performed without a stabilisation time before data collection highlighted results comparable to *ex-situ* ones: (i) till 1098 °C the mineral assemblage is composed of lime, mayenite, brownmillerite, fluorapatite-ellestadite s.s., α'_L-C_2S and minor amount of anhydrite; (ii) ternesite crystallised at T 1098-1123 °C and fastly increased till 1170 °C, following a gradual reduction ending with the total decomposition at 1232-1235 °C; (iii) ye'elimite appeared at 1123-1146 °C leading mayenite consumption, and from 1244 °C to room temperature decreased; (iv) Fap-ell strongly decreased after stabilisation of ternesite and ye'elimite, completely disappeared when hatrurite occurred at T 1235-1244 °C, and finally re-crystallised during cooling; (v) α'_L-C_2S firstly turned into α'_H-C_2S from 1123 to 1146 °C, at T > 1189 °C definitly changed in α-C_2S, and after queching only α-C_2S occurred with no α'_H or β-C_2S modifications; (vi) hatrurite started

crystallising from 1235-1244 °C, which is in good agreement with *ex-situ* results, and remained stable during cooling.

Ex-situ experiments on *RM* fragments (labelled as *RF*) were performed at different heating temperatures (900, 1200, 1250 and 1350 °C) leading a direct comparison of mineral assemblage in *RM* pellets heated at the same temperatures and natural larnite-ye'elimite rocks (Table 10.2). At 900 °C no big changes occurred compared to *RM* one, excepted for twice larnite content, lower lime and fluorapatite-ellestadite, and the occurrence of gehlenite, hematite and perovskite as minor crystal phases. *RM* fragments heated at 1200 °C showed two main colours and with quite different mineral assemblages (Table 10.2):

(i) *RFa* sample revealed a light brown homogenous colour (Fig A1a) with a mineral assemblage close to *RM* heated at 1300 °C, with a high content of hatrurite, the occurrence of both larnite and flamite polymorphs and the lack of ternesite (Fig. 10.9). Furthermore, fluorapatite-ellestadite s.s. and ye'elimite wt.% occurred as minor crystal phases;

(ii) *RFb* sample showed homogenous dark colour (Fig. A2a) and a mineral assemblage similar to *RM* heated at 1200 °C, excepted for the occurrence of minor minerals as rankinite (C_3S_2), gehlenite, wollastonite (CS), flamite and anhydrite (Fig. 10.10). The wt.% of crystal phases is different compared to *RM*, especially for the increase of ye'elimite and lower content of fluorapatite-ellestadite s.s..

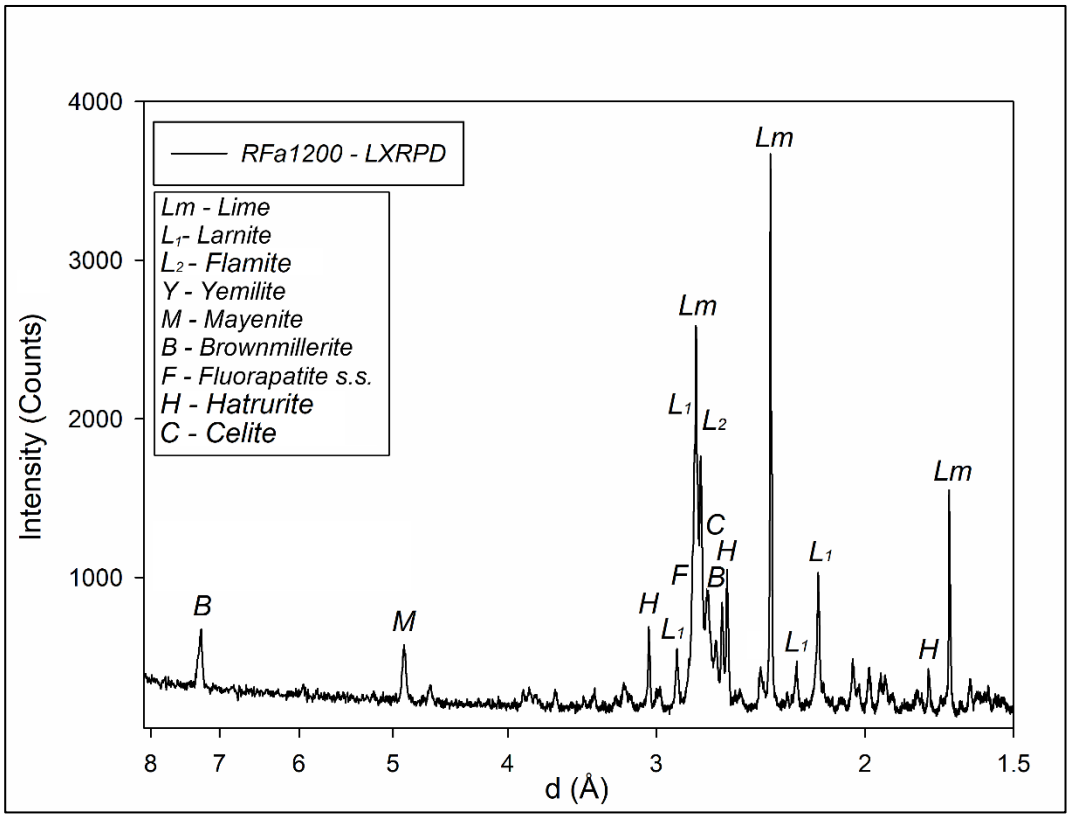

Fig. 10.9 –LXRPD patterns of *RM* fragment heated at 1200 °C (*RFa*); main Bragg peaks of major crystal phases are highlighted.

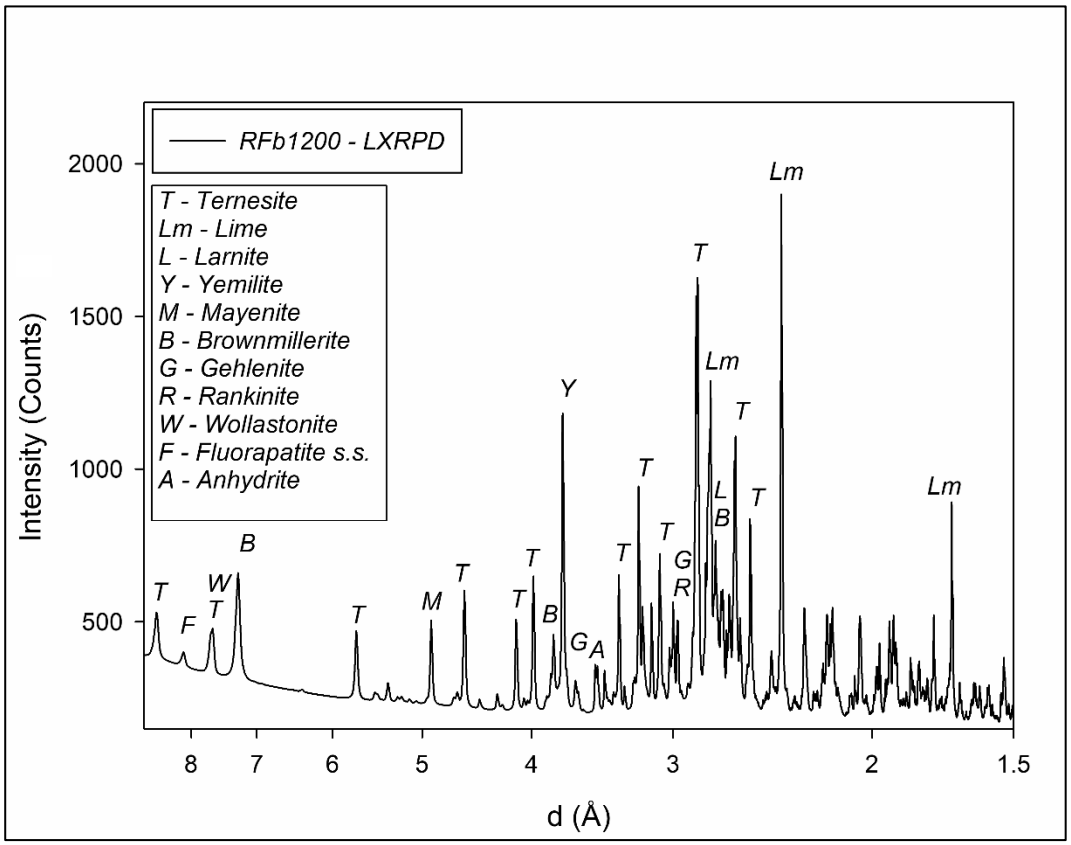

Fig. 10.10 –LXRPD patterns of *RM* fragment heated at 1200 °C (*RFb*); main Bragg peaks of major crystal phases are highlighted.

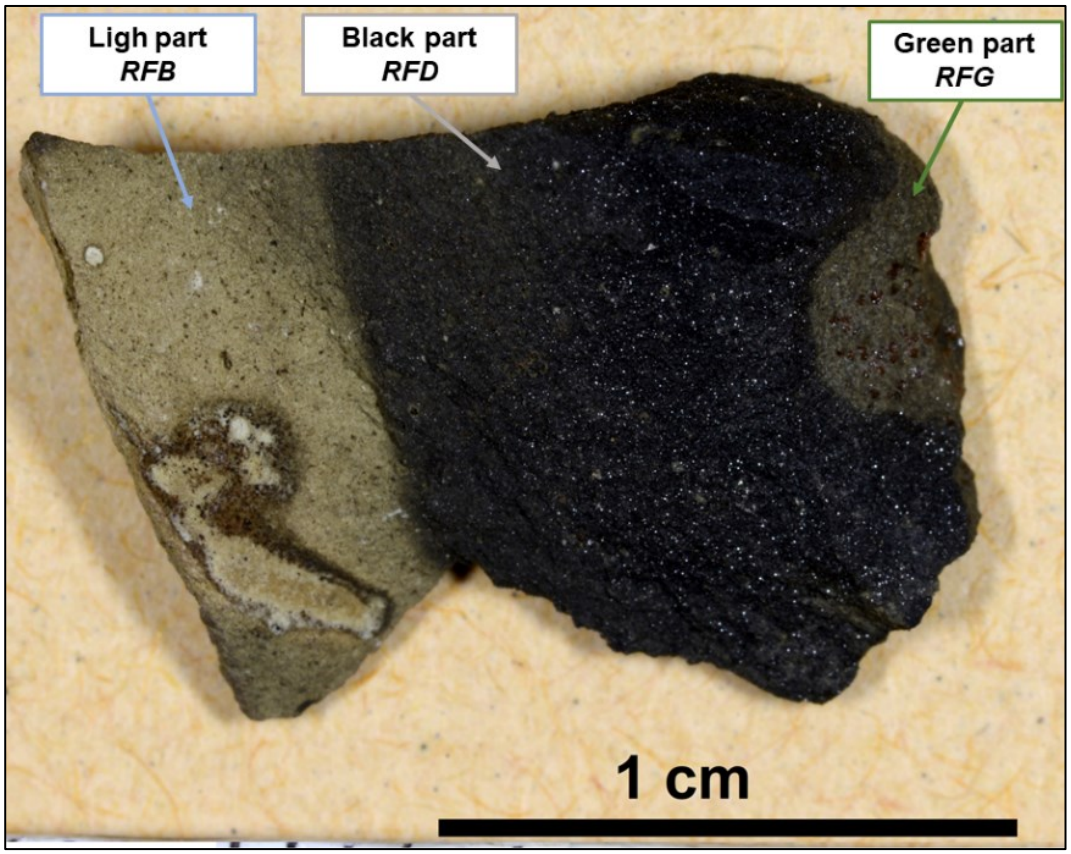

Fig. 10.11 – *RM* rock fragment heated at 1250 °C for 4 h at laboratory scale; three different coloured parts are highlighted and labelled: light brown parts (*RFB*) with low crystal size and sparce black micrometric crystals; homogenous black parts with coarser crystal size (*RFD*); green parts made of rounded to rhombic orange crystals with < 200 μm in a green matrix.

RM fragments heated at 1250 °C often showed sharp internal divisions made of three different coloured parts (light green, dark and green parts) that revealed changes in mainly calcium silicate phases occurrence and abundance (Fig. 10.11, Table 10.2):

(i) *RFB* part represents the most common part of heated fragments with light green colour, homogenous low crystal size with sparce micrometric black spots. Larnite, flamite, mayenite, brownmillerite, fluorapatite-ellestadite s.s. is the mineral assemblage, which is different compared to *RM* heated at 1250 °C due to the lack of ye'elimite, hatrurite, ternesite and lime;

(ii) dark coloured parts are labelled as *RFD* with and mineral assemblage similar to *RFB*, excepted for hatrurite occurrence, high fluorapatite-ellestadite s.s. content and lack of flamite. *RFD* has a higher crystal size compared to *RFD*;

(iii) *RFG* represents green parts inside *RFD*, with submillimetric rounded to pseudorhombic dark orange crystals. Hatrurite, larnite, brownmillerite, mayenite, fluorapatite-ellestadite s.s. is the mineral assemblage, which is close to *RFD* with low brownmillerite content.

Afterwards, no lime occurred in all *RF* samples heated at 1250 °C (Table 10.2) suggesting higher SiO_2 content that led an increase in calcium silicate phases (larnite, flamite and hatrurite) associated with a slight increase in Al_2O_3 allowing higher amount of mayenite compared to *RM ex-situ* results.

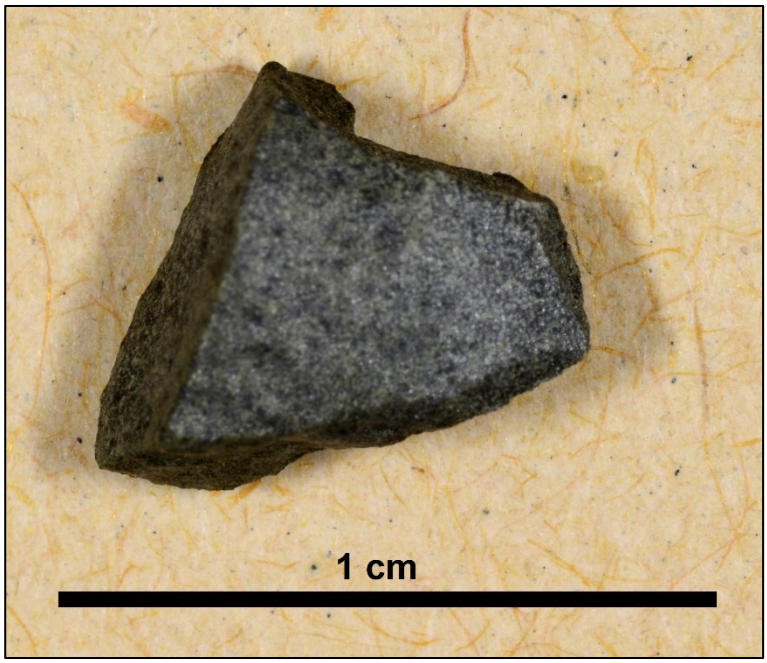

Fig. 10.12 – *RM* rock fragment heated at 1350 °C for 4 h at laboratory scale (*RF1350*), showing a homogenous texture, dark colour and lower porosity compared to other rock fragments heated at lower temperatures.

RM fragments heated at 1350 °C revealed a homogenous texture with black colour, low crystal size and densification, confirmed by the increase in hardness during grinding. Mineral assemblage and abundances of phases are close to *RM* pellets heated at 1350 °C, excepted the lack of ye'elimite, lime and lower amount of fluorapatite-ellestadite s.s..

Heating Temperature	***900 °C***	***1200 °C***		***1250 °C***			***1350 °C***
Sample Name / Mineral	***RF900***	***RFa1200***	***RFb1200***	***°RFB1250***	****RFG1250***	***$ RFD 1250***	***RF1350***
Lime CaO	3.37(.12)	15.15(.12)	11.33(.10)	*n.d.*	*n.d.*	*n.d.*	*n.d.*
Larnite β-Ca_2SiO_4	66.46(.49)	37.95(.38)	18.65(.40)	44.13(.42)	47.22(.79)	60.48(.43)	65.49(.43)
Flamite α'_H-Ca_2SiO_4	*n.d.*	14.86(27)	6.62(.39)	36.01(.56)	*n.d.*	4.54(.25)	9.30(.35)
Hatrurite Ca_3SiO_5	*n.d.*	12.28(.25)	*n.d.*	*n.d.*	32.52(.57)	9.13(.28)	4.66(.35)
Gehlenite $Ca_2Al_2SiO_7$	1.47(.18)	*n.d.*	3.39(.19)	*n.d.*	*n.d.*	*n.d.*	*n.d.*
Wollastonite $CaSiO_3$	*n.d.*	*n.d.*	3.78(.21)	*n.d.*	*n.d.*	*n.d.*	*n.d.*
Rankinite $Ca_3Si_2O_7$	*n.d.*	*n.d.*	2.02(.29)	*n.d.*	*n.d.*	*n.d.*	*n.d.*
Anhydrite $CaSO_4$	*n.d.*	*n.d.*	0.90(.21)	*n.d.*	*n.d.*	*n.d.*	*n.d.*
Ternesite $Ca_5(SiO_4)_2SO_4$	*n.d.*	*n.d.*	28.40(.27)	*n.d.*	*n.d.*	*n.d.*	*n.d.*
Fluorapatite $Ca_5(Si_{x/2}, S_{x/2}, P_{1-x}O_4)_3F$	14.71(.35)	2.28(.14)	5.67(.22)	1.26(.14)	11.34(.44)	9.81(.20)	0.60(.16)
Brownmillerite $Ca_2(Al,Fe)_2O_5$	8.92(.20)	11.09(.17)	9.48(.21)	8.43(.16)	2.33(.24)	7.56(.15)	9.27(.20)
Ye'elimite $Ca_4(AlO_2)_6SO_4$	*n.d.*	0.21(6)	7.14(.17)	*n.d.*	*n.d.*	*n.d.*	*n.d.*
Mayenite $Ca_{12}Al_{14}O_{33}$	*n.d.*	4.42(.12)	1.52(.13)	10.17(.17)	6.59(.33)	8.50(.12)	10.68(.18)
Celite $Ca_3Al_2O_6$	*n.d.*	1.77(9)	*n.d.*	*n.d.*	*n.d.*	*n.d.*	*n.d.*
Quartz α-SiO_2	0.45(8)	*n.d.*	*n.d.*	*n.d.*	*n.d.*	*n.d.*	*n.d.*
Hematite Fe_2O_3	0.68(8)	*n.d.*	*n.d.*	*n.d.*	*n.d.*	*n.d.*	*n.d.*
Perovskite $CaTiO_3$	3.94(.15)	*n.d.*	*n.d.*	*n.d.*	*n.d.*	*n.d.*	*n.d.*
Rexp	6.51	6.57	6.24	6.48	10.12	6.49	6.44
Rwp	13.99	10.90	12.59	9.40	12.04	9.22	9.60
GoF	2.15	1.66	2.02	1.45	1.19	1.42	1.49

Table 10.2 – RQPA results for ex-situ *RM* samples heated at laboratory scale as rock fragments (RF); e.s.d. is reported in rounded brackets; °light brown part of heated *RM* fragment; *green part of heated *RM* fragments; $dark part of heated *RM* fragments; n.d., not detected.

Sample	*T (°C)*	*a (Å)*	*b (Å)*	*c (Å)*	*β (°)*	*V/Z (Å³)*	*Crystallite Size (μm)*	*μstrain* $\left(\Delta d/_{d}\,10^{6}\right)$	*Instr. Set-Up*
RFa	1200	5.5153(5)	6.7625(5)	9.328(1)	94.482(6)	86.713(8)	0.2	1000	***LXRPD***
RFb	1200	5.5109(3)	6.7528(4)	9.3261(8)	94.420(4)	86.501(9)	0.2	1000	***LXRPD***
RFB	1250	5.5172(4)	6.7656(5)	9.3264(8)	94.404(5)	86.778(9)	0.11(4)	1881(134)	***LXRPD***
RF	1350	5.5136(3)	6.7700(3)	9.3433(6)	94.402(4)	86.933(8)	0.13(1)	1538(92)	***LXRPD***
RM	1200	5.51911(8)	6.76629(8)	9.3326(2)	94.534(1)	86.856(1)	0.38(1)	1518(24)	***SXRPD (ID22)***
	1250	5.5131(8)	6.7713(8)	9.334(2)	94.282(9)	86.868(.013)	0.12(1)	3842(244)	***LXRPD+Si***
	1300	5.5152(5)	6.7745(5)	9.339(1)	94.354(6)	86.980(9)	0.11(1)	2456(150)	***LXRPD+Si***
	1350	5.5174(4)	6.7718(4)	9.3389(9)	94.503(5)	86.968(7)	0.15(9)	1662(134)	***LXRPD+Si***
BC	1200	5.51483(2)	6.76035(2)	9.32105(4)	94.5522(2)	86.603(1)	1.36(2)	1017(5)	***SXRPD (ID22)***
	1250	5.51389(9)	6.75822(9)	9.3175(3)	94.570(2)	86.526(8)	1.04(8)	1421(35)	***LXRPD+Si***
	1300	5.51516(9)	6.75996(9)	9.3195(2)	94.572(1)	86.586(6)	1.02(6)	658(26)	***LXRPD+Si***
	1350	5.51479(9)	6.75971(9)	9.3191(2)	94.572(1)	86.574(.012)	1.30(9)	712(26)	***LXRPD+Si***
Referee	1300 [169]	5.502(1)	6.745(1)	9.297(1)	94.59(2)	85.975(1)	-	-	***SCXRD***
6BWO	1170-1350 [21]	5.50899(3)	6.75733(3)	9.31427(6)	94.5067(4)	86.4155(5)	1.21(.14)	1767(21)	***SXRPD (ID22)***

Table 10.3 – Crystallographic parameters of larnite in synthetic laboratory prepared samples, also comparing results coming from larnite in natural CP rocks (*6BWO*) and pure synthetic larnite; -, not available data; e.s.d. is reported in rounded brackets.

Sample		*T (°C)*	*a (Å)*	*b (Å)*	*c (Å)*	*β (°)*	*V/Z (Å³)*	*Crystallite Size (μm)*	*μstrain* $\left(\Delta d/_{d}\,10^{6}\right)$	*Instr. Set-Up*
RF	***a***	1200	9.299(3)	7.0806(5)	12.257(5)	116.119(8)	120.764(7)	*n.e.*	*n.e.*	***LXRPD***
	G	1250	9.297(4)	7.0821(8)	12.265(7)	116.038(9)	120.93(2)	1.16(.20)	804(91)	***LXRPD***
	D	1250	9.288(6)	7.081(2)	12.25(1)	116.00(2)	120.79(2)	0.26(1)	761(229)	***LXRPD***
		1350	9.288(9)	7.090(1)	12.26(2)	115.98(3)	120.93(3)	*n.e.*	*n.e.*	***LXRPD***
RM		1250	9.295(5)	7.079(1)	12.26(1)	116.05(2)	120.79(1)	0.35(3)	961(122)	***LXRPD+Si***
		1300	9.305(4)	7.080(8)	12.26(1)	116.13(1)	120.88(1)	0.27(1)	885(234)	***LXRPD+Si***
		1350	9.309(.017)	7.084(2)	12.26(3)	116.13(5)	120.95(5)	*n.e.*	*n.e.*	***LXRPD+Si***
Referee		1300 [157]	9.295(4)	7.079(3)	12.221(5)	116.08(1)	120.386(5)	-	-	***XRPD***

Table 10.4 – Crystallographic parameters of hatrurite in synthetic laboratory prepared samples; -, not available data; *n.e.,* not estimated; e.s.d. is reported in rounded brackets.

Crystallographic investigation on larnite occurring in *BC*, *RM* and *RF* XRD patterns highlighted similar cell volume (V/Z), but different from pure synthetic larnite (Table 10.3): (i) *RF* and *RM* samples showed a slight increasing trend with the temperature rise; whereas, (ii) *BC* displayed almost constant values over the studied temperature window.

Crystallite size and microstrain parameters of larnite were evaluated using Rietveld method with GSAS-ii, and were simultaneous refined only for SXRPD patterns. Moreover, crystallite size for *RFa,b* samples were empirically estimated during the refinement because the automatic refinement always gave too low values: microstrain was fixed to 1000 and not refined, whereas crystallite size was gradually step-by-step reduced starting from 1 μm, till no improvement in the fitting was observed. Three main trends were observed with the temperature rise (Table 10.3): (i) *RF* displayed a slight reduction and increase in crystallite size and microstrain, respectively; (ii) *RM* depicted a similar trend of *RF*, showing lowest crystallite size and highest microstrain at 1250 °C, strictly related to the crystallisation of hatrurite and flamite (Table 10.3,4); (iii) *BC* pointed out similar crystallite size and microstrain over the entire temperature range, excepted for a slight microstrain increase at 1250 °C.

Haturite occurred in *RM* only at T > 1250 °C and at different temperature and with variable content in *RF* samples above 1200 °C (Table 10.2). Crystallographic investigation on hatrurite revealed an upward cell volume trend with the temperature rise was, excepted for *RFG* which showed higher value out from the trend, close to 1350 °C ones (Table 10.4, Fig. 10.13). However, all hatrurite-bearing samples revealed higher cell volume compared to OPC one [164]. Crystallite size and microstrain parameters were not estimated (labelled as *n.e.* in Table 10.4) for samples with low hatrurite content: hatrurite has most intense Bragg peaks overlapped with larnite ones, and peaks out of overlapping are only at 3.04 Å (~ 29.375° 2θ with Cu-Kα) and at 1.769 Å (~ 51.620° 2θ with Cu-Kα), not allowing a suitable evaluation for microstrain and crystallite size. However, microstrain values remained almost constant for all studied samples; whereas, crystallite size displayed similar values among *RM* and *RF*, excepted for *RFG* sample that has the highest value probably related to the coarser grain size (Fig. 10.11).

Ternesite should be considered as solid solution with pure ternesite and silicocarnotite as end members; it occurred in *RM* samples from 1100 to 1300 °C showing a cell volume close to pure ternesite with no changes over the temperature window (Fig. 10.14).

Apatite represents a constituent of *RM* raw meals and occurred in all *ex-situ* experiments. A steep cell volume rise took place from 700 to 900 °C, moving from values close to pure fluorapatite to fluorellestadite ones. Cell volume slightly reduced from 900 °C to 1350 °C, probably related to the lesser stability at HT of fluorellestadite [319], which start decomposing at T > 1220 °C [319]. Microstrain and crystallite size were evaluated only from 1100 °C: microstrain increased especially at T > 1300 °C; whereas, crystallite size showed constant values, with high *e.s.d.* only at 1350 °C not allowing a correct estimation (Fig. 10.15).

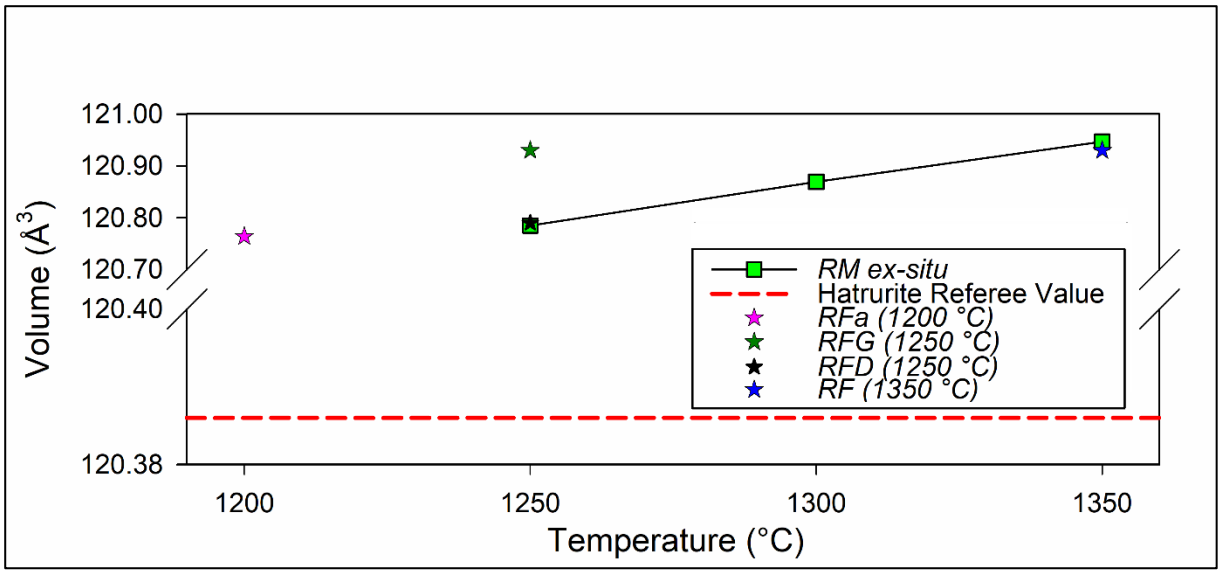

Fig. 10.13 – Hatrurite cell volume changes for ex-situ experiments of *RM* heated as fragments (*RFa* purple star, *RFG* light green star, *RFD* dark green star and RF at 1350 °C with blue star) and pellets (green square); M_1-C_3S of De Noirfontaine [164] was used as referee value for hatrurite.

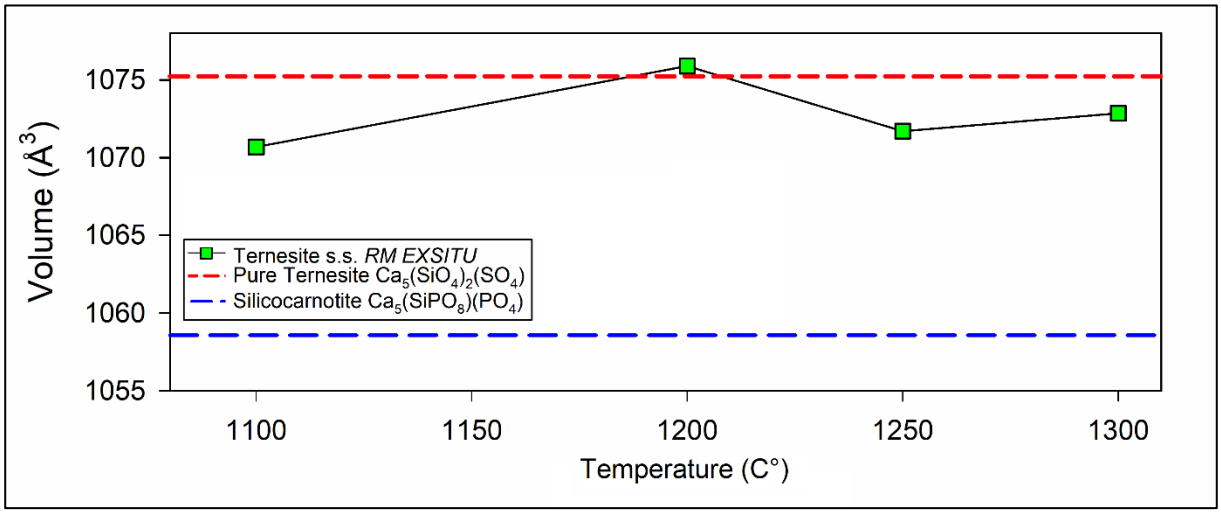

Fig. 10.14 – Ternesite cell volume changes for ex-situ experiments of *RM* heated as pellets (green squares); pure ternesite [344] and silicocarnotite [329] cell volume values were reported to show the possible cell volume variation range.

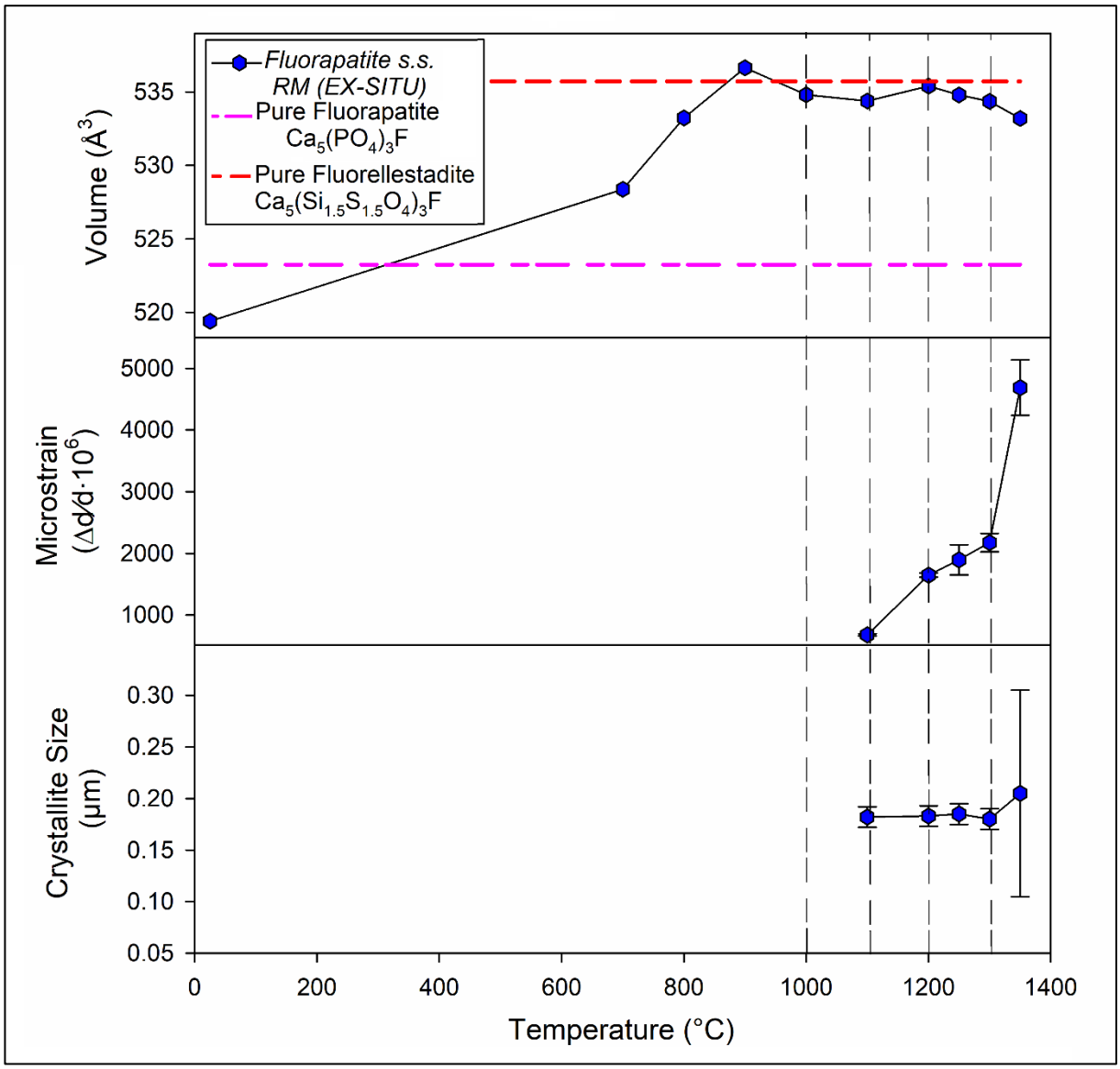

Fig. 10.15 – Fluorapatite s.s. crystallographic parameters are reported for *RM* ex-situ experiments, highlighting changes on cell volume, microstrain and crystallite size at different heating temperatures; fluorellestadite [345] and fluorapatite [346] cell volume values were used to display the cell volume range of the complete solid solution.

Microtextural investigation performed by means of RLM and SEM on *BC* samples heated at different temperatures (1200, 1250, 1300 and 1350 °C) revealed several important changes:

(i) from 1200 to 1250 °C no microtextural changes in *BC* samples occurred which is composed of rounded to polygonal larnite, brownmillerite and sporadic anhedral ye'elimite crystals (Fig. 10.16,17). Only a slight increase of crystal size occurred for brownmillerite at 1250 °C, especially inside dense aggregates reaching ~ 10 μm and subhedral prismatic shape (Fig. 10.17a,c). The general lack of ye'elimite, especially for *BC* heated at 1200 °C, despite its occurrence was confirmed by LXRPD, could be explained by its very low crystal size, high porosity and lower hardness (3.5 Moh's) compared to brownmillerite (5.5 Moh's) and larnite (6 Moh's) [7,8].

(ii) a clear decrease in porosity and increase of crystal size occurred for all phases at 1300 °C (Fig. 10.18,19), especially for brownmillerite showing euhedral prismatic shape (8-18 μm) (Fig. 10.18b,c). Brownmillerite-rich dense aggregates (30-150 μm) still occurred with euhedral prismatic coarser crystals (< 15 μm) compared to ones in matrix (Fig. 10.18a,b,c). Furthermore, bigger brownmillerite-rich aggregates revealed lighter crystals at the core compared to ones on the rims, suggesting a Fe-enrichment in the aggregate centre (Fig. 10.18b).

(iii) intense changes occurred at 1350 °C due to partial melting. Sample is made of (*a*) melt-richer portions with coarse prismatic brownmillerite (< 60 μm) with sometimes small larnite inclusions and enveloping rounded fractured larnite crystals (10-30 μm) with frequent undulated rims (Fig. 10.20a,d); whereas, (*b*) melt-poorer parts are made of rounded fractured crystals always enveloped by brownmillerite with predominant xenomorphic crystal shape (Fig. 10.20a,b,c,21a). Ye'elimite often occurred as pseudocubic crystals (~ 10 μm) (Fig. 10.20,21) with rare small larnite inclusions only in melt-richer portions (Fig. 10.20a,d). Furthermore, syngenite ($K_2Ca(SO_4)_2H_2O$) occurred as interstitial phase in melt-poorer portion with anhedral shape, strong fractured and lined, due to its low hardness (2.5 Moh's) (Fig. 10.20c); whereas, it occurred with xenomorphic texture in melt-rich portions with numberless micrometric larnite inclusions often occurring close to anhedral ye'elimite crystals (Fig. 10.20d). Nital etching on polished sections was performed for RLM investigation showing the turning of larnite to orange brown colours and leaving unchanged ye'elimite and brownmillerite (Fig. A.10b,c).

More images of *BC* samples at RLM and SEM investigation are reported and described in the Appendix (1200 °C, Fig. A.7; 1250 °C, Fig. A.8; 1300 °C, Fig. A.9; 1350 °C, Fig. A.10).

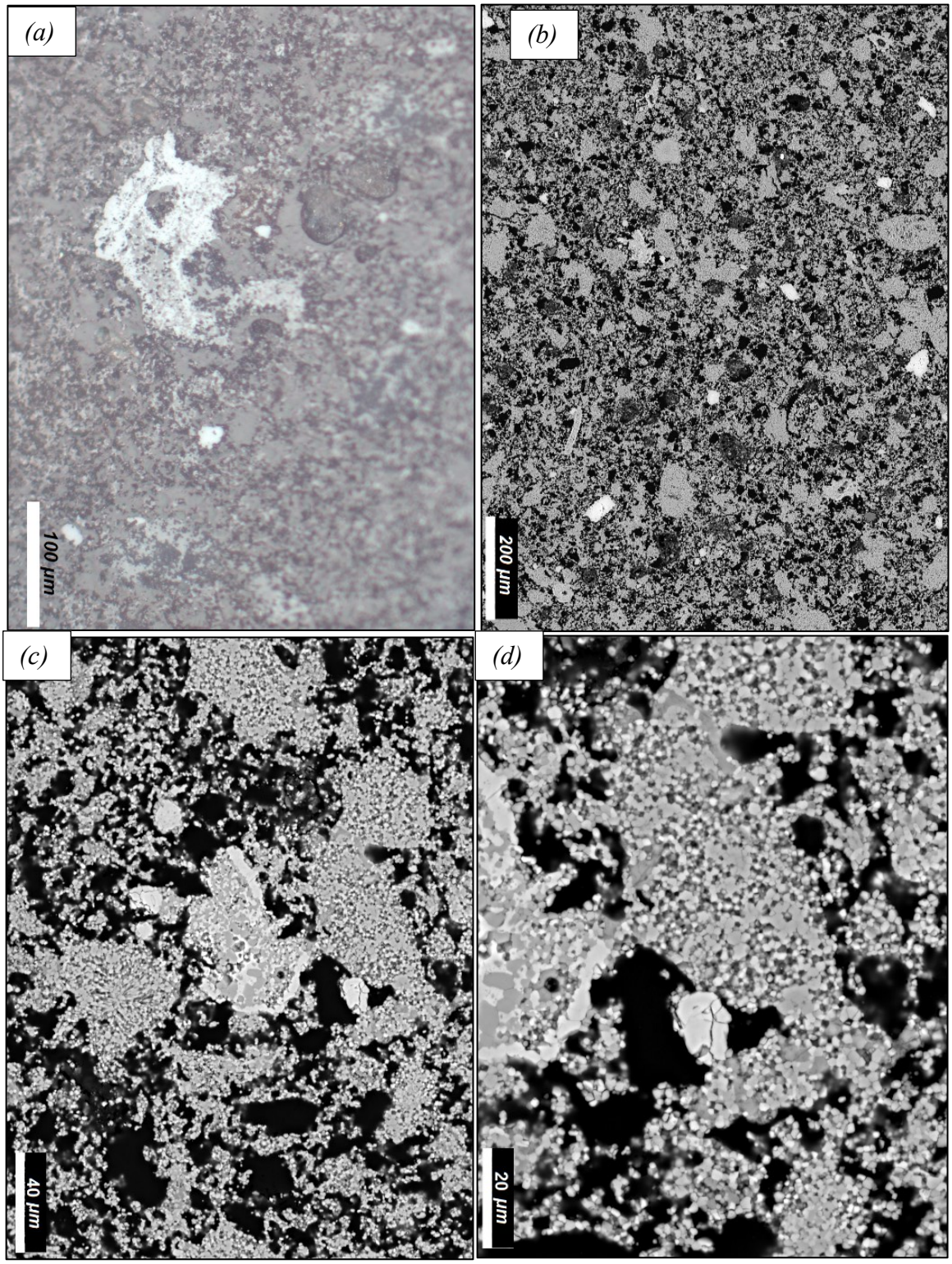

Fig. 10.16 – Microtextural features od *BC* sample heated at 1200 °C at laboratory scale: (a) RLM image highlighting the low crystal size and the occurrence of brownmillerite enrichment as dense aggregates; (b) BSE image at low magnification revealing the high porosity of the sample, with the occurrence of medium grey clusters ~ 150 µm (larnite-rich portions) and white ones of 75-85 µm (brownmillerite-rich regions); (c,d) BSE images at high magnification showing the extremely low crystal size of larnite (grey rounded crystals ~ 1-4 µm) and anhedral brownmillerite (white crystals ~ 1-10 µm), whereas no ye'elimite and mayenite were found despite were detected at LXRPD.

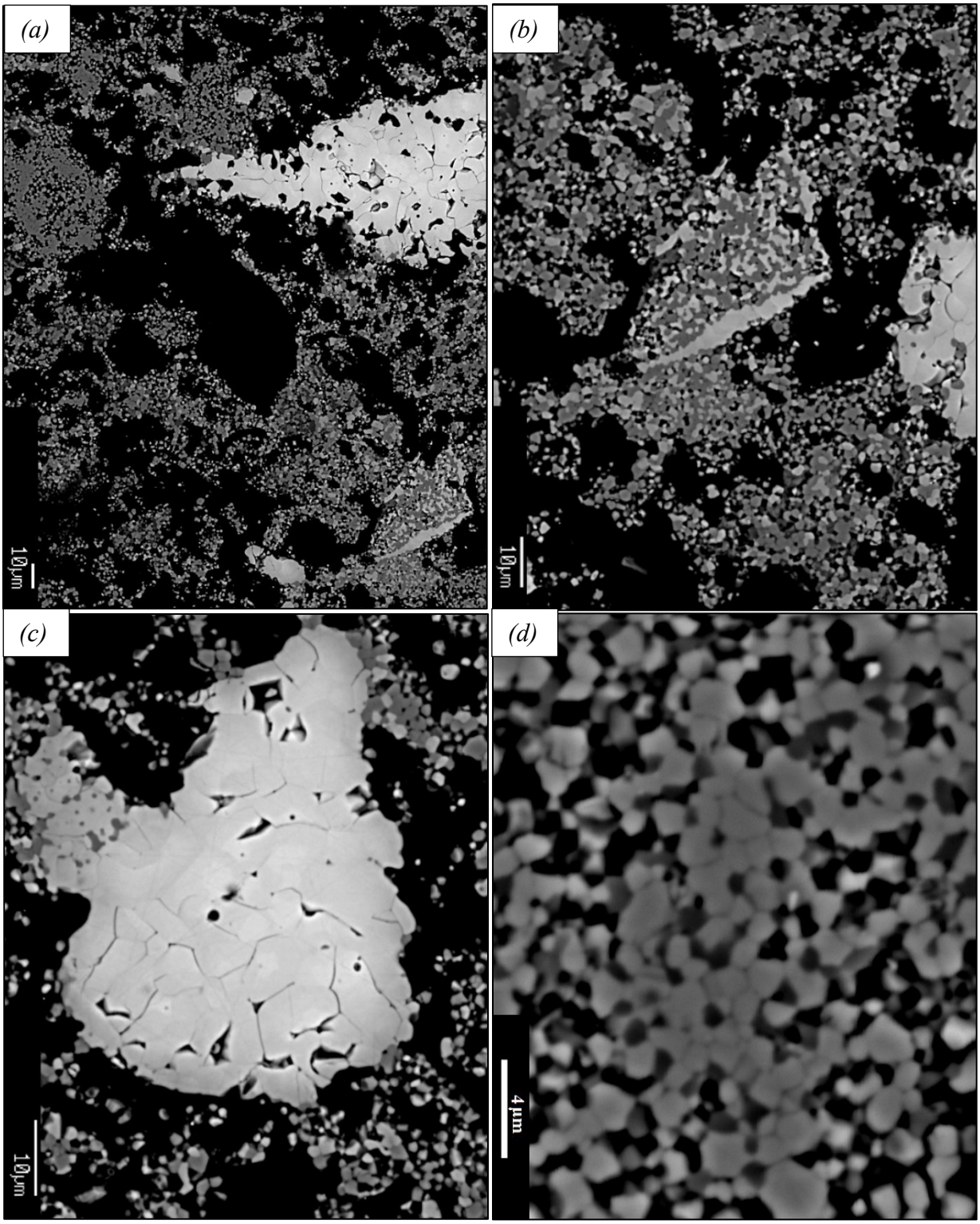

Fig. 10.17 – BSE images of *BC* sample heated at 1250 °C at laboratory scale: (a,b) microtexture at low magnification showing high porosity, low crystal size and a mineral assemblage composed of larnite (grey rounded to polygonal shape crystals), brownmillerite (white prismatic to rounded shape crystals) and ye'elimite (dark grey rounded shape crystals) with sparce dense aggregates (40-100 µm) of subhedral coarser brownmillerite (10-15 µm); (c) detail of a dense brownmillerite aggregate revealing the coarser and subhedral crystal shape compared to ones occurring among larnite crystals; (d) micrometric crystal size of larnite with polygonal to rounded shape, associated with dark grey crystals of ye'elimite often occurring within larnite crystals triple junctions.

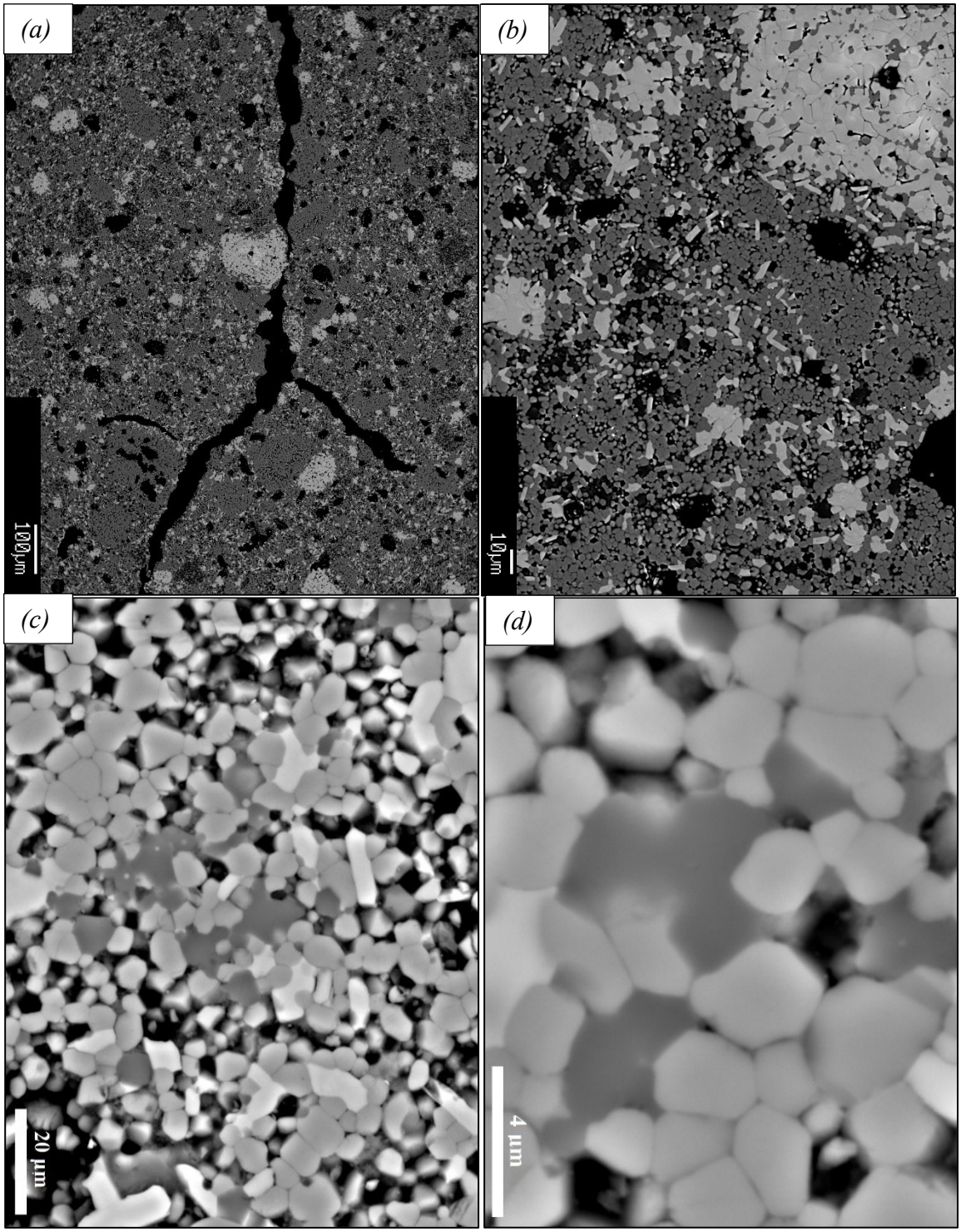

Fig. 10.18 – BSE images of *BC* sample heated at 1300 °C at laboratory scale: (a) microtexture overview at low magnification showing white brownmillerite-rich rounded clusters (30-150 µm), grey low crystal size matrix with high porosity mainly made of larnite crystals; (b) enlargement of the central part of the previous image, revealing sparce white euhedral prismatic brownmillerite, dark grey anhedral ye'elimite and polygonal to rounded larnite, with brownmillerite-rich nodules with coarser crystals (10-15 µm); (c,d) microtexture details better revealing shape and distribution of all occurring crystal phases.

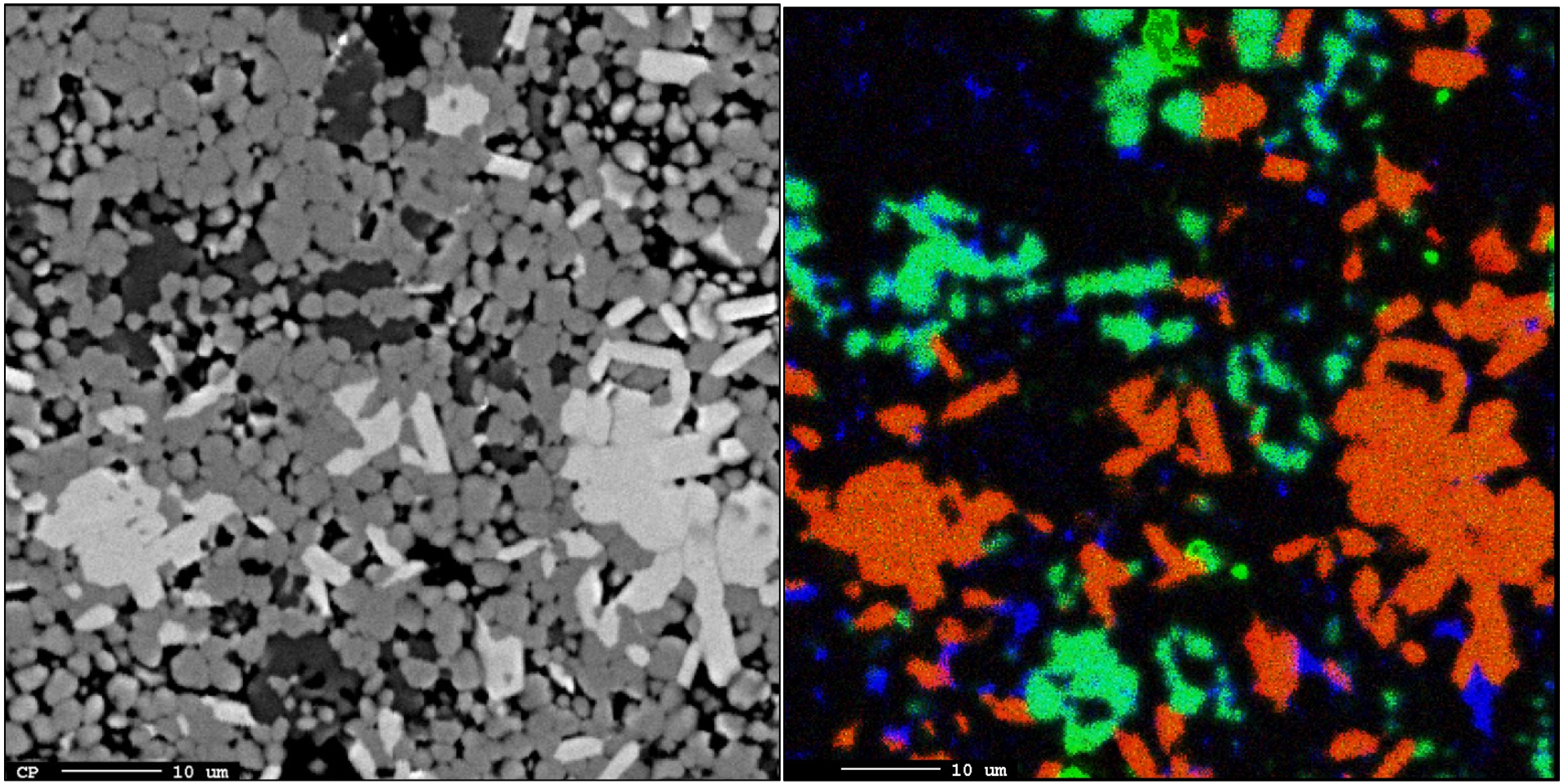

Fig. 10.19 – (a) BSE image of *BC* sample heated at 1300 °C at laboratory scale, highlighting white euhedral coarser prismatic brownmillerite, grey rounded to polygonal micrometric larnite, dark grey anhedral ye'elimite often occurring inside denser larnite-rich portions and black voids; (b) element map of previous BSE image with RGB scale (Red = Fe, Green = Al, Blue = S) showing brownmillerite and ye'elimite as red-orange and cyano green portions, respectively, moreover, blue pixels should represent S-rich phases but they often point on pores.

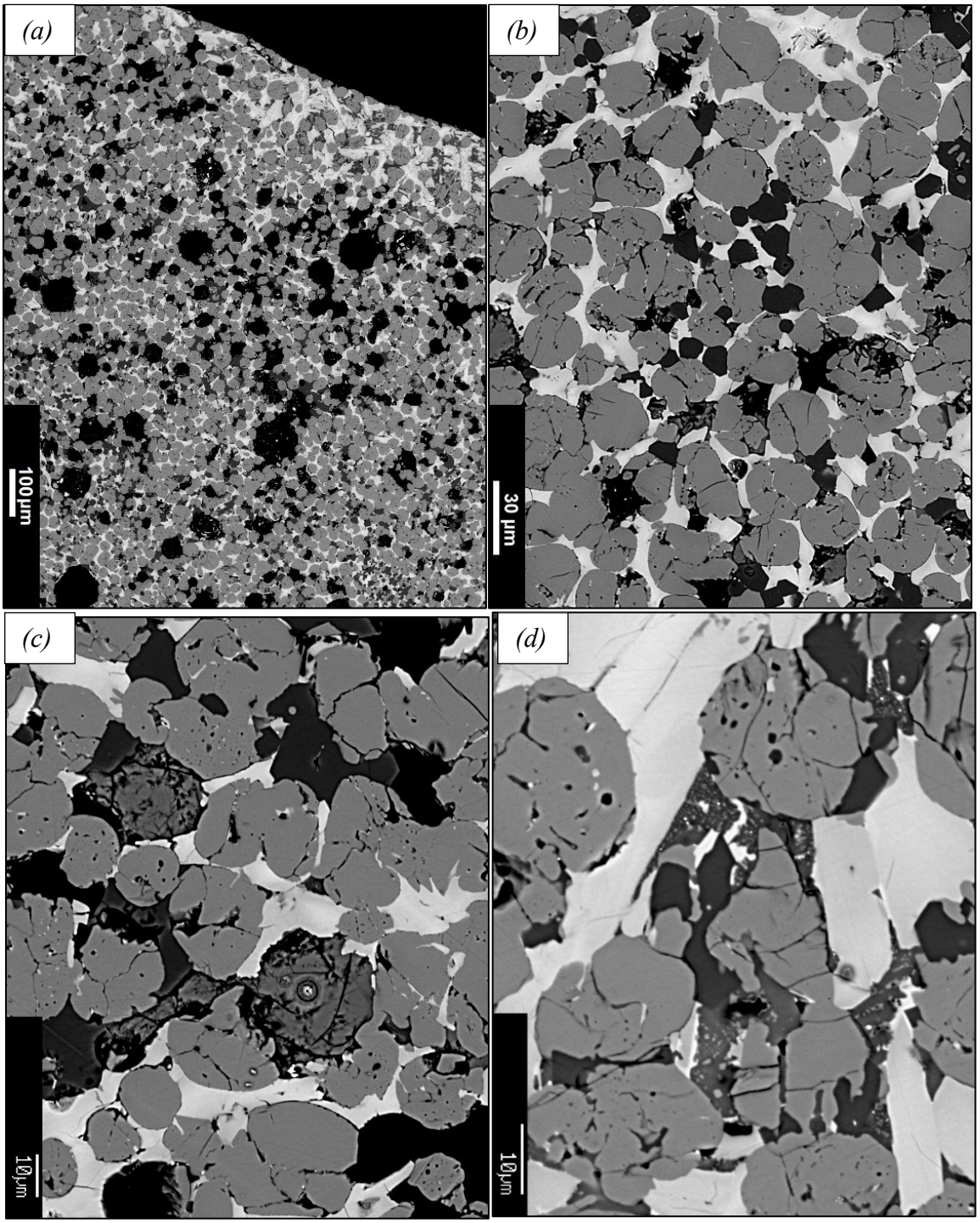

Fig. 10.20 – BSE images of *BC* sample heated at 1350 °C at laboratory scale showing microtextural features: (a) low magnification image highlighting white melt-richer portion close to bottom part of heated pellet and melt-poorer regions with higher porosity; (b) detail of melt-poorer portion displaying grey rounded fractured larnite (< 30 µm), white xenomorphic brownmillerite enveloping all other phases, dark euhedral ye'elimite (< 10 µm); (c) dark grey fractured anhedral syngenite crystals inside melt-poorer portion associated with rounded larnite with often undulated rims enveloped in brownmillerite matrix; (d) detail of melt-richer portion with grey fractured larnite, white coarse prismatic brownmillerite, dark anhedral ye'elimite and dark grey syngenite rich in larnite inclusions often close to ye'elimite crystals.

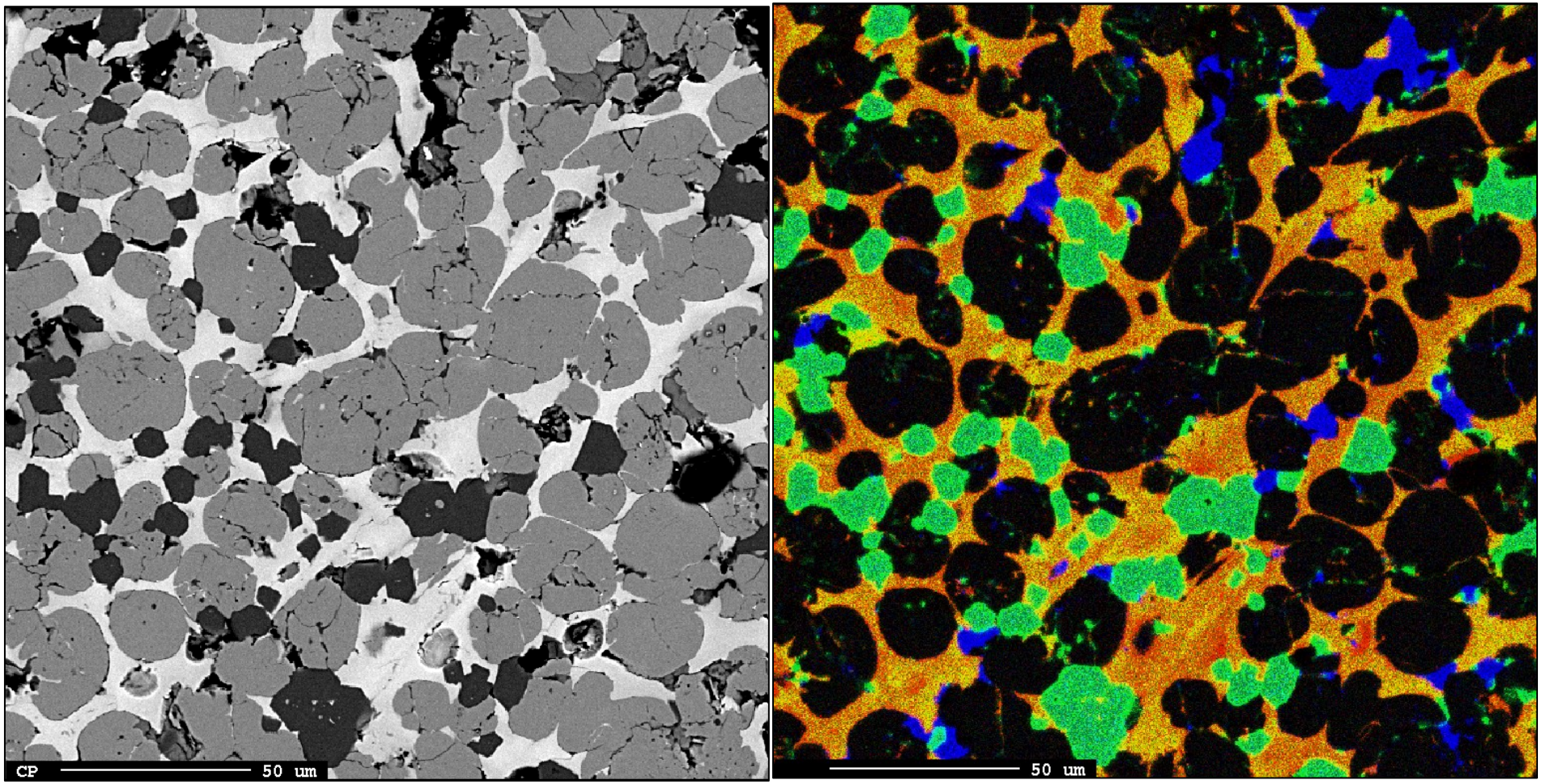

Fig. 10.21 – (a) BSE image of *BC* sample heated at 1350 °C of a melt-poorer portion made of white xenomorphic brownmillerite, grey fractured rounded larnite, dark pseudocubic shaped ye'elimite and sporadic dark grey fractured anhedral syngenite; (b) element map in RGB (Red = Fe, Green = Al, Blue = S) of the previous BSE image, better showing brownmillerite, ye'elimite and syngenite as red orange, cyan and blue, respectively, furthermore, larnite is represented by rounded black portions which often revealed brownmillerite orange inclusions.

Only *RM* fragments heated at 1200 °C, such as *RFa* and *RFb*, were studied for microtextural investigation, showing two distinct microtextures:

(i) *RFa* revealed a fine grain size microtexture composed of rounded fluorapatite pellets (30-50 μm) and brownmillerite dense nodules (15-25 μm) enveloped in a matrix of xenomorphic larnite with sparce micrometric brownmillerite and high porosity (Fig. 10.22a). Furthermore, fluorapatite pellets have numberless micrometric brownmillerite inclusions and voids (Fig. 10.22d); whereas, brownmillerite-rich aggregates displayed coarser crystals (3-5 μm) compared to ones in the fine matrix (Fig. 10.22a,b). Part of the porosity seems to be related to the detachment of phosphatic nodules during polishing procedure, due to the similar rounded shape and size (Fig. 10.22c). RLM investigation on polished sections was only able to reveal brownmillerite aggregates due to the global ultra-fine texture (Fig. A.1b,c); however, Nital etching was useful to confirm the occurrence of small hatrurite crystals due to its distinctive bluish to orange colours (Fig. A.1d, Table 10.2);

(ii) *RFb* is composed of rounded fractured lime (10-15 μm), representing coarser crystals, enveloped in a matrix of mainly xenomorphic ternesite, euhedral prismatic brownmillerite (< 10 μm) and anhedral larnite, ye'elimite and anhydrite (Fig. 10.23a,b). Brownmillerite occurred in the matrix as both sparce crystals and dense aggregates (20-40 μm) with coarser crystals, as found in *RFa* (Fig. 10.23b). Larnite and anhydrite always occurred inside ternesite with anhedral shapes and undulated to interdigitated rims, suggesting its formation from the high temperature decomposition of ternesite (Fig. 10.23b,c). *RFb* showed a lesser porosity and a lack phosphatic nodules compared to *RFa*. RLM investigation pointed out similar features observed during SEM analysis as the occurrence of ternesite-rich matrix with anhedral larnite and sparce prismatic brownmillerite, also occurring as dense aggregates (Fig. A.2b,c,d).

All *RM* pellets heated from 1200 to 1350 °C were studied for textural analysis showing relevant changes at each 50 °C increase:

(i) *RM* at 1200 °C showed a microtexture similar to *RFb* sample, excepted for lower porosity, lesser occurrence of brownmillerite-rich aggregates and higher larnite content. Microtexture is made of rounded high fractured lime crystals (< 15 μm) enveloped in a matrix of mainly xenomorphic ternesite, anhedral larnite, rounded to subhedral ye'elimite and mayenite (5 μm), and euhedral prismatic brownmillerite (< 10 μm) (Fig. 10.24a,b,c). Larnite always showed undulated to interdigitated rims in contact with ternesite matrix (Fig. 10.24b,c). Despite fluorapatite represents a constituent mineral (Fig. 10.3,4), no clear crystals were identified only using BSE images, suggesting that should have xenomorphic shape, low crystal size and similar grey scale colour of ternesite as confirmed by element map analysis (Fig. 10.25): fluorapatite s.s. showed similar grey scale colour of ternesite and was identified by the enrichment in all analysed elements, such as P, S and F (Fig. 10.25b). Furthermore, portions only rich in F and others in S represent mayenite and ye'elimite crystals, respectively; whereas larnite showed a slight enrichment only in P (Fig. 10.25b).

(ii) *RM* heated at 1250 °C showed intense changes in both microtexture and mineral assemblage, as revealed by XRD analysis (Fig. 10.3,4): peciloblastic rhombic hatrurite (100-250 μm) and rounded to subhedral fractured lime (10-25 μm) in a matrix made of mainly xenomorphic larnite, prismatic brownmillerite (< 10 μm), micrometric subhedral ye'elimite and mayenite, and residual anhedral fluorapatite and ternesite (Fig. 10.26c,d). Peciloblastic hatrurite has numberless inclusions of all occurring crystal phases and rims are strait and undulated in contact with ternesite and larnite, respectively (Fig. 10.27a). An increase of larnite and a reduction in ternesite and porosity occurred comparing results with *RM* heated at 1200 °C (Fig. 10.3,4,24c,26c). The identification of ternesite *vs* fluorapatite s.s. and mayenite *vs* ye'elimite were clarified by element map analysis (Fig. 10.27), confirming that these minerals pairs have similar grey colours in BSE images: mayenite was corresponding to elemental map portions only rich in F, while, portions only enriched in S were related ye'elimite; P-S-F rich areas were related to fluorapatite s.s., whereas, P-S for ternesite (Fig. 10.27b). Furthermore, P-F and P were found in hatrurite and larnite crystals, respectively (Fig. 10.27b). RLM showed same textural features of SEM analysis thanks to higher crystal size and the lower porosity compared to lower temperature heated samples (Fig. 10.26a,A.3,A.4). Nital etching on polished sections observed with RLM clearly revealed hatrurite, which turned to light blue and orange colours, larnite, which changed to brown colour, and other phases (ternesite, fluorapatite, mayenite and ye'elimite) that remained unchanged (Fig. 10.26b);

(iii) *RM* heated at 1300 °C showed microtextural features close to OPC ones [304]: rounded coarse hatrurite (100-200 μm), rounded fractured larnite (10-30 μm) and subhedral lime (10-15 μm) enveloped in a matrix of xenomorphic brownmillerite, minor fluorapatite, ternesite, mayenite and rare ye'elimite (Fig. 10.28,29). Brownmillerite dramatically changed its shape suggesting a partial melting (Fig. 10.28a,b). Coarse hatrurite crystals revealed less larnite inclusions but bigger and more rounded compared to sample heated at 1250 °C (Fig. 10.28c). Rounded larnite crystals often displayed an internal complex structure of mainly ternesite and lesser brownmillerite inclusions (Fig. 10.28d). Element map analysis highlighted fluorapatite-rich portions (P-F-S rich regions), often occurring outside larnite or hatrurite clusters, anhedral mayenite (F-rich portions) and ye'elimite (S-rich areas) (Fig. 10.29). Furthermore, hatrurite showed enrichment in P and F; whereas, larnite is only P-rich (Fig. 10.29b);

(iv) *RM* heated at 1350 °C revealed similar microtexture to sample heated at 1300 °C, with changes in hatrurite crystal shape and inclusion, and abundances of occurring crystal phases (Fig. 10.3,4). Hatrurite crystals showed more rounded shape and smaller size, with less inclusions with bigger anhedral larnite and sparce mayenite-brownmillerite exsolution (Fig. 10.30a,b). Mayenite-brownmillerite exsolution inside hatrurite crystals typical showed skeletal intergrowth suggesting a partial melting. Lime has more euhedral pseudocubic shape fully internal fractured. Rounded larnite (15-40 μm) still revealed the internal complex texture with fluorapatite and minor brownmillerite (Fig. 10.30d). RLM images are reported in the Appendix showing larnite and hatrurite with similar features at parallel nicols (Fig. A.6b), but different at crossed ones (Fig. A.6c),

due to brownish colours of hatrurite. Mayenite, ye'elimite and brownmillerite could be identified with RLM: the two formers have darker colour compared to larnite and fluorapatite at parallel nicols, whereas the latter has the lightest colours in the samples and dark colour with no internal reflection at crossed nicols (Fig. A.6b,c). Nital etching was helpful to distinguish hatrurite and larnite at RLM, also in revealing fluorapatite crystals (Fig. A.6d).

More images of *RM* heated pellets observed at RLM and SEM investigation are reported and described in the Appendix (1200 °C, A1; 1250 °C, A2; 1300 °C, A3; 1350 °C, A4).

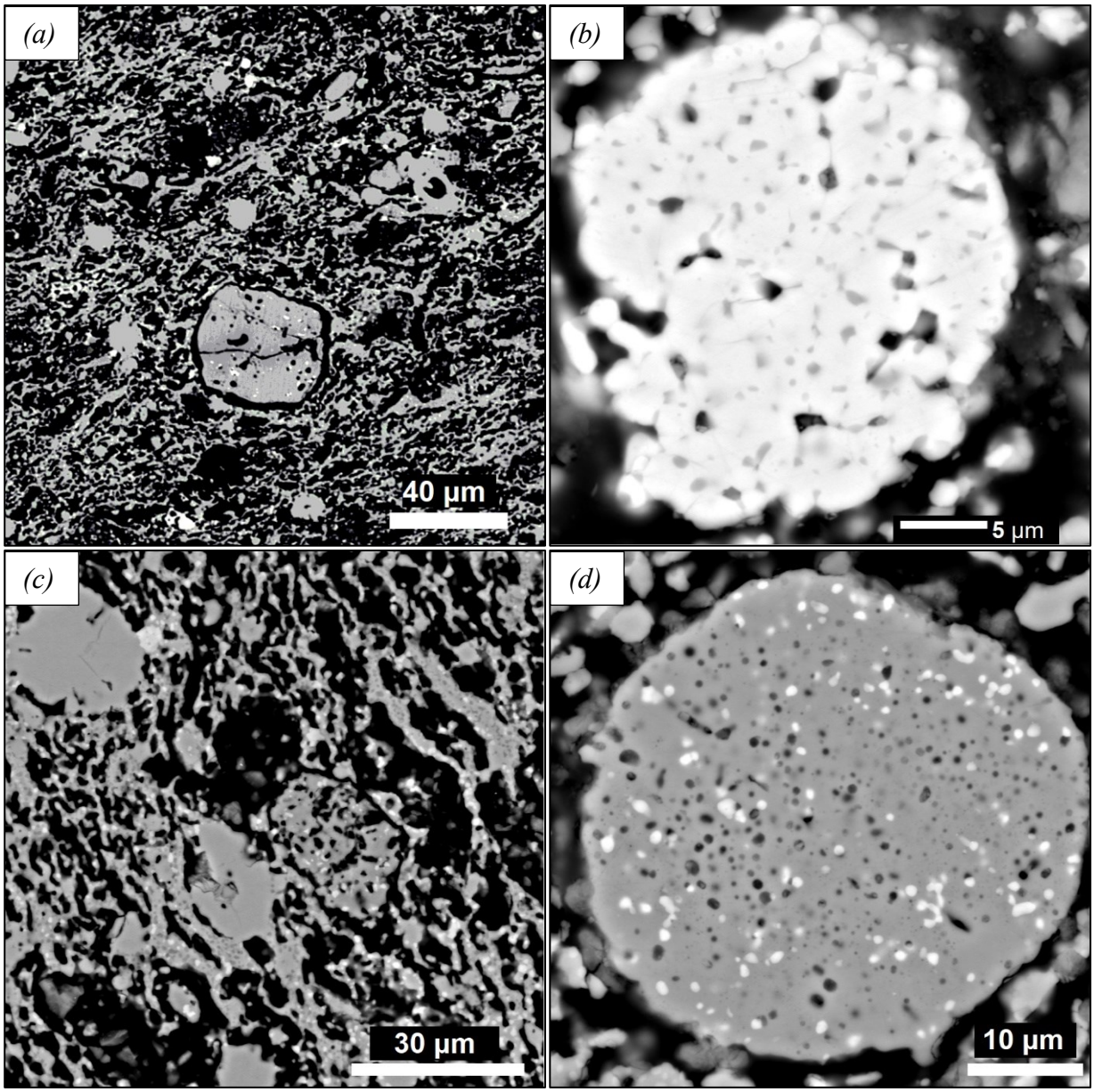

Fig. 10.22 – BSE images acquired at SEM for *RM* rock fragment heated at 1200 °C (*RFa* sample) highlighting its microtexture at different magnification scale: (a) high porosity sample with numerous rounded shape voids, pellets made of fluorapatite s.s, general low crystal size with homogenous grey colour (larnite crystals) and white spots or aggregates (brownmillerite crystals);(b) high magnification of a dense aggregate of micrometric rounded to polygonal brownmillerite crystals; (c) low crystal size microtexture with medium grey anhedral larnite and micrometric white rounded crystals of brownmillerite; (d) detail of fluorapatite nodule with numerous brownmillerite (white anhedral crystals) inclusions and rounded to elongated pores.

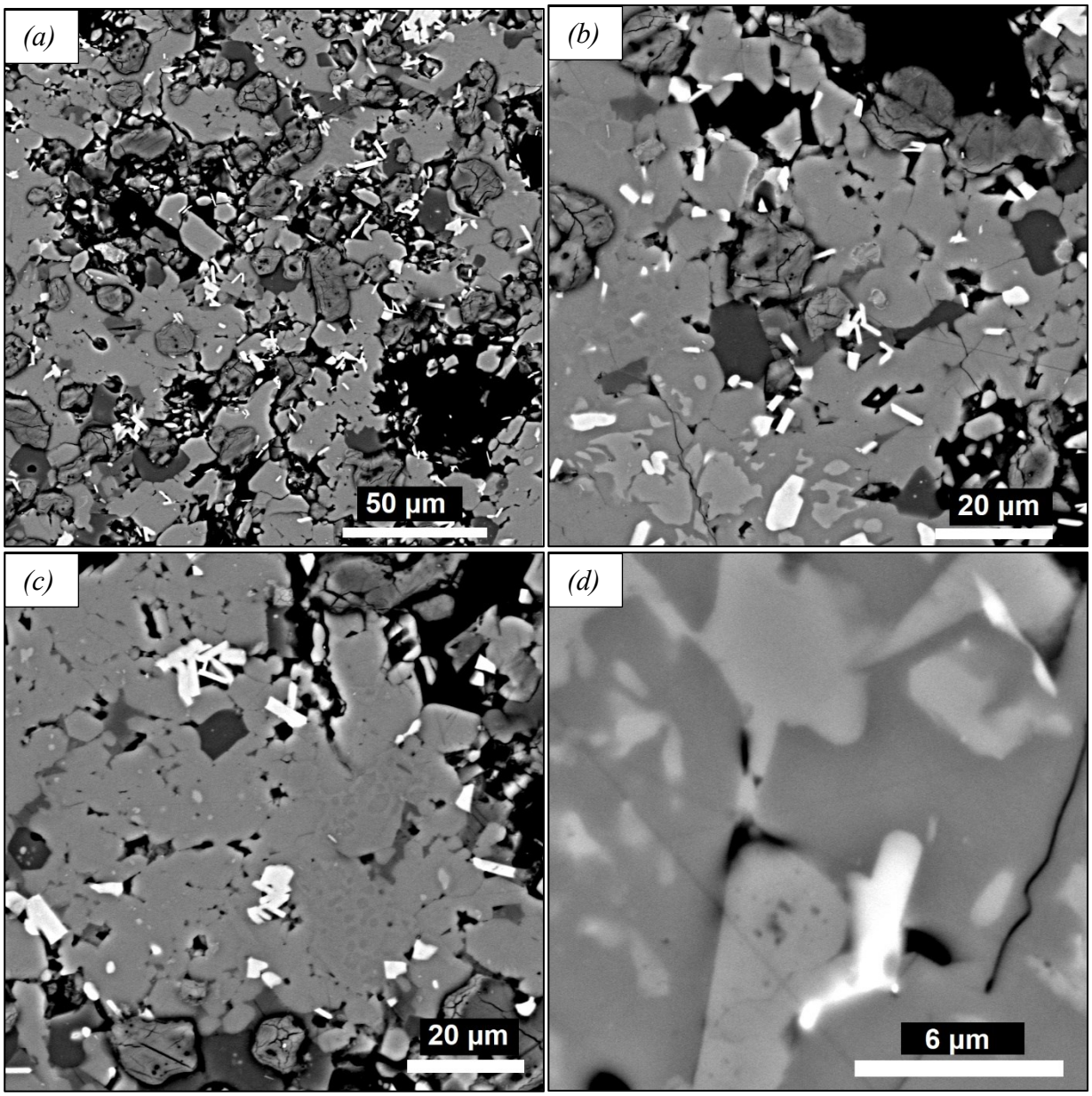

Fig. 10.23 – BSE images acquired at SEM for *RM* rock fragment heated at 1200 °C (*RFb* sample) highlighting microstructural details at different observation scale: (a) overview at low magnification showing rounded fractured lime aggregates (inhomogeneous dark grey colour), a matrix of ternesite and larnite (grey to light grey colours), euhedral prismatic to acicular brownmillerite (white), anhedral ye'elimite (dark grey), xenomorphic anhydrite (dark grey lighter than ye'elimite) and black pores; (b,c) details at higher magnification revealing the abundance of anhedral ternesite (grey colour) with light grey anhedral crystals of larnite, acicular to prismatic white brownmillerite, anhedral dark grey and darker anhydrite and ye'elimite, respectively; (d) detail of the ternesite-larnite association, exhibiting anhedral larnite crystals with undulated and indented borders, suggesting the gradual decomposition of ternesite forming larnite and residual anhydrite.

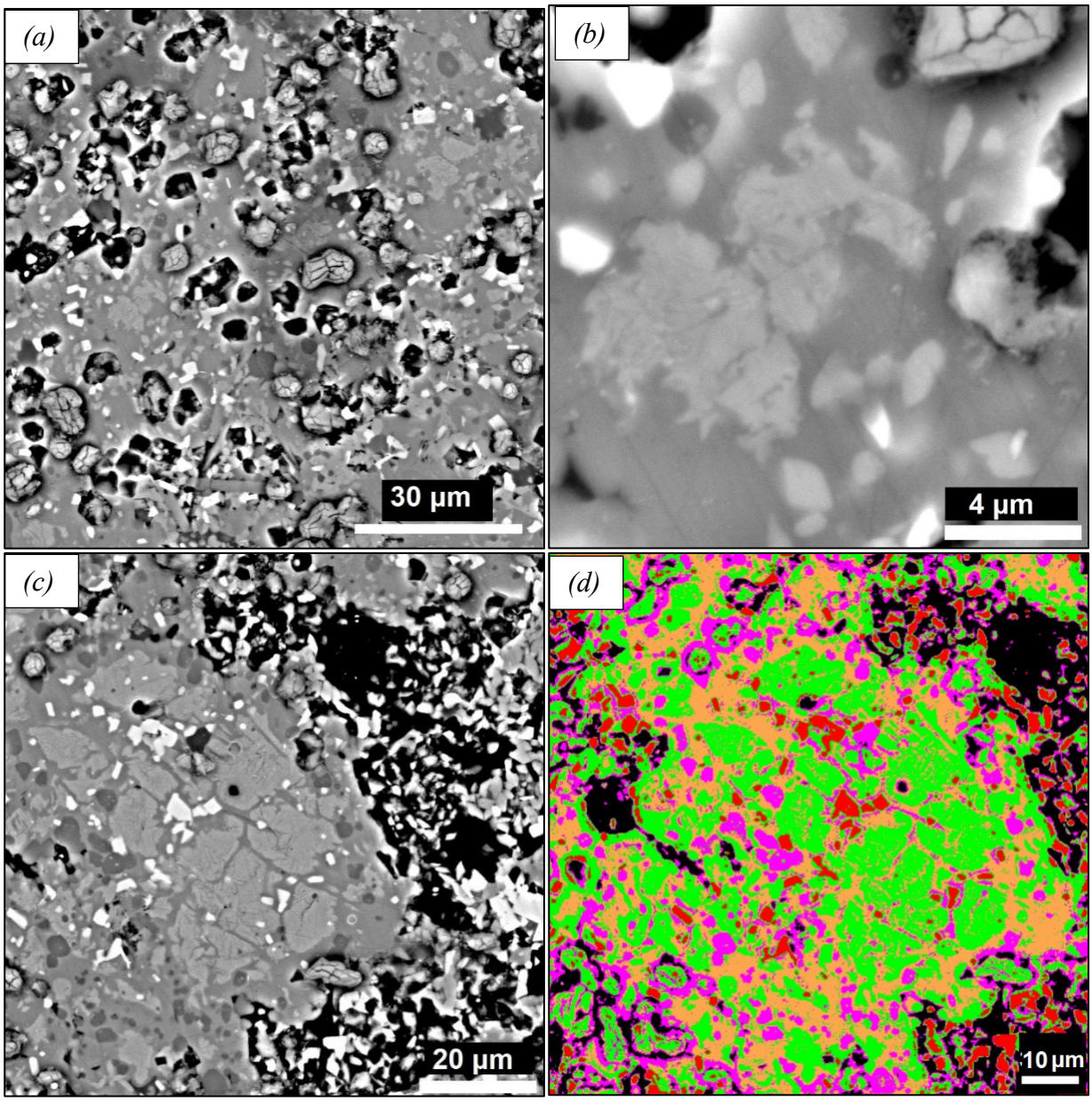

Fig. 10.24 – BSE images acquired at SEM for *RM* pellets heated at 1200 °C highlighting microstructural details: (a) overview at low magnification showing revealing coarse rounded fractured lime (grey), prismatic brownmillerite (white) and ternesite-fluorapatite-rich matrix (medium grey) with anhedral larnite (light grey), mayenite (dark grey) and ye'elimite (darker grey); (b) details of the ternesite-fluorapatite-rich matrix with micrometric larnite with undulated to interdigitated rims and white brownmillerite crystals; (c) anhedral larnite crystals enrichment enveloped in xenomorphic ternesite (medium grey) with sparce euhedral brownmillerite and anhedral ye'elimite and/or mayenite; (d) coloured segmentation of previous image, using red for brownmillerite, green for larnite, light orange for ternesite and fluorapatite, and purple for ye'elimite and mayenite.

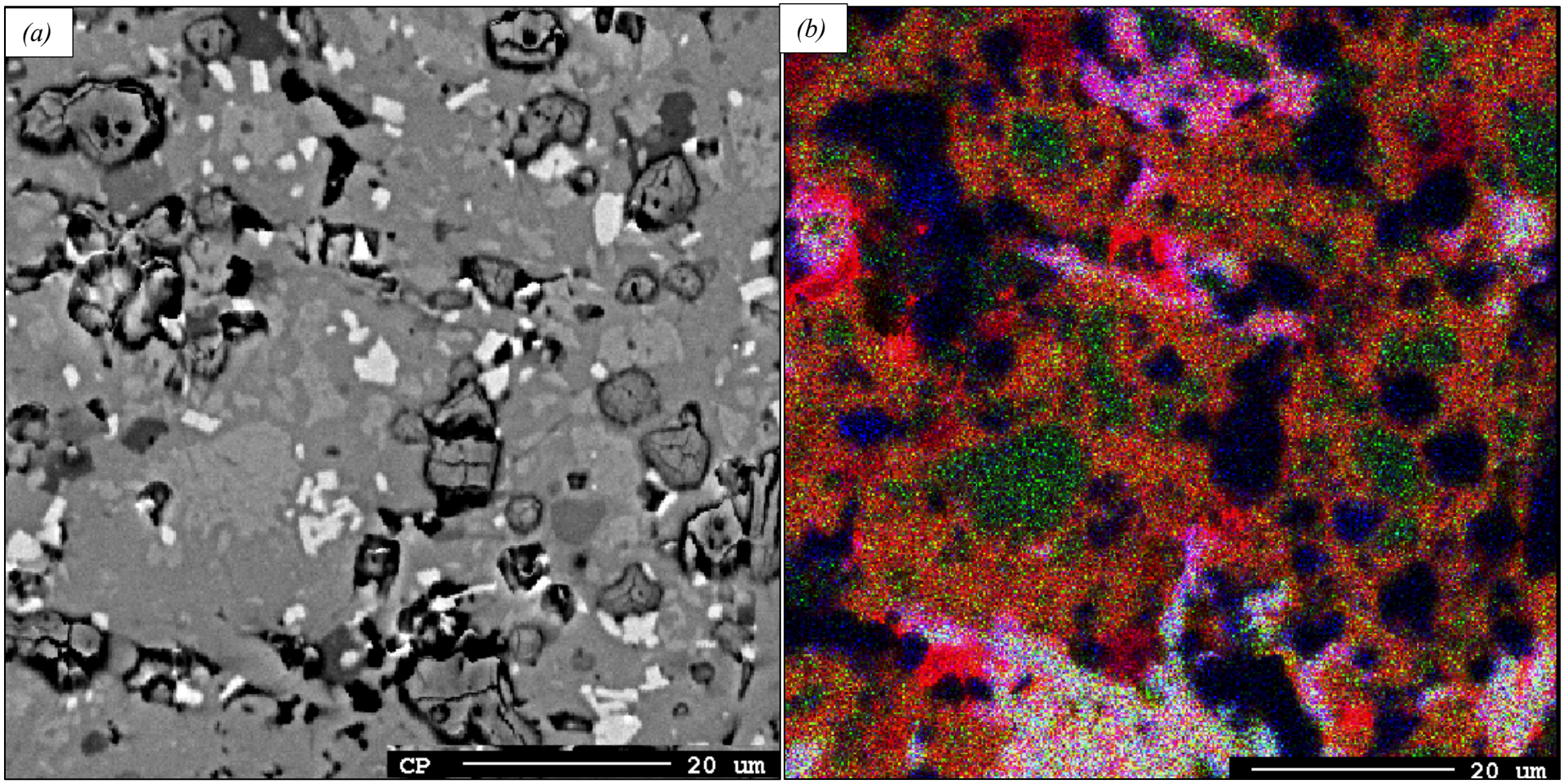

Fig. 10.25 – (a) BSE images acquired at SEM for *RM* pellet heated at 1200 °C highlighting microtextural features marked by the occurrence of rounded fully fractured lime crystals (dark grey), euhedral prismatic brownmillerite (white), anhedral larnite with undulated rims (light grey), anhedral ye'elimite and mayenite (dark grey) all enveloped in a ternesite-fluorapatite xenomorphic matrix; (b) element map analysis of previous BSE image with RGB scale (Red = S; Green = P; Blue = F) clearly revealing light pink portions made of fluorapatite-ellestadite s.s., abundant orange yellowish regions of ternesite-silicocarnotite s.s, only red parts represent ye'elimite, whereas, blue areas are related to mayenite; moreover, all larnite crystals showed a slight enrichment in phosphorus due to greenish shade.

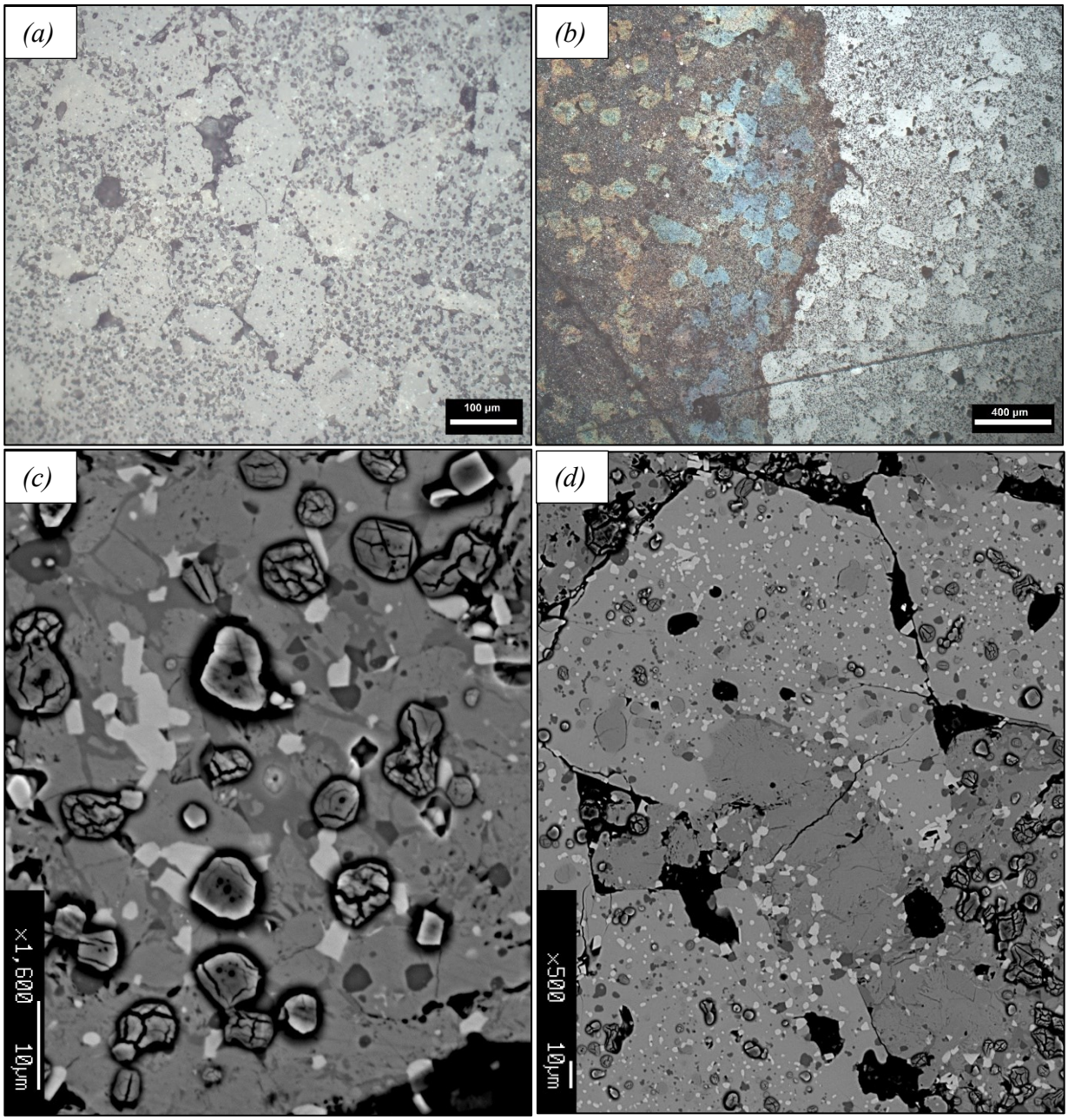

Fig. 10.26 – BSE images acquired at SEM and RLM ones for *RM* pellet heated at 1250 °C highlighting microstructural details: (a) RLM image at low magnification coarse rhombic pecilitic hatrurite crystals (100-150 µm) (dull grey), rounded lime crystals (dark grey), sparce white brownmillerite and a grey matrix made of larnite, ternesite and fluorapatite that are not distinguished at this observation scale; (b) polished section half Nital etched (left part) observed at RLM revealing abundance and euhedral shape of hatrurite crystals turning from dull grey to light blue and orange colours, whereas larnite-rich matrix turned to brown colour; (c) BSE image highlighting matrix microtexture made of mainly anhedral larnite (grey), xenomorphic ternesite and fluorapatite s.s. (darker grey than larnite), rounded fractured lime (dark grey, < 10 µm), prismatic brownmillerite (white, < 6 µm), subhedral ye'elimite and mayenite (dark grey, 1-3 µm); (d) BSE image displaying peciloblastic euhedral hatrurite crystals with larnite crystals cluster extending inside with undulated rims locally rich in brownmillerite and ye'elimite.

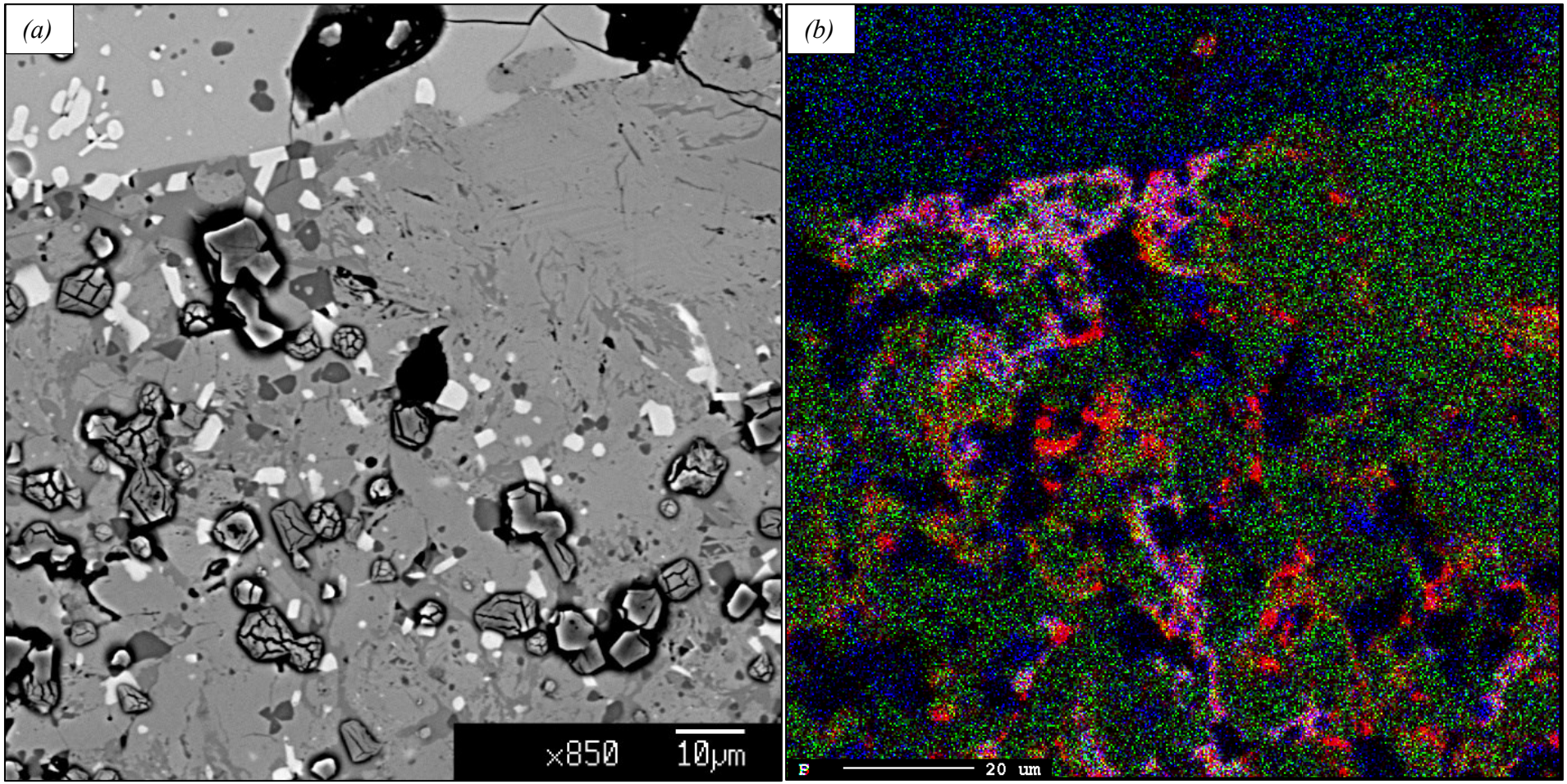

Fig. 10.27 – (a) BSE image of *RM* pellet heated at 1250 °C highlighting hatrurite crystal side on the top (light grey) with straight and undulated rims in contact with ternesite-fluorapatite (dark grey) and anhedral larnite (medium grey), respectively; moreover, rounded fully fractured lime (dark grey, ~ 10 µm), subhedral ye'elimite and mayenite (darker grey, 1-5 µm), prismatic brownmillerite (white, < 10 µm) and xenomorphic larnite (medium grey) associated with ternesite and fluorapatite s.s. (darker than larnite); (b) element map analysis on the same sample portion reported in previous BSE image reported in RGB scale (Red = S, Green = P, Blue = F), distinguishing fluorapatite s.s. in pink, ternesite s.s. in yellow orange, mayenite in blue and ye'elimite in red; furthermore, hatrurite crystal showed a slight enrichment in P and F, whereas larnite crystals only in P as revealed by the greenish shade.

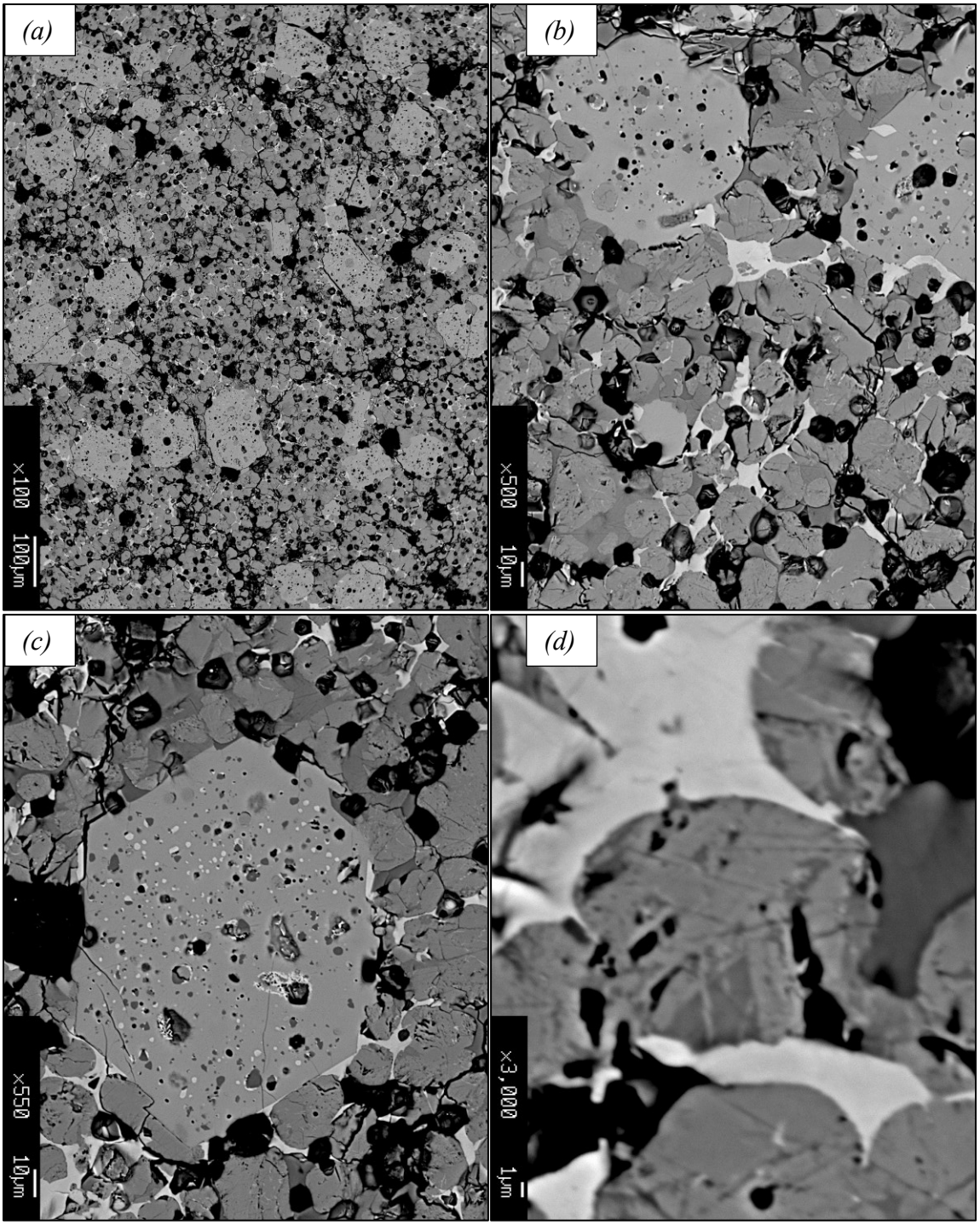

Fig. 10.28 – BSE images acquired at SEM and RLM ones for *RM* pellet heated at 1300 °C highlighting microstructural details: (a) low magnification image reporting coarse rhombic pecilitic hatrurite crystals (100-150 μm) (dull grey), xenomorphic white brownmillerite and rounded larnite (grey); (b) subhedral hatrurite with undulated rims and inclusions, subhedral fractured lime crystals (10 μm), sparce subhedral to rounded ye'elimite and mayenite, rounded larnite crystals (medium grey) enveloped in matrix of white xenomorphic brownmillerite and fluorapatite-ternesite s.s.; (c) details of pseudohexagonal peciloblastic hatrurite crystal with inclusions of all other phases; (d) microtexture details of rounded larnite crystals revealing the occurrence of ternesite and fluorapatite as inclusions.

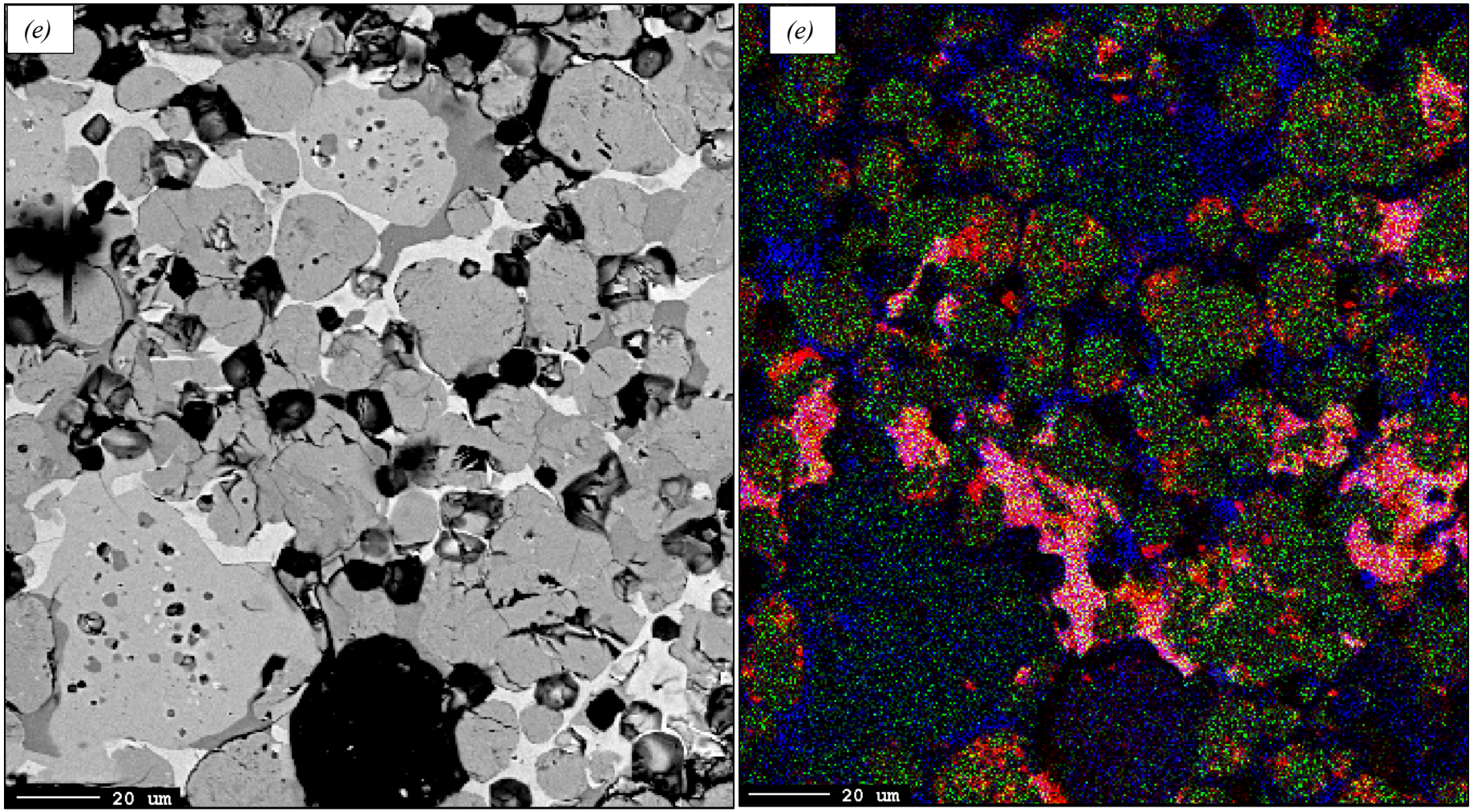

Fig. 10.29 – (a) BSE image of *RM* pellet heated at 1300 °C highlighting subhedral hatrurite crystals with undulated rims (light grey), subhedral lime (dark grey), anhedral ye'elimite and mayenite (darker grey), rounded larnite (medium grey) and a matrix of xenomorphic brownmillerite (white), fluorapatite and ternesite s.s. (darker than larnite); (b) element map analysis of previous BSE investigated portion in RGB scale (Red = S, Green = P, Blue = F) distinguishing fluorapatite s.s. (pink), ternesite s.s. (yellow orange), mayenite (blue), ye'elimite (red) and slight enrichment of P+F (bluish-green shade) and P (greenish shade) of hatrurite and larnite, respectively.

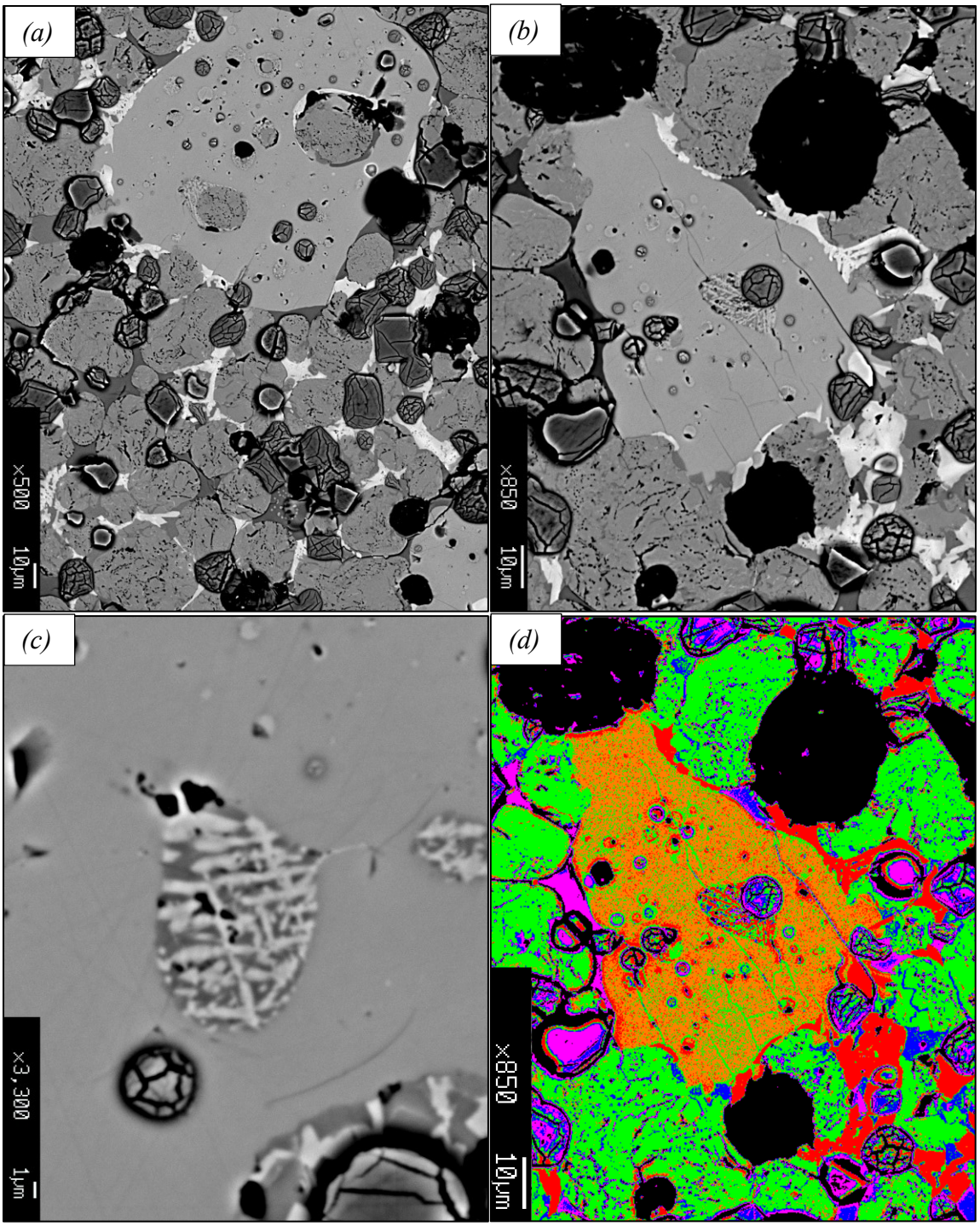

Fig. 10.30 – BSE images acquired at SEM of *RM* pellet heated at 1350 °C showing microtextural details: (a,b) coarse subhedral hatrurite with several large inclusions, rounded larnite (medium grey, 10-35 µm), subhedral lime (dark grey, 10-20 µm) and matrix of xenomorphic brownmillerite (white), fluorapatite s.s. (darker grey than larnite), mayenite and ye'elimite (dark grey colour); (c) micrometric rounded inclusion inside hatrurite of mayenite-brownmillerite exsolution with skeletal intergrowth suggesting partial melting during heating at high temperature; (d) segmentation of previous (b) BSE image using orange for hatrurite, green for larnite, red for brownmillerite, blue fluorapatite s.s. and purple for remaining mayenite, ye'elimite and rounded lime crystals due to similar grey scale tone.

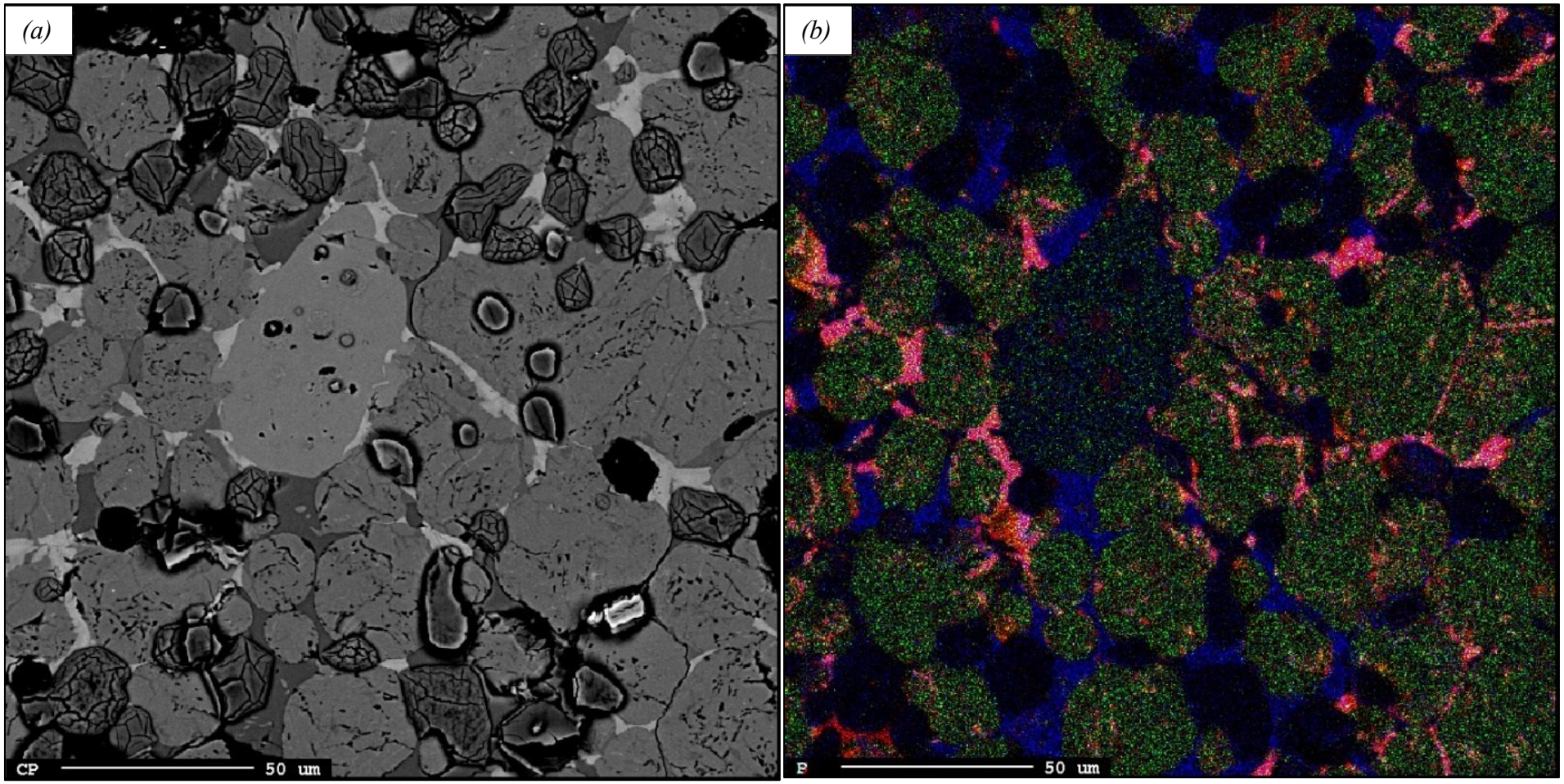

Fig. 10.31 – (a) BSE image of *RM* pellet heated at 1350 °C highlighting rounded hatrurite crystals (light grey) with pronounced lobed rims in contact with larnite, subhedral fractured lime (dark grey) and rounded slight porous larnite (medium grey) enveloped by a matrix of xenomorphic brownmillerite (white), fluorapatite s.s. (darker than larnite), mayenite and rare ye'elimite (dark grey); (b) element map analysis of previous BSE investigated portion in RGB scale (Red = S, Green = P, Blue = F) useful to distinguishing minerals in xenomorphic matrix, such as fluorapatite s.s. (pink), mayenite (blue), rare ye'elimite (red); furthermore, a slight P-S-enrichment (greenish-yellowish shade) in rounded larnite crystals occurred.

Punctual chemical investigation was performed on larnite, hatrurite, brownmillerite, ye'elimite and some mayenite crystals. Fluorapatite and ternesite crystals were tried to be investigated but mixed analysed were obtained due to their complex xenomorphic microtexture and low crystal size.

Chemical investigation on larnite occurring in all samples pointed out three main features (Table 10.5):

(i) *RM* pellets heated at different temperatures showed a mostly constant average chemical composition of larnite with P^{5+} and Al^{3+} as main ionic substituent of $^{IV}Si^{4+}$ and Fe^{3+} as minor one; whereas, Na^{+} and low amount of Mg^{2+}, Fe^{2+} and K^{+} represent ionic substituents of Ca^{2+}. Any trend was identified observing EMPA results, due to narrow chemical composition variation among all analysis. All samples revealed low amount of iron that should be both occur as Fe^{3+} and Fe^{2+}, because if only Fe^{3+} is considered, a slight excess of tetrahedral site happens. Furthermore, Fe^{3+} could not well fit calcium sites due to its lesser size, therefore Fe^{2+} should fit better in calcium site: $^{VIII}Fe^{3+}$-O bond is ~ 2.18 Å and $^{VIII}Fe^{2+}$-O is ~ 2.32 Å [291], whereas, the average Ca-O bond distance is 2.50 Å for both calcium sites [169];

(ii) only *RM* fragments heated at 1200 °C (*RFa* and *RFb*) were investigated for punctual chemical investigation and larnite crystals showed a chemical composition close to stoichiometry compared to *RM* heated pellet one: *RFa* revealed purest larnite crystals with only slight $^{IV}Al^{3+}$ and $^{IV}P^{5+}$ ionic substitution on $^{IV}Si^{4+}$; whereas, *RFb* highlighted higher amount of $^{IV}Al^{3+}$, $^{IV}P^{5+}$ and $^{IV}S^{6+}$ associated with low-amount of Ca^{2+} vacancies;

(iii) larnite in *BC* pellets heated at different temperatures figured out only an increasing trend of $^{IV}Al^{3+}$ and $^{IV}S^{6+}$, which are substituting $^{IV}Si^{4+}$, with the temperature rise, especially from 1300 to 1350 °C (Table 10.5). Furthermore, negligible amount of K^{+}, Na^{+}, Mg^{2+} and Fe^{2+} occurred, which are substituting Ca^{2+}.

Brownmillerite crystals were analysed in *BC* and *RM* pellets heated at different temperatures, excepted for *BC* at 1200 °C, whereas, no analysis was performed on *RFa* and *RFb* samples, due to low crystal size (Table 10.6). Results figured out two main features:

(i) brownmillerite crystal in *RM* samples showed an almost constant Al^{3+} and Fe^{3+}, excepted for a slight decreasing trend of the latter with the increase in temperature, whereas Mg^{2+} associated with Si^{4+} strongly increase with the temperature rise. Calcium site was always fully covered by only Ca^{2+} and no other possible substituent was found;

(ii) brownmillerite in *BC* and *RM* revealed same trends: $^{VI}Mg^{2+} + {}^{IV}Si^{4+} \rightarrow {}^{VI}Fe^{3+} + {}^{IV}Fe^{3+}$ took place with temperature increase; Al-content mainly rose from 1250 to 1300 °C, and later slightly decreased. Calcium site was fully filled by Ca^{2+}. Some brownmillerite dense aggregates showed coarser crystals with lighter colour at BSE investigation, pointing out higher and lower Fe_2O_3 and Al_2O_3 contents, respectively.

Punctual chemical investigation on hatrurite crystals were performed only *RM* pellets heated at 1250, 1300 and 1350 °C. As previously described, hatrurite always occurred as coarse euhedral to subhedral peciloblastic crystals with inclusions of all other phases (Fig. 10.26d,28c,30a,b). Results showed a constant chemical composition for each sample, only highlighting a slight increase and reduction of SiO_2 and P_2O_5, respectively, from 1250 to 1300 °C. Fluorine occurred in all samples as ionic substituent of oxygen by the reaction $^{IV}Al^{3+} + F^{-1} \rightarrow {}^{IV}Si^{4+} + O^{-2}$,

hence a normalisation to the sum of theorical cations or anions is needed to calculate the general formula. In Table 10.7 are reported two different general formulas: (i) type *A* was obtained by normalising to 5 anions (sum of O and F) and considering Fe^{2+} when tetrahedral site was fulfilled and only being hosted in Ca-site; whereas, Fe^{3+} and Al^{3+} are only found in tetrahedral site; (ii) type *B* was calculated by normalising to 4 cations, considering only Fe^{3+} and Ca-site could host Al^{3+} and Fe^{3+} but preferentially the latter; moreover, type *B* considered the ionic substitution $2^{IV}Al^{3+} + Vac.^{-2} \rightarrow 2^{IV}Si^{4+} + O^{-2}$ creating oxygen vacancies. Both types of general formula pointed out: (i) a slight increase in positive charge for Ca-site, due to a slight excess of divalent cations, mainly Fe^{2+} for type *A* and Fe^{3+} for type *B*; (ii) a decrease of positive charge on tetrahedron site due to high Al^{3+} content, which led the occurrence of oxygen vacancies for type *B*.

Ye'elimite crystals available for punctual chemical investigation were found only in *BC* samples heated at 1300 and 1350 °C, while crystals in other samples gave mixed analysis useless for chemical composition study (Table 10.8). Mg^{2+}, K^{+} and Na^{+} slightly substituted Ca^{2+}; however, monovalent cations (K^{+} and Na^{+}) are charge balanced by Si^{4+} substituting Al^{3+}. Iron was fully considered as Fe^{3+}, representing an important substituent of Al^{3+}. Fe^{3+} and Mg^{2+} content slightly increased with the temperature rise.

Punctual chemical investigation on mayenite was performed only on *RM* pellet heated at 1250 °C because tries on other samples, both *RM* and *BC* ones, gave mixed chemical analysis especially with larnite and ye'elimite. Results highlighted that Mg^{2+} and Fe^{3+} are the main substituent of Ca^{2+} and Al^{3+}, respectively, whereas the substitution $Na^{+} + Si^{4+} \rightarrow Ca^{2+} + Al^{3+}$slightly occurred (Table 10.9). Moreover, mayenite in *RM* sample should be considered closer to fluormayenite end member due to its fluorine-rich content.

Samples	*RM*				*RFa*	*RFb*	*BC*			
T vs Oxide (wt.%)	***1200 °C (n = 11)°***	***1250 °C (n =9)°***	***1300 °C (n = 5)°***	***1350 °C (n = 11)°***	***1200 °C (n = 5)°***	***1200 °C* (n = 4)°***	***1200 °C* (n = 4)°***	***1250 °C (n = 5)°***	***1300 °C (n = 9)°***	***1350 °C (n = 25)°***
F	*b.d.*	*b.d.*	*b.d.*	*b.d.*	*b.d.*	*b.d.*	*b.d.*	*b.d.*	*b.d.*	*b.d.*
Na_2O	0.41(.11)	0.47(.13)	0.38(6)	0.32(8)	0.16(7)	*b.d.*	*b.d.*	0.10(8)	0.05(2)	0.17(9)
P_2O_5	4.54(.19)	4.54(.54)	4.54(.22)	4.30(.35)	1.40(.91)	2.96(.61)	*b.d.*	0.12(3)	0.14(7)	0.57(7)
Fe_2O_3	1.34(.39)	1.11(.32)	1.25(23)	1.19(.26)	0.23(.13)	0.29(.33)	*b.d.*	0.30(9)	0.30(9)	0.63(7)
K_2O	0.06(3)	0.12(4)	0.12(2)	0.09(8)	0.02(2)	*b.d.*	*b.d.*	0.39(.41)	0.11(7)	0.13(5)
MgO	0.09(6)	0.17(.15)	0.21(.11)	0.16(.11)	0.02(2)	*b.d.*	*b.d.*	0.01(2)	0.04(2)	0.17(4)
SO_3	1.79(6)	1.35(9)	1.71(.11)	1.71(.44)	0.04(3)	1.43(1.14)	0.45(.35)	1.10(1.05)	0.58(.16)	1.00(.23)
CaO	61.27(.35)	62.33(.42)	63.68(.45)	62.16(1.77)	63.76(.45)	63.67(0.91)	65.02(.95)	64.95(1.06)	63.78(.37)	63.08(.30)
Al_2O_3	3.00(.28)	3.17(.26)	3.27(.29)	3.43(.20)	0.69(.55)	1.59(0.80)	0.59(.39)	0.75(.14)	0.79(.22)	1.44(.43)
Cl	0.01(7)	*b.d.*	*b.d.*	*b.d.*	0.01(1)	*b.d.*	*b.d.*	*b.d.*	*b.d.*	*b.d.*
TiO_2	0.24(2)	*b.d.*	0.24(5)	0.23(4)	0.07(3)	*b.d.*	*b.d.*	*b.d.*	0.09(3)	0.17(4)
SiO_2	24.41(.43)	24.50(.94)	24.45(.90)	24.51(.69)	32.86(1.77)	30.18(2.94)	33.95(.58)	33.50(.63)	33.27(.47)	31.33(.49)
Cr_2O_3	0.08(4)	*b.d.*	0.11(1)	0.08(4)	0.09(7)	*b.d.*	*b.d.*	*b.d.*	0.02(2)	0.01(1)
Total	97.24(.55)	97.84(.50)	99.96(.44)	98.18(1.49)	99.44(.58)	101.12(3)	100.01(.25)	101.22(.17)	99.17(.17)	98.70(.55)
X_2YO_4 – Larnite (Ca_2SiO_4)$^{\$}$										
	Ca^{2+}	1.939(.016)	1.963(.011)	1.963(8)	1.947(.039)	1.967(9)	1.982(.038)	1.990(.030)	1.971(.037)	1.974(8)	1.983(.019)
	Mg^{2+}	0.004(3)	0.007(6)	0.009(5)	0.007(5)	0.001(7)	-	-	0.001(4)	0.002(1)	0.007(2)
X	**Na^{+}**	0.023(6)	0.027(7)	0.021(3)	0.018(5)	0.009(4)	-	-	0.006(2)	0.003(5)	0.005(2)
	K^{+}	0.002(1)	0.004(2)	0.004(8)	0.003(3)	0.001(1)	-	-	0.014(5)	0.004(2)	0.005(2)
	Fe^{2+}	0.011(9)	-	-	0.011(9)	0.005(3)	-	-	0.004(2)	0.006(2)	0.008(5)
	Si^{4+}	0.721(.016)	0.720(.027)	0.703(.030)	0.716(.019)	0.946(.049)	0.863(.085)	0.970(.021)	0.949(.05)	0.961(.010)	0.919(.01)
	P^{5+}	0.113(4)	0.113(.013)	0.111(5)	0.106(8)	0.034(.019)	0.054(.037)	-	0.003(1)	0.004(2)	0.004(2)
	Al^{3+}	0.104(9)	0.110(9)	0.111(.010)	0.118(7)	0.027(.018)	0.040(.041)	0.020(4)	0.025(5)	0.027(7)	0.050(2)
Y	**Fe^{3+}**	0.013(3)	0.025(7)	0.027(5)	0.016(9)	-	-	-	0.002(3)	0.001(2)	0.005(5)
	S^{6+}	0.039(.016)	0.030(2)	0.037(8)	0.038(9)	0.001(1)	0.031(3)	0.010(3)	0.023(.02)	0.013(4)	0.022(5)
	Ti^{4+}	0.005(1)	-	0.005(1)	0.003(3)	0.001(1)	-	-	-	0.002(6)	0.001(2)
	Cr^{3+}	0.002(1)	-	0.002(1)	0.001(1)	0.002(2)	-	-	-	0.001(1)	0.001(1)
O^{2-}	4	4	4	4	4	4	4	4	4	4

Table 10.5 – EMPA results from punctual chemical investigation on larnite in synthetic samples laboratory prepared; e.s.d. is reported in rounded brackets; *results are coming from SEM-EDS analysis; b.d., below detection limit; °number of analysis; $the general formula was calculated based on normalisation to 8 negative charges, Fe^{2+} molar value was considered and estimated only when the Y site was completely fulfilled.

Samples		*RM*				*BC*			
Temperature / Oxide (wt.%)		*1200 °C (n = 3)°*	*1250 °C (n =6)°*	*1300 °C (n = 5)°*	*1350 °C (n =5)°*	*1250 °C (n = 5)°*	*1300 °C* (n = 6)°*	*1300 °C (n = 7)°*	*1350 °C (n = 10)°*
F		0.00	0.02(2)	0.00	0.00	0.11(2)	0.01(2)	0.03(2)	0.02(3)
Na_2O		0.25(4)	0.01(9)	0.19(2)	0.03(2)	0.02(3)	0.02(2)	0.02(2)	0.04(4)
P_2O_5		0.04(4)	0.01(8)	0.20(5)	0.28(8)	0.01(3)	0.01(1)	0.01(1)	0.03(.04)
Fe_2O_3		28.50(.33)	26.52(1.11)	24.19(1.38)	25.77(1.86)	54.62(1.94)	29.70(1.27)	41.39(3.44)	29.22(.99)
K_2O		0.04(8)	0.07(.10)	0.03(3)	0.01(1)	0.01(1)	0.030(2)	0.01(1)	0.11(.23)
MgO		1.30(.16)	1.35(5)	2.00(.17)	2.42(.13)	0.84(.16)	1.30(9)	1.08(9)	0.06(.20)
SO_3		0.07(.20)	0.13(.20)	0.17(.12)	0.15(4)	0.01(1)	0.04(3)	0.00	0.16(22)
CaO		46.17(.22)	47.08(.21)	47.59(.53)	45.96(.40)	41.22(.35)	46.41(.50)	44.13(.62)	45.51(.43)
Al_2O_3		20.41(1.22)	22.54(.75)	20.30(1.33)	19.16(2.23)	2.06(1.25)	20.03(.75)	12.09(3.16)	17.47(1.71)
Cl		0.01(1)	0.00	0.00	0.00	0.00	0.00	0.00	0.00
TiO_2		1.36(7)	0.00	1.26(18)	0.00	0.00	0.88(.12)	0.27(7)	0.00
SiO_2		0.40(2)	0.43(.10)	2.03(.40)	2.31(.31)	0.32(7)	0.64(4)	0.63(3)	3.13(.91)
Cr_2O_3		0.02(2)	0.00	0.00	0.00	0.00	0.01(2)	0.01(2)	0.00
Total		98.57(1.26)	98.88(.36)	98.67(76)	96.09(.52)	99.22(.30)	99.07(.44)	99.67(.57)	97.75(.78)
X_2YO_5 – Brownmillerite ($Ca_2(Al,Fe)_2O_5$)$^{\$}$									
X	**Ca^{2+}**	2.01(5)	2.04(6)	2.06(3)	2.03(2)	1.98(1)	2.02(3)	1.99(2)	2.01(1)
Y	**Mg^{2+}**	0.08(1)	0.08(3)	0.12(.11)	0.15(8)	0.06(1)	0.068(2)	0.079(5)	0.11(1)
	Fe^{2+}	0.00	0.00	0.01(5)	0.00	0.00	0.00	0.00	0.04(1)
	Si^{4+}	0.02(1)	0.02(4)	0.08(2)	0.10(2)	0.01(1)	0.03(1)	0.03(1)	0.13(4)
	Al^{3+}	0.98(4)	1.08(3)	0.95(6)	0.93(9)	0.11(7)	0.957(.032)	0.60(.15)	0.85(8)
	Fe^{3+}	0.87(1)	0.81(4)	0.73(4)	0.80(6)	1.84(8)	0.91(4)	1.31(.14)	0.87(6)
	Ti^{4+}	0.04(3)	0.00	0.04(5)	0.00	0.00	0.03(4)	0.01(1)	0.00
O^{2-}		5	5	5	5	5	5	5	5

Table 10.6 – EMPA results from punctual chemical investigation on brownmillerite in synthetic samples laboratory prepared; e.s.d. is reported in rounded brackets; °number of analysis; $^{\$}$the general formula was calculated by normalising to 10 negative charges, the Fe^{2+} was considered and estimated only when the site Y was not completely fulfilled; *, analysis on coarser brownmillerite crystals in *BC* sample heated at 1300 °C.

Sample / Oxide (wt.%)	*RM*		
	1250 °C (n = 5)°	*1300 °C (n = 5)*	*1350 °C (n = 10)*
F	0.10(.11)	0.07(.10)	0.12(.11)
Na_2O	0.06(4)	0.04(.03)	0.08(2)
P_2O_5	2.26(.28)	1.93(.08)	1.93(0.15)
Fe_2O_3	0.88(5)	0.78(.17)	0.79(.21)
K_2O	0.01(1)	0.01(1)	0.01(1)
MgO	0.76(5)	0.68(4)	0.73(7)
SO_3	0.13(4)	0.08(4)	0.14(.16)
CaO	71.13(.27)	72.18(.64)	70.90(1.62)
Al_2O_3	3.21(.20)	2.60(.24)	2.94(.77)
Cl	0.00	0.00	0.00
TiO_2	0.00	0.21(5)	0.19(6)
SiO_2	20.02(.16)	21.35(.50)	20.72(.92)
Cr_2O_3	0.0	0.02(2)	0.04(2)
Total	98.55(.18)	99.94(.68)	98.46(1.64)

Table continue below with formula calculation

X_3YZ_5 – Hatrurite							
	Calcul. Type	***A*$**	***B*^**	***A*$**	***B*^**	***A*$**	***B*^**
X	**Ca^{2+}**	2.952(8)	2.933(9)	2.951(6)	2.937(6)	2.940(3)	2.927(2)
	Mg^{2+}	0.044(3)	0.044(3)	0.039(3)	0.039(2)	0.042(2)	0.042(4)
	Na^{+}	0.005(3)	0.005(3)	0.003(2)	0.003(2)	0.006(1)	0.006(1)
	Fe^{2+}	0.020(6)	-	0.020(5)	-	0.017(9)	-
	Fe^{3+}	-	0.018(8)	-	0.021(6)	-	0.023(6)
	Al^{3+}	-	-	-	-	-	0.002(2)
	Sum	3.021(8)	3.000	3.013(4)	3.000	3.006(.014)	3.000
	Pos. Charges	6.036(.012)	6.013(.01)	6.023(8)	6.018(5)	6.005(.033)	6.019(.021)
Y	**Si^{4+}**	0.775(7)	0.770(7)	0.815(2)	0.811(9)	0.802(3)	0.798(.034)
	P^{5+}	0.074(9)	0.074(9)	0.062(3)	0.062(3)	0.063(5)	0.063(5)
	Al^{3+}	0.146(9)	0.144(9)	0.117(9)	0.117(9)	0.134(.036)	0.132(.025)
	Fe^{3+}	0.006(5)	0.008(3)	0.002(2)	0.001(1)	0.004(6)	-
	S^{6+}	0.004(1)	0.004(1)	0.002(2)	0.002(1)	0.004(3)	0.004(5)
	Ti^{4+}	0.000	0.000	0.006(1)	0.006(2)	0.003(3)	0.003(3)
	Cr^{3+}	0.000	0.000	0.001(6)	0.001(6)	0.001(8)	0.001(3)
	Sum	1.006(5)	1.000	1.005(2)	1.000	1.012(.010)	1.00
	Pos. Charges	3.951(.019)	3.930(.014)	3.968(.011)	3.947(9)	3.980(.030)	3.941(.025)
Z	**O^{2-}**	4.988(.013)	4.966(.010)	4.992(.012)	4.978(9)	4.986(.013)	4.972(.021)
	F^{-}	0.012(.013)	0.012(.010)	0.008(.012)	0.008(.012)	0.014(.013)	0.014(.013)
	Sum	5.000	4.977(.014)	5.000	4.986(.014)	5.000	4.986(.022)
	Vacancies	-	0.023(9)	-	0.014(4)	-	0.013(.013)
	Neg. Charges	9.988(.013)	9.942(.017)	9.992(.012)	9.965(6)	9.986(.013)	9.958(3)

Table 10.7 – EMPA results for hatrurite punctual chemical investigation in *RM* samples heated at 1250, 1300 and 1350 °C; e.s.d. is reported in rounded brackets; °number of analysis; $, general formula was calculated by firstly normalising to 10 negative charges, following by normalisation to 5 for Z site (sum of O^{2-} and F^{-}), and Fe^{2+} was taken into consideration only when Y site was completely filled by the other elements also Fe^{3+}; ^, other general formula was calculated by firstly normalising to 10 negative charges, following by normalisation to 4 cations (sum of Y and X sites), considering all Fe as trivalent and X site hosting Fe^{3+} and the remaining Al^{3+} to fulfil the calcium site.

Sample / Oxide (wt.%)		*BC*	
		1300 °C (n = 5)°	*1350 °C (n = 13)°*
F		0.00	0.00
Na_2O		0.02(3)	0.06(2)
P_2O_5		0.02(4)	0.01(3)
Fe_2O_3		1.28(.18)	1.80(.17)
K_2O		0.14(.13)	0.11(5)
MgO		0.09(2)	0.09(3)
SO_3		12.98(9)	13.22(.22)
CaO		36.39(.20)	36.13(.22)
Al_2O_3		48.91(.22)	49.79(.28)
Cl		0.00	0.00
TiO_2		0.01(1)	0.00
SiO_2		0.49(.24)	0.41(.17)
Cr_2O_3		0.01(2)	0.00
Total		100.34(.51)	100.62(.47)
$X_4Y_6ZO_{16}$ – Ye'elimite			
X	**Ca^{2+}**	2.95(1)	2.95(1)
	Mg^{2+}	0.01(1)	0.01(1)
	Na^{+}	0.01(1)	0.01(1)
	K^{+}	0.02(2)	0.01(1)
Y	**Si^{4+}**	0.05(2)	0.04(2)
	Al^{3+}	5.86(3)	5.84(4)
	Fe^{3+}	0.10(1)	0.14(1)
Z	**S^{6+}**	0.99(1)	0.99(2)
O^{2-}		16	16

Table 10.8 – EMPA results for ye'elimite punctual chemical investigation in *BC* samples laboratory prepared; e.s.d. is reported in rounded brackets; °number of analyses; $^{\$}$the general formula was calculated by normalising to 32 negative charges.

Sample / Oxide (wt.%)		*RM 1250 °C (n = 4)°*
F		1.73(.13)
Na_2O		0.07(2)
P_2O_5		0.04(4)
Fe_2O_3		2.26(2.35)
K_2O		0.05(4)
MgO		0.24(.25)
SO_3		0.04(9)
CaO		45.32(.94)
Al_2O_3		46.81(1.06)
Cl		0.00
TiO_2		0.00
SiO_2		0.15(6)
Cr_2O_3		0.00
Total		96.71(1.77)
General formula X_{12} Y_{14} $O_{33-x/2}$ W_x (normalised to 66 negative charges§)		
X	**Ca^{2+}**	11.87(2)
	Mg^{2+}	0.09(1)
	Na^{+}	0.03(1)
	K^{+}	0.01(1)
Y	**Si^{4+}**	0.04(2)
	Al^{3+}	13.48(5)
	Fe^{3+}	0.43(1)
	S^{6+}	0.02(1)
O	**O^{2-}**	32.32(1)
W	**F^{-1}**	1.34(.12)

Table 10.9 – EMPA results for mayenite punctual chemical investigation in *RM* sample heated at 1250 °C; e.s.d. is reported in rounded brackets; °number of analyses; $the general formula was calculated by firstly normalising to 66 negative charges, and the stochiometric value of O was calculated by 33-(W/2).

QTA was performed by means of NXRD on fragment and pellet of *RM* heated at 1200 °C (*RFb* and *RM* samples) using larnite and ternesite as proxy for preferred crystallographic orientations due to their major abundances in the samples (Table 10.2, Fig. 10.4). Ternesite and larnite reconstructed pole figures were made using main intense Bragg peaks. *RM* pellet heated at 1200 °C should be considered as a standard sample with no preferred orientation due to its preparation: sample was obtained from homogenous fine grinded powder of Ghareb Formation rocks, firstly decarbonated at 950 °C, re-grinded and pelletised at high pressured, following by thermal treatment at 1200 °C for 8 hours. Results highlighted no preferred crystallographic orientation inside both samples giving similar reconstructed pole figures, as confirmed by the almost constant multiple of random distribution (m.r.d.) than remained in the range 0.75-1.20 (Fig. 10.32-35).

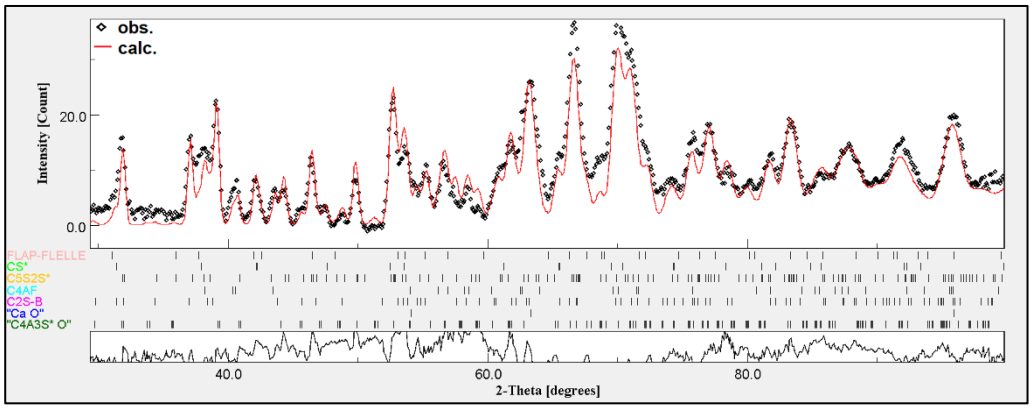

Fig. 10.32 – NXRD pattern fitting of *RFb* sample showing the goodness of fitting between observed (black rhombs) and calculated (red line) patterns.

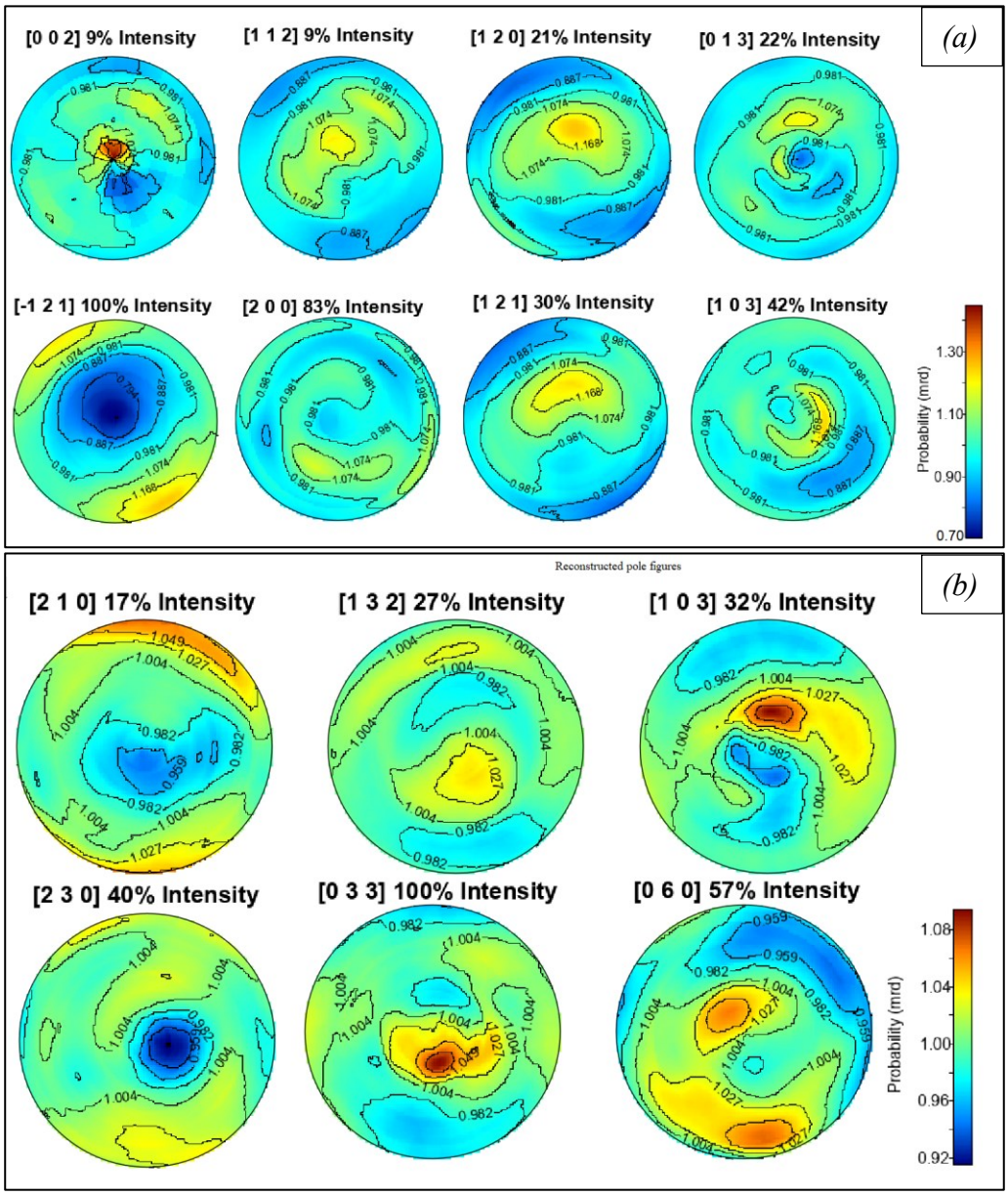

Fig. 10.33 – Reconstructed pole figures from NXRD for QTA on *RFb* sample showing main Bragg peaks of (a) larnite and (b) ternesite, both revealing no preferred crystallographic orientation.

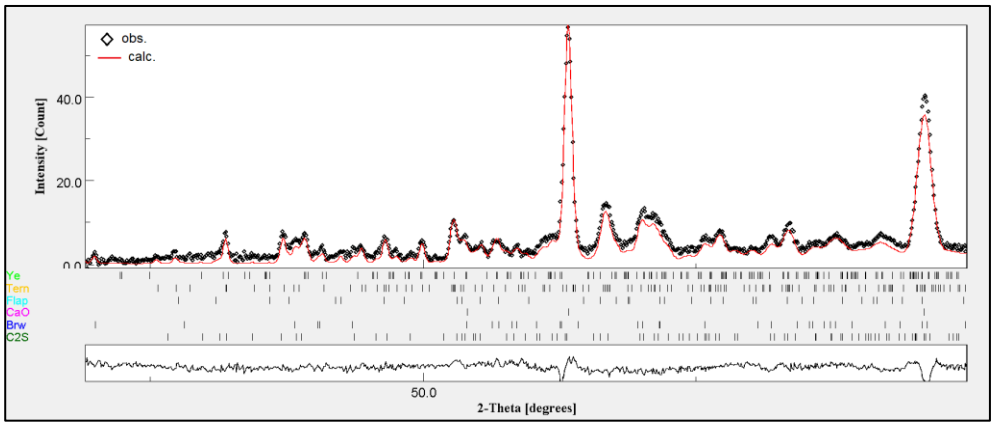

Fig. 10.34 – NXRD pattern fitting of *RM* sample heated at 1200 °C showing the goodness of fitting between observed (black rhomb) and calculated (red line) patterns.

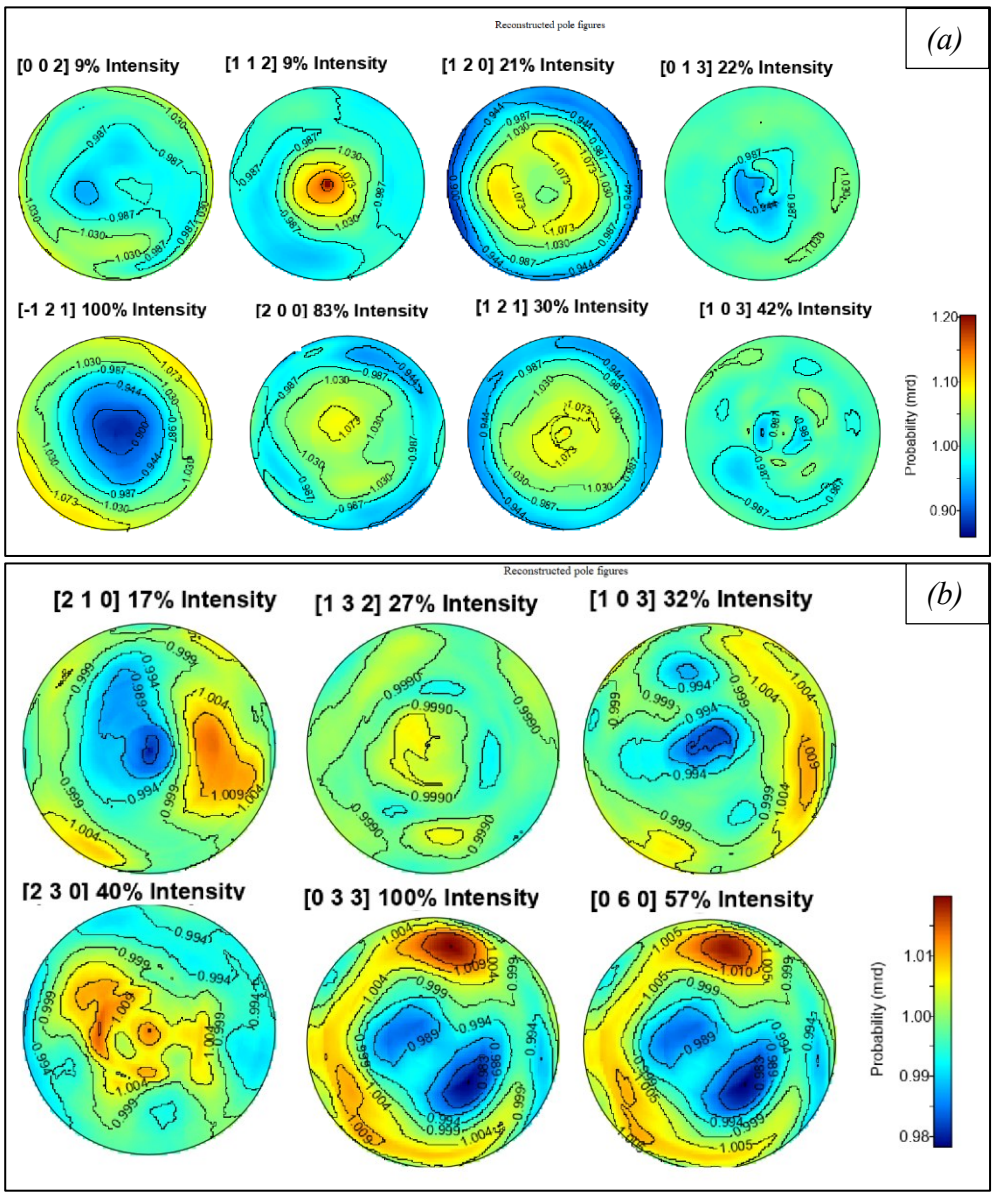

Fig. 10.35 – Reconstructed pole figures from NXRD for QTA on *RM* pellet heated at 1200 °C showing main Bragg peaks of (a) larnite and (b) ternesite, both revealing no preferred crystallographic orientation.

BC pellet heated at 1200 °C was also studied by means of SXRPD at ID22 (ESRF) leading detailed crystallographic information. Due to the high larnite content crystal structure refinement of β-C_2S was made following this refinement strategy: (i) RQPA on all occurring phases, also refining crystallite size and microstrain for main crystal phases (larnite, brownmillerite and ye'elimite), was made; (ii) larnite crystal structure from Jost et al. [169] was used as starting point, but punctual chemical investigation results (Table 10.5) were considered, fixing the atomic fraction of tetrahedral site to 0.97 Si^{4+}, 0.02 Al^{3+} and S^{+6}; (iii) stopping the refinement of crystallite size and microstrain values for all phases, refining all atomic position and thermal parameters (Uiso) for larnite.

Crystallographic parameters of larnite in *BC* sample revealed values closer to larnite found in OPC [170], and higher compared to pure synthetic larnite [169], excepted for slight lower β angle (Table 10.10). Furthermore, tetrahedron bond distances with oxygen slightly reduced, but no changes on O-Si-O angle value occurred (Table 10.12); whereas, a general stretch of Ca-O bonds in polyhedron (sevenfold and eightfold coordination for Ca1 and Ca2, respectively) occurred, excepted for a few Ca1-O bonds (Table 10.13,14).

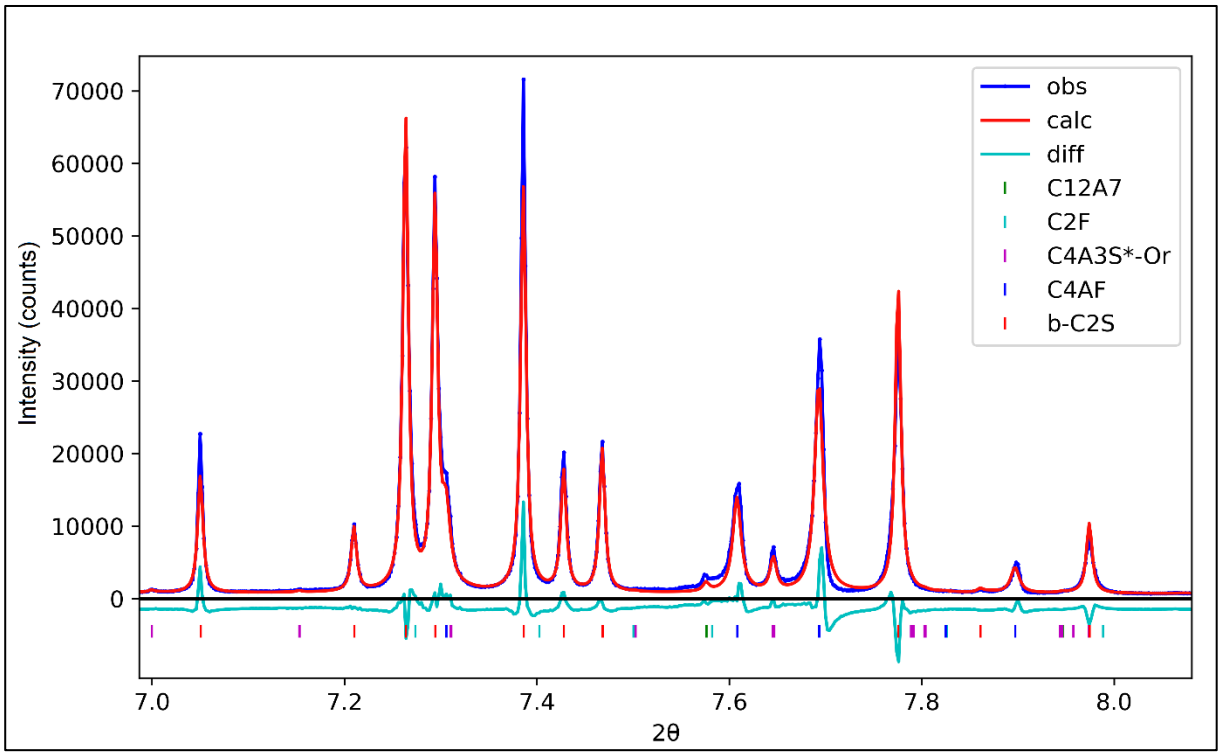

Fig. 10.36 – Fitted SXRPD pattern (*BC* heated at 1200 °C) after crystal structure refinement of larnite using GSAS-ii software; blue line the observed pattern, red line the calculated one and the lower coloured sticks represent Bragg peaks of occurring crystal phases.

Crystal Phase	Larnite (β-Ca_2SiO_4, β-C_2S)		
Configuration	*SXRPD (ID22)* (our study)	*SCXRD* [169]	*NXRPD* [170]
λ (Å)	0.354109	0.710749 (Mo)	1.478
Chemical Composition*	$Ca_2Si_{0.97}Al_{0.02}S_{0.01}O_4$	Ca_2SiO_4	-
Space Group	*P2₁/n*	*P2₁/n*	*P2₁/n*
a (Å)	5.51483(2)	5.5020(1)	5.5172(4)
b (Å)	6.76035(2)	6.745(1)	6.76996(6)
c (Å)	9.32106(4)	9.297(3)	9.32298(8)
β (°)	94.5522(2)	94.59(4)	94.336(2)
V (Å³)	346.413(1)	343.9(1)	347.228(1)
Z	4	4	4
R-Factor (%)	2.87	-	-
Number of Reflections	2601	995	-
Range of d (Å) investigated	0.5177 – 5.4666	1.37 – 5.47	0.93 – 5.67
Rexp	1.00	-	-
Rwp	8.623	-	-
GoF	8.59	-	-

Table 10.10 – Crystallographic parameters for larnite crystal structure refinement from *BC* pellet heated at 1200 °C analysed with SXRPD (ID22) and bibliographic data [169,170]; *, chemical composition reported is coming from SEM-EDS punctual chemical investigation (Table 10.5); -, not available data.

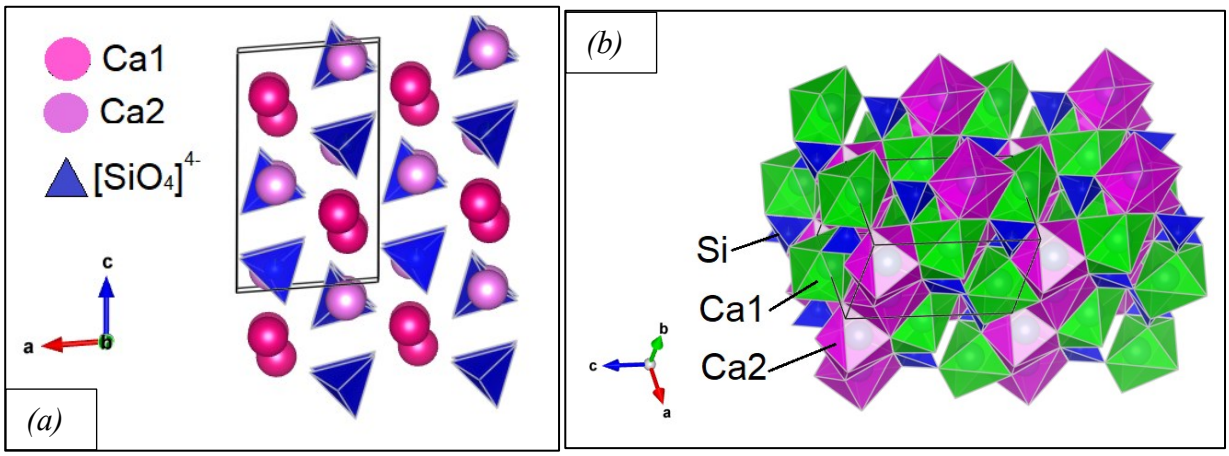

Fig. 10.37 – Crystal structure of the refined larnite along b vector ([010] direction): (a) highlighting the nesosilicate structure with two different calcium sites; (b) the different coordination polyhedral for Ca1 and Ca2, 7 and 8, respectively.

Label	Type	x	y	z	frac.	Uiso	m*
Ca1	Ca^{2+}	0.2723(2)	0.34281(1.4)	0.56959(1.0)	1	0.0081(3)	4
Ca2	Ca^{2+}	0.2794(2)	0.99755(1.4)	0.29776(1.0)	1	0.0084(3)	4
	Si^{4+}	0.2330(3)	0.7816(2)	0.5821(2)	0.97	0.003(4)	4
Si1	Al^{3+}	0.23299(3)	0.7816(2)	0.5821(2)	0.02	0.003(4)	4
	S^{6+}	0.2330(3)	0.7816(2)	0.5821(2)	0.01	0.003(4)	4
O1	O^{2-}	0.28254(5)	0.0106(4)	0.5599(3)	1	0.0153(8)	4
O2	O^{2-}	0.0223(5)	0.7491(4)	0.6899(3)	1	0.0140(9)	4
O3	O^{2-}	0.4823(5)	0.6691(4)	0.6377(3)	1	0.0131(8)	4
O4	O^{2-}	0.1553(5)	0.6727(4)	0.4301(3)	1	0.0179(9)	4

Table 10.11 – Atomic positions and crystallographic parameters of the refined larnite crystal structure for *BC* heated at 1200 °C collected at SXRPD (ID22) by means of Rietveld method with GSAS-ii; e.s.d. is reported is rounded brackets; *multiplicity number of the atomic site.

Bond	New Bond Distance (Å)	Previous Bond Distance (Å)
(Si1-O1)	1.58935	1.61464
(Si1-O2)	1.61134	1.62737
(Si1-O3)	1.62036	1.64586
(Si1-O4)	1.62370	1.65870
Angle	**New Angle (°)**	**Previous Angle (°)**
(O3-Si1-O2)	111.85	111.74
(O2-Si1-O4)	109.24	110.15
(O4-Si1-O3)	103.01	102.83
(O1-Si1-O3)	110.42	110.97
(O1-Si1-O2)	110.71	109.44
(O1-Si1-O4)	111.40	111.46

Table 10.12 – Angle and bond values for atomic site Si1, which includes Si, S and Al, and oxygens belonging to silicon tetrahedron, calculated for refined and referee larnite crystal structures [169].

Bond	New Bond Distance (Å)	Previous Bond Distance (Å)
(Ca2-O2)	2.40825	2.39159
(Ca2-O4)	2.63630	2.62844
(Ca2-O1)	2.66335	2.64908
(Ca2-O3)	2.40651	2.40076
(Ca2-O2)	2.39710	2.38768
(Ca2-O1)	2.44434	2.44495
(Ca2-O4)	2.48310	2.45098
(Ca2-O3)	2.65401	2.65097

Table 10.13 – Bond distance values for atomic site Ca2, which is connected with 8 neighbour oxygen, calculated for refined and referee larnite crystal structures [169].

Bond	New Bond Distance (Å)	Previous Bond Distance (Å)
(Ca1-O3)	2.44710	2.42614
(Ca1-O1)	2.24950	2.23208
(Ca1-O2)	2.51134	2.50840
(Ca1-O3)	2.54807	2.55348
(Ca1-O4)	2.36140	2.37210
(Ca1-O4)	2.63620	2.64872
(Ca1-O2)	2.87300	2.89715

Table 10.14 – Bond distance values for atomic site Ca1, which is connected with 7 neighbour oxygens, calculated for refined and referee larnite crystal structures [169].

Euhedral hatrurite crystals were selected from *RM* pellet heated at 1250 °C and investigated by SCXRD at PXI beamline at PSI synchrotron. Collected data was refined using CrysAlisPro v. 1.171.40.36a software: results from unit cell finding and space group identification revealed a good fitting with $R\bar{3}m$ space group, despite none previous study reported the centre of symmetry for hatrurite. The two modification of monoclinic polymorphs (M1 and M3) are usually found in OPC; furthermore, rhombohedral space group R3m had been firstly identified as pseudo-rhombohedral average structure for hatrurite, later identifying a monoclinic cell (Cm) due to the occurrence of extra Bragg spots [347]. Moreover, hatrurite crystals often display twinning form, thus making the problem of solving the structure highly difficult [161]. Further investigation will be performed in other to solve its crystal structure.

Crystal phase	Hatrurite (also called alite, tricalcium silicate, C_3S)
Chemical Composition*	$(Ca_{2.94}Mg_{0.04}Fe^{2+}_{0.02})(Si_{0.8}P_{0.1}Al_{0.1})O_{4.99}F_{0.01}$ $(Ca_{2.94}Mg_{0.04}Fe^{3+}_{0.02})(Si_{0.79}P_{0.07}Al_{0.14})O_{4.97}F_{0.01}$ $\square_{0.02}$
Crystal size (mm)	0.15 x 0.05 x 0.03
Space Group from refinement	$R\bar{3}m$
***a* (Å)**	7.07873(1)
***b* (Å)**	7.07873(2)
***c* (Å)**	25.0565(5)
α (°)	89.9934(2)
β (°)	90.0068(2)
γ (°)	120.005(2)
***V* (Å^3)**	1087.35(4)
Synchrotron Wavelength (Å)	0.70848
Range for data collection, θ (°)	3.4105-34.7859
Reciprocal space range hkl	$-11 \leq h \leq 11$ $-11 \leq k \leq 11$ $-31 \leq l \leq 32$
Set of measured reflections	3774
Absorption correction method	Empirical correction (ABSPACK) using spherical harmonics

Table 10.15 – Parameters and results from SCXRD (at PXI beamline at PSI synchrotron) investigation on hatrurite crystal in *RM* pellet heated at 1250 °C; *, simplified chemical formulas from EMPA results (reported in Table 10.7) considering the two different calculations.

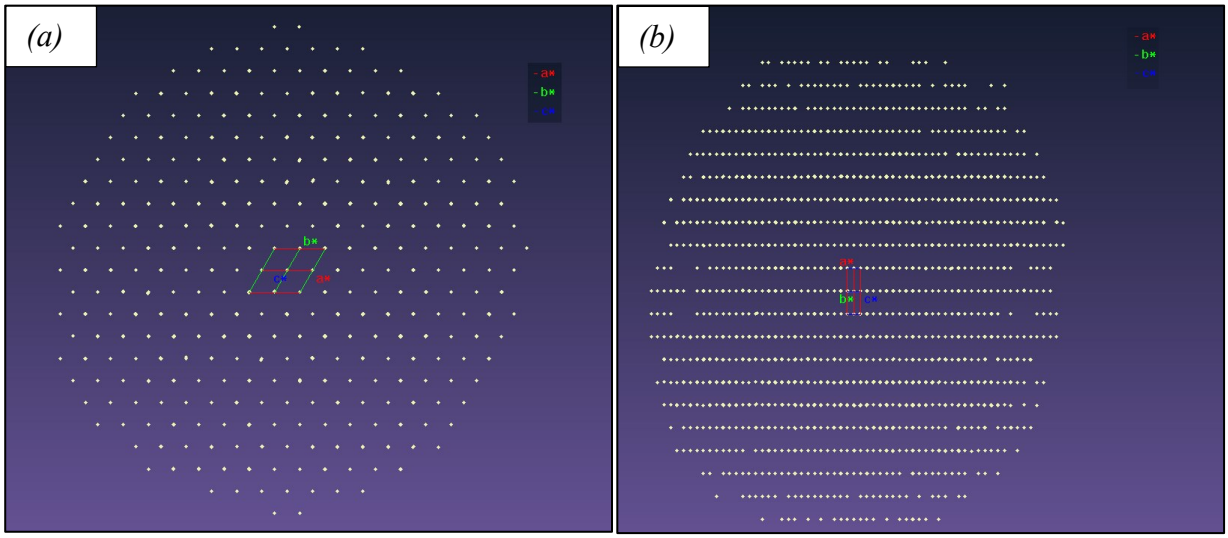

Fig. 10.38 – Reciprocal space projection of Bragg peaks (a) along c vector [001] and (b) b vector [010] for an hatrurite crystal in RM1250 analyzed by SCXRD at synchrotron facility source.

In-situ HT X-ray μ-CT was performed on Ghareb Fm. fragment at RT, 900, 1150, 1250 °C and after heating at 1350 °C. Results allowed to highlight changes in porosity, voids distribution and shape; whereas crystal phase identification and distribution was not practicable due to the extreme low crystal size and similar density among phases. Rock fragment showed changes of total voids amount at different temperatures: 7.81vol.% of voids at RT before heating, which could be even higher considering the pixel resolution (2.4 μm) and fine microtexture of chalk [348]; 2.47vol.% at 900 °C; 3.64vol.% at 1150 °C; 6.61vol.% at 1250 °C; 7.16vol.% at RT after heating at 1350 °C.

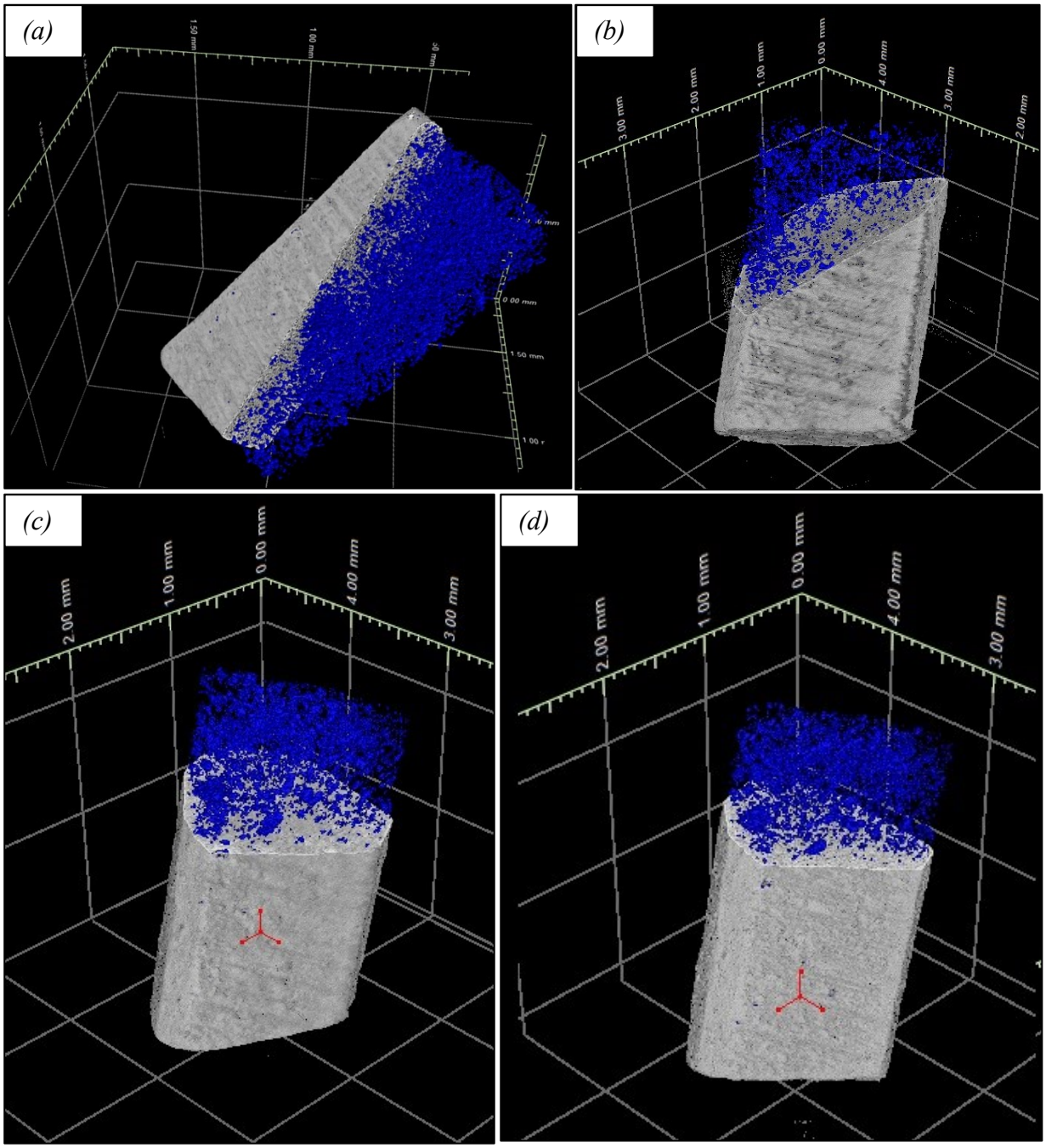

Fig. 10.39 – Volume rendering of Ghareb Fm. fragment during *in-situ* experiment by means of synchrotron X-ray μ-CT, highlighting in blue voids: (a) sample collected at RT before thermal treatment with a clipping plane parallel to the elongation; (b) sample at 900 °C with a crossing clipping plane; (c) sample at 1150 °C with a clipping plane in the middle; (d) sample at 1250 °C with a clipping plane in the middle.

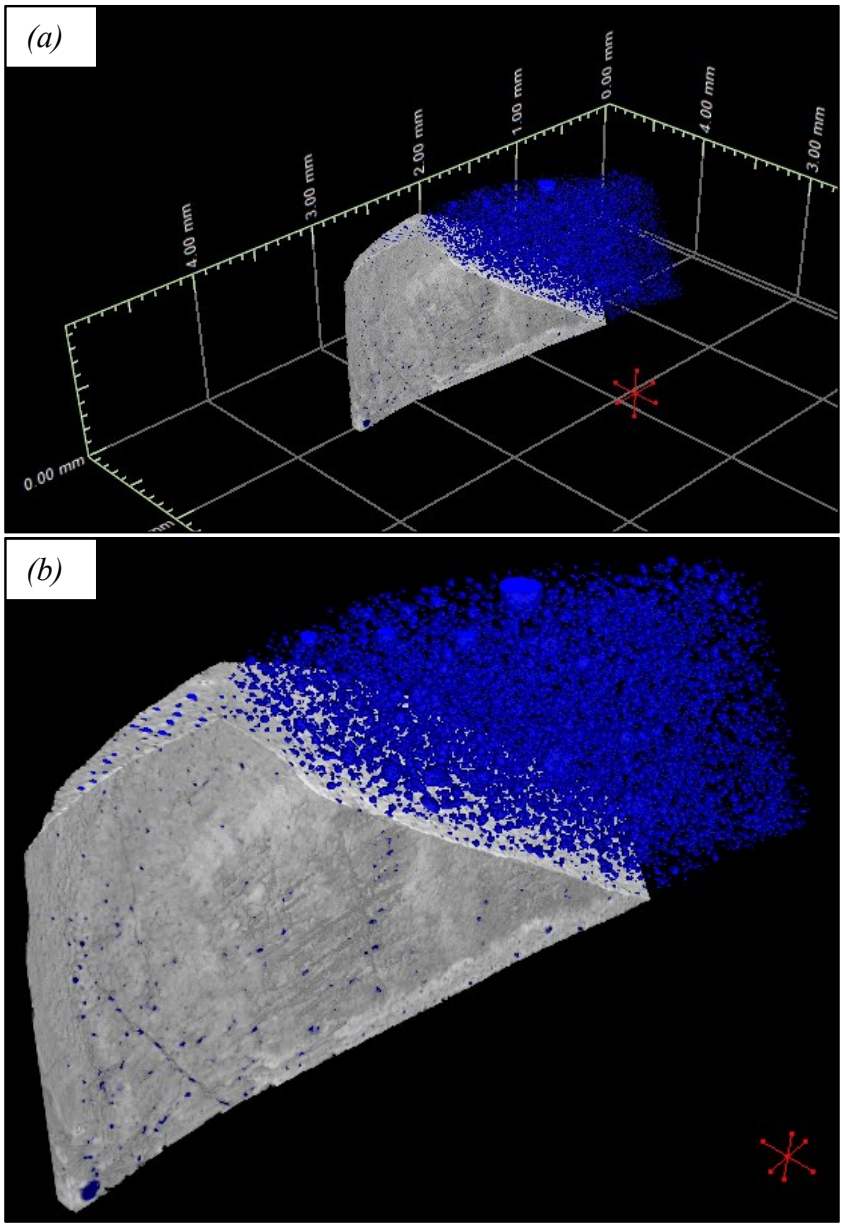

Fig. 10.40 – Volume rendering of Ghareb Fm. fragment after *in-situ* heated at 1350 °C and studied by means of X-ray μ-CT at room temperature; a diagonal clipping plane was used to better show voids distribution in blue.

Voids reduction (vol.%) from RT to 900 °C should be due to the effect of thermal expansion and low size of porosity leading an underestimation (Fig 10.39a,b): furthermore, most calcite has to be decarbonated at 900 °C as highlighted during *in-situ* HT SXRPD experiment (Fig. 10.5), leading an increase of porosity due to CO_2 release. The increasing voids trend from 900 to 1250 °C could be ascribable to a gradual and progressive evolution of voids shape increasing the size and being more clustered (Fig. 10.39b,c,d). Rock fragment melted from 1250 and 1350 °C, leading a complete change in sample shape and not allowing a reconstruction at 1350 °C due to the continuous movement of the sample during measurement. Therefore, the sample was studied at RT after heating at 1350 °C, showing similar voids vol.% but with the common occurrence coarse rounded shape voids (10-70 μm).

Ex-situ X-ray μ-CT analysis performed at RT on *RM* fragments laboratory heated at 900 °C (Fig. 10.40a), 1250 °C (Fig. 10.40b) and 1350 °C (Fig. 10.40c,d) showed changes in voids vol.%

and a direct comparison with *in-situ* results: 11.17vol.% of voids for sample heated at 900 °C with homogeneous voids distribution and rare open fractures; 11.94vol.% of voids for sample heated at 1250 °C with coarser and clustered voids; 7.49vol.% of voids for sample heated at 1350 °C with lesser porosity but coarser and more rounded.

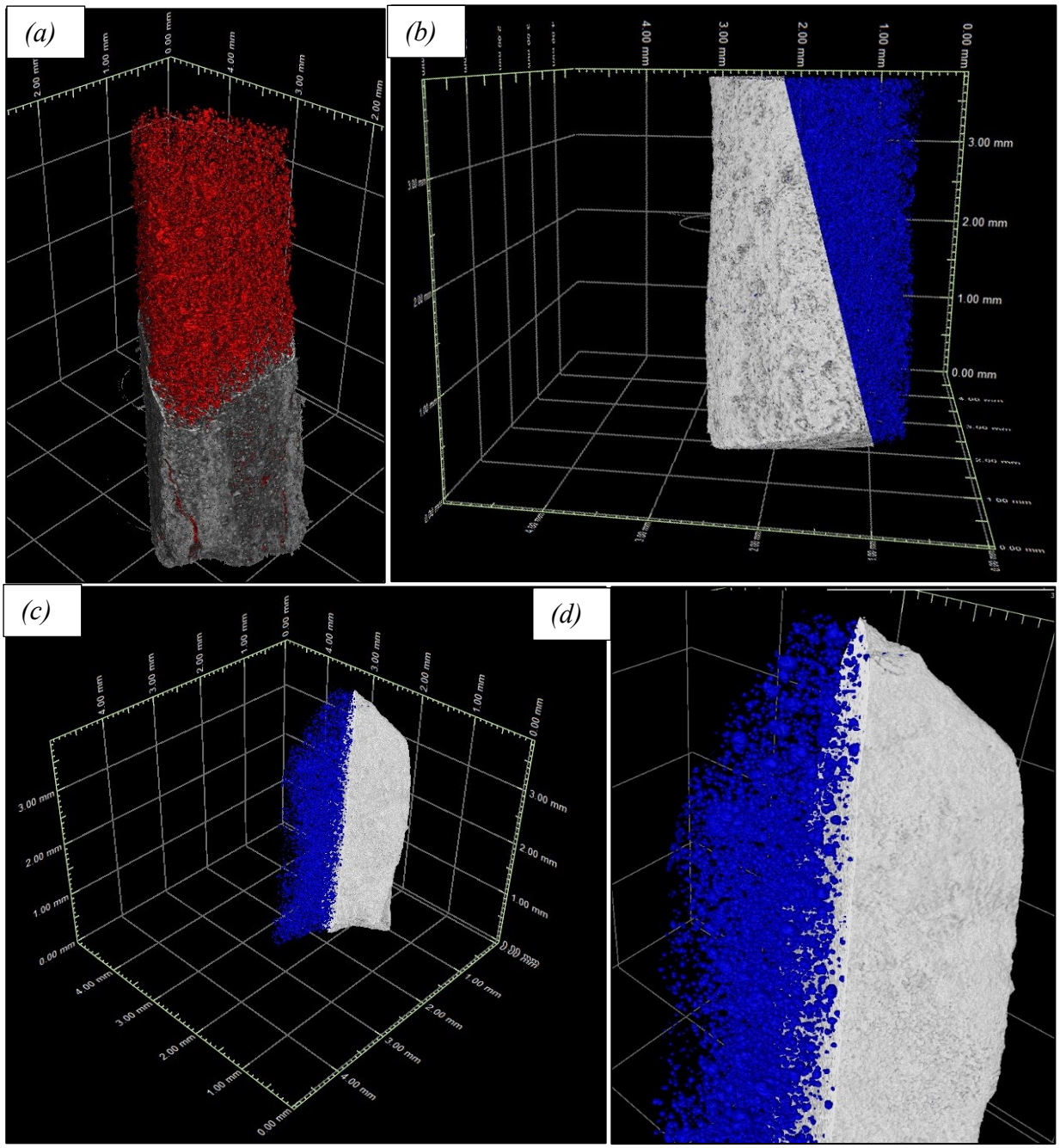

Fig. 10.41 – Volume rendering of Ghareb Fm. fragments laboratory heated at different temperatures: (a) 900 °C; (b) 1250 °C; (c,d) 1350 °C; a clipping plane was used to better highlight voids distribution reported in blue or red.

BC pellet fragment laboratory heated at 1350 °C (Fig. 10.20,21) was studied by means of X-ray μ-CT revealing a voids vol.% of 8.00, close to one observed for *RM* both *in-situ* and *ex-situ* heated at 1350 °C (Fig. 10.40,41c,d) but with larger voids (Fig. 10.42). Furthermore, the identification of brownmillerite, dicalcium silicate and ye'elimite, representing constituent crystal phases, was allowed thank to higher density contrast and pixel resolution (0.9 μm) (Fig. 10.42a,b).

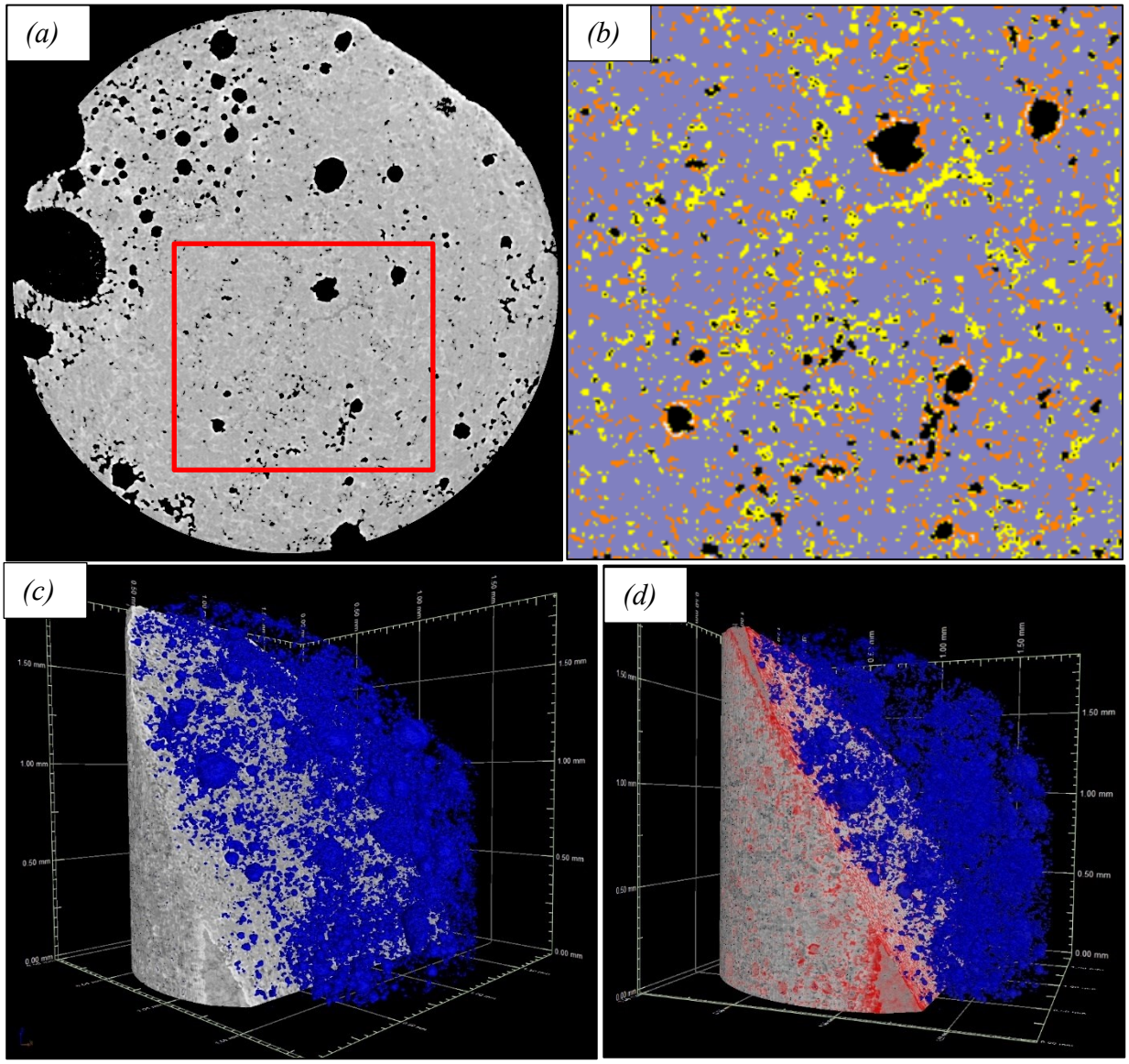

Fig. 10.42 – *BC* sample laboratory heated at 1350 °C and studied by means of synchrotron X-ray μ-CT: (a) sample slice reporting voids in black, brownmillerite in light grey, dicalcium silicate in medium grey and ye'elimite in dark grey; (b) color segmentation of the red square region of previous sample slice, reporting brownmillerite in orange, dicalcium silicate in pale purple and ye'elimite in yellow; (c) volume rendering with a diagonal clipping plane better showing voids distribution in blue; (d) volume rendering reporting in blue voids and in red brownmillerite.

10.2 – Discussion

Green-cements were prepared at laboratory scale at selected heating temperatures starting with two different raw meals: (i) Ghareb Formation (labelled as *RM*, Table 7.1.) and (ii) High Ferrite Belite Clinker S-doped (labelled as *BC* Table 7.3). Samples were studied by means of both conventional analytical techniques (XRF, RLM, SEM, EMPA and *ex-situ* LXRPD) and innovative ones (*ex-situ* and *in-situ* XRPD, μ-CT, SCXRD and NXRD-QTA all performed at synchrotron scale facility) leading detailed information and clarifying changes occurring during heating. Furthermore, the effect of grain size and natural anisotropies (microtextural and chemical inhomogeneities) at different temperatures were investigated by heating Ghareb Formation rock fragments (labelled as *RF*) at laboratory scale.

The study of microtextural and mineralogical changes occurring from room to high temperatures is extremely crucial in cement manufacture because allows to design the correct thermal treatment and starting raw meal (e.g., minor elements occurrence, raw meal grain size, etc.) for improving cement properties (i.e., increasing the amount water-reactive phases, mainly $C_4A_3\bar{S}$ and C_3S; polymorphism control of crystal phases, appropriate crystal grain size, etc.), reducing cost expenditure which includes wasted energy and starting raw materials supply.

Cement production always starts with fine homogenous raw materials powder firstly thermal treated by means of a preheater, which uses part of hot exhausted gases coming from the kiln and some fuel to reach 900-1000 °C, leading the complete decarbonation around 2 min [8]. The obtained mineral assemblage for an OPC is made of lime (CaO), quartz, periclase (MgO), Larnite (β-C_2S), mayenite ($C_{12}A_7$), brownmillerite (C_4AF), srebrodolskite (C_2F), spurrite and minor amount of sulphate-bearing phases (anhydrite, sylvite, aphthitalite, halite, arcanite and syngenite) that usually coat grains [7,8]. BC, CSA and all other *green-cements* types are obtained with the same procedure, only changing chemical composition of the starting raw meal and maximum heating temperature that is 100-150 °C less than OPC one [147,148].

Ex-situ experiments on *BC* sample revealed that calcite starts to decompose at ~ 700 °C and fully breaks down < 800 °C (Fig. 10.1,2), agreeing well with previous *in-situ* HT experiments on pure calcite [333]. Even recent study using TGA-DSC on different *green-cements* raw meals (BC, ABCSA and BCSA) confirmed that calcite breakdown starts at 696-715 °C and complete at 800 °C [349–351]. At 700 °C no calcium aluminate and/or ferrite phases occurred, only anhydrite, low amount of lime, quartz, k-feldspar, hematite and calcite were found (Fig. 10.1,2). XRF calculated from RQPA showed a strong and slight underestimation of Al_2O_3 and SiO_2, respectively, that could be explained by the occurrence of an Al-Si-rich amorphous phase, linked to the thermal decomposition of kaolinite and other clays, which is not detected by diffraction analysis: pure kaolinite dehydroxylates at ~ 550 °C turning into an amorphous-like phase (metakaolinite) with a general chemical composition of $Al_2O_3{\cdot}2SiO_2$ usually rising the background intensity on XRD patterns [342,352]. Furthermore, mostly aluminium should be retained in the metakaolinite because no Al-bearing phases (mayenite, brownmillerite, celite or gehlenite) occurred. Only at > 700 °C

mayenite, brownmillerite and srebrodolskite crystallised along with larnite when more lime was available to react with hematite, metakaolinite and quartz. The complete decomposition of calcite led to the occurrence of periclase that could replace Ca^{2+} in calcium-rich phases at HT, suggesting a Mg-rich calcite source in the raw meal. Till 900 °C no changes in the mineral assemblages occurred, excepted the occurrence of low amount of celite (C_3A) that should be related to the reaction among free-lime and metakaolinite. Ye'elimite starts occurring at 1000 °C by the reaction among anhydrite and celite or mayenite, despite the main formation reactions need krotite (CA) and anhydrite, or krotite, mayenite and anhydrite [317,318,326]. Therefore, our ye'elimite formation reactions, which involve celite and/or mayenite with anhydrite, release lime to compensate the CaO difference: (i) $2C_3A + C_{12}A_7 + 3C\bar{S} \rightarrow 3C_4A_3\bar{S} + 9C$ or (ii) $3C_3A + C\bar{S} \rightarrow C_4A_3\bar{S} + 6C$, both reported using the cement chemistry notation [7,8]. Moreover, celite and mayenite fully reacted from 1000 to 1100 °C, leading the highest ye'elimite content (Fig. 10.1). Similar values were obtained in a previous study showing a maximum ye'elimite content for a BCSA cement at ~ 1105 °C or lower T in the case of boron-doping (~ 1070 °C) [353]; whereas, experiments performed on pure system CaO-Al_2O_3-SO_3 revealed the highest ye'elimite content at 1300 °C independently from the sintering time [326]. This feature may be explained by the effect of impurities compared to the pure system, commonly improving reactivity at lower temperature [7,150]. Furthermore, Fe_2O_3 represents a component which could reach up to 12wt.% in ye'elimite by the ionic substitution $^{IV}Fe^{3+} \rightarrow {}^{IV}Al^{3+}$ in the crystal structure [354], leading two main features: (i) the ionic substitution leads higher availability of aluminium improving the crystallisation of ye'elimite and other Al-rich phases; (ii) high iron content in ye'elimite leads lower temperature for the polymorphic transition from orthorhombic (*Pcc2*) to cubic crystal structure ($I\bar{4}3m$) that could remain metastable at room temperature improving water-reactivity [354]. Ternesite crystallised from 1000 to 1100 °C and later broke down at < 1200 °C, agreeing well with previous study: $C_5S_2\bar{S}$ slowly starts crystallising at ~ 882 °C around α'_L-C_2S crystals in presence of anhydrite ($2\alpha'_L\text{-}C_2S + C\bar{S} \rightarrow C_5S_2\bar{S}$) by a solid-state-reaction, and starts to break down at 1020 °C in open system and from 1172 to 1264 °C for OPC kiln conditions [318,330,355]. Oxygen and sulphur dioxide fugacities are relevant for ternesite and ye'elimite stability fields at HT because both represent reaction products: (i) $C_5S_2\bar{S} \rightarrow 2C_2S + CaO + SO_2 + \frac{1}{2}O_2$ [330,355,356]; (ii) $C_4A_3\bar{S} \rightarrow \frac{1}{5}C_{12}A_7 + CA + SO_2 + \frac{1}{2}O_2$ [318]. Therefore, in open heating conditions ternesite and ye'elimite exhibit lower decomposition temperatures, 1020 °C [355] and 1200-1250 °C [318], respectively; whereas, in close system their upper stability limits rise to ~ 1298 °C [330,356,357] and ~ 1400 °C [318] for ternesite and ye'elimite, respectively. *Ex-situ* experiments on *BC* were performed on heated pellets in open environment till 1200 °C (see section 7.1.2), explaining the earlier decomposition of ternesite at 1100-1200 °C compared to cement kiln condition and assessing more reliability on results from previous studies. Lime completely reacted from 1100 to 1200 °C with residual quartz, amorphous metakaolinite and k-feldspar increasing larnite content, which also strongly increased due to ternesite break down (Fig. 10.1,2). Furthermore, even brownmillerite content rose due to the availability of Al_2O_3 from k-feldspar and metakaolinite, and Fe_2O_3 from srebrodolskite. XRF calculated from RQPA and EMPA results showed a loss of SO_3 which could be accounted to ternesite decomposition and slight reduction of ye'elimite from 1100 °C to 1350 °C, passing from 3.3wt.% to ~ 1.6wt.% of SO_3;

nevertheless, XRF on *BC* after heating at 1350 °C showed similar SO_3 compared to raw meal (Table 7.3): this SO_3 gap observed with RQPA could be explained by the occurrence of low amount (< 3-4wt.%) of sulphate bearing phases (syngenite, arcanite, Ca-langbeinite, etc.), which were observed during EMPA investigation (Fig. 10.20,21), not detected during XRD analysis thanks to their low crystallite size. The chance of sulphur and other volatile elements (chlorine, fluorine, sodium, etc.) loss has been broadly reported and is considered as a problem for cement manufacture: (i) alkali sulphates, spurrite and ternesite form rings in OPC kiln in lower temperature zones by reaction among raw material and vapour phase [7,358]; (ii) sulphur dioxide fugacity is a key-control factor for ye'elimite stability and its reduction limits ye'elimite crystallisation, rising the difficulty to control and predict the final mineral assemblage and content. From 1250 to 1350 °C no relevant changes on mineral assemblage occurred with only a slight increase of larnite and reduction of ye'elimite and periclase, explained by two ionic substitutions involving dicalcium silicate and one for brownmillerite that were confirmed by EMPA results (Table 10.5,6): (i) dicalcium silicate hosts higher amount of dopants at HT, especially Al and S ($^{IV}S^{6+} + 2\,^{IV}Al^{6+} \rightarrow 3\,^{IV}Si^{4+}$) [150,181,359], and minor Mg ($^{VI}Mg^{2+} \rightarrow {}^{VI}Ca^{2+}$) [7,150,162], leading more Si and Ca available to increase dicalcium silicate at the expense of ye'elimite; (ii) brownmillerite can host magnesium inside octahedral atomic site which is charge balanced by silicon intake in tetrahedral position ($^{VI}Mg^{2+} + {}^{IV}Si^{4+} \rightarrow {}^{IV}Al^{3+} + {}^{VI}Fe^{3+}$). Furthermore, only orthorhombic ye'elimite occurred in all heated samples probably due to lesser extent of ionic substituents, mainly iron [354], and slow cooling from HT. Final mineral assemblage for *BC* raw meal from 1250 to 1350 °C is β-C_2S–C_4AF–$C_4A_3\bar{S}$ plus minor MgO and $C_{12}A_7$, the latter should probably form by partial decomposition of ye'elimite at HT. This final mineral assemblage corresponds to common BCSA cements one, which its thermodynamic stability was confirmed by previous experiments [315,360,361]. Considering microtextural features observed some considerations could be made:

(i) *BC* raw meal started melting from 1300-1350 °C considering brownmillerite microtexture (Fig. 10.18,20), giving similar melting point to previous *in-situ* experiments on BCSA raw meal (1270-1309 °C) [362];

(ii) The occurrence of a liquid phase led a strong development of larnite crystals, as showed by its crystal size increase (Fig. 10.20,21);

(iii) No hatrurite occurred despite the HT due to the high-S content and lack of C_3S mineralisers (i.e., MgO, F, ZnO, etc. [7,150]), as stated in other studies [186,363];

(iv) Syngenite occurrence as interstitial phase close to ye'elimite and larnite suggests the presence of an immiscible S-rich melt, especially at low-T during cooling, which is also rich in alkali leading the formation of alkali sulphates (Fig. 10.20,21) [7,8].

Experiments on *RM* raw meal are described by the chemical system CaO-Al_2O_3-SiO_2-Fe_2O_3-P_2O_5-SO_3-CaF_2 that represents the phosphorous and fluorine doped system of standard BCSA. *Ex-situ* experiments on *RM* showed several differences compared to *BC* ones (Fig. 10.1-4):

(i) spurrite ($C_5S_2\bar{C}$) was stable from 700 °C to 800-900 °C decomposing to $2C_2S + CaO + CO_2$, while it did not occur in all *BC* samples;

(ii) $C_{12}A_7$, C_4AF, C_2F and β-C_2S were already stable at 700 °C, suggesting higher reactivity of the system compared to pure system (C-A-S-F-$\bar{S}$);

(iii) Fap-ell was an ever-present crystal phase over the explored temperature range (RT-1350 °C), especially increasing till 900-1000 °C and strongly reducing at 1200-1250 °C;

(iv) ternesite and ye'elimite appeared at 1100 °C, 100 °C higher than *BC*, and the former remained stable up to 1300 °C, whereas the latter even occurred at 1350 °C but strongly reduced from 1200-1300 °C;

(v) flamite (α'_H-C_2S) and hatrurite (C_3S) crystallised at 1200-1250 °C and both remained stable at room temperature even with slow cooling.

Spurrite is considered as a transient crystal phase as C_2AS and C_2F in OPC, with higher temperature stability field compared to calcite but strictly depend on the CO_2 pressure: spurrite has upper limit at 790 °C with low-CO_2 pressure (0.08 atm) and at 915 °C with high-CO_2 pressure (1 atm) [332]. Moreover, DTA experiments on spurrite extracted from cement kiln decomposed at different temperature in the range 857-915 °C, probably related to slightly different chemical composition and crystallographic features (crystallite size and microstrain) [364]. However, many experiments performed in the spurrite stability field failed in its crystallisation [365]; whereas, spurrite always grew when mineralisers occurred, such as CaF_2, $CaCl_2$ or alkali carbonates, even at low amount [332,365]: therefore, *RM* should have low amount of fluorite, as showed in some Ghareb Formation residues (*SE* and *SO*) (Table 8.2,3) and the corresponding Maastrichtian limestone on Jordan area [366]. The occurrence of minor amount of fluorite agrees well with the increase of Fap-ell content, especially from 800 to 900 °C (Fig. 10.4), explained by fluorellestadite formation reaction: $3\alpha'_L$-$C_2S + 3C\bar{S} + CaF_2 \rightarrow 2Ca_5(S_{0.5}Si_{0.5}O_4)_3F$. The hypothesis of hydroxyellestadite formation instead of fluorellestadite should be rejected due to its dehydroxylation at 850-900 °C, leading a cell volume reduction and oxyellestadite ($Ca_{10}(Si_{0.5}S_{0.5}O_4)_6O$) formation that is later decomposed at 1050 °C [367,368]: our experiments showed a constant volume increase toward fluorellestadite end member (Fig. 10.15). Furthermore, previous study reported the chance of crystallising fluorellestadite halogen deficient ($Ca_{10}(SiO_4)_{3+x}(SO_4)_{3-x}F_{2-2x}\square_{2x}$), thus even little halogen amount (CaF_2 for *RM*) could strongly increase Fap-ell content [369].

In-situ HT results from RT to 1000 °C starting with *RM* limestone confirmed the crystallisation of fluorellestadite from 750°C to 1000 °C consuming anhydrite, quartz and lime, instead of dicalcium silicate as a source of silicon and calcium: $6CaO + 3SiO_2 + 3CaSO_4 + CaF_2 \rightarrow 2Ca_5(S_{0.5}Si_{0.5}O_4)_3F$. The lack of brownmillerite, lime, larnite, srebrodolskite, spurrite, mayenite and gehlenite at 700 °C compared to *ex-situ* results is explained considering the kinetics of their formation reactions, requiring more heating time than 15 min; consequently, brownmillerite and mayenite occurred only at higher temperature at 800-850 °C and 925-950 °C, respectively (Fig. 10.5). Lime was detected only at 975-1000 °C on SXRD patterns, but it should be considered earlier formed by $CaCO_3$ decomposition from 700-750 °C, due to the formation of larnite and gehlenite at the same temperature (Fig. 10.5). Furthermore, *in-situ* experimental condition (pure SiO_2 capillary heated) influenced the thermal stability of carbonate phases increasing around 200 °C their upper limits, thanks to the rise of CO_2 fugacity compared to open system in *ex-situ* in laboratory condition: (i) calcite occurred up to 975 °C; whereas, (ii) spurrite was stable from 925 to 1000 °C. Higher CO_2 fugacity was also proved by the formation of calcite during cooling to RT (Fig. 10.5) by the reaction among lime and carbon dioxide.

Ternesite and ye'elimite were found in *RM ex-situ* experiments at 1100 °C (Fig. 10.4), similar to *in-situ* one without stabilisation time (Fig. 10.6): ternesite and ye'elimite crystallised at 1098-1123 °C and 1123-1146 °C, respectively, during *in-situ* experiments without stabilisation. Whereas, ternesite and ye'elimite both crystallised at 966-1029 °C for *in-situ* experiments with stabilisation time of 10 min., which is close to previous study reporting ye'elimite formation at 940-1000 °C [317,326,353], and ternesite at 882-927 °C [355]. Ternesite formation is also marked by the decrease of larnite, anhydrite (only in *ex-situ* experiments) and Fap-ell previously formed, suggesting the crystallisation of ternesite-silicocarnotite s.s. (tern-silc) ($Ca_5\left(Si_{1-\frac{x}{2}}P_{\frac{x}{2}}O_4\right)_2$ ($P_xS_{1-x}O_4$), which for pure silicocarnote *x* is equal to 1). The partial involvement of Fap-ell in tern-silc crystallisation released CaF_2 which should be hosted in mayenite crystals [207] and the excess forms a melt at 1054 °C: C_2S-fluorellestadite-CaF_2 assemblage at T ~ 1054 °C reaches a peritectic point incongruently melting (C_2S-fluorellestadite-Liq) with an approximately composition of the liquid phase of 50wt.% CaF_2, 25wt.% C_2S and 25wt.% of $CaSO_4$ [319]. Therefore, two different formation reactions of tern-silc were identified in this study depending on the availability of anhydrite: (i) if no anhydrite is available $Fap\text{-}ell + larnite \rightarrow tern\text{-}silc + CaF_2$, if halogen deficient apatite is not considered $\left(Ca_5\left(P_{(1-2x)}Si_xS_xO_4\right)_3F + \frac{3}{2}Ca_2SiO_4 \rightarrow \frac{3}{2}Ca_5\left(Si_{\frac{2x+1}{2}}P_{\frac{1-2x}{2}}O_4\right)_2(P_{1-2x}S_{2x}O_4) + \frac{1}{2}CaF_2\right)$; (ii) when anhydrite is available, $2\,larnite + anhydrite \rightarrow ternesite$ $\left(2\,Ca_2SiO_4 + CaSO_4 \rightarrow Ca_5(SiO_4)_2(SO_4)\right)$, or $4\,lime + 2\,quartz + anhydrite \rightarrow ternesite$ $\left(4\,CaO + 2SiO_2 + CaSO_4 \rightarrow Ca_5(SiO_4)_2(SO_4)\right)$, leading the formation of only pure ternesite as occurred in *BC* sample (Fig. 10.1,2). Ternesite started breaking down at different temperatures considering the experimental conditions: at 1200-1250 °C, 1170-1189 °C and 1111-1133 °C for *ex-situ*, *in-situ* without and with stabilisation time, respectively. Furthermore, ternesite was fully decomposed at 1232-1235 °C in *in-situ* condition without stabilisation time, whereas, *ex-situ* results showed low amount even at 1300 °C, suggesting that ternesite could re-crystallise during slow cooling: Böhme et al. [355] showed the formation of ternesite and anhydrite during cooling on larnite and lime crystals, respectively, suggesting their formation from 1020 to 882 °C if sulphur dioxide occurs. Afterwards, ternesite in *RM* experiments displayed higher temperature stability compared to *BC* ones that could be explained by the silicocarnotite fraction in solid solution that has higher decomposition temperature: silicocarnotite is stable up to 1450 °C, after which decomposes to α-C_2S-α-C_3P s.s. [195,197,198].

Dicalcium silicate highlighted during *in-situ* experiments all polymorphic transitions with slightly higher temperatures when no stabilisation time was used: 1123-1146 °C and 1095-1111 °C for α'$_L$-C_2S → α'$_H$-C_2S; 1189-1220 °C and 1150-1182 °C α'$_H$-C_2S → α-C_2S (Fig. 10.6,7). Results figured out temperatures lower than ones reported for stoichiometric dicalcium silicate, such as 1160 °C and 1425 °C for α'$_H$-C_2S and α-C_2S transitions, respectively [7,8,370]: polymorphic transition temperatures for dicalcium silicate are strongly influenced by dopants, especially Na^+, K^+, Sr^{2+}, P^{5+}, B^{3+}, S^{6+} and Al^{3+}, which differently act increasing or even decreasing the stability field of a specific polymorph. Al^{3+} and S^{6+} enhance the stabilisation of β-C_2S, whereas, P^{5+} alone or coupled with Na^+ and/or K^+ increase the stability field of HT polymorphs (α'$_L$, α'$_H$, α-C_2S) [183,195–200].

EMPA on larnite crystals of *RM* sample heated at 1200 °C (Table 10.5) confirmed the occurrence of mainly Al^{3+} and P^{5+}, and minor S^{6+}, Na^{+} and Fe^{2+} as ionic substituents of Ca^{2+} and Si^{4+} with an average chemical formula $(Ca_{1.94}Na_{0.02}Fe^{2+}_{0.01}\square_{0.03})(Si_{0.74}P_{0.11}Al_{0.1}Fe^{3+}_{0.01}S_{0.04}O_4)$, proving their stabiliser effect during heating.

The breakdown of tern-silc (occurring at 1111-1133 °C and 1170-1189 °C for *in-situ* with and without stabilisation time, respectively) and Fap-ell (starting at 1150-1182 °C and 1170-1189 °C for *in-situ* with and without stabilisation time, respectively) released significant amount of phosphorous, which could be hosted inside larnite by the following two breakdown reactions:

(i) $Ca_5\left(S_{\frac{1}{2}-\frac{x}{2}}Si_{\frac{1}{2}-\frac{x}{2}}P_xO_4\right)_3F \rightarrow \left(\frac{3+3x}{2}\right)Ca_{2-\frac{1}{2}x}\square_{\frac{1}{2}x}\left(Si_{\frac{1-x}{x+1}}P_{\frac{2x}{x+1}}O_4\right)+\left(\frac{3-3x}{2}\right)SO_2+\left(\frac{3-3x}{4}\right)O_2+\frac{1}{2}CaF_2+\left(\frac{3-3x}{2}\right)CaO$

(ii) $Ca_5\left(Si_{1-\frac{x}{2}}P_{\frac{x}{2}}O_4\right)_2(P_xS_{1-x}O_4) \rightarrow (2+x)Ca_{2-\frac{2x}{4+2x}}\square_{\frac{2x}{4+2x}}\left(Si_{\frac{2-x}{2+x}}P_{\frac{2x}{2+x}}O_4\right)+(1-x)SO_2+\left(\frac{1-x}{2}\right)O_2+(1-x)\,CaO$

These two reactions could be considered only for a limited amount of P_2O_5, around $x \leq 0.6$ and 0.8 at 1200 °C for Fap-ell and tern-silc, respectively, corresponding to a maximum content of P_2O_5 in dicalcium silicate of ~ 27wt.%: at higher phosphorus content P-doped dicalcium silicate is no longer stable alone, leading the formation of nagelschimidite ($Ca_7P_2Si_2O_{16}$) associated with α-C_2S at HT (Fig. 9.23) [196,197]. Lower breakdown temperature of Fap-ell at 1150-1182 °C compared to the pure system CaO-SiO_2-SO_3-CaF_2 at 1220 °C, should be due to the occurrence of Al_2O_3, Fe_2O_3 and low amount of MgO as reported in previous study giving a melting point at 1160-1180 °C [8,204,371]. Fap-ell should breakdown over a temperature range because is a solid solution, leading at the beginning a fluorellestadite richer melt which is gradually enriched in fluorapatite content during heating [3]. The sulphur released by previous reported reactions could also hosted inside C_2S but requires Al^{3+} to be charge balanced, both substituting silicon in tetrahedron: $2^{IV}Al^{3+} + {}^{IV}S^{6+} \rightarrow 3^{IV}Si^{4+}$ [359]; Al^{3+} should be considered as an even-present element available from Al-bearing phases as mayenite, brownmillerite and ye'elimite (Fig. 10.4-8).

The strong increase of dopants, especially in phosphorous and aluminium (Table 10.5), in dicalcium silicate justify the occurrence of α-C_2S at lower temperature, leading the formation of R-C_3S at 1235-1244 °C, due to higher reactivity of α-C_2S with lime compared to α'$_H$-C_2S (Fig. 10. 6) [7,8]. Furthermore, despite the slow cooling in *ex-situ* experiments, hatrurite and α'$_H$-C_2S occurred even at room temperature (Fig. 10.3,4), suggesting a high content of dopants that stabilised HT polymorphs (Table 10.5,7). Whereas, α-C_2S and hatrurite were found at room temperature for *in-situ* experiment that underwent a quenching from 1244 °C, representing an extremely important evidence useful for cement manufacture: the formation of hatrurite associated with α-C_2S, instead of other lower polymorphs, should improve hydration reactivity, limiting the main drawback of BCs, and reducing energy expenditure by the lower T formation.

The lack of a clear decrease of mayenite and brownmillerite content at HT suggests no clear evidence of a partial melting during *in-situ* experiments [147,362]. However, previous studies in the system C-S-A-F-$\bar{F}$-$\bar{S}$ figured out a first melt appearance at T as low as 1180-1189 °C and for brownmillerite-fluorellestadite mixture at 1193-1204 °C [190,204]; moreover, C-S-$\bar{F}$-$\bar{S}$ system showed a first melting at 1220 °C for fluorellestadite-C_2S with a melt composition of 55wt.% $CaSO_4$, 35wt.% Ca_2SiO_4 and 10wt.% CaF_2 [319]. Furthermore, the gradual breakdown of Fap-ell, starting at T > 1150 °C, released CaF_2 that is partially hosted in mayenite and the remaining developed a melt [319]. Therefore, this low-T melt has a strong different chemical composition

compared to the main clinker liquid phase that is produced at higher T (here after called as high-T melt), which is rich in Al_2O_3, Fe_2O_3 and CaO [7,8]: OPC liquid phase mainly comes from mayenite, brownmillerite and celite melting, which during cooling crystallise as an interstitial phases. Low-T melt should be high in SO_3, CaF_2, SiO_2, CaO and alkali; whereas, it is also enriched in P_2O_5 after fully Fap-ell breakdown at 1180-1235 °C [204]: the lack of Fap-ell and ternesite at T > 1232 °C in *in-situ* experiments (Fig. 10.6) and their occurrence at *RM* after a slow cooling (Fig. 10.3,4), point out that they crystallised from a low-T melt as suggested by their xenomorphic microtexture (Fig. 10.26,27). Moreover, low-T melt has different properties (viscosity, wettability and density) compared to high-T one due to the different chemical composition; hence, it is able to modify the stability filed of crystal phases and promoting metamorphic reactions: the occurrence of a melt rich in P, F, S, Si, Ca, K and Na strongly promoted diffusion of CaO toward reactive α-C_2S crystals leading the crystallisation of hatrurite (R-C_3S at HT) at 1235-1244 °C that grew fast forming coarse (100-200 μm) peciloblastic rhombic or pseudohexagonal crystals plenty of inclusions (Fig. 10.26,27a) [372].

RM high-T melt should have formed from 1250 to 1300 °C, estimated by microstructural features of brownmillerite that changed its microstructure: brownmillerite at 1250 °C occurred as sparce subhedral to euhedral prismatic crystals, while at 1300 °C revealed a xenomorphic microtexture enveloping all other crystal phases, such as larnite, hatrurite and lime (Fig. 10.28,29). Previous study reported a melting point of 1280 °C and 1338 °C for C_2S-$C_{12}A_7$-C_4AF-C_3A and C_3S-C_2S-C_4AF-C_3A assemblages for pure C-A-S-F system, respectively, but the effect of minor elements strongly reduce melting point and influence crystal phase stability [8]. *RM* mineral assemblage observed in *in-situ* experiments at HT (~ 1244 °C) is made of C-C_3S-C_2S-$C_{12}A_7$-C_4AF, suggesting the reduction of C_3A stability field since no tie-lie between CaO and $C_{12}A_7$ occur in pure system: the increase in $C_{12}A_7$ stability field should be related to fluorine occurrence. Experiments on pure CSA cements revealed a melting point of 1259-1270 °C [190,353]; while, a starting raw mixture of fluorellestadite-brownmillerite showed two main melting points during heating, a first one at 1193-1208 °C, related to the gradual decomposition of fluorellestadite (low-T melt), and a second one at 1269-1306 °C (high-T melt) [190]. The occurrence of high P_2O_5 content in *RM* sample compared to previous study should lead lower melting point, due to the increase of chemical component [3], estimating a main melting point between 1250 and 1259-1270 °C. When high-T melt is formed in *RM* sample, which is rich in Al_2O_3, Fe_2O_3, CaO and minor SiO_2 [8], it interacts with other phases and previously formed melt: low-T and high-T melts interact mixing and exchanging chemical components; however, an immiscibility gap between sulphur-rich melt and Al-Fe-rich one occurs [7,8]. Hatrurite content reduced in *RM* samples heated at 1300 and 1350 °C, which could be explained by a strong enrichment in phosphorous and sulphur of high-T melt due to the interaction with low-T melt, which reduced C_3S stability field turning into α-C_2S+CaO despite fluorine doping (Fig. 10.30,31).

During cooling hatrurite commonly partially decomposes to α'$_H$-C_2S and CaO at temperature around 1200 °C, thus a fast cooling is always performed. Nervetheless, no lime and larnite enrichment was found around hatrurite crystals, suggesting that hatrurite crystals were stable even with slow cooling, probably caused by foreign ions (Table 10.4). The occurrence at RT of α'$_H$-C_2S in *ex-situ* experiments between 1250 and 1350 °C highlights an incomplete polymorphic

transition between α-C_2S to α'$_H$-C_2S despite the slow cooling, which could be explained by the high phosphorous and aluminium content (Table 10.3) [7,122,187].

Experiments on *RM* fragments heated at different temperatures showed the effects of grain size during heating and helped to estimate the combustion temperature of natural larnite-rich rocks. Differences in mineral assemblage and microtexture, as revealed by LXRPD and SEM (Table 10.2, Fig 10.4) should be mainly related to different mineral distribution and natural anisotropies occurring in pristine limestone. *RF* heated at 900 °C showed higher larnite content, quartz and perovskite compared to *RM* at the same temperature: (i) higher content of Si-rich phases (clay minerals, quartz and opal) allowed higher larnite wt.%; (ii) titanite was found inside black nodules in limestone (Fig. 8.21,22) which at HT reacts with lime to crystallise perovskite, which is even found in larnite-rich rocks [122]. Strong differences occurred among *RFa* and *RFb*, especially considering microtexture (Fig. 10.22,23,A.1,2). *RFa* is made of hatrurite along with larnite and flamite at 1200 °C that could be explained by considering local strong enrichment in a low-T melt, especially rich in F and P, promoting α-C_2S that reacted at lower T to form R-C_3S, as for *RM* sample at T > 1235-1244 °C. Furthermore, *RFa* microtexture showed the occurrence of very low crystallite size and previous phosphate pellets turned into fluorapatite-ellestadite aggregates (Fig. 10.22). *RFb* showed similar RQPA and microtexture of *RM* pellet heated at 1200 °C, despite for the occurrence of rankinite, gehlenite and wollastonite which are not stable in contact with lime: the occurrence of local enrichment of aluminium and silicon (clay-enriched portions) could explain this feature. Even at 1250 °C inhomogeneities occurred for *RM* heated fragments, suggesting the lack of the high-T melt as for *RM* pellets: portions strongly enriched in hatrurite, larnite and fluorapatite and lower in Al-Fe-bearing phases occurred (Table 10.2, Fig. 10.4), suggesting a local strong enrichment of pristine phosphate pellets, calcite, and fine quartz with low gypsum, hematite and clay content; other portions highlighted similar RQPA of *RM* pellet at same temperature with lower free lime and lack of ye'elimite, suggesting lower calcite and gypsum in pristine limestone portions. At 1350 °C after the occurrence of high-T melt, the mineral assemblage of *RF* is close to *RM* one, excepted for the lack of ye'elimite, lime, lower fluorapatite (Table 10.2): lower calcite, phosphate pellets and gypsum should occur in pristine *RM* fragments limestone compared to homogenous *RM* pellet. Therefore, even at HT after the partial melting, natural anisotropies have a strong impact on the final mineral assemblage, crystal phase distribution and their wt.% with laboratory.

SCXRD on hatrurite crystals in *RM* pellet heated at 1250 °C belonging to $R\bar{3}m$ (Fig. 10.15), despite only *R*3*m* has been reported as the highest temperature tricalcium silicate polymorph [163]. Several studies reported the frequent misinterpretation of monoclinic hatrurite crystals as rhombic [177]. Tricalcium silicate forms at HT by the reaction among lime and dicalcium silicate as *R*3*m* space group forming rhombic or pseudohexagonal shape crystals when euhedral, but during cooling undergoes in displacive polymorphic transition [159,373] passing to *Cm* (M_3) or *Pc* (M_1) space group by complex twinning: two sets of twinning are simultaneous introduced from R to M_3 structure, one forms due to the disappearance of trigonal threefold axes and the other is a fine polysynthetic [374]. Observing hatrurite Bragg peaks on all hatrurite-bearing patterns (*RM* heated at 1250, 1300, 1350 °C and *RFa*, *RFD* , *RFG* and *RF* heated at 1350 °C), M_1 or R polymorphs can occur because they have similar powder pattern, whereas M_3-C_3S polymorph could not occur due to absence of the doublet at 1.76-1.74 Å [375]. Considering the high dopants content in hatrurite

crystals (Table 10.4) the chance of R polymorph occurrence should be taken into consideration due to the very high doping content of P^{5+} and Al^{3+}: previous study reported the positive effect of P_2O_5 to stabilise R polymorph at high content (≥ 1wt.%) [376]. However, only high content of ZnO content was able to stabilise at RT the R polymorph after heating at 1400 °C [159]. General formula calculated for hatrurite crystals by EMPA analysis always showed lower tetrahedral positive charge for tetrahedral site due to high Al^{3+} not fully compensated by only P^{5+} and S^{6+} substitutions (Table 10.4). Cationic normalisation (type B general formula in Table 10.4) of hatrurite charge balanced the lower tetrahedral positive charge with the ionic substitution involving trivalent iron in Ca-site ($^{VI}Fe^{3+} + {}^{IV}Al^{3+} \rightarrow {}^{VI}Ca^{2+} + {}^{IV}Si^{4+}$) and oxygen vacancy formation ($2Al^{3+} + V.^{-2} \rightarrow 2Si^{4+} + O^{2-}$): previous study reported that silicon substitution by aluminium associated with oxygen vacancy is energy favoured than aluminium substituting both Ca^{2+} and Si^{4+} [377,378] in dicalcium and tricalcium silicate but with limited amount [379]. Otherwise, the higher Al^{3+} molar content could be explained by the occurrence of micro-exsolution of Al-rich bearing phases (celite and/or mayenite) increasing Al_2O_3. Afterward, the occurrence of highly doped hatrurite crystals should strongly improve hydration reactivity due to the higher defects content and metastability of crystal structure.

RM in-situ results suggest a combustion temperature for ye'elimite-larnite granofels (*YC2O* and *6BWO*) lower than Fap-ell decomposition (1150-1182 °C), due to the occurrence of coarse pecilitic euhedral Fap-ell (Fig. 9.12,13c,14,15d,16) with S-rich rim (fluorellestadite-rich rim, Fig.9.14b) and no xenomorphic crystals: microtextural features suggest equilibrium with other occurring phases. The coarse pecilitic Fap-ell crystals could have crystallised thanks to the occurrence of a low-T melt during tern-silc crystallisation: tern-silc formation in absence of anhydrite partially involve Fap-ell releasing fluorine, which associated with larnite and fluorellestadite (C_2S-Fluorellestadite-CaF_2) promotes incongruent melting a 1054 °C consuming CaF_2 [319]. Whereas, if anhydrite occurs along with Fap-ell and the released low amount of CaF_2 a melt occurs even at 960 °C [319]. Flamite did not occur in our ye'elimite-larnite rocks suggesting a lack of α-C_2S during heating and/or a slow cooling, which the latter usually leads a complete transition between α-C_2S to α'$_H$-C_2S: flamite occurrence at RT depends on (i) thermal treatment (T and cooling regime) and (ii) foreign ions, especially P_2O_5 content. Low-P_2O_5 flamite (*c* point in Fig. 9.23) occurred in larnite-rich rocks with low or no Fap-ell [122], suggesting T ≥ 1225 °C that is higher than Fap-ell stability. Whereas, P_2O_5-rich flamite (c_1 composition in Fig. 9.23) was always associated with Fap-ell [122], suggesting a T between 1098 °C and 1150-1182 °C, allowing the simultaneous stability of α-C_2S, α'$_H$-C_2S and Fap-ell at HT. Considering (i) the upper limit of Fap-ell stability (1150-1182 °C) and (ii) ternesite (1111-1133 °C), which the latter occurs only in minor amount in *YC2O* (Table 9.1), the SO_2 fugacity could be roughly estimated for our ye'elimite-larnite granofels: ternesite starts decomposing at 1111 °C with 2% O_2 (v/v) and -5 $log_{10}P_{SO_2}(atm)$, while at 1133 °C with 2% O_2 (v/v) -4.8 $log_{10}P_{SO_2}(atm)$; whereas at upper Fap-ell limits ternesite is not stable with -3.8 and -5 $log_{10}P_{SO_2}(atm)$ at 1150 and 1180 °C , respectively [330]. SO_2 fugacity values are partially included cement kiln ones, which usually range from -2.5 and -4 [338].

10.3 – Conclusion

The multidisciplinary apporach on *green-cement* raw mixture simultaneously doped with P_2O_5, SO_3 and fluorine (*RM* sample) were crucial for allowing a complete and detailed study on crystal phase assemblage, microtextural and crystallographic changes during heating. Experiments highlighted four main features with significant relevance for designing new *green-cements* and also capable to better explain CP process involving impure limestone: (i) the occurrence at lower T (1235-1244 °C) of C_3S and α-C_2S compared to OPC after quenching; (ii) ternesite-silicocarnotite s.s. forms at 966-1029 °C involving fluorapatite-ellestadite s.s. releasing CaF_2 which should be hosted in $C_{12}A_7$ and the excess forms a low-T melt at 1054 °C (C_2S-Fluorellestadite-CaF_2); (iii) ternesite-silicocarnotite and fluorapatite-ellestadite s.s. decompose at 1111-1133 °C and 1150-1182 °C, respectively, leading the formation of a low-T melt F, S, P and Si-rich in which CaO can fast diffuse promoting C_3S formation which growths as coarse peciloblastic crystals; (iv) high-T melt Al-Fe-rich occurs at 1250-1270 °C that is immiscible with the low-T one but able to partially exchange ions, especially P and S, leading a gradual and temperature progressive dissolution of euhedral C_3S crystals previously crystallised. These results helped in better constraining combustion temperature of ye'elimite-larnite granofels (*YC2O* and *6BWO*), describing metamorphic reactions during heating and clarifying microtextural features: (v) ye'elimite-larnite granofels should have formed at T higher than ternesite breakdown T (1111-1133 °C) and lower than fluorellestadite ones (1150-1182 °C); (vi) coarse peciloblastic fluorapatite crystals could be explained by the occurrence of the above mentioned low-T melt after ternesite breakdown; (vii) ye'elimite-larnite granofels estimated temperature formation (~ 1111 to 1182°C) along with microtextural features can exclude the reaching of main melting point (1250-1270 °C, high-T melt) during CP.

Consequently, (a) the simultaneous occurrence of F, S and P in cement raw meals lowers the heating T at ~ 1244 °C (~ 216 °C less than OPC one) reducing fuel consumption and CO_2 emissions, especially if are used wastes as alternative raw materials which often have lower CO_2 emitting phases and finer starting grain size. Furthermore, (b) the occurrence of HT polymorphs of C_2S (β and α'_H) associated with highly doped C_3S, even with slow cooling, should strongly increase water-reactivity overcoming the main drawback of belite-rich cement and further reduce energy consumption; whereas, (c) in the case of fast cooling, only α-C_2S occurred along with highly doped C_3S which boost more the hydration reactivity. Therefore, results pointed out several benefits of reusing Ghareb Formation rock wastes (*RM* sample, impure limestone) from Rotem Amfort plant as alternative raw material for designing new *green-cements* with better hydration properties compared to standard Belite Cement thanks to simultaneous minor elements effects (F-P-S-doping): this study figured out the availability of wastes valorisation (e.g., phosphogypsum, solid urban wastes, F-rich sludges, P-S-F-rich rock wastes, etc.) as partially replacing raw materials in cement manufacture being able to cope with the aim of managing waste-related problems (dangerous elements pollution, reducing land use for landfills and waste treatment costs) and reducing CO_2 emissions (lowering combustion T, grinding energy expenditure, fuel and natural raw materials consumption).

Experiments on synthetising High Ferrite Belite Cement S-doped (*BC* sample) showed same stable crystal phase assemblage (β-C_2S-$C_4A_3\bar{S}$-$C_{12}A_7$-C_4AF), microtexture and melting point (1300-1350 °C) of common BCSA cements. Furthermore, (i) final mineral assemblage was already occurring at 1200 °C, excepted for minor amount of k-feldspar, with high porous and fine microtexture; (ii) β-C_2S was always stable at RT without γ-C_2S retrograde polymorphic transition even with a slow cooling. These outcomes allow (a) a strong reduction of energy expenditure and CO_2 emission for cement plant, thanks for the lower temperature combustion and soft microtexture for lowering grinding costs; (b) the reuse of Fe-S-rich wastes as alternative raw material helps in handling bauxite supply and landfill related problems.

Experiments on heating at different temperatures of Ghareb Formation fragments outlined the effects of natural anisotropies (pristine limestone features) on leading strong changes on final mineral assemblage and microtexture compared to rock powder heating (*RM ex-situ* and *in-situ* experiments): (i) natural anisotropies mainly affect mineral assemblage at T below the high-T melt occurrence (1250-1270 °C), while, they are less relevant when high-T melt occurs; (ii) C_3S enriched portions (~ 30wt.%) occurred at 1250 °C with no S-rich phases ($C_4A_3\bar{S}$ and $C_5S_2\bar{S}$) and high fluorapatite content, which could be linked to a phosphatic pellets enrichment and low gypsum content portions in pristine limestone; (iii) C_3S_2-C_2AS-CS occurrence at 1200 °C should be related to local enrichment of quartz and clay minerals in pristine limestone, moving the average chemical composition to higher-SiO_2 and Al_2O_3 not allowing C_2S stability inside those rock portions. Furthermore, (a) hatrurite occurred even at T as low as 1200 °C along with flamite highlighting the possibility of producing *green-cements* at lower T compared to previous rock powder experiments on Ghareb Formation, even with higher starting raw material grain size.

Chapter 11
Hydration property comparison between Belite Cement and natural larnite-rocks

11.1 – Introduction

This chapter is focused on the hydration property comparison between Belite Cement (BC) and natural larnite-rocks (ye'elimite-larnite granofels), which their mineral assemblage, crystallographic and microstructural features were deeply studied and described in previous chapters.

Cements are water-reactive material leading mechanical strength, mostly compressive resistance, allowing their use for building. Cement hydration tests are focused on obtaining data related to: (i) Specific Surface Area estimation (SSA), which strong influence hydration reactivity, obtained by BET and Blaine methods; (ii) crystal phase assemblage and amorphous content evolution, obtained by RQPA with internal standard on XRD patterns collected at different hydration time; (iii) Thermal Gravimetric Analysis (TGA) useful to quantify the amount of water (absorbed and bonded-water content) in anhydrous and hydrated cement pastes at different hydration time, strictly needed to estimate the Free-Water Content (FWC) in cement pastes; (iv) Isothermal Calorimetric Analysis (ICA) that records the produced heat flow during hydration over the time.

Two different cements were prepared and studied: (i) High Ferrite Belite Cement S-doped (HFBC), previously obtained by heating at 1350 °C a *BC* raw meal doped with gypsum (Fig. 10.1,2,20,21); (ii) natural ye'elimite-larnite rock belonging to Hatrurim Basin Formation in Israel (*Nat*, Table 9.1, Fig. 9.9,15,16).

Furthermore, ye'elimite-larnite rock (*6BWO* sample) was further tested, comparing its hydration as a powder and fragments by means of LXRPD (Table 9.1, Fig. 9.4,6,7,12,13,14), reproducing the natural hydration conditions of larnite-rich rocks.

11.2 – Results

Clinker samples were studied by LXRPD analysis showing their starting crystal phase assemblage (Table 11.1). *Nat* sample was obtained by fine grinding and homogenising 1 kg of natural ye'elimite-larnite rock (*YC2O* fragments), highlighting same mineral assemblage of *YC2O*, excepted for ternesite occurrence. Whereas, *BC* sample was prepared by heating ~ 500 g of *BC* raw meal at 1350 °C obtaining ~ 350 g of clinker, showing a mineral assemblage composed of dicalcium silicate polymorphs (both larnite and calcio-olivine), ye'elimite and brownmillerite associated with minor amount of periclase.

In both clinker samples (*Nat* and *BC*) occurred calcio-olivine with different content, in contrast on what was observed in previous XRD analysis (Table 9.1, Fig. 10.1,2) suggesting the influence of fine grinding on its occurrence.

Crystal phases	***Nat***	***BC***
Larnite *(β-Ca_2SiO_4)*	72.58(.37)	66.58(.38)
Calcio-olivine *(γ-Ca_2SiO_4)*	3.41(.17)	8.17(.16)
Ye'elimite *($Ca_4Al_6SO_{16}$)*	5.64(.15)	6.26(.18)
Mayenite *($Ca_{12}Al_{14}O_{33}$)*	3.26(.15)	-
Fluorapatite-ellestadite*	2.86(.20)	-
Brownmillerite *($Ca_2(Al,Fe)_2O_5$)*	-	18.74(.21)
Ternesite *($Ca_5(SiO_4)_2(SO_4)$)*	1.68(.15)	-
Shulamitite *($Ca_3TiAlFeO_8$)*	2.45(.18)	-
Spinel *($MgAl_2O_4$)*	5.60(.31)	-
Periclase *(MgO)*	-	0.25(.12)
Gibbsite *$Al(OH)_3$*	0.40(9)	-
Hydrogarnet *($Ca_3Al_2(O_4H_4)_3$)*	0.73(8)	-
Afwillite *($Ca_3Si_2O_4(OH_6)$)*	1.39(.14)	-

Table 11.1 – RQPA results (wt.%) of anhydrous natural larnite-rich rocks (Nat) and synthetic Belite Clinker (BC) selected for hydration studies; *, $Ca_5\left(Si_{\frac{x}{2}}S_{\frac{x}{2}}P_{1-x}\right)_3F$; -, not detected.

TGA was performed on both samples showing higher water content for *Nat* (3.68wt.%) compared to *BC* (0.17wt.%), which is strongly related to hydrated phases occurrence in the former (Fig. 11.2) and absorbed water for the latter (Fig. 11.1).

Gypsum addition on clinker samples for preparing cement powders was calculated considering ye'elimite hydration reaction in presence of sulphate-bearing phases (anhydrite, bassanite or gypsum), leading the formation of ettringite and AH_3 [285,380] (*Eq.11.1*):

(Eq.11.1) $Ca_4(AlO_4)_6(SO_4) + 2CaSO_4 \cdot n(H_2O) + (38 - 2n)H_2O \rightarrow Ca_6Al_2(OH)_{12}(SO_4)_3 \cdot 26H_2O + 4Al(OH)_3$

Furthermore, *BC* clinker has high brownmillerite content (Table 11.1), which can interact with sulphate-bearing phases during hydration, leading more ettringite (*Eq.11.2*) or monosulphate (*Eq.11.3*); whereas, hydrogarnet (*Eq.11.4,5*) and iron hydroxide (*Eq.10.5*) are hydration products in the case of no sulphate source [381–383]:

(*Eq.11.2*) $Ca_4(Al,Fe)_4O_{10} + 3CaSO_4 \cdot 2(H_2O) + 30H_2O \rightarrow Ca_6Al_2(OH)_{12}(SO_4)_3 \cdot 26H_2O + Ca(OH)_2 + 2Fe(OH)_3$

(*Eq.11.3*) $Ca_4(Al,Fe)_4O_{10} + CaSO_4 \cdot 2(H_2O) + (n+2)H_2O \rightarrow Ca_4Al_2O_6(SO_4) \cdot 14H_2O + Ca(OH)_2 + 2Fe(OH)_3$

(*Eq.11.4*) $Ca_4(Al,Fe)_4O_{10} + 2Ca(OH)_2 + 10H_2O \rightarrow Ca_3(Al,Fe)_2(OH)_{12}$

(*Eq.11.5*) $Ca_4(Al,Fe)_4O_{10} + 10H_2O \rightarrow \frac{4}{3}Ca_3(Al_{0.75}Fe_{0.25})_2(OH)_{12} + \frac{4}{3}Fe(OH)_3$

Estimated amount of gypsum and anhydrite to fully react ye'elimite (*Eq.11.1*) and brownmillerite (*Eq.11.2*) in *BC* and *Nat* clinker samples are reported in Table 11.2: *Nat* clinker requires ~ 3wt.% of gypsum; whereas, *BC* clinker needs ~ 19wt.% of gypsum, representing a strongly different sulphate addition which limits the comparison with *Nat* cement. Therefore, two different *BC* cements were prepared, one with 3wt.% and the other with 5wt.%, and the released heat flow was tested with ICA till 3 hydration days. All cement pastes were prepared using a water cement powder ratio of 0.5.

Sulphate-bearing phases	***Nat***	***BC***
Gypsum *($CaSO_4 \cdot 2H_2O$)*	3.18(*)	23.30 [3.53(*)+19.77(“)]
Anhydrite *($CaSO_4$)*	2.52(*)	18.42 [2.79(*)+18.42(”)]

Table 11.2 – Sulphate-bearing phases amount reported in grams to fully react ye'elimite (*) and brownmillerite (“) with water following the Eq10.1,2.

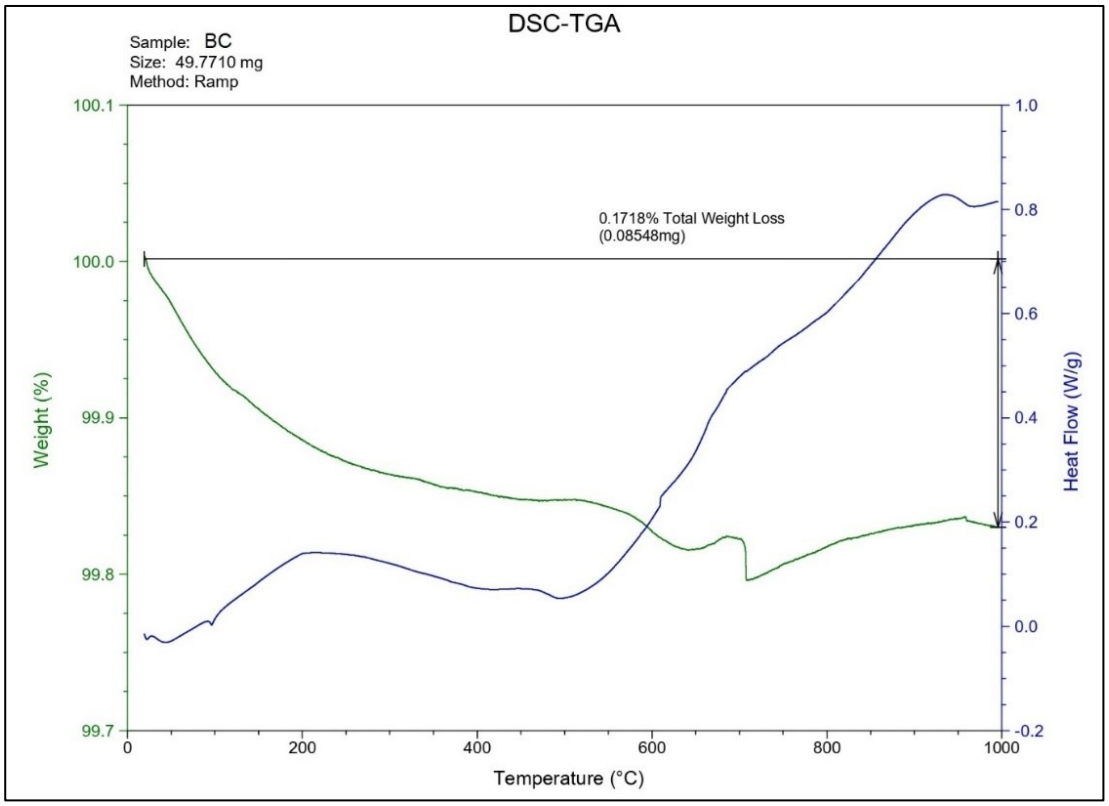

Fig. 11.1 – DSC-TGA of anhydrous synthetic Belite Clinker (*BC*); blue curve is the heat flow (W/g), whereas the green one represents the weight loss (wt.%) upon heating. In black is reported the total weight loss.

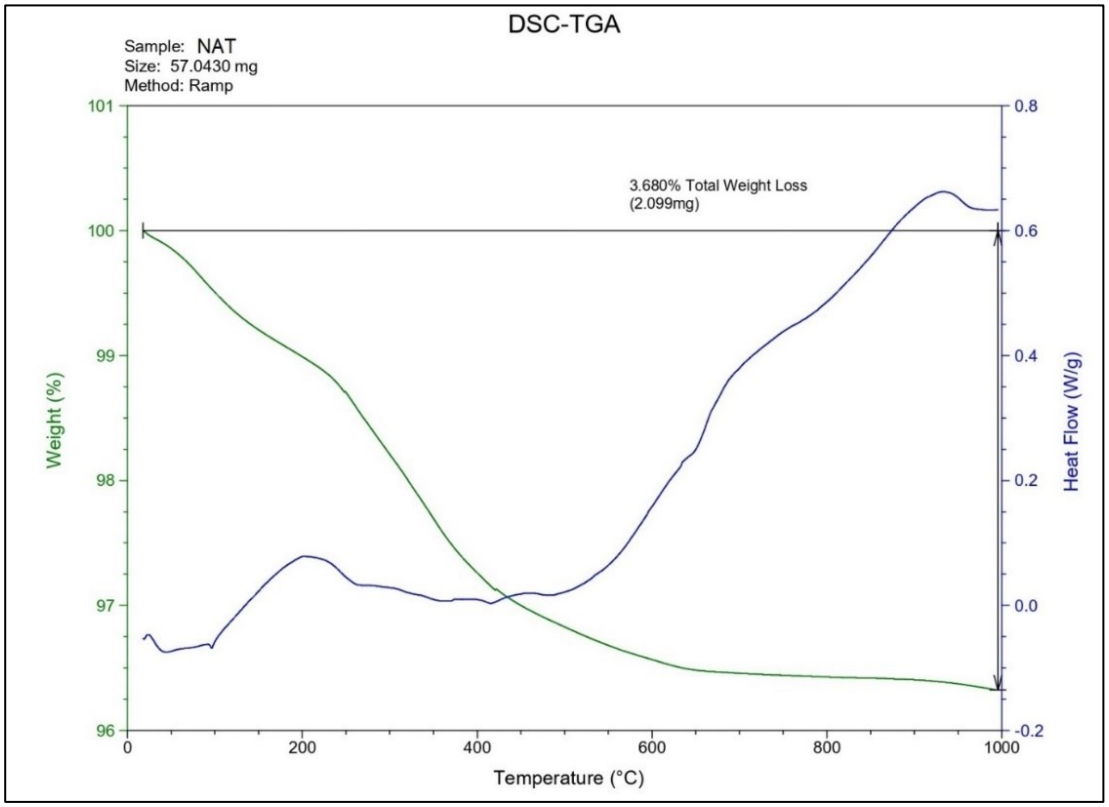

Fig. 11.2 – DSC-TGA of *Nat*, the blue curve is the heat flow (W/g), whereas the green one represents the weight loss (wt.%) upon heating. In black is reported the total weight loss.

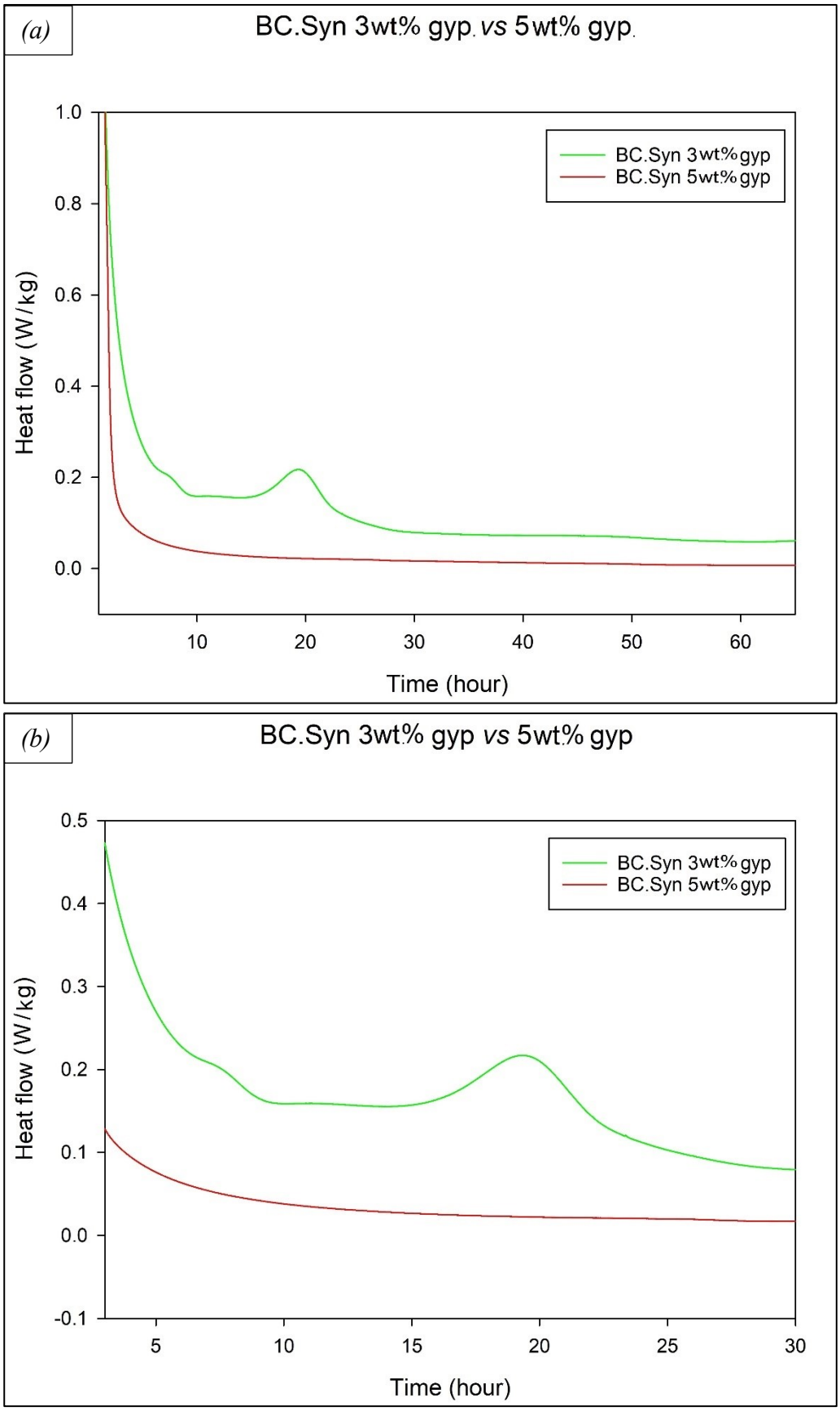

Fig. 11.3 – Heat flow (W/kg) vs time (hour) was reported for *BC* with 3 and 5wt.% of gypsum with 0.5 water cement ratio (a) till 65 hours and (b) a detailed inspection from 3 to 30 hours.

BC cement pastes prepared with 3wt.% and 5wt.% of gypsum showed different heat flows during the hydration: one main hydration peak occurred at 15-22 hours adding 3wt.% of gypsum; whereas, no clear hydration peak raised adding 5wt.% (Fig. 11.3). However, both pastes highlighted a first strong hydration peak related to gypsum and ye'elimite dissolution in water.

Therefore, the addition of 3wt.% of gypsum was used to prepare *BC* (labelled as *3GBC*) and *Nat* (labelled as *3GNat*) pastes, comparing their hydration performances by means of: (i) LXRPD with internal standard method to quantify amorphous content evolution over the time; (ii) TGA calculating bonded and Free-Water Contents (Fig. 11.5,6); (iii) ICA to evaluate the heat flow evolution during hydration till 7 days.

SSA of anhydrous cement powders was checked by both BET and Blaine methods: cements have similar SSA obtained Blaine method, falling in the common values of cement powders [7,8]; whereas, BET results gave higher values for *3GNat* compared to *3GBC* (Table 11.3).

Sample Name	***3GNat***	***3GBC***
Density (g/cm^3)	3.10(1) | 3.11*	3.22(1) | 3.26*
BET (m^2/kg)	2.26(1)	1.55(1)
Blaine (m^2/kg)	542(30)	505(34)

Table 11.3 – Density, BET and Blaine values are reported for both natural (*3GNat*) and synthetic (*3GBC*) cements; e.s.d is reported in round brackets; *predicted values using crystallographic density of gypsum [384] associated with its addition to clinker.

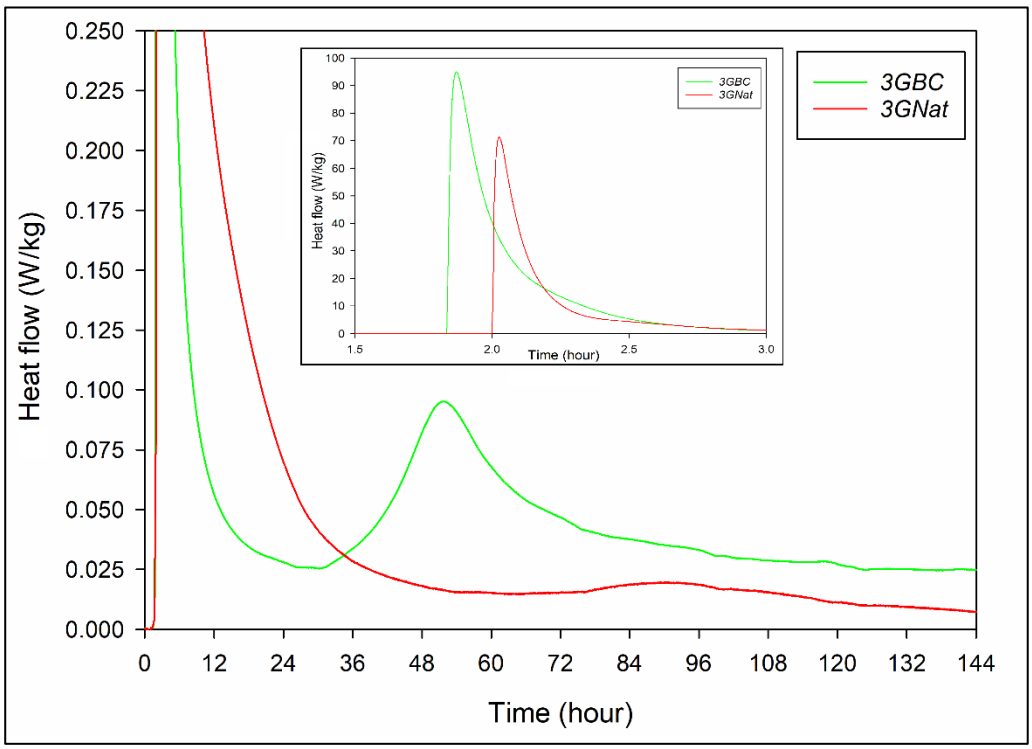

Fig. 11.4 – Heat flow (W/kg) vs time (hour) obtained with ICA for *3GNat* (red curve) and *3GBC* (green curve) pastes prepared with 0.5 water cement ratio, reporting in the small box detail of the first hydration peak.

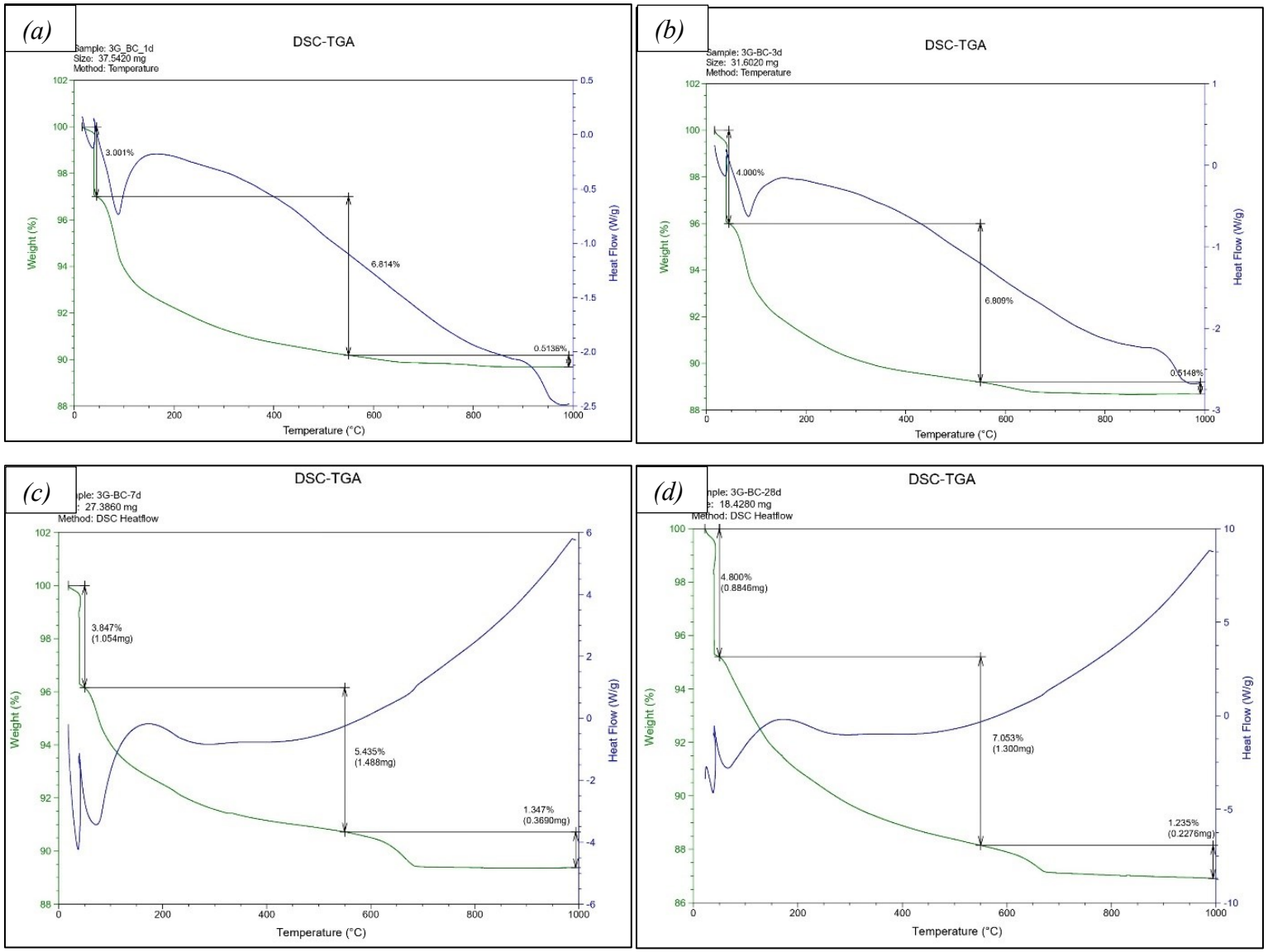

Fig. 11.5 – DSC-TGA of *3GBC* at (a) 1 day, (b) 3 days, (c) 7 days, (d) 28 hydration days; in blue the heat flow (W/g); in green weight loss (%, g) over the heating up to 1000 °C.

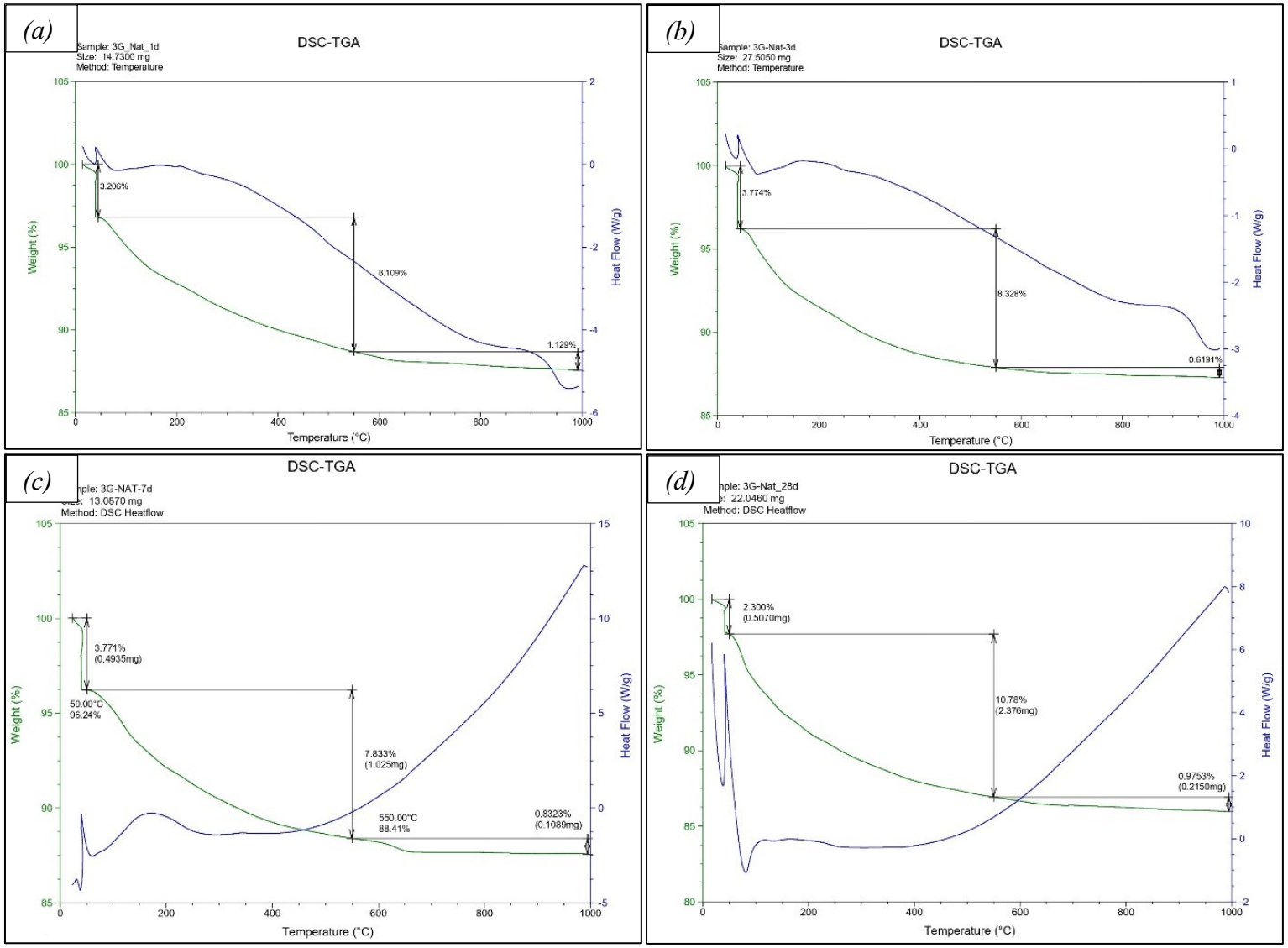

Fig. 11.6 – DSC-TGA of *3GNat* at (a) 1 days, (b) 3 days, (c) 7 days, (d) 28 days of hydration; in blue the heat flow (W/g); in green weight loss (%, g) over the heating up to 1000 °C.

Results of the RQPA with the internal standard method of both cement pastes at 0, 1, 3, 7, 28 hydration days are reported in Table 11.4. Furthermore, amorphous content and Free-Water Content evolution over the hydration time are reported. Both cements showed comparable hydration properties and mineral assemblages (Table 11.4; Fig. 11.7):

(i) *3GNat* cement hydration at from 0 to 1 day of hydration all mayenite, ye'elimite and gypsum completely dissolved with water, leading the formation of calcium aluminate decahydrated, ettringite, aluminium hydroxide and a slight increase of hydrogarnet. Even a limited hydration of β-C_2S occurred after 1 day but its hydration was clear at 28 hydration days. Amorphous content strongly increased after 1 day due to the dissolution of gypsum, ye'elimite, mayenite and minor larnite; whereas slowly reduced from 1 to 7 days thanks to stratlingite and ettriginte precipitation; finally amorphous content re-increased from 7 to 28 days due to larnite hydration. Free-Water Content was almost stable from 1 to 7 hydration days and then started reducing due to the increase in amorphous content and hydrated crystal phases, as confirmed the weight loss from 45 to 550 °C. However, spinel, fluorapatite-ellestadite s.s. and calcio-olivine unreacted, whereas, shulamitite slowly reduced till 7 hydration days and later reacted faster halving its starting content. Ternesite exhibited its hydration reactivity only at 28 hydration days. Ettringite continuously increased over the hydration, whereas, stratlingite started occurring from 7 hydration days when calcium aluminate decahydrated was no longer stable;

(ii) *3GBC* cement hydration revealed a similar behaviour of *3GNat*, especially for larnite hydration, which slightly reacted with water after 1 day. Ettringite occurred since 1 hydration day and continuously increased, excepted from 3 to 7 days which remained almost constant. Amorphous content strongly raised up after 1 day of hydration and remained almost constant till 7 days, after which started increasing probably due to larnite hydration. No aluminium hydroxide, calcium aluminate hydrated phases, portlandite and brucite were formed up to 28 hydration days. Free-Water Content remained almost constant over the entire hydration time studied, as highlighted observing weight loss from 45 to 550 °C.

ICA on cement pastes highlighted a completely different heat flow release between *3GBC* and *3GNat*, excepted for the first hydration peak related to gypsum and ye'elimite break down*: 3GBC* showed a main hydration peak starting and lowering at 36 and 72 hours, respectively; while, *3GNat* revealed only a flat hydration peak from 72 to 100 hydration hours. Both cement pastes showed heat flow similar to BCSA or CSA cements after 20 hours of hydration [385–387]. However, *3GBC* has always a higher heat flow compared to *3GNat* from 36 hours (Fig. 11.4). LXRPD patterns in the window range from 2.70 to 2.80 Å of both cement pastes are reported in Fig. 11.8 highlighting changes in intensity and peaks shape of main Bragg peaks of larnite.

CRYSTAL PHASES	0 day		1 day		3 days		7 days		28 days	
	3GNat	*3GBC*	*3GNat*	*3GBC*	*3GNat*	*3GBC*	*3GNat*	*3G BC*	*3GNat*	*3GBC*
Larnite *(β-Ca_2SiO_4)*	37.49(1.26)	35.35(1.71)	30.96(.42)	30.09(.58)	31.03(.46)	29.46(.51)	30.80(.46)	29.82(.55)	27.96(.37)	27.15(.47)
Calcio-olivine *(γ- Ca_2SiO_4)*	2.05(.12)	4.45(.22)	1.47(8)	4.24(.13)	1.34(8)	3.24(.12)	1.03(8)	2.81(.12)	1.13(8)	3.07(.12)
Ye'elimite *($Ca_4Al_6SO_{16}$)*	2.80(.13)	3.16(.15)	-	-	-	-	-	-	-	-
Mayenite *($Ca_{12}Al_{14}O_{33}$)*	1.65(9)	-	-	-	-	-	-	-	-	-
Brownmillerite *($Ca_4Al_2Fe_2O_{10}$)*	-	10.11(.49)	-	8.04(.18)	-	7.72(.17)	-	8.16(.18)	-	5.59(.14)
Shulamitite *($Ca_3TiAlFeO_8$)*	0.89(7)	-	0.82(6)	-	1.03(6)	-	0.97(6)	-	0.77(6)	-
Fluorapatite*	0.96(.11)	-	1.00(9)	-	1.16(9)	-	1.09(9)	-	1.18(9)	-
Spinel *($MgAl_2O_4$)*	2.46(.11)	-	2.23(7)	-	2.25(7)	-	2.24(7)	-	2.20(7)	-
Ternesite *($Ca_5(SiO_4)_3(SO_4)$)*	0.41(.15)	-	0.53(.12)	-	0.67(.12)	-	0.48(.12)	-	0.06(.12)	-
Periclase *(MgO)*	-	0.14(1)	-	0.19(4)	-	0.12(4)	-	0.20(4)	-	0.06(5)
Hydrogarnet *($Ca_3Al_2(O_4H_4)_3$)*	0.14(8)	-	0.59(8)	-	0.55(8)	-	0.42(8)	-	0.30(8)	-
Gibbsite *$Al(OH)_3$*	0.14(.10)	-	0.35(8)	-	0.66(9)	-	0.85(9)	-	0.06(9)	-
Gypsum *($CaSO_4$ $2H_2O$)*	1.98(.10)	1.86(9)	-	-	-	-	-	-	-	-
Afwillite *($Ca_3Si_2O_4(OH_6)$)*	0.68(.12)	-	0.64(.11)	-	0.67(.11)	-	0.54(.10)	-	0.42(.10)	-
Ettringite *($Ca_6Al_2(SO_4)_3(OH)_{12}\cdot 26H_2O$)*	-	-	1.29(9)	2.85(.12)	2.56(.09)	3.81(.13)	2.01(9)	4.63(.14)	4.74(.10)	6.70(.17)
Calcium Aluminate decahydrate *CAH_{10}*	-	-	0.41(5)	-	0.43(.05)	-	-	-	-	-
Riversidite *(Tobermorite 9Å)* *($Ca_3(HSi_3O_9)_2\cdot 2H_2O$))*	-	-	-	-	-	-	-	1.36(.15)	-	-
Stratlingite *($Ca_2Al_2SiO_2(OH)_{10}\cdot 3H_2O$)*	-	-	-	-	-	-	1.69(7)	-	1.54(7)	0.86(.11)
Amorphous Content	15.03(.49)	11.60(.56)	32.46(.36)	26.29(.46)	30.63(.38)	27.41(.42)	30.45(.39)	26.10(.40)	34.57(.35)	28.57(.40)
Free Water Content	33.33(1)	33.33(1)	27.24(1)	28.30(1)	27.02(1)	28.24(1)	27.43(1)	26.92(1)	25.07(1)	28.00(1)

Table 11.4 – RQPA results for *3GNat* and *3GBC* at 1, 3, 7, 28 days of hydration considering both Free Water Content and Amorphous Content; *, $Ca_5\left(Si_{\frac{x}{2}}S_{\frac{x}{2}}P_{1-x}\right)_3F$; e.s.d. is reported in rounded brackets and was calculated using the propagation error rules [388].

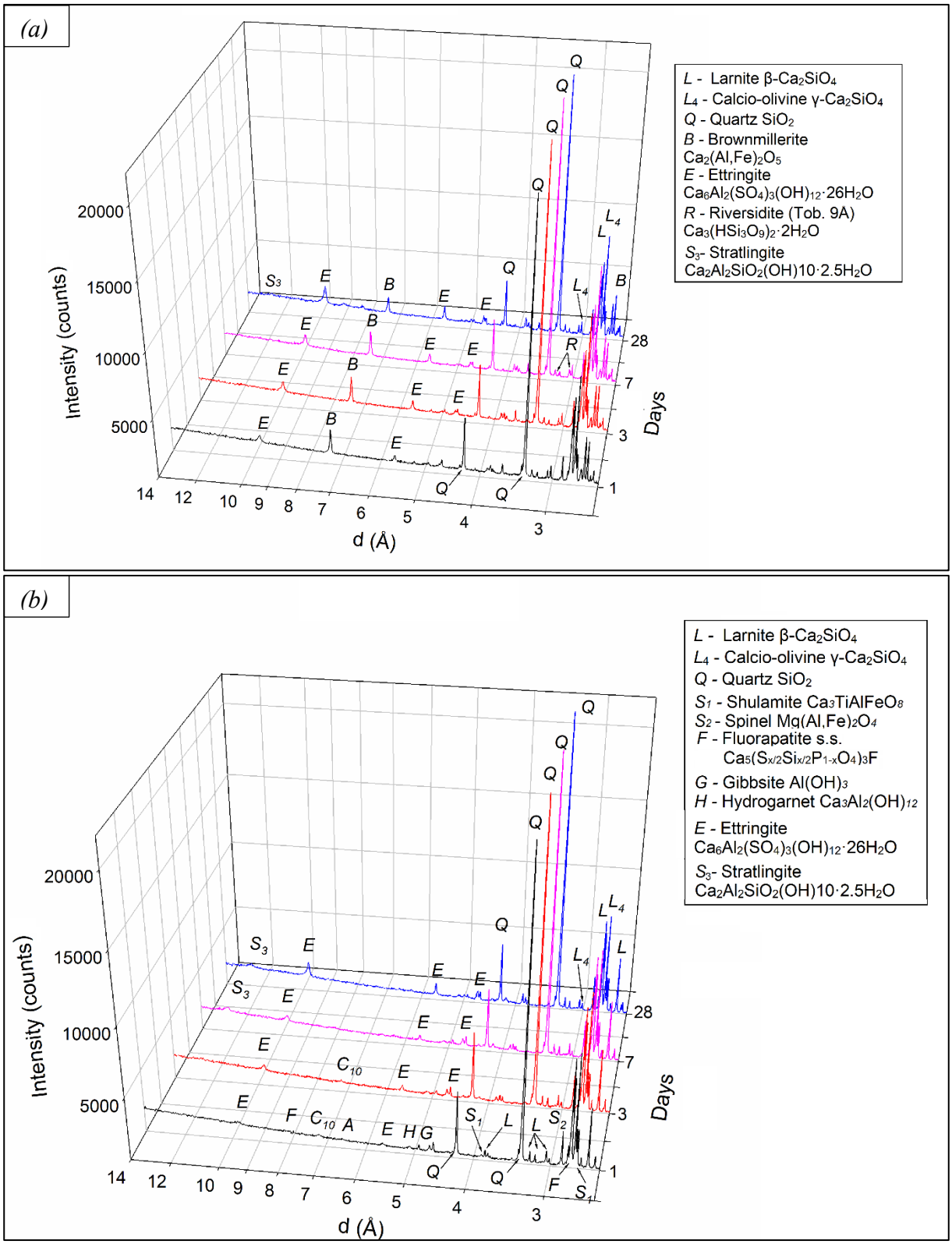

Fig. 11.7 – LXRPD patterns of cement pastes from 0 to 28 hydration days with quartz as internal standard and highlighting main Bragg peaks of occurring crystal phases: (a) *3GBC*; (b) *3GNat*.

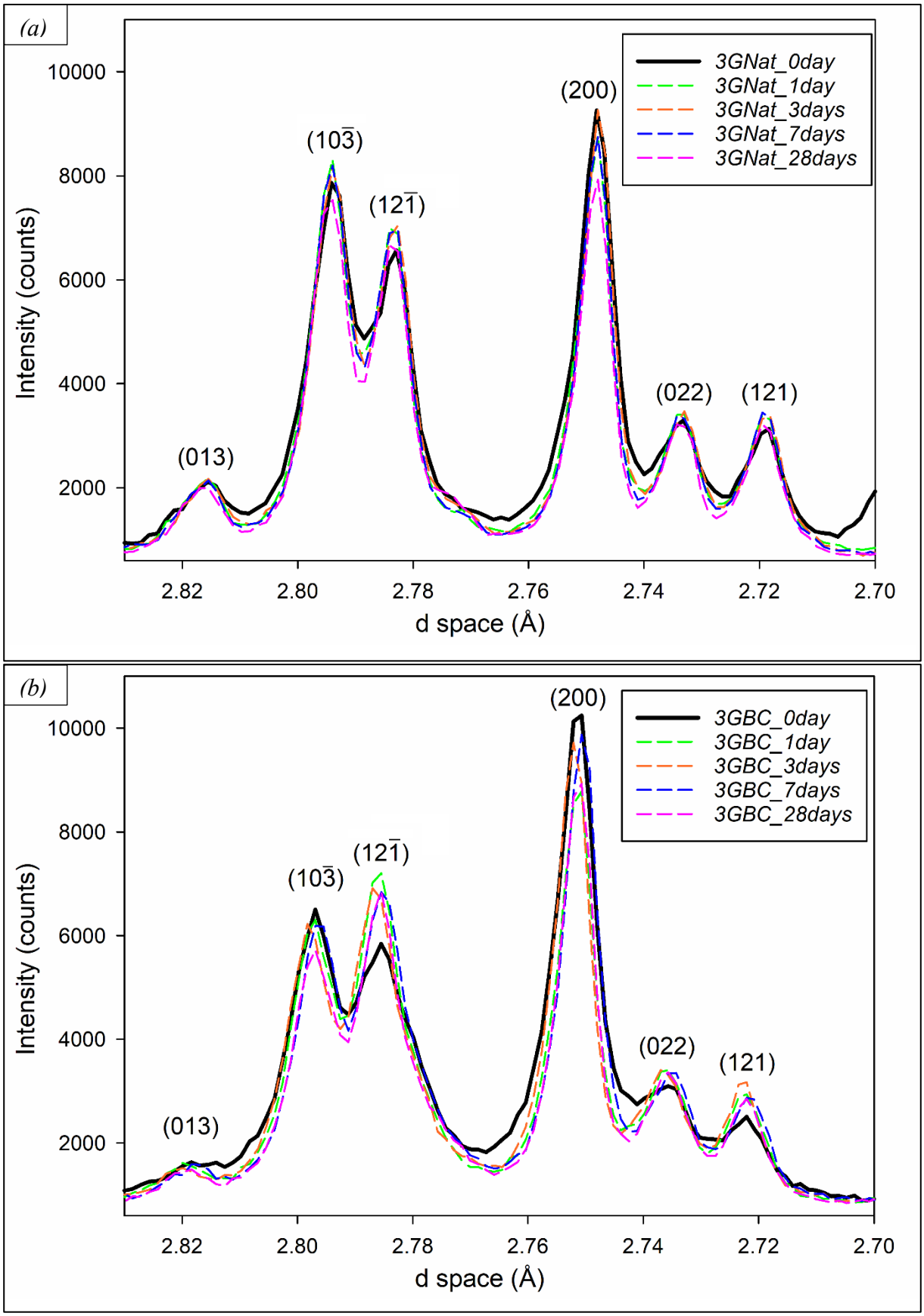

Fig. 11.8 – LXRPD patterns of cement pastes from 0 to 28 hydration days highlighting β-C_2S Bragg peaks shape in the window range from 2.80 to 2.70 Å: (a) *3GNat*; (b) *3GBC*.

X-ray μ-CT tomography was performed on sample *3GBC* hydrated for 1 month highlighting voids crystal phase distribution. *3GBC* sample after 1 hydration month has 8.00 vol.% of voids with both large well-rounded pores (Fig. 11.9a) and small micrometric ones. Unreacted dicalcium silicate and brownmillerite occurred as coarse and small clusters, respectively. Furthermore, the wide low-density matrix is related to hydrated phases, such as ettringite, stratlingite and C-S-H amorphous phase. These results are in good agreement with previous LXRPD analysis (Table 11.4).

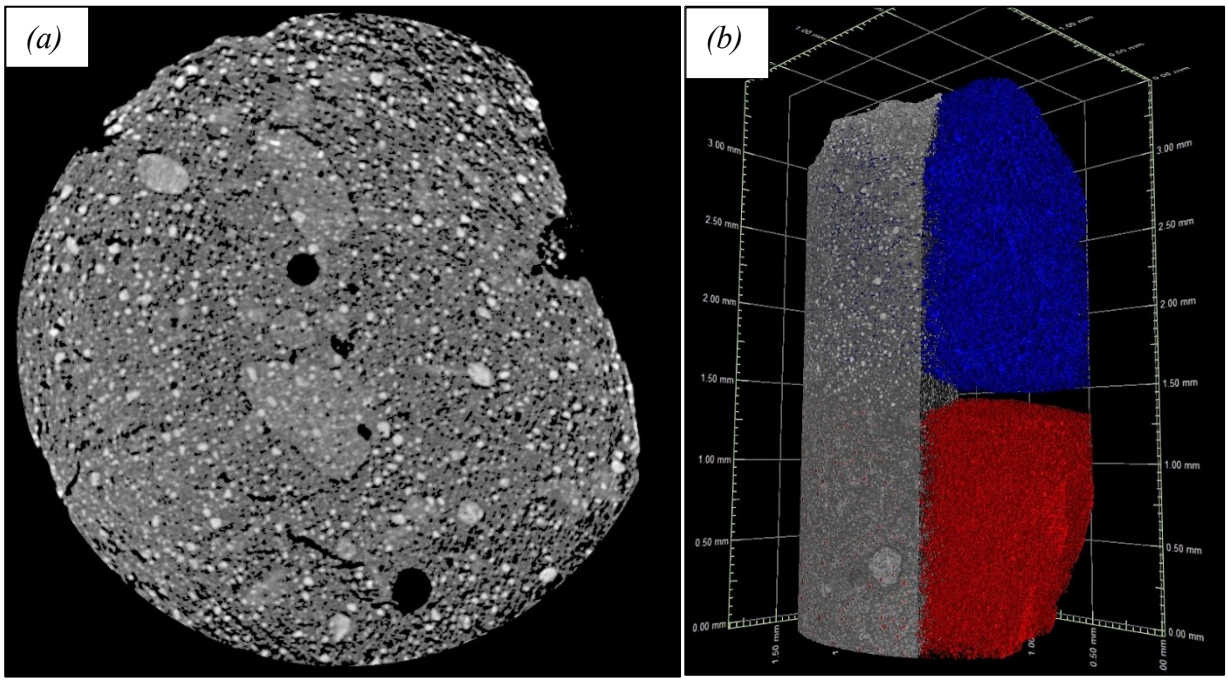

Figure 11.9 – *3GBC* sample hydrated for 1 month and studied by means of synchrotron X-ray μ-CT at Elettra: (a) sample slice highlighting brownmillerite in white (high density phase), not water-reacted dicalcium silicate in medium grey (medium density phase), hydrated phases (ettringite, stratlingite and amorphous C-S-H phase, representing low density phases) and voids in black; (b) volume rendering with a clipping plane parallel to the elongation of the sample, showing on the top half voids distribution in blue and unreacted brownmillerite in red in the bottom half.

Natural ye'elimite-larnite rock (*6BWO*, Table 11.5) powder was directly mixed with water (water cement ratio equal to 0.6) and the crystal phase assemblage evolution over the hydration time was studied by means of RQPA. Furthermore, *6BWO* rock fragments were immersed in water in a sealed box, avoiding water loss, at a constant temperature of 20 °C and after 5 months of hydration the white precipitation was sampled, dried with absolute ethanol and studied by means of LXRPD (Table 11.5).

Sample	***6BWO***				
Starting material	***Powder***				***Fragments***
Time	***0 days***	***3 weeks***	***3 months***	***4 months***	***5 months***
Experimental Set-Up	***SXRPD (ID22)***	***SXRPD (MCX)***	***LXRPD***	***LXRPD***	***LXRPD***
Larnite *(β-Ca_2SiO_4)*	68.15(.14)	66.28(.27)	64.47(.33)	42.87(.29)	-
Brownmillerite *($Ca_2(Al,Fe)_2O_5$)*	0.18(2)	-	-	-	-
Ye'elimite *($Ca_4Al_6SO_{16}$)*	15.04(.10)	-	-	-	-
Shulamitite *($Ca_3TiAlFeO_8$)*	2.08(3)	1.93(7)	1.91(.12)	2.20(.10)	-
Fluorapatite-ellestadite $Ca_5\left(Si_{\frac{x}{2}}S_{\frac{x}{2}}P_{1-x}\right)_3 F$	8.41(7)	9.47(.20)	9.63(.28)	10.03(.27)	-
Spinel *($Mg(Al,Fe)_2O_4$)*	4.04(3)	4.21(8)	4.07(.10)	4.05(.12)	-
Hydrogarnet *($Ca_3Al_2(O_4H_4)_3$)*	0.67(3)	1.13(.10)	1.11(.12)	1.33(.12)	-
Gibbsite *($Al(OH)_3$)*	0.43(4)	0.73(9)	0.54(.12)	0.24(.12)	2.93(.20)
Bayerite *($Al(OH)_3$)*	-	0.51(9)	0.19(.12)	-	8.89(.23)
Nordstrandite *($Al(OH)_3$)*	0.37(4)	0.78(.10)	0.71(.13)	0.43(.13)	3.51(.21)
Gypsum *($CaSO_4{\cdot}2H_2O$)*	-	-	-	0.87(9)	20.83(.24)
Ettringite *($Ca_6Al_2(SO_4)_3(OH)_{12}{\cdot}26H_2O$)*	-	8.14(.15)	8.97(.15)	10.96(.33)	-
Stratlingite *($Ca_2Al_2SiO_2(OH)_{10}{\cdot}3H_2O$)*	-	4.48(.19)	6.17(.24)	18.76(.33)	-
Quartz *(α-SiO_2)*	0.11(3)	0.27(4)	0.43(5)	0.26(5)	0.35(7)
Calcite *($CaCO_3$)*	0.52(4)	2.07(4)	1.82(8)	8.00(.14)	57.28(.35)
Syngenite *($K_2Ca(SO_4)_2{\cdot}H_2O$)*	-	-	-	-	2.58(.17)

Table 11.5 – RQPA results (wt.%) of *6BWO* (ye'elimite-larnite rock) hydration as powder and the precipitate from rock fragments hydration at different curing time; -, not detected.

RQPA results are reported in Table 11.5 useful to (i) identify mineral assemblage changes and (ii) major wt.% variation of crystal phases during hydration.

Hydration of *6BWO* cement without gypsum or anhydrite addition figured out an almost constant wt.% of hydrogarnet and low water-reactive phases (spinel, fluorapatite-ellestadite s.s. and shulamitite); whereas, larnite strongly reacted with water at 4 hydration months. Ettringite and stratlingite represent the main hydrated crystallite phases, which the former continued slowly increasing from 3 weeks to 4 months, whereas the latter strongly raised up at 4 months. Calcite and aluminium hydroxides (gibbsite, nordstrandite and bayerite) represent minor crystal phases produced during hydration; calcite already occurred after 3 weeks of hydration and clearly increased at 4 months; aluminium hydroxides continuously reduced after 3 weeks of hydration due to stratlingite precipitation.

6BWO fragments hydration produced a white crystalline precipitate made of calcite, representing the main crystal phase, gypsum and aluminium hydroxide, which the latter is mostly composed of bayerite (Table 11.5). Furthermore, minor amount of syngenite and quartz occurred.

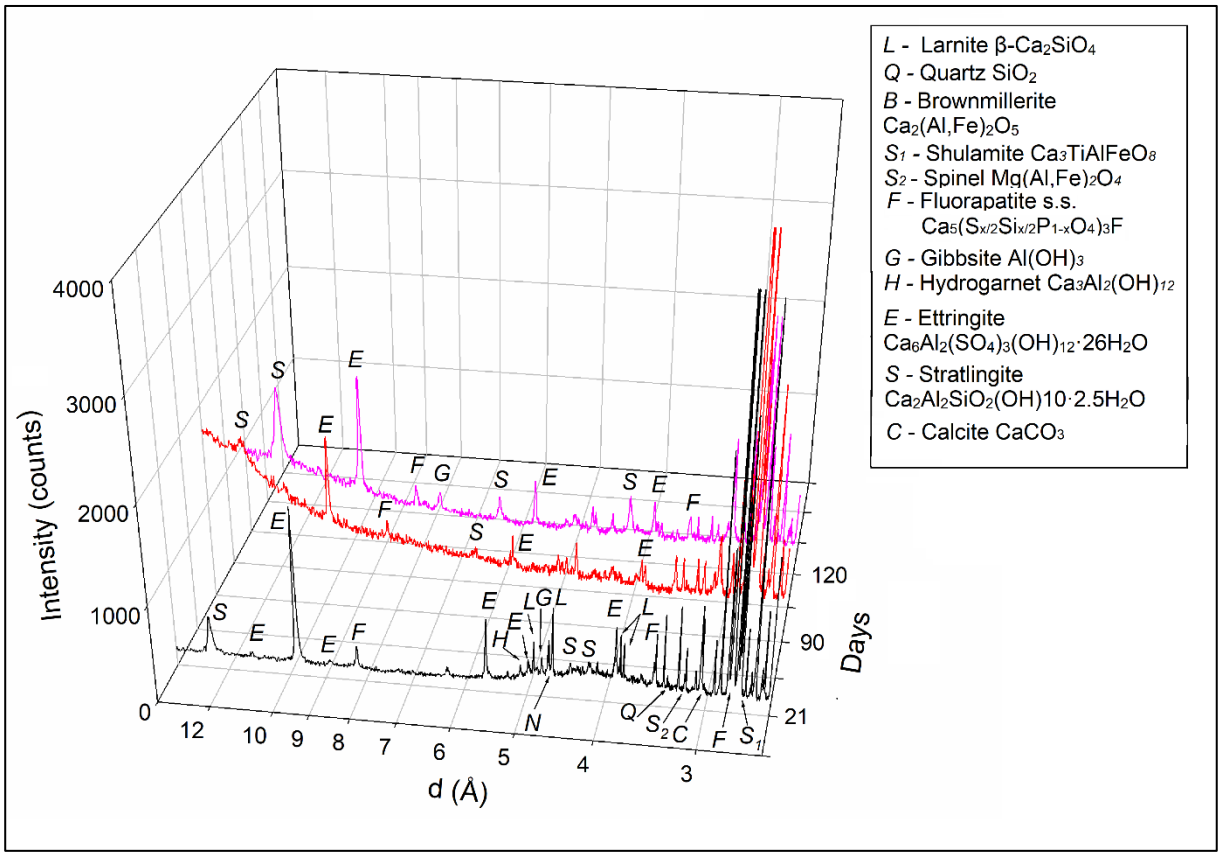

Figure 11.10 – LXRPD patterns of *6BWO* pastes at 3 weeks, 3 and 4 months of hydration, highlighting main Bragg peaks of occurring crystal phases.

11.3 – Discussion

The hydration properties of Belite Cements based on natural ye'elimite-larnite rocks (*Nat*) and synthetic High Ferrite Belite Clinker sulphur doped (*BC*) were tested and compared by means of SSA, TGA, ICA and LXRD.

Both *BC* and *Nat* samples, corresponding to large volume of homogeneous fine grinded powder of *BC* heated at 1350 °C and *YC2O* ye'elimite-larnite rocks, respectively, showed the occurrence of calcio-olivine, which did not occur previously (Table 11.1, Fig. 10.1,2). Calcio-olivine could form in the case of: (i) prolonged heating at high temperature, enhancing large and purer dicalcium silicate crystals; (ii) slow cooling after heating, promoting the gradual expulsion of foreign ions leading purer crystals and enhancing complete retrograde polymorphic transitions; (iii) low amount of dopants (Na_2O, K_2O, B_2O_3, P_2O_5, SO_3, etc. [7,8]) in the starting raw meal, inhibiting the stabilisation of high temperature polymorphs after cooling [389]. However, γ-C_2S occurrence in *BC* and *Nat* clinkers should be related to the prolonged grinding: fine grinding leads an increase in crystal structural defects and provides energy for the polymorphic transition to metastable high-defective larnite crystals [390,391].

SSA results revealed similar values for both cements considering Blaine method, while, *3GNat* has higher SSA value with BET method compared to *3GBC*: BET method should be considered with higher sensitivity compared to Blaine one [392].

The hydration of *BC* and *Nat* cements with 3wt.% of gypsum with a water cement ratio of 0.5 pointed out some differences and similarities:

(i) Both cements showed a slight larnite hydration even after 1 day, which could be explained by the occurrence of low crystallite size crystals highly reactive with water, leading the formation of amorphous CSH (with an approximately chemical composition of $C_{1.61\text{-}2}SH_4$) and low amount of CH [7,8]: LXRPD patterns revealed a sharpening of larnite Bragg peaks during the hydration, suggesting the first dissolution of low crystallite larnite which contributes to the broad parts of peaks (Fig. 11.8). However, this hypothesis needs further research in order to confirm the occurrence of CSH gel due to belite hydration;

(ii) Ettringite is an ever-present hydrated crystal phase always crystallising in both cements by the hydration reaction $C_4A_3\bar{S} + 2C\bar{S}H_2 + 34H \rightarrow C_6A\bar{S}_3H_{32} + 2AH_3$ among ye'elimite, gypsum and water, which also forms amorphous aluminium hydroxide [389]. Considering gypsum and ye'elimite contents (Table 11.4) the expected ettringite for sample *3GBC* is 6.50wt.%, consuming 1.78wt.% of the starting gypsum; whereas the remaining 0.10wt.% should react with 0.08wt.% brownmillerite leading 0.20wt.% of ettringite, 0.01wt.% portlandite and 0.03wt.% of $Fe(OH)_3$ (see section 6.5.4): the total expected ettringite for *3GBC* is 6.70wt.% which goodly fits with the RQPA values at 28 hydration days. Whereas, sample *3GNat* has 5.76wt.% of expected ettringite from ye'elimite hydration consuming 1.58wt.% gypsum and the remaining 0.40wt.% of gypsum could react with 1.1wt.% of mayenite leading the formation of 1wt.% ettringite [393], 0.52wt.% portlandite and 0.74wt.% AH_3 ($C_{12}A_7 + 3C\bar{S}H_2 + 53H \rightarrow C_6A\bar{S}_3H_{32} + 6AH_3 + 9CH$): the overall expected ettringite formation for *3GNat* is 6.76wt.% but at 28 hydration days only 4.75wt.% occurred, pointing out a slower reaction formation of ettringite compared to *3GBC*;

(iii) Stratlingite occurred in both cements but early crystallised in *3GNat* after 7 hydration days, while it occurred only at 28 days in *BC* based cement: stratlingite usually crystallises after several hydration days [394] by the reaction $C_2S + AH_3 + 5H \rightarrow C_2ASH_8$ [395], which could be also re-written as $C_{1.8}SH_4 + 0.2CH + AH_3 + 0.8H \rightarrow C_2ASH_8$ considering the early hydration of belite [7,8]. Stratlingite crystallisation is favoured by a pH rise and the availability of CAH phases as nuclei for growing, such as CAH_{10}, C_2AH_8 and C_3AH_6 [396,397]. Therefore, the occurrence of mayenite hydration in *3GNat*, in absence of available sulphate, led the formation of CAH_{10} and low amount of C_3AH_6 [398,399] suggesting the hydration reaction $2C_{12}A_7 + 120H \rightarrow 9CAH_{10} + 5C_3AH_6$, which improved the early formation of stratlingite after 7 days by the following reaction: $2CAH_{10} + 2C_{1.8}SH_4 + 0.4CH \rightarrow C_2ASH_8 + AH_3 + 9.4H$ only considering the participation of calcium aluminate decahydrated as aluminium source and larnite hydration products;

(iv) Low amount of ternesite occurred in *3GNat* which at 28 hydration days showed slow water-reactivity increasing ettringite and amorphous CSH phase: pure ternesite hydration could be described by the reaction $C_5S_2\bar{S} + 10.8H \rightarrow 2C_{1.8}SH_4 + 0.4CH + C\bar{S}H_2$ [338]. The formation of CSH and low amount of CH raises pH, improving larnite hydration, whereas gypsum precipitation increases sulphate availability for ettringite crystallisation. However, ternesite hydration associated with AH_3, as occurring in *3GNat*, produces stratlingite, ettringite and CSH, as reported in previous studies [400,401]. Furthermore, previous

experiments showed thaumasite ($C_3S\bar{S}\bar{C}H_{15}$) crystallisation by ternesite hydration from 28 to 180 days when CO_3^{2-} occurs [337,402]. Ternesite has higher reactivity than larnite and similar to brownmillerite, high SO_4^{4-} content and low pH reduce its water-reactivity [403];

(v) Brownmillerite only occurred in *3GBC* and partially reacted with water after 1 day and only later re-started slowly reacting with water after 7 hydration days probably due to the pH rise by larnite dissolution [7]. Brownmillerite hydration should have participated in ettringite precipitation as reported in *Eq.11.2,3* because no hydrogarnet occurred in XRD patterns (*Eq11.4,5)*;

(vi) The increasing trend in amorphous content after 7 hydration days of *3GNat* could be explained by ternesite and shulamitite hydration which slowly reacted leading early amorphous phases: ternesite dissolution led amorphous CSH and CH; while, main shulamitite hydration product is $CaTiFe^{3+}AlO_8 \cdot 3H_2O$ [34], which should be also associated with portlandite formation to balance the calcium excess, as reported in the reaction $Ca_3TiFe^{3+}AlO_8 + 5H_2O \rightarrow CaTiFe^{3+}AlO_8 \cdot 3H_2O + 2Ca(OH)_2$.

Hydration of ye'elimite-larnite rock powder without gypsum or anhydrite showed a similar mineral assemblage of *3GNat*, excepted for the continuous crystallisation of calcite by the reaction between CO_2 and $Ca(OH)_2$ [7,8]. Furthermore, larnite strongly hydrated after 3 months leading the formation of stratlingite by the consumption of aluminium hydroxides (gibbsite, bayerite and nordstrandite) and CSH previously formed by ye'elimite and larnite hydration, respectively. The slight fluorapatite increase should be related to the release of phosphorous and portlandite by larnite hydration [404]. Gypsum precipitation after 3 months of could be due to the increase in pH and oversaturation of SO_4^{2-}.

Precipitation produced by the hydration of ye'elimite-larnite granofels fragments highlighted a crystal phase assemblage close to white veins of larnite-rich rocks (Table 9.3), excepted for higher gypsum, AH_3 and the lack of tobermorite 11 Å.

These results give more credit to a precipitation of crystals from a circulating solution inside fractures to explain white veins formation in larnite-rich rocks: a circulating solution resulting from the interaction of anhydrous natural clinker is enriched in $Ca(OH)_2$, AH_3, SO_4^{2-} and CO_3^{2-} leading the formation of large amount of calcite ($Ca(OH)_2 + CO_2 \rightarrow CaCO_3 + H_2O$), representing the main phase, ettringite, aluminium hydroxides and gypsum. Therefore, CSH phases (tobermorite, jennite, afwillite, stratlingite, thaumasite, bulfoteinite, apophyllite, etc.) should occur mainly in brown parts of hydrated larnite-rich rocks, which represent the direct hydration of anhydrous natural clinker. The overall lack of stratlingite in natural hydrated larnite-rich rocks veins could be explained by an increase in temperature higher than 90 °C and/or high content of $Ca(OH)_2$, destabilising stratlingite which turns into hibschite ($Ca_3Al_2(SiO_4)_{3-x}(OH)_{4x}$), portlandite and calcium aluminate hydrates (C_4AH_x) [405,406].

11.4 – Conclusion

The comparison between natural larnite-based cement (*Nat* sample), prepared from ye'elimite-larnite granofels collected in Hatrurim Basin, and laboratory prepared HFBC S-doped (*BC* sample heated at 1350 °C) showed similar hydration properties and mineral assemblage after 28 hydration days. Larnite and ye'elimite both represent main hydrating crystal phases of these two cements but exhibited different water-reactivity: the simultaneous occurrence of ye'elimite and gypsum during hydration led ettringite and aluminium hydroxides formation since 1 day of hydration; while, larnite started hydrating at 28 hydration days producing amorphous CSH and low amount of CH, reacting with AH_3 to form stratlingite. Nevertheless, slight hydration-degree occurred for larnite since 1 day of hydration thanks to high defective crystals. However, secondary phases should be taken into consideration during hydration experiments: brownmillerite represents an important constituent in Belite Cements, and influences hydration properties especially with high sulphate ion availability, despite its slow hydration reactivity; whereas, minor crystal phases only occurring in natural larnite-based cement (shulamitite, ternesite and mayenite) influenced hydration increasing amorphous content, CAH_x, $Ca(OH)_2$ and SO_4^{2-} which can modify pH, availability of ions and stability of anhydrous phases. Nonetheless, both cement pastes highlighted similar crystal phase assemblage after 28 hydration days, which is well comparable to commercial BCSA cements.

Laboratory hydration of ye'elimite-larnite granofels fragments and powder without sulphate-bearing phases reproduced conditions similar to natural hydration of ye'elimite-larnite granofels in Hatrurim Basin at early ages. Hydrated larnite-rich rocks commonly occur as veins made of (i) white central part, strongly enriched in calcium carbonate and minor ettringite and CSH phases, and (ii) brown borders with wide mineral assemblage usually richer in CSH minerals, ettringite, aluminium hydroxides and katoite. Laboratory hydration of ye'elimite-larnite granofels powder gave XRD results similar to brown parts of natural veins: stratlingite, ettringite, calcite and gypsum are main hydration products after 4 months, which should gradually turn into higher hydrogarnet, calcite and crystalline CSH phases. CSH phases formation is related to the gradual conversion of the amorphous CSH and by the probable decomposition of stratlingite at high pH with $Ca(OH)_2$ linked with fully larnite hydration.

Ye'elimite-larnite granofels fragments hydration produced a white precipitation, which is composed of mainly calcite and lesser gypsum, ettringite and aluminium hydroxides with no CSH crystalline phases at 5 hydration months, representing the early corresponding of white cores of natural veins: ye'elimite-larnite granofels during hydration by weathering led the dissolution of anhydrous water-reactive phases (ye'elimite, larnite, mayenite, brownmillerite, etc.) leading a circulating solution mainly rich in $Ca(OH)_2$, SO_4^{2-}, AH_3 and minor amorphous CSH filling pores and fractures, which gradually crystallised as main calcite and ettringite associated with minor phases.

Chapter 12
General conclusions

This study aimed to compare the natural process of Combustion Pyrometamorphism (CP) that involved impure limestone occurring in Hatrurim Basin (Israel) and the synthetic analogous process of cement production by means of a multidisciplinary approach based on both conventional and innovative analytical techniques.

Filed trip in Hatrurim Basin area allowed to collect both CP rocks and protolith of larnite-rich rocks, and relevant geological features making a direct comparison with available bibliographic data. Chemical composition differences (CaO-SiO_2-Al_2O_3) observed along the metamorphic sequence by changes on mineral phase assemblage are well linked to chemical composition and microtextural changes occurring inside the pristine sedimentary sequence: (i) metamorphosed Mishash Formation (also called bake-line) corresponds to the base of metamorphosed sequence; (ii) gehlenite-wollastonite and anorthite-diopside hornfels represent brown to black layers corresponding to the metamorphism of marls belonging to Lower Member of Taqiye Formation; (iii) stratified larnite-rich rocks and calcite-spurrite well-fit with HT metamorphism of well-stratified marly limestone of Hafir Member. Furthermore, HT rocks usually occur at the metamorphic sequence top or close portions which were featured by higher oxygen availability improving combustion reaction. Therefore, results confirmed the general hypothesis of HT *in-situ* metamorphism of a sedimentary sequence by the combustion of methane-rich gases coming from deep hydrocarbon reservoirs along fractures and faults for a prolonged heating period (mud volcanism), leading the formation of a metamorphic sequence; hence, the previous bitumen self-ignition model should be rejected as formation mechanism of Hatrurim Basin rocks.

The study on protolith of larnite-rich rocks (Ghareb Fm.) was crucial to reveal detailed mineralogical and crystallographic information and to highlight natural anisotropies (such as goethite-rich layers, Fe-Ti-rich nodules, phosphatic-rich portions and gypsum-rich veins), which have a strong influence on final mineral assemblage and microtexture during CP. The link between anisotropies occurring in pristine limestone and ye'elimite-larnite granofels was confirmed even by laboratory heating of protolith fragments: (i) millimetric black nodules rich in spinel and Ti-bearing phases in ye'elimite-larnite granofels should be correlated with millimetric dark nodules rich in Fe-phases and with minor titanite occurring inside pristine limestone; (ii) coarse fluorapatite crystals occurring inside ye'elimite-larnite granofels should be linked to the occurrence of phosphatic pellets inside protolith rocks, as confirmed by Ghareb Formation fragments heating.

Detailed crystallographic and microtextural investigations on ye'elimite-larnite granofels and the equivalent *green-cement* fluorine, sulphur and phosphorous doped, which was laboratory prepared using ye'elimite-larnite granofels protolith (Ghareb Formation), revealed crystal phase evolution upon heating till 1350 °C showing two main melting events: (i) low-T melt rich in $CaSO_4$-C_2S-CaF_2 is produced at $T \geq 1054$ °C when CaF_2 is released by ternesite-silicocarnotite crystallisation at 966-1029 °C and by fluorapatite-ellestadite breakdown at 1150-1182 °C; (ii) high-T Al-Fe-rich melt occurs at 1250-1270 °C, leading microtextural features close to OPC and BC

ones. Furthermore, highly doped hatrurite and HT dicalcium silicate polymorphs (larnite and flamite) occurred at room temperature after heating at 1244 °C of Ghareb Formation powder even with a slow cooling, representing an important outcome suitable for designing *green-cements* and improving cement manufacture: phosphorous, sulphur and fluorine raw meal doping should strongly improve hydration properties, limiting the main drawback of belite-rich cements. Therefore, this study figured out the availability of P-S-F-rich wastes reuse (e.g., phosphogypsum, solid urban wastes, F-rich sludges, P-S-F-rich rock wastes, etc.) as partially replacing raw materials in cement manufacture being able to cope with the aim of managing waste-related problems (dangerous elements pollution, reducing land use for landfills and waste treatment costs) and reducing CO_2 emissions (lowering combustion T, grinding energy expenditure, fuel and natural raw materials consumption). Furthermore, results could be employed not only for improving cement manufacture but also for advancing oil fields exploration, due to the vicinity of CP rocks to oil and gas reservoirs: CP rocks could be used as a proxy especially for methane-rich reservoirs.

High Ferrite Belite Cement S-doped laboratory prepared showed same mineral assemblage and hydration properties of BCSA cements, supporting the chance of partial substituting of bauxite with Fe-rich wastes as starting raw materials. Moreover, two important features were observed: (i) the final mineral assemblage (larnite-brownmillerite-ye'elimite) was already occurring at 1200 °C, excepted for minor minerals occurrence, with high porous and fine microtexture; (ii) larnite was always stable at RT without γ-C_2S retrograde polymorphic transition even with a slow cooling. These relevant results allow: (a) a strong reduction of energy expenditure and CO_2 emission for cement plant, thanks for the lower combustion T compared to common Belite Cements (1250-1350 °C); (b) lower grinding energy costs thanks to the advantageous porous-soft microtexture, which represents a main item of expenditure in cement manufacture; (c) the positive reuse of Fe-S-rich wastes as alternative raw material helps in handling bauxite supply and landfill related problems.

Natural ye'elimite-larnite granofels figured out similar hydration reactions of HFBC S-doped ones, with differences mainly due to minor hydrating crystal phases, such as ternesite, mayenite. Furthermore, hydration experiments on ye'elimite-larnite granofels clarified the formation process of natural hydrated larnite-rocks veins better explain their textural features: (i) the weathering of ye'elimite-larnite granofels outcrops caused the water interaction with reactive anhydrous phases (larnite, ye'elimite, mayenite, brownmillerite and ternesite) leading the formation of a circulating pore solution and a hydration products, such as CSH phases, hydrogarnet, gibbsite, ettringite, etc.; (ii) the circulating pore solution can move along cracks and fractures and is rich in $Ca(OH)_2$, SO_4^{2-} and AH_3, which gradually leads the precipitation of mainly calcite and minor ettringite and gypsum, forming white core of hydration veins; (iii) the hydration products, which during the early hydration stage occur as amorphous phases, remain in the same position and gradually crystallise as CSH phases (tobermorite, jennite, afwillite, etc.), hydrogarnet, gibbsite associated with calcite, gypsum and ettringite coming from the pore solution, representing brown parts of hydration veins.

Appendix

Additional images of studied samples

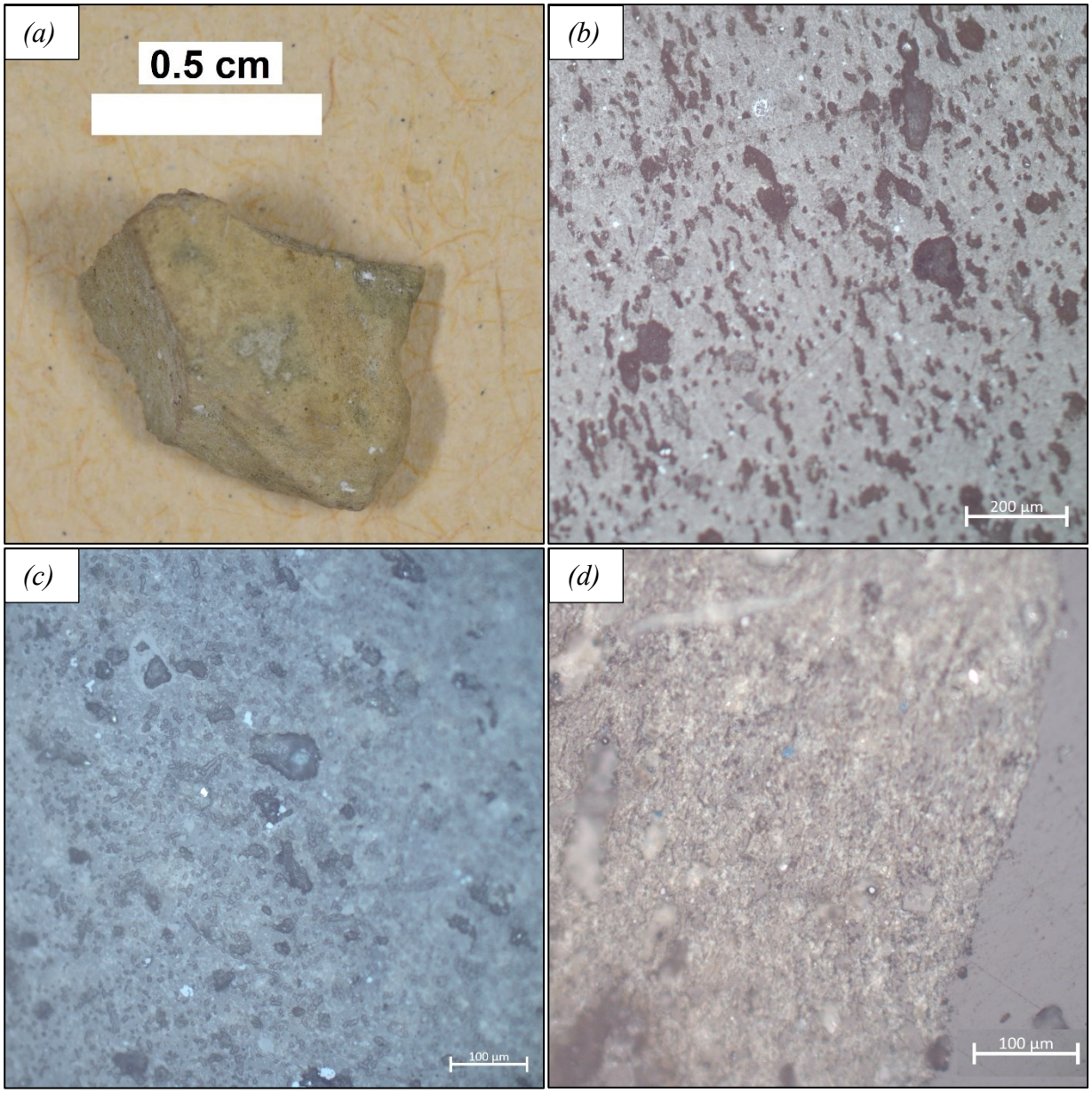

Fig. A.1 – (a) Ghareb Fm. fragment heated at 1200 °C (*RFa*); (b,c) RLM images of *RFa* at // nicols highlighting the fine grain size and high porosity, with a visible mineral assemblage made of dicalcium silicate (medium grey portions), lime (dull grey in relief) and brownmillerite (white rounded nodules 15-25 µm); (d) RFM image of *RFa* at // nicols etched with Nital with dicalcium silicate with brown colour and clearly revealed small anhedral hatrurite crystals with blue colour.

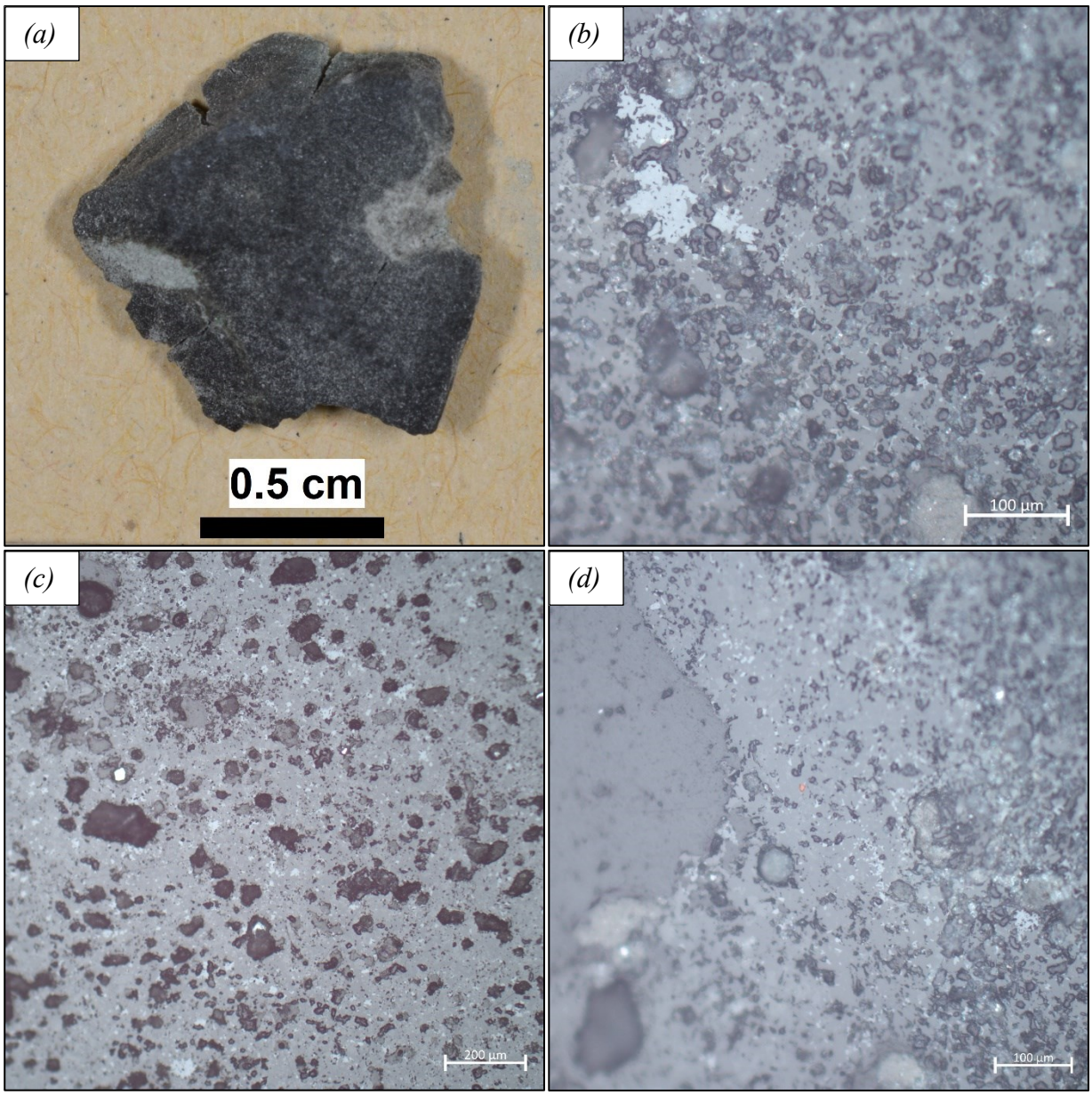

Fig. A.2 – (a) Ghareb Fm. fragment heated at 1200 °C (*RFb*) at laboratory scale showing darker and greener colours than *RFa* (Fig. A.1a) due to ternesite abundance; (b,c,d) RLM images of *RFb* at // nicols highlighting a fine grain microstructure with high porosity and an observable mineral assemblage made of euhedral prismatic to acicular brownmillerite (white) even forming rounded enrichments, anhedral lime (dull grey in relief) and a xenomorphic matrix composed of larnite (medium grey) and ternesite (medium grey darker than larnite one).

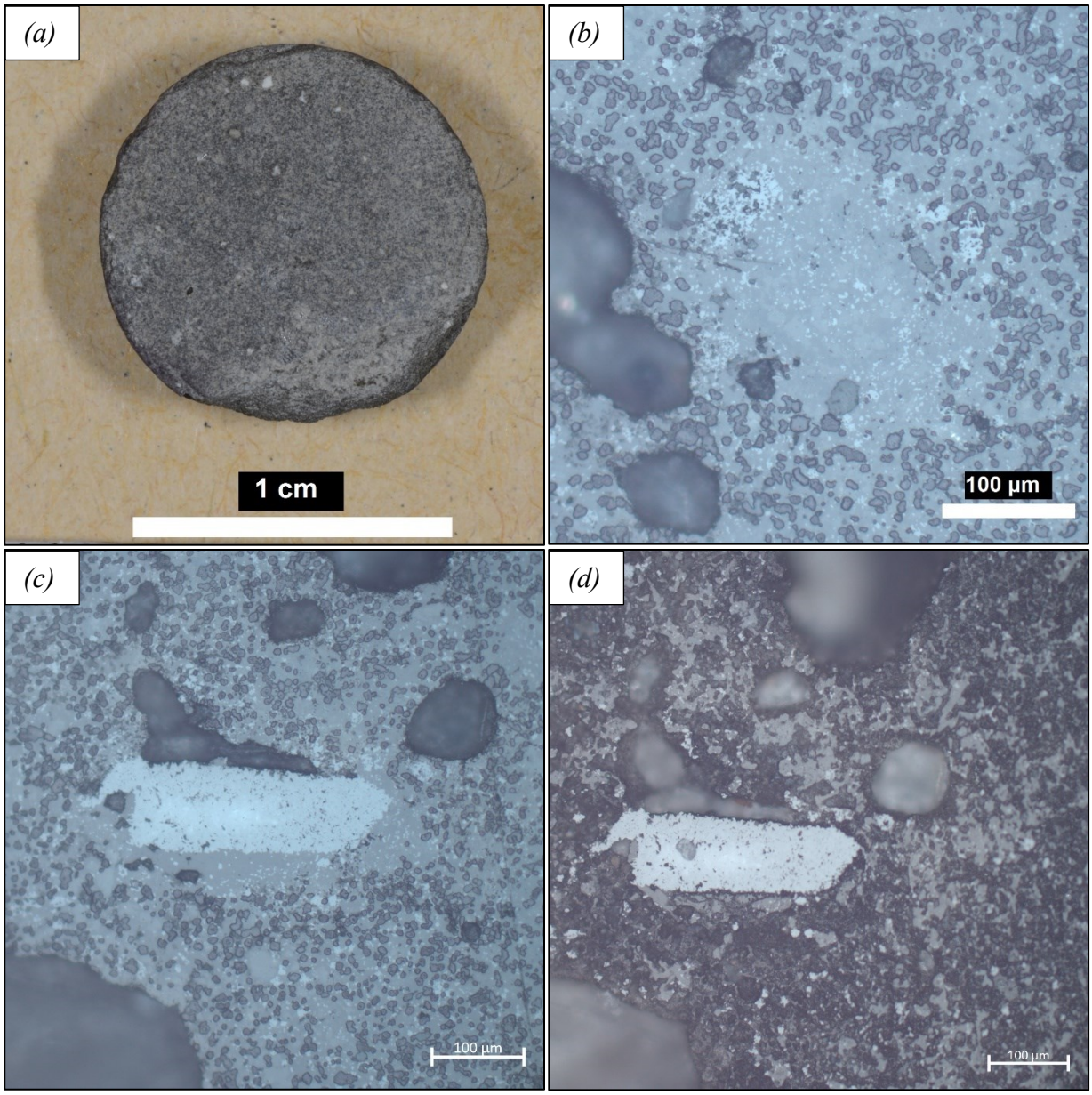

Fig. A.3 – *RM* (Ghareb Fm. powder) heated at 1200 °C as pellets: (a) *RM* pellet after heating at 1200 °C at laboratory scale for 8 hours; (b) RLM image at // nicols revealing anhedral rounded lime crystals (dull grey in relief), euhedral to subhedral brownmillerite crystals (white) also forming enriched rounded portions and a matrix made of larnite (medium grey), ternesite and fluorapatite-ellestadite (medium grey darker than larnite); (c) RLM image at // nicols showing submillimetric brownmillerite enrichment surrounded with the ternesite-larnite-fluorapatite-made xenomorphic matrix; (d) RLM image at // nicols of the previous polished section portion Nital etched revealing the distribution of larnite, which turned to brown colour, and no reactive phases in the matrix, such as ternesite and fluorapatite-ellestadite.

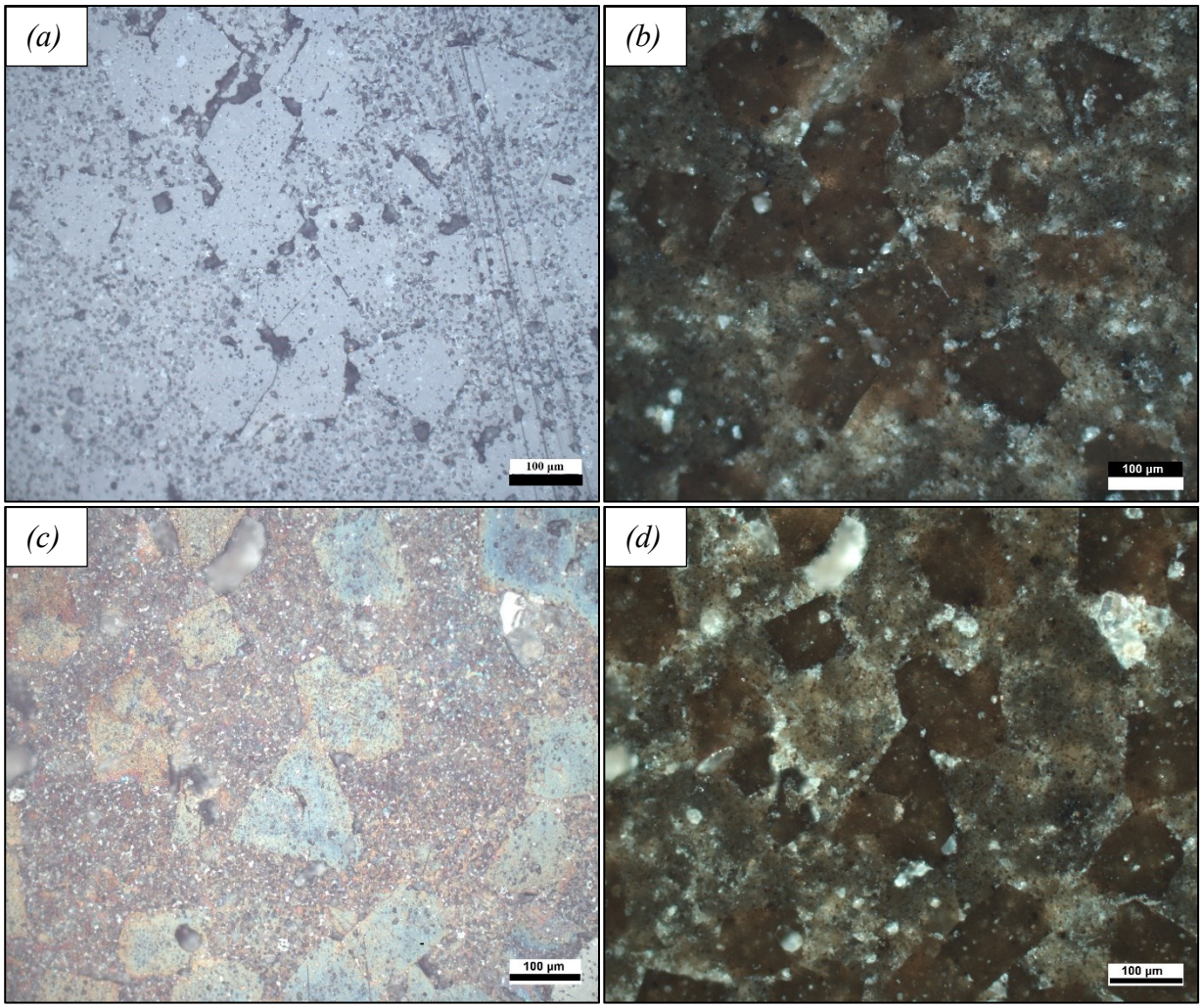

Fig. A.4 – *RM* (Ghareb Fm. powder) heated at 1250 °C as pellets: RLM at // (a) and + (b) nicols, highlighting a microtexture made of large (100-150 µm) peciloblastic euhedral rhombic-shape hatrurite crystals (medium grey //, dark brown +), subhedral lime (dark grey //), euhedral brownmillerite (white //, black + with sporadic orange internal reflections) and matrix made of rounded larnite (medium grey //, light brown +) and xenomorphic ternesite and fluorapatite-ellestadite (darker grey than larnite //, brown +); RLM at // (c) and + (d) nicols of polished section etched with Nital revealing peciloblastic rhombic shape hatrurite crystals (light blue and orange //, dark brown), anhedral larnite (light brown to orange //, light brown +), brownmillerite crystals (white //, black +) and xenomorphic ternesite and fluorapatite-ellestadite crystals which showed same optical properties.

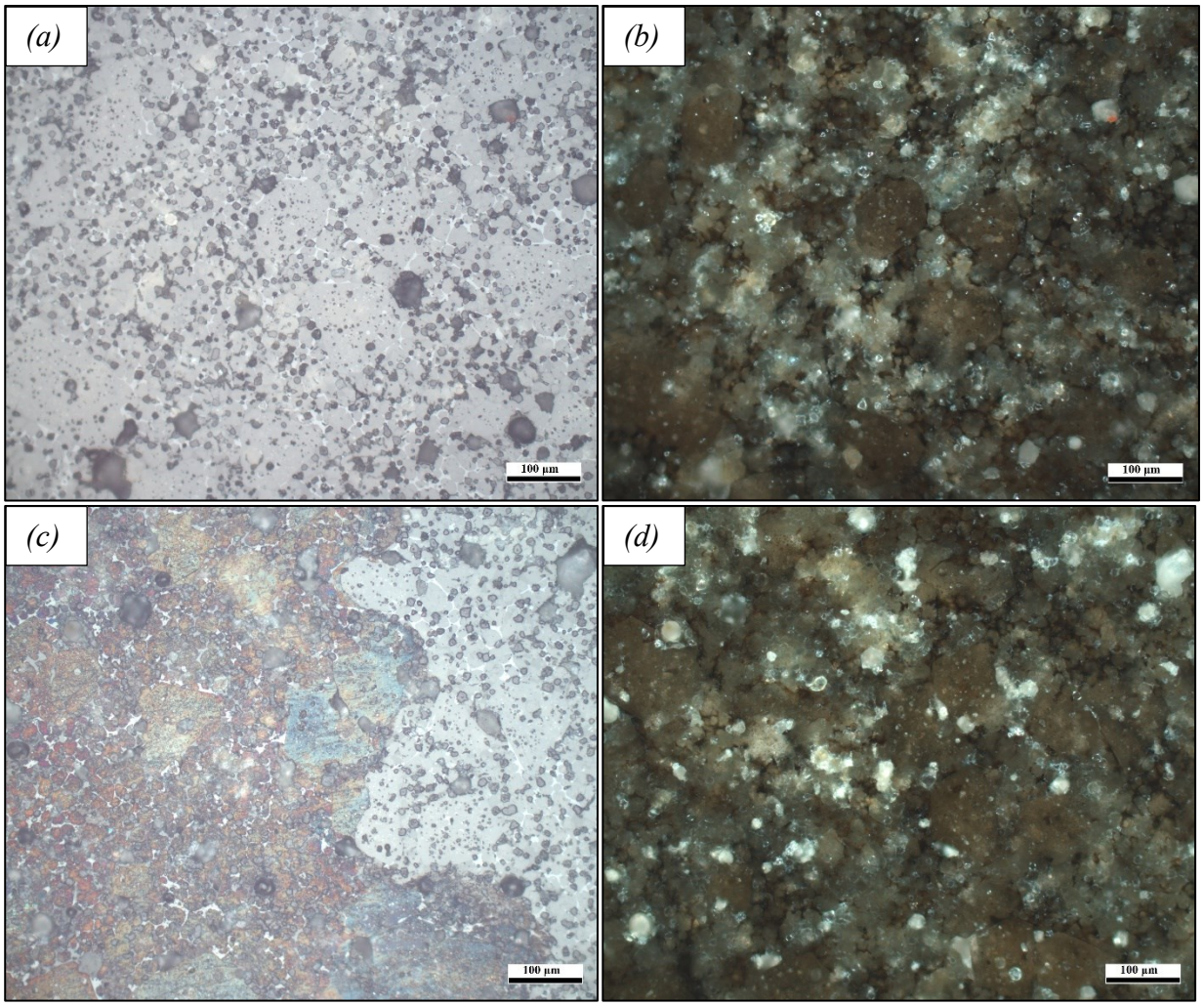

Fig. A.5 – *RM* (Ghareb Fm. powder) heated at 1300 °C as pellets: RLM at // (a) and + (b) nicols, highlighting a microtexture made of large (100-150 µm) peciloblastic subhedral hatrurite crystals (medium grey //, dark brown +), rounded lime (dark grey // in relief), rounded larnite (medium grey //, light brown +) and matrix made of xenomorphic brownmillerite (white //, dark + with sporadic orange internal riflections) and ternesite plus fluorapatite-ellestadite (darker grey than larnite //, brown +) which could not be distinguished each other; RLM at // (c) and + (d) nicols of polished section etched with Nital clearly revealing rounded larnite crystals (brown //, light brown +), hatrurite crystals (yellowish to bluish colours //, brown +), rounded lime (dark grey // in relief) and the matrix with brownmillerite (white //, black +) and no reactive fluorapatite-ellestadite and ternesite (dark //).

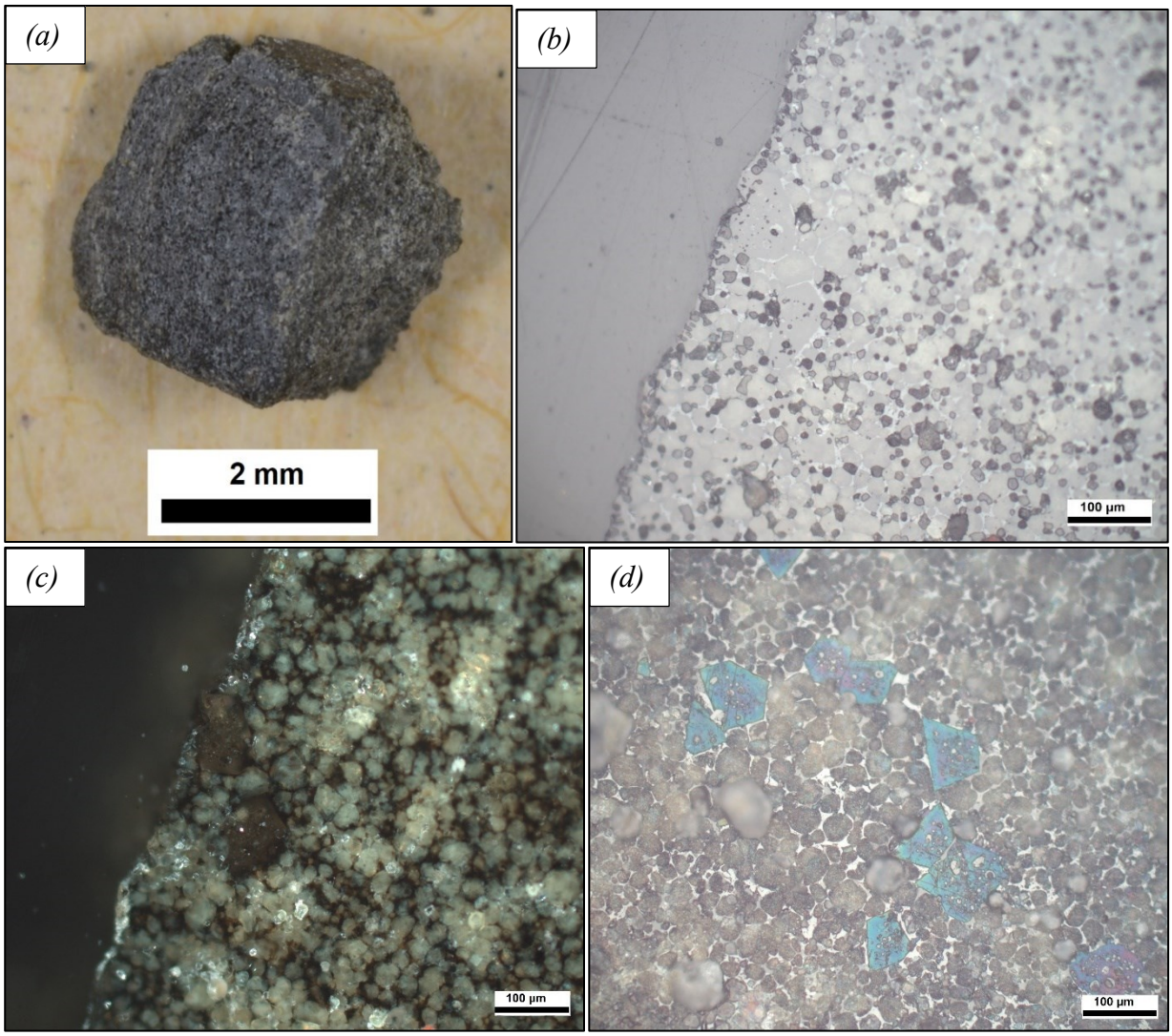

Fig. A.6 – *RM* (Ghareb Fm. powder) heated at 1350 °C as pellets: (a) black sintered pellet after heating process at laboratory scale; RLM images at // (b) and + (c) nicols showing a microtexture made of rounded larnite crystals (30 µm, medium grey //, light brown +), subhedral to rounded hatrurite crystals (medium grey //, dark brown +), subhedral lime (dark grey //) and a matrix mainly composed of xenomorphic brownmillerite (white //, dark +); RLM image at // nicols of a polished section Nithal etched clearly revealing hatrurite crystals (bluish to purple //), rounded larnite (dark brown //) and the brownmillerite-made matrix.

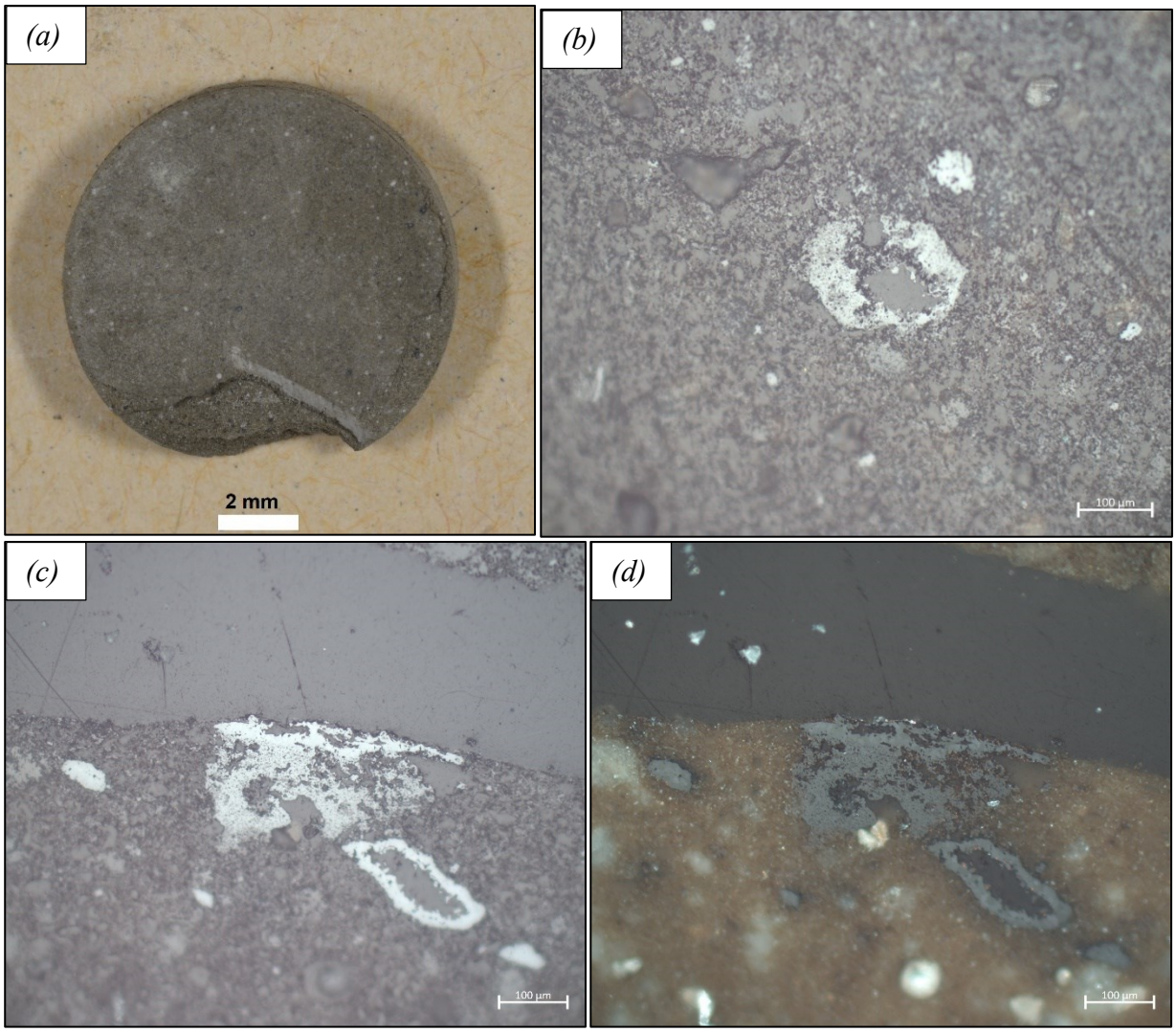

Fig. A.7 – Belite Clinker (*BC*) heated at 1200 °C as pellets at laboratory scale: (a) *BC* pellet after heating process showing a brown colour with rounded white nodules; (b) RLM image at // nicols highlighting a general low crystal size and high porosity, with a microtexture made of larnite (medium grey //, light brown +), rare anhedral ye'elimite (dark grey //) and brownmillerite (white //, black +) occurring as sparce micrometric crystals of submillimetric dense aggregates; RLM images at // (c) and + (d) nicols showing details of a dense aggregated made of anhedral brownmillerite (white //, dark grey + with nicols slight phase-shifted) and xenomorphic larnite (medium grey //, light brown +).

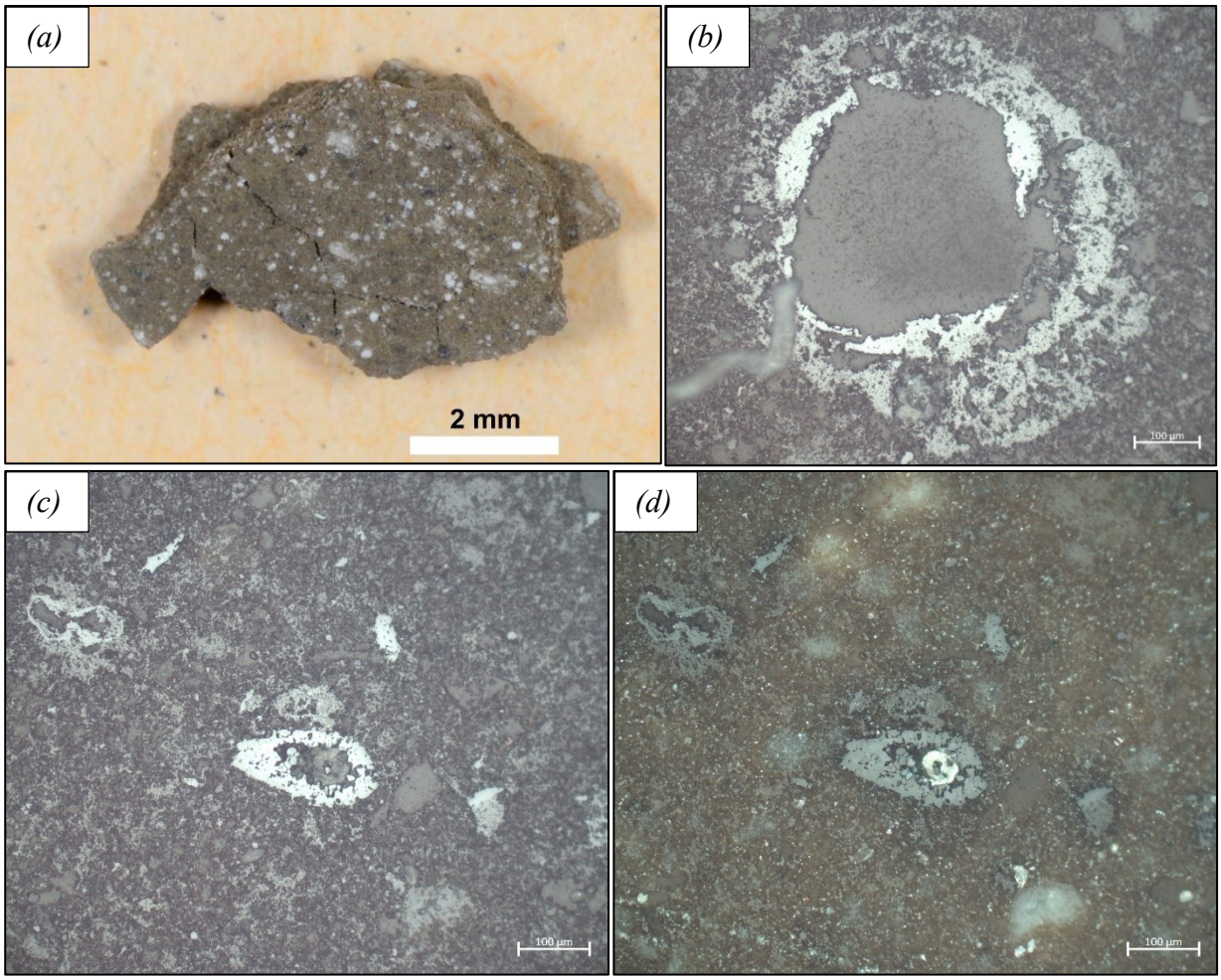

Fig. A.8 – Belite Clinker (*BC*) heated at 1250 °C as pellets at laboratory scale: (a) *BC* pellet after thermal treatment at 1250 °C for 4 hours highlighting brown colour with white and black submmillimetric nodules; (b) RLM image at // nicols revealing the microstructure of a brownmillerite (white //) enrichment with some anhedral larnite (medium grey //); RLM images at // (c) and + (d) nicols revealing a microtexture made of submillimetric nodules made of brownmillerite (white //, dark grey + with nicols slight phase-shifted) and a low grain size matrix of anhedral larnite (medium grey //, light brown +) and sparce micrometric brownmmilerite crystals.

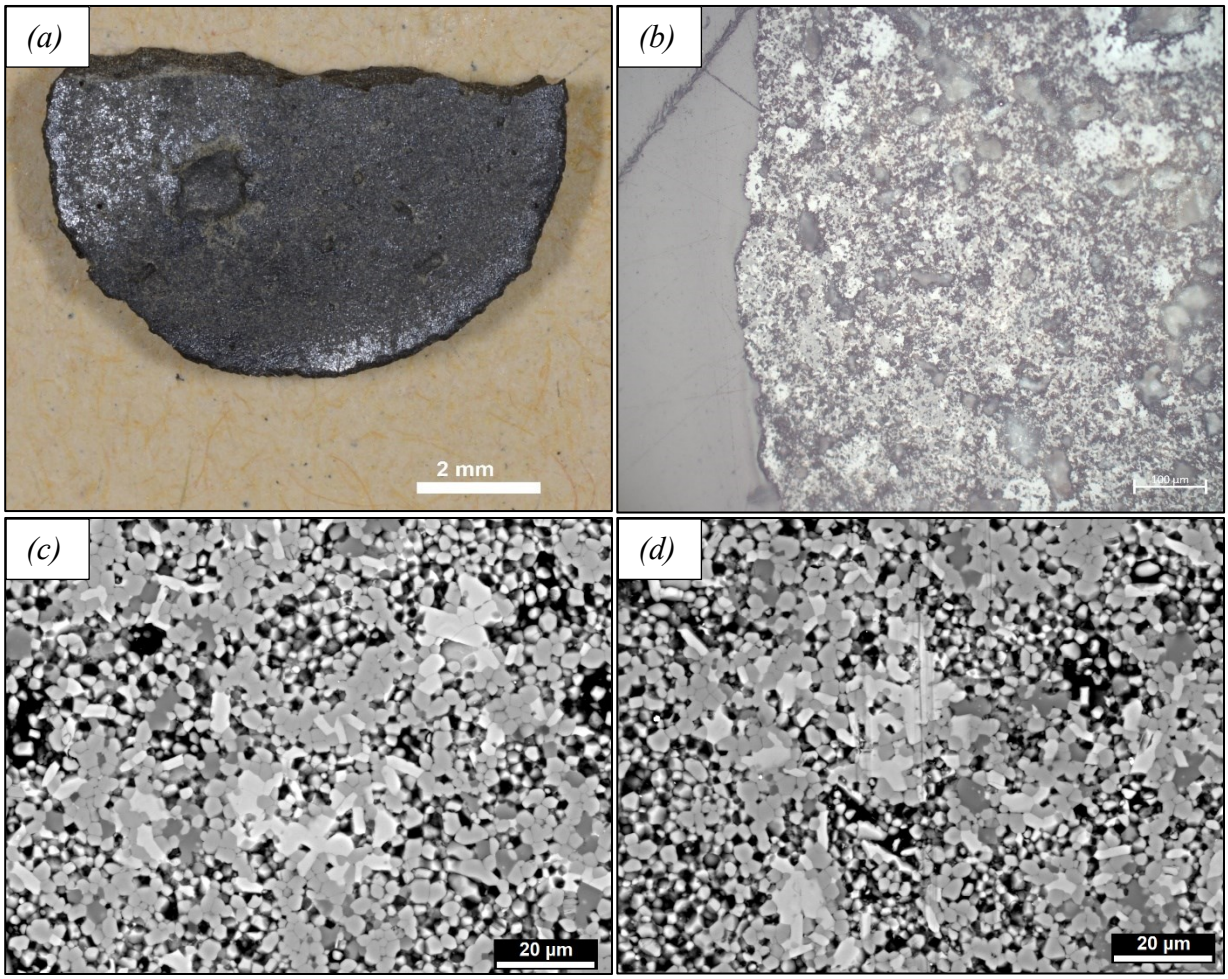

Fig. A.9 – Belite Clinker (*BC*) heated at 1300 °C as pellets at laboratory scale: (a) *BC* pellet after thermal treatment at 1300 °C for 4 hours showing an homogenous dark colour with submetallic luster, (b) RLM image at // nicols revealing a matrix made of anhedral larnite (medium grey //), subhedral brownmillerite (white //) and sparce anhedral ye'elimite (dark grey //) with brownmillerite-rich dense submillimetric nodules; (c,d) BSE images highlighting rounded to polygonal micrometric larnite (medium grey), prismatic to subhedral brownmillerite (white), anhedral ye'elimite (dark grey) and porosity (black).

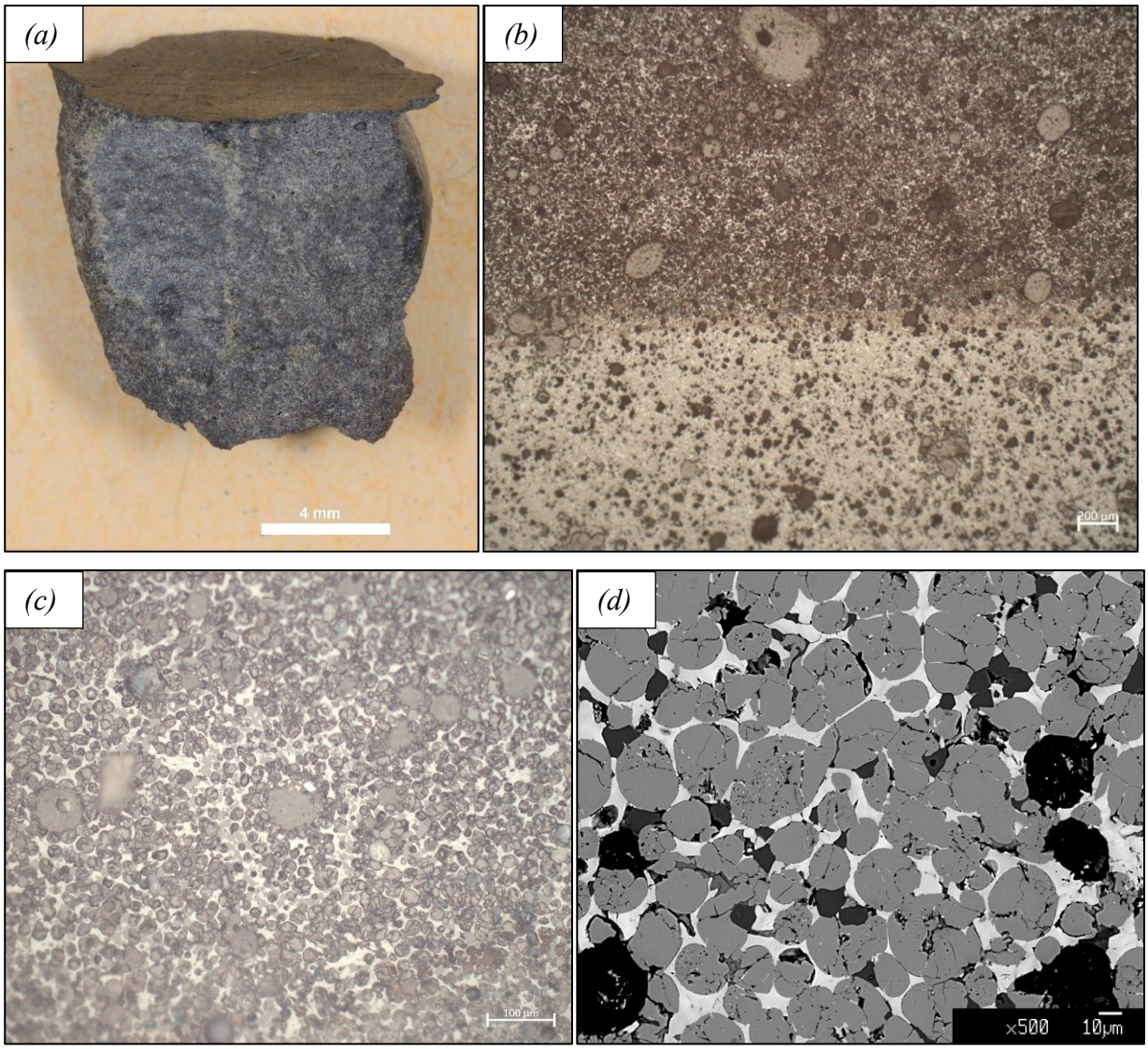

Fig. A.10 – Belite Clinker (*BC*) heated at 1350 °C as pellets at laboratory scale: (a) *BC* pellet after thermal treatment at 1350 °C for 4 hours showing black colour; (b) RLM image at // nicols of polished section half Nital etched (upper portion) revealing larnite as main mineral (medium grey and brown when etched) and the xenormorphic brownmillerite-made matrix (white); (c) RLM image at // nicols of Nital etched polished section highlighting micrometric fractured rounded larnite (brown //) enveloped in matrix mainly composed of xenomorphic brownmillerite and subhedral micrometric ye'elimite crystals (dark grey //); (d) BSE image showing rounded fractured larnite crystals (medium grey), subhedral to euhedral ye'elimite (dark grey) and the matrix made of anhedral brownmillerite (white) and sparce interstitial syngenite (darker than larnite).

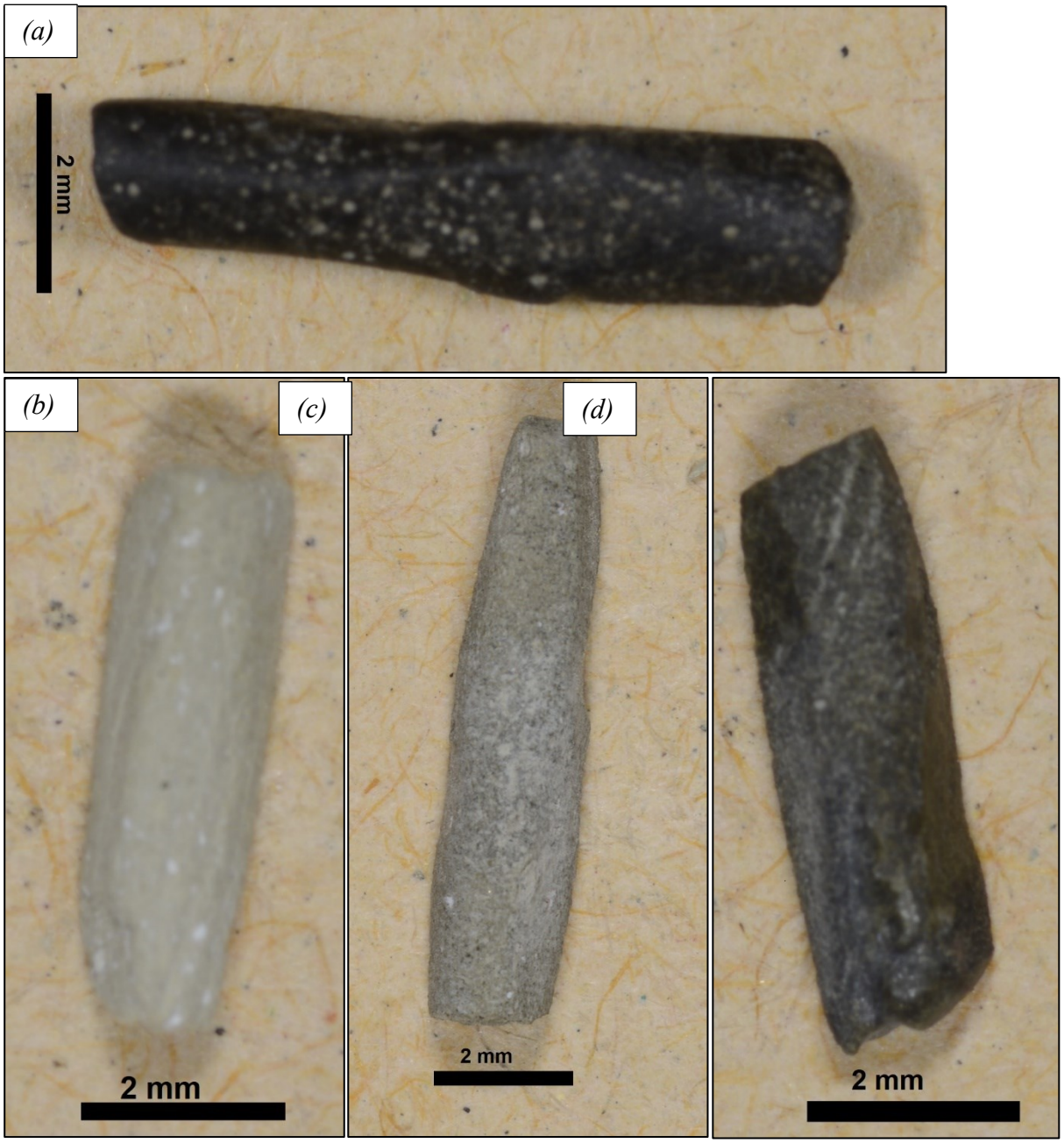

Fig. A.10 – Synthetic *green-cements* samples laboratory prepared for synchrotron X-ray μ-CT analysis: (a) *BC* sample heated at 1350 °C; (b) Ghareb Fm. sample heated at 900 °C; Ghareb Fm. fragment heated at 1250 °C; Ghareb Fm. fragment heated at 1350 °C.

Reference

[1] R. Grapes, Pyrometamorphism, Springer Berlin Heidelberg, Berlin, Heidelberg, 2010. https://doi.org/10.1007/978-3-642-15588-8.

[2] E. V. Sokol, S.N. Kokh, Y. Vapnik, V. Thiéry, S.A. Korzhova, Natural analogs of belite sulfoaluminate cement clinkers from Negev Desert, Israel, Am. Mineral. 99 (2014) 1471–1487. https://doi.org/10.2138/am.2014.4704.

[3] J.D. Winter, An Introduction to Igneous and Metamorphic Petrology, (2001). https://www.researchgate.net/publication/44564973_An_Introduction_to_Igneous_and_Metamorphic_Petrology/citation/download (accessed July 2, 2020).

[4] K. Bucher, R. Grapes, Petrogenesis of Metamorphic Rocks, 2011. https://doi.org/10.1007/978-3-540-74169-5.

[5] E. V. Sokol, N.I. Volkova, Combustion metamorphic events resulting from natural coal fires, GSA Rev. Eng. Geol. 18 (2007) 97–115. https://doi.org/10.1130/2007.4118(07).

[6] Y.K. Bentor, M. Kastner, Combustion metamorphism in Southern California, Science (80-.). (1976). https://doi.org/10.1126/science.193.4252.486.

[7] H.F.W. Taylor, Cement chemistry. 2nd ed., Acad. Press. (1997).

[8] W. Kurdowski, Cement and concrete chemistry, 2014. https://doi.org/10.1007/978-94-007-7945-7.

[9] E.A. Brandes, G.B. Brook, Smithells Metals Reference Book: Seventh Edition, 2013. https://doi.org/10.1016/C2009-0-25363-3.

[10] R. Clocchiatti, Les fulgurites et roches vitrifiées de l'Etna / Fulgurites and vitreous rocks from Etna: a preliminary petrochemical study, Eur. J. Mineral. (1990). https://doi.org/10.1127/ejm/2/4/0479.

[11] G. Frenzel, V. Stahle, Uber Alumosilikatglas mit Lechatelierit-Einschlussen von einer Fulguritrohre des Hahnenstockes (Glarner Freiberg, Schweiz)., Chemie Der Erde - Geochemistry. (1984).

[12] R.H. Grapes, H. Müller-Sigmund, Lightning-strike fusion of gabbro and formation of magnetite-bearing fulgurite, Cornone di Blumone, Adamello, Western Alps, Italy, Mineral. Petrol. (2010). https://doi.org/10.1007/s00710-009-0100-3.

[13] A. BURG, A. STARINSKY, Y. BARTOV, Y. KOLODNY, Geology of the Hatrurim Formation (Mottled Zone') in the Hatrurim basin, Isr. J. Earth-Sciences. 40 (1991) 107–124.

[14] A.R. Zilberfarb, Metamorphic of Cretaceous Sandstones by Natural Coal-Fires, San Rafael Swell, Utah, 2014.

[15] B.H. Clark, D.R. Peacor, Pyrometamorphism and partial melting of shales during combustion metamorphism: mineralogical, textural, and chemical effects, Contrib. to Mineral. Petrol. (1992). https://doi.org/10.1007/BF00310784.

[16] M. Cosca, E.J. Essene, J.W. Geissman, W.B. Simmons, D.A. Coates, Pyrometamorphic rocks associated with naturally burned coal beds , Powder River Basin , Wyoming, Am. Mineral. (1989).

[17] A.H. Jones, J.W. Geissman, D.A. Coates, Clinker deposits, Powder River Basin, Wyoming and Montana: A new source of high-fidelity paleomagnetic data for the Quaternary, Geophys. Res. Lett. (1984). https://doi.org/10.1029/GL011i012p01231.

[18] Y.K. Bentor, M. Kastner, I. Perlman, Y. Yellin, Combustion metamorphism of bituminous sediments and the formation of melts of granitic and sedimentary composition, Geochim. Cosmochim. Acta. (1981). https://doi.org/10.1016/0016-7037(81)90074-0.

[19] B.N. Church, A. Matheson, Z.D. Hora, Combustion metamorphism in the Hat Creek area, British Columbia, Can. J. Earth Sci. (1979). https://doi.org/10.1139/e79-173.

[20] E. V. Sokol, S.N. Kokh, V. V. Sharygin, V.A. Danilovsky, Y. V. Seryotkin, R. Liferovich, A.S. Deviatiiarova, E.N. Nigmatulina, N.S. Karmanov, Mineralogical diversity of Ca2SiO4-bearing combustion metamorphic rocks in the Hatrurim Basin: Implications for storage and partitioning of elements in Oil Shale Clinkering, Minerals. (2019). https://doi.org/10.3390/min9080465.
[21] V. V. Sharygin, E. V. Sokol, Y. Vapnik, Minerals of the pseudobinary perovskite-brownmillerite series from combustion metamorphic larnite rocks of the Hatrurim Formation (Israel), Russ. Geol. Geophys. 49 (2008) 709–726. https://doi.org/10.1016/j.rgg.2008.03.001.
[22] Y. Vapnik, V. V. Sharygin, E. V. Sokol, R. Shagam, Paralavas in a combustion metamorphic complex: Hatrurim Basin, Israel, GSA Rev. Eng. Geol. 18 (2007) 133–153. https://doi.org/10.1130/2007.4118(09).
[23] M.N.N. Masalehdani, P.M. Black, H.W. Kobe, Mineralogy and petrography of iron-rich slags and paralavas formed by spontaneous coal combustion, Rotowaro coalfield, North Island, New Zealand, in: GSA Rev. Eng. Geol., 2007. https://doi.org/10.1130/2007.4118(08).
[24] L.E.M. Elluso, S.A.C. Onticelli, M.A.D.A. Ntonio, N.I.P.M. Irco, E.M.S. Accani, C. Nazionale, Petrology and mineralogy of wollastonite- and melilite-bearing paralavas from the Central Apennines , Italy, 88 (2003) 1287–1299.
[25] E. V. Sokol, S.N. Kokh, H.N. Khoury, Y. V. Seryotkin, S. V. Goryainov, S.A. Novikova, I.A. Sokol, Natural analogue approaches to prediction of long-term behaviour of Ca2UO5·2-3H2O X-phase: case study from Tulul Al Hammam site, Jordan, Arab. J. Geosci. 10 (2017). https://doi.org/10.1007/s12517-017-3305-5.
[26] E. V. Sokol, S.N. Kokh, Y. Vapnik, V. Thiéry, S.A. Korzhova, Natural analogs of belite sulfoaluminate cement clinkers from Negev Desert, Israel, Am. Mineral. (2014). https://doi.org/10.2138/am.2014.4704.
[27] R. Grapes, Pyrometamorphism, Springer-Verlag, Berlin/Heidelberg, 2006. https://doi.org/10.1007/3-540-29454-6.
[28] A. Burg, Y. Kolodny, V. Lyakhovsky, Hatrurim - 2000: The “Mottled Zone” revisited, forty years later, Isr. J. Earth Sci. 48 (1999) 209–223.
[29] E. Sokol, I. Novikov, S. Zateeva, Y. Vapnik, R. Shagam, O. Kozmenko, Combustion metamorphism in the Nabi Musa dome: new implications for a mud volcanic origin of the Mottled Zone, Dead Sea area, Basin Res. 22 (2010) 414–438. https://doi.org/10.1111/j.1365-2117.2010.00462.x.
[30] R. Grapes, Pyrometamorphism, 2010. https://doi.org/10.1007/978-3-642-15588-8.
[31] S. Kokh, A. Dekterev, E. Sokol, S. Potapov, Numerical simulation of an oil-gas fire: A case study of a technological accident at Tengiz oilfield, Kazakhstan (June 1985-July 1986), Energy Explor. Exploit. (2016). https://doi.org/10.1177/0144598715623670.
[32] V.Y.K. V. I. Feldman, A. M. Dikov, P. Yu, Tengizites - Glasses from center of oil fire, Dokl. Russ. Acad. Sci. 339 (1994) 239–242.
[33] R. Juroszek, H. Krüger, I. Galuskina, B. Krüger, L. Jeżak, B. Ternes, J. Wojdyla, T. Krzykawski, L. Pautov, E. Galuskin, Sharyginite, Ca3TiFe2O8a new mineral from the bellerberg Volcano, Germany, Minerals. (2018). https://doi.org/10.3390/min8070308.
[34] V. V. Sharygin, B. Lazic, T.M. Armbruster, M.N. Murashko, R. Wirth, I.O. Galuskina, E. V. Galuskin, Y. Vapnik, S.N. Britvin, A.M. Logvinova, Shulamitite Ca3TiFe3+AlO8 - A new perovskite-related mineral from Hatrurim Basin, Israel, Eur. J. Mineral. 25 (2013) 97–111. https://doi.org/10.1127/0935-1221/2013/0025-2259.
[35] V. V. Sharygin, A hibonite-spinel-corundum-hematite assemblage in plagioclase-clinopyroxene pyrometamorphic rocks, Hatrurim Basin, Israel: mineral chemistry, genesis and formation temperatures, Mineral. Mag. 83 (2019) 123–135. https://doi.org/10.1180/mgm.2018.138.
[36] S.I. Tomkeieff, The Dolerite Plugs of Tieveragh and Tievebulliagh near Cushendall, Co.

Antrim, with a Note on Buchite, Geol. Mag. (1940). https://doi.org/10.1017/S0016756800070382.
[37] D. Fettes, J. Desmons, Metamorphic rocks: a classification and glossary of terms: recommendations of the International Union of Geological Sciences Subcommission on the Systematics of Metamorphic Rocks, Choice Rev. Online. (2008). https://doi.org/10.5860/choice.45-4741.
[38] G.C. Brown, A.E. Mussett, The inaccesible earth. An integrated view of its structure and composition, 276 S, Chapman & Hall), London. (1993).
[39] L.L. Fermor, Preliminary note on the burning of coal seams at the outcrop, Trans. Min. Geol. Met. Inst. India. 12 (1918) 50–63.
[40] A. Prakash, R.P. Gupta, A.K. Saraf, A Landsat TM based comparative study of surface and subsurface fires in the Jharia coalfield, India, Int. J. Remote Sens. (1997). https://doi.org/10.1080/014311697217738.
[41] S. Sen Gupta, Petrology of the para-lavas of the eastern part of Jharia coalfield, Q J Geol Min Met. Soc India. 29 (1957) 79–101.
[42] E. L. Heffern, D. A. Coates, C. W., Distribution and Age of Clinker in Northern Powder River Basin, Montana: ABSTRACT, Am. Assoc. Pet. Geol. Bull. (1983). https://doi.org/10.1306/03b5b8b2-16d1-11d7-8645000102c1865d.
[43] C.W.N. D. A. Coates, Mao showing fissio-track ages of clinker in the Rochelle Hills, southern Campbell Country, Wyoming, US Geol Surv Misc Inv Map. I (1984).
[44] M.A. Cosca, D.R. Peacor, Chemistry and structure of esseneite (CaFe3+AlSiO6), a new pyroxene produced by pyrometamorphism., Am. Mineral. (1987).
[45] R.M. Bustin, W.H. Mathews, In situ gasification of coal, a natural example: history, petrology, and mechanics of combustion., Can. J. Earth Sci. (1982). https://doi.org/10.1139/e82-042.
[46] S. Estrada, K. Piepjohn, M.J. Frey, L. Reinhardt, H. Andruleit, W. Von Gosen, Pliocene coal-seam fires on southern Ellesmere Island, Canadian Arctic, Neues Jahrb. Fur Geol. Und Palaontologie - Abhandlungen. (2009). https://doi.org/10.1127/0077-7749/2009/0251-0033.
[47] H.F. Whitworth, The occurrence of some fused sedimentary rocks at Ravensworth, N.S.W.J R Soc N S W. 92 (1958) 204–210.
[48] D.R.G. B. J. Hensen, Clinohypersthene and hypersthene from a coal fire buchite near Ravensworth, N.S.W., Australia, Am Miner. 64 (1979) 131–135.
[49] J.H. Rattingan, Phenomenon about burning mountain, Wingen, New South Wales, Aust J Sci. 30 (1967) 183–184.
[50] A.J. Tulloch, J.K. Campbell, Clinoenstatite-bearing buchites possibly from combustion of hydrocarbon gases in a major thrust zone: Glenroy Valley, New Zealand, J. Geol. (1993). https://doi.org/10.1086/648233.
[51] B.P. Belikov, Composition of some burned rocks from the Kuzbass, Tr Petrog Inst Akad Nauk SSSR. 4 (1933) 91–100.
[52] I.S. Novikov, E. V. Sokol, A. V. Travin, S.A. Novikova, Signature of Cenozoic orogenic movements in combustion metamorphic rocks: mineralogy and geochronology (example of the Salair-Kuznetsk Basin transition), Russ. Geol. Geophys. (2008). https://doi.org/10.1016/j.rgg.2007.11.011.
[53] V.A.B. I. A. Kalugin, G. A. Tret'Yakov, Iron-Ore basalts in fused rocks of Eastern Kazakhstan, Nauk. Novosib. (1991).
[54] X.M. Zhang, C.J.S. Cassells, J.L. Van Genderen, Multi-sensor data fusion for the detection of underground coal fires, Geol. En Mijnbouw/Netherlands J. Geosci. (1998).
[55] D. Cole, A recent example of spontaneous combustion of oil-shale, Geol. Mag. (1974). https://doi.org/10.1017/S0016756800038802.
[56] J.F. Sauvage, M. Sauvage, Tectonique, néotectonique et phénomènes ignés à l'extrémité est

du fossé de Nara (Mali): Daounas et lac Faguibine, J. African Earth Sci. (1992). https://doi.org/10.1016/0899-5362(92)90003-U.
[57] H. Svensen, D.K. Dysthe, E.H. Bandlien, S. Sacko, H. Coulibaly, S. Planke, Subsurface combustion in Mali: Refutation of the active volcanism hypothesis in West Africa, Geology. (2003). https://doi.org/10.1130/0091-7613(2003)031<0581:SCIMRO>2.0.CO;2.
[58] N.P. Ermankow, Pasrud-Yagnob coal deposit and burning mines of Kan-Tag mountain. In: Geology of Tadjikistan Coal Deposits. Moscow, 1935.
[59] V.P. Novikov, A thousand-year old fire, Nauk. i Zhizn'. 9 (1989) 30–32.
[60] D. Belakvski, The minerals of the burning coal seams at Ravat, tadshikistan, Lapis. 15 (1990) 21–26.
[61] V. V. Sharygin, E. V. Sokol, D.I. Belakovskii, Fayalite-sekaninaite paralava from the Ravat coal fire (central Tajikistan), Russ. Geol. Geophys. (2009). https://doi.org/10.1016/j.rgg.2009.01.001.
[62] M. Zbarski, Mineralogical and petrographical features of burned rocks from central Asia, Zap. Kirg. Otd. Vses Miner. Obs. 4 (1963) 53–67.
[63] W.F.P. McLintock, On the Metamorphism Produced by the Combustion of Hydrocarbons in the Tertiary Sediments of South-West Persia, Mineral. Mag. 23 (1932) 207–227. https://doi.org/10.1180/minmag.1932.023.139.01.
[64] S.Z.J. M. A. Basi, Baked and fused Miocene sediments from the Injana area, Hemrin South, Iraq, J Geo Soc Iraq. 7 (1974) 1–17.
[65] Y. Kolodny, A. Burg, Petrographic atlas of the Hatrurim Formation by Shulamit Gross, (2016).
[66] E. V. Sokol, O.L. Gaskova, O.A. Kozmenko, S.N. Kokh, E.A. Vapnik, S.A. Novikova, E.N. Nigmatulina, Clastic dikes of the Hatrurim basin (western flank of the Dead Sea) as natural analogues of alkaline concretes: Mineralogy, solution chemistry, and durability, Dokl. Earth Sci. 459 (2014) 1436–1441. https://doi.org/10.1134/S1028334X14100122.
[67] I. Novikov, Y. Vapnik, I. Safonova, Mud volcano origin of the Mottled Zone, South Levant, Geosci. Front. (2013). https://doi.org/10.1016/j.gsf.2013.02.005.
[68] E. V. Sokol, O.A. Kozmenko, S.N. Kokh, Y. Vapnik, Gas reservoirs in the Dead Sea area: Evidence from chemistry of combustion metamorphic rocks in Nabi Musa fossil mud volcano, Russ. Geol. Geophys. (2012). https://doi.org/10.1016/j.rgg.2012.06.003.
[69] H.N. Khoury, E. Salameh, I.D. Clark, P. Fritz, W. Bajjali, A.E. Milodowski, M.R. Cave, W.R. Alexander, A natural analogue of high pH cement pore waters from the Maqarin area of northern Jordan. I: introduction to the site, J. Geochemical Explor. 46 (1992) 117–132. https://doi.org/10.1016/0375-6742(92)90103-F.
[70] S. Fourcade, L. Trotignon, P. Boulvais, I. Techer, M. Elie, D. Vandamme, E. Salameh, H. Khoury, Cementation of kerogen-rich marls by alkaline fluids released during weathering of thermally metamorphosed marly sediments. Part I: Isotopic (C,O) study of the Khushaym Matruk natural analogue (central Jordan), Appl. Geochemistry. 22 (2007) 1293–1310. https://doi.org/10.1016/j.apgeochem.2007.02.012.
[71] H.N. Khoury, Long-term analog of carbonation in travertine from Uleimat Quarries, Central Jordan, Environ. Earth Sci. 65 (2012) 1909–1916. https://doi.org/10.1007/s12665-011-1173-y.
[72] H.N. Khoury, E. V. Sokol, I.D. Clark, Calcium uranium oxide minerals from central Jordan: Assemblages, chemistry, and alteration products, Can. Mineral. 53 (2015) 61–82. https://doi.org/10.3749/canmin.1400071.
[73] E. V. Sokol, S.N. Kokh, H.N. Khoury, Y. V. Seryotkin, S. V. Goryainov, Long-term immobilisation of Cd2+ at the Tulul Al Hammam natural analogue site, central Jordan, Appl. Geochemistry. 70 (2016) 43–60. https://doi.org/10.1016/j.apgeochem.2016.05.002.
[74] V. Žáček, R. Skála, Z. Dvořák, Combustion Metamorphism in the Most Basin, Czech

Republic, in: Coal Peat Fires A Glob. Perspect., 2014. https://doi.org/10.1016/B978-0-444-59509-6.00006-5.
[75] Z.D. V. Zacek, R. Skàla, M. Chulupàcova, Ca-Fe3+-rich, Si-undersaturated buchite from Zelensky, North-Bohemian Brwon Coal Basin, Czech Republic, Eur J Miner. 4 (2005) 623–634.
[76] M.C.G. Juenger, F. Winnefeld, J.L. Provis, J.H. Ideker, Advances in alternative cementitious binders, Cem. Concr. Res. 41 (2011). https://doi.org/10.1016/j.cemconres.2010.11.012.
[77] Y.K. Bentor, S. Gross, L. Heller, © 1963 Nature Publishing Group, 199 (1963) 478–479. https://doi.org/10.1038/199478a0.
[78] S. Gross, The Mineralogy of the Hatrurim formation, Israel, Bull. - Geol. Surv. Isr. (1977).
[79] L. Picard, Geological research in the Judean Desert, Jerusalem, 1931.
[80] A.V. Y. K. Bentor, The Geological Map of Israel 1:100’000, Sheet 16-Mount Sedom (with explanatory text), (1960).
[81] B.B. G. Gvirtzman, The Tertiary Project in Semi-Annual Progress Report on The Geol. Res. Project., Inst. Pet. Res. Geophys. (1966) 11–17.
[82] S.N. Britvin, M.N. Murashko, Y. Vapnik, Y.S. Polekhovsky, S. V. Krivovichev, M.G. Krzhizhanovskaya, O.S. Vereshchagin, V. V. Shilovskikh, N.S. Vlasenko, Transjordanite, Ni2P, a new terrestrial and meteoritic phosphide, and natural solid solutions barringerite-transjordanite (hexagonal Fe2P-Ni2P), Am. Mineral. (2020). https://doi.org/10.2138/am-2020-7275.
[83] I. Galuskina, E. Galuskin, Y. Vapnik, G. Zeliński, K. Prusik, Priscillagrewite-(Y), (Ca2Y)Zr2Al3O12: A new garnet of the bitikleite group from the Daba-Siwaqa area, the Hatrurim Complex, Jordan, Am. Mineral. (2021). https://doi.org/10.2138/am-2021-7692.
[84] E. V. Galuskin, I.O. Galuskina, J. Kusz, T. Armbruster, K.M. Marzec, P. Dzierżanowski, M. Murashko, Vapnikite Ca 3 UO 6 – a new double-perovskite mineral from pyrometamorphic larnite rocks of the Jabel Harmun, Palestinian Autonomy, Israel , Mineral. Mag. 78 (2014) 571–581. https://doi.org/10.1180/minmag.2014.078.3.07.
[85] E. V. Sokol, Y. V. Seryotkin, S.N. Kokh, Y. Vapnik, E.N. Nigmatulina, S. V. Goryainov, E. V. Belogub, V. V. Sharygin, Flamite, (Ca,Na,K) 2 (Si,P)O 4 , a new mineral from ultrahightemperature combustion metamorphic rocks, Hatrurim Basin, Negev Desert, Israel , Mineral. Mag. 79 (2015) 583–596. https://doi.org/10.1180/minmag.2015.079.3.05.
[86] I.O. Galuskina, S. Britvin, E. Galuskin, The Hatrurim Complex - the New Unique Locality on World Mineral Map : the Review of Mineral Discoveries, (2014) 3–5.
[87] M. Rukieh, V.G. Trifonov, A.E. Dodonov, H. Minini, O. Ammar, T.P. Ivanova, T. Zaza, A. Yusef, M. Al-Shara, Y. Jobaili, Neotectonic map of Syria and some aspects of Late Cenozoic evolution of the northwestern boundary zone of the Arabian plate, J. Geodyn. (2005). https://doi.org/10.1016/j.jog.2005.07.016.
[88] I. Novikov, Y. Vapnik, I. Safonova, Mud volcano origin of the Mottled Zone, South Levant, Geosci. Front. 4 (2013) 597–619. https://doi.org/10.1016/j.gsf.2013.02.005.
[89] A. Kröner, Ophiolites and the evolution of tectonic boundaries in the late proterozoic Arabian-Nubian shield of northeast Africa and Arabia, Precambrian Res. (1985). https://doi.org/10.1016/0301-9268(85)90016-6.
[90] F. Hirsch, Geological Map of Israel (1:50’000, Bet Guvrin), Sheet 11-III, (1983).
[91] V.B.O. I. V. Visotzkiy, Oil-and-gas Basin of Foreign Countries, Nedra. (1990).
[92] C. Homberg, E. Barrier, M. Mroueh, W. Hamdan, F. Higazi, Basin tectonics during the Early Cretaceous in the Levant margin, Lebanon, J. Geodyn. (2009). https://doi.org/10.1016/j.jog.2008.09.002.
[93] M.A. Ziegler, Late Permian to Holocene paleofacies evolution of the Arabian Plate and its hydrocarbon occurrences, GeoArabia. 6 (2001) 445–504.
[94] J. Hall, V. Krasheninnikov, F. Hirsch, C. Benjamini, A. Flexer, J. Hall, Geological

Framework of the Levant, Vol. II Levantine …. II (2005) 836. https://doi.org/10.1016/j.gloenvcha.2011.08.005.
[95] Z. Garfunkel, Relation between continental rifting and uplifting: evidence from the Suez rift and northern Red Sea, Tectonophysics. (1988). https://doi.org/10.1016/0040-1951(88)90294-6.
[96] C.D. Walley, Some outstanding issues in the geology of Lebanon and their importance in the tectonic evolution of the Levantine region, Tectonophysics. (1998). https://doi.org/10.1016/S0040-1951(98)00177-2.
[97] R. Freund, Geological Magazine, Geol. Mag. 102 (1965) 189–205.
[98] Y.B. G. Steinitz, The Miocene-Pleistocene history of Dead Sea segment of the Rift in light of K-Ar ages basalts, Isr. J. Earth Sci. 40 (1991) 199–208.
[99] A.H. M. I. Kopp, J. Adjamyan, K. Il'yas, F. Fakiani, The mechanism of formation of the slip graben El Gab (Syria) and the problem of the propagation of the Levantine Transform, Geotectonika. 5 (1999) 77–92.
[100] H. Gvirtzman, E. Stanislavsky, Palaeohydrology of hydrocarbon maturation, migration and accumulation in the Dead Sea rift, Basin Res. 12 (2000) 79–93. https://doi.org/10.1046/j.1365-2117.2000.00111.x.
[101] J. Hall, V. Krasheninnikov, F. Hirsch, C. Benjamini, A. Flexer, J. Hall, Geological Framework of the Levant, 2005.
[102] R.W. A. Shen, Major Geological Structures of Israel and environs 1:500'000, (2014). https://www.gov.il/en/departments/general/geological-stractures-israel-area-embossed.
[103] R. Freund, A Model of the Structural Development of Israel and Adjacent Areas Since Upper Cretaceous Times, Geol. Mag. 103 (1965) 13–20.
[104] Y.A. Hirsch, F., A. Burg, Geological Map of Israel 1:50'000, Arad, Sheet 15-IV, (2008).
[105] F. Hirsch, Geological Map of Israel 1:50'000, Hamakhtesh Haqatan, Sheet 19-II, (1995).
[106] D. Soudry, Z. Lewy, Microbially influenced formation of phosphate nodules and megafossil moulds (Negev, Southern Israel), Palaeogeogr. Palaeoclimatol. Palaeoecol. 64 (1988) 15–34. https://doi.org/10.1016/0031-0182(88)90139-3.
[107] A. Schneider-Mor, H. Alsenz, S. Ashckenazi-Polivoda, P. Illner, S. Abramovich, S. Feinstein, A. Almogi-Labin, Z. Berner, W. Püttmann, Paleoceanographic reconstruction of the late Cretaceous oil shale of the Negev, Israel: Integration of geochemical, and stable isotope records of the organic matter, Palaeogeogr. Palaeoclimatol. Palaeoecol. (2012). https://doi.org/10.1016/j.palaeo.2012.01.003.
[108] H. Alsenz, J. Regnery, S. Ashckenazi-Polivoda, A. Meilijson, L. Ron-Yankovich, S. Abramovich, P. Illner, A. Almogi-Labin, S. Feinstein, Z. Berner, W. Püttmann, Sea surface temperature record of a Late Cretaceous tropical Southern Tethys upwelling system, Palaeogeogr. Palaeoclimatol. Palaeoecol. (2013). https://doi.org/10.1016/j.palaeo.2013.09.013.
[109] A. Gütlein, M. Kersten, S. Feinstein, P. Illner, Mobility of Cr and V in Spent Oil Shale: Impact of Thermal Treatment, Procedia Earth Planet. Sci. (2013). https://doi.org/10.1016/j.proeps.2013.03.001.
[110] H. Alsenz, P. Illner, S. Ashckenazi-Polivoda, A. Meilijson, S. Abramovich, S. Feinstein, A. Almogi-Labin, Z. Berner, W. Püttmann, Geochemical evidence for the link between sulfate reduction, sulfide oxidation and phosphate accumulation in a late cretaceous upwelling system, Geochem. Trans. (2015). https://doi.org/10.1186/s12932-015-0017-1.
[111] A. ALMOGI-LABIN, A. FLEXER, A. HONIGSTEIN, A. ROSENFELD, E. ROSENTHAL, Biostratigraphy and tectonically controlled sedimentation of the Maastrichtian in Israel and adjacent countries, Rev. Esp. Paleontol. (1990).
[112] Y.N. D. Soudry, R. Roded, The Ashosh-Haroz facies and their significance for the Mishash palaeogeography and phosphorite accumulation in the northern and central Negev, southern

Israel, Isr. J. Earth-Sciences. 34 (1985) 211–220.
[113] E. Sass, Y. Kolodny, Stable isotopes, chemistry and petrology of carbonate concretions (Mishash formation, Israel), Chem. Geol. 10 (1972) 261–286. https://doi.org/10.1016/0009-2541(72)90022-8.
[114] S. Ashckenazi-Polivoda, S. Abramovich, A. Almogi-Labin, A. Schneider-Mor, S. Feinstein, W. Püttmann, Z. Berner, Paleoenvironments of the latest Cretaceous oil shale sequence, Southern Tethys, Israel, as an integral part of the prevailing upwelling system, Palaeogeogr. Palaeoclimatol. Palaeoecol. (2011). https://doi.org/10.1016/j.palaeo.2011.02.018.
[115] T.M. Shirav, M., Oil Shale in Israel, Geol. Surv. Isr. 24 (1984) 1–32.
[116] U.W. Y. Shahar, A new oil shale deposit in the Northern Negev, Israel, Mexico, 1967.
[117] D. Gur, G. Steinitz, Y. Kolodny, A. Starinsky, M. McWilliams, 40Ar39Ar dating of combustion metamorphism ("Mottled Zone", Israel), Chem. Geol. 122 (1995) 171–184. https://doi.org/10.1016/0009-2541(95)00034-J.
[118] B. Spiro, Bacterial sulphate reduction and calcite precipitation in hypersaline deposition of bituminous shales, Nature. 269 (1977) 235–237.
[119] Y. Shahar, The Hazeva Formation in the Oron-Ef'e syncline, Israel, Isr. J. Earth Sci. 22 (1973) 31–49.
[120] I.H. Z. Garfunkel, The Upper Tertiary and Qauternary morphology of the Negev, Israel, Isr. J. Earth Sci. 15 (1966) 101–117.
[121] A. Matthews, Y. Nathan, The decarbonation of carbonate-fluorapatite (francolite), Am. Mineral. (1977).
[122] E. V. Sokol, S.N. Kokh, V. V. Sharygin, V.A. Danilovsky, Y. V. Seryotkin, R. Liferovich, A.S. Deviatiiarova, E.N. Nigmatulina, N.S. Karmanov, Mineralogical diversity of ca2 sio4-bearing combustion metamorphic rocks in the hatrurim basin: Implications for storage and partitioning of elements in oil shale clinkering, Minerals. 9 (2019). https://doi.org/10.3390/min9080465.
[123] Y. Kolodny, S. Gross, Thermal Metamorphism by Combustion of Organic Matter: Isotopic and Petrological Evidence, J. Geol. (1974). https://doi.org/10.1086/627995.
[124] H.B. Tristram, The Land of Israel. A journal of travels in Palestine, undertaken with special reference to its physical character, Soc. Promot. Christain Knowl. (1865) 651.
[125] E. Hull, The survery of western Palestine Memoir on the geology and geography of Arabia Petraea, Palestine and adjoining districs, Palest. Expl. Fund. (1886) 154.
[126] M. Blackenhorn, Naturwissenschaftliche studien am Toten Meer und im Jordantal, Friedlander Sohn. (1912) 478.
[127] M. Avnimelech, Remarks on the occurrence of unsual high-temperature minerals in the so-called "Mottled Zone" complex of Israel, Isr. J. Earth Sci. 13 (1964) 102–110.
[128] Y.K. Y. K. Bentor, A. Vroman, New evidence on the origin of the high-temperature mineral assemblage of the "Mottled Zone" (Israel), 24th Intl. Geol. Congr. (1972) 267–275.
[129] A. Matthews, Y. Kolodny, Oxygen isotope fractionation in decarbonation metamorphism: the Mottled Zone event, Earth Planet. Sci. Lett. (1978). https://doi.org/10.1016/0012-821X(78)90154-1.
[130] Y. Vapnik, V. V. Sharygin, E. V. Sokol, R. Shagam, Paralavas in a combustion metamorphic complex: Hatrurim Basin, Israel, in: GSA Rev. Eng. Geol., 2007. https://doi.org/10.1130/2007.4118(09).
[131] V. V. Sharygin, A hibonite-spinel-corundum-hematite assemblage in plagioclase-clinopyroxene pyrometamorphic rocks, Hatrurim Basin, Israel: mineral chemistry, genesis and formation temperatures, Mineral. Mag. (2019). https://doi.org/10.1180/mgm.2018.138.
[132] P.C. Hewlett, Lea's Chemistry of Cement and Concrete, 2003. https://doi.org/10.1016/B978-0-7506-6256-7.X5007-3.
[133] Y.I. Geller, Small-scale mobilization of trace elements as evidenced by mineralogy and

chemistry of veins in the Hatrurim Formation calcite-spurrite rocks, Rep. Geol. Surv. Isr. (2013).
[134] D. Turcotte, G. Schubert, Geodynamics, 2nd ed, 2002.
[135] M. In, I. Hatrurim, A. Gilat, Hydrothermal activity and hydro-explosions as a cause of natural combustion and pyrolysis of bituminous rocks : the case of Pliocene metamorphism in Israel (Hatrurim Formation) HYDROTHERMAL ACTIVITY AND HYDRO-EXPLOSIONS AS A CAUSE OF NATURAL COMBUSTION, GSI Curr. Res. 11 (1998) 96–102.
[136] O. Amit, A. Bein, THE GENESIS OF THE ZOHAR GAS AS DEDUCED FROM ITS CHEMICAL AND CARBON ISOTOPE COMPOSITION, J. Pet. Geol. (1979). https://doi.org/10.1111/j.1747-5457.1979.tb00694.x.
[137] A. Meilijson, S. Ashckenazi-Polivoda, L. Ron-Yankovich, P. Illner, H. Alsenz, R.P. Speijer, A. Almogi-Labin, S. Feinstein, Z. Berner, W. Püttmann, S. Abramovich, Chronostratigraphy of the Upper Cretaceous high productivity sequence of the southern Tethys, Israel, Cretac. Res. (2014). https://doi.org/10.1016/j.cretres.2014.04.006.
[138] J. Wei, K. Cen, Y. Geng, China's cement demand and CO 2 emissions toward 2030: from the perspective of socioeconomic, technology and population, Environ. Sci. Pollut. Res. (2019). https://doi.org/10.1007/s11356-018-04081-2.
[139] U.S Geological Survey, Mineral commodity summaries 2020: U.S. Geological Survey, 2020.
[140] H.G. van Oss, USGS, Cement Statistics, U.S. Geol. Surv. Miner. Commod. Summ. (2014).
[141] A. Hasanbeigi, L. Price, E. Lin, Emerging energy-efficiency and CO 2 emission-reduction technologies for cement and concrete production: A technical review, Renew. Sustain. Energy Rev. (2012). https://doi.org/10.1016/j.rser.2012.07.019.
[142] H.G. Van Oss, A.C. Padovani, Cement manufacture and the environment - Part I: Chemistry and technology, J. Ind. Ecol. (2002). https://doi.org/10.1162/108819802320971650.
[143] H.G. Van Oss, A.C. Padovani, Cement manufacture and the environment, Part II: Environmental challenges and opportunities, J. Ind. Ecol. (2003). https://doi.org/10.1162/108819803766729212.
[144] M. a. G. Aranda, a. G.D. La Torre, K. Morsli, M. Zahir, In-situ Clinkerization Study of Belite Portland Clinkers by Synchrotron X-ray Powder Diffraction, in: 12th Int. Congr. Chem. Cem., 2007.
[145] E. Gartner, Industrially interesting approaches to "low-CO2" cements, Cem. Concr. Res. (2004). https://doi.org/10.1016/j.cemconres.2004.01.021.
[146] C.D. Popescu, M. Muntean, J.H. Sharp, Industrial trial production of low energy belite cement, Cem. Concr. Compos. (2003). https://doi.org/10.1016/S0958-9465(02)00097-5.
[147] Á.G. De La Torre, K. Morsli, M. Zahir, M.A.G. Aranda, In situ synchrotron powder diffraction study of active belite clinkers, J. Appl. Crystallogr. (2007). https://doi.org/10.1107/S0021889807042379.
[148] M.A.G. Aranda, A.G. De la Torre, Sulfoaluminate cement, in: Eco-Efficient Concr., 2013. https://doi.org/10.1533/9780857098993.4.488.
[149] J.H. Sharp, C.D. Lawrence, R. Yang, Calcium sulfoaluminate cements - Low-energy cements, special cements or what?, Adv. Cem. Res. (1999). https://doi.org/10.1680/adcr.1999.11.1.3.
[150] M. Segata, N. Marinoni, M. Galimberti, M. Marchi, M. Cantaluppi, A. Pavese, Á.G. De la Torre, The effects of MgO, Na2O and SO3 on industrial clinkering process: phase composition, polymorphism, microstructure and hydration, using a multidisciplinary approach, Mater. Charact. (2019). https://doi.org/10.1016/j.matchar.2019.109809.
[151] M. Marroccoli, M.L. Pace, A. Telesca, G.L. Valenti, Synthesis of calcium sulfoaluminate cements from Al 2O 3-rich by-products from aluminium manufacture, in: 2nd Int. Conf. Sustain. Constr. Mater. Technol., 2010.

[152] Z. Li, L. Huang, S. Wang, Z. Yang, L. Yu, Using alumina-rich sludge and phosphogypsum manufactures low-CO2 cement, Constr. Build. Mater. (2021). https://doi.org/10.1016/j.conbuildmat.2021.123016.
[153] N.V.B. N. I. Golovastikov, R. G. Matveeva, Crystal structure of tricalcium silicate, 3CaO.SiO2 = C3S, Sov. Pjys. Crystallogr. 20 (1975) 441.
[154] M.N. De Noirfontaine, F. Dunstetter, M. Courtial, G. Gasecki, M. Signes-Frehel, Tricalcium silicate Ca3SiO5, the major component of anhydrous Portland cement: On the conservation of distances and directions and their relationship to the structural elements, Zeitschrift Fur Krist. (2003). https://doi.org/10.1524/zkri.218.1.8.20769.
[155] V.K. Peterson, B.A. Hunter, A. Ray, Tricalcium silicate T1 and T2 polymorphic investigations: Rietveld refinement at various temperatures using synchrotron powder diffraction, J. Am. Ceram. Soc. (2004). https://doi.org/10.1111/j.1551-2916.2004.01625.x.
[156] Á.G. De la Torre, R.N. De Vera, A.J.M. Cuberos, M.A.G. Aranda, Crystal structure of low magnesium-content alite: Application to Rietveld quantitative phase analysis, Cem. Concr. Res. (2008). https://doi.org/10.1016/j.cemconres.2008.06.005.
[157] F. Dunstetter, M.N. De Noirfontaine, M. Courtial, Polymorphism of tricalcium silicate, the major compound of Portland cement clinker: 1. Structural data: Review and unified analysis, Cem. Concr. Res. (2006). https://doi.org/10.1016/j.cemconres.2004.12.003.
[158] M.N. De Noirfontaine, M. Courtial, F. Dunstetter, G. Gasecki, M. Signes-Frehel, Tricalcium silicate Ca3SiO5 superstructure analysis: A route towards the structure of the M1 polymorph, Zeitschrift Fur Krist. (2012). https://doi.org/10.1524/zkri.2012.1425.
[159] M. BIGARÉ, A. GUINIER, C. MAZIÈRES, M. REGOURD, N. YANNAQUIS, W. EYSBL, T. HAHN, E. WOERMANN, Polymorphism of Tricalcium Silicate and Its Solid Solutions, J. Am. Ceram. Soc. (1967). https://doi.org/10.1111/j.1151-2916.1967.tb15009.x.
[160] W.G. Mumme, Crystal-Structure of tricalcium silciate from a Portland-cement clinker and its application to quantitative XRD analysis, Neues Jahrb. Miner. Monatsh.. (1995).
[161] F. Nishi, Y. Takeuchi, I. Maki, Tricalcium silicate Ca30[Si04]:The monoclinic superstructure, Zeitschrift Fur Krist. - New Cryst. Struct. (1985). https://doi.org/10.1524/zkri.1985.172.3-4.297.
[162] Á.G. De La Torre, S. Bruque, J. Campo, M.A.G. Aranda, The superstructure of C3S from synchrotron and neutron powder diffraction and its role in quantitative phase analyses, Cem. Concr. Res. (2002). https://doi.org/10.1016/S0008-8846(02)00796-2.
[163] F. Nishi, Y. Takeuchi, The rhombohedral structure of tricalcium silicate at 1200 °C, Zeitschrift Fur Krist. - New Cryst. Struct. (1984). https://doi.org/10.1524/zkri.1984.168.1-4.197.
[164] M.N. De Noirfontaine, F. Dunstetter, M. Courtial, G. Gasecki, M. Signes-Frehel, Polymorphism of tricalcium silicate, the major compound of Portland cement clinker: 2. Modelling alite for Rietveld analysis, an industrial challenge, Cem. Concr. Res. (2006). https://doi.org/10.1016/j.cemconres.2004.12.004.
[165] H. Saalfeld, X-ray investigation of single crystals of β-Ca2SiO4 (larnite) at high temperature, Am. Mineral. 60 (1975) 824–827.
[166] G. YAMAGUCHI, Y. ONO, S. KAWAMURA, Y. SODA, Synthesis of the Modifications of Ca_2SiO_4 and the Determination of their Powder X-ray Diffraction Patterns, J. Ceram. Assoc. Japan. (1963). https://doi.org/10.2109/jcersj1950.71.806_63.
[167] S. Udagawa, K. Urabe, M. Natsume, T. Yano, Refinement of the crystal structure of γ-Ca2SiO4, Cem. Concr. Res. (1980). https://doi.org/10.1016/0008-8846(80)90070-8.
[168] C.M. Midgley, The crystal structure of β dicalcium silicate, Acta Crystallogr. (1952). https://doi.org/10.1107/s0365110x52000964.
[169] K.H. Jost, B. Ziemer, R. Seydel, Redetermination of the structure of β-dicalcium silicate, Acta Crystallogr. Sect. B Struct. Crystallogr. Cryst. Chem. (1977).

https://doi.org/10.1107/s0567740877006918.
[170] R. Berliner, C. Ball, P.B. West, Neutron powder diffraction investigation of model cement compounds, Cem. Concr. Res. (1997). https://doi.org/10.1016/S0008-8846(97)00028-8.
[171] K. Mori, R. Kiyanagi, M. Yonemura, K. Iwase, T. Sato, K. Itoh, M. Sugiyama, T. Kamiyama, T. Fukunaga, Charge states of Ca atoms in β-dicalcium silicate, J. Solid State Chem. (2006). https://doi.org/10.1016/j.jssc.2006.06.018.
[172] N.A. Yamnova, N. V. Zubkova, N.N. Eremin, A.E. Zadov, V.M. Gazeev, Crystal structure of larnite β-Ca2SiO4 and specific features of polymorphic transitions in dicalcium orthosilicate, Crystallogr. Reports. (2011). https://doi.org/10.1134/S1063774511020209.
[173] M.Y.B. A. M. Il'inets, V. I. Simonov, New data concerning atomic structures of Portland cement silicates, in: 8th ICCC, 1986: pp. 498–491.
[174] W. Mumme, L.M.D. Cranswick, B. Chakoumakos, Rietveld crystal structure refinements from high temperature neutron powder diffraction data for the polymorphs of dicalcium silicate, Neues Jahrb. Fur Mineral. Abhandlungen. (1996).
[175] S. V. Rashchenko, Y. V. Seryotkin, E. V. Sokol, S.N. Kokh, Incommensurately modulated crystal structure of flamite - Natural analogue of -Ca2SiO4, Acta Crystallogr. Sect. B Struct. Sci. Cryst. Eng. Mater. (2019). https://doi.org/10.1107/S2052520619013623.
[176] W.G. Mumme, R.J. Hill, G. Bushnell-Wye, E.R. Segnit, Rietveld crystal structure refinements, crystal chemistry and calculated powder diffraction data for the polymorphs of dicalcium silicate and related phases, Neues Jahrb. Fuer Mineral. (1995).
[177] P. Mondal, J.W. Jeffery, The crystal structure of tricalcium aluminate, Ca 3 Al 2 O 6 , Acta Crystallogr. Sect. B Struct. Crystallogr. Cryst. Chem. (1975). https://doi.org/10.1107/s0567740875003639.
[178] F. Nishi, Y. Takéuchi, The A1 6 O 18 rings of tetrahedra in the structure of Ca 8.5 NaAl 6 O 18 , Acta Crystallogr. Sect. B Struct. Crystallogr. Cryst. Chem. (1975). https://doi.org/10.1107/s0567740875004736.
[179] Y. Takéuchi, F. Nishi, Crystal-chemical characterization of the 3CaO·Al 2 O 3 —Na 2 O solid-solution series , Zeitschrift Für Krist. - Cryst. Mater. (1980). https://doi.org/10.1524/zkri.1980.152.14.259.
[180] G.J. Redhammer, G. Tippelt, G. Roth, G. Amthauer, Structural variations in the brownmillerite series Ca2(Fe2-xAlx)O5: Single-crystal X-ray diffraction at 25 °C and high-temperature X-ray powder diffraction (25 °C ≤ T ≤ 1000 °C), Am. Mineral. (2004). https://doi.org/10.2138/am-2004-2-322.
[181] J.I. Bhatty, Role of Minor elements in Cement manufacturing, Innov. Portl. Cem. Manuf. PCA. (2011).
[182] A. Elhoweris, I. Galan, F.P. Glasser, Stabilisation of α ′ dicalcium silicate in calcium sulfoaluminate clinker, Adv. Cem. Res. (2020). https://doi.org/10.1680/jadcr.18.00050.
[183] M. Marchi, M. Segata, F. Scotti, Effect of minor elements on clinker mineralogy and reactivity, in: 36th Int. Conf. Cem. Microsc. 2014, 2014.
[184] K. Kolovos, S. Tsivilis, G. Kakali, The effect of foreign ions on the reactivity of the CaO-SiO2-Al2O3-Fe2O3 system: Part II: Cations, Cem. Concr. Res. (2002). https://doi.org/10.1016/S0008-8846(01)00705-0.
[185] K. Kolovos, P. Loutsi, S. Tsivilis, G. Kakali, The effect of foreign ions on the reactivity of the CaO-SiO2-Al2O3-Fe2O3 system: Part I. Anions, Cem. Concr. Res. (2001). https://doi.org/10.1016/S0008-8846(00)00461-0.
[186] S. Uda, E. Asakura, M. Nagashima, Influence of SO3 on the phase relationship in the system CaO-SiO2-Al2O3-Fe2O3, J. Am. Ceram. Soc. (1998). https://doi.org/10.1111/j.1151-2916.1998.tb02398.x.
[187] T. Staněk, P. Sulovský, Active low-energy belite cement, Cem. Concr. Res. (2015). https://doi.org/10.1016/j.cemconres.2014.11.004.

[188] T. Stanek, P. Sulovský, D. Vsianský, Active Belite Clinker doped with SO3, in: 13th Int. Congr. Chem. Cem., 2011.
[189] L. Kacimi, A. Simon-Masseron, A. Ghomari, Z. Derriche, Reduction of clinkerization temperature by using phosphogypsum, J. Hazard. Mater. (2006). https://doi.org/10.1016/j.jhazmat.2005.12.053.
[190] T. Hanein, T.Y. Duvallet, R.B. Jewell, A.E. Oberlink, T.L. Robl, Y. Zhou, F.P. Glasser, M.N. Bannerman, Alite calcium sulfoaluminate cement: Chemistry and thermodynamics, Adv. Cem. Res. (2019). https://doi.org/10.1680/jadcr.18.00118.
[191] T. Staněk, P. Sulovský, Dicalcium silicate doped with sulfur, Adv. Cem. Res. (2012). https://doi.org/10.1680/adcr.11.00021.
[192] Y. Huang, J. Qian, X. Kang, J. Yu, Y. Fan, Y. Dang, W. Zhang, S. Wang, Belite-calcium sulfoaluminate cement prepared with phosphogypsum: Influence of P 2 O 5 and F on the clinker formation and cement performances, Constr. Build. Mater. (2019). https://doi.org/10.1016/j.conbuildmat.2019.01.112.
[193] S. Kramar, L. Žibret, E. Fidanchevska, V. Jovanov, B. Angjusheva, V. Ducman, Use of fly ash and phosphogypsum for the synthesis of belite-sulfoaluminate clinker, Mater. Constr. (2019). https://doi.org/10.3989/mc.2019.11617.
[194] S. Boughanmi, I. Labidi, A. Megriche, H. Tiss, A. Nonat, Does phosphorus affect the industrial Portland cement reactivity?, Constr. Build. Mater. (2018). https://doi.org/10.1016/j.conbuildmat.2018.08.060.
[195] W. FIX, H. HEYMANN, R. HEINKE, Subsolidus Relations in the System 2CaO·SiO2-3CaO·P2O5, J. Am. Ceram. Soc. (1969). https://doi.org/10.1111/j.1151-2916.1969.tb11948.x.
[196] V. Rubio, M.A. De La Casa-Lillo, S. De Aza, P.N. De Aza, The system Ca3(PO4)2-Ca 2SiO4: The sub-system Ca2SiO 4-7CaOP2O52SiO2, J. Am. Ceram. Soc. (2011). https://doi.org/10.1111/j.1551-2916.2011.04716.x.
[197] M. Hasegawa, Y. Kashiwaya, M. Iwase, Thermodynamic properties of solid solutions between di-calcium silicate and tri-calcium phosphate, High Temp. Mater. Process. (2012). https://doi.org/10.1515/htmp-2012-0077.
[198] R. Widmer, F. Gfeller, T. Armbruster, Structural and Crystal Chemical Investigation of Intermediate Phases in the System Ca2SiO4-Ca3(PO4)2-CaNaPO4, J. Am. Ceram. Soc. (2015). https://doi.org/10.1111/jace.13850.
[199] M.N. De Noirfontaine, S. Tusseau-Nenez, M. Signes-Frehel, G. Gasecki, C. Girod-Labianca, Effect of phosphorus impurity on tricalcium silicate T1: From synthesis to structural characterization, J. Am. Ceram. Soc. (2009). https://doi.org/10.1111/j.1551-2916.2009.03092.x.
[200] S.L. Poulsen, H.J. Jakobsen, J. Skibsted, Incorporation of phosphorus guest ions in the calcium silicate phases of portland cement from 31P MAS NMR spectroscopy, Inorg. Chem. (2010). https://doi.org/10.1021/ic100140j.
[201] W. Gutt, Manufacture of Portland Cement from Phosphatic Raw Materials, 5th Int. Congr. Chem. Cem. Part 1. (1968).
[202] K.G. Kolovos, S. Tsivilis, G. Kakali, Study of clinker dopped with P and S compounds, J. Therm. Anal. Calorim. (2004). https://doi.org/10.1023/B:JTAN.0000041655.82776.09.
[203] A.P. Osokin, E.N. Potapova, Properties of local melts formed during dissolution of siliceous components, Melts Moscow. (1990).
[204] M.T. Blanco-Varela, T. Vázquez, A. Palomo, A study of a new liquid phase to obtain low-energy cements, Cem. Concr. Res. (1986). https://doi.org/10.1016/0008-8846(86)90073-6.
[205] I. Odler, H. Zhang, Investigations on high SO3 Portland clinkers and cements, Cem. Concr. Res. (1996).
[206] GUTT W, OSBORNE GJ, EFFECT OF MANGANESE, IRON AND FLUORINE ON

PROPERTIES OF TRICALCIUM SILICATE, Brit Cer Soc-Trans. (1969).
[207] E. V. Galuskin, F. Gfeller, T. Armbruster, I.O. Galuskina, Y. Vapnik, M. Dulski, M. Murashko, P. Dzierżanowski, V. V. Sharygin, S. V. Krivovichev, R. Wirth, Mayenite supergroup, part III: Fluormayenite, Ca12Al14O32[〈4F2], and fluorkyuygenite, Ca12Al14O32[(H2O)4F2], two new minerals from pyrometamorphic rocks of the Hatrurim Complex, South Levant, Eur. J. Mineral. (2015). https://doi.org/10.1127/ejm/2015/0027-2420.
[208] Z. Guan, Y. Chen, S. Guo, S. Qin, X. Zhu, Crystal lattice constant change and polymorph of alite caused by impurity defects, Kuei Suan Jen Hsueh Pao/ J. Chinese Ceram. Soc. (2006).
[209] Y. Da, T. He, C. Shi, M. Wang, Y. Feng, Studies on the formation and hydration of tricalcium silicate doped with CaF2 and TiO2, Constr. Build. Mater. (2021). https://doi.org/10.1016/j.conbuildmat.2020.121128.
[210] J. Skibsted, T.F. Sevelsted, S.L. Poulsen, T.T. Tran, Studies on guest-ion incorporation in Portland cement - Part 2, ZKG Int. 66 (2013).
[211] T.T. Tran, Fluoride Mineralization of Portland cement. pplications of Double-Resonance NMR Spectroscopy in Structural Investigations of Guest Ions in Cement Phases, Aarhus Univ. (2011).
[212] T.T. Tran, D. Herfort, H.J. Jakobsen, J. Skibsted, SITE PREFERENCES OF F □ , Al 3 + AND Fe 3 + GUEST IONS IN THE CALCIUM SILICATE PHASES OF PORTLAND CEMENT FROM SOLID-STATE NMR SPECTROSCOPY, Fluoride. (2011).
[213] T.T. Tran, D. Herfort, H.J. Jakobsen, J. Skibsted, Site preferences of fluoride guest ions in the calcium silicate phases of portland cement from 29Si{19F} CP-REDOR NMR spectroscopy, J. Am. Chem. Soc. (2009). https://doi.org/10.1021/ja905223d.
[214] K. Enemark-Rasmussen, T.T. Tran, J. Skibsted, Fluoride ions as structural probe-ions in 19F MAS NMR studies of cement materials and thermally activated SCMs, Adv. Cem. Res. (2014). https://doi.org/10.1680/adcr.13.00024.
[215] C. M., SISTEMA CaO-Al2O3-SiO2: INDAGINI CRISTALLOGRAFICHE E MINERALOGICHE MEDIANTE DIFFRAZIONE E FLUORESCENZA A RAGGI X, Università degli Studi di Milano, 2019.
[216] H.E. Borgholm, A new heat recovery and desulphurization plant for 4 wet kilns in Aalborg Portland, in: 2002. https://doi.org/10.1109/citcon.1993.296973.
[217] H.E. Borgholm, F. Feige, New heat recovery and desulphurization plant for 4 wet kilns in Aalborg Portland State of the art in high compression comminution, in: IEEE Cem. Ind. Tech. Conf., 1993.
[218] C. Gilioli, F. Massazza, M. Pezzuoli, A new compound containing five components: 17.2CaO·O.8K2O·6SiO2·3SO3·CaF2, Cem. Concr. Res. (1979). https://doi.org/10.1016/0008-8846(79)90064-4.
[219] R. Li, W. He, J. Zhang, Y. Wang, Y. Zhang, D. Nie, Preparation of belite–sulphoaluminate cement using phosphate rock acid-insoluble residue, Constr. Build. Mater. (2022). https://doi.org/10.1016/j.conbuildmat.2022.126573.
[220] Y.I. Geller, A. Burg, L. Halicz, Y. Kolodny, System closure during the combustion metamorphic “Mottled Zone” event, Israel, Chem. Geol. (2012). https://doi.org/10.1016/j.chemgeo.2012.09.029.
[221] E. V. Sokol, I.S. Novikov, S.N. Zateeva, V. V. Sharygin, Y. Vapnik, Pyrometamorphic rocks of the spurrite-merwinite facies as indicators of hydrocarbon discharge zones (the Hatrurim formation, Israel), Dokl. Earth Sci. 420 (2008) 608–614. https://doi.org/10.1134/S1028334X08040181.
[222] M. Galimberti, N. Marinoni, G. Della Porta, M. Marchi, M. Dapiaggi, Effects of limestone petrography and calcite microstructure on OPC clinker raw meals burnability, Mineral. Petrol. (2017). https://doi.org/10.1007/s00710-016-0485-8.

[223] K. Zhang, P. Shen, L. Yang, M. Rao, S. Nie, F. Wang, Development of high-ferrite cement: Toward green cement production, J. Clean. Prod. (2021). https://doi.org/10.1016/j.jclepro.2021.129487.
[224] Y. Elakneswaran, N. Noguchi, K. Matumoto, Y. Morinaga, T. Chabayashi, H. Kato, T. Nawa, Characteristics of ferrite-rich portland cement: Comparison with ordinary portland cement, Front. Mater. (2019). https://doi.org/10.3389/fmats.2019.00097.
[225] Y.N. Dhoble, S. Ahmed, Review on the innovative uses of steel slag for waste minimization, J. Mater. Cycles Waste Manag. (2018). https://doi.org/10.1007/s10163-018-0711-z.
[226] G. Sarapajevaite, K. Baltakys, Purification of Sulfur Waste Under Hydrothermal Conditions, Waste and Biomass Valorization. (2021). https://doi.org/10.1007/s12649-020-01206-y.
[227] V.K. Shen, D.W. Siderius, W.P. Krekelberg, H.W. Hatch, NIST Standard Reference Simulation Website - National Institute of Standards and Technology, NIST Stand. Ref. Database Number 173. (2018).
[228] L. Rebuffi, J.R. Plaisier, M. Abdellatief, A. Lausi, A.P. Scardi, Mcx: A synchrotron radiation beamline for X-ray diffraction line profile analysis, Zeitschrift Fur Anorg. Und Allg. Chemie. (2014). https://doi.org/10.1002/zaac.201400163.
[229] J.R. Plaisier, L. Nodari, L. Gigli, E.P.R.S. Miguel, R. Bertoncello, A. Lausi, The X-ray diffraction beamline MCX at Elettra: A case study of non-destructive analysis on stained glass, Acta IMEKO. (2017). https://doi.org/10.21014/acta_imeko.v6i3.464.
[230] M. Ortolani, C.L.A. Ricardo, A. Lausi, P. Scardi, Thin film stress and texture analysis at the MCX synchrotron radiation beamline at ELETTRA, in: Mater. Sci. Forum, 2011. https://doi.org/10.4028/www.scientific.net/MSF.681.115.
[231] A. Lausi, E. Busetto, M. Leoni, P. Scardi, The MCX project: a Powder Diffraction beamline at ELETTRA, PSRS Bull. (2006).
[232] J.-L. Hodeau, P. Bordet, M. Anne, A. Prat, A.N. Fitch, E. Dooryhee, G. Vaughan, A.K. Freund, Nine-crystal multianalyzer stage for high-resolution powder diffraction between 6 keV and 40 keV, in: Cryst. Multilayer Opt., 1998. https://doi.org/10.1117/12.332525.
[233] C. Dejoie, M. Coduri, S. Petitdemange, C. Giacobbe, E. Covacci, O. Grimaldi, P.O. Autran, M.W. Mogodi, D.Š. Jung, A.N. Fitch, Combining a nine-crystal multi-analyser stage with a two-dimensional detector for high-resolution powder X-ray diffraction, J. Appl. Crystallogr. (2018). https://doi.org/10.1107/S1600576718014589.
[234] C. Dejoie, P.-O. Autran, E. Covacci, A. Fitch, Combining a nine-crystal multianalyser stage with a hybrid CdTe photon-counting detector for high-resolution X-ray powder diffraction at ESRF-ID22, Acta Crystallogr. Sect. A Found. Adv. (2019). https://doi.org/10.1107/s2053273319089332.
[235] A. Fitch, C. Dejoie, Combining a multi-analyzer stage with a two-dimensional detector for high-resolution powder X-ray diffraction: Correcting the angular scale, J. Appl. Crystallogr. (2021). https://doi.org/10.1107/S1600576721005288.
[236] J.W. Edwards, R. Speiser, H.L. Johnston, High temperature structure and thermal expansion of some metals as determined by x-ray diffraction data. I. Platinum, tantalum, niobium, and molybdenum, J. Appl. Phys. (1951). https://doi.org/10.1063/1.1699977.
[237] and G.N. T.Degen, M. Sadik, E. Broh, PANalytical X'Pert HighScore Plus, 2014.
[238] S. Gates-Rector, T. Blanton, The Powder Diffraction File: a quality materials characterization database, Powder Diffr. (2019). https://doi.org/10.1017/S0885715619000812.
[239] M. Quirós, S. Gražulis, S. Girdzijauskaitė, A. Merkys, A. Vaitkus, Using SMILES strings for the description of chemical connectivity in the Crystallography Open Database, J. Cheminform. (2018). https://doi.org/10.1186/s13321-018-0279-6.
[240] S. Graulis, D. Chateigner, R.T. Downs, A.F.T. Yokochi, M. Quirós, L. Lutterotti, E. Manakova, J. Butkus, P. Moeck, A. Le Bail, Crystallography Open Database - An open-

access collection of crystal structures, J. Appl. Crystallogr. (2009). https://doi.org/10.1107/S0021889809016690.
[241] A. Vaitkus, A. Merkys, S. Grazulis, Validation of the Crystallography Open Database using the Crystallographic Information Framework, J. Appl. Crystallogr. (2021). https://doi.org/10.1107/S1600576720016532.
[242] A. Merkys, A. Vaitkus, J. Butkus, M. Okulič-Kazarinas, V. Kairys, S. Gražulis, COD::CIF::Parser: An error-correcting CIF parser for the Perl language, J. Appl. Crystallogr. (2016). https://doi.org/10.1107/S1600576715022396.
[243] R.T. Downs, M. Hall-Wallace, The American Mineralogist crystal structure database, Am. Mineral. (2003). https://doi.org/10.5860/choice.43sup-0302.
[244] S. Gražulis, A. Merkys, A. Vaitkus, M. Okulič-Kazarinas, Computing stoichiometric molecular composition from crystal structures, J. Appl. Crystallogr. (2015). https://doi.org/10.1107/S1600576714025904.
[245] H.M. Rietveld, Rietveld; J. Appl. Cryst, 1969, 2, 65-71.pdf, J. Appl. Cryst. (1969).
[246] P. Paufler, The Rietveld Method, Cryst. Res. Technol. (1995). https://doi.org/10.1002/crat.2170300412.
[247] D.J. Morgan, D.L. Bish & J.E. Post (Editors) Modern Powder Diffraction. (Reviews in Mineralogy, Volume 20). Mineralogical Society of America, Washington, D.C., 1989. xi + 369 pp. Price US$20 (prepayment required on orders less than $70). ISBN: 0.939950.24.3., Clay Miner. (1990). https://doi.org/10.1180/claymin.1990.025.4.12.
[248] B.H. Toby, R.B. Von Dreele, GSAS-II: The genesis of a modern open-source all purpose crystallography software package, J. Appl. Crystallogr. 46 (2013). https://doi.org/10.1107/S0021889813003531.
[249] P. Thompson, D.E. Cox, J.B. Hastings, Rietveld refinement of Debye–Scherrer synchrotron X-ray data from Al2O3, J. Appl. Crystallogr. (1987). https://doi.org/10.1107/S0021889887087090.
[250] C.J. Howard, The approximation of asymmetric neutron powder diffraction peaks by sums of Gaussians, J. Appl. Crystallogr. (1982). https://doi.org/10.1107/s0021889882012783.
[251] G. Caglioti, A. Paoletti, F.P. Ricci, Choice of collimators for a crystal spectrometer for neutron diffraction, Nucl. Instruments. (1958). https://doi.org/10.1016/0369-643X(58)90029-X.
[252] L.W. Finger, D.E. Cox, A.P. Jephcoat, Correction for powder diffraction peak asymmetry due to axial divergence, J. Appl. Crystallogr. (1994). https://doi.org/10.1107/S0021889894004218.
[253] B. van Laar, W.B. Yelon, PEAK IN NEUTRON POWDER DIFFRACTION., J. Appl. Crystallogr. (1984). https://doi.org/10.1107/S0021889884011006.
[254] A.C. Larson, R.B. Von Dreele, GSAS Manual, Structure. (2004).
[255] P. Scherrer, Bestimmung der Größe und der inneren Struktur von Kolloidteilchen mittels Röntgenstrahlen, Nachrichten von Der Gesellschaft Der Wissenschaften Zu Göttingen, Math. Klasse. (1918).
[256] J.I. Langford, A.J.C. Wilson, Scherrer after sixty years: A survey and some new results in the determination of crystallite size, J. Appl. Crystallogr. (1978). https://doi.org/10.1107/s0021889878012844.
[257] A. Leineweber, E.J. Mittemeijer, Notes on the order-of-reflection dependence of microstrain broadening, J. Appl. Crystallogr. (2010). https://doi.org/10.1107/S0021889810030451.
[258] A.G. De La Torre, S. Bruque, M.A.G. Aranda, Rietveld quantitative amorphous content analysis, J. Appl. Crystallogr. (2001). https://doi.org/10.1107/S0021889801002485.
[259] A.G. De La Torre, S. Bruque, M.A.G. Aranda, Applied Crystallography Rietveld quantitative amorphous content analysis, J. Appl. Cryst. (2001).
[260] F. Guirado, S. Galí, S. Chinchón, Quantitative Rietveld analysis of aluminous cement clinker

phases, Cem. Concr. Res. (2000). https://doi.org/10.1016/S0008-8846(00)00289-1.
[261] L. Lutterotti, R. Ceccato, R. Dal Maschio, E. Pagani, Quantitative analysis of silicate glass in ceramic materials by the Rietveld method, Mater. Sci. Forum. (1998). https://doi.org/10.4028/www.scientific.net/msf.278-281.87.
[262] Agilent, CrysAlisPro Data Collection and Processing Software for Agilent X-ray Diffractometers, 2014.
[263] S. Basu, A. Finke, L. Vera, M. Wang, V. Olieric, Making routine native SAD a reality: lessons from beamline X06DA at the Swiss Light Source, Acta Crystallogr. Sect. D Struct. Biol. (2019). https://doi.org/10.1107/S2059798319003103.
[264] A. Pauluhn, C. Pradervand, D. Rossetti, M. Salathe, C. Schulze-Briese, Automatic loop centring with a high-precision goniometer head at the SLS macromolecular crystallography beamlines, J. Synchrotron Radiat. (2011). https://doi.org/10.1107/S0909049511011848.
[265] R. Bingel-Erlenmeyer, V. Olieric, J.P.A. Grimshaw, J. Gabadinho, X. Wang, S.G. Ebner, A. Isenegger, R. Schneider, J. Schneider, W. Glettig, C. Pradervand, E.H. Panepucci, T. Tomizaki, M. Wang, C. Schulze-Briese, SLS crystallization platform at beamline X06DA-A fully automated pipeline enabling in situ X-ray diffraction screening, Cryst. Growth Des. (2011). https://doi.org/10.1021/cg101375j.
[266] J. Diez, M. Wang, E. Pohl, T. Tomizaki, A. Bertrand, Q. Chen, P. Dietrich, G. Ingold, M. Knecht, A. Meents, V. Olieric, E. Panepucci, A. Pauluhn, C. Pradervand, M. Roccamante, R. Schneider, I. Walthert, E. Zimoch, C. Schulze-Briese, Industrial use of the SLS-MX beamlines, Synchrotron Radiat. News. 20 (2007) 19–22. https://doi.org/10.1080/08940880701510787.
[267] L. Jacquamet, J. Ohana, J. Joly, P. Legrand, R. Kahn, F. Borel, M. Pirocchi, P. Charrault, P. Carpentier, J.L. Ferrer, A new highly integrated sample environment for protein crystallography, Acta Crystallogr. Sect. D Biol. Crystallogr. (2004). https://doi.org/10.1107/S0907444904005232.
[268] J. Aishima, R.L. Owen, D. Axford, E. Shepherd, G. Winter, K. Levik, P. Gibbons, A. Ashton, G. Evans, High-speed crystal detection and characterization using a fast-readout detector, Acta Crystallogr. Sect. D Biol. Crystallogr. (2010). https://doi.org/10.1107/S0907444910028192.
[269] F.P. J. L. Pouchou, Microbeam Analysis, 1st ed., San Francisco, 1988.
[270] J. Schindelin, I. Arganda-Carreras, E. Frise, V. Kaynig, M. Longair, T. Pietzsch, S. Preibisch, C. Rueden, S. Saalfeld, B. Schmid, J.Y. Tinevez, D.J. White, V. Hartenstein, K. Eliceiri, P. Tomancak, A. Cardona, Fiji: An open-source platform for biological-image analysis, Nat. Methods. (2012). https://doi.org/10.1038/nmeth.2019.
[271] C.A. Schneider, W.S. Rasband, K.W. Eliceiri, NIH Image to ImageJ: 25 years of image analysis, Nat. Methods. (2012). https://doi.org/10.1038/nmeth.2089.
[272] C.T. Rueden, J. Schindelin, M.C. Hiner, B.E. DeZonia, A.E. Walter, E.T. Arena, K.W. Eliceiri, ImageJ2: ImageJ for the next generation of scientific image data, BMC Bioinformatics. (2017). https://doi.org/10.1186/s12859-017-1934-z.
[273] M. Kudrna Prašek, M. Pistone, D.R. Baker, N. Sodini, N. Marinoni, G. Lanzafame, L. Mancini, A compact and flexible induction furnace for in situ X-ray microradiograhy and computed microtomography at Elettra: design, characterization and first tests, J. Synchrotron Radiat. (2018). https://doi.org/10.1107/S1600577518005970.
[274] M. Zucali, D. Chateigner, M. Dugnani, L. Lutterotti, B. Ouladdiaf, Quantitative texture analysis of glaucophanite deformed under eclogite facies conditions (Sesia-Lanzo Zone, Western Alps): Comparison between X-ray and neutron diffraction analysis, Geol. Soc. Spec. Publ. (2002). https://doi.org/10.1144/GSL.SP.2001.200.01.14.
[275] A.I. Saville, A. Creuziger, E.B. Mitchell, S.C. Vogel, J.T. Benzing, J. Klemm-Toole, K.D. Clarke, A.J. Clarke, MAUD Rietveld Refinement Software for Neutron Diffraction Texture

Studies of Single- and Dual-Phase Materials, Integr. Mater. Manuf. Innov. (2021). https://doi.org/10.1007/s40192-021-00224-5.
[276] L. Lutterotti, Total pattern fitting for the combined size-strain-stress-texture determination in thin film diffraction, Nucl. Instruments Methods Phys. Res. Sect. B Beam Interact. with Mater. Atoms. (2010). https://doi.org/10.1016/j.nimb.2009.09.053.
[277] L. Lutterotti, M. Bortolotti, G. Ischia, I. Lonardelli, H.R. Wenk, Rietveld texture analysis from diffraction images, in: Zeitschrift Fur Krist. Suppl., 2007. https://doi.org/10.1524/zksu.2007.2007.suppl_26.125.
[278] L. Lutterotti, S. Matthies, H.R. Wenk, A.S. Schultz, J.W. Richardson, Combined texture and structure analysis of deformed limestone from time-of-flight neutron diffraction spectra, J. Appl. Phys. (1997). https://doi.org/10.1063/1.364220.
[279] L. Yansheng, W. Fu, X. Jiazheng, L. Zhide, Estimation of the true orientation distribution function determination of the maximum-entropy method by the Taylor model, J. Appl. Crystallogr. (1993). https://doi.org/10.1107/S002188989201149X.
[280] R.B. Von Dreele, Quantitative texture analysis by Rietveld refinement, J. Appl. Crystallogr. (1997). https://doi.org/10.1107/S0021889897005918.
[281] H.R. Wenk, Application of neutron scattering in earth sciences, JOM. (2012). https://doi.org/10.1007/s11837-011-0223-y.
[282] S. Ober, K. Frederick, A Study of the Blaine Fineness Tester and A Determination of Surface Area From Air Permeability Data, in: Symp. Part. Size Meas., 2009. https://doi.org/10.1520/stp39302s.
[283] J.D. Zea-Garcia, A.G. De la Torre, M.A.G. Aranda, I. Santacruz, Processing and characterisation of standard and doped alite-belite-ye'elimite ecocement pastes and mortars, Cem. Concr. Res. (2020). https://doi.org/10.1016/j.cemconres.2019.105911.
[284] L. Wadsö, Operational issues in isothermal calorimetry, Cem. Concr. Res. (2010). https://doi.org/10.1016/j.cemconres.2010.03.017.
[285] J.D. Zea-Garcia, S.G. Sanfelix, O. Vallcorba, M.A.G. Aranda, I. Santacruz, A.G. De La Torre, Hydration Activation of Alite-Belite-Ye'elimite Cements by Doping with Boron, ACS Sustain. Chem. Eng. (2020). https://doi.org/10.1021/acssuschemeng.9b05975.
[286] R.J. Dunham, Classification of Carbonate Rocks According to Depositional Textures, in: Classif. Carbonate Rocks--A Symp., 1962.
[287] A.F. Embry, J.E. Klovan, A Late Devonian reef tract on northeastern Banks Island, NWT, Bull. Can. Pet. Geol. (1971).
[288] Y. Kolodny, M. Bar, E. Sass, Fission track age of the Mottled Zone event' in Israel, Earth Planet. Sci. Lett. (1971). https://doi.org/10.1016/0012-821X(71)90178-6.
[289] F.D. Smitho, Planktonic Foraminifera as Indicators of Depositional Environment, Micropaleontology. (1955). https://doi.org/10.2307/1484167.
[290] A. Flexer, Late cretaceous paleogeography of northern Israel and its significance for the Levant geology, Palaeogeogr. Palaeoclimatol. Palaeoecol. 10 (1971) 293–316. https://doi.org/10.1016/0031-0182(71)90053-8.
[291] R.D. Shannon, Revised effective ionic radii and systematic studies of interatomic distances in halides and chalcogenides, Acta Crystallogr. Sect. A. (1976). https://doi.org/10.1107/S0567739476001551.
[292] L. Lutterotti, D. Chateigner, S. Ferrari, J. Ricote, Texture, residual stress and structural analysis of thin films using a combined X-ray analysis, in: Thin Solid Films, 2004. https://doi.org/10.1016/j.tsf.2003.10.150.
[293] D. SOUDRY, Ultra-fine structures and genesis of the Campanian Negev high-grade phosphorites (southern Israel), Sedimentology. (1987). https://doi.org/10.1111/j.1365-3091.1987.tb00792.x.
[294] S. Shoval, Clay sedimentation along the southeastern Neo-Tethys margin during the oceanic

convergence stage, Appl. Clay Sci. (2004). https://doi.org/10.1016/j.clay.2003.08.010.
[295] G.P. Illner, Depositional environment of the Upper Cretaceous oil shales in the Negev Desert, Israel: Geochemical constraints based on trace elements and stable isotopes, Karlsruher Instituts für Technologie (KIT), 2014.
[296] C. Robert, H. Chamley, Development of early Eocene warm climates, as inferred from clay mineral variations in oceanic sediments, Glob. Planet. Change. (1991). https://doi.org/10.1016/0921-8181(91)90114-C.
[297] Z. Lewy, Pebbly phosphate and granular phosphorite (Late Cretaceous, southern Israel) and their bearing on phosphatization processes, Geol. Soc. Spec. Publ. (1990). https://doi.org/10.1144/GSL.SP.1990.052.01.12.
[298] Z. Lewy, H. Cappetta, Senonian Elasmobranch teeth from Israel Biostratigraphic and paleoenvironmental implications, Neues Jahrb. Für Geol. Und Paläontologie - Monatshefte. (1989). https://doi.org/10.1127/njgpm/1989/1989/212.
[299] J. Bartov, Y. Eyal, Z. Garfunkel, G. Steinitz, Late Cretaceous and Tertiary stratigraphy and paleogeography of southern Israel, Isr. J. Earth Sci. 21 (1972) 69–97.
[300] E. Sass, Y. Nathan, A. Nissenbaum, Mineralogy of certain pyrite concretions from Israel and their alteration products, Mineral. Mag. J. Mineral. Soc. (1965). https://doi.org/10.1180/minmag.1965.035.269.11.
[301] W.D. Birch, A. Pring, A. Reller, H. Schmalle, Bernalite : a new ferric hydroxide with perovskite structure, Naturwissenschaften. (1992). https://doi.org/10.1007/BF01135768.
[302] R.E. Westland, New phases in the hydous ferric sulfate system, a suppoting argument that the mineral lausenite is of formula FE2(SO4)3·5H2O and the crystal structure refinement and hydrogen bonding scheme of the minerals quenstedtite and romerite, Queen's University, 2012.
[303] A.G. De la Torre, M.A.G. Aranda, Accuracy in Rietveld quantitative phase analysis of Portland cements, J. Appl. Crystallogr. (2003). https://doi.org/10.1107/S002188980301375X.
[304] D.H. Campbell, Microscopical Examination and Interpretation of Portland Cement and Clinker, 1999.
[305] P. Ramdohr, The ore minerals and their intergrowths, New York, Pergamon Press. (1969).
[306] A.D. Elliot, Structure of pyrrhotite 5C (Fe9S10), Acta Crystallogr. Sect. B Struct. Sci. (2010). https://doi.org/10.1107/S0108768110011845.
[307] H. Saalfeld, W. Depmeier, Silicon-Free Compounds with Sodalite Structure, Krist. Und Tech. (1972). https://doi.org/10.1002/crat.19720070125.
[308] S.M. Antao, I. Hassan, J.B. Parise, Cation ordering in magnesioferrite, MgFe2O4, to 982 °C using in situ synchrotron X-ray powder diffraction, Am. Mineral. (2005). https://doi.org/10.2138/am.2005.1559.
[309] R.C. Peterson, G.A. Lager, E.L. Hitterman, A time-of-flight neutron powder diffraction study of MgAl2O 4 at tempratures up to 1273 K, Am. Mineral. (1991).
[310] V. V. Sharygin, B. Lazic, T.M. Armbruster, M.N. Murashko, R. Wirth, I.O. Galuskina, E. V. Galuskin, Y. Vapnik, S.N. Britvin, A.M. Logvinova, Shulamitite Ca3TiFe3+ AlO8 - a new perovskite-related mineral from Hatrurim Basin, Israel, Eur. J. Mineral. (2013). https://doi.org/10.1127/0935-1221/2013/0025-2259.
[311] Y. Vapnik, I. Novikov, Reply to Comment of Y. Kolodny, A. Burg and A. Sneh on "Combustion metamorphism in the Nabi Musa dome: New implications for a mud volcano origin of the Mottled Zone, Dead Sea area", by E. Sokol, I. Novikov, S. Zateeva, Ye. Vapnik, R. Shagam and O. Kozmenk, Basin Res. 25 (2013) 115–120. https://doi.org/10.1111/bre.12007.
[312] Y. Kolodny, A. Burg, A. Sneh, Comment on "Combustion metamorphism (CM) in the Nabi Musa dome: New implications for a mud volcanic origin of the Mottled Zone, Dead Sea area", by: E. Sokol, I. Novikov, S. Zateeva, Ye. Vapnik, R. Shagam and O. Kozmenko, Basin

Research (2010) 22, 414-438, Basin Res. 25 (2013) 112–114. https://doi.org/10.1111/bre.12009.
[313] R. Bogoch, A. Gilat, O. Yoffe, S. Ehrlich, Rare earth and trace element distributions in the Mottled Zone complex, Israel, Isr. J. Earth Sci. 48 (1999) 225–234.
[314] E. V. Sokol, S.N. Kokh, H.N. Khoury, Y. V. Seryotkin, S. V. Goryainov, S.A. Novikova, I.A. Sokol, Natural analogue approaches to prediction of long-term behaviour of Ca2UO5·2-3H2O X-phase: case study from Tulul Al Hammam site, Jordan, Arab. J. Geosci. (2017). https://doi.org/10.1007/s12517-017-3305-5.
[315] I. Galan, T. Hanein, A. Elhoweris, M.N. Bannerman, F.P. Glasser, Phase compatibility in the system CaO-SiO2-Al2O3-SO3-Fe2O3 and the effect of partial pressure on the phase stability, Ind. Eng. Chem. Res. 56 (2017) 2341–2349. https://doi.org/10.1021/acs.iecr.6b03470.
[316] Y. Harada, N. Saito, K. Nakashima, Crystallinity of supercooled oxide melts quantified by electrical capacitance measurements, ISIJ Int. (2017). https://doi.org/10.2355/isijinternational.ISIJINT-2016-299.
[317] Y. El Khessaimi, Y. El Hafiane, A. Smith, Examination of ye'elimite formation mechanisms, J. Eur. Ceram. Soc. (2019). https://doi.org/10.1016/j.jeurceramsoc.2019.07.042.
[318] T. Hanein, A. Elhoweris, I. Galan, F.P. Glasser, M.N. and Bannerman, Thermodynamic data of ye'elimite (C4A3$) for cement clinker equilibrium calculations, Conf. 35th Cem. Concr. Sci. Conf. (2015).
[319] S. Giminez-Molina, M.T. Blanco, J. Marr, F.P. Glasser, Phase relations in the system Ca 2 SiO 4 -CaO-CaSO 4 -CaF 2 relevant to cement clinkering , Adv. Cem. Res. (1992). https://doi.org/10.1680/adcr.1992.4.14.81.
[320] E. V. Galuskin, J. Kusz, T. Armbruster, I.O. Galuskina, K. Marzec, Y. Vapnik, M. Murashko, Vorlanite, (CaU6+)O4, from Jabel Harmun, Palestinian Autonomy, Israel, Am. Mineral. 98 (2013) 1938–1942. https://doi.org/10.2138/am.2013.4548.
[321] L. Halicz, Y. Kolodny, System closure and isochemistry during the Mottled Zone event , Israel, (2017) 1–8.
[322] sokol E.V. Sharygin, Viktor V., Phase FeAlO3 in plagioclase clinopyroxene rock in Hatrurim Basin, Israel., in: 200th Anniv. Meet. Russ. Mineral. Soc., 2017.
[323] S. Popović, M. Ristić, S. Musić, Formation of solid solutions in the system Al2O3-Fe2O3, Mater. Lett. (1995). https://doi.org/10.1016/0167-577X(95)00019-4.
[324] A.D. Polli, F.F. Lange, C.G. Levi, J. Mayer, Crystallization behavior and microstructure evolution of (Al,Fe)2O3 synthesized from liquid precursors, J. Am. Ceram. Soc. (1996). https://doi.org/10.1111/j.1151-2916.1996.tb07991.x.
[325] J. Majzlan, A. Navrotsky, B.J. Evans, Thermodynamics and crystal chemistry of the hematite-corundum solid solution and the FeAlO3 phase, Phys. Chem. Miner. (2002). https://doi.org/10.1007/s00269-002-0261-7.
[326] Y. El Khessaimi, Y. El Hafiane, A. Smith, R. Trauchessec, C. Diliberto, A. Lecomte, Solid-state synthesis of pure ye'elimite, J. Eur. Ceram. Soc. (2018). https://doi.org/10.1016/j.jeurceramsoc.2018.03.018.
[327] E. V. Galuskin, I.O. Galuskina, F. Gfeller, B. Krüger, J. Kusz, Y. Vapnik, M. Dulski, P. Dzierżanowski, Silicocarnotite, Ca5 [(SiO4)(PO4)](PO4), a new ,,old'' mineral from the Negev Desert, Israel, and the ternesite–silicocarnotite solid solution: indicators of high-temperature alteration of pyrometamorphic rocks of the Hatrurim Complex, Southern Levant, Eur. J. Mineral. 28 (2016) 105–123. https://doi.org/10.1127/ejm/2015/0027-2494.
[328] M.M. Galuskina, Irina O., galuskin E.V., Pakhomova A.S., Widmer R., Armbruster T., Lazic B., Grew E.S., Vapnik Y., Dzierazanowski P., Khesinite, in: IMA2014-033 CNMNC Newsl., 2014: pp. 797–804.
[329] E. V. Galuskin, I.O. Galuskina, F. Gfeller, B. Krüger, J. Kusz, Y. Vapnik, M. Dulski, P.

Dzierżanowski, Silicocarnotite, Ca5 [(SiO4)(PO4)](PO4), a new ,,old'' mineral from the Negev Desert, Israel, and the ternesite–silicocarnotite solid solution: indicators of high-temperature alteration of pyrometamorphic rocks of the Hatrurim Complex, Southern Levant, Eur. J. Mineral. (2016). https://doi.org/10.1127/ejm/2015/0027-2494.

[330] T. Hanein, I. Galan, F.P. Glasser, S. Skalamprinos, A. Elhoweris, M.S. Imbabi, M.N. Bannerman, Stability of ternesite and the production at scale of ternesite-based clinkers, Cem. Concr. Res. (2017). https://doi.org/10.1016/j.cemconres.2017.04.010.

[331] D.H. Lindsley, Oxide Minerals: Petrologic and Magnetic Significance, 2019. https://doi.org/10.1016/0037-0738(93)90062-a.

[332] F.P. Glasser, The formation and thermal stability of spurrite, Ca5(SiO4)2CO3, Cem. Concr. Res. (1973). https://doi.org/10.1016/0008-8846(73)90058-6.

[333] K.S.P. Karunadasa, C.H. Manoratne, H.M.T.G.A. Pitawala, R.M.G. Rajapakse, Thermal decomposition of calcium carbonate (calcite polymorph) as examined by in-situ high-temperature X-ray powder diffraction, J. Phys. Chem. Solids. (2019). https://doi.org/10.1016/j.jpcs.2019.05.023.

[334] N. Spanos, P.G. Koutsoukos, The transformation of vaterite to calcite: Effect of the conditions of the solutions in contact with the mineral phase, J. Cryst. Growth. (1998). https://doi.org/10.1016/S0022-0248(98)00385-6.

[335] M.S. Hashim, S.E. Kaczmarek, The transformation of aragonite to calcite in the presence of magnesium: Implications for marine diagenesis, Earth Planet. Sci. Lett. (2021). https://doi.org/10.1016/j.epsl.2021.117166.

[336] Y. Kolodny, A. Burg, Y.I. Geller, L. Halicz, Y. Zakon, Veins in the combusted metamorphic rocks, Israel; Weathering or a retrograde event?, Chem. Geol. 385 (2014) 140–155. https://doi.org/10.1016/j.chemgeo.2014.07.006.

[337] S. Skalamprinos, G. Jen, I. Galan, M. Whittaker, A. Elhoweris, F. Glasser, The synthesis and hydration of ternesite, Ca5(SiO4)2SO4, Cem. Concr. Res. (2018). https://doi.org/10.1016/j.cemconres.2018.06.012.

[338] S. Skalamprinos, I. Galan, T. Hanein, F. Glasser, Enthalpy of formation of ye'elimite and ternesite, J. Therm. Anal. Calorim. (2018). https://doi.org/10.1007/s10973-017-6751-0.

[339] F. Winnefeld, B. Lothenbach, Phase equilibria in the system Ca4Al6O12SO4 – Ca2SiO4 – CaSO4 – H2O referring to the hydration of calcium sulfoaluminate cements, RILEM Tech. Lett. (2016).

[340] M.A.G. Aranda, A.G. De la Torre, L. Leon-Reina, 5. Rietveld Quantitative Phase Analysis of OPC Clinkers, Cements and Hydration Products, in: Appl. Mineral. Cem. Concr., 2018. https://doi.org/10.1515/9781501508356-007.

[341] I.D. Clark, R. Dayal, H.N. Khoury, The Maqarin (Jordan) natural analogue for 14C attenuation in cementitious barriers, Waste Manag. 14 (1994) 467–477. https://doi.org/10.1016/0956-053X(94)90050-7.

[342] S. Lee, Y.J. Kim, H.S. Moon, Phase transformation sequence from kaolinite to mullite investigated by an energy-filtering transmission electron microscope, J. Am. Ceram. Soc. (1999). https://doi.org/10.1111/j.1151-2916.1999.tb02165.x.

[343] M. Popescu, A. Simion, V. Matei, Study of thermal behaviour up to 1550° of materials containing calcium sulphate, J. Therm. Anal. (1985). https://doi.org/10.1007/BF02156495.

[344] E. Irran, E. Tillmanns, G. Hentschel, Ternesite, Ca5(SiO4)2SO4, a new mineral from the Ettringer Bellerberg/Eifel, Germany, Mineral. Petrol. (1997). https://doi.org/10.1007/BF01163138.

[345] I. Pajares, Á.G. De la Torre, S. Martínez-Ramírez, F. Puertas, M.-T. Blanco-Varela, M.A.G. Aranda, Quantitative analysis of mineralized white Portland clinkers: The structure of Fluorellestadite, Powder Diffr. (2002). https://doi.org/10.1154/1.1505045.

[346] P. Comodi, Y. Liu, M.L. Frezzotti, Structural and vibrational behaviour of fluorapatite with

pressure. Part II: In situ micro-Raman spectroscopic investigation, Phys. Chem. Miner. (2001). https://doi.org/10.1007/s002690100155.
[347] J.W. Jeffery, The crystal structure of tricalcium silicate, Acta Crystallogr. (1952). https://doi.org/10.1107/s0365110x52000083.
[348] I.L. Fabricius, Chalk: Composition, diagenesis and physical properties, Bull. Geol. Soc. Denmark. (2007). https://doi.org/10.37570/bgsd-2007-55-08.
[349] H.Y. Ghorab, M. Rizk, B. Ibrahim, M.M. Allam, High belite cement from alternative raw materials, Mater. Constr. (2014). https://doi.org/10.3989/mc.2014.01913.
[350] Y. Hu, S. Ma, W. Li, X. Shen, The preparation and composition analysis of alite-ye'elimite with industrial wastes, Ceram. - Silikaty. (2016). https://doi.org/10.13168/cs.2016.0027.
[351] A.G. De la Torre, A.J.M. Cuberos, G. Alvarez-Pinazo, A. Cuesta, M. a G. Aranda, In-Situ Clinkering Study of Belite Sulfoaluminate Clinkers by Synchrotron X-Ray Powder Diffraction, in: 13th Int. Congr. Chem. Cem., 2011.
[352] G. Cultrone, C. Rodriguez-Navarro, E. Sebastian, O. Cazalla, M.J. De La Torre, Carbonate and silicate phase reactions during ceramic firing, Eur. J. Mineral. (2001). https://doi.org/10.1127/0935-1221/2001/0013-0621.
[353] Á.G. De La Torre, A.J.M. Cuberos, G. Álvarez-Pinazo, A. Cuesta, M.A.G. Aranda, In situ powder diffraction study of belite sulfoaluminate clinkering, J. Synchrotron Radiat. (2011). https://doi.org/10.1107/S0909049511005796.
[354] J.S. Ndzila, S. Liu, G. Jing, S. Wang, Z. Ye, The effect of Fe3+ ion substitution on the crystal structure of Ye'elimite, Ceram. - Silikaty. (2020). https://doi.org/10.13168/cs.2019.0044.
[355] N. Böhme, K. Hauke, M. Neuroth, T. Geisler, In situ hyperspectral raman imaging of ternesite formation and decomposition at high temperatures, Minerals. (2020). https://doi.org/10.3390/min10030287.
[356] Y.B. Pliego-Cuervo, F.P. Glasser, The role of sulphates in cement clinkering: Subsolidus phase relations in the system CaO-Aℓ2O3-SiO2-SO3, Cem. Concr. Res. (1979). https://doi.org/10.1016/0008-8846(79)90094-2.
[357] W. Gutt, M.A. Smith, A new calcium silicosulphate [7], Nature. (1966). https://doi.org/10.1038/210408a0.
[358] G.S. Choi, F.P. Glasser, The sulphur cycle in cement kilns: Vapour pressures and solid-phase stability of the sulphate phases, Cem. Concr. Res. (1988). https://doi.org/10.1016/0008-8846(88)90071-3.
[359] L. Bonafous, C. Bessada, D. Massiot, J. -P Coutures, B. Le Holland, P. Colombet, 29Si MAS NMR Study of Dicalcium Silicate: The Structural Influence of Sulfate and Alumina Stabilizers, J. Am. Ceram. Soc. (1995). https://doi.org/10.1111/j.1151-2916.1995.tb08029.x.
[360] S. Sahu, J. Majling, Phase compatibility in the system CaOSiO2Al2O3Fe2O3SO3 referred to sulphoaluminate belite cement clinker, Cem. Concr. Res. (1993). https://doi.org/10.1016/0008-8846(93)90070-P.
[361] J. Strigáč, S. Sahu, M. Lopašovská, R. Ďurovčíková, V. Kovár, J. Majling, Phase compatibility in the system CaO - SiO2 - Al2O3 - So3, Ceram. - Silikaty. (1998).
[362] A.G. De la Torre, A.J.M. Cuberos, G. Álvarez-Pinazo, A. Cuesta, M.A.G. Aranda, In situ powder diffraction study of belite sulfoaluminate clinkering, J. Synchrotron Radiat. 18 (2011) 506–514. https://doi.org/10.1107/S0909049511005796.
[363] Y. Gao, Z. Li, J. Zhang, Q. Zhang, Y. Wang, Synergistic use of industrial solid wastes to prepare belite-rich sulphoaluminate cement and its feasibility use in repairing materials, Constr. Build. Mater. (2020). https://doi.org/10.1016/j.conbuildmat.2020.120201.
[364] G. Goswami, B.P. Padhy, J.D. Panda, Thermal analysis of spurrite from a rotary cement kiln, J. Therm. Anal. (1989). https://doi.org/10.1007/BF01913030.
[365] H. Bolio-Arceo, F.P. Glasser, Formation of spurrite, Ca5(SiO4)2CO3, Cem. Concr. Res. (1990). https://doi.org/10.1016/0008-8846(90)90084-B.

[366] E. V. Sokol, O.A. Kozmenko, H.N. Khoury, S.N. Kokh, S.A. Novikova, A.A. Nefedov, I.A. Sokol, P. Zaikin, Calcareous sediments of the Muwaqqar Chalk Marl Formation, Jordan: Mineralogical and geochemical evidences for Zn and Cd enrichment, Gondwana Res. (2017). https://doi.org/10.1016/j.gr.2017.03.008.
[367] J.C. Trombe, G. Montel, Some features of the incorporation of oxygen in different oxidation states in the apatitic lattice-I On the existence of calcium and strontium oxyapatites, J. Inorg. Nucl. Chem. (1978). https://doi.org/10.1016/0022-1902(78)80298-X.
[368] K. Tõnsuaadu, K.A. Gross, L. Pluduma, M. Veiderma, A review on the thermal stability of calcium apatites, in: J. Therm. Anal. Calorim., 2012. https://doi.org/10.1007/s10973-011-1877-y.
[369] Y. Pliego-Cuervo, F.P. Glasser, Phase relations and crystal chemistry of apatite and silicocarnotite solid solutions, Cem. Concr. Res. (1978). https://doi.org/10.1016/0008-8846(78)90033-9.
[370] C. Remy, D. Andrault, M. Madon, High-temperature, high-pressure X-ray investigation of dicalcium silicate, J. Am. Ceram. Soc. (1997). https://doi.org/10.1111/j.1151-2916.1997.tb02914.x.
[371] Z.L. Damao T., The Role of CaF2 and CaSO4 in Cement Clinkering, in: 8th ICCC, Rio de Janeiro, 1986: p. Vol. II, 117.
[372] M. I., Formation and microscopic textures of Portland cement clinker minerals. Part 1, Organ Stowarzyszenia Prod. Cem. (2006).
[373] A. Guinier, M. Regourd, Structure of Portland Cement Minerals, in: 5th Int. Congr. Chem. Cem. Part 1, 1968.
[374] I. Maki, S. Chromý, Microscopic study on the polymorphism of Ca3SiO5, Cem. Concr. Res. (1978). https://doi.org/10.1016/0008-8846(78)90020-0.
[375] M. Courtial, M.-N. de Noirfontaine, F. Dunstetter, G. Gasecki, M. Signes-Frehel, Polymorphism of tricalcium silicate in Portland cement: A fast visual identification of structure and superstructure, Powder Diffr. (2003). https://doi.org/10.1154/1.1523079.
[376] X. Ren, W. Zhang, S. Ouyang, Effect of multiple foreign ions doping on metastable structure of alite, Kuei Suan Jen Hsueh Pao/Journal Chinese Ceram. Soc. (2012).
[377] A. Cuesta, M.A.G. Aranda, J. Sanz, Á.G. De La Torre, E.R. Losilla, Mechanism of stabilization of dicalcium silicate solid solution with aluminium, Dalt. Trans. (2014). https://doi.org/10.1039/c3dt52194j.
[378] P. Guo, B. Wang, M. Bauchy, G. Sant, Misfit Stresses Caused by Atomic Size Mismatch: The Origin of Doping-Induced Destabilization of Dicalcium Silicate, Cryst. Growth Des. (2016). https://doi.org/10.1021/acs.cgd.5b01740.
[379] J.M. Porras-Vázquez, Á.G. De la Torre, D. Marrero-López, E.R. Losilla, M.A.G. Aranda, A new family of oxide ion conductors based on tricalcium oxy-silicate, J. Chem. Soc. Dalt. Trans. (2006). https://doi.org/10.1039/b516324b.
[380] G. Álvarez-Pinazo, I. Santacruz, M.A.G. Aranda, Á.G. De La Torre, Hydration of belite-ye'elimite-ferrite cements with different calcium sulfate sources, Adv. Cem. Res. (2016). https://doi.org/10.1680/jadcr.16.00030.
[381] D.E. Rogers, L.P. Aldridge, Hydrates of calcium ferrites and calcium aluminoferrites, Cem. Concr. Res. (1977). https://doi.org/10.1016/0008-8846(77)90068-0.
[382] N. Meller, C. Hall, A.C. Jupe, S.L. Colston, S.D.M. Jacques, P. Barnes, J. Phipps, The paste hydration of brownmillerite with and without gypsum: A time resolved synchrotron diffraction study at 30, 70, 100 and 150 °C, J. Mater. Chem. (2004). https://doi.org/10.1039/b313215c.
[383] F. Brown, Barret, The hydration of tricalcium aluminate and tetracalcium aluminoferrite in the presence of calcium sulfate, Mater. Struct. (1986). https://doi.org/10.1007/BF02481758.
[384] P. Comodi, S. Nazzareni, P.F. Zanazzi, S. Speziale, High-pressure behavior of gypsum: A

single-crystal X-ray study, in: Am. Mineral., 2008. https://doi.org/10.2138/am.2008.2917.
[385] V. Morin, G. Walenta, E. Gartner, P. Termkhajornkit, I. Baco, J.M. Casabonne, Hydration of a Belite-Calcium Sulfoaluminate-Ferrite cement : Aether TM, 13th Int. Congr. Chem. Cem. (2011).
[386] I.A. Chen, M.C.G. Juenger, Synthesis and hydration of calcium sulfoaluminate-belite cements with varied phase compositions, J. Mater. Sci. (2011). https://doi.org/10.1007/s10853-010-5109-9.
[387] M.A.G. Aranda, A.J.M. Cuberos, A. Cuesta, G. Alvarez-Pinazo, a G.D. La Torre, Hydrating Behaviour of Activated Belite Sulfoaluminate Cements, in: 13th Int. Congr. Chem. Cem., 2011.
[388] J.G. Goldsmith, Modern Analytical Chemistry, 1st Edition (Harvey, David), J. Chem. Educ. (2000). https://doi.org/10.1021/ed077p705.2.
[389] D. Londono-Zuluaga, J.I. Tobón, M.A.G. Aranda, I. Santacruz, A.G. De la Torre, Clinkering and hydration of belite-alite-ye´elimite cement, Cem. Concr. Compos. (2017). https://doi.org/10.1016/j.cemconcomp.2017.04.002.
[390] C.G. M. Milanesio, G. Artioli, G. Cruciani, P. Scardi, A. Guagliardi, N. Masciocchi, R. Caliandro, R. Rizzi, A. Sironi, M. Dapiaggi, L. Luterotti, P. Canton, Analisi di materiali policristallini mednaite tecniche di diffrazione, Martina Franca (Ta) - Palazzo Ducale, 2006.
[391] I.J. Lin, Implications of fine grinding in mineral processing: Mechanochemical approach, J. Therm. Anal. Calorim. (1998). https://doi.org/10.1023/A:1010178413725.
[392] S. Mantellato, M. Palacios, R.J. Flatt, Reliable specific surface area measurements on anhydrous cements, Cem. Concr. Res. (2015). https://doi.org/10.1016/j.cemconres.2014.10.009.
[393] K. Piekkari, V. Isteri, K. Ohenoja, M. Illikainen, Hazardous industrial filter sludge immobilization with mayenite and gypsum, J. Clean. Prod. 387 (2023) 135873. https://doi.org/10.1016/j.jclepro.2023.135873.
[394] M. Ben Haha, F. Winnefeld, A. Pisch, Advances in understanding ye'elimite-rich cements, Cem. Concr. Res. (2019). https://doi.org/10.1016/j.cemconres.2019.105778.
[395] J. Wang, Hydration mechanism of cements based on low-CO2 clinkers containing belite, ye'elimite and calcium alumino-ferrite, 7th Int. Symp. Cem. Concr. (2010).
[396] J. Ding, J.J. Beaudoin, Y. Fu, Strätlingite formation in high-alumina cement-zeolite systems, Adv. Cem. Res. (1995). https://doi.org/10.1680/adcr.1995.7.28.171.
[397] J. Ding, Y. Fu, J.J. Beaudoin, Strätlingite formation in high alumina cement - silica fume systems: Significance of sodium ions, Cem. Concr. Res. (1995). https://doi.org/10.1016/0008-8846(95)00124-U.
[398] H. Pöllmann, Calcium aluminate cements - Raw materials, differences, hydration and properties, Rev. Mineral. Geochemistry. 74 (2012). https://doi.org/10.2138/rmg.2012.74.1.
[399] C.K. Park, Characteristics and hydration of C12-x A7·X(CaF2) (X = 0 ~ 1.5) minerals, Cem. Concr. Res. (1998). https://doi.org/10.1016/S0008-8846(98)00105-7.
[400] M. Ben Haha, F. Bullerjahn, M. Zajac, On the reactivity of ternesite, in: Proc. 14th Int. Congr. Chem. Cem., 2015.
[401] Y. Shen, X. Chen, J. Li, P. Wang, J. Qian, Preparation and Performance of Ternesite – Ye ' elimite Cement, (2022) 1–17.
[402] K. Dvořák, D. Všianský, D. Gazdič, M. Fridrichová, D. Vaičiukynienė, Thaumasite formation by hydration of sulphosilicate clinker, Mater. Today Commun. (2020). https://doi.org/10.1016/j.mtcomm.2020.101449.
[403] F. Bullerjahn, D. Schmitt, M. Ben Haha, Effect of raw mix design and of clinkering process on the formation and mineralogical composition of (ternesite) belite calcium sulphoaluminate ferrite clinker, Cem. Concr. Res. (2014). https://doi.org/10.1016/j.cemconres.2014.02.004.
[404] M.W. Barnes, M. Klimkiewicz, P.W. Brown, Hydration in the System Ca2SiO4–Ca3(PO4)2

at 90°C, J. Am. Ceram. Soc. (1992). https://doi.org/10.1111/j.1151-2916.1992.tb04204.x.
[405] M.U. Okoronkwo, F.P. Glasser, Stability of strätlingite in the CASH system, Mater. Struct. Constr. (2016). https://doi.org/10.1617/s11527-015-0789-x.
[406] M.U. Okoronkwo, F.P. Glasser, Strätlingite: compatibility with sulfate and carbonate cement phases, Mater. Struct. Constr. (2016). https://doi.org/10.1617/s11527-015-0740-1.

Acknowledgments

I am really thankful to my tutor Nicoletta for supporting me and always giving helpful advice in all field during my academic path.

A most special thanks to Prof. Fernando Cámara for his constant support from all sides, being always available to share his viewpoint for purposeful dialogs.

Thanks to Dr. S. Milani for training me on single crystal X-ray diffraction and giving precious advice on my thesis.

Thanks to Dr. R. Wald, Dr. V. Toledo and Dr. M. Taub for their significant help during field trip in Israel and the precious supply of mined rock samples.

A special thanks to Prof. M. Angeles de la Torre and her team for having hosted and helped me in pursuing my aims.

I would also to show my gratitude to Dr. M. Prasek, Dr. L. Gigli, Dr. G. Confalonieri and Dr. M. I. Marchi for their help received during synchrotron experiments.

A very special thanks to Prof. M. Voltolini, Prof. M. Zucali and Prof. G. Della Porta for their helpful advice during data treatment.

Thank to Prof. M. Dapiaggi, Prof. A. Pavese and Prof. V. Diella for their useful tips during my academic path.

I would also to express my sincere thanks to Phil. C. Cantaluppi, E. Arcellaschi, Dr. M. Maspero, Dr. G. Cocomazzi, Dr. O. B. Brunetti for both material and mental support, being essential for the achievement of this project.

Thanks to Dr. E. Ferrari, M. Buono, A. Risplendente, F. Marchesini and C. Malinverno for their important support during experimental procedure and sample preparation.

I would also like to thank Dr. A. Zanon for her perseverance in giving me always her essential assistance in all hard times.

Thanks again to all my classmates, especially Dr. T. Battison, Dr. J. Zamudio García, Dr. G. Casiraghi, Dr. F. Pagliaro, Dr. A. Morales, Dr. S. Monico, Dr. G. Massinelli, Dr. L. Baratelli and Dr. A. Mosconi.